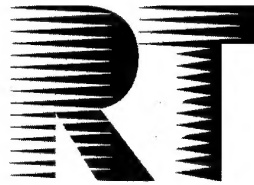


NORTH ATLANTIC TREATY ORGANIZATION



RESEARCH AND TECHNOLOGY ORGANIZATION

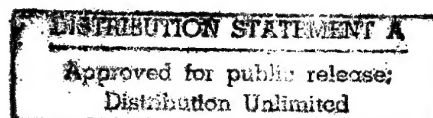
BP 25, 7 RUE ANCELLE, F-92201 NEUILLY-SUR-SEINE CEDEX, FRANCE

RTO MEETING PROCEEDINGS 1

# **E-O Propagation, Signature and System Performance Under Adverse Meteorological Conditions Considering Out-of-Area Operations**

(La propagation, la signature et les performances des systèmes  
optroniques dans des conditions météorologiques défavorables,  
compte tenu des opérations hors zone)

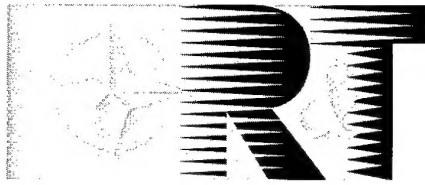
*Papers presented at the Sensors & Electronics Technology Panel Symposium held at the Italian  
Air Force Academy, Naples, Italy, 16-19 March 1998.*



Published September 1998

*Distribution and Availability on Back Cover*

**NORTH ATLANTIC TREATY ORGANIZATION**



**RESEARCH AND TECHNOLOGY ORGANIZATION**

BP 25, 7 RUE ANCELLE, F-92201 NEUILLY-SUR-SEINE CEDEX, FRANCE

**RTO MEETING PROCEEDINGS 1**

**E-O Propagation, Signature and System  
Performance Under Adverse Meteorological  
Conditions Considering Out-of-Area Operations**

(La Propagation, la signature et les performances des systèmes optroniques dans des conditions météorologiques défavorables, compte tenu des opérations hors zone)

*Papers presented at the Sensors & Electronics Panel Symposium held at the Italian Air Force Academy, Naples, Italy, 16-19 March 1998.*



19981102 124

**DTIC QUALITY INSPECTED 4**

AQF99-01-012 0

# The Research and Technology Organization (RTO) of NATO

RTO is the single focus in NATO for Defence Research and Technology activities. Its mission is to conduct and promote cooperative research and information exchange. The objective is to support the development and effective use of national defence research and technology and to meet the military needs of the Alliance, to maintain a technological lead, and to provide advice to NATO and national decision makers. The RTO performs its mission with the support of an extensive network of national experts. It also ensures effective coordination with other NATO bodies involved in R&T activities.

RTO reports both to the Military Committee of NATO and to the Conference of National Armament Directors. It comprises a Research and Technology Board (RTB) as the highest level of national representation and the Research and Technology Agency (RTA), a dedicated staff with its headquarters in Neuilly, near Paris, France. In order to facilitate contacts with the military users and other NATO activities, a small part of the RTA staff is located in NATO Headquarters in Brussels. The Brussels staff also coordinates RTO's cooperation with nations in Middle and Eastern Europe, to which RTO attaches particular importance especially as working together in the field of research is one of the more promising areas of initial cooperation.

The total spectrum of R&T activities is covered by 6 Panels, dealing with:

- SAS Studies, Analysis and Simulation
- SCI Systems Concepts and Integration
- SET Sensors and Electronics Technology
- IST Information Systems Technology
- AVT Applied Vehicle Technology
- HFM Human Factors and Medicine

These Panels are made up of national representatives as well as generally recognised 'world class' scientists. The Panels also provide a communication link to military users and other NATO bodies. RTO's scientific and technological work is carried out by Technical Teams, created for specific activities and with a specific duration. Such Technical Teams can organise workshops, symposia, field trials, lecture series and training courses. An important function of these Technical Teams is to ensure the continuity of the expert networks.

RTO builds upon earlier cooperation in defence research and technology as set-up under the Advisory Group for Aerospace Research and Development (AGARD) and the Defence Research Group (DRG). AGARD and the DRG share common roots in that they were both established at the initiative of Dr Theodore von Kármán, a leading aerospace scientist, who early on recognised the importance of scientific support for the Allied Armed Forces. RTO is capitalising on these common roots in order to provide the Alliance and the NATO nations with a strong scientific and technological basis that will guarantee a solid base for the future.

The content of this publication has been reproduced directly from material supplied by RTO or the authors.



*Printed on recycled paper*

Published September 1998

Copyright © RTO/NATO 1998  
All Rights Reserved

ISBN 92-837-0001-5



*Printed by Canada Communication Group Inc.  
(A St. Joseph Corporation Company)  
45 Sacré-Cœur Blvd., Hull (Québec), Canada K1A 0S7*

# **E-O Propagation, Signature and System Performance Under Adverse Meteorological Conditions Considering Out-of-Area Operations**

**(RTO MP-1)**

## **Executive Summary**

If a system, for example a sighting system, which operates in the electro-optic wavebands is considered, large amounts of time are devoted to the design and modification of the detectors and emitters. Furthermore, the science behind the operation of these devices is understood. This understanding and the mathematical processing of their signals facilitate the improvement and development of system characteristics. For example, different operational wavelengths can be used for improved detector suitability, filters can be added to remove unwanted energies, and automatic detection algorithms can be incorporated.

However, in an operational situation, between the emitter (for example a target) and the detector there is a layer of intervening atmosphere. Within reason this layer of atmosphere cannot be modified, yet the atmosphere has as much effect on system performance as any other aspect of the total system.

The operational performance of an electro-optic system will vary under different meteorological or weather conditions, and adverse weather conditions in particular will affect and degrade system performance. Similarly the weather varies in different geographical areas and deployment zones, and the implication of this is that an electro-optic system that operates with a certain level of performance in one location will operate at a different level of performance in a different location. Issues such as these were the subject matter of the symposium.

The value and relevance of the meeting was demonstrated during the presentation of the invited introductory paper, "The reconnaissance, search and target acquisition cycle; lessons learned", by B. Gen. G. Marani. Aspects of the presentation detailed an analysis of operational data that indicated that a significant number of missions in the region of the Adriatic failed or had to be aborted due to weather-related phenomena. Presenters during the technical visit to NATO AIRSOUTH reinforced these findings.

The symposium comprised four sessions, in which 34 papers were presented.

- Modelling
- EOPACE (Electro-optical Propagation Assessment on Coastal Environments)
- System performance
- Sensing.

The modelling session concentrated on the development and applications of computer codes. In particular, codes, such as MODTRAN, which are associated with the prediction of atmospheric transmission and radiance codes were discussed. However, measurement and comparison programmes that used atmospheric prediction codes were also presented.

Results from the EOPACE project demonstrated the importance and effect of aerosols in the near-surface coastal environment, and their implications for system operation in this layer of the atmosphere. EOPACE also demonstrated the synergetic ability of different Nations to work together for a common goal. It could be clearly seen that the results from the project would eventually be able to support the improvement of the models presented in the first session of the symposium.

The system modelling session suffered from an unprecedented number of cancelled papers. However, the remaining papers demonstrated techniques that could be employed to mitigate the effect of adverse weather conditions. The effect of battlefield contamination was also addressed.

The session on sensing produced a selection of presentations on satellite and ground based sensing projects. Projects were described which produced valuable results that could be used to improve and supplement modelling activities, whereas other projects were concentrating on military operational issues.

The symposium should be considered a great success and contained presentations that covered fundamental atmospheric research to the operational performance of systems related to propagation phenomena. Many of the operational problems that are associated with system operation in adverse meteorological conditions were also addressed and possible solutions were presented.

The meeting produced a clear understanding that propagation related issues will directly effect the ultimate operational performance of electro-optical systems and therefore cannot be separated from other aspects of system specification, design, and performance evaluation life cycle.



# **La propagation, la signature et les performances des systèmes optroniques dans des conditions météorologiques défavorables, compte tenu des opérations hors zone**

**(RTO-MP-1)**

## **Synthèse**

Pour tout système fonctionnant dans les gammes d'onde électromagnétiques, comme les systèmes de visée par exemple, il faut beaucoup de temps pour concevoir et modifier les émetteurs et les détecteurs. Pourtant, les sciences qui régissent le fonctionnement de ces dispositifs sont parfaitement maîtrisées. Cette maîtrise, associée au traitement mathématique de leurs signaux, facilite l'amélioration et le développement des caractéristiques systèmes.

À titre d'exemple, pour optimiser la conception des détecteurs, des gammes d'onde opérationnelles différentes peuvent être utilisées; des filtres peuvent être ajoutés pour éliminer d'éventuelles énergies parasites, et des algorithmes de détection automatique peuvent être incorporés.

Cependant, en situation opérationnelle, il existe une couche intermédiaire de l'atmosphère entre l'émetteur (par exemple une cible) et le détecteur. Cette couche ne peut-être modifiée que dans des limites très raisonnables et pourtant l'atmosphère exerce autant d'effet sur les performances des systèmes que tout autre élément du système global.

Les performances opérationnelles d'un système électro-optique varient selon les conditions météorologiques, et le mauvais temps, en particulier, a pour effet de dégrader les performances des systèmes. De la même façon, les conditions météorologiques varient en fonction du lieu géographique et de la zone de déploiement, ce qui signifie qu'un système électro-optique avec des performances données sur un site aura des performances différentes sur un autre site. Le symposium s'est donné pour objectif d'examiner des questions de cet ordre.

L'intérêt et la pertinence de la réunion ont été démontrés lors de la présentation de l'exposé liminaire sur "Le cycle de reconnaissance, recherche et acquisition de la cible - enseignements à tirer", qui a été préparée par le Général de brigade G. MARANI. Parmi d'autres aspects, l'exposé a fourni une analyse de données opérationnelles indiquant qu'un certain nombre de missions réalisées en Adriatique avaient échouées, soit été annulées à cause de phénomènes météorologiques. Les présentations données à l'occasion de la visite du commandement AFSOUTH/OTAN ont confirmé ces conclusions.

Le symposium a été organisé en quatre sessions, avec un total de 34 présentations.

- modélisation
- EOPACE (évaluation de la propagation électro-optique dans un environnement côtier)
- performances systèmes
- détection

La session sur la modélisation a été axée sur le développement et la mise en œuvre de codes machine tels que MODTRAN, qui sont associés à la prévision de la transmission atmosphérique, ainsi que sur les codes de luminance énergétique. Cependant, des programmes de mesure et de comparaison faisant appel à des codes de prévision atmosphérique ont également été présentés.

Les résultats obtenus du projet EOPACE ont démontré l'importance et les effets des aérosols dans l'environnement côtier proche de la surface de la mer et les conséquences en ce qui concerne l'exploitation des systèmes dans cette couche atmosphérique. Le projet EOPACE a également témoigné de la capacité synergétique des différents pays œuvrant ensemble pour un objectif commun. Il est apparu très clairement que les résultats du projet pourraient à terme servir à améliorer les modèles présentés lors de la première session du symposium.

La session sur la modélisation a été pénalisée par un grand nombre de présentations annulées au dernier moment. Cependant, les communications présentés ont mis en évidence des techniques permettant d'atténuer les effets du mauvais temps et la dégradation des conditions visuelles sur le champ de bataille.

La session sur la détection a été caractérisée par une série de présentations sur des projets de détection au sol et par satellite. Certains projets donnent des résultats pouvant servir à améliorer et à compléter les activités de modélisation, tandis que d'autres concernent plus particulièrement des questions militaires opérationnelles.

Le symposium a obtenu un succès incontestable. Des domaines variés, allant de la recherche atmosphérique fondamentale aux performances opérationnelles des systèmes relatifs aux phénomènes de propagation ont été couverts. De nombreux problèmes opérationnels associés à l'exploitation de systèmes dans des conditions météorologiques défavorables ont été examinés et des solutions présentées.

Il a permis de clairement prendre conscience que la programmation a une influence directe sur les performances opérationnelles des systèmes électro-optiques et que, par conséquent, elle doit être prise en compte dans les spécifications techniques dans la phase de conception et dans le cycle d'évaluation des performances.

# Contents

	Page
Executive Summary	iii
Synthèse	iv
Theme/Thème	ix
Sensors and Electronics Technology Panel	x
	Reference
<b>INVITED PAPER</b>	
<b>R.S.T.A. Cycle Lessons Learned</b> by G. Marani	<b>1</b>
<b>SESSION I: MODELLING</b>	
<b>MODTRAN4: Simulating Atmospheric Radiation for Cloudy Conditions</b> by G.P. Anderson, J.H. Chetwynd, A. Berk, L.S. Bernstein, P.K. Acharya, H.E. Snell and E.P. Shettle	<b>2</b>
<b>The MOSART Code</b> by W.M. Cornette, S.J. Westmoreland, P.K. Acharya, A. Berk, D.C. Robertson, G.P. Anderson, W.A.M. Blumberg, L.S. Jeong and F.X. Kneizys	<b>3</b>
<b>A Comparison of Atmospheric Transmittance Measurements in the 3-5 <math>\mu\text{m}</math> and 8-12 <math>\mu\text{m}</math> Spectral Regions with MODTRAN: Considerations for Tropospheric Operations Requiring Long, Near-Horizontal Path Geometries</b> by A.J. Ratkowski, G.P. Anderson, J.H. Chetwynd, R.M. Nadile, A.D. Devir and T.D. Conley	<b>4</b>
<b>Effets de la réfraction atmosphérique sur la propagation infrarouge dans la basse atmosphère marine — comparaison des modèles SEACLUSE et PIRAM</b> by J. Claverie, B. Tranchant, P. Mestayer, A.M.J. Van Eijk and Y. Hurtaud	<b>5</b>
<b>A Rapid 3-5 Micron TDA Simulation Based on MODTRAN4</b> by L.S. Bernstein, S.M. Adler-Golden, A. Berk, M.M. Edwards, E.E. Hume, F.A. Zawada, J. Mozer, G.P. Anderson, J.H. Chetwynd and H. Gilliam	<b>6</b>
<b>IR-Range Forecasts with NAVFLIR</b> by C. von Ruesten and F. Theunert	<b>7</b>
<b>Weather Effects and Modeling for Simulation and Analysis</b> by A.E. Wetmore, P. Gillespie and D. Ligon	<b>8</b>
<b>Automatic Correction for Atmospheric Degradation in Infrared Images</b> by D.R. Edmondson, L.A. Wainwright, E.J. Price, S.A. Parrish, M. Godfrey, N.M. Faulkner, S.P. Brooks, J.P. Oakley and M.J. Robinson	<b>9</b>
<b>Paper 10 withdrawn</b>	

<b>The Infra-Red Signature of a Hot Scattering Plume Calculated by the SCATAX Method</b> by M.J. Caola	11
-----------------------------------------------------------------------------------------------------------	----

<b>Effects of Obscurants on the Performance of Laser Range Finders</b> by A. Dimmeler, D. Clement and W. Büchtemann	12
------------------------------------------------------------------------------------------------------------------------	----

## SESSION II: EOPACE

<b>Electrooptical Propagation Assessment in Coastal Environments (EOPACE)</b> by J.H. Richter	13
--------------------------------------------------------------------------------------------------	----

<b>Electro-Optical Propagation Just Above Wave Tops as Predicted by ANAM, the Advanced Navy Aerosol Model</b> by S.G. Gathman and A.M.J. van Eijk	14
------------------------------------------------------------------------------------------------------------------------------------------------------	----

<b>Long-Range Transmission at Low Elevations Over The Ocean</b> by A.N. de Jong, G. de Leeuw, P.J. Fritz and M.M. Moerman	15
------------------------------------------------------------------------------------------------------------------------------	----

<b>Near Surface Scintillation (<math>Cn^2</math>) Estimates from a Buoy Using Bulk Methods during EOPACE</b> by P. Frederickson, K. Davidson, C. Zeisse and I. Bendall	16
---------------------------------------------------------------------------------------------------------------------------------------------------------------------------	----

<b>Air Mass Characterization for EO Propagation Assessment</b> by T.E. Battalino	17
-------------------------------------------------------------------------------------	----

<b>Aerosol Transport and Origins</b> by J. Rosenthal, T. Battalino, L. Eddington, R. Helvey, C. Fisk and D. Lea	18
--------------------------------------------------------------------------------------------------------------------	----

<b>Air Trajectories and Air Mass Characteristics in the Southern California Coastal Region</b> by R.A. Helvey and T.E. Battalino	19
-------------------------------------------------------------------------------------------------------------------------------------	----

<b>Air Mass Parameterization and Coastal Aerosol Modeling</b> by D.R. Jensen, C.H. Wash and M.S. Jordan	20
------------------------------------------------------------------------------------------------------------	----

<b>Analysis of Three Methods of Characterizing an Air Mass</b> by K. Littfin, S. Gathman, D. Jensen and C. Zeisse	21
----------------------------------------------------------------------------------------------------------------------	----

<b>Analysis of Nephelometer Observations during EOPACE IOP-7</b> by A.K. Goroch and K. Littfin	22
---------------------------------------------------------------------------------------------------	----

<b>Satellite and Ship-based Lidar Estimates of Optical Depth during EOPACE</b> by C.H. Wash, M.S. Jordan, P.A. Durkee, P. Veefkind and G. de Leeuw	23
-------------------------------------------------------------------------------------------------------------------------------------------------------	----

<b>Aerosol Production in the Surf Zone and Effects on IR Extinction</b> by F.P. Neele, G. de Leeuw, A.M.J. van Eijk, E. Vignati, M.H. Hill and M.H. Smith	24
--------------------------------------------------------------------------------------------------------------------------------------------------------------	----

## SESSION III: SYSTEM PERFORMANCE

<b>Optimizing Infrared and Night Vision Goggle Sensor Performance by Exploiting Weather Effects</b> by P. Tattelman, D.M. Madsen, J.B. Mozer and T.C. Hiatt	25
----------------------------------------------------------------------------------------------------------------------------------------------------------------	----

Paper 26 withdrawn

Paper 27 withdrawn

<b>Performance Assessment of an Active Imaging System in Degraded Weather Conditions</b>	<b>28</b>
by V. Larochelle, D. Bonnier, G. Roy and P. Mathieu	

<b>Tactical Laser Systems Performance Analysis in Various Weather Conditions</b>	<b>29</b>
by R. Sabatini	

**Paper 30 withdrawn**

**Paper 31 withdrawn**

#### **SESSION IV: SENSING**

**Paper 32 withdrawn**

<b>Midcourse Space Experiment (MSX): Overview of Mid-Wave Infrared Atmospheric Gravity Waves in Earth Limb and Terrestrial Backgrounds</b>	<b>33</b>
by R.R. O'Neil, H.A.B. Gardiner, J.J. Gibson and A.T. Stair	

<b>An Investigation of Methods to Improve the Estimation of Battlefield Ground Conditions</b>	<b>34</b>
by A. Whitelaw, S. Howes, J. Brownscombe, O. Greening, J. Turton and D. Bennetts	

<b>Evaluation of Concurrent Thermal IR Atmospheric Propagation and Aerosol Particle Size Distribution Measurements at Gotland, Sweden</b>	<b>35</b>
by R. Carlson, R. Tong, G. De Leeuw, P. Fritz, H. Garner and E. Vignati	

<b>Low-Altitude Point-Target EXperiment (LAPTEX): Analysis of Horizon Target Detection</b>	<b>36</b>
by D. Dion, P. Schwering, K. Stein, A. de Jong and H. Winkel	

**Paper 37 withdrawn**

<b>Dependence of Aerosol Size Distribution on Different Sea Bottom Types</b>	<b>38</b>
by A. Zielinski, T. Zielinski and J. Piskozub	

<b>HADES: Hot and Dusty Environment Survey</b>	<b>39</b>
by A.R. Tooth and J. Rogge	

<b>Atmospheric Optical Extinction Measured by Lidar</b>	<b>40</b>
by C.R. Philbrick and D.B. Lysak	

<b>Lidar Remote Sensing of Adverse Weather for Performance Assessment of EO Sensors and Weapons</b>	<b>41</b>
by L.R. Bissonnette, G. Roy and J-M. Thériault	

<b>Measurement of the Distortion Generated in a Laser Beam's Characteristics Resulting from Passage Through an Engine's Wake</b>	<b>42</b>
by D.H. Titterton	

<b>LEXTAB: Long term Experiment on Targets, Atmosphere, and Backgrounds in the Desert</b>	<b>43</b>
by K. Weiss-Wrana, A. Dimmeler, W. Jessen and L. Balfour	

# Theme

During "favourable" weather conditions the operational performance of the majority of the UV, visible, and IR Wave weapon systems that are used by NATO forces is nominally equivalent to the performance that is achieved by most opposing forces. However, the most important factor in weapon systems design is very often not the final performance of a system but the performance differential between the system and the threat. In the presence of adverse weather conditions, for example, rain, fog, snow, and cloud, the performance of systems will be degraded but it may be possible, by way of an improved understanding of adverse weather conditions, that a performance differential can be achieved. It is reported that the success of Desert Storm was, in part, achieved by the differential superiority of the coalition forces.

Historically, both the threat and the location of the next conflict were "assumed", and systems were optimised accordingly. However, the concept of modern Rapid Reaction Forces troops may now be deployed in any location, including desert, arid, and polar regions. In these regions, systems that were once optimised for use in temperate locations may now prove to be sub-optimal.

The ability to maintain weapon system performance during adverse weather conditions is essential. A small improvement in performance may yield a significant advance under such conditions. It is of considerable importance to NATO that the full impact of out-of-area operations on electro-optic system performance be addressed.

The following topics are appropriate for consideration:

- Theoretical and practical aspects of atmospheric propagation under adverse conditions
- Out-of-area operations, variations in weather conditions and propagation phenomena
- System optimisation techniques for out-of-area applications
- Modelling techniques
- Measurement programmes, including existing collaborations
- Applications of dual use technologies for adverse conditions (military/commercial).

# Thème

Avec des conditions météorologiques favorables, les performances opérationnelles de la plupart des systèmes d'armes UV, visibles et IR mise en œuvre par les forces de l'OTAN sont en principe équivalentes à celles de la majorité des forces d'opposition. Cependant, les performances définitives d'un système d'armes ne sont pas toujours considérées comme l'élément le plus important lors de sa conception; une attention particulière est souvent accordée au différentiel de performances entre le système et la menace.

En présence de conditions météorologiques défavorables, par exemple pluie, brouillard, neige ou nuages, les performances des systèmes sont dégradées, mais un différentiel de performances peut néanmoins être obtenu grâce à une meilleure appréhension de ces conditions météorologiques. Les rapports indiquent que la réussite des opérations "Tempête de Désert" est en partie due à la supériorité différentielle des forces de la coalition.

En réalité le type de menace et la situation géographique du conflit avaient été "présumés" et les systèmes optimisés en conséquence. Cependant, conformément au concept de la force d'intervention rapide, des troupes peuvent, dorénavant, être déployées partout, y compris dans des régions désertiques, arides ou polaires. Il se pourrait alors que les systèmes optimisés pour les régions tempérées s'avèrent moins performants.

La capacité de maintien des performances d'un système d'armes dans des conditions météorologiques défavorables est vitale. Toute amélioration opérationnelle peut produire des avantages non négligeables dans de telles conditions. Il est d'une importance considérable pour l'OTAN que la véritable incidence des opérations hors zone sur les performances des systèmes optroniques soit prise en compte.

Les sujets suivants doivent être examinés:

- les aspects théoriques et pratiques de la propagation atmosphérique dans des conditions météorologiques défavorables
- les opérations hors zone et la variation des conditions météorologiques et des phénomènes de propagation
- les techniques d'optimisation de systèmes pour d'applications hors zone
- les techniques de modélisation
- les programmes de contrôle, y compris les projets collaboratifs en cours
- l'application des technologies duales (militaires/commerciales) en cas de conditions défavorables

## **SENSORS & ELECTRONICS TECHNOLOGY PANEL**

**Chairman:** Dr. L. MARQUET  
Director, CECOM Research  
Development & Engineering Center  
AMSEL-RD  
Fort Monmouth  
New Jersey 07703-5201  
USA

**Deputy Chairman:** Mr. F. CHRISTOPHE  
Adjoint au Directeur du Departement  
Electromagnetisme et Radar  
CERT/ONERA  
BP 4025  
31055 Toulouse Cedex  
FRANCE

### **SYMPOSIUM TECHNICAL PROGRAMME COMMITTEE**

**Chairmen:** Dr J.H. RICHTER (United States)  
Prof. J. ROGGE (Netherlands)  
Mr. A.R. TOOTH (United Kingdom)

**Members:** Ms. G.P. ANDERSON (United States)  
Dr. D. CLEMENT (Germany)  
Dr. D. DION (Canada)  
Dr. A.K. GOROCH (United States)  
Mme. A-M. BOUCHARDY (France)

### **PANEL EXECUTIVE**

Lt. Col. G. DEL DUCA (Italy)

**from Europe:**  
RTANATO  
ATTN: SET Executive  
BP 25  
7, rue Ancelle  
F-92201 Neuilly-sur-Seine Cedex  
France

**from North America:**  
RTANATO-SET  
PSC 116  
APO AE 09777

Tel: 33 1 55 61 22 68

Fax: 33 1 55 61 22 99/98

## R.S.T.A. CYCLE LESSONS LEARNED

**Brig. Gen. Giuseppe Marani**

Headquarters 5<sup>th</sup> Allied Tactical Air Forces Chief of Staff

Viale A. Ferrarin, 138, 36100 Vicenza, Italy

SLIDE NR. 3

### OVERVIEW

I would like to start my presentation with a bit of history and statistics, just to give you an idea of the efforts which has been put into B-H by allied air forces in the past five years.

We'll see how Coalition Ground Forces are deployed in B-H and what the Air Power tasks are.

Then we'll get into the Reconnaissance Surveillance Target Acquisition, the topic of this presentation; what it is and how the process works; the people who work on it from initial requests to the issue of the Air Task Order.

Even if SIGINT, ELINT and Early Warning are to be considered part of the Surveillance job, those will not be covered in this presentation.

SLIDE NR. 4

A few words about C2 Systems used in the CAOC and connectivity's.

Some assets capabilities, and to conclude, some lessons learned.

SLIDE NR. 5

- Allied Nations began their involvement in B-H in 1992 with the humanitarian effort called Operation PROVIDE PROMISE. This Operation official closure was held in Sarajevo on 09 Jan. 1996 after over 160,000 metric tons of humanitarian materials had been delivered.
- 31 march 1993, the united nations security council resolution 816

created a "no flight zone" over Bosnia Herzegovina. The UN requested and the north Atlantic Council approved NATO's enforcement of the NFZ..

- since then, over 180.000 sorties have been flown in that theater, including two months of air strike operations conducted against bosnian serb army targets (Sep-Oct '95).

SLIDE NR. 6

Some other current figures.

- ~ 3,500 personnel from 15 nations
- 19 Air bases in 6 European countries
- 84 land-based aircraft -- less airlift
- Periodic deployments of carrier aviation in the Adriatic Sea
- 100 - 200 sorties per day
- Unique air assets

SLIDENR.7



NATO stepped up to enforce implementation of the peace plan and formed, initially, the IFOR (Implementation Forces) and then the SFOR (Stabilization Forces). The country has been divided into three geographical areas of responsibility,

each one assigned to a Commander of a Multi-National Division (MND).

As you can see on the slide, MND-N is led by the Americans, MND-SE is led by the French, and MND-SW is led by the British. All of these districts are truly multi-national.

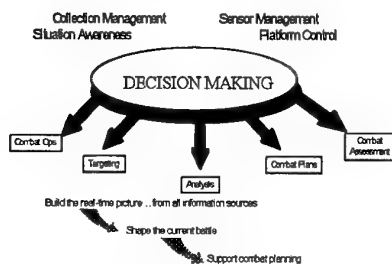
With this situation of our ground forces,

SLIDE NR. 8

these, and many others, are the main tasks of the air OPS in Bosnia.

SLIDE NR. 9

### RSTA Cycle



Situational awareness is vital; any situation / contingency can be managed at the very best if current information is available. This is why a great deal of effort is needed in the management of reconnaissance and surveillance information. The RSTA cycle includes collection and sensor management, situation awareness and platform control; from these efforts, multinational and multi-source intelligence, surveillance and reconnaissance information can be integrated to provide decision makers with a comprehensive understanding of the battlespace. This understanding provides more effective target analysis, combat plans, combat operation and combat assessment. In this way, we see how both raw and analyzed data can be fused to build a common

picture from which all Component Commanders can operate.

SLIDE NR. 10

### Aerial Reconnaissance Needs

- POINT TARGET COVERAGE
  - compliance monitoring
  - mass graves
  - joint target list sites
  - check points
  - demonstrations
- SURVEILLANCE/ MONITORING OF WIDE AREAS
  - situation awareness
  - force protection
  - compliance monitoring

Our principal customer (SFOR) requests two types of aerial reconnaissance: point target coverage (compliance monitoring, mass graves, joint target list sites) and SURVEILLANCE (situation awareness, force protection, compliance monitoring).

Different sensors are required for the different products desired (glossy prints, real-time motion video, reporting), at varying times of day and weather conditions.

Since Operations began in 1993, to comply with all the "requests for information", over 16,000 sorties (Manned / Unmanned) have been flown by the best assets available, for recce / reconnaissance purposes in an AOR of over 10.000 Km<sup>2</sup>

SLIDE NR. 11

### Collection and Coordination Intelligence Requirements

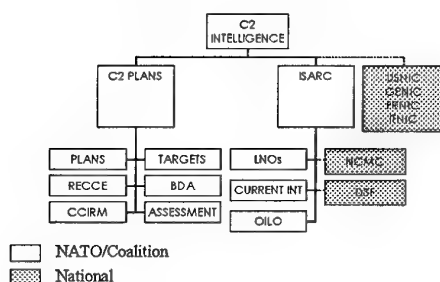
As you know, to optimize results, the challenge is to correctly associate target



to sensor to platform, keeping in mind capabilities and limitations, threat level and, of course, weather conditions. CCIRM is the process for reviewing and coordinating intelligence requirements and collection. It is essential to implement the priority set to minimize duplication of the same intelligence requests; and it is necessary to ensure deconfliction and mutual support between intelligence collection assets.

SLIDE NR. 12

### CAOC C2 ORGANIZATION



In the CAOC structure, this process takes place every day in the C2, or Intelligence, area.

SLIDE NR. 13

### Intelligence Surveillance And Reconnaissance Cell

In the CAOC /C2 Structure, the ISARC is the focal point for all RFI'S and can also be considered a kind of CAOC-SFOR interface. Established in January '96, the mission of the ISARC is to provide responsive and coordinated reconnaissance and surveillance support to Forces in Bosnia plus

SLIDE NR. 14

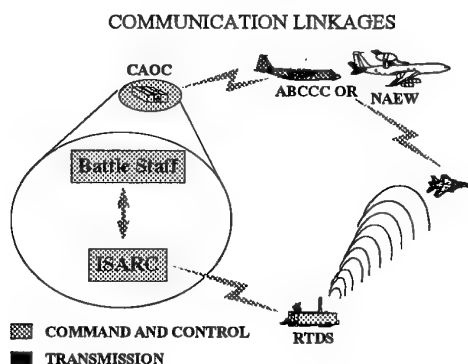
### KEY TASKS

- ◆ REACH-BACK TASKING/REQUESTS
- ◆ PRODUCE DAILY CAOC REPORTS
- ◆ REVIEW ALL MISREPS FOR PERTINENT INFO
- ◆ PROVIDE INDICATIONS AND WARNING
- ◆ SITUATIONAL AWARENESS
- ◆ THREAT WARNING
- ◆ ALL-SOURCE ANALYSIS AND REPORTING

other key tasks as indicated in this slide. This Cell basically manages the collection process especially in the execution phase of operations, coordinating efforts of the Tactical Reconnaissance Cell, SIGINT Reconnaissance Cell, Dynamic Retasking Cell, Electronic Warfare Cell, National Intelligence Cells, but...

SLIDE NR. 15

### RAPID TARGETING SYSTEM (RTS)

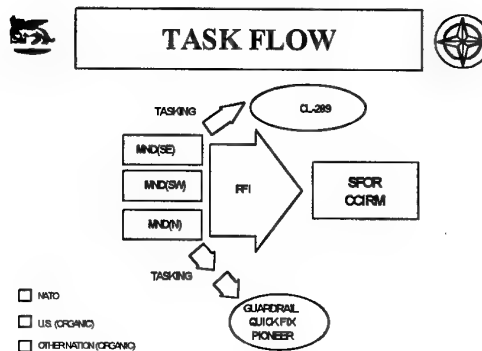


... dynamic retasking is a core attribute of the ISARC. Being almost collocated with the Battle Staff and Unit representatives, the ISARC can provide

immediate inputs to an evolving situation and the means to react. This can be done by re-directing the collection platforms and associated sensors to support operations with coverage of targets of opportunity and fleeting targets, ensuring, at the same time, that operations are conducted safely with no airspace conflicts. In the same way, a better platform can be re-directed over a target which has not been positively identified in the first place. The look-shoot-look ability is a developing program that uses the RTS to first look at a scene both here with the targeting decision-makers and the pilot in the area for bomb-dropping. The decision-makers decide if the target is appropriate and then direct the pilot to get a real-time view of the target. We can revisit the site immediately to see if the objective was met.

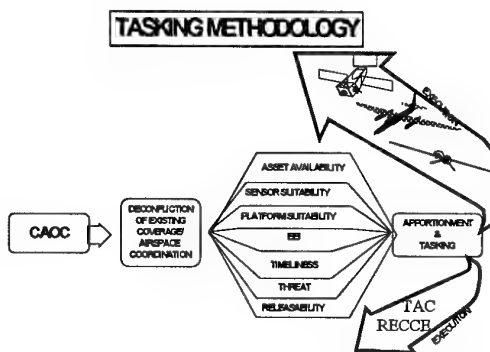
Some of the tools used include Binocular and JSAS, which provide situational awareness. The sensors currently being used include Predator, the U-2 (supported by CARS Alternative workstation) and the P-3 Photo-Telesis System. Intelligence systems include the Combat Intelligence System (CIS), the Video Exploitation Workstation Software (VIEWS) and Powerscene.

SLIDE NR. 16



Let's now see very briefly what the tasking methodology is. "Requests for information" from our ground customers that can not be directly satisfied by using their own assets, are forwarded to SFOR CCIRM in Sarajevo for coordination.

SLIDE NR. 17



These are then sent to the CAOC. Here, the people I just talked about, take proper actions to have the daily ATO message issued.

SLIDE NR. 18

Throughout the process, we retain the capability to operate inside the ATO cycle for maximum operational effectiveness. We have the opportunity to minimize uncertainty & delays in the decision process...to exploit

opportunities...and to maintain the offensive initiative.

One of the means the Combat Staff has available in the CAOC to maintain situation awareness is the JSAS ( JFACC Situational Awareness System)

- displays target locations, flight routes and ground force locations
- tailor to commander's desires for optimal views or the battlefield

SLIDE NR. 20

This slide shows the complexity of connectivity in theater, in addition to the importance of communications linkage.

SLIDE NR. 21

Several platforms have been employed for surveillance, monitoring and targeting over Bosnia. Red ones are "national assets" in support of operations, blue are dedicated to Coalition forces. Let's go quickly through the most common ones.

SLIDE NR. 22

Joint STARS is a Joint Air Force/Army Surveillance, Targeting and Battle Management System, designed to support air/land component commanders with:

Near-real time wide-area surveillance and targeting information on moving and stationary ground targets. Its primary mission is monitoring cantonment sites.

Enhanced theater battlefield management through deep attack operations C<sup>3</sup> and support directed at delaying, disrupting, or destroying enemy forces

SLIDE NR. 23


JSTARS (when in theater) uses orbits in Hungary, Croatia, and the Adriatic to provide information about ground activity. From these locations, the

SLIDE NR. 19

**JSAS**

JFACC (Joint Forces Air Component Commander)

Situational Awareness System



- COMBINES NEAR-REALTIME AND RECON INFORMATION WITH MAPS, IMAGERY, AND ANNOTATIONS/OVERLAYS FOR ENHANCED BATTLEFIELD PICTURE
- DISPLAYS COMBINED TADIL(ADSI), TRAP/TIBS PICTURE
- DISPLAYS PROJECTED THEATER/NATIONAL RECON COVERAGE
- DISPLAYS TARGET LOCATIONS, FLIGHT ROUTES AND GROUND FORCE LOCATIONS
- TAILOR TO COMMANDER'S DESIRES FOR OPTIMAL VIEWS OR THE BATTLEFIELD

Few words about this "CAOC wall, BARCO displayed" system; all sorts of current multi-source information is fed into this system which then...

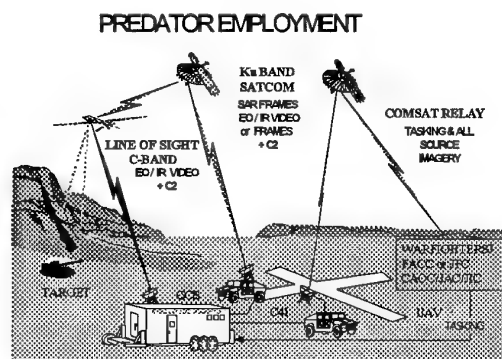
- combines near-real-time and recon information with maps, imagery, and annotations/overlays for enhanced battlefield picture
- displays combined tadil(adsi), trap/tibs picture
- displays projected theater/national recon coverage

aircraft sends the radar imagery to one of the Ground Station Modules (in Sarajevo), which injects it in the Joint Broadcast System. Users are again HQ-SFOR, MNDs, and CAOC.

SLIDE NR. 24

It produces freeze frame images of limited quality. Good quality real-time video is injected into the Joint Broadcast System for dissemination to HQ SFOR, MNDs and CAOC;  
With a long dwell time, it's easy to quickly retask, but ...weather must be clear and free of clouds and distance from ground-station must be not greater than 100NM.

SLIDE NR. 25



•With its EO / IR / SAR payload, Predator can be used day and night and in any weather (of course using different sensors); it has been employed quite extensively when available in theater. Its products are:

- real time EO / IR video,
  - SAR still imagery,
- all of which are widely disseminated via JBS.

During "Deliberate Force" (1995), Predator was used to provide near real-

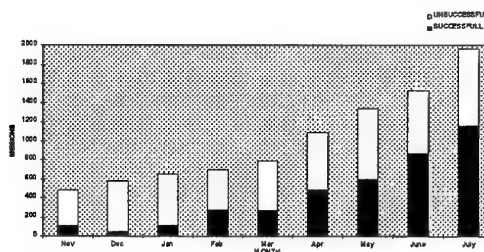
time pre-strike target reconnaissance, followed by battle damage assessment. Its contribution was very valuable during the Pope's visit in Sarajevo and during the Municipal elections last year. This unmanned platform is optimum for high threat or denied areas.

SLIDE NR. 26

Tactical, fixed wing reconnaissance aircraft consistently provide the best imagery. They are the key to maintaining good quality, up-to-date imagery of targets or any other key site of interest. Aircraft are currently provided by five Nations, to include Italy, France, United Kingdom, the Netherlands, Germany.  
Tactical aircraft can fly under most weather to image targets. Unfortunately, these aircraft also require escort when imaging targets in high threat areas. Tactical aircraft should not be used to image targets in denied areas; for example, areas where air superiority has not been established

SLIDE NR. 27

#### MONTHLY SUCCESS RATES



Talking about reconnaissance we cannot forget ... "weather". The best EO Sensor in the world cannot defeat clouds. The best EO Sensor in the world

on a platform that cannot descend through clouds or operate in poor weather cannot take the best EO picture in the world. The constant factor in Bosnia is precipitation. No matter what form it takes, rain, snow, sleet or hail, water will fall over there. Weather has a significant impact on aerial reconnaissance collection success over Bosnia. Average success rates for TACRECCE during the year are approximately:  
40% in Sep-Oct, 20% in Nov-Feb, 40% in Mar-Apr and 50-75% in May-Aug.

SLIDE NR. 28

### LESSONS LEARNED

- Joint, coalition operations are essential ... unified approach into a sometimes uncertain, battlespace ensures unity of effort and fosters the common purpose ensuring mission success. As with any mission, competing interests degrade mission effectiveness for reconnaissance and surveillance, and can degrade the targeting cycle.

- Information must be timely ... Commanders cannot wait for information requirements to be filled 48 to 72 to 96 hours from the time the situation arises ... Commanders need answers sooner rather than later in order to take a proactive, not reactive, approach to the emerging battlespace. A robust communication architecture is essential to the dissemination of both a single-source and fused picture of the battlespace. This picture must be disseminated simultaneously to Commanders at both the operational and tactical levels of war to a level of detail and fidelity that sufficiently supports their operations.

- More attention must be paid to information integration ... single-source information can provide timely collection tippers, but a fused, integrated picture built from multi-discipline sources provides the best battlespace awareness for operational and tactical Commanders.

SLIDE NR. 29

- Intelligence data must be releasable ... Coalition Commanders must have the same "view" of the battlespace as each of their counterparts; coalition military operations can be effective only if national Intelligence information is fused into a correlated "all-hands" picture of the battlespace in joint, coalition command centers.

- Mobile targets are a difficult nut to crack ... tactical air missions dynamically retasked against mobile targets present the most difficult targeting dilemma. Good-quality information about the emerging target, such as key descriptive data, geological accuracy target movement and surrounding terrain features, can prove to be the difference between mission success and failure. Timing and synchronization are critical to successfully executing a mobile targeting scenario, with information flowing near-simultaneously from "sensor-to-shooter".

SLIDE NR. 30

- Virtual connectivity is today's reality, not tomorrow's pipe dream ... Today HQ SFOR, the MNDs and the CAOC are virtually connected through the Bosnia Command and Control

Augmentation (BC2A) network, which directly links each C2 node through video teleconferencing and share files. Other communication networks enable processing and evaluating of information collected on the Balkans at intelligence production nodes far removed from the area of operations.

- Airmen are most suited to tasking air and space platforms, including reconnaissance and surveillance assets (self explanatory).

expensive and ecologically-unsound task indeed- or scanned into an electronic file, resulting in a degradation in quality. Digital imagery retains its original quality and is far more economically available.

SLIDE NR. 31

## CONCLUSIONS

Advanced systems can enhance our warfighting capability. Real-time or near real-time information on enemy location, dispositions, capabilities, and indicators of intentions from surveillance and reconnaissance assets gives Commanders the needed situational awareness. The ability to effectively utilize the platforms and associated sensors available, in any weather condition regardless of whether the operational theater is out of area or

- Real time video is a success story, it provides Commanders real-time situational awareness and it is the most highly demanded product in Bosnia operations. However it is a story with many chapters to come: mechanisms and methodologies to exploit, store, and retrieve video have yet to meet or match the needs of the supported users.

Digital imagery is the future. In order to distribute wet film imagery, it must either be mass-produced in hard copy - an not, is the most challenging and demanding task for any Force Commander, but this is not related to sensors themselves. What we are concerned about is:

- well trained both crews and operators,
- a robust communication linkage for optimum and widest range of communication and data dissemination,
- timely and complete situation awareness available to decision makers,
- a C3 structure designed to manage the whole process.

If we are not able to have this, even the most advanced sensors in the world are nearly useless. Improving capabilities of sensors, of course, is something worthy and demanding, but improving our managing skills is essential.

# MODTRAN4: SIMULATING ATMOSPHERIC RADIATION FOR CLOUDY CONDITIONS

G.P. Anderson, J.H. Chetwynd

PL/Geophysics Directorate, 29 Randolph Rd., Hanscom AFB, MA 01731  
617-377-2335, Fax 377-8900, 'ganderson@plh.af.mil'

A. Berk, L.S. Bernstein, P.K. Acharya

Spectral Sciences, Inc., 99 S. Bedford St., Burlington, MA 01803

H.E. Snell

Atmospheric and Environmental Research, Inc., 840 Memorial Dr., Cambridge, MA 02139

E.P. Shettle

Naval Research Laboratory, Washington, D.C. 20375

## ABSTRACT

The new MODTRAN4 band model, with its Correlated- $k$  (CK) Beer's Law algorithm, can efficiently and correctly (usually within 3-5%) calculate the scattering and absorption signatures of realistic molecular, aerosol and cloudy environments in the lower and middle atmosphere. The current approach for molecular scattering accommodates line overlap and partial correlations between both molecular species and the solar irradiance, while maintaining automated band model spectral resolution at 2 or 15  $\text{cm}^{-1}$ . This new level of evolution and validation will permit improved syntheses and analyses of actinic (direct plus scattered) solar and thermal energy budgets within the stratosphere and troposphere, including potential compensation for optically thin clouds. Such validated energy budgets can then serve as validation surrogates for applications related to surveillance and background simulations within clouded environments.

Comprehensive validation is usually provided through two basic avenues: model to model and model to measurement. The first involves direct comparisons with line-by-line calculations, as exemplified by FASE (the line-by-line algorithm jointly developed from FASCODE by DoD and DOE) which provides the molecular standard for layer effective optical depths, single scattering albedos, and transmittances. This enables the MODTRAN4 algorithm to be refined for more adaptable spectral resolution plus efficient determination of those layer quantities necessary for multiple scattering applications; e.g. DISORT. The second validation step centers on comparisons against

a variety of measurements, mostly airborne visible and IR up-welling radiances, including both clear and clouded skies. However, in this instance, only simulations and sensitivity studies will be presented.

## 1. INTRODUCTION

With the development of MODTRAN4 (Bernstein, et al., 1996), a flexible tool for radiative energy budget calculations is now available. While this version of MODTRAN is grounded in the prior series of AF radiative transfer band model (BM) algorithms (LOWTRAN, Kneizys, et al., 1980, 1983, 1988, through MODTRAN3, Berk et al., 1989, 1995), it is distinct in its ability to employ Beer's law ( $T_v = \exp(-k_{v,i} n_i)$ ) to describe local layer, species-specific transmittance for input to the radiance calculations. While this capability is not always necessary, it allows appropriate handling of multiple scattering (m.s.) using existing non-BM algorithms (DISORT, Stammes et al., 1988, and Isaacs et al., 1987). MODTRAN4, while maintaining the basic 2  $\text{cm}^{-1}$  spectral resolution, can now complement the m.s. routines by introducing a Correlated- $k$  (CK) capability that is expressly compatible with Beer's law formulations.

MODTRAN4 also provides greatly improved predictive capabilities under cloudy and/or heavy aerosol loading conditions in both the visible and IR.

It does so by allowing the explicit definition of water and ice cloud vertical profiles and spectral data, either by scaling and combining default model clouds or by redefining entirely new model clouds with micro-layering options.

It can be shown that this combination of improvements will permit rapid identification of atmospheric contaminants/signatures in window regions as well as accurate spectral calculations of

heating/cooling budgets in the presence of clouds for both thermal and solar spectral regimes. Finally, in the regions of molecular opacity, where weighting functions peak in the atmosphere, it is expected that MODTRAN4 can play a role in very quick 'primitive' retrievals, avoiding the large number of line-by-line (LBL) calculations necessary for initiating derivative (perturbation) matrices (Anderson et al., 1993). While the error estimates and residuals associated with a  $2\text{ cm}^{-1}$  algorithm will be larger than those associated with LBL retrievals, the speed advantage for image processing might warrant this initial approach.

## 2. ADDITION OF A CORRELATED- $k$ CAPABILITY TO MODTRAN

Addition of a CK capability to MODTRAN (Bernstein et al., 1995) provides an accurate and fast means for evaluation of the effects of clouds and heavy aerosol loading on retrievals (both surface properties and species concentration profiles) and on atmospheric radiative heating/cooling calculations. These radiative transfer computations require coupling the effects of gaseous molecular absorption due primarily to water vapor, carbon dioxide, and ozone, with particulate multiple scattering due to volcanic aerosols, ice crystals, and water droplets. In order to adapt a band model approach for use in scattering calculations it is necessary to express the band model transmission function in terms of a weighted sum of Beer's law exponential terms. Thus, a method for determining the weighing factors and monochromatic absorption coefficients for the MODTRAN band model is required. A discussion of the CK approach as tailored for integration into a TDA (Tactical Decision Aid) MODTRAN-based algorithm is provided in a companion paper (Bernstein et al., 1998); for a more complete discussion of the CK method the reader is referred to Lacis and Oinas (1991).

The MODTRAN band model for a single species is based on four parameters: (1) the integrated line strength  $S$  in a spectral interval  $\Delta\omega$  ( $\Delta\omega = 1\text{ cm}^{-1}$  in MODTRAN), (2) the effective number of equivalent lines  $n$  (non-integer values of  $n$  are acceptable) in the interval, (3) the average pressure broadening Lorentz line width  $\gamma_L$ , and (4) the Doppler line width  $\gamma_D$ . These parameters are determined directly from the

1997 HITRAN parameter line compilation (Rothman et al., 1997).

## 3. INITIAL VALIDATION OF MODTRAN4 MULTIPLE SCATTER SOLAR

Development of MODTRAN4 was necessary because MODTRAN3 predictions of multiply scattered solar and molecular radiances in spectral regions with non-continuum molecular absorption may be inaccurate. This scenario cannot be validated by comparisons to FASCODE (Clough et al., 1988) because FASCODE currently lacks a solar capability. Thus, initial validation of MODTRAN4 multiply scattered solar calculations was made directly to measurements.

In previous studies (Anderson et al., 1997) a comparison of calculated radiance predictions to airborne measurements (Malherbe et al., 1995) was performed against a circular variable filter cryogenic spectrometer (1500-5500 nm, 2% spectral resolution). From an aircraft of 3.0 km, the cloud top at 2.5 km was observed at two angles relative to the sun-sensor configuration. The MODTRAN4 cloud model upgrade enabled the cloud profile and spectral data to be explicitly entered for the MODTRAN calculations. Both MODTRAN calculations employed a simpler two-stream multiple scattering model (Isaacs et al., 1987); the discrete ordinate model in MODTRAN, DISORT (Stamnes et al., 1988), was run with 8-streams over a limited spectral sub-region and produced similar results. The fit was excellent when the sun was positioned behind the line-of-sight. However, when the sun fell into the near line of sight (e.g.  $11^\circ$ ), the fit could not properly capture the forward scattering lobe. This unresolved problem has led to these sensitivity studies plus investigations into specific scattering geometries.

## 4. VISIBLE AND IR EXAMPLES OF THIN CIRRUS CLOUDS WITH MODTRAN4

MODTRAN4 has the ability to import arbitrary cloud and aerosol descriptions, as developed for particular measurement scenarios. The entire spectral range (UV through far-IR) is impacted by clouds and it is generally accepted that thick cumulus clouds cannot be penetrated by standard electro-optical techniques. For the present study, only thin cirrus (ice clouds) have been examined, with the intent to explore the optical depths which might be



'corrected'; that is, what level of cloud opacity might constitute an irretrievably cloud-contaminated scene or line-of-sight?

4.1 Visible and Near-IR (400-2500 nm) instruments, as exemplified by the AVIRIS (Airborne Visible and IR Imaging Spectrometer, an ER-2 aircraft-mounted instrument; see Green et al 1996), provide a growing resource for hyperspectral imaging for surface characterization. Typically such data are specifically collected during clear-sky conditions. As such methodologies are moved to space, the options of taking measurements only when clouds are not present become a less viable option. Hyperspectral imaging (HSI) through 'thin' clouds is one important application. Figure 1 a/b demonstrate a pair of simulations for AVIRIS, 1a on a log scale, 1b on linear. In each case, the darker of the two curves is for clear-sky conditions, a surface albedo for dry grass (Mustard, 1991), and a solar zenith angle of 50°. The cirrus cloud inserted for the second simulation (lighter color) shows a distinctive pattern that is currently being used in AVIRIS analyses to determine ice cloud contamination. The pivotal frequency for initial detection is 1380 nm, the center of an H<sub>2</sub>O band that becomes sensitively opaque at concentrations associated with cirrus cloud altitudes. At shorter wavelengths there is a crossover, where, in the presence of ice clouds, the visible wavelengths scatter more brightly, while longward of 1380 nm, the H<sub>2</sub>O and particulate absorption within the cloud makes the scene darker.

This response, first reported by B.-C. Gao (1993, 1995), is being included in the NASA Mission to Planet Earth (MTPE) Earth Observing System Experiments, explicitly to determine cirrus cloud occurrence. Note that the molecular absorption signatures in these simulations are primarily H<sub>2</sub>O (the most prevalent), O<sub>2</sub> (at 760 nm), and CO<sub>2</sub> (at 2350 nm). Other structure comes from the combination of surface albedo and solar Fraunhofer signatures, both very indistinct in this presentation, except for the overall envelope of the solar Planck function (for T~6000K) peak near 500 nm.

Equally important in this spectral range are slant-path observations, as exemplified by aircraft instrumentation in the visible and near-IR. While HSI must see through such clouds in the near-nadir direction, aircraft must detect the existence of such

clouds and adjust their flight plans accordingly. It might be necessary to move above, into, or below the contaminating scattering source. This scenario is examined with MODTRAN simulations by demonstrating the impact of observing such thin clouds from aircraft at assorted slant paths and opacities. The selected cirrus cloud, while spatially thick (3 km), is represented by three opacities that vary from 'very thin' (1.e-4 optical depth, essentially transparent) to 'thick' (1.0, still a 'thin' ice cloud). The altitudes for the observing aircraft have been set at 9 and 13 km, below the cloud and at its center. Observation angles have been varied from below, looking up through a 70° slant path, or 88°, the latter mimicking an essentially horizontal observing path.

Again, both log and linear formats are presented (Figures 2a/b). The roles of scattering within and below the cloud appear separable. The two uppermost curves (in 2a) are the simulations for looking under and through the thickest cloud almost horizontally (at 9 km and 13 km, respectively). At 9 km there is a significant particulate component to the secondary scattering of the solar irradiance that has penetrated and been 'forward scattered' through the cloud. At the center of the 13 km 'in cloud' observation, the scattering from the cloud, both along the line-of-sight and from above, compensate for the lack of additional molecular scattering. This distinction can be most readily discerned in the depth of the H<sub>2</sub>O absorption features; at 13 km there is less water and these features are shallower.

The third brightest curve is also 'observed' under a cloud (at 9 km 'horizontal' viewing), but this thinnest cloud did not contribute any additional forward scattering, providing essentially a clear-sky view. The scattering is almost entirely single scattering, dominated by the Rayleigh molecular component, thus producing the brightest signature at the shortest wavelengths (most readily noted in the linear plot). The two dimmest curves are both 'slant' paths, from 9 km up through the cirrus cloud. The differences in these two curves are only discernible in the log plot, demonstrating two intermediate opacities (OD= .01 and 1.0). The thinner cloud is moderately brighter with deeper H<sub>2</sub>O absorption features; the forward scattering (particulate) component is less dominant than the absorption by the cloud itself. Observing directly through an ice cloud can (at least for this configuration from 2 km below the cloud

base) make the more opaque cloud appear darker. Other configurations relative to solar position could provide the opposite impact. More controlled sensitivity studies need to be undertaken.

4.2 Moving to the IR simulations (Figure 3 a/b), the consequences of the cloud become quite different. It must be remembered that in this case there is only a small solar component ( $>2500 \text{ cm}^{-1}$ ) and all views are to cold space with an intervening warm cloud, so surface emissivity is almost irrelevant except as a component to the multiple scattering. The thermal structure of the atmosphere plays an important role in the radiance of the major molecular radiators ( $\text{CO}_2$  centered at  $600 \text{ cm}^{-1}$  (15  $\mu\text{m}$ ) and  $2300 \text{ cm}^{-1}$  (4.3  $\mu\text{m}$ ),  $\text{O}_3$  at  $1000 \text{ cm}^{-1}$  (9.6  $\mu\text{m}$ ), and  $\text{H}_2\text{O}$ ). The two brightest curves are for paths looking directly up from the surface at the thickest ( $\text{OD}=1.0$ ) cirrus clouds, one located at 20 km (emulating a polar stratospheric cloud), the other at 11 km (typical cirrus). Both clouds are equally bright in the opaque regions, due primarily to  $\text{CO}_2$  and coincident  $\text{H}_2\text{O}$  strong emissions from the lower troposphere (and at higher temperatures), reflecting the temperature profile of the sub-arctic summer conditions selected for these simulations. The high opacity level is readily noted when the smooth emission curves (Planck curve for  $T=260\text{K}$ ) dominate the signature. Where these two profiles differ is in the ozone signature that, by itself, is not generally opaque in the vertical. However, because of the intervention of the opaque 11 km cloud, the 20 km cloud view detects additional lower stratospheric ozone emission between 11 and 20 km. The spectrally broad 'bites' out of the pure Planck function demonstrate that both cirrus clouds remain optically thin in the windows at these nearly vertical observing angles, seeing the colder temperatures at the top of the atmosphere.

The second set of curves (all labeled 'slant') are generally of lower brightness. In each case the path has been chosen to begin at 9 km (aircraft altitude), intersecting the 11 km cloud base at a range of over 10 km, by choosing an observation angle of  $80^\circ$ . The thinnest cloud (opacity of  $1.0\text{e-}4$ ) is again typical of clear-sky conditions. Over most of the path the window regions between molecular emissions are transparent (seeing through to cold space) and systems based on observing within these 'windows' (3-5  $\mu\text{m}$ , 8-12  $\mu\text{m}$ ) would be fully operative,

recording very low background values. Ozone appears in emission for both the clear-sky and the thinner cloud, relative to the neighboring 'windows'. The  $\text{CO}_2$  and  $\text{H}_2\text{O}$  features both become optically thick at the cloud intercept. The thickest cloud is almost optically thick throughout for this slant path (as indicated by the quasi-Planck shape), thus filling the windows that would otherwise be used for systems operations.

## 5. CONCLUSIONS

MODTRAN4 shows great promise as a research tool for better understanding of the role of clouds in the atmosphere, providing components for sensitivity studies around and within the visual 'field of operation', actual and simulated. In general the calculations can be done rapidly and with accuracy that approaches LBL numerical solutions. Important current caveats center on improved optical properties of clouds and their physical descriptions (ice and water), both issues of current research activity. Additionally, none of these current calculations was done with sufficient multiple scattering streams to support definitive conclusions. Evaluations of cloud transparency and opacities must be continued.

## 6. REFERENCES

- G.P. Anderson, J.H. Chetwynd, A. Berk, L.S. Bernstein, P.K. Acharya, 'An Algorithm for Hyperspectral Remote Sensing: Solar and Thermal Regimes, 4', *Optical Society of America, Proceedings of Optical Remote Sensing of the Atmosphere*, Santa Fe, Feb 10-14, 1997.
- Anderson, G.P., Kneizys, F.X., M.L. Hoke, L.W. Abreu, E.P. Shettle, 'MODTRAN2: Suitability for Remote Sensing', *Proc. of SPIE, 1954, Remote Sensing*, 1993.
- Berk, A., "Upgrades to the MODTRAN Layer Cloud/Rain Models," Report. No. SSI-SR-56, Spectral Sciences, Inc., 99 S. Bedford St., Burlington, MA, 1995..
- Berk, A., L. S. Bernstein, and D. C. Robertson, "MODTRAN: A Moderate Resolution Model for LOWTRAN7," Rep. GL-TR-89-0122, Air Force Geophys. Lab., Bedford, MA, 1989.
- Bernstein, L. S., A. Berk, D. C. Robertson, P. K. Acharya, G. P. Anderson, and J. H. Chetwynd, "Addition of a Correlated- $k$  Capability to MODTRAN," *Proceeding of the 1996 IRIS Targets, Backgrounds, and Discrimination Meeting*, 1996.
- Bernstein, L.S., A. Berk, P.K. Acharya, D.C. Robertson, G.P. Anderson, J.H. Chetwynd, L.M. Kimball, "Very Narrow Band Model

Calculations of Atmospheric Fluxes and Cooling Rates Using the MODTRAN Code," *J. Atm. Sci.*, 53, 2887-2904, 1996.

Clough, S. A., F. X. Kneizys, G. T. Anderson, E. P. Shettle, J. H. Chetwynd, L. W. Abreu, and L. A. Hall, 1988, "FASCOD3 Spectral Simulation", *Proceedings of the International Radiation Symposium*, Lenoble and Geleyn, Deepak Publishing.

Clough, S.A., M.J. Iacono, J.-L. Moncet, "Line-by-Line Calculations of Atmospheric Fluxes and Cooling Rates: Applications to Water Vapor", *J. Geophys. Res.*, 97, 15761, 1992.

Gao, B.-C., Alexander F. H. Goetz, and Warren J. Wiscombe: Cirrus cloud detection from airborne imaging spectrometer data using the 1.38 micron water vapor band, *Geophys. Res. Lett.*, 20, 301-304, 1993.

Gao, B.-C. and Yoram J. Kaufman, Selection of the 1.375-micron MODIS channel for remote sensing of cirrus clouds and stratospheric aerosols from space, *J. Atmos. Sci.*, 52, 4231-4237, 1995.

Green, R.O., D.A. Roberts, and J.E. Conel, "Characterization and Compensation of the Atmosphere for Inversion of AVIRIS Calibrated Radiance to Apparent Surface Reflectance," *Summaries of the Sixth Annual JPL Airborne Earth Science Workshop*, JPL Publication 96-4, Vol. 1, Pasadena, California, pp. 135-146, 1996.

Isaacs, R. G., W. C. Wang, R. D. Worsham, and S. Goldenberg, 1987, "Multiple Scattering LOWTRAN and FASCODE Models," *Applied Optics*, 26, 1272-1281.

Kimball, L.M., "Investigation of Atmospheric Heating and Cooling Balance Using MODTRAN3", *AFOSR Summer Faculty Report*, 1995.

Kneizys, F.X., Shettle, E.P., Gallery, W.O., Chetwynd, J.H., Abreu, L.W., Selby, J.E.A., Fenn, R.W., McClatchey, R.A., **Atmospheric Transmittance/Radiance: Computer Code LOWTRAN 5**, AFGL-TR-80-0067, AD A058643, 1980.

Kneizys, F.X., Shettle, E.P., Gallery, W.O., Chetwynd, J.H., Abreu, L.W., Selby, J.E.A., Clough, S.A., Fenn, **Atmospheric Transmittance/Radiance: Computer Code LOWTRAN 6**, AFGL-TR-83-0187, AD A137796, 1983.

Kneizys, F.X., Shettle, E.P., Chetwynd, J.H., Abreu, L.W., Anderson, G.P., Gallery, W.O., Selby, J.E.A., Clough, S.A., **Users Guide to LOWTRAN 7**, AFGL-TR-88-0177, 1988.

Lacis, A. A., and V. Oinas, "A description of the Correlated K Distribution Method

for Modeling Nongray Gaseous Absorption, Thermal Emission, and Multiple Scattering in Vertically in Homogeneous Atmospheres," *J. Geophys. Res.*, 96, 9027 - 9063, 1991.

Malherbe, C., P. Simoneau, A. Boischot, G. Durand, J. Deschamps, and G. Gregoire, , "Radiative Transfer Model in a Cloudy Atmosphere: A Comparison with Airborne Cumulus Measurement," *Proceedings of the SPIE Conference on Passive IR Remote Sensing of Clouds and the Atmosphere III.*, 1995

Mustard, J.F., "Distribution of Soil, Rock, and Grass in the Western Foothills of the Sierra Nevada", in *Proceedings of the Third Airborne Visible/Infrared Imaging Spectrometer (AVIRIS) Workshop*, JPL 91-28, pp 14-22, 1991.

Rothman, L. S. et al., 1997, "The again, HITRAN Molecular Database: Edition of 1997," Released as a CD-Rom, June, 1997. ('rothman@plh.af.mil')

Stamnes, K., S. C. Tsay, W. J. Wiscombe, and K. Jayaweera, "Numerically Stable Algorithm for Discrete-Ordinate-Method Radiative Transfer in Multiple Scattering and Emitting Layered Media," *Applied Optics*, 27, 2502-2509, 1988.

Figure 1a/b: Clear and cloudy AVIRIS simulations; see discussion.

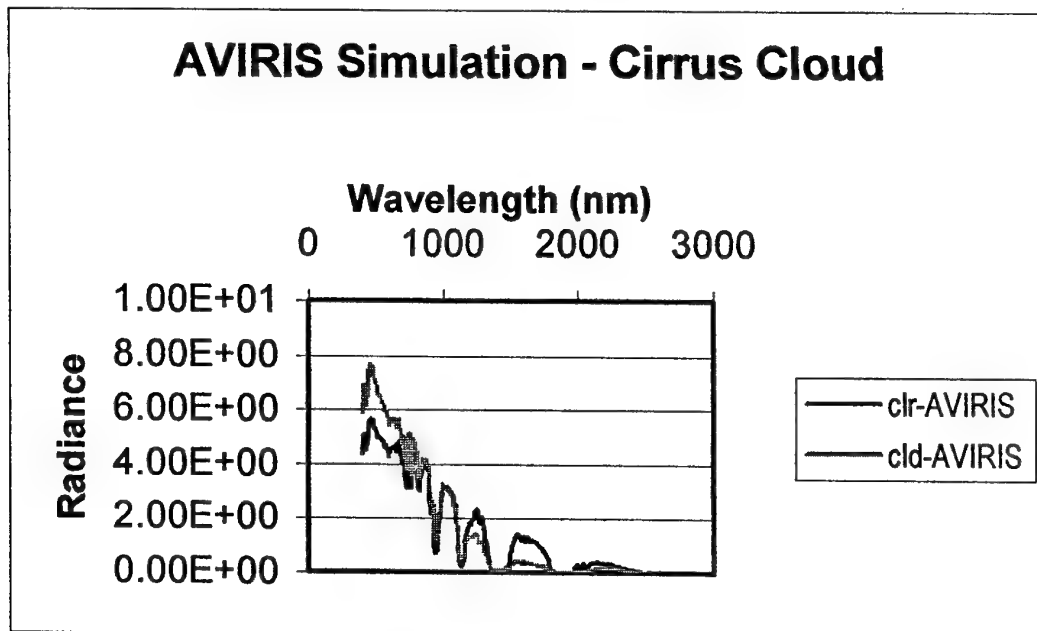
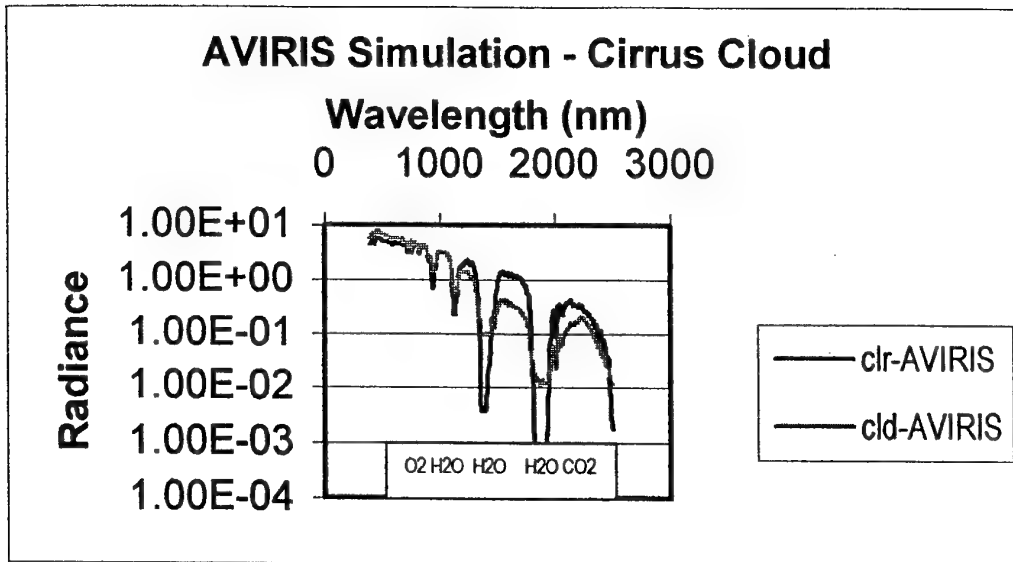


Figure 2 a/b: Vis/Near-IR observations from aircraft altitudes; see discussion.

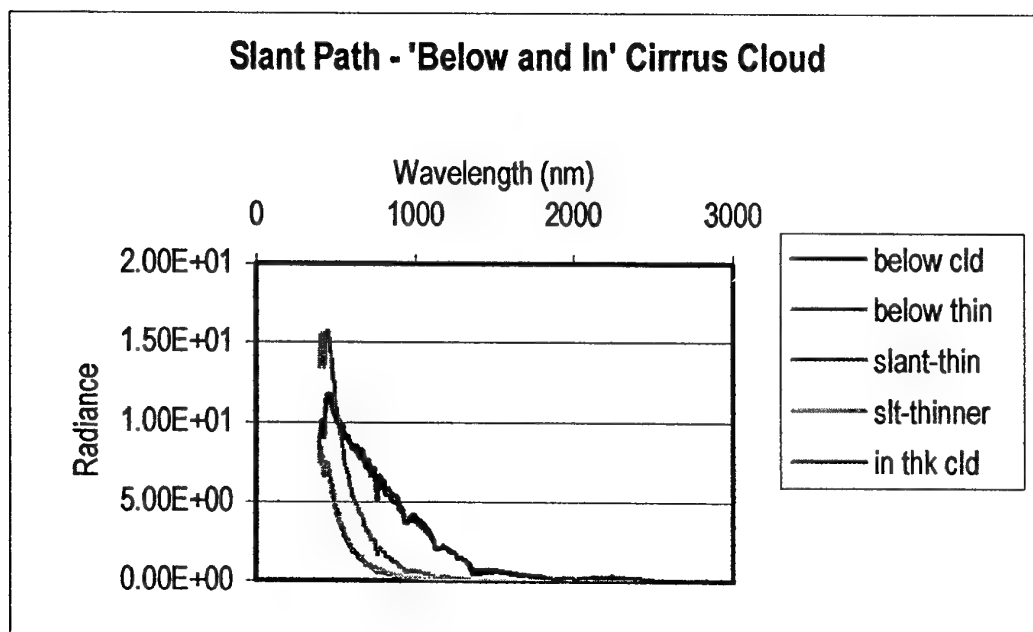
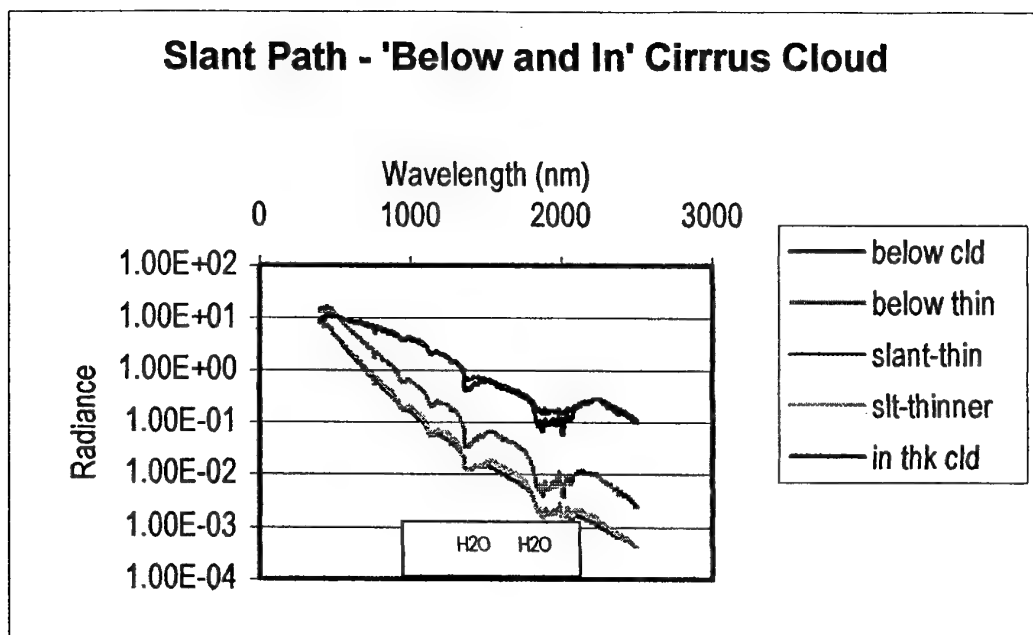
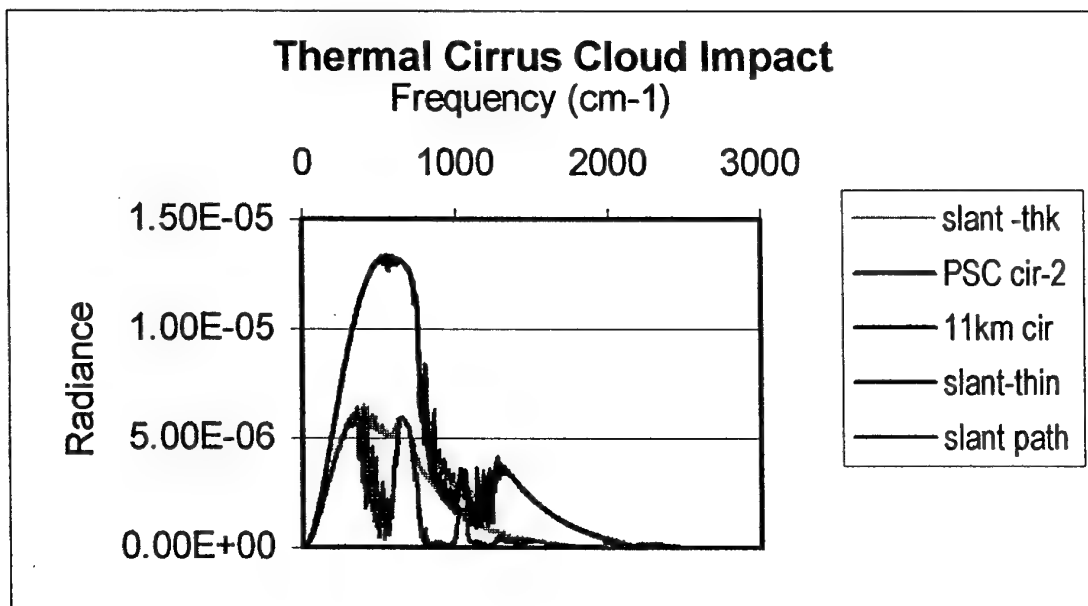
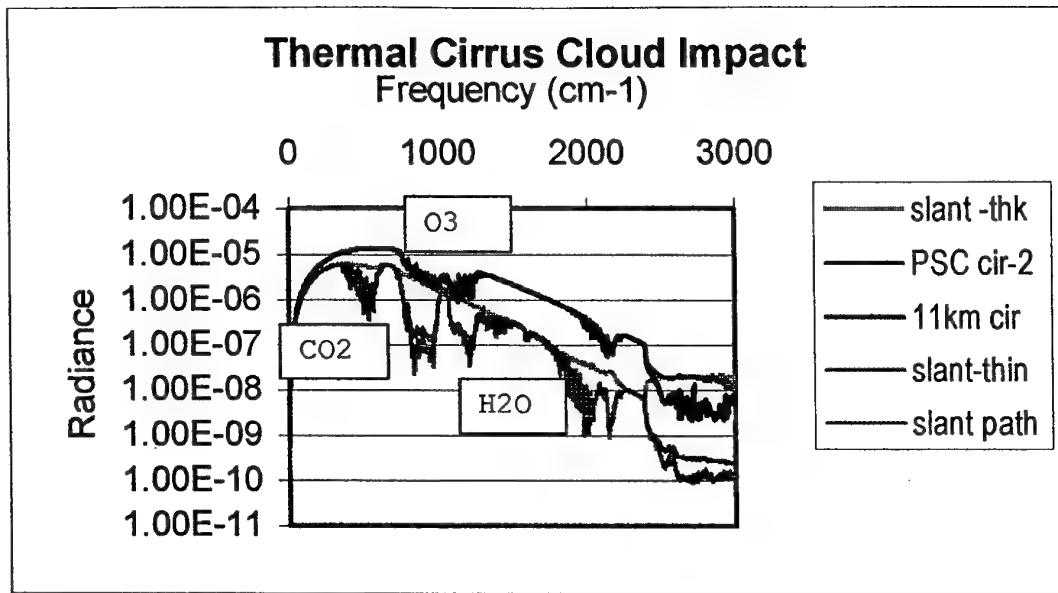


Figure 3 a/b: Thermal IR observations from aircraft; see discussion.



PAPER No. 2

DISCUSSOR'S NAME: E. Schweicher

COMMENT/QUESTION:

What kind of devices did you envision especially when you mentioned "adaptive optics".

AUTHOR/PRESENTER'S REPLY:

"Adaptive Optics", in the sense to which I alluded, embodies the selective choice of the hyperspectral channels which contain the most information content for deriving sets of physical parameters (temperature, pressure, surfaces, constituent, aerosol). This subset of channels would depend upon the type of scene (image) being observed; e.g. desert, forest, water for visible to near-IR nadir observations. Such adaptive choices will minimize "on-board" processing times for surveillance applications.

Note: this choice of vocabulary is totally unrelated to "adaptive optics" as related to wavefront optics.

## The MOSART Code

by

Dr. William M. Cornette  
National Imagery and Mapping Agency  
4600 Sangamore Road, D-33  
Bethesda, MD 20816-5003, USA  
CornetteW@nima.mil

Sally J. Westmoreland  
Photon Research Associates, Inc.  
5720 Oberlin Drive  
San Diego, CA 92121-1723, USA

Dr. Prabhat K. Acharya, Dr. Alexander Berk, Dr. David C. Robertson  
Spectral Sciences, Inc.  
99 South Bedford Street, #7  
Burlington, MA 01803-5169, USA

Gail P. Anderson, Dr. William A.M. Blumberg, Dr. Laila S. Jeong,  
and Dr. Francis X. Kneizys  
Air Force Research Laboratory  
29 Randolph Road  
Hanscom AFB, MA 01731-3010, USA

### 1. SUMMARY

The MODerate Spectral Atmospheric Radiance and Transmittance (MOSART) code is the U.S. Department of Defense standard code for calculating accurate and realistic atmospheric transmission along sensor-target line-of-sight (LOS) paths and optical radiance backgrounds against which targets are detected by sensor systems. MOSART uses the same band model and  $1\text{ cm}^{-1}$  resolution band parameter data base found in MODTRAN, which have been derived from the 1996 HITRAN line atlas. In the ultraviolet and visible regions, MOSART contains additional molecular absorption bands at a coarser resolution. The line-of-sight geometries include all MODTRAN3 geometries, plus some new geometries, including Observer-Source, Observer-Background, Observer-Source-Background, Earth limb, Horizontal, At-Source (i.e., Observer and Source are co-located). An X-Windows- and Motif-based MOSART Input GUI is available, as is a simple scrolling input file builder.

An extensive set of global data bases is incorporated into the code, including climatologies (e.g., diurnal surface air temperature, three-etae cloud cover, cirrus presence), terrain elevation (10 arcmin

resolution), water/snow composition, and ecosystem type (10 arcmin resolution). Coupled with the ecosystem and terrain elevations are composite terrain scene types with appropriate boundary layer aerosol composition. Each scene includes appropriate parameters for determining the terrain temperature for each material in the scene, together with the reflected and emitted radiances for determining the mean and standard deviation for the scene. The Global Data Base Model allows a full 3-D representation of the earth's atmosphere (i.e., altitude, latitude, and longitude) with radiative transfer varying as the line-of-sight moves within the spatially changing atmosphere.

The MOSART code is approximately 190,000 lines of ANSI FORTRAN 77 code, including 12 utility codes and manuals (4 volumes: Installation, User's, Technical, and Software Reference Manuals). Version 1.50 of MOSART was released in September 1997. The status of MOSART, along with appropriate upgrades will be presented, together with information on how to obtain the code and who to contact for technical information and "bug" reporting.



## 2. INTRODUCTION

The MODerate Spectral Atmospheric Radiance and Transmittance (MOSART) code is the U.S. Department of Defense standard code for calculating accurate and realistic atmospheric transmission along sensor-target line-of-sight (LOS) paths and optical radiance backgrounds against which targets are detected by sensor systems. As such, it has the capability to support both scene and signature simulations. It grew out of a merging of the MODTRAN [Ref. 1] and APART [Ref. 2] codes with some additional capabilities added.

Except for DISORT, MOSART Version 1.50 contains all MODTRAN 3.5 capabilities (and some of the MODTRAN 3.7 capabilities) and has been compared to it for a number of conditions by Spectral Sciences, Inc. and Photon Research Associates, Inc. The version of the DISORT code in MODTRAN 3.6 is still under beta testing and further work is on-going at Spectral Sciences, Inc. (SSI) and at the Air Force Research Laboratory, Hanscom AFB, MA. When it is approved by Air Force Research Laboratory, it will be incorporated into MOSART.

Some features in the MOSART code are:

- observables-driven architecture (see Figure 1)
  - ⇒ observer-to-source radiative transfer
  - ⇒ observer-to-background radiative transfer
  - ⇒ full radiative environment
- MODTRAN molecular absorption
  - ⇒ three-flux multiple scattering
  - ⇒ turbulence & sky noise
  - ⇒ forward in-scatter
- global data bases
- atmospheres
- climatologies
- terrain
  - ⇒ terrain altitude
  - ⇒ ecosystems/terrain type
  - ⇒ contrast
  - ⇒ structured background
  - ⇒ bidirectional/directional reflectivities
- hydrometeors
  - ⇒ clouds (water/ice)
  - ⇒ fog
  - ⇒ rain
  - ⇒ snow

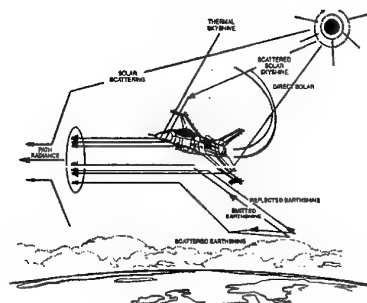


Figure 1. MOSART Observables-Driven Architecture

## 3. ATMOSPHERIC MODELS

The MOSART code has a number of model atmosphere and climatological models to assist the user in creating atmospheres appropriate for any spot on the globe. The user can also define a specific atmosphere, if desired.

### 3.1 Model Atmospheres

The MOSART code contains twenty-three (23) model atmospheres that include profiles of pressure, temperature, wind speed, and molecular concentrations. These model atmospheres include Summer and Winter variations for:

- Equatorial
- Tropical
- Subtropical
- Midlatitude
- Subarctic
- Arctic
- Polar

plus an Annual Tropical Atmosphere from MODTRAN, a Spring/Fall Atmosphere for the midlatitudes, four (4) special Subarctic Winter atmospheres, the U.S. Standard 1976 Atmosphere, and the Israeli Standard Atmosphere. The Israeli Standard Atmosphere has a day and a night version. A User-Defined Atmosphere is also allowed.

### 3.2 Molecular Concentrations

The molecular species included with MOSART are the twelve (12) molecules on the MODTRAN molecular data base:

- Water vapor
- Carbon Dioxide
- Nitrous oxide
- Carbon monoxide

- Methane
- Oxygen
- Nitric oxide
- Sulfur dioxide
- Nitrogen dioxide
- Ammonia
- Nitric acid

plus the following:

- Nitrogen
- Hydrogen peroxide
- Carbon tetrachloride
- CFC-11
- CFC-12
- CFC-13
- CFC-14
- CFC-21
- CFC-22
- CFC-113
- CFC-114
- CFC-115
- $\text{ClONO}_2$
- $\text{HNO}_4$
- Nitrogen Pentoxide

### 3.2 Global Atmospheres

While MOSART is fully capable of calculating the atmospheric propagation for a single atmosphere (e.g., Midlatitude Summer), it is also capable of assuming the atmospheric parameters vary along the line-of-sight. Currently, MOSART only considers variations in latitude, but variations in longitude will be included in Version 2.00. With the variable atmosphere, a north-looking line-of-sight will have a different path radiance than a south-looking line-of-sight. Samples of the output from a variable atmosphere are shown in Figures 2 and 3, which show the transmittance, path radiance, earth radiance, and total radiance for a nadir viewing satellite as it traverses Greenwich Meridian from one pole to the other. Included in both figures are the terrain altitude and the location of land and ocean masses. The location of the sun is shown graphically.

### 3.3 Climatological Data Base

The Global Climatological Data Base contains data that allows the code to modify the model atmospheres to represent the climatology more closely at a given location. Within this data base, the code has access to information such as:

- Surface Air Temperature
- Cloud Cover (low, mid, and high etage, plus total)
- Cloud Altitude (low, mid, and high etage)
- Cirrus Cloud Cover
- Snow and Ice Cover
- Land Cover (not used)

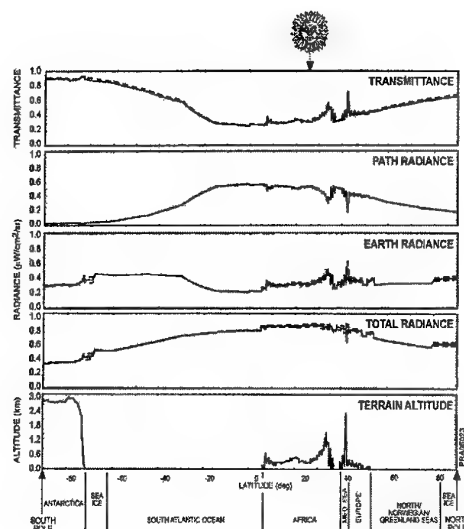


Figure 2 Longitudinal Profiles  $11 \mu\text{m}$   
21 June 1993 at 1200 hours

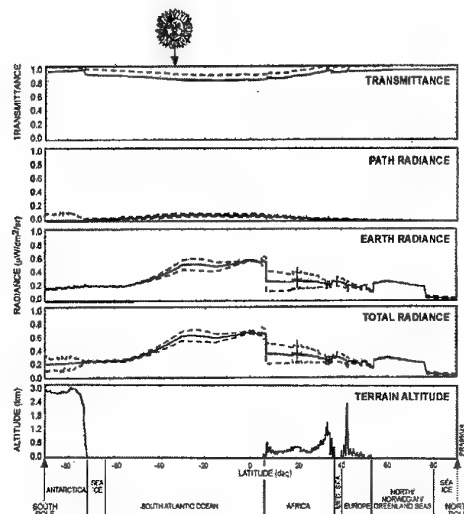
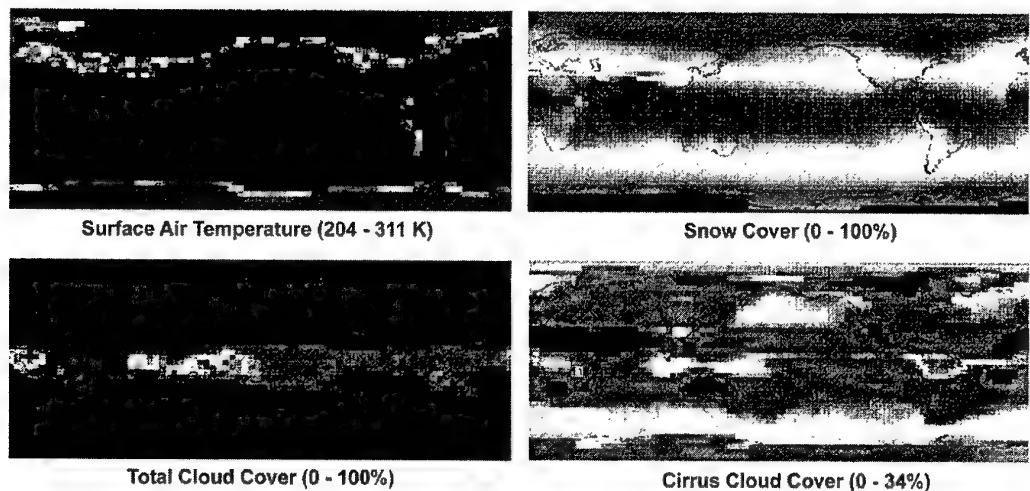


Figure 3. Longitudinal Profiles  $4 \mu\text{m}$   
21 December 1993 at 1200 hours

**Note:** Solid lines are transmittance and mean radiances; dashed lines are in-scattered transmittance and mean  $\pm$  one standard deviation radiances. The solar position is as shown. The observer is looking from a nadir view from space.



Five Year (1985 - 89) Average From NOAA Nimbus-7

Figure 4. Climatology Maps for April

The Surface Air Temperature, Cloud Cover, and Cloud Altitude are monthly averages for at local noon and midnight, while the other parameters are simply monthly averages. The data has a latitudinal resolution of  $4.5^\circ$  and a longitudinal resolution of  $4.5^\circ$  at the equator, degrading to  $120^\circ$  at the poles (see Figure 4).

The MOSART code includes temporal (e.g., seasonal, annual) changes to the molecular concentration of certain molecules (e.g.,  $\text{CO}_2$ ,  $\text{CH}_4$ ,  $\text{CO}$ ,  $\text{N}_2\text{O}$ ). A global climatology data base of tropospheric water vapor will be incorporated in the near future.

### 3.4 Aerosol Haze Profiles

The aerosol haze profiles, i.e., the extinction versus altitude at  $0.55 \mu\text{m}$ , in MOSART are of two types. The first type is the MODTRAN profiles with fixed altitude divisions between the different altitude types. The second type is the profiles whose transition points depend upon the atmosphere. The boundary layer transition is the same for the two types. The troposphere-stratosphere transition for MODTRAN is 10 km, while MOSART uses the actual tropopause. Similarly, where MODTRAN uses 35 km to transition from stratosphere to mesosphere, MOSART uses the actual stratopause.

For the boundary layer, the sea level visibility (or meteorological range) can be defined or estimated from the aerosol type and relative humidity.

### 3.5 Aerosol Models

MOSART contains all the aerosol models (i.e., the models that translate the haze extinction at  $0.55 \mu\text{m}$  to some other wavelength) in MODTRAN. In addition, MOSART contains a temperature-dependent background stratospheric model. The capability to calculate a user-defined aerosol model from a built-in Mie scattering code is also included.

The boundary layer aerosol type can be approximated by the terrain type. Work is ongoing to include wind effects (e.g., the blowing of Sahara Dust out into the Atlantic Ocean) and to allow mixing of aerosol models.

### 3.6 Hydrometeors

Fifteen (15) non-precipitating low altitude water clouds (see Table 1) are included in the code, together with five (5) precipitating clouds with rain profiles (see Table 2).

For temperatures below 273.15 K, the water clouds are assumed to be a mixture of water and ice, eventually becoming all ice at colder temperatures. Similarly, the rain may be a mixture of rain and snow, or all snow, at temperatures below freezing.

Table 1. Non-Precipitating Clouds

CLOUD	ALTITUDE (KM)
Advection Fog No. 1	0.00 - 0.15
Advection Fog No. 22	0.00 - 0.15
Radiation Fog No. 1	0.00 - 0.075
Radiation Fog No. 2	0.00 - 0.075
Cumulus	0.66 - 2.70
Altostratus	2.40 - 2.90
Stratocumulus I	0.66 - 1.32
Stratocumulus II	0.66 - 2.00
Nimbostratus I	0.16 - 1.00
Nimbostratus II	0.16 - 0.66
Stratus I	0.16 - 0.66
Stratus II	0.33 - 1.00
Stratus-Stratocumulus	0.66 - 2.00
Cumulus-Cumulus Congestus I	0.66 - 2.70
Cumulus-Cumulus Congestus II	0.66 - 3.40

Table 2 Precipitating Clouds

CLOUD	ALTITUDE (KM)	RAIN RATE (MM/HR)	
Stratus II	0.33-1.00	Drizzle	2.0
Nimbostratus II	0.16-0.66	Light	5.0
Nimbostratus II	0.16-0.66	Med.	12.5
Cumulus	0.66-2.70	Heavy	25.0
Cumulus	0.66-2.70	Extreme	75.0

The type of rain drop distribution varies with the rain rate:

- Marshall-Palmer
- Drizzle (Joss and Waldvogel)
- Widespread rain (Joss and Waldvogel)
- Thunderstorm (Joss and Waldvogel)
- Thunderstorm (Sekhon and Srivastava)

Six different snow models are included:

- Needle crystals
- Plain dendritic crystals
- Spatial dendritic crystals
- Powder snow crystals
- Crystal with droplet
- Graupel

Three (3) cirrus cloud models are the LOWTRAN Standard (64  $\mu\text{m}$  mode radius), the LOWTRAN Subvisual (4  $\mu\text{m}$  mode radius), and a model based on the work on Heymsfield, where the particle size distribution and ice content are temperature dependent.

#### 4. BACKGROUND MODELS

The background is defined in MOSART as the object at which the line-of-sight terminates, namely, the terrain, the ocean, or space.

##### 4.1 Terrain

The terrain is defined as the configuration, composition, and representation of the surface of the earth, including its relief, natural features, permanent or semi-permanent man-made features, and related processes. The MOSART code provides a detailed description of the terrain.

##### 4.1.1 Ecosystem Data Base

The Global Ecosystem Data Base consists of the basic information required to construct a terrain composite scene:

- Terrain Altitude (Figure 5)
- Ecosystem Type (Figure 6)
- Fraction Water Cover (Figure 7)

All these parameters are provided at a spatial resolution of 10 arcminutes.

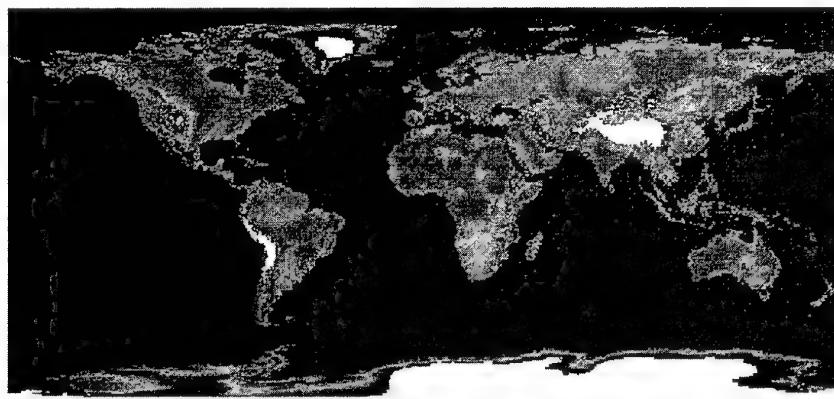


Figure 5. Terrain Altitude [Ref. 11]

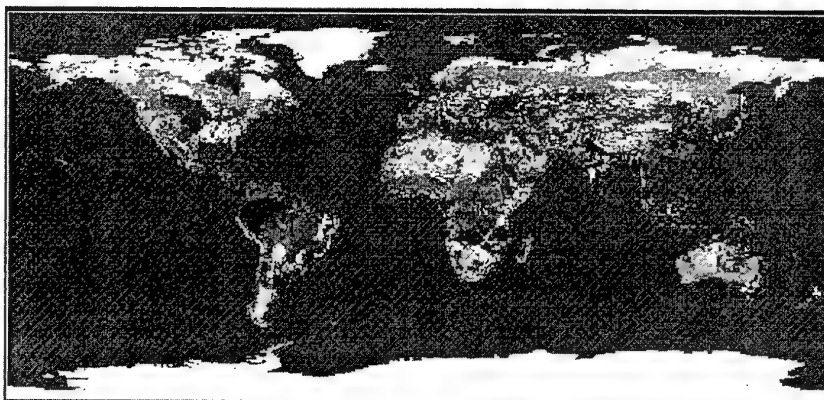


Figure 6. Ecosystem Type [Ref. 11]



Figure 7. Fraction Water Coverage [Ref. 11] Note the dry Northern Africa contrasting with the wet area around the Congo River.

Using this data it is possible to assign a scene type from the library of 39 scene types (see Table 3).

Some of the scene types are geo-specific, while others are geo-typical. However, it is felt that this set of scenes represents a spanning set of scene types for approximating any location on the globe. One element that is still needed is a soil moisture data base.

Although there are approximately 300 urban areas in the MOSART code, it is planned to upgrade this capability, perhaps using something like Figure 8. One deficiency in the current MOSART Terrain/Ecosystem Data Base is the lack of an geospecific soil classification (see Figure 9). This is planned for a future release.

#### 4.1.2 Terrain Materials

The individual terrain materials are represented by their optical parameters (e.g., reflectance, index of refraction) and thermal properties (e.g., specific heat, conductance, characteristic

length). They are shown in Table 4. A user-defined material is also included.

#### 4.1.3 Terrain Temperature Calculations

The MOSART code calculates the terrain surface temperature for each material at the specified time of day in the terrain background scene. The TERTEM utility performs identical calculations for a complete 24-hour diurnal cycle for a user-defined set of altitudes and surface orientations. Temperatures are calculated for materials that are always shadowed from the direct solar loading and for materials that are always under direct solar loading.

Each material is fully defined for the thermal calculations, including:

- Specific heat
- Conductivity
- Characteristic length
- Film coefficient
- Density
- Substructure

Table 3 Scene Types

SCENE TYPE	LOCATION
City/Harbor Land/Sea Interface	San Diego, CA
Arctic Tundra Land/Sea Interface	Pt. Barrow, AK
Forested Low Relief	Wa Wa, Ontario, Canada
Subarctic Rocky Land/Sea Interface	Trondheim, Norway
Forested Terrain/Agricultural	Fulda, Germany
Flat Agricultural	Alberta, Canada
Desert Pavement with Dunes	Imperial Valley, CA
Desert Land/Sea Interface	Salton Sea, CA
Forested Mountains/Cultural	Santa Cruz, CA
Multi-Year Sea Ice	Beaufort Sea
Arctic Mountains with Scrub	Brooks Range, AK
Arctic Tundra with Melt Lakes	Geotypical
Open Ocean/Lake	Geotypical
Mixed Farmland/Orchards	Camarillo, CA
Southern California Land/Sea Interface	Southern California
Tundra (Type No. 1)	Geotypical
Tundra (Type No. 2)	Geotypical
Pine Forest	Geotypical
Mixed Forest/Farmland	Geotypical
Grassland/Savannah	Geotypical
Scrub/Chaparral	Geotypical
Scrub Desert	Geotypical
Urban	Geotypical
Rural Land/Sea Interface	Geotypical
Tropical Forest	Geotypical
Tropical Savannah	Geotypical
Tropical Desert	Geotypical
Tropical Land/Sea Interface	Geotypical
Continental Ice	Geotypical
Urban/Commercial	Geotypical
Urban/Residential	Geotypical
Tilled Soil/Farmland	Geotypical
Iraq and Syria	Iraq and Syria
Iran	Iran
North Korea	North Korea
Pakistan	Pakistan
Kern River, California	Kern River, California
USA (North America)	USA (North America)
Global	Global

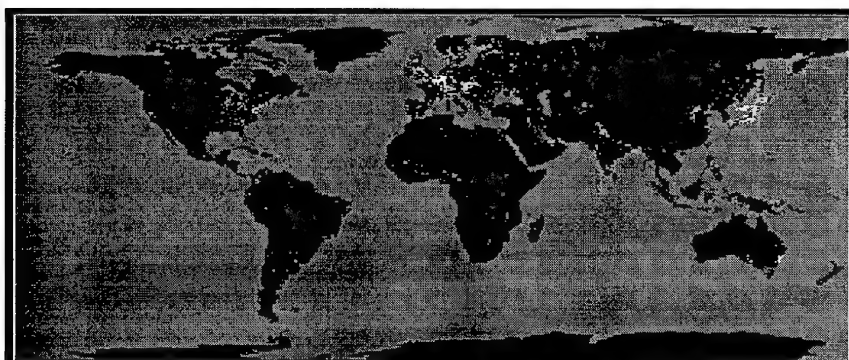


Figure 8. World at Night [Ref. 8]

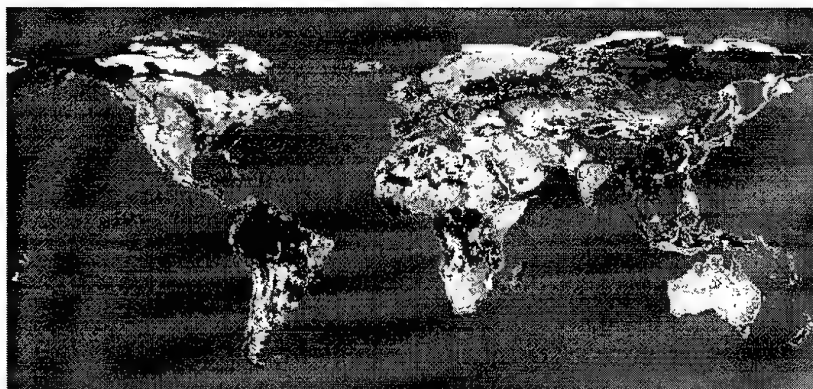


Figure 9. FAO Soil Classification [Ref.11]

Table 4. Terrain Materials

Water	Vegetation	Soil & Rocks
Fresh Water	Dry grass	Packed Soil
Sea Water	MODTRAN Grass	Beach sand
MODTRAN Ocean	MODTRAN Dead Grass	Limestone-Silt-Sand
GENESSIS Water Ocean	MODTRAN Burnt Grass	Limestone-Silt
GENESSIS Water Ocean	Lawn grass	Salt-Silt
First Year Ice	Scrub	Silt-Sand
Multi-Year Ice	Pine Trees	Limestone Rock
Dry Snow	Broadleaf Trees (Summer)	Sandstone Rock
Wet Snow	Broadleaf Trees (Winter)	Varnished Sand
MODTRAN Snow Cover (Fresh)	MODTRAN Forest	Varnished Sandstone
GENESSIS Fresh Snow	MODTRAN Farm	Dry Silt Playa
GENESSIS Old Snow	MODTRAN Maple Leaf	Wet Silt Playa
MODTRAN Cloud Deck		Dry Silt-Salt Flats
	<b>Man-made &amp; Miscellaneous</b>	Wet Silt-Salt Flats
	Blackbody	MODTRAN Desert
	Whitebody	Lake sand
	Still Air	Desert sand
	Asphalt	Black sand
	Concrete	White sand
	Building Roof (Galvanized Iron)	Clay soil
	Block concrete	Loam soil
	Pebbled asphalt	Sandy loam
	Paved concrete	Silty clay
	Black asphalt	Silty loam
	Road gravel	Loamy sand

Using a broad-band atmospheric propagation model that includes multiple scattering due to the percentage cloudiness at three different altitude layers, MOSART determines the solar and thermal loading upon the material.

The other sources of heat flux are:

- Self-emission
- Radiation
- Conductance
- Free convection

- Forced convection
- Evaporation (some materials)

The substructure allows for multiple materials with a film coefficient defined between materials. If an air gap exists between materials, multiple reflections can occur between materials. Also, a simplistic buoyancy model is used for the air gap to allow the hotter air to rise.

Convection is both forced (i.e., wind) and free (i.e., heated air rising). For some materials

(e.g., trees, scrub), a wind profile through the material is assumed. For evaporation, a modified Penman equation is used to obtain the Bowman ratio of sensible (convection) heat to latent heat.

A sample set of calculated terrain temperatures as a function of the time of day is shown in Figure 9, together with some measured temperatures.

#### 4.1.4 Terrain Radiance

For water, snow, and ice materials, the directional emissivity and bidirectional

reflectivity are calculated from spectral indices of refraction, composition (e.g., percentage of water, air, and ice), and roughness specifications. All other materials are represented by a spectral reflectance value that is separated into a directional and a diffuse component for both emissivity and reflectivity.

Using data from geo-specific scenes, each material has a variance and a power spectral density slope associated with it. Therefore, the calculated scene radiances are represented by a

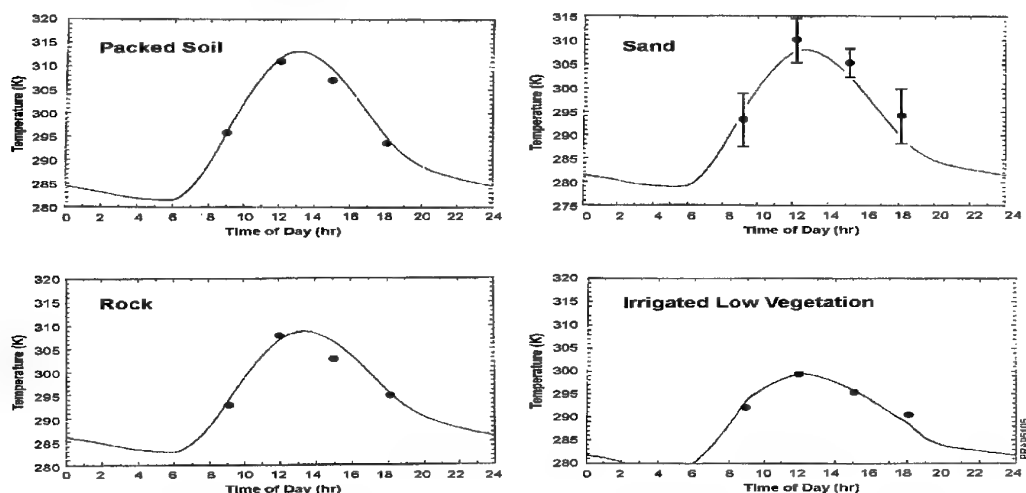
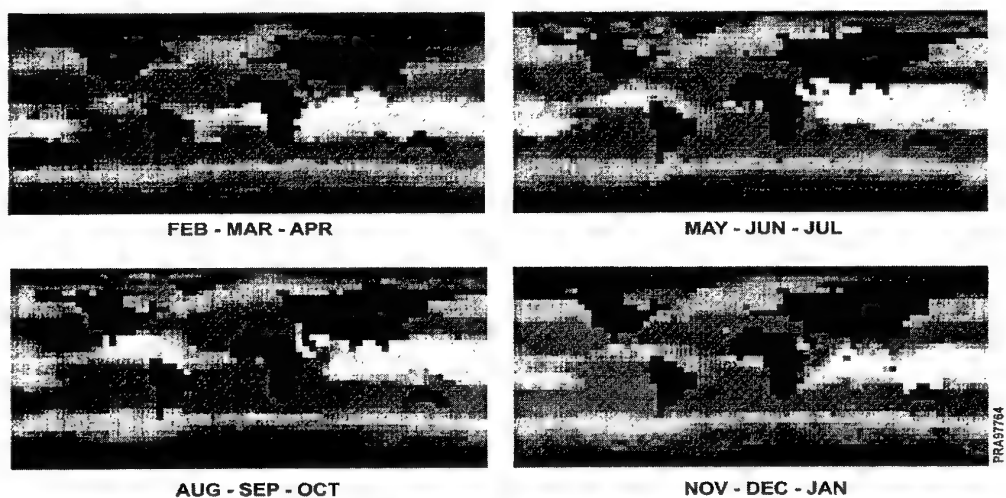


Figure 9. Terrain Material Temperatures. Dots represent measurement points; bars represent variation in measurements. Santa Cruz, CA, 21 September 1982



Ref.: S. Levitus, Climatological Atlas of the World Ocean

Figure 11 Sea Surface Temperature [Ref. 9]



mean value, a standard deviation, and a power spectral density slope.

#### 4.2 Ocean

The ocean background, while treated as part of the terrain insofar as the radiance calculations are concerned, is handled differently with respect to temperature. The sea surface temperature is determined from an internal data base at  $5^\circ$  spatial resolution, as shown in Figure 11.

A  $1^\circ$  spatial resolution data base of maximum and minimum sea ice extents is contained in MOSART for estimating the amount of sea ice present. The sea roughness, which has an impact on the bi-directional reflectance function, is estimated from the local wind speed.

#### 4.3 Space

The space background in MOSART consists of simple models of zodiacal light, mean star radiance, galactic radiance, and extra-galactic radiance.

### 5. GEOMETRY

The viewpath geometries include all MODTRAN geometries, plus some new geometries, including:

- Observer-Source
- Observer-Background
- Observer-Source-Background (for contrast calculations)
- Earthlimb
- Horizontal
- At-Source (i.e., Observer & Source are co-located).

The user can specify a number of different parameters; for example:

- observer altitude, source altitude, and range
- observer and source altitude, latitude, and longitude
- observer altitude, latitude and longitude with the tangent latitude and longitude
- observer altitude, latitude and longitude with the tangent altitude

Any potential geometry is capable of being requested. Since the MOSART code works internally with elevation angle, and MODTRAN users are accustomed to zenith angle, the user can specify either.

### 6. RADIATIVE TRANSFER

Some of the special aspects of the MOSART code and the methods it uses to calculate the equation of radiative transfer are discussed below. All radiative transfer calculations are performed at a user-specified wavenumber or wavelength interval and then degraded to any desired spectral resolution, using either a triangular slit function, a rectangular slit function, or a slit function of the user's design.

#### 6.1 Molecular Band Model

MOSART uses the same  $1\text{ cm}^{-1}$  resolution set of band parameters that is in MODTRAN 3.7. This set of band parameters is derived from the 1997 HITRAN line atlas, including the latest change to partition the  $1\text{ cm}^{-1}$  region into four sections for better representation of the continuum. Based on comparisons with degraded spectral created by the line-by-line code FASCODE, the actual resolution of both MODTRAN and MOSART are slightly greater than  $1\text{ cm}^{-1}$  and are usually advertised as  $2\text{ cm}^{-1}$ . In the UV/ Visible region, MOSART has a few more molecular absorption bands than MODTRAN.

#### 6.2 Layer Model

The uniform layer approach to solving the equation of radiative transfer used in LOWTRAN and early versions of MODTRAN have been replaced by a continuous approximation. The uniform layers are replaced by altitude grid points through which the lines-of-sight are propagated. The equation of radiative transfer is solved assuming that the transmittance along the line-of-sight varies exponentially between grid points. Other atmospheric parameters (e.g., temperature, blackbody radiance, scattered solar radiance) are assume to vary either linearly or exponentially between grid points. This approach to solving the equation of radiative transfer provides more accurate results, particularly for optically thick layers and near-horizontal viewing [Ref. 4].

#### 6.3 Single Scattering Phase Function

An analytic single scattering phase function is used in the multiple scattering calculations and in the single scattering calculations for all aerosols and hydrometeors that are defined in terms of an asymmetry parameter. This phase function is more realistic than the traditional Henyey-Greenstein [Refs. 3 & 5].

#### 6.4 Turbulence

The turbulence parameter,  $C_n^2$ , is included in the MOSART code as an analytic function that can be modified near the surface with a user-supplied value. This profile depends upon the background altitude, the location of the tropopause, and the stratospheric wind speed, along with the surface value of turbulence. The turbulence is used to calculate the scintillation of the source and the background. The scintillation is aperture averaged if the sensor aperture is provided.

The statistical variations in the path radiance are determined by using the turbulence values. The emitted path radiance is calculated by transforming the structure constant of the index of refraction,  $C_n^2$ , to the structure constant of the temperature,  $C_T^2$ . The molecular scattering component can be derived directly from  $C_n^2$ . The aerosol scattering component is derived assuming that the variability in aerosol number density follows the variability in atmospheric density.

#### 6.5 In-scattered Transmittance

Besides calculating the transmittance, in which scattering is considered a loss mechanism, an "in-scattered transmittance" is calculated. In MODTRAN, any scattered transmittance is assumed lost to the observer. However, in the in-scattered transmittance, a first order approximation is made to account for those photons that are scattered into the forward direction, and hence into the sensor's field-of-view and aperture.

#### 6.6 Multiple Scattering

The multiple scattering module uses a multiple-flux technique to account for both solar and lunar irradiances. Thermal fluxes are calculated with a standard two-stream technique. The boundary conditions are defined by the terrain and space radiance models. The band model transmittance curve of growth for molecular transmittance is represented by an exponential sum fit using a Malkmus band model [Ref. 9]

The MOSART code uses an analytic exponential sum fit algorithm (sometimes called a correlated-k method) to more accurately model the multiple scattering.

#### 6.7 Correlated Paths

Whenever two paths need to be combined (e.g., combining the solar-source and observer-source paths to determine the source-reflected solar radiance at the observer's aperture), the

spectral line correlation between the two paths must be considered. MOSART treats all multiple line-of-sight as a "bent path," and the line correlation along each bent path uses the Curtis-Godson approximation

#### 6.8 Comparisons Between MODTRAN and MOSART

As part of the testing of MOSART, comparisons have been made between MODTRAN 3.5-1.2 and MOSART Version 1.50. Figures 12 and 13 show the comparisons for the MODTRAN case1 output and its equivalent MOSART output. The MODTRAN test case, case1, uses the LOWTRAN band model; for this comparison, the test case was changed to use the MODTRAN band model. The difference in the 32,000 to 34,000  $\text{cm}^{-1}$  is due to a difference in the temperature correction of the extinction coefficients for the Hartley-Huggins band of ozone. MOSART has since been updated to agree with the MODTRAN parameters.

Some causes of other differences include:

1. MOSART uses a different altitude grid for integration
2. The two codes use different analytical phase function
3. The two codes use different multiple scattering algorithms

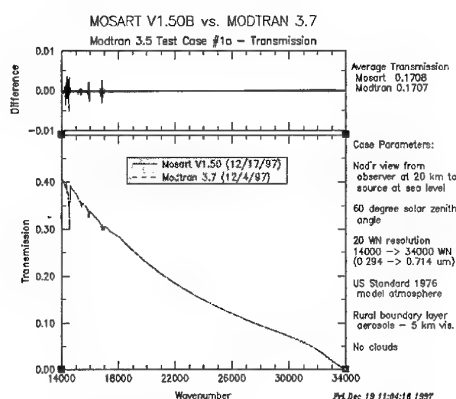


Figure 12. Comparison Between MODTRAN and MOSART Transmittance

#### 7. CODE DESCRIPTION

The MOSART code consists of a main program and several utility programs. The source code, which is written in ANSI X3.9-1978 FORTRAN, consists of over 190,000 lines of code. A C++ "wrapper" and an Input File Building Graphical User Interface (GUI)

are also included. The GUI uses X-Windows and MOTIF.

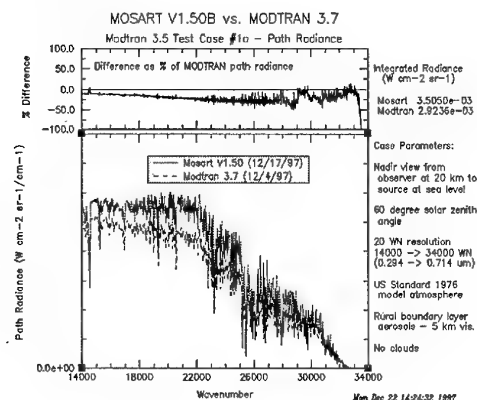


Figure 13. Comparison Between MODTRAN and MOSART Multiple Scattered Path Radiances

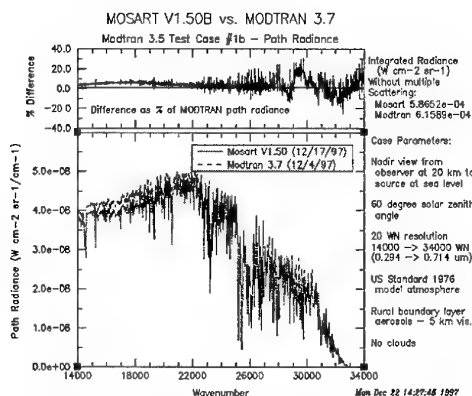


Figure 14. Comparison Between MODTRAN and MOSART Single Scattered Path Radiances

The utilities include:

- Data Base Installation Code
- Floating Point Arithmetic and Machine Parameter Testing Code
- ASCII-Binary File Conversion Code
- Input File Creation Code, Including a MODTRAN-to-MOSART Input File Transformation
- NCAR-based Plotting Program
- Filter Function/Spectral Resolution Convolution Code
- Terrain Material Temperature Model (diurnal, altitude, orientation, and shade)
- Blackbody Temperature Converter
- Visual Conversion Code (radiance to luminance; illumination dependent)

- Facet Signature Code
- Spectral Filter Optimizer
- Statistical Scene Generator

Four (4) data bases are included with the code:

1. MODTRAN 3.7 molecular band parameters
2. Global terrain altitude and terrain classification
3. Global climatology
4. NRL/SAG atmospheric data

MOSART has been installed and tested on a number of machine, including:

- SGI (IRIX)
- Sun (OS & Solaris)
- HP 9000
- Data General
- IBM 3094 (VM/CMS) (Early Version)
- High End PCs (Windows 95 and Windows NT) (Lahey & Microsoft compilers)
- DEC VAX/VMS & Alpha 3000
- Prime (Early Version)

Recommended platforms are workstations (SGI, Sun, HP, DEC Alpha), although it will run on a high end PC (e.g., 200+ MHz, 128 Mb RAM, 100 Mb of free disk space). It has been thoroughly tested on machines that use the IEEE 754 floating point standard (e.g., SGI, Sun, HP), but there may be some minor numerical bugs encountered on VAX/VMS machines due to the hard underflow (i.e., one known case crashed on a VAX but ran on the other IEEE 754-compliant machines; the fix was simple and was purely numerical).

An X-Windows/Motif Input GUI is available, as is a simple scrolling input file builder. However, once the user becomes familiar with the input file structure (it is self-documenting with full text descriptions of the inputs being included in the input file), an editor such as vi or emacs is quite adequate.

To install MOSART (values are for a SGI machine), approximately 100 Mbytes of Disk Space is required, along with a FORTRAN 77 Compiler (ANSI X3.9-1978); libraries satisfying MIL-STD 1753 are helpful, but not necessary. Requirement for X-Windows/MOTIF and the National Center for Atmospheric Research (NCAR) plotting package are optional (for GUI and plotting utility, respectively).

To date, the MOSART code has been utilized by a number of simulations and applications, including:

- Synthetic Scene Generation Model (SSGM) BMDO/NRL/PRA
- Environment Effect in Distributed Interactive Systems (E<sup>2</sup>dis) DMSO/NRL/PRA/SSI
- Flexible Infrared Signature Tools (FIST) RL/NAIC/PRA
- SPIRITS (in development) PL/SSI
- SAMM2 (in planning) PL/SSI
- HYPEX (Hyperspectral Atmospheric Correction) PRA [Ref. 5]
- National Polar-orbiting Operational Environmental Satellite System (NPOESS) Analysis (proposed) (AFRL/SSI)
- Scene Simulators:
  - GENESSIS (PRA)
  - CLDSIM (PRA)
  - GCI Toolkit (PRA)
  - SensorVision (PSI)
  - CloudScape (Visidyne)

One question that a number of users raise is why two codes (i.e., MODTRAN and MOSART) and which one should be used. MODTRAN is a small, efficient code with representative environmental conditions (e.g., six model atmospheres) that performs point-to-point or point-to-space calculations. MODTRAN uses line-of-sight radiative transfer (i.e., a "soda straw" viewpoint). MOSART, on the other hand, has access to

- global environmental conditions and climatologies
- global terrain altitude, scene, and material data bases

and provides output to support scene simulation and signature models. MOSART calculates a comprehensive radiative environment, but is rather large and is not very fast. Each code has its own purpose.

## 8. CODE STATUS

The initial release version of the MOSART code is Version 1.41, which was delivered in September 1995. Version 1.50 was delivered in November 1997. This latest version of MOSART has been approved for public release, distribution unlimited by Air Force Public Affairs and Ballistic Missile Defense Office; release by Air Force Research Laboratory is pending further testing.

The MOSART documentation has been released as PL-TR-94-2244 (4 Volumes) in May 1996. The documentation [Ref.7] consists of:

1. Installation Reference Manual
2. Users' Reference Manual
3. Technical Reference Manual
4. Software Reference Manual
5. Addendum (Dec 1997)

### 8.1 Code Upgrades

As of June 1997, Version 1.41 has undergone significant testing and evaluation by several users, resulting in some general clean-up, "bug" fixes and code modifications, documentation corrections, clarifications (resulting from questions from various users), and an explanation of FTNCHEK warnings. The major upgrades that have been implemented since the initial September 1995 release are:

1. improved layer coupling for the multiple scattering calculations
2. new forward scattering algorithm
3. new terrain temperature algorithm
  - wind and free convection through material (e.g., Grass, Scrub, Tree)
  - transmissive layers
  - air gap
  - multiple reflections
4. modified algorithm for the calculation width
5. User-Defined atmospheres upgraded
6. full MODTRAN 3.6 compatibility (except for DISORT)
7. MOLBMP97 regular molecular and CFCBMP96 heavy molecular data bases
8. adjustable clouds
9. molecular concentration normalization (User-Defined)

### 8.2 Potential Upgrades

Plans are in the works for a release of Version 2.00 in 1998 that will include:

1. atmosphere characterization
  - model-driven & user-defined 3-D atmospheres
  - broken cloud fields
  - global humidity data base
2. diffuse transmission (off-axis, single scatter) through clouds
3. analytic (Robertson) model of skyshine
4. microwave/millimeter wave capability

5. multiple, overlapping sensor response curves
6. higher resolution/expanded terrain material data base
7. global snow cover & sea ice data bases
8. cooling rate calculations
9. more flexible input file structure

Potential future growth may occur in the following areas:

1. DISORT N-stream multiple scattering integration
2. new exponential sum fit (correlated-k) algorithm
3. polarization
4. insertion of user-defined elements (e.g., clouds, smoke)
5. Navy Oceanic Vertical Aerosol Model (NOVAM)
6. interface with weather data bases (e.g., NORAPS, NOGAPS, COAMPS)
7. aerosol mixtures (e.g., smooth altitude transitions)
8. geographical assignment of boundary layer aerosol model, including prevailing winds)
9. integration of non-Lambertian surface reflectance with multiple scattering
10. Cox and Munk treatment of sea surface normals
11. variable spectral gridding
12. incorporation of fast MS correction procedures for 2-stream calculations

This list is not definite, nor is it all inclusive. If you require some additional capabilities, please contact Dr. William M. Cornette (see below).

## 9. OBTAINING THE CODE AND POINTS OF CONTACT

MOSART (both code and documentation) is distributed by the US Government. The first step in obtaining the MOSART code is to download a Non-Disclosure Agreement from the web-site

<<http://www.plh.af.mil/VSBM/index.html>>.

Once the Non-Disclosure Agreement has been completed and submitted, a password will be provided that will allow the user to download (FTP) the MOSART code, along with the documentation in Adobe Reader format. For additional information on obtaining the MOSART code and documentation, please contact:

Dr. Laila S. Jeong (AFRL/VSBM)

(617) 377-3671

jeong@plh.af.mil

For technical information, please contact:

Dr. William M. Cornette (NIMA/TMPO)

(301) 227-3492

CornetteW@nima.mil

Please send all potential "bug" reports, along with sample input and output to:

Ms Sally J. Westmoreland (PRA)

mosart@photon.com

## 10. REFERENCES

1. Anderson, G.P., J.H. Chetwynd, J.-M. Theriault, P. Acharya, A. Berk, D.C. Robertson, F.X. Kneizys, M.L. Hoke, L.W. Abreu, and E.P. Shettle. MODTRAN2: Suitability for Remote Sensing. SPIE Proc. (1968)
2. Cornette, W.M., Atmospheric Propagation and Radiative Transfer (APART) Computer Code. Vol I: Installation Reference Manual (R-024-90), Vol II: User Reference Manual (R-062-90), Vol III: Technical Reference Manual (R-077-90), Vol IV: Software Reference Manual (R-075-90). Photon Research Associates, Inc., 5720 Oberlin Drive, San Diego, CA 92121 (1990)
3. Cornette, W.M. and J.G. Shanks, Physically reasonable analytic expression for the single-scattering phase function. Applied Optics 31, 3152-3160 (1992)
4. Cornette, W.M., Robust algorithm for correcting the layer problem in LOWTRAN. Applied Optics 31, 5767-5769 (1992)
5. Cornette, W.M., P.K. Acharya, and G.P. Anderson, "Using the MOSART Code For Atmospheric Correction." Invited Paper. 1994 International Geoscience and Remote Sensing Symposium Proc. Pp. 215-219 (1994)
6. Cornette, W.M. and J.G. Shanks, Physically reasonable analytic expression for the single-scattering phase function: errata. Applied Optics 34, 641 (1995)
7. Cornette, W.M., P.K. Acharya, D.C. Robertson, and G.P. Anderson, Moderate

Spectral Atmospheric Radiance and Transmittance Code (MOSART). PL-TR-94-2244 (4 Volumes) USAF Phillips Laboratory, Directorate of Geophysics, Hanscom AFB, MA 01731-3010 (1995)

8. Feldman, G.C., Private communication. Created from a mosaic satellite image compiled by W.T. Sullivan III, University of Washington, from satellite photographs acquired by the Defense Meteorological Satellite Program of the U.S. Air Force (1995)
9. Levitus, S., Climatological Atlas of the World Ocean. National Oceanic and Atmospheric Administration Professional Paper 13 (1982)
10. Malkmus, W., Random Lorentz Band Model with Exponentially-Tailed Line-Intensity Distribution Function. J. Opt. Soc. Am. 57, 323-329 (1967)
11. National Geophysical Data Center, Global View, National Oceanic and Atmospheric Administration (1994)

## A comparison of atmospheric transmittance measurements in the 3-5 $\mu\text{m}$ and 8-12 $\mu\text{m}$ spectral regions with MODTRAN: considerations for tropospheric operations requiring long, near-horizontal path geometries

A. J. Ratkowski\*, G. P. Anderson\*, J. H. Chetwynd\*, R. M. Nadile\*, A. D. Devir\*\* and T. D. Conley\*\*\*

(\*) USAF Research Laboratory, Battlespace Environment Division (AFRL/VSB),  
29 Randolph Road, Hanscom AFB, MA 01731-3010, USA

(\*\*) Technion Research and Development Foundation, Electro-Optics Research and  
Development Division (EORD), Technion City, Haifa 32000, Israel

(\*\*\*) Boston College, Institute for Scientific Research, Newton, MA, 02159-1164, USA

### 1. ABSTRACT

Radiance measurements conducted during tropospheric operations to detect objects on the Earth's surface from a manned aircraft or from an unmanned airborne vehicle (UAV) will involve long, near-horizontal viewing geometries. The computer code MODTRAN is widely used for the prediction of the propagation of infrared radiation through the lower atmosphere. Consequently, we have undertaken to test the predictions of MODTRAN for the 3-5 and 8-12 micron spectral regions under mid-Eastern desert conditions.

### 2. MODTRAN

The new MODTRAN4 band model, with its correlated-k Beer's Law algorithm, can efficiently and correctly (usually within 3-5%) calculate the scattering and absorption properties of realistic molecular, aerosol and cloudy environments in the lower and middle atmosphere. The current approach for molecular scattering accommodates line overlap and partial correlations between both molecular species and the solar irradiance, while maintaining automated band model spectral resolution at 2 or 15  $\text{cm}^{-1}$ . This new level of evolution and validation will permit improved syntheses and analyses of solar (direct or scattered) and thermal energy as observed from a variety of platforms. This capability is a product of the standard MODTRAN calculations of transmittance, radiance and irradiance, including thermal, solar and lunar sources.

Comprehensive validation is provided through two basic avenues. The first involves direct comparisons with line-by-line (LBL) calculations, as exemplified by FASE (the LBL

algorithm jointly developed from FASCODE1 by DoD and DOE) which provides the molecular standard for layer-effective optical depths, single-scattering albedos, and transmittances. This enables the MODTRAN4 algorithm to be refined for more adaptable spectral resolution plus efficient determination of those layer quantities necessary for multiple-scattering applications, (DISORT2, for example). The second validation step centers on comparisons with a variety of measurements. Among the latter are ground-based measurements of atmospheric transmission using the sun as a source in the SWIR (3-5  $\mu\text{m}$ ) and LWIR (8-12  $\mu\text{m}$ ); examples for such validation are presented here.

With the development of MODTRAN4<sup>3,4</sup>, a flexible tool for radiative energy budget calculations is now available. While this version of MODTRAN is grounded in the prior series of USAF radiative-transfer low-resolution band-model (BM) algorithms<sup>5-7</sup> and moderate-resolution BM algorithms<sup>8-10</sup>, it is distinct in its ability to employ Beer's law to describe local-layer, species-specific transmittance for input to the radiance calculations. While this capability is not always necessary, it allows appropriate handling of multiple scattering (MS) using existing non-BM algorithms<sup>2,11</sup>. MODTRAN4, while maintaining the basic 2  $\text{cm}^{-1}$  spectral resolution, can now complement the MS routines by introducing a correlated-k (CK) capability which is compatible with Beer's law formulations. MODTRAN4 also provides greatly improved predictive capabilities under cloudy and/or heavy aerosol loading conditions in both the visible and IR. It allows the explicit definition of water and ice cloud vertical profiles

and spectral data, either by scaling and combining default model clouds or by redefining entirely new model clouds with micro-layering options. More information on MODTRAN4 and its beta release has already been presented<sup>12</sup>. Significant changes have been made in MODTRAN4 to the models of the H<sub>2</sub>O continuum, the N<sub>2</sub> pressure-induced continuum, the radiance algorithms, and the band models. Calculations in the IR, when compared to both measurement<sup>13</sup> and to LBL calculations, usually fall within 5% for all spectral ranges, even at relatively high spectral resolution (less than 5 cm<sup>-1</sup>, for example).

### 3. MEASUREMENTS

As noted above, comparisons with measurements are a required validation step. In this paper we compare MODTRAN4 predictions with atmospheric transmittance measurements made from Mount Miron at an altitude of 1200m using the rising Sun as a source<sup>14</sup>. Accurate radiometric measurements of the Sun were performed for long, near-horizontal-paths. Measurements of atmospheric profiles of pressure, temperature, water vapor density (in gr/m<sup>3</sup>) along the path are highly desired for the interpretation of such radiometric measurements. The theoretical calculations in this paper employ radiosonde data obtained from the Israeli Meteorological Service to specify the pressure, temperature and relative humidity (or water vapor density) of the different atmospheric layers. In the absence of a complete *in situ* sonde measurements (since the sonde profiles were not intersected by the spectroradiometer's line of sight), the sonde profile was modified: this modification was based on the results of a sensitivity analysis of the climatology of the desert atmosphere - an analysis which was conducted to assess the importance of variations in temperature, pressure and water density along long optical paths<sup>14</sup>. This sensitivity study indicated that the temperature profiles of four different months, for altitudes up to 11km, can be approximated by a single profile shifted by a constant temperature difference, as is shown in Figure 1. In the same way, the study indicated that the profiles of the water vapor density (in gr/m<sup>3</sup>) of four different months for altitudes up to 11 km can be approximated by a single profile that is shifted by a constant multiplicative factor, as is shown in Figure 2. A similar (but almost negligible) multiplicative factor is also used for shifting the respective pressure profiles. Following these models, the sonde temperature and water vapor density data were corrected by clamping their profiles to the ground temperature

and to the water vapor density conditions that were measured on the ground at an altitude of 1200 m. This kind of scaling was found to be within a few percent of the actual measured values. The visibility was measured with a VF-500 visibility sensor (HSS, Inc.). The values of the visibility were found to vary between 35 km and 45 km during the field test, and were consistent with the observed values (as evaluated by a trained observer) for that day. A rural aerosol model was used since the wind speed was too low to use a desert model and since the values of the visibility confirmed this model.

The actual measurement technique employs the sun as a 5900 K blackbody source for transmittance measurements conducted in a near-horizontal, long-slant-path geometry. The measurements were conducted with a dual-channel spectroradiometer with an aperture of 20 cm and a field of view (FOV) of 2 mrad. A circular-variable filter (CVF) with spectral resolution of 4% of the transmitted wavelength covering the spectral regions from 2.8 to 5.6  $\mu\text{m}$  and from 6.9 to 13.8  $\mu\text{m}$  was employed to measure the transmitted solar spectral radiance. A dichroic mirror separated these two spectral regions to two separate InSb and MCT detectors. The center of the FOV was aligned with a precise theodolite and the spectral measurements were performed at predetermined zenith angles, when the FOV was filled by the disc of the Sun. After each measurement of the Sun, the FOV was aimed outside the Sun's disc to check for scattered radiation. The scattered IR radiation was negligible in comparison to the direct Sun radiation. The same can be said about the effect of the radiation from the internal blackbody of the radiometer and the calculated path radiance. The measured transmittance values were obtained from a comparison between the radiometric signal of the sun and that of a 1273 K blackbody source. Additional details on the experiment and the measurements can be found in the literature<sup>14</sup>.

### 4. CALCULATED RESULTS

The measurements reported earlier<sup>14</sup> were for 11 different solar elevations: 0°, 1°, 2°, 4°, 6° (90° is the zenith angle). In this paper, the results for four solar elevations (1°, 2°, 8° and 30°) will be reported. Initial calculations were based on the predictions of the old (and now obsolete) LOWTRAN7 code. The predicted transmittance values were convolved to match the slit-response-function of the CVF used for



wavelength dispersion of the measured spectral data. It should be noted that MODTRAN4 has a new capability to register the calculations in wavelength with wavelength-driven scanning and/or filter functions. The earlier predicted transmittance values (after the above mentioned convolution) indicated that, especially for very low observing angles ( $1^\circ$  and  $2^\circ$ ), the spectral match between the measured data and a LOWTRAN7 calculation, was not good. This discrepancy is more pronounced when the shape factor in the  $3\text{--}5\text{ }\mu\text{m}$  spectral region is considered. However, there is now an excellent agreement in this spectral region when the data is compared with MODTRAN4, as shown in Figures 3 and 4. Similar agreement was obtained for moderate and high solar elevation angles ( $8^\circ$  and  $30^\circ$ ), as is shown in Figures 5 and 6.

The differences between the experimental data and the predictions of MODTRAN4 in the  $8\text{--}12\text{ }\mu\text{m}$  spectral region at very low observing angles ( $1^\circ$  and  $2^\circ$ ) remain in the shape of the predicted spectra. The differences are more pronounced with respect to the relative magnitudes of the two transmittance peaks, at  $8.5\text{ }\mu\text{m}$  and at  $10.5\text{ }\mu\text{m}$ . These feature differences still appear in the MODTRAN4 calculations and require further investigation, as can be seen from Figures 7 and 8. However, the growth rate of the measured transmittance at high solar elevation angles ( $8^\circ$  and  $30^\circ$ ) is in excellent agreement with the measurements, as shown in Figures 9 and 10. It should be noted that the  $8\text{--}12\text{ }\mu\text{m}$  spectral region is very sensitive to changes in the water density - changes that can occur in the lower layers of the atmosphere at very long distance from the radiometer, especially for nearly horizontal optical paths.

## 5. CONCLUSIONS

This paper compares experimental measurements (in geometries of interest to the UAV or manned-aircraft communities) with calculations using the latest version of MODTRAN. Previous results indicate a strong dependence of the spectral features of signatures transmitted through the lower atmosphere on the aerosol and on the water vapor content. We plan to conduct sensitivity studies to address their relative importance.

## 6. REFERENCES

1. S.A. Clough, F. X. Kneizys, G. T. Anderson, E. P. Shettle, J. H. Chetwynd, L. W. Abreu, and L. A. Hall, "FASCOD3 spectral simulation" Proceedings of the International Radiation Symposium 1988, Lenoble and Geleyn, Deepak Publishing.
2. K.S. Stamnes, S. C. Tsay, W. J. Wiscombe, and K. Jayaweera, "Numerically stable algorithm for Discrete-Ordinate-Method Radiative Transfer in multiple scattering and emitting layered media", *Appl. Optics*, 27, pp. 2502-2509, 1988.
3. L.S. Bernstein, A. Berk, D. C. Robertson, P. K. Acharya, G. P. Anderson, and J. H. Chetwynd, "Addition of a correlated-k capability to MODTRAN," Proceeding of the 1996 IRIS Targets, Backgrounds, and Discrimination Meeting, 1996.
4. L.S. Bernstein, A. Berk, P.K. Acharya, D.C. Robertson, G.P. Anderson, J.H. Chetwynd and L.M. Kimball, "Very narrow band model calculations of atmospheric fluxes and cooling rates using the MODTRAN code", *J. Atm. Sci.*, 53, pp. 2887-2904, 1996.
5. F.X. Kneizys, E.P. Shettle, W.O. Gallery, J.H. Chetwynd, L.W. Abreu, J.E.A. Selby, R.W. Fenn and R.A. McClatchey, "Atmospheric Transmittance/Radiance: Computer Code LOWTRAN 5", AFGL-TR-80-0067, AD A058643, 1980.
6. F.X. Kneizys, E.P. Shettle, W.O. Gallery, J.H. Chetwynd, L.W. Abreu, J.E.A. Selby, S.A. Clough and R.W. Fenn, "Atmospheric Transmittance/Radiance: Computer Code LOWTRAN 6", AFGL-TR-83-0187, AD A137796, 1983.
7. F.X. Kneizys, E.P. Shettle, J.H. Chetwynd, L.W. Abreu, G.P. Anderson, W.O. Gallery, J.E.A. Selby and S.A. Clough, "Users Guide to LOWTRAN 7", AFGL-TR-88-0177, 1988.
8. A. Berk, L. S. Bernstein, and D. C. Robertson, "MODTRAN: A Moderate Resolution Model for LOWTRAN7", GL-TR-89-0122, Air Force Geophysics Lab., Hanscom AFB, MA, 1989.
9. F.X. Kneizys, M.L. Hoke, L.W. Abreu, E.P. Shettle, "MODTRAN2: Suitability for remote sensing", *Proc. SPIE*, 1954, Remote Sensing, 1993.
10. A. Berk, "Upgrades to the MODTRAN layer cloud/rain models," Report. SSI-SR-56,

Spectral Sciences, Inc., 99 S. Bedford St., Burlington, MA, 1995.

11. R.G. Isaacs, W. C. Wang, R. D. Worsham, and S. Goldenberg, "Multiple-scattering LOWTRAN and FASCODE models", Appl. Optics, 26, pp. 1272-1281, 1987.

12. G.P. Anderson, J.H. Chetwynd, A. Berk, L.S. Bernstein and P.K. Acharya, "An algorithm for hyperspectral remote sensing: solar and thermal regimes", Optical Society of America, Proceedings of Optical Remote Sensing of the Atmosphere, Sante Fe, February 10-14, 1997.

13. J. Wang, G.P. Anderson, H.E. Revercomb and R.O. Knuteson, "Validation of FASCOD3 and MODTRAN3: Comparison of model calculations with ground-based and airborne interferometer observations under clear-sky conditions", Appl. Optics, 35, pp. 6028-6039, 1996.

14. A.D. Devir, N. Brandman, B. Barzilai and A. Ben-Shalom, "Ground-to-space atmospheric transmittance measurements in the 3-5  $\mu\text{m}$  and 8-12  $\mu\text{m}$  spectral regions: comparisons with LOWTRAN7", SPIE, 1971, Proceedings of the 8th Meeting on Optical Engineering in Israel, pp. 35-49, 1992.

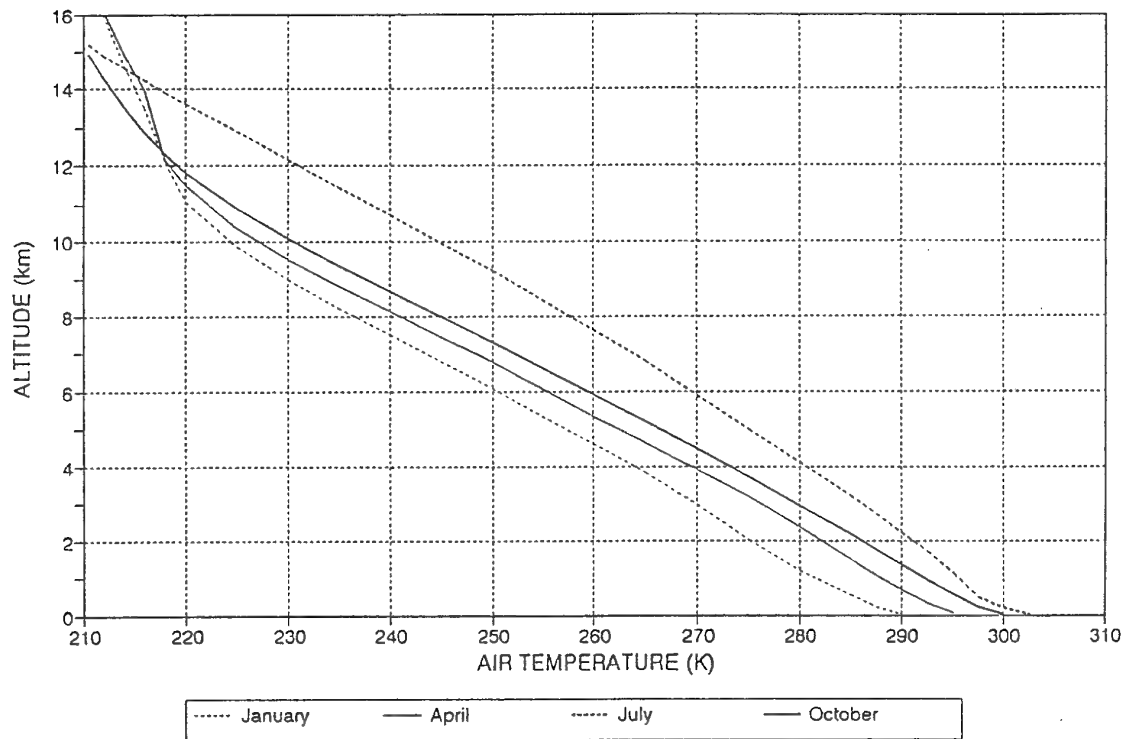


Figure 1: The altitude dependence of day-time temperature profile for four different months.

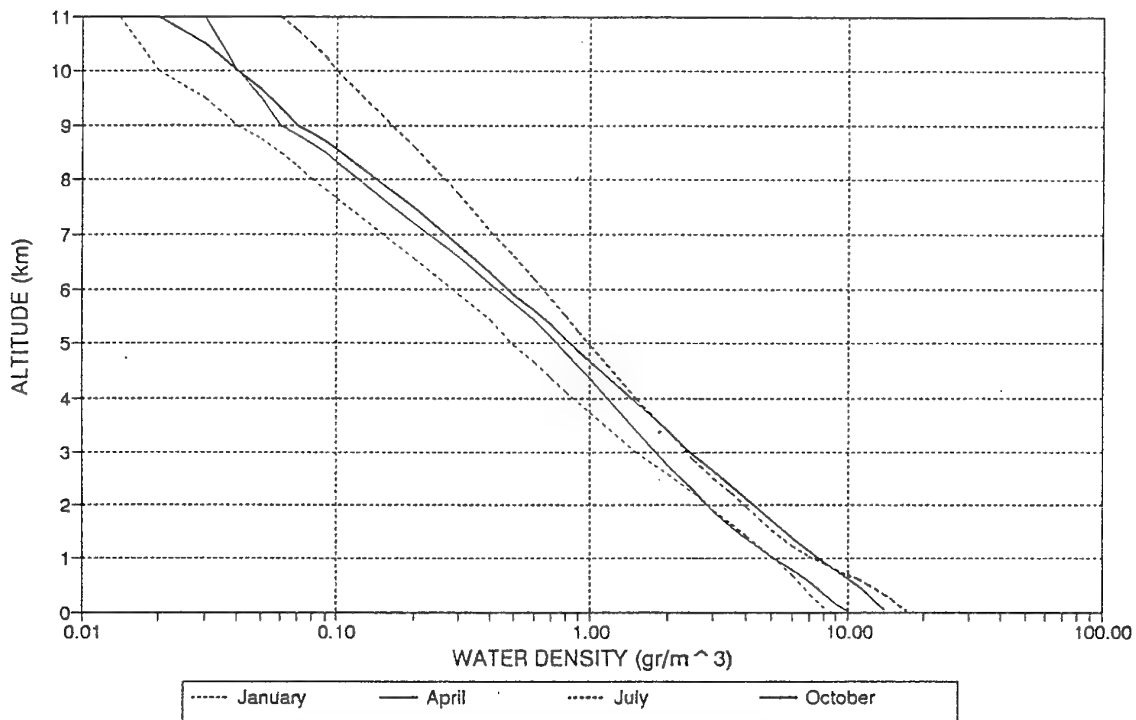


Figure 2: The altitude dependence of day-time water vapor density (gr/m<sup>3</sup>) profile for four different months.

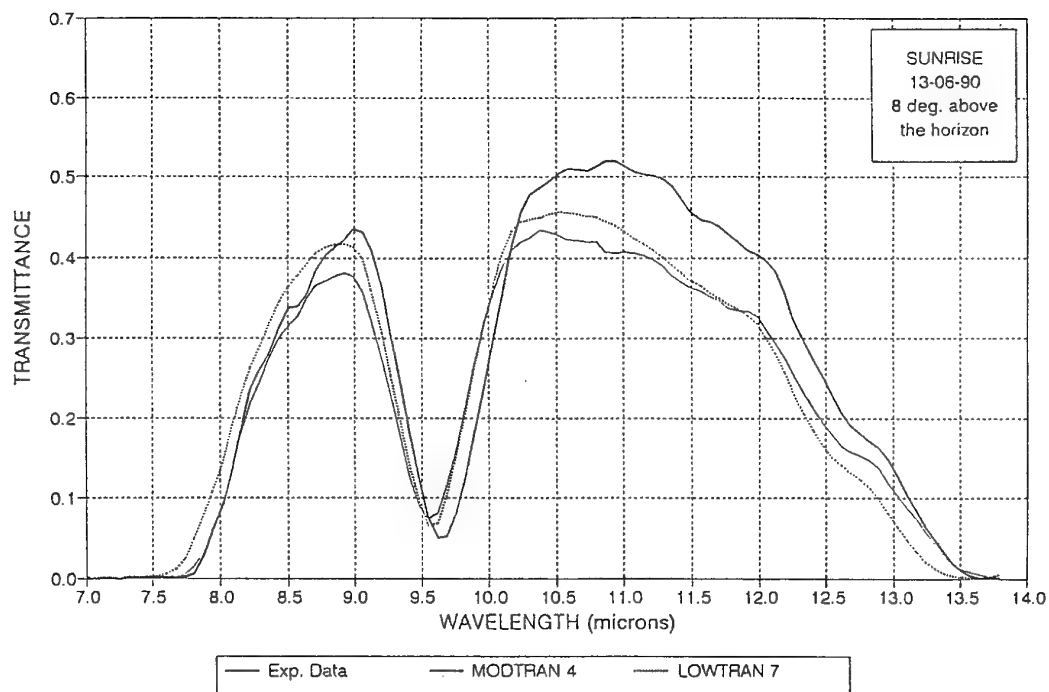


Figure 9: Predicted and measured atmospheric transmittance in the 8-12 $\mu$ m spectral region for 8° ground-to-space slant path.

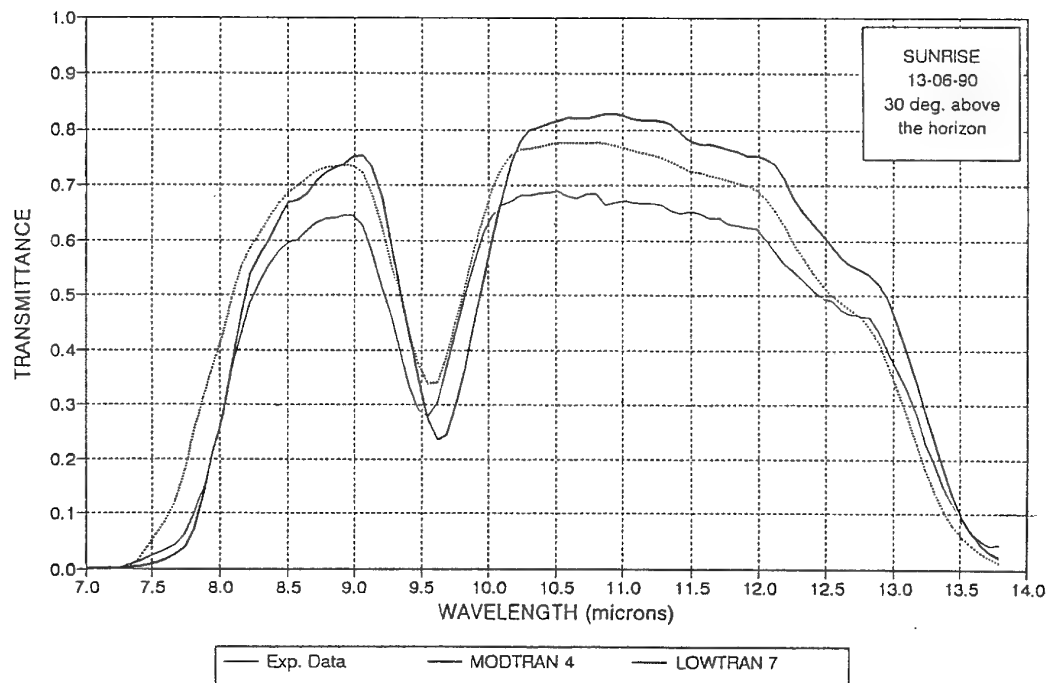


Figure 10: Predicted and measured atmospheric transmittance in the 8-12 $\mu$ m spectral region for 30° ground-to-space slant path

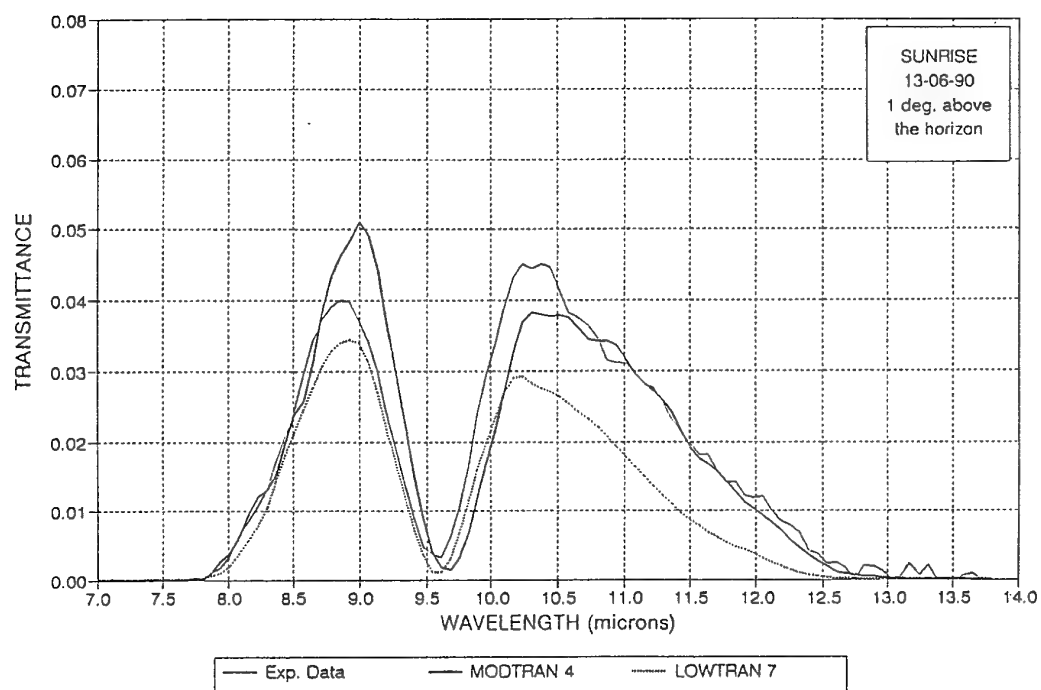


Figure 7: Predicted and measured atmospheric transmittance in the 8-12 $\mu$ m spectral region for 1° ground-to-space slant path.

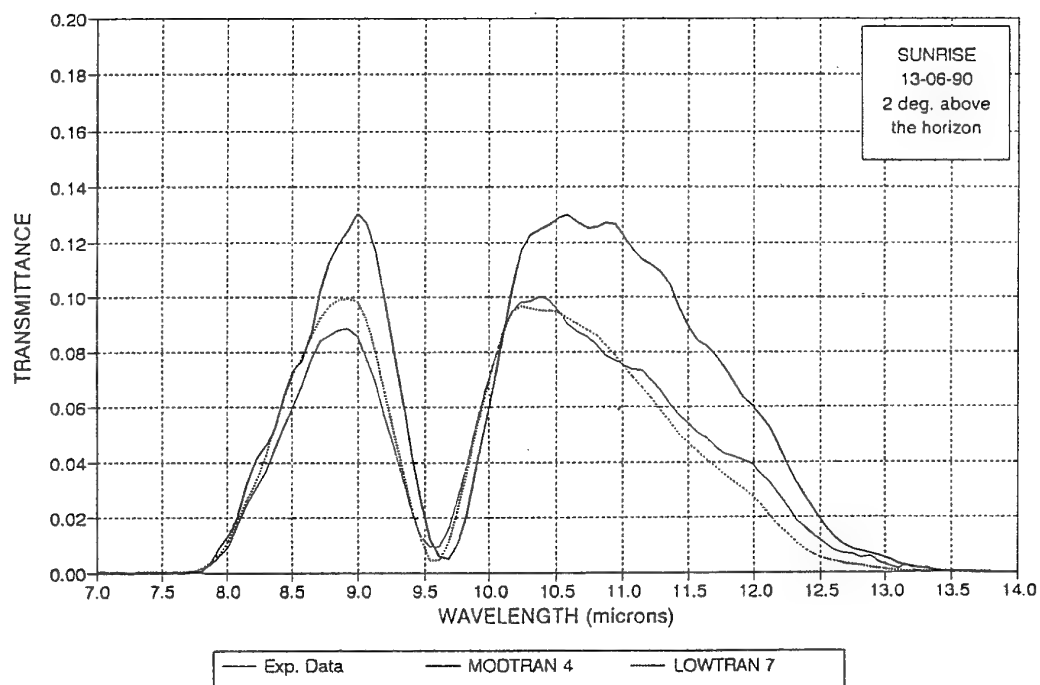


Figure 8: Predicted and measured atmospheric transmittance in the 8-12 $\mu$ m spectral region for 2° ground-to-space slant path.

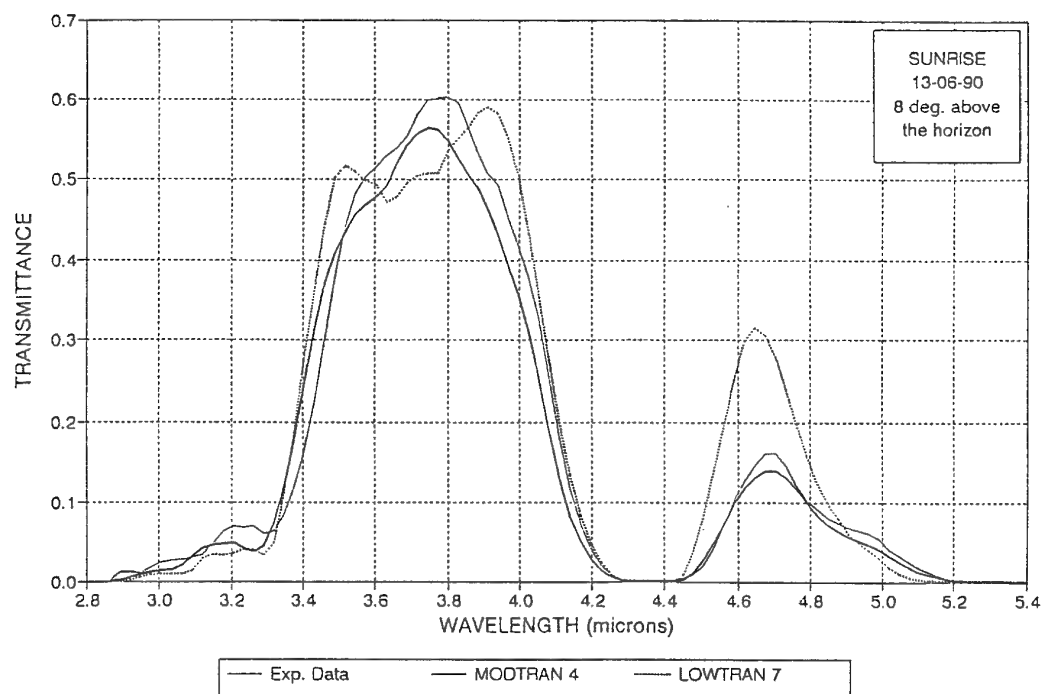


Figure 5: Predicted and measured atmospheric transmittance in the 3-5 $\mu$ m spectral region for 8° ground-to-space slant path.

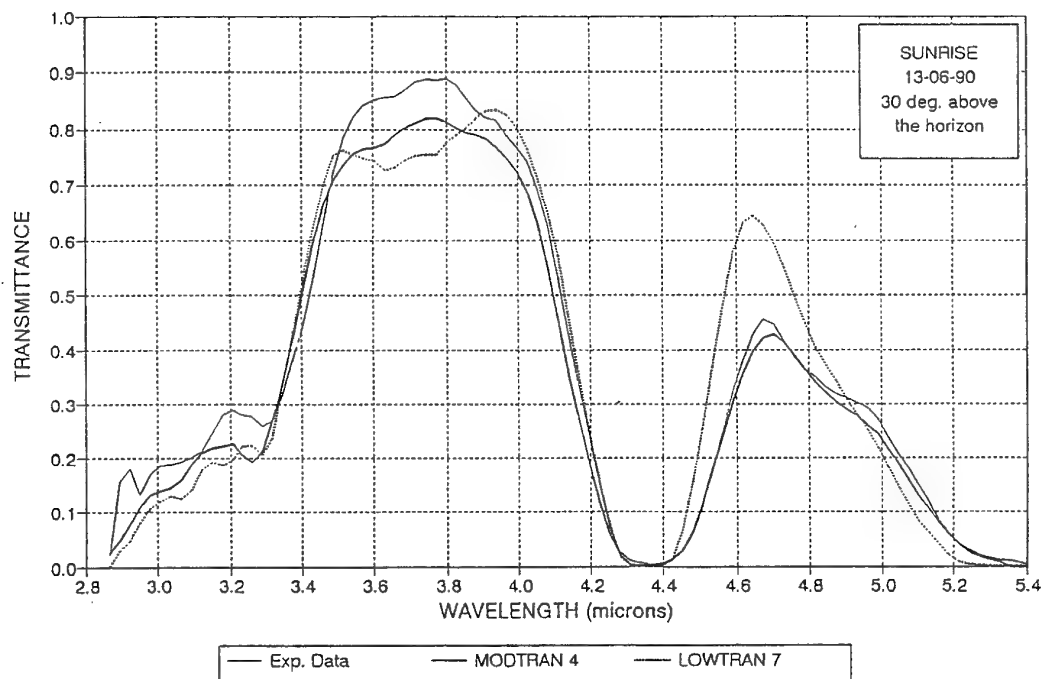


Figure 6: Predicted and measured atmospheric transmittance in the 3-5 $\mu$ m spectral region for 30° ground-to-space slant path.

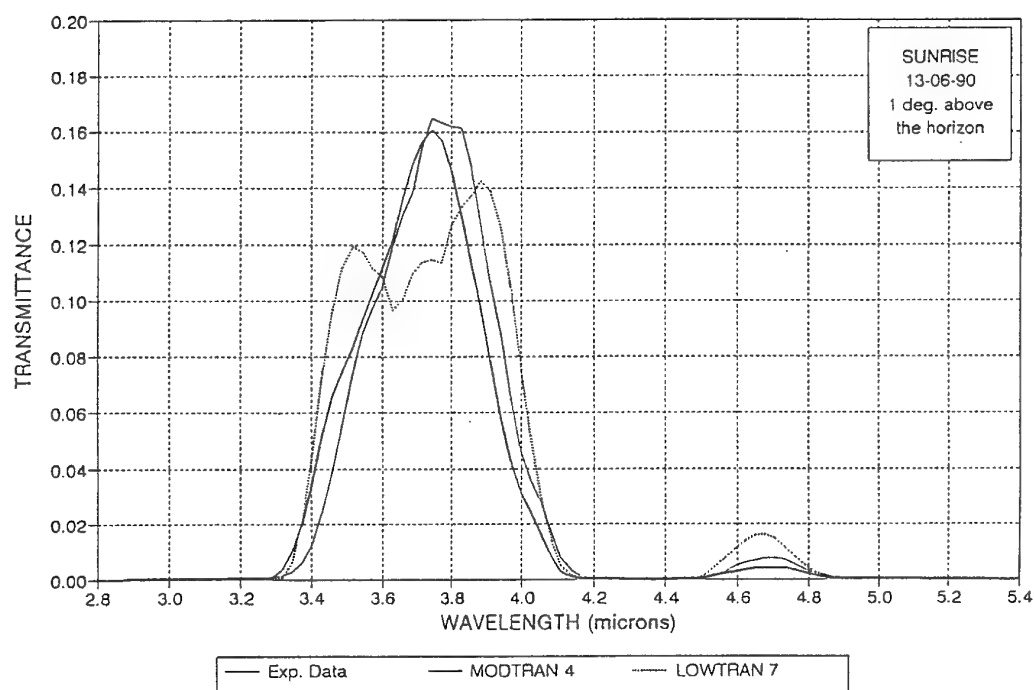


Figure 3: Predicted and measured atmospheric transmittance in the 3-5 $\mu$ m spectral region for 1° ground-to-space slant path.

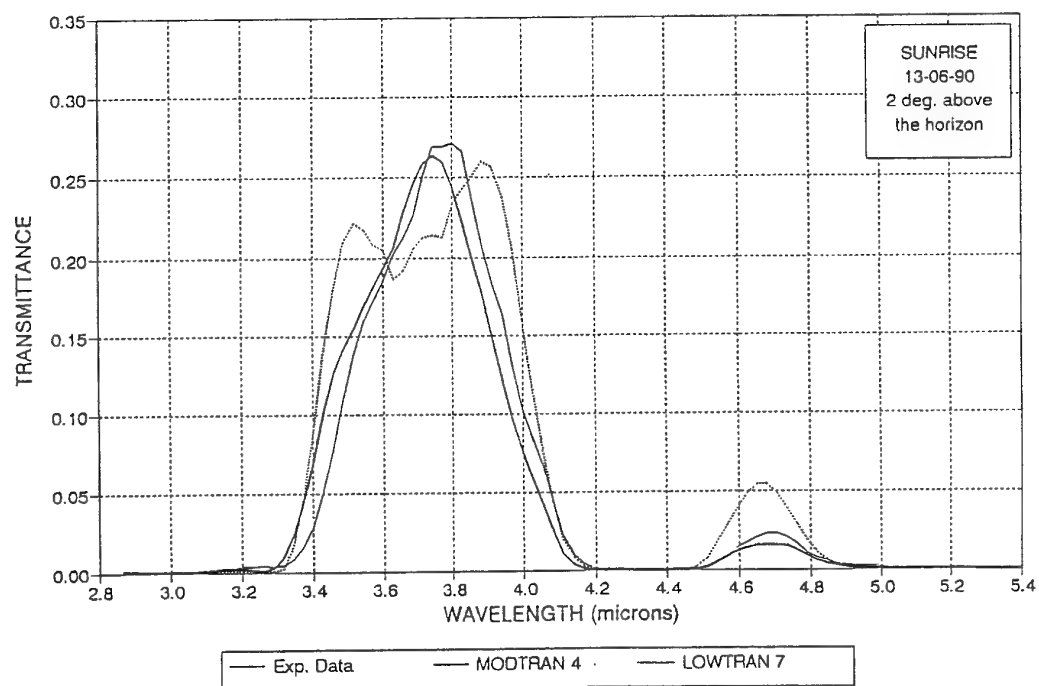


Figure 4: Predicted and measured atmospheric transmittance in the 3-5 $\mu$ m spectral region for 2° ground-to-space slant path.

# EFFETS DE LA REFRACTION ATMOSPHERIQUE SUR LA PROPAGATION INFRAROUGE DANS LA BASSE ATMOSPHERE MARINE COMPARAISON DES MODELES SEACLUSE ET PIRAM.

**J. CLAVERIE**

Ecoles Militaires de Coëtquidan - CREC - 56381 GUER CEDEX - FRANCE.

**B. TRANCHANT, P. MESTAYER**

CNRS - Ecole Centrale de Nantes - 44321 NANTES CEDEX 3 - FRANCE.

**A.M. J. VAN EIJK**

FEL TNO - P. O. Box 96864 - 2509 JG THE HAGUE - THE NETHERLANDS.

**Y. HURTAUD**

CELAR - 35174 BRUZ CEDEX - France

## SOMMAIRE

Dans la Couche de Surface Atmosphérique Marine, la réfraction atmosphérique conduit notamment, aux longueurs d'onde optiques (visible et infrarouge) à des diminutions de portées des systèmes. Ces phénomènes peuvent être décrits en associant un programme de tracé de rayons à un modèle d'indice de réfraction dans la CSAM. Deux modèles sont décrits dans cet article :

- le modèle PIRAM basé sur une méthode *bulk* classique,

- le modèle SeaCluse qui analyse finement les interactions aérosols-atmosphère en présence de vagues, ce qui lui permet de calculer également les profils de concentration aérosolaire dans la CSAM.

A partir des données expérimentales de l'expérience MAPTIP, on peut conclure globalement que :

- les 2 modèles présentés, malgré leurs natures et objectifs différents, conduisent à des résultats en bon accord global avec les observations.

- faute de données suffisantes, les profils calculés par SeaCluse, ne sont pas encore optimisés pour les tous premiers mètres d'altitude.

## INTRODUCTION

Les performances des systèmes infrarouges de détection, de d'observation et de veille fonctionnant à proximité immédiate de la surface de la mer sont étroitement dépendants des conditions de propagation. La portée maximale de ces systèmes dépend du profil vertical d'indice de réfraction de l'air dans les premières dizaines de mètres d'altitude qui constituent la Couche de Surface Atmosphérique Marine, notée CSAM par la suite. Dans des conditions de plein océan, on pourrait penser que l'atmosphère est quasi neutre, et se contenter d'utiliser, pour la propagation des ondes aux fréquences optiques, un modèle d'atmosphère standard. Cependant, au voisinage des

côtes, mais pas seulement, on rencontre des situations atmosphériques très instables (le température de l'air est inférieure de plusieurs °C à celle de l'eau). On enregistre alors une réduction très sensible de l'horizon optique, ainsi que l'apparition de zones de mirages. Ces phénomènes peuvent conduire à une interprétation erronée des informations délivrées par les capteurs optiques.

Les profils d'indice de réfraction calculés par les méthodes *bulk* classiques rendent bien compte de ces aléas de propagation, liés aux conditions de réfraction de grande échelle. Néanmoins, la propagation infrarouge dépend également de l'extinction moléculaire (absorption par la vapeur d'eau et le dioxyde de carbone) et de l'extinction aérosolaire causée notamment, pour le milieu marin, par les gouttelettes d'eau éjectées par les vagues. De plus, dans les cas de vent fort, le champ de vagues modifie sensiblement les profils de température et d'humidité aux très basses altitudes, par rapport à ceux calculés par les méthodes *bulk* classiques. Afin d'essayer de décrire aussi finement que possible l'ensemble de ces interactions, une coopération entre l'Ecole Centrale de Nantes (France) et le FEL-TNO (Pays-Bas) a permis le récent développement du modèle SeaCluse.

Dans cet article, nous nous proposons de comparer les prédictions, vis à vis de la réfraction uniquement, déduites du modèle SeaCluse à celles du modèle PIRAM, développé aux Ecoles Militaires de Coëtquidan (France) et mettant en œuvre une méthode *bulk* classique.

Dans une première partie, nous rappellerons brièvement la nature des principaux effets de réfraction dans la CSAM. Nous donnerons ensuite les caractéristiques essentielles du modèle PIRAM (partie 2), avant de décrire les spécificités du modèle SeaCluse (partie 3). Les données expérimentales utilisées dans cet article, issues de l'expérience MAPTIP, réalisée aux Pays-Bas durant l'automne 1993, à l'initiative du groupe OTAN AC243/RSG 8 seront présentées dans la partie 4. La comparaison des 2



modèles étudiés, tant sur le plan des profils verticaux calculés, que sur leurs conséquences en terme de calcul d'horizons optiques ou de zones de dédoublements, fera l'objet de la partie 5.

## 1. EFFETS DE LA REFRACTION DANS LA CSAM.

Dans un milieu stratifié, la prédiction des phénomènes de réfraction est liée à la connaissance du profil vertical d'indice de réfraction  $n(z)$ ,  $z$  désignant l'altitude. Au voisinage du sol  $n$  est voisin de 1, aussi on utilise plus volontiers le coïndice de réfraction  $N$  défini par :

$$N = (n-1) \cdot 10^6 \quad (1)$$

Il est également commode d'employer le module de réfraction  $M$  donné par :

$$M = 10^6 \left( n - 1 + \frac{z}{a} \right) \approx N + 0,157z \quad (2)$$

où  $a$  désigne le rayon de la Terre ( $a \approx 6371$  km).

Aux longueurs d'onde optiques, le coïndice  $N$  est relié à la pression atmosphérique  $p$  (en HPa), à la température thermodynamique  $T$  (en K) et à l'humidité spécifique  $q$  (en kg/kg) par :

$$N = \frac{p}{T(1+\alpha q)} \left[ A(1-q) + \frac{Bq}{\mu} \right] \quad (3)$$

avec  $\alpha \approx 0,608$  et  $\mu \approx 0,622$ .

Les valeurs de  $A$  et  $B$  dépendent de la longueur d'onde  $\lambda$ . En adoptant la démarche suivie par FORAND [1], on peut assimiler  $A$  et  $B$  à des constantes pour chacune des principales fenêtres de transmission atmosphérique. Les valeurs utilisées pour ces coefficients  $A$  et  $B$  sont résumées dans le tableau 1 ci-après.

Domaine spectral	$\lambda$ ( $\mu\text{m}$ )	$A$ (K/HPa)	$B$ (K/HPa)
Visible	0,4 – 1,0	78,5	67,0
IR proche	1,0 – 3,0	77,7	65,5
IR moyen	3,0 – 5,0	77,5	65,0
IR lointain	8,0 – 12,0	77,5	40,0

Tableau 1 : Valeurs des Coefficients  $A$  et  $B$  en fonction de la longueur d'onde.

On peut constater, d'une part, que les valeurs numériques de ces coefficients sont très voisines, mis à part pour l'IR lointain. Mais, d'autre part, à ces longueurs d'onde et contrairement au cas des radiofréquences, l'humidité n'intervient que pour 2 à 3 % de la valeur totale de l'indice. Comme le profil vertical de pression atmosphérique est quasiment linéaire dans la CSAM, le profil d'indice de réfraction est essentiellement lié au profil de température. De fait, pour les longueurs d'onde évoquées dans le tableau 1, le milieu, vis à vis de la réfraction, n'est quasiment pas dispersif. Les conclusions obtenues à partir de mesures et/ou modèles concernant le domaine visible peuvent donc facilement s'étendre à l'infrarouge.

La trajectoire des rayons optiques dépend du gradient vertical de l'indice de réfraction. L'atmosphère standard est caractérisé par un gradient  $\frac{dM}{dz} = 132$  M/km. Cependant, dans la CSAM, le profil vertical d'indice de réfraction est rarement standard. Selon la stabilité atmosphérique, 3 cas sont possibles :

- atmosphère neutre ou quasi-neutre.

Les températures de l'air et de la mer sont alors voisines (écart inférieur à 0,5 °C). Le profil d'indice de réfraction est proche du profil standard. L'horizon optique n'est que légèrement modifié par rapport au cas standard.

- atmosphère instable.

La température de l'air est alors inférieure à la température de l'eau. Le gradient vertical d'indice est supérieur au gradient standard, surtout au proche voisinage de l'interface air-mer. La courbure des rayons est alors accentuée vers le haut. On est alors dans une situation d'infraréfraction caractérisée par un horizon optique réduit.

Pour une source placée en deçà de cet horizon, tout en étant proche, le profil d'indice de réfraction génère une situation de double trajet entre la source et le point d'observation. La source est vue sous deux élévations distinctes. Il y a donc dédoublement ; on parle encore d'une zone de mirage.

- atmosphère stable.

La température de l'air est alors supérieure à la température de l'eau. Cette situation est propice à l'existence d'un conduit de guidage des ondes optiques (cas de supraréfraction), dont la hauteur atteint au plus quelques mètres. Une source située au-delà de l'horizon standard, mais à l'intérieur du conduit peut malgré tout être observée. Parallèlement, le conduit est surmonté d'une zone d'ombre. Nous ne traiterons pas ces cas stables par la suite car nous ne disposons pas de données complètes pour les analyser. De plus leur modélisation reste très délicate du point de vue météorologique.

Cette brève description appelle deux remarques :

- Dans la CSAM, les conduits pour les fréquences optiques n'existent que dans les cas stables (peu fréquents en pleine mer) et sont de hauteurs faibles, contrairement au cas des radiofréquences où l'existence d'un conduit d'évaporation est quasi permanente, sauf pour les cas très stables où il existe de l'infraréfraction. En optique l'infraréfraction existe dans les cas instables. Il y a, et ceci est bien connu, une complémentarité des modes de propagation entre les radiofréquences et les fréquences optiques.

- Un modèle complet de propagation optique dans la CSAM doit prendre en compte, outre la réfraction, l'absorption atmosphérique, l'atténuation due à la pluie et au brouillard, l'extinction aérosolaire importante pour les rayons lumineux qui "passent" près de la surface de l'eau, à cause des gouttelettes en suspension. Tous ces phénomènes contribuent à diminuer la visibilité optique et empêchent bien souvent l'observation d'éventuels mirages. Il est néanmoins très important de connaître les limites de visibilité, les zones de dédoublement, imposées par les lois de la réfraction.

Si le profil d'indice est supposé connu, les effets de la réfraction atmosphérique peuvent être quantifiés au moyen d'un programme de tracé de rayons. Un exemple, correspondant à une des situations instables observées durant la campagne MAPTIP (voir partie 4), est donné sur la figure 1. Le phénomène de dédoublement (ou mirage) apparaît nettement en limite d'horizon. Pour tenir compte de l'effet d'écran causé par les vagues, seuls les rayons dont l'altitude reste supérieure à  $0,65H_{1/3}$ ,  $H_{1/3}$  désignant la hauteur significative des vagues, sont calculés<sup>1</sup>.

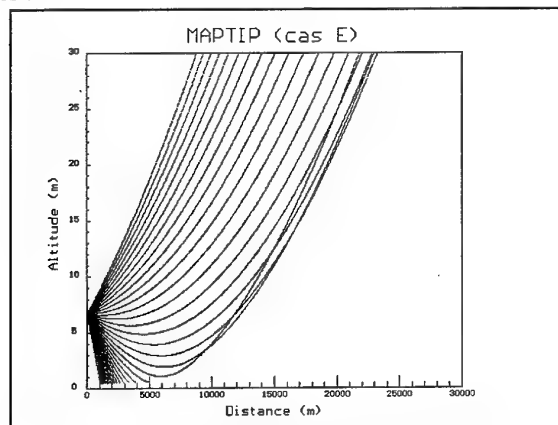


Figure 1 : MAPTIP cas E (voir partie 4)

Exemple de tracé de rayons.

On observe un dédoublement en limite d'horizon.

Une étude plus quantitative nécessite de calculer davantage de rayons, notamment ceux qui correspondent aux limites de la zone de mirage. Pour l'exemple précédent (MAPTIP, cas E) un tel calcul conduit à la figure 2.

On constate que les résultats obtenus diffèrent très nettement de ceux que l'on déduirait de la simple hypothèse d'atmosphère standard. Pour une source lumineuse située à une altitude quelconque, on peut calculer  $D_{max}$  la distance correspondant à la limite supérieure de la zone de mirage (qui est aussi l'horizon optique),  $D_{min}$ , la distance correspondant à la limite inférieure de la zone, ainsi que les élévations apparentes vues du point d'observation. Comme  $D_{min}$  est directement liée aux coordonnées du premier rayon qui réussit à passer au-dessus des vagues, cette valeur dépend beaucoup du profil d'indice de réfraction dans sa partie basse (les quelques premiers mètres d'altitude). En fonction de l'altitude de la source observée,  $D_{max}$  dépendra davantage de la partie "haute" du profil d'indice.

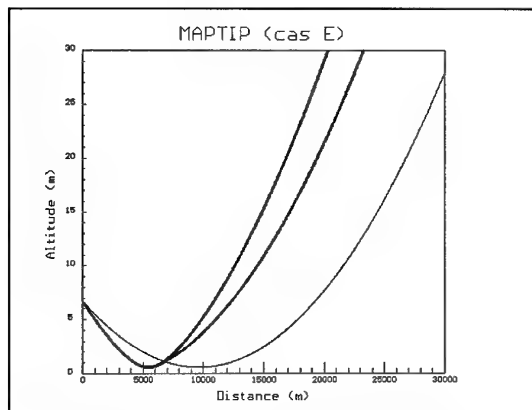


Figure 2 : MAPTIP cas E (voir partie 4).

Limites de la zone de mirage (trait gras).

Horizon optique en atmosphère standard (trait fin).

## 2. METHODES BULK ET MODELE PIRAM

De part sa relative simplicité, la méthode *bulk* est assez populaire dès qu'il s'agit de calculer l'ensemble des profils météorologiques verticaux et par suite le profil vertical d'indice de réfraction dans la CSAM. Parmi les réalisations mettant en œuvre cette méthode, figure en bonne place le modèle français baptisé PIRAM (Profils d'Indices de Réfraction en Atmosphère Marine) [2]<sup>2</sup>. Outre les profils météorologiques "classiques" (pression, température, humidité et vitesse du vent), le modèle PIRAM calcule les profils d'indice de réfraction, de constantes de structure de l'indice de réfraction ( $C_n^2$ ), les hauteurs de conduits lorsque ceux-ci existent, tout ceci aux radiofréquences comme aux longueurs d'onde optiques.

Dans les modèles *bulk*, les calculs de profils sont initialisés par la connaissance des paramètres météorologiques suivants (paramètres *bulk*) :

- pression atmosphérique  $p_1$  mesurée à l'altitude  $z_1$ ,
- température de l'air  $T_1$  mesurée à l'altitude  $z_1$ ,
- humidité relative  $H_1$  mesurée à l'altitude  $z_1$ ,
- vitesse du vent  $u_1$  mesurée à l'altitude  $z_1$  (on peut aussi s'accommoder d'une valeur  $u_2$  mesurée à une altitude  $z_2$  différente de  $z_1$ ),
- température de l'eau  $T_0$ .

La mesure de  $p_1$ , notamment, combinée avec la loi de l'hydrostatique permet la détermination du profil de pression atmosphérique. Pour obtenir les profils de température (via la température potentielle virtuelle notée  $\theta_v$ ), d'humidité spécifique et de vitesse du vent notée  $u$ , on s'appuie sur la théorie de Monin-Obukhov qui introduit les paramètres suivants :

- une échelle de vent,  $u_*$ , appelée aussi vitesse de frottement,

<sup>1</sup> Le choix du coefficient 0,65 peut paraître arbitraire ; il permet un assez bon accord entre les prédictions et les observations expérimentales. Il serait cependant souhaitable de pouvoir étayer ce choix par des considérations plus théoriques.

<sup>2</sup> Le modèle PIRAM a subi quelques améliorations par rapport à la référence indiquée. Un document complet sur la version actuelle du modèle est actuellement en cours de rédaction.

- une échelle de température,  $\theta_{v*}$ ,
- une échelle d'humidité,  $q_*$ ,
- une échelle de longueur,  $L$ , appelée longueur de Monin-Obukhov, définie par :

$$L = \frac{\overline{\theta_v u_*^2}}{\kappa g \theta_{v*}} \quad (4)$$

avec :

- $g = 9.81 \text{ m.s}^{-2}$ , accélération de la pesanteur,
- $\kappa = 0.4$ , constante de von Karman,
- $\overline{\theta_v}$ , température potentielle virtuelle moyenne de la CSAM.

La longueur de Monin-Obukhov est un indicateur de stabilité. Quand la stratification est instable,  $L$  est négative; quand elle est stable,  $L$  est positive.  $L$  est infinie pour une atmosphère neutre.

Monin et Obukhov ont postulé l'existence, pour les cas stables comme pour les cas instables, de fonctions universelles  $\phi_m$  et  $\phi_h$  reliant les flux aux gradients verticaux de vitesse du vent  $u$ , de température potentielle virtuelle  $\theta_v$  et d'humidité spécifique  $q$ . On a alors, en posant

$$\xi = \frac{z}{L} :$$

$$\left. \begin{aligned} \frac{du}{dz} &= \left( \frac{u_*}{\kappa z} \right) \phi_m(\xi) \\ \frac{d\theta_v}{dz} &= \left( \frac{\theta_{v*}}{\kappa z} \right) \phi_h(\xi) \\ \frac{dq}{dz} &= \left( \frac{q_*}{\kappa z} \right) \phi_h(\xi) \end{aligned} \right\} \quad (5)$$

Les fonctions  $\phi_m$  et  $\phi_h$  décrivent la forme spécifique des relations flux-profil. Dans le cas d'une atmosphère neutre, ces fonctions sont simplement égales à 1. L'ensemble des profils verticaux suivent alors une loi purement logarithmique. Pour les cas instables traités dans cet article, le modèle PIRAM utilise les relations suivantes :

$$\left. \begin{aligned} \phi_h(\xi) &= (1 - 16\xi)^{-\frac{1}{2}} \\ \phi_m(\xi) &= (1 - 16\xi)^{-\frac{1}{4}} \end{aligned} \right\} \quad (6)$$

Pour obtenir les profils de vent, température et humidité, il suffit d'intégrer les relations (5) en ayant défini au préalable les conditions aux limites. L'intégration ne commence pas à l'altitude nulle, premièrement parce qu'il faut tenir compte du caractère rugueux de surface de la mer et deuxièmement parce qu'il y aurait une impossibilité mathématique.

Les bornes inférieures d'intégration sont les longueurs de rugosité en vent, température et humidité, respectivement notées  $z_{0u}$ ,  $z_{0t}$  et  $z_{0q}$ . Ces longueurs de rugosité sont, par définition, les altitudes où les variables correspondantes seraient égales à leurs valeurs actuelles à la sur-

face si les relations (7) étaient encore valables à cette altitude. En réalité, les profils  $u(z)$ ,  $\theta_v(z)$  et  $q(z)$  ne vérifient plus les relations (7) pour les valeurs de  $z$  inférieures à environ  $20 \cdot z_{0x}$  ( $x = u, t$  ou  $q$ ), notamment dans la sous-couche visqueuse où ils deviennent généralement linéaires en  $z$ . Les longueurs de rugosité sont donc des constantes d'intégration pour obtenir les relations (7) à partir de (5), dont la réalité physique a été souvent discutée, notamment pour la surface marine où leurs valeurs sont inférieures au millimètre. Cependant, pour les surfaces solides, on a pu montrer leur permanence en fonction de la forme et de la densité des éléments de rugosité de la surface, indépendamment de leur nature physico-chimique et des caractéristiques de l'écoulement. Pour la mer, le couplage dynamique entre le vent et les vagues dû à la déformabilité de la surface rompt cette indépendance, et on exprime généralement ces longueurs de rugosité en fonction de l'état de la mer et/ou du frottement du vent.

Néanmoins, en supposant ces rugosités calculables et préalablement calculées (voir la fin de cette partie), on aboutit pour les profils verticaux à :

$$\left. \begin{aligned} u(z) &= u_0 + \frac{u_*}{\kappa} \left[ \ln \left( \frac{z}{z_{0u}} \right) - \Psi_m \left( \frac{z}{L} \right) \right] \\ \theta_v(z) &= \theta_{v0} + \frac{\theta_{v*}}{\kappa} \left[ \ln \left( \frac{z}{z_{0t}} \right) - \Psi_h \left( \frac{z}{L} \right) \right] \\ q(z) &= q_0 + \frac{q_*}{\kappa} \left[ \ln \left( \frac{z}{z_{0q}} \right) - \Psi_h \left( \frac{z}{L} \right) \right] \end{aligned} \right\} \quad (7)$$

avec :

$$\left. \begin{aligned} -\Psi_m(\xi) &= \int_0^\xi \frac{1 - \phi_m(\xi')}{\xi'} d\xi' \\ -\Psi_h(\xi) &= \int_0^\xi \frac{1 - \phi_h(\xi')}{\xi'} d\xi' \end{aligned} \right\} \quad (8)$$

-  $q_0$  et  $\theta_{v0}$ , les valeurs de l'humidité spécifique et de la température potentielle virtuelle à l'altitude nulle. Ces grandeurs sont calculées à partir de la mesure de la température de la mer  $T_0$  et en supposant que l'humidité relative à l'altitude zéro est de 98%.

-  $u_0$ , la vitesse du vent à l'altitude zéro, supposée nulle dans PIRAM.

$$-\Psi_m \left( \frac{z_{0u}}{L} \right) = \Psi_h \left( \frac{z_{0t}}{L} \right) = \Psi_h \left( \frac{z_{0q}}{L} \right) \approx 0.$$

Compte tenu de (6) et de la définition (8), on a :

$$\left. \begin{aligned} \Psi_m(\xi) &= 2 \ln \left( \frac{1+x}{2} \right) + \ln \left( \frac{1+x^2}{2} \right) - 2 \arctg(x) + \frac{\pi}{2} \\ \Psi_h(\xi) &= 2 \ln \left( \frac{1+y}{2} \right) \end{aligned} \right\} \quad (9)$$

avec  $x = (1 - 16\xi)^{\frac{1}{4}}$  et  $y = (1 - 16\xi)^{\frac{1}{2}}$

En utilisant les valeurs de  $u_1$ ,  $\theta_{v1}$ ,  $q_1$ , déduites de la mesure des paramètres *bulk* effectuée à l'altitude  $z_1$  on obtient :

$$\left. \begin{aligned} u_* &= \kappa u_1 \left[ \ln \left( \frac{z_1}{z_{0u}} \right) - \Psi_m \left( \frac{z_1}{L} \right) \right]^{-1} \\ \theta_{v*} &= \kappa (\theta_{v1} - \theta_{v0}) \left[ \ln \left( \frac{z_1}{z_{0t}} \right) - \Psi_h \left( \frac{z_1}{L} \right) \right]^{-1} \\ q_* &= \kappa (q_1 - q_0) \left[ \ln \left( \frac{z_1}{z_{0q}} \right) - \Psi_h \left( \frac{z_1}{L} \right) \right]^{-1} \end{aligned} \right\} \quad (10)$$

Les 3 équations (10) ajoutées à (4) qui définit  $L$ , forment un système de quatre équations non linéaires à quatre inconnues :  $u_*$ ,  $\theta_{v*}$ ,  $q_*$  et  $L$ . Une fois ces quatre paramètres d'échelle calculés, les profils verticaux de vent, de température et d'humidité et par suite le profil d'indice de réfraction sont parfaitement déterminés.

En ce qui concerne les longueurs de rugosité, PIRAM dispose de plusieurs options de calcul. Nous nous limitons ici à présenter celle qui a été utilisée pour l'analyse de la campagne MAPIP. Une façon assez simple, mais réaliste de calculer la rugosité en vent  $z_{0u}$  est donnée dans [3] :

$$z_{0u} = \frac{1,65 \cdot 10^{-6}}{u_*} + \alpha_c \frac{u_*^2}{g} \quad (11)$$

où  $\alpha_c$  désigne la "constante" de Charnock dont la valeur communément admise pour la pleine mer est 0.011. Pour les régions côtières, la valeur 0.017 a été utilisé dans PIRAM.

Pour calculer, les rugosités en température et en humidité,  $z_{0t}$  et  $z_{0q}$ , on introduit les coefficients de transfert en température et en humidité (à 10 m), notés  $C_{HN}$  et  $C_{EN}$ , et qui peuvent s'exprimer par :

$$\left. \begin{aligned} C_{HN} &= \frac{\kappa^2}{\ln \left( \frac{10}{z_{0u}} \right) \cdot \ln \left( \frac{10}{z_{0t}} \right)} \\ C_{EN} &= \frac{\kappa^2}{\ln \left( \frac{10}{z_{0u}} \right) \cdot \ln \left( \frac{10}{z_{0q}} \right)} \end{aligned} \right\} \quad (12)$$

A l'instar du modèle canadien LW(W)KD [1], nous avons utilisé ici les résultats de SMITH [4] :

$$C_{HN} = 1 \cdot 10^{-3} \text{ et } C_{EN} = 1,2 \cdot 10^{-3} \quad (13)$$

La détermination de  $z_{0t}$  et  $z_{0q}$  est donc immédiate dès lors que l'on a calculé  $z_{0u}$ . On remarquera que compte tenu de la forme particulière de la relation (11), cette détermination nécessite un couplage itératif avec les équations (10) et (4).

### 3. LE MODELE SEACLUSE

SeaCluse est un modèle numérique développé pour simuler la dispersion des aérosols marins, principalement les embruns générés par les vagues déferlantes, leur évaporation dans les basses couches de l'atmosphère marine, et l'influence du couplage entre ces deux processus simultanés. En effet les embruns, de toutes tailles entre 1 et 500  $\mu\text{m}$ , sont entraînés par les mouvements de l'air au ras des vagues et diffusés par la turbulence ; changeant d'altitude en permanence, ils se retrouvent sans cesse en déséquilibre thermodynamique et hydrique avec leur environnement immédiat, ce qui provoque leur évaporation et recondensation partielles. Le cœur du modèle SeaCluse calcule à chaque altitude les bilans de concentration de particules, de concentration de vapeur d'eau et de chaleur sensible qui déterminent ces échanges thermodynamiques et hydriques. Pour cela, il est nécessaire d'établir au préalable les profils moyens de vitesse, diffusivité turbulente, température et humidité "de référence" obtenus en l'absence d'embruns : ce calcul est réalisé par un module appelé "pré-processeur météorologique" basé sur une approche voisine de celle décrite dans la section précédente. Cependant, l'évolution initiale des embruns dès leur éjection de la surface marine étant une phase cruciale de ces processus, on a été amené à développer ce pré-processeur de telle sorte que non seulement il prenne en compte l'influence des vagues en moyenne mais aussi qu'il décrive l'écoulement et les répartitions de température et d'humidité entre creux et crêtes [5].

En réalité, c'est donc seulement ce pré-processeur qui a été utilisé ici pour déterminer les paramètres de l'écoulement et les profils verticaux de température et d'humidité en prenant en compte l'influence des vagues à très basse altitude. L'influence de la présence des embruns sur la réfraction infrarouge restant assez limitée, dans les exercices décrits ici le cœur du modèle SeaCluse n'a pas été utilisé pour calculer la répartition des particules. Cependant, les premiers tests ont montré que, pour  $u_{10} = u(z=10\text{m}) > 10 \text{ m/s}$ , la présence des embruns peut dans certaines conditions induire des différences de quelques dixièmes de  $^\circ\text{C}$  et quelques % d'humidité dans les profils immédiatement au-dessus des vagues. D'autre part la détermination des distributions d'aérosols, en tailles et en altitudes, est très importante dans les calculs d'extinction aérosolaire infrarouge.

Le pré-processeur météorologique de SeaCluse s'appuie sur une paramétrisation très proche de celle de LIU et al. [6] souvent appelée "modèle LKB". Au lieu des relations (6) on a retenu les résultats de EDSON et al. [7], soit

$\phi_m(\xi) = (1 - 20\xi)^{-1/4}$  pour les conditions de stratification instable. Les variables thermodynamiques utilisées sont la température potentielle  $\theta$  et :

- l'humidité absolue  $q_v$  en kg de vapeur d'eau par  $\text{m}^3$  d'air (variable conservative), dans le cœur du modèle,
- l'humidité spécifique  $q$  dans le pré-processeur par cohérence avec le modèle LKB initial, avec  $q_v = q \rho$  où  $\rho$  est la masse volumique de l'air.

Le calcul commence (théoriquement) par l'évaluation des échelles de frottement  $u_*$ , de température  $\theta_*$  et d'humidité  $q_*$  en s'appuyant sur les formules *bulk* exprimées sous leur forme standard :

$$\left. \begin{aligned} \tau &= \rho u_*^2 = \rho C_D u_{10}^2 \\ H &= -\rho c_p u_* \theta_* = -\rho c_p C_H u_{10} (\theta_{10} - \theta_o) \\ E &= -\rho L_v u_* q_* = -\rho L_v C_E u_{10} (q_{10} - q_o) \end{aligned} \right\} \quad (14)$$

Les coefficients de frottement  $C_D$  et de transferts  $C_H$  et  $C_E$  sont obtenus à partir de  $C_{DN}$ ,  $C_{HN}$  et  $C_{EN}$ , leurs valeurs à la neutralité ( $\xi = 0$ ), en tenant compte de la correction de stratification thermique [8], ce qui implique de calculer les valeurs de  $\xi$ ,  $\psi_m(\xi)$  et  $\psi_h(\xi)$  (voir relations (9)) qui dépendent elles-mêmes de  $u_*$ ,  $\theta_*$  et  $q_*$ . Ce système complet de paramètres est obtenu par itérations successives doubles : pour obtenir  $\xi$  et pour tenir compte d'une hauteur de référence  $z_1$  (altitude des mesures) éventuellement différente de 10 m. En s'appuyant sur les résultats et synthèses récentes [9], [10], on retient :

$$\left. \begin{aligned} C_{HN} &= C_{EN} = 1,1 \cdot 10^{-3} \\ C_{DN} &= 0,61 + 0,063 u_{10} \text{ (pleine mer)} \\ C_{DN} &= 0,43 + 0,10 u_{10} \text{ (zones côtières)} \end{aligned} \right\} \quad (15)$$

On notera que les formules (14) font apparaître  $u_{10}$  et non  $(u_{10} - u_o)$ , où  $u_o$  est la vitesse de l'air à la surface, non nulle du fait du glissement de la surface induit par le frottement, parce que les paramétrisations des coefficients  $C_{iN}$  ne prennent pas en compte cette vitesse de glissement.

L'établissement des profils au dessus de la surface marine sépare la CSAM en une couche directement influencée par les vagues et une couche non-perturbée par leur mouvement. La hauteur de la frontière entre les 2 couches dépend de la hauteur des vagues et elle est fixée ici à  $z = H_0$ , l'origine des altitudes étant située au niveau moyen de la surface et  $H_0$  étant la hauteur creux-à-crête de l'onde dominante. Pour  $z > H_0$ , les profils sont obtenus à l'aide de formules identiques à (7) dans lesquelles les rugosités  $z_{0x}$  sont déduites des valeurs de  $u$ ,  $\theta$ ,  $q$  à la hauteur de référence et des valeurs de  $u_*$ ,  $\theta_*$ ,  $q_*$  précédemment calculées : on n'utilise donc pas les paramétrisations supplémentaires (11) et (12).

Pour la couche de l'atmosphère directement influencée par le mouvement des vagues, on réalise le calcul des champs bi-dimensionnels  $(x, z)$  de vent, température et humidité au-dessus de la surface. La forme de la surface  $\eta(x)$  des vagues dominantes est assimilée à une onde de Stokes d'ordre 8.

Pour les conditions de pleine mer on considère que le champ de vagues est pleinement développé ; les paramètres du profil  $\eta(x)$  sont donc totalement fixés par le choix du paramètre de Stokes  $h = 0,135$  et de l'âge de la vague  $\Gamma = 0,85$ , sachant que l'on a :

$$h = \frac{kH_0}{2} \text{ avec } k = \frac{2\pi}{\Lambda}, \text{ nombre d'onde de la vague,}$$

$$\Gamma = \frac{c_v}{u_{10}} \text{ avec } c_v \text{ célérité de la vague.}$$

Pour les zones côtières le champ de vagues n'est pas établi et il dépend de la profondeur d'eau et de la distance à la côte, ou fetch. Le calcul fait alors intervenir un modèle de l'énergie des vagues et de leur distribution spectrale, fonction de ces paramètres et de la vitesse de frottement  $u_*$ .

Le calcul du champ de vent dans la zone des vagues,  $-H_0/2 < z < H_0$ , est basé sur une approche minimisant les hypothèses, sans paramètre arbitraire. On suppose que localement l'écoulement est suffisamment peu perturbé (les pentes restent faibles) pour retrouver la forme logarithmique du profil de vent en variables locales :

$$u(x, z) - u_{0L}(x) = \frac{u_*}{\kappa} \left[ \ln \left( \frac{z - \eta(x)}{z_{0L}(x)} \right) - \Psi_m(\xi) \right] \quad (16)$$

$$\text{où } \xi = \frac{[z - \eta(x)]}{L}$$

Ici  $u_{0L}(x)$  est la vitesse du vent locale (pour chaque abscisse  $x$ ) à la surface de la vague, égale à la vitesse de glissement local de la surface. Elle se décompose en une composante locale due aux mouvements orbitaux de l'eau à la surface et une composante moyenne due au glissement d'ensemble de la surface dans le sens du vent :

$$u_{0L}(x) = u(x, \eta(x)) = \omega \eta(x) + \kappa u_* \quad (17)$$

où  $\omega$  est la pulsation de l'onde de Stokes. Les profils locaux de température et d'humidité sont obtenus sur les mêmes bases :

$$\left. \begin{aligned} \theta(x, z) - \theta_o &= \frac{\theta_* P_{rt}}{\kappa} \left[ \ln \left( \frac{z - \eta(x)}{z_{0t}(x)} \right) - \Psi_h(\xi) \right] \\ q(x, z) - q_o &= \frac{q_* S_{ct}}{\kappa} \left[ \ln \left( \frac{z - \eta(x)}{z_{0q}(x)} \right) - \Psi_h(\xi) \right] \end{aligned} \right\} \quad (18)$$

$P_{rt}$  (respectivement  $S_{ct}$ ) désigne le nombre de Prandtl (respectivement Schmidt) turbulent.

$z_{0L}(x)$ ,  $z_{0t}(x)$  et  $z_{0q}(x)$  sont des paramètres identiques à des longueurs de rugosité locales, qui sont déterminées en imposant que tous les profils locaux convergent pour  $z = 10$  m, soit :

$$u(x, 10) = u_{10} ; \theta(x, 10) = \theta_{10} ; q(x, 10) = q_{10} ;$$

On observe que les valeurs de ces paramètres ainsi obtenues sont assez proches en moyenne des longueurs de rugosité fournies par les modèles de Charnock, LKB, ou plus élaborés [5]. Les profils moyens utilisés dans la suite sont obtenus par intégration en  $x$  des profils locaux, sur une longueur d'onde  $\Lambda$  de la vague dominante :

$$\phi(z) = \overline{\phi(x, z)} = \frac{1}{\Lambda} \int_0^{\Lambda} \phi(x, z) dx ; \phi = u, \theta \text{ ou } q \quad (19)$$

$$\text{pour } -\frac{H_0}{2} < z < H_0.$$

Bien que le choix de la hauteur de raccordement des 2 couches,  $z = H_0$ , paraisse arbitraire et ne prenne pas en compte la cambrure des vagues, on observe un très bon raccordement des profils calculés dans les 2 couches [5].

#### 4. DONNEES EXPERIMENTALES

Les données utilisées ici sont issues de l'expérience OTAN MAPTIP (Marine Aerosol Properties and Thermal Imager Properties) qui s'est déroulée durant l'automne 1993, du 11 octobre au 5 novembre, sur les côtes néerlandaises, à proximité de Katwijk.

Le dispositif expérimental et l'ensemble des instruments mis en œuvre sont décrits en détail dans [11]. Nous ne présentons par la suite que les moyens directement liés à l'analyse des effets de réfraction dans la CSAM [12].

Afin de quantifier ces effets, plusieurs lampes halogènes d'une puissance de 500 W ont été installées sur un navire océanographique hollandais, le Tydeman, à différentes hauteurs indiquées sur la figure 3.

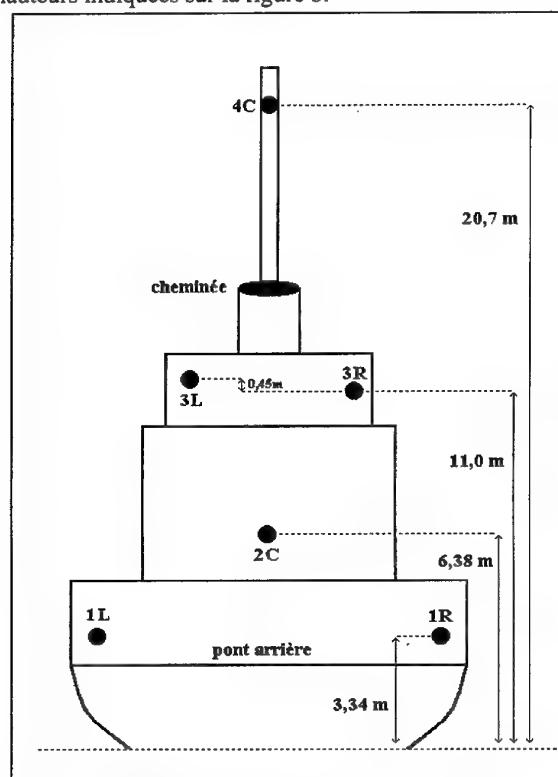


Figure 3 : Vue arrière du Tydeman.  
Position des lampes halogènes par rapport  
à la ligne de flottaison

Lorsque le bateau s'éloignait du rivage, les différentes lampes atteignaient l'horizon les unes après les autres

puis disparaissaient. Avant qu'elles ne disparaissent, de longues périodes de dédoublement (plusieurs minutes) ont été observées. La disparition complète des lampes était généralement précédée de clignotements dont la période coïncidait avec celle du mouvement des vagues.

L'observation des lampes installées sur le bateau se faisait depuis la plage de Katwijk à partir de caméras fonctionnant soit dans le visible, soit dans l'infrarouge. Nous utiliserons les mesures fournies par une des caméras "visibles". Comme nous l'avons déjà dit, toutes les conclusions que l'on pourra tirer de notre étude sont transposables au domaine infrarouge.

Par ailleurs deux bouées instrumentées ont été mouillées en mer à 4 km des côtes :

- une bouée météorologique mesurant notamment les paramètres *bulk* ainsi que la direction du vent et le rayonnement solaire

- une bouée océanographique mesurant la hauteur significative et le spectre monodimensionnel des vagues.

Durant la campagne, la CSAM était toujours en situation instable, avec des écarts de température entre la mer et l'air allant de 0.3°C à 9°C. Les vents étaient en général relativement modérés mais, et cette situation est plutôt atypique, il s'agissait de vent d'est donc continentaux, alors que sur les côtes hollandaises de la mer du Nord les vents dominants sont habituellement d'origine océanique. Parmi les données disponibles, nous avons sélectionné 2 événements particuliers, mais représentatifs des conditions météorologiques rencontrées :

- le cas E (situation très instable) enregistré le 22/10/93 pour un déplacement du navire Tydeman débutant à 20h45 et se terminant à 21h55.

- le cas H (situation quasi-neutre) enregistré le 26/10/93 pour un déplacement du navire Tydeman débutant à 08h35 et se terminant à 09h45.

La durée "utile" de ces 2 événements (de la disparition des lampes les plus basses à la disparition des lampes les plus hautes) était de l'ordre de 30 minutes. Durant ces laps de temps, on a pu vérifier que l'ensemble des paramètres météorologiques et océanographiques était quasiment invariant. La valeur de tous ces paramètres est indiquée sur le tableau 2 ci-après.

	Cas E	Cas H
$p_1$ (hPa)	1027	1031
$T_1$ (°C)	7,4	11,2
$H_1$ (%)	76	85
$u_1$ (m/s)	9,1	7,0
Direction (°)	60	40
$z_1 = z_2$ (m)	3,4	3,4
$T_0$ (°C)	12,4	11,5
$H_{1/3}$ (m)	0,91	0,68
$T_{1/3}$ (s) <sup>3</sup>	4,8	4,6
Marée (m)	0,32	-0,59

Tableau 2 : Valeurs des paramètres météorologiques  
et océanographiques correspondant  
aux cas E et H de MAPTIP

<sup>3</sup>  $T_{1/3}$  désigne la période significative des vagues.

Pour les 2 cas étudiés, l'altitude, par rapport au niveau moyen de la mer, de la caméra d'observation était de 7.04 mètres. Dans le programme de tracé de rayons, cette valeur doit être corrigée par la hauteur de marée.

## 5. COMPARAISON DE PIRAM ET SEACLUSE

Les profils de température, de vitesse de vent et d'indice de réfraction correspondant aux cas précédemment définis sont tracés sur les figures 4a à 6a (MAPTIP cas E) et 7a à 9a (MAPTIP cas H). Les profils d'indice M déduits du modèle SeaCluse sont, et ceci pour des raisons de commodité de mise en œuvre informatique, calculés par la relation (3) à partir :

- du profil de température SeaCluse,
- des profils de pression et d'humidité PIRAM.

Comme le profil d'humidité n'intervient que très peu pour calculer l'indice de réfraction dans le domaine optique, le biais introduit par cette procédure est tout à fait minime. De plus, de par la nature même des paramétrisations utilisées par les 2 modèles, les conclusions que l'on peut tirer de la comparaison des profils de température sont aisément transposables aux profils d'humidité.

Afin de mieux apprécier les différences éventuelles, les écarts en fonction de l'altitude entre les valeurs SeaCluse et les valeurs PIRAM sont reportés sur les figures 4b à 6b (MAPTIP cas E) et 7b à 9b (MAPTIP cas H).

L'ensemble de ces figures appelle les commentaires suivants :

- Tous les profils se coupent à l'altitude de mesure (ou altitude de référence)  $z_1 = 3,4$  m. Cette constatation n'est pas aussi triviale qu'il y paraît, car SeaCluse, en interne, utilise comme contraintes les valeurs à l'altitude 10 m. Il faut donc itérer pour calculer la valeur de ces contraintes compatible avec les valeurs effectivement mesurées.
- En ce qui concerne les profils de température, les écarts observés aux très basses altitudes de doivent pas surprendre. En effet, la température de la mer  $T_0$  est prise comme température à l'altitude nulle par PIRAM alors que, comme la présence des vagues est explicitement prise en compte par SeaCluse, le profil de température calculé par ce modèle s'étend jusqu'à l'altitude  $-H_0/2$ . Ces écarts sont d'autant plus grands que l'instabilité, mesurée en première approximation par la différence de température entre l'eau et l'air, augmente (voir figures 4b et 6b).
- Les profils de température s'écartent de nouveau lorsque l'altitude augmente à raison d'environ  $0,1^\circ\text{C}/10\text{m}$ . Ce comportement s'explique par les choix différents faits par les 2 modèles aussi bien pour les fonctions de stabilité que pour les longueurs de rugosité.
- Les profils de vitesse de vent diffèrent sensiblement aux très basses altitudes, pour les mêmes raisons que celles invoquées à propos des profils de température. Naturellement, les écarts enregistrés

augmentent avec la vitesse du vent mesurée à l'altitude de référence. A plus haute altitude, les profils ne convergent pas tout à fait vers la même valeur, mais l'écart, de l'ordre de quelques dixièmes de m/s, devient, pour toutes les données analysées (y compris celles non présentées ici), quasiment constant.

- Pour les profils d'indice de réfraction, les comportements respectifs des 2 modèles ne sont que la conséquence de ce qui a déjà été remarqué à propos des profils de température. Aux altitudes supérieures à une dizaine de mètres, les profils s'écartent d'environ  $0,1 \text{ M}/10\text{m}$ .

Vis à vis des calculs des horizons optiques ( $D_{\text{max}}$ ) et/ou des limites des zones de mirage ( $D_{\text{min}}$  et  $D_{\text{max}}$ ) les résultats obtenus sont résumés dans les tableaux 3 et 4.

Lampes		A. S.	P.	S.	O.
3,34 m	Dmin (km)	16,09	8,71	7,53	8,53
	Dmax (km)		9,55	9,17	11,08
6,38 m	Dmin (km)	19,00	10,67	8,76	10,08
	Dmax (km)		12,08	11,81	12,95
11 m	Dmin (km)	22,19	13,06	11,64	-
	Dmax (km)		15,04	14,89	-
20,7 m	Dmin (km)	27,09	17,09	15,60	-
	Dmax (km)		19,68	19,73	21,08

**Tableau 3 : MAPTIP (cas E)**

Valeurs des limites des zones de mirage ( $D_{\text{max}}$  correspond en outre à l'horizon optique) pour les différentes hauteurs de lampes du Tydeman.

A.S. : valeurs pour l'atmosphère standard (pas de dédoublement).

P. : valeurs calculées à partir de PIRAM.

S. : valeurs calculées à partir de SeaCluse.

O. : observations expérimentales (- indique l'absence de données).

Lampes		A. S.	P.	S.	O.
3,34 m	Dmin (km)	17,06	15,56	14,81	16,41
	Dmax (km)			15,29	
6,38 m	Dmin (km)	19,92	18,28	17,53	18,98
	Dmax (km)			18,19	
11 m	Dmin (km)	23,08	21,34	20,64	21,82
	Dmax (km)			21,40	
20,7 m	Dmin (km)	27,96	26,10	25,51	26,67
	Dmax (km)		26,14	26,38	

**Tableau 4 : MAPTIP (cas H)**

Valeurs des limites des zones de mirage ( $D_{\text{max}}$  correspond en outre à l'horizon optique) pour les différentes hauteurs de lampes du Tydeman.

A.S. : valeurs pour l'atmosphère standard (pas de dédoublement).

P. : valeurs calculées à partir de PIRAM.

S. : valeurs calculées à partir de SeaCluse.

O. : observations expérimentales.

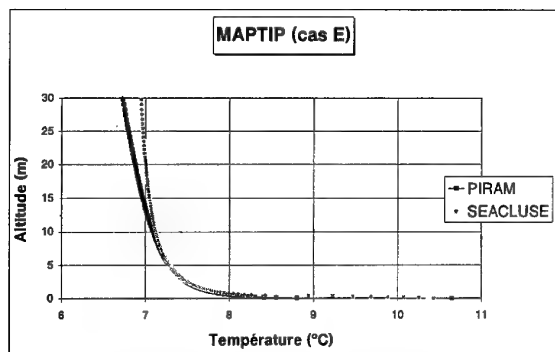


**Figure 4a : MAPTIP (cas E)**  
*Profils de température calculés  
 par PIRAM et SeaCluse.*

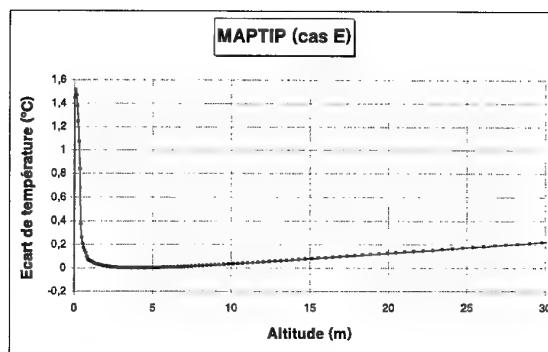


**Figure 4b : MAPTIP (cas E)**  
*Ecart entre les profils de température  
 PIRAM et SeaCluse en fonction de l'altitude*

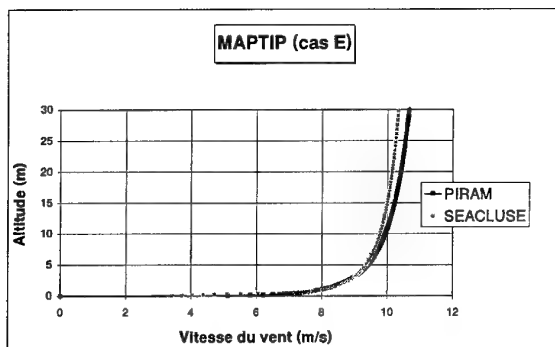


**Figure 5a : MAPTIP (cas E).**  
*Profils de vitesses vent calculés  
 par PIRAM et SeaCluse.*

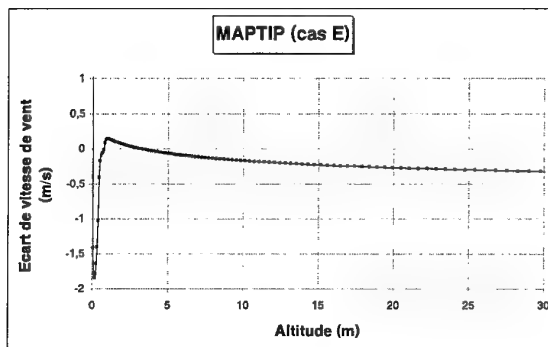


**Figure 5b : MAPTIP (cas E)**  
*Ecart entre les profils de vitesse de vent  
 PIRAM et SeaCluse en fonction de l'altitude*

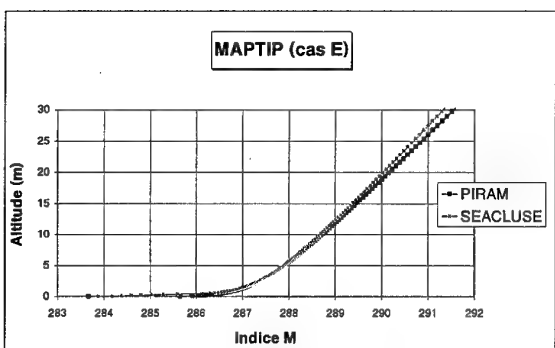


**Figure 6a : MAPTIP (cas E).**  
*Profils d'Indice M calculés à partir :*  
 - des profils de température PIRAM ou SeaCluse,  
 - des profils de pression et d'humidité PIRAM

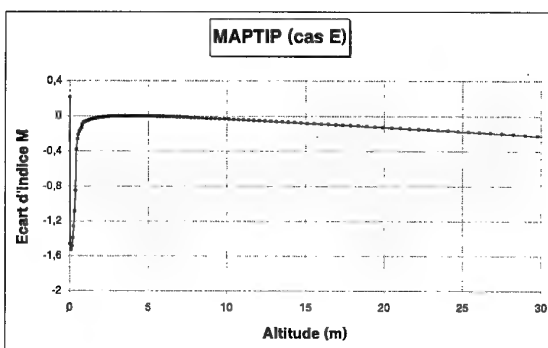


**Figure 6b : MAPTIP (cas E)**  
*Ecart entre les profils d'indice M déduits  
 des profils de température PIRAM et SeaCluse  
 en fonction de l'altitude*



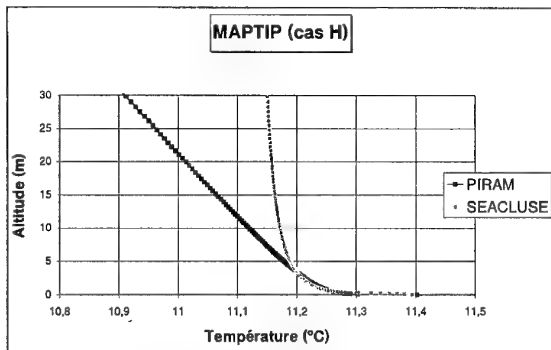


**Figure 7a : MAPTIP (cas H)**  
*Profils de température calculés  
 par PIRAM et SeaCluse.*

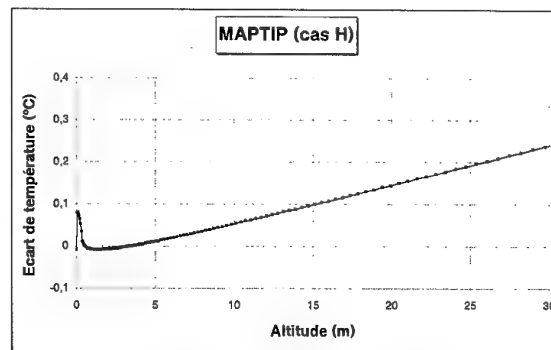


**Figure 7b : MAPTIP (cas H)**  
*Ecart entre les profils de température  
 PIRAM et SeaCluse en fonction de l'altitude*

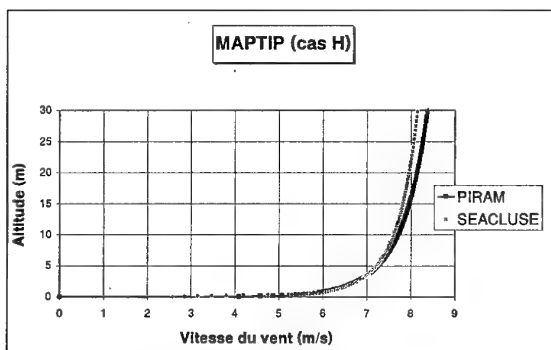


**Figure 8a : MAPTIP (cas H).**  
*Profils de vitesses vent calculés  
 par PIRAM et SeaCluse.*

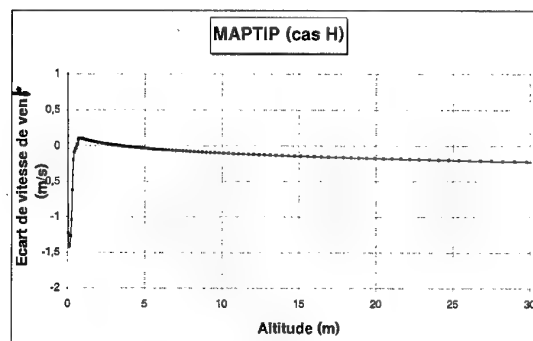


**Figure 8b : MAPTIP (cas H)**  
*Ecart entre les profils de vitesse de vent  
 PIRAM et SeaCluse en fonction de l'altitude*

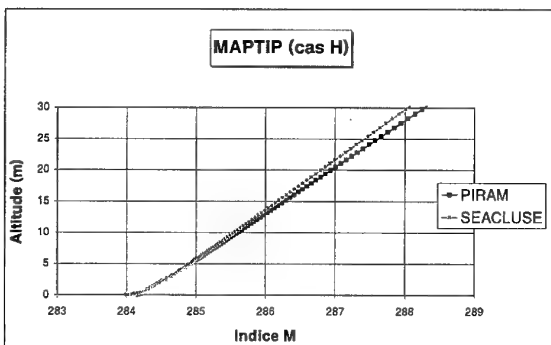


**Figure 9a : MAPTIP (cas H).**  
*Profils d'Indice M calculés à partir :*  
 - des profils de température PIRAM ou SeaCluse,  
 - des profils de pression et d'humidité PIRAM

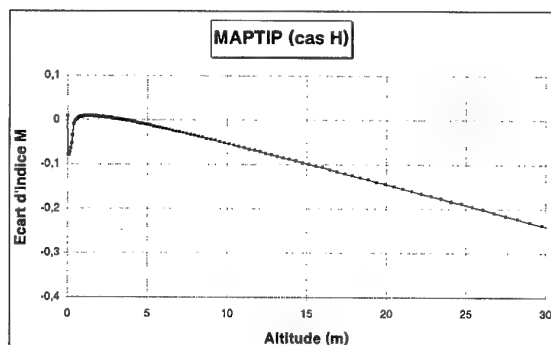


**Figure 9b : MAPTIP (cas H)**  
*Ecart entre les profils d'indice M déduits  
 des profils de température PIRAM et SeaCluse  
 en fonction de l'altitude*

Avec une hypothèse d'atmosphère standard, on ne prédit évidemment aucun dédoublement ; il n'y a donc pas lieu de distinguer  $D_{min}$  et  $D_{max}$  dans les tableaux 3 et 4. Pour des atmosphères quasi-neutres, comme le cas H, les observations n'indiquent pas non plus d'existence de dédoublements, contrairement à ce que semble prédire le programme de tracé de rayons utilisant les profils issus de PIRAM ou de SeaCluse. En fait, à partir du programme de tracé de rayons, on raisonne pour des sources ponctuelles. En réalité, les sources observées (lampes halogènes situées à l'arrière du Tydeman) ne le sont pas et il faut des effets de réfraction suffisamment importants pour observer des dédoublements. Pour une atmosphère quasi-neutre, on n'observera simplement un léger étirement de l'image dans le sens vertical. Les phénomènes de scintillation, de flou et d'étalement rendent délicate l'observation de petits mirages.

Il faut également remarquer que le programme de tracé de rayons utilisé suppose une atmosphère horizontalement homogène ; cette hypothèse n'est jamais complètement vérifiée surtout lors de MAPIP puisque l'on avait plutôt des vents dominants d'origine continentale.

Compte tenu des remarques énoncées dans les 2 paragraphes précédents, tout écart inférieur au km, entre les valeurs de  $D_{min}$  et  $D_{max}$  calculées et celles observées, sera jugé très satisfaisant.

En ce qui concerne l'étude comparative des résultats issus de SeaCluse et de PIRAM, la lecture des tableaux 3 et 4 appelle les commentaires suivants :

- Les valeurs de  $D_{max}$  calculées par PIRAM et SeaCluse sont relativement proches et en assez bon accord avec les observations expérimentales. A cause des différences de pentes, mentionnées plus haut, dans les profils, les valeurs de  $D_{max}$  calculées à partir de SeaCluse sont inférieures à celles calculées à partir de PIRAM, pour les lampes les plus basses et supérieures pour les lampes les plus hautes. Cependant ces écarts ne sont pas suffisamment importants pour que l'on se hasarde à en tirer des conclusions hâtives.

- Les valeurs de  $D_{min}$  (très sensibles, rappelons-le, à la partie basse des profils) déduites de SeaCluse sont systématiquement inférieures à celles déduites de PIRAM et aux observations expérimentales. Le fait "d'éliminer" les rayons dont l'altitude devient inférieure à  $0,65H_{1/3}$  revient à ne pas tenir compte des profils pour ces altitudes où l'on n'observe les écarts maximum entre SeaCluse ET PIRAM. Les différences qui subsistent sur les valeurs de  $D_{min}$  peuvent avoir deux origines qui ne sont pas du tout incompatibles :

- La "troncature" à  $0,65H_{1/3}$  est un choix optimum lorsque le profil est calculé par une méthode bulk [12]. Néanmoins, comme SeaCluse prend en compte les interactions avec le champ de vagues, le choix d'un autre seuil de troncature pourrait conduire à des résultats en meilleur accord avec les observations. Il man-

que des éléments théoriques pour pouvoir conclure quant au choix de ce seuil dont l'existence physique est pourtant indiscutable.

- Les paramètres du modèle de Stokes pour le champ de vagues ont été obtenus à partir des valeurs expérimentales de la hauteur significative des vagues, de la période significative des vagues et de la vitesse du vent, valeurs reportées dans le tableau 2. Ces valeurs conduisent à un champ de vagues relativement développé : typiquement  $\Gamma = 0,7$  et  $h = 0,09$ . Ces résultats semblent peu réalistes en raison de l'origine continentale des vents dominants et du fetch variant de 4 à 20 km. Par comparaison, et pour des conditions similaires, on trouve dans [13] et [14] les valeurs typiques suivantes :  $\Gamma = 0,35$  et  $h = 0,25$ . On peut penser que les paramètres de Stokes utilisés par SeaCluse pour les résultats présentés ici ne sont peut-être pas représentatifs du champ de vagues réel.

## CONCLUSION

Cette étude montre qu'il est important de connaître le profil d'indice de réfraction dans la CSAM afin de déterminer la portée réelle maximum des systèmes optiques fonctionnant dans le visible ou dans l'infrarouge. Le calcul du profil vertical d'indice par un modèle *bulk* tel que PIRAM conduit à des résultats qui sont généralement en bon accord avec les observations expérimentales effectuées durant la campagne MAPIP.

Le modèle numérique SeaCluse qui prend en compte les interactions et échanges d'énergie entre le champ de vagues et l'écoulement d'air a pour objectif majeur le calcul de la concentration d'aérosols marins, mais il permet également le calcul du profil d'indice de réfraction. Pour les effets de réfraction, l'analyse des résultats de MAPIP avec le modèle SeaCluse s'avère très encourageante. Cependant, les points suivants méritent d'être approfondis :

- Etude de la sensibilité des résultats de SeaCluse aux paramètres de STOKES décrivant le champ de vagues.

- Amélioration de la détermination de ces paramètres de Stokes obtenus ici à partir des hauteurs et périodes des vagues et de la vitesse du vent. A cet effet, l'utilisation prochaine des spectres de vagues mesurées lors de MAPIP devrait être un atout précieux.

- Analyse de l'effet de la surface de la mer sur la propagation des rayons optiques lorsque l'altitude de ceux-ci devient du même ordre de grandeur que la hauteur des vagues.

## REMERCIEMENTS

Ce travail de comparaison a été réalisé avec le soutien de la DGA/CELAR. Les auteurs expriment leur plus chaleureuse gratitude à Denis DION et Luc FORAND du CRDV (CANADA) pour l'accès aux données issues des matériels canadiens mis en œuvre durant la campagne MAPTIP. Ils remercient également la Marine Néerlandaise pour l'utilisation du navire océanographique "Hr.Ms.Tydeman" lors de la campagne MAPTIP, et pour le soutien apporté au TNO pour le développement du modèle SeaCluse.

## REFERENCES

- [1] FORAND J.L., "The L(W)WKD Marine Boundary Layer Model", DREV-R 9618, Mars 1997.
- [2] CLAVERIE J. et al., "Modélisation des profils verticaux d'indice de réfraction et de  $C_n^2$  en atmosphère marine", 2<sup>nd</sup> AGARD SPP Symposium, *L'évaluation de la propagation en régions côtières*, 19-22 Sept. 1994, Bremerhaven, Allemagne, pp 29-1, 29-11.
- [3] GARRATT J. R., "The atmospheric boundary layer", Cambridge University Press, 316 p, 1992.
- [4] SMITH S.D., "Water vapour flux at the sea surface", *Bound. Layer Meteorol.*, 47, 1989, pp 277-293.
- [5] MESTAYER P.G. et al., "Numerical simulation of the dynamics of sea spray over the waves", *J. Geophys. Res.*, 101, 1996, pp 20771-20797.
- [6] LIU W.T., KATSAROS K.B., BUSINGER J.A., "Bulk parameterization of the air-sea exchange of heat and water vapor including the molecular constraints at the interface", *J. Atmos. Sci.*, 36, 1979, pp 1722-1735.
- [7] EDSON J.B. et al., "A study of the inertial dissipation method for computing air-sea fluxes", *J. Geophys. Res.*, 96, 1991, pp 10689-10711.
- [8] GEERNAERT G.L., KATSAROS K.B., RICHTER K., "Variation of the drag coefficient on sea state", *J. Geophys. Res.*, 91, 1986, pp 7667-7679.
- [9] DECOSMO J. et al., "Air-sea exchange of water vapor and sensible heat: The Humidity Exchange over the Sea (HEXOS) results", *J. Geophys. Res.*, 101, 1996, pp 12001-12016.
- [10] SMITH S.D., "Coefficients for sea surface wind stress, heat flux, and wind profiles as a function of wind speed and temperature", *J. Geophys. Res.*, 93, 1988, pp 15467-15472.
- [11] JENSEN D.R., DE LEEUW G., VAN EIJK A.M.J., "Summary of the Marine Aerosol Properties and Thermal Imager Performance Trial (MAPTIP)", 2<sup>nd</sup> AGARD SPP Symposium, *L'évaluation de la propagation en régions côtières*, 19-22 Sept. 1994, Bremerhaven, Allemagne.
- [12] FORAND J.L. et al., "MAPTIP Work Group Report: Refractive effects in the visible and the infrared", DREV-R 9621, Juin 1997.
- [13] GEERNAERT G.L., "Bulk parametrisations for the wind stress and heat fluxes", in "Surface waves and fluxes I", 91-172, G.L. GEERNAERT and W.J. PLANT (eds), Kluwer Academic Press, The Netherlands, 1990.
- [14] TRANCHANT B., "Simulations numériques des aérosols marins", Ph.D Thesis, Ecole Centrale de Nantes, Mars 1997.

PAPER No. 5

DISCUSSOR'S NAME: W. Cornette

COMMENT/QUESTION:

The paper's assumption is that the index of refraction is non-dispersive and that the water vapour term is small (2-3%). However, in the LWIR (above 10-12 $\mu$ m), the index of refraction becomes dispersive with a large dependence on water vapour. Are there any plans to evaluate the effect of the MBL in the LWIR?

AUTHOR/PRESENTER'S REPLY:

Actually, the bands of interest are the ones listed in the paper: visible, [1.3  $\mu$ m], [3.5  $\mu$ m] and [8.12  $\mu$ m]. For each of these bands we used simplified relationships between the index of refraction and the wavelength. But these relationships give very good accuracy.

You can use more complex formulae, for all IR bands including LWIR. (See the reference [1] in the paper for more details).

Actually we do not study propagation for wavelengths > 12  $\mu$ m.

## A RAPID 3-5 MICRON TDA SIMULATION BASED ON MODTRAN4

L. S. Bernstein, S. M. Adler-Golden, and A. Berk  
Spectral Sciences, Inc, Burlington, MA 01803 USA

M. M. Edwards, E. E. Hume, F. A. Zawada, J. Mozer,  
G. P. Anderson, and J. H. Chetwynd  
USAF Research Laboratory, Space Vehicles Directorate  
Hanscom AFB, MA 01730 USA

H. Gilliam  
Radex, Inc., Bedford, MA 01730 USA

### SUMMARY

A real-time atmospheric attenuation model for the 3-5  $\mu\text{m}$  wavelength region has been developed for use as a weather effects Tactical Decision Aid. The TDA algorithm is based on a correlated- $k$  (CK) method developed for MODTRAN4. The CK parameters for water vapor, ozone, aerosols, and uniformly mixed gases are pre-computed without making any assumptions about the target or sensor locations or the weather-dependent species concentrations. The TDA has been used to compute the atmospheric transmittance for a series of lines of sight between a sensor and theater ballistic missile target through a 3D-heterogeneous atmosphere defined by a weather simulation model. The CPU time is 0.01 s per line of sight on a 100 MIPS computer, and the transmittance accuracy is within a few percent. These results show that the CK algorithm has considerable promise as a general-purpose, real-time radiation transport tool.

### 1. INTRODUCTION

There are a variety of environmental optical effects that need to be accounted for in realistic scene renditions. They include atmospheric transmittance losses, radiance sources in the line of sight such as thermal IR emission and scattering of sunlight and earthshine, background environments, and ambient radiation reflected from the target. To incorporate these effects in real-time engagement simulations, very fast

computation methods are required. Typically these methods rely on either crude mathematical approximations or interrogation of a pre-computed database that has been customized for a particular scenario. With the database approach, there are constraints on the movements of the scene objects (targets, sensor platforms, etc.), because it is not practical to pre-compute the atmospheric and object lighting conditions for all possible geometries. Thus, there is a need for real-time, realistic environmental optical effects models which do not rely on database assembly and interrogation.

The Air Force Research Laboratory's Wargaming and Technology Assessment Branch has developed the Atmospheric Effects Server (AES) to incorporate weather effects into distributed simulations.<sup>(1)</sup> The development of a 3-5  $\mu\text{m}$  transmission capability was required to add capability to the AES. The AES is based on a client-server based architecture and provides computer generated entities access to realistic effects computed in accordance with weather data distributed by a central weather server. The AES has been used to add 8-12  $\mu\text{m}$  transmission capability and high resolution clouds to an engagement level simulation.<sup>(2)</sup> The calculation are physics-based using models developed by AFRL and its predecessor organizations, Phillips Laboratory and the Geophysics Laboratory. These include thermal signatures for targets and backgrounds, atmospheric transmission loss, and sensor performance. The AES architecture provides a unique testbed for developing models

and incorporating realistic effects into distributed simulations.

This paper describes a real-time atmospheric attenuation model for the 3-5  $\mu\text{m}$  wavelength region. The objective of this work, which was sponsored by the Air Force Phillips Laboratory Geophysics Directorate/Modeling and Simulation Facility, was to embed a 3-5  $\mu\text{m}$  weather effects Tactical Decision Aid (TDA) into Distributed Interactive Simulations (DIS) for stand-off detection of the bright plumes from theater ballistic missiles. The objective was to achieve around  $\pm 20\%$  in-band radiance accuracy with sufficient speed (around 0.01 s or less of computation time per display frame) for real-time (30 frame/s) image generation. To do this, the atmospheric transmittance calculation is carried out using the correlated-k (CK) method. Since

transmittance is a fundamental quantity needed to describe the transport of radiation to a sensor from targets and backgrounds as well as radiation generated from thermal emission and scattering, and the CK method is very general, the current approach can be readily extended from the present application to the other simulation problems (i.e., other wavelength regions, plume emissions, solar scattering, etc.).

The algorithm developed for this work is an extension of the CK algorithm recently incorporated into MODTRAN4.<sup>(3)</sup> In the CK approach, the transmittance for a finite spectral interval is described by a weighted sum of a few exponential (Beer's Law) terms. The weighting factors and effective monochromatic absorption coefficients are calculated using the method developed for MODTRAN4, which has recently

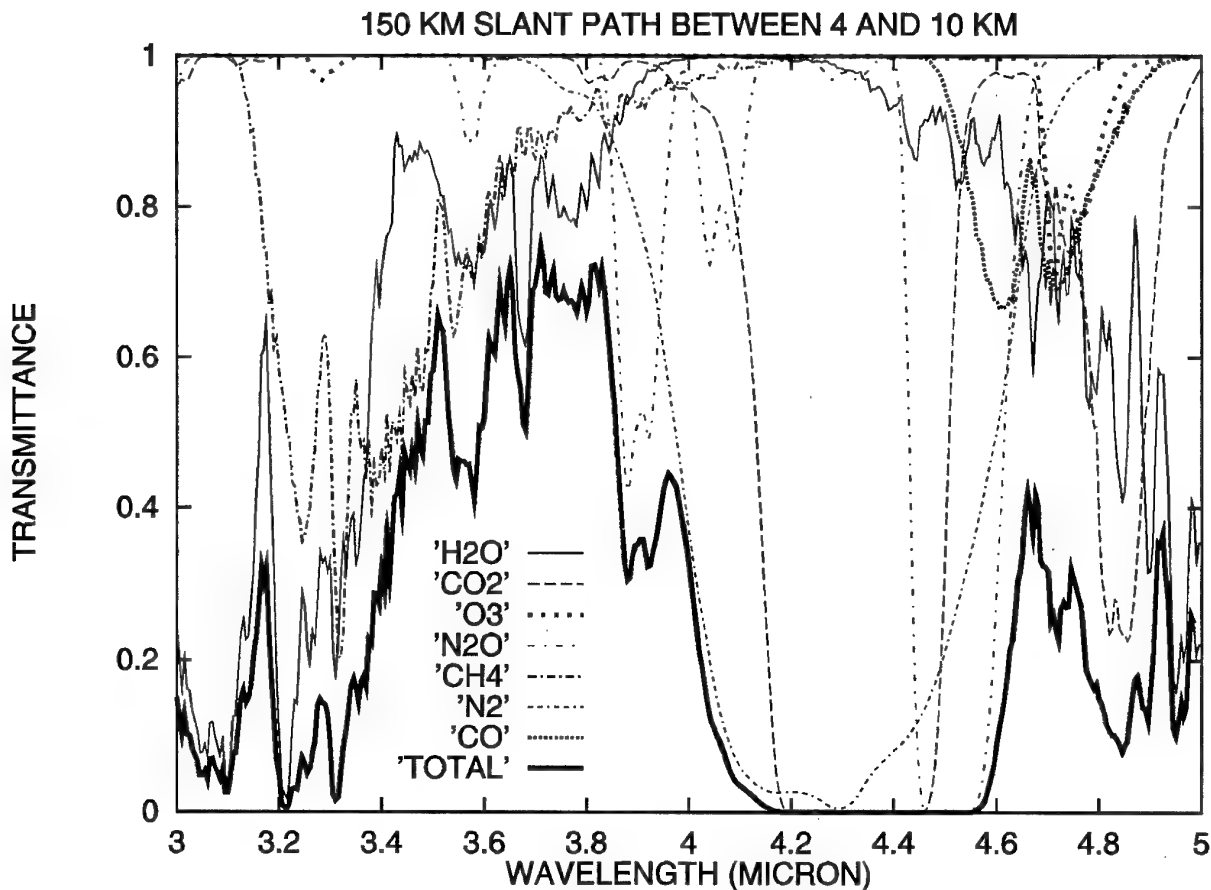


**Figure 1** MODTRAN Calculation of Line-of-Sight Transmittance Showing Molecular Species Contributions.

been validated against both earlier MODTRAN band model algorithms<sup>(4)</sup> and "exact" (but very time-consuming) line-by-line calculations. The CK approach has a number of computational advantages over the band model method. For the current application a particularly important one is its ability to rapidly perform a large number of calculations over inhomogeneous paths (i.e., lines of sight through spatially varying water vapor, clouds, and aerosols for arbitrary sensor and target locations) simply by summing a small number of monochromatic optical depths along the path.

## 2. TECHNICAL APPROACH

The 3-5  $\mu\text{m}$  "window" region contains absorption bands from a number of different molecular species which can result in substantial attenuation over paths of the order of 100 km. As shown in the MODTRAN calculation in Fig. 1, important contributors include water vapor, carbon dioxide, ozone, methane, nitrogen, and other species. Clouds and aerosols provide additional, unstructured sources of attenuation. The total monochromatic transmittance is the product of the monochromatic transmittances for each species. To an excellent approximation a spectrally degraded or binned total transmittance may also be represented by the product of correspondingly degraded or binned species transmittances, provided that the degradation or binning is not too coarse.

In the CK method the transmittance in a spectral bin, referred to hereafter as a sub-interval, is described by a weighted sum of a few exponential (Beer's Law) terms. For a broad sensor bandpass, the net transmittance is the sum of the sub-interval transmittances:

$$T_{12} = \sum_i \sum_j g_{ij} \exp(-\tau_{ij}) \quad (1)$$

Here  $i$  is an index for the set of sub-intervals,  $j$  is an index for a set of optical depths,  $\tau$ , in each sub-interval, and  $g$  is a weighting factor for each optical depth. The optical depths are given by

species density-weighted sums of absorption coefficients,  $k$ , over the line-of-sight path  $s$ :

$$\tau_{ij} = \sum_l k_{ij} \rho(x, y, z) ds_l \quad (2)$$

Here  $\rho$  is the local species density at point  $(x, y, z)$  in space and  $ds_l$  is the length of the  $l$ 'th increment of the path. A method for calculating appropriate  $g$  and  $k$  values has been worked out and incorporated in MODTRAN4.

The CK approach has a number of important computational advantages over the traditional band model approach. For engagement simulations three particularly important ones are: (1) its ability to treat "L-shaped" paths (e.g., a sun-sensor-target path) simply by summing monochromatic optical depths for each path; (2) the ability to rapidly perform calculations for a large number of heterogeneous paths, such as lines of sight for arbitrary sensor and target locations through an atmosphere containing spatially varying water vapor, clouds, and aerosols, and (3) the ability to accurately treat molecular absorption lines over paths through high-temperature exhaust plumes, which contain very large variations in temperature and number density.

An overview of the TDA implementation is depicted in Figure 2. The 3-5  $\mu\text{m}$  region was divided into 15  $\text{cm}^{-1}$  sub-intervals, and MODTRAN4 calculations were used to establish species- and altitude-dependent matrices of  $k_{ij}$  and  $g_{ij}$  values in each sub-interval. (These values needed to be determined only once; they do not depend on the simulation scenario.) For each scenario a weather model is run, resulting in a 3D grid of temperature (T), pressure (P) and water vapor concentration over the DIS volume. In the current application the DIS volume was quite large, encompassing a ground footprint of up to 200 km by 200 km and extending vertically to high altitude (missile burnout can exceed 50 km altitude).

The TDA consists of a FORTRAN subroutine

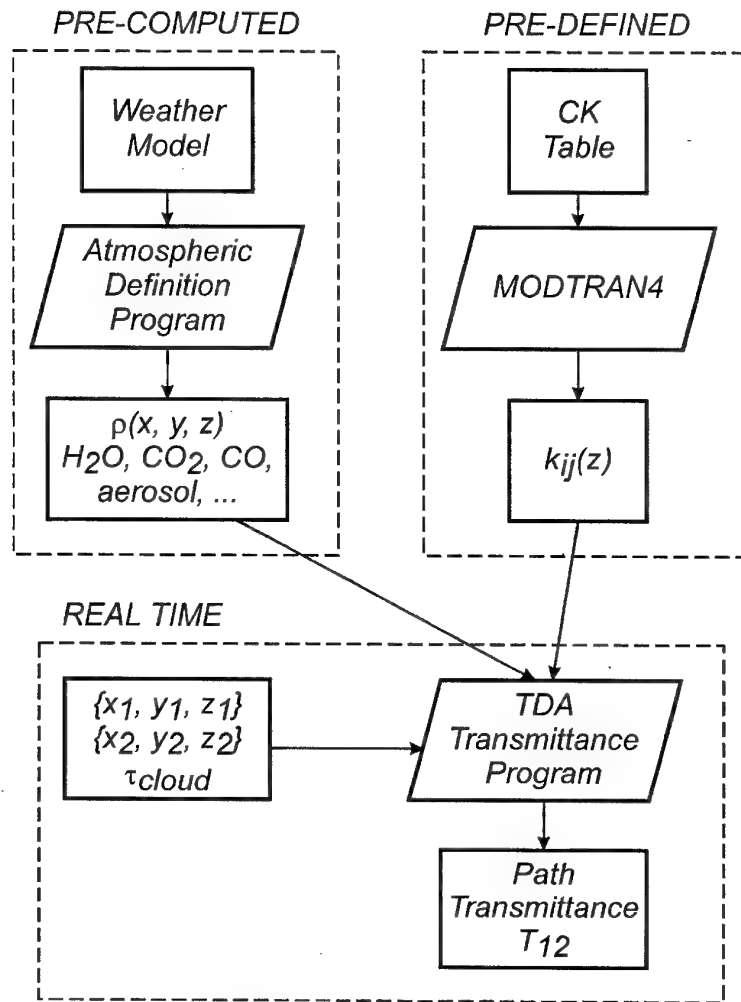


**Figure 2** Flow Chart for the CK Real-Time Transmittance Algorithm.

called from a C-language main program. When the TDA is called, the 3D weather grid is accessed to define the T, P, and water vapor concentration for points along the line-of-sight path between the sensor  $(x_1, y_1, z_1)$  and target  $(x_2, y_2, z_2)$  coordinates, and the clear atmosphere transmittance is calculated by averaging the individual sub-interval transmittances. The sub-interval transmittances are calculated as the products of separate transmittances for water vapor, ozone, the uniformly mixed gases (all remaining molecular species), and aerosols. Finally, the total 3-5  $\mu\text{m}$  transmittance is taken as the product of the clear atmosphere transmittance and a separately specified cloud transmittance.

A sample calculation is displayed in Figure 3 for a sensor at 10 km altitude viewing the vertical ascent of a missile at a constant slant range of 150 km. The curves correspond to 5 km increments in missile altitude from 0-30 km and 10 km increments from 30-100 km. Note that there is very good agreement between the MODTRAN transmittance calculation in Figure 1 with the TDA calculation for a similar geometry (second curve from the bottom in Figure 3). The accuracy of the TDA-computed  $T_{12}$  value is within several percent for all paths, and thus more than satisfies the  $\pm 20\%$  requirement for the present application.

The CPU time required to compute the total transmittance for a 150 km slant path sub-divided



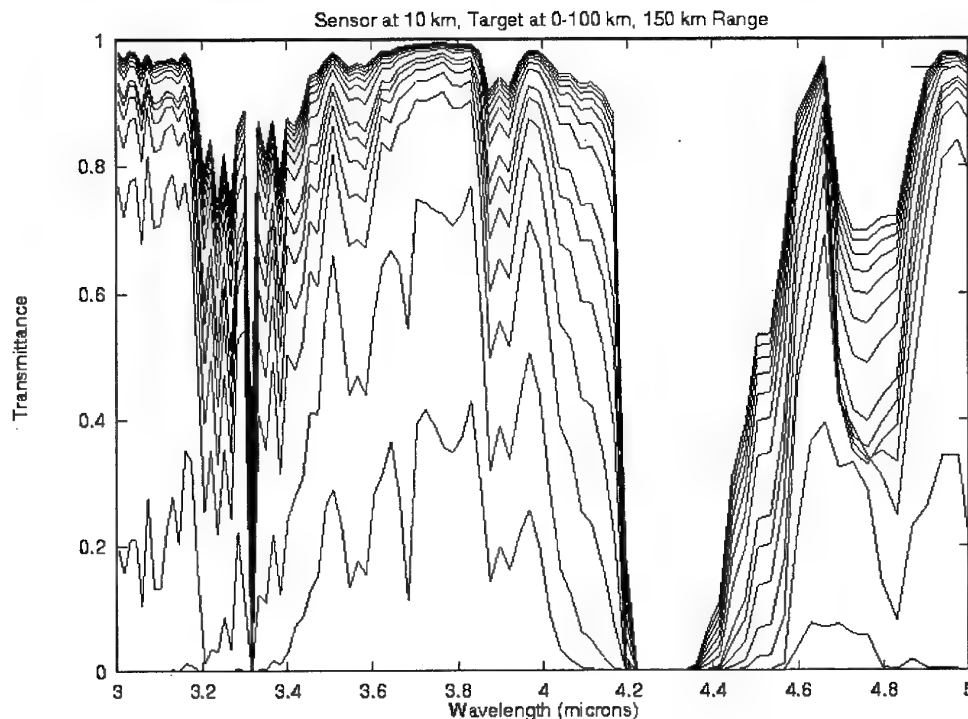


**Figure 3** Sample Transmittance Calculation from the Real-Time 3-5  $\mu\text{m}$  Region TDA.

into 150 segments for the RT calculation is around 10 msec on a 100 MIPS computer. The calculation will be even faster for the narrower (in wavenumbers) 8-12  $\mu\text{m}$  window region. For equivalent resolution the number of spectral sub-intervals would be reduced by a factor of four compared to the 3-5  $\mu\text{m}$  region, resulting in a corresponding fourfold speed improvement.

### 3. CONCLUSIONS AND FUTURE DIRECTIONS

This work has demonstrated that by using the correlated-k (CK) method it is possible to perform accurate calculations of in-band radiation transport with sufficient speed (0.01 second or less for a transmittance calculation) for real-time TDA applications, without resorting to pre-computed databases that are limited to specific geometries. The method is general enough to be extended to other wavelength regions and to other radiation transport problems such as thermal emission and solar scattering which require the calculation of transmittance.

In separate work not reported here, we have also found that the CK method satisfactorily handles the transport of gaseous species radiation in the presence of large temperature inhomogeneities, such as occur in the propagation of rocket plume radiation through the atmosphere. With some additional time saving strategies it should be possible in the near future to extend this approach to radiometrically accurate real-time rendering of entire engagement scenes.

### REFERENCES

1. Edwards, M. M., Hume, E. E., Zawada, F. A., and Mozer, J., "Realizing Environmental Effects Within a Distributed Simulation," Proceedings of Electromagnetic/Electro-Optics Prediction Requirements & Products Symposium, pp 345-354, June 1997.
2. Edwards, M. M., Hume, E.E., Zawada, F. A., and Mozer, J., "The Impact of Clouds on an Engagement-Level Simulation," Cloud Impacts on DoD Operations and Systems 1997

Conference, PL-TR-97-2112 Environmental research Papers, No. 1209, pp 31-34, Paul Tattleman, Ed., September 1997.

3. Bernstein, L. S., Berk, A., Robertson, D. C., Acharya, P. K., Anderson, G. P., and Chetwynd, J. H., "Addition of a Correlated- $k$  Capability to MODTRAN," Proceedings of the 1996 IRIS Targets, Backgrounds, and Discrimination Meeting, January 1996.

4. Berk, A., Bernstein, L. S., and Robertson, D. C., "MODTRAN: A Moderate Resolution Model for LOWTRAN7," Rpt. No. GL-TR-89-0122, Air Force Geophysics Lab., Bedford, MA, 01731, pp. 1-38.

#### **ACKNOWLEDGEMENTS**

The authors thank the Air Force Research Laboratory for support of the work performed by Spectral Sciences, Inc. under Contract No. F19628-91-C-0145.

## IR-RANGE FORECASTS WITH NAVFLIR

Christian von Ruesten  
Friedrich Theunert  
German Military Geophysical Office  
Mont Royal  
D-56841 Traben-Trarbach  
Germany

### SUMMARY

First the influence of meteorological parameters on IR-range are described. Especially fog and precipitation reduce IR-ranges. NAVFLIR consists of three components: the contrast model, the transmission model, and the sensor model. Measurements of IR-ranges in Meppen (NW-Germany) are well in line with the calculations of NAVFLIR. The deviations between different types of IR-measurements of the same target are at the same magnitude as the deviations between calculations and measurements. Reflection effects are also considered by NAVFLIR. Charts of IR-ranges over Germany and over the Adriatic area show typical distributions of weather dependence.

### LIST OF SYMBOLS

ETD	effective temperature difference
MNTD	minimum necessary temperature difference
MRTD	minimum resolvable temperature difference
$n_D$	pairs of lines / object length
L	object length
L	perpendicular object length
p	probability
R	distance
$R_{max}$	range of a given view task
$\lambda$	wave-length

### 1 INTRODUCTION

Navflir was developed for forecasting IR-ranges of FLIRs installed in helicopters and jets. In contrast to night vision goggles, FLIRs work with the thermal spectral range. The dominant factor of shortwave ( $\lambda < 3 \mu\text{m}$ ) spectral data is the reflection of illuminated objects. This reflected light moves through a predominantly scattering atmosphere to the sensor. On the other hand, longwave radiation is emitted by the objects themselves and moves through a mostly absorbing atmosphere (Fig 1).

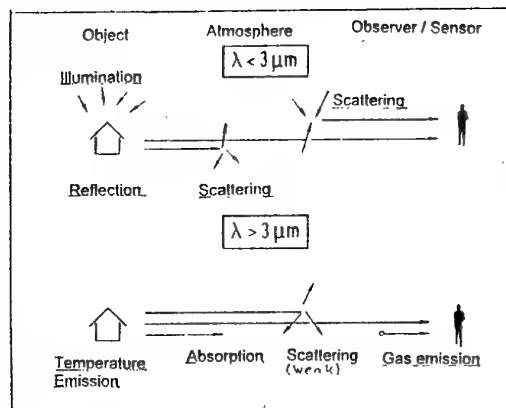


Fig. 1: Principles of measuring in different spectral regions

### 2 INFLUENCE OF GEOPHYSICAL PARAMETERS ON FLIR RANGES

The thermal signal is affected in two ways: First, the atmosphere weakens the signal directly due to absorbing particles like gas molecules, dust, mist, fog and precipitation. Opposite to the absorbing gases having a nearly constant concentration, absolute humidity strongly modifies the atmospheric transmission. An indirect effect of increasing absolute humidity is the swelling of aerosol particles like dust, salt, and soot. In the thermal range the scattering effect of aerosol particles is reduced and almost comparable to the increased absorption effect. Fog reduces the atmospheric transmission on the same order of magnitude as in the visual range. In low radiation fog slightly better ranges occur, because the droplet size distribution is different here. Precipitation reduces the atmospheric transmission significantly, depending of the droplet size distribution.

Further, geophysical parameters change the temperature contrasts of the objects of a scene. Cloudiness diminishes irradiation and, thus the longwave radiation of the objects of the scene. Especially, low and medium clouds cause significantly reduced signatures, especially under broken or overcast conditions. Precipitation causes a film of wetness blurring the thermal contrasts of the scene. Additionally, precipitation produces clutter due to the cooling effect of

evaporation. Wind increases turbulent heat exchange. Especially oscillating wind may produce enormous variations of thermal contrast. Crossover situations due to different heat capacities or conductivities of the objects arise as a typical problem, when measuring thermal infrared signatures. In this way, contrasts may vanish frequently, accompanied by fair weather conditions, in the morning and evening.

### 3 Structure of NAVFLIR

NAVFLIR consists of three components: the contrast model, the transmission model, and the sensor model. The contrast model calculates the surface temperatures of the objects in the scene. It is based on the heat balance equation using time, location, and meteorological parameters as input. Additionally, the calculated radiant fluxes in the scene are needed. The transmission model (LOWTRAN or MODTRAN) calculates the atmospheric extinction depending on the spectral range. In addition, meteorological parameters like aerosol data (air mass) need to be known. The temperature difference between two objects reduced by the extinction of the atmosphere is named effective temperature difference (ETD). The ETD reaches the sensor and is combined with the characteristic curve of the sensor (MRTD) and with the view task (demand of resolution). This calculation is done by the sensor model with the result of IR-ranges.

#### NAVFLIR

Input

S <-> NSI  
 U <-> Lowtran <-> incl. subroutines  
 R <-> Canopy <-> Strahl  
 F <-> Objtemp <-> Strahl, Ninter, Eddy  
 A <-> Reichw <-> Reflex  
 C  
 E

Output <-> Visual <-> Reflex

Fig. 2: Structure of NAVFLIR

The structure of NAVFLIR (Fig. 2) shows the main program SURFACE, which controls in- and output. The contrast model consists of the modules STRAHL, OBJTEMP and CANOPY. STRAHL calculates the short- and longwave radiant fluxes and the radiation budget by using the two-stream approximation. OBJTEMP solves the energy budget for surfaces of buildings, roads, or metals and calculates radiative temperatures of the surfaces. CANOPY solves the energy budget for six layers of a canopy and produces the surface temperatures of vegetation (trees, meadows, and forests). Additionally, botanical parameters (leaf area index, size of leaves, height of canopy etc.) is

needed. The transmission model LOWTRAN 6 calculates the atmospheric extinction on the optical path. A possible change to MODTRAN 4 is being considered.

The sensor model REICHW calculates the FLIR-ranges from ETD, sensor data (MRTD) and view task. The combination of view task and MRTD leads to the minimum necessary temperature difference (MNTD):

$$\text{MNTD (R)} = \text{FAK} \cdot \text{MRTD} (n_D \cdot R / L) ; \quad (1)$$

$$\text{FAK} = \sqrt{3.5 \cdot L / (n_D \cdot L')}$$

e.g.:  $n_D$  (detection,  $p = 50\%$ ) = 1 pair of lines / objectlength (L)  
 $n_D$  (identificat.,  $p = 50\%$ ) = 7 pair of lines / objectlength

$$\text{ETD (R}_{\max}) = \text{MNTD (R}_{\max}) \quad (2)$$

The resolution required for the view tasks is shown in Fig. 3 and the resulting ranges ( $R_{\max}$ ) can be seen in Fig. 4 (W. Schuberth et al., 1991)

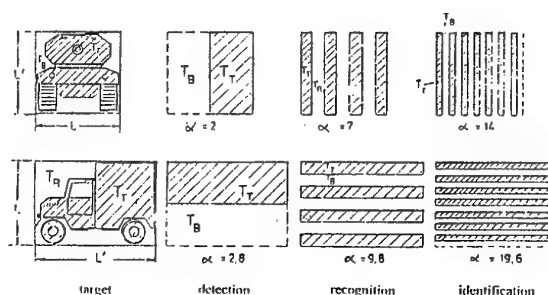


Fig. 3: Relation between view task and resolution

The module VISUAL changes the surface temperatures into grey-shades, so that an IR-image showing the blurring effect caused by the atmosphere is simulated. It increases with increasing distance sensor - object until the range  $R_{\max}$  is reached and the temperature-contrast disappears. Then, the two considered objects cannot be distinguished. Reflection effects are calculated by the subroutine REFLEX using the Fresnel equations. The module EDDY is used for computing the turbulent fluxes of heat and humidity. NINTER interpolates meteorological parameters with respect to time and NSI estimates the precipitation rate from the synop code.

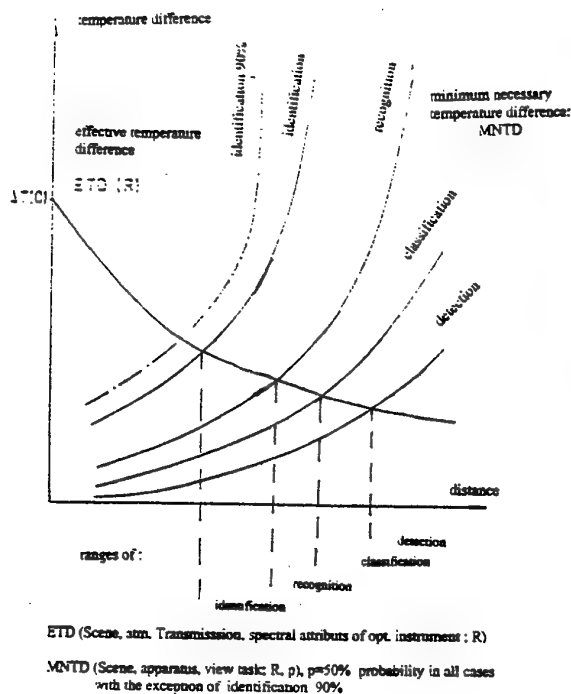


Fig. 4 : Ranges depending on different view tasks (MNTD) (Schuberth et al., 1991)

There are three modes of starting NAVFLIR: The interactive mode, the file mode using examples or prepared data-records, and the OMNIS-mode using model weather forecasts for a chosen area of the GMGO-network. The next menu gives the possibility of changing the input parameters time, distance, altitude, view tasks, probability, and sensor types (Fig.5). After selecting the correct input parameters, you select a scene out of a set of 15 scenes containing 13 different objects (Fig.6). Then, NAVFLIR calculates temperature differences and ranges of the objects with respect to the background of the chosen scene.

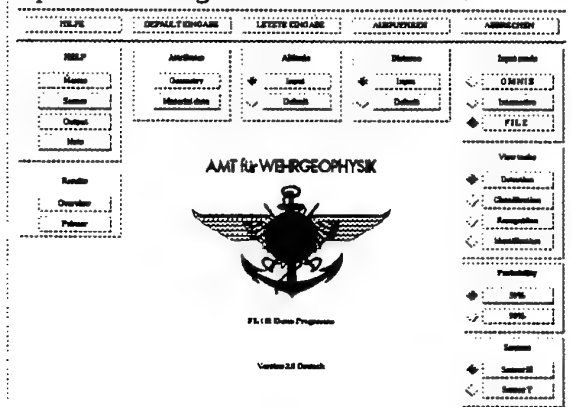


Fig. 5: Starting menu of NAVFLIR containing input parameters

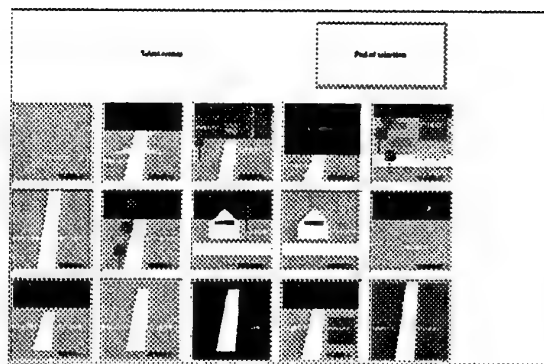


Fig.6: Menu of scenes

#### 4 COMPARISON WITH MEASUREMENTS

During the development of NAVFLIR IR-measurements were conducted in the Meppen area (NW-Germany). The IR-emission of different targets ( mast, bushes, road, etc.) were recorded by an IR-AGA-camera placed on a truck and by FLIR. This mast was also used for measuring the meteorological data. The narrow road was sometimes covered with puddles, which reflected the cold IR-emission of the clear sky. A special object is a large hollow plate filled with water, which therefore had a very large heat capacity.

8 Dec. 1993 was a very interesting measuring day, because a warmfront with heavy rain crossed the area during the evening. In the late afternoon, the rain started (Fig. 7) and the hollow plate was still warmer than its background. At six o'clock the rain became heavy and conditions were extremely bad. Therefore, the plate disappeared in the IR-image. Air temperature was significantly increasing from 4 to 10 centigrades.

Comparison of IR-Measurements in Meppen (NW-Germany) with calculations of the NAVFLIR-Model

weather conditions in the evening of 8th of Dec 1993:  
warmfront crossing Meppen area

time:	16:30	18:20	20:15Z
airtemperature/dewpoint in C:	3.8 / 2.0	4.8 / 3.3	9.8 / 7.3
visibility in km:	5.0	3.0	4.0
weather:	light rain	heavy rain	light rain
clouds (cover, height(ft), type):	8 008 St	8 006 St	6 006 St
	8 080 As	8 080 As	8 080 As
	8 200 Cs	8 200 Cs	8 200 Cs
humidity of soil:	moist	wet	wet
Tmin/Tmax:		-1.3 / +10.0	

Fig. 7: Weather situation during the IR-measurements in Meppen

Later the rain abated and the plate became visible again at 8 o'clock. The plate, however, was cooler then, because its large heat capacity caused a relatively slower warming. An additional cooling was caused by evaporation. These results could also be simulated by NAVFLIR (Fig. 8, 8a, 9 and 9a). Calculations are well in line with the measurements.

The accuracy of calculations and different measurements are comparable, because the deviations between contact and camera measurements are similar to the deviations between measurements and calculations. The variations concerning the bushes are caused by the higher amount of inhomogenities.

Nevertheless the deviations never exceed two centigrates (Fig. 10). Another interesting effect is the reflection of the sky, especially when the sky is clearing up. There are two calculated curves of surface temperatures concerning the road. With the lower curve, the reflection of the sky is considered. The cloudiness (mostly low clouds) decreased during the period. The measured curve suddenly decreased, with disappearing clouds. There is, however, only a slight decrease of the mast temperature (Fig. 11).



Fig. 8-8a: Calculated and measured surface temperature of the Meppen scene before warmfront crossing

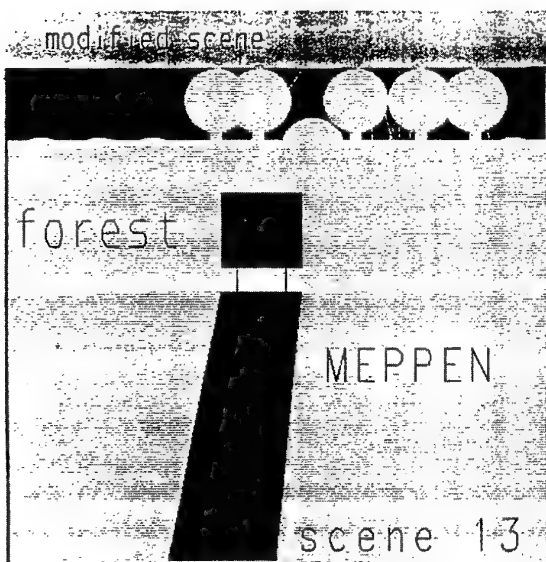
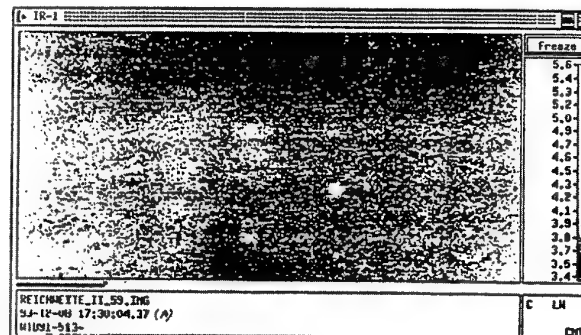
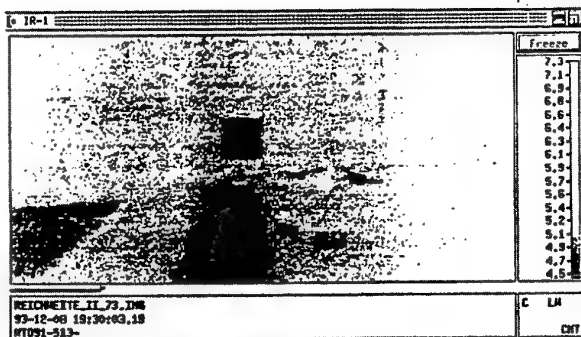


Fig. 9-9a: Measured and calculated surface temperature of the Meppen scene after warmfront crossing



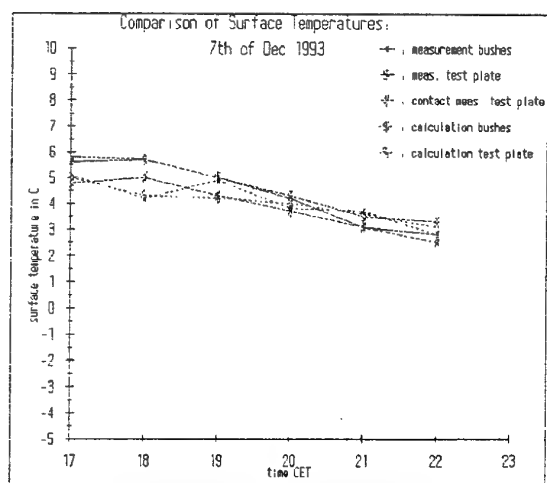


Fig. 10: Comparison of calculation with different IR-measurement methods

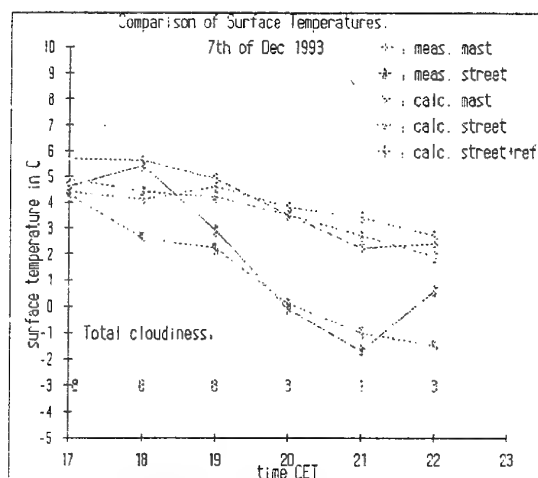


Fig. 11: Influence of reflection on measurements

## 5 CHARTS OF IR-RANGE FORECASTS

The OMNIS- method developed by GMGO enables us to make weather forecasts for every weather station in a region of our choice. It uses weather forecast models and, if necessary, statistical methods as input. NAVFLIR then calculates IR-ranges for the stations. These ranges are interpolated on a grid with a grid-point distance of 50km. The charts were produced for Germany and for the Adriatic area. Lots of object combinations may be calculated. The temperature contrast between street and meadow was chosen, because it is one of the most frequent combinations. The geometrical dimensions of the objects are typical (street: 10m\*1km; meadow: 1km\*1km). The ranges refer to detection with a probability of 50%.

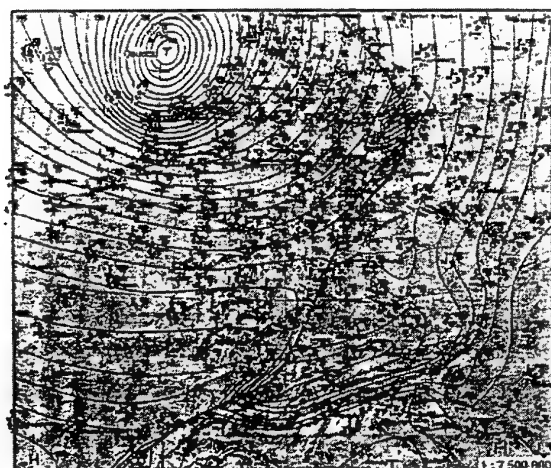


Fig. 12: Low pressure influence over Germany on the 3 Mar 1995

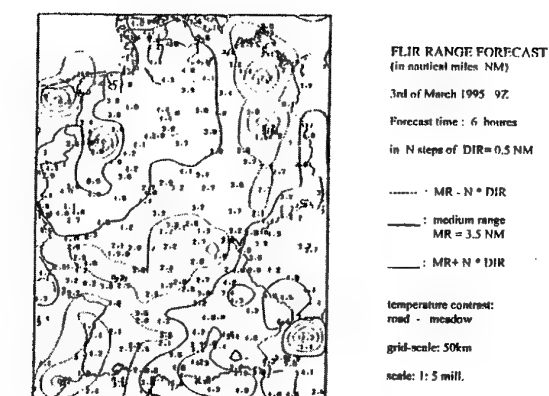
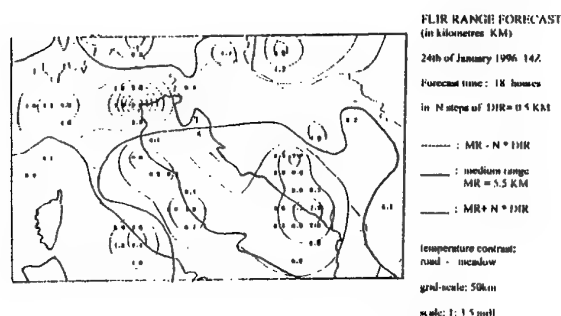


Fig. 13: IR-ranges over Germany resulting from Fig. 12

An interesting weather situation is shown for 3 Mar 1995, where a storm low over the North Sea with a well defined occlusion front extending from the western Baltic to the French Alps caused strong precipitation over East and Southwest Germany. Some showers occurred over North Netherlands (Fig. 12). The IR-range chart (Fig. 13) shows strongly reduced values along the occlusion front, especially along the precipitation area and over the shower area. Low pressure influence caused an inhomogeneous range distribution combined with relatively low values, whereas high pressure gives a homogenous distribution combined with high values.

An example of an IR-chart over the Adriatic region is given for 24 Jan 1996, where low pressure dominates the West Mediterranean and high pressure occurs over SE-Europe. Therefore, reduced ranges are found over North and West Italy where a warmfront produced precipitation combined with reduced visibilities (Fig. 14). Additionally, precipitation is enhanced by a southerly flow moving toward the Alps. Therefore, heavy rain occurred in the region of Venice.



**Fig. 14: IR-range chart over the Adriatic region on 24 Jan 1996**

## 6 Further Outlook

NAVFLIR will be installed in the GeoBerT- network of GMGO. Therefore, each military weather information center in Germany will be able to use NAVFLIR and give IR-range forecasts. Also, it will be possible to calculate IR-ranges all over the world, whenever forecast weather data are available. The non-availability of actual sensor data is a problem furtheron, especially actual MRTD-curves are scarcely available. Hence, there is the problem to adapt NAVFLIR calculations to real sensors.

## References:

### Reports:

- 1 Theunert, F. (1996):  
Navflir, ein Verfahren zur IR-Reichweitenvorhersage. Fachliche Mitteilungen Nr. 221, Amt fuer Wehrgeophysik
- 2 Schuberth, W., W. Wittenstein and D.H. Hoehn (1991):  
Thermisches Reichweitenmodell 2 des FfO (TRM2). Manuscript No.:4 CCG- course "Infrarottechnik -Grundlagen und moderne Anwendungen"



# Weather Effects and Modeling for Simulation and Analysis

Dr. Alan E. Wetmore and Dr. Patti Gillespie and Dr. David Ligon  
US Army Research Laboratory  
2800 Powder Mill Road  
Adelphi, MD 20783 USA

## Abstract

In the past, the US Army developed the Electro-Optical Systems Atmospheric Effects Library (EOSAEL) [1, 2, 3] as analysis tool to investigate and predict impacts of weather on EO systems. This Tri-Service effort has also been extended to NATO countries through collaboration in several research study groups. As new tools for simulation and analysis are developed to support increasingly sophisticated weapons systems, the US Army in collaboration with the Air Force and Navy has been developing a new generation of tools for this support mission. One of our current efforts is the Weather and Atmospheric Visualization Effects for Simulation (WAVES) series of models. These models are designed to increase our analysis and simulation capabilities through both more sophisticated treatment of complex weather conditions as well as supporting imaging and image modification tools.

Historically, analysts have wanted "one number" effects for weather impacts; future developmental systems will need to be modeled from a physical basis that implements the real impacts of weather on notional systems. Imaging sensors must be able to deal with complex targets, backgrounds and camouflage embedded in an inhomogeneous atmosphere. Truly robust systems require testing in all extremes and variations of weather and climatic conditions, testing that can only be carried out through physics based simulations. The WAVES tools are designed to immerse an imaging system in a consistent atmospheric environmental simulation that allows investigation of illumination, shadow, radiance, transmission and turbulence effects on sensor and algorithm performance.

This presentation will describe the existing models in the WAVES toolbox, their interactions with other envi-

ronmental models and an outline of the future research directions we will be undertaking.

## 1 Introduction

Historically the US Army has developed and supported the Electro-Optical System Atmospheric Effects Library (EOSAEL) as the tool to address impacts of the environment on weapons system performance. Development and support for the EOSAEL has been ongoing since the late 1970's. From the beginning this toolkit was envisioned (and implemented) to support Army, Naval, and Air Forces requirements for transmission and visibility calculations in the near earth environment in the presence of battlefield debris. During the design and implementation for the original EOSAEL computer capabilities of the target users forced a focus on straightforward single line-of-sight calculations. Local weather was represented by a single representative vertical sounding that represented the battlefield. Very high resolution effects such as turbulent structure in smoke plumes could not be exploited by the customers, and was not included.

Many EOSAEL models make a calculation of the point-to-point transmission between a target and a sensor. This arises from the way EOSAEL models treat obscuration in the atmosphere as a series of effects that can be superimposed. For instance, if there are several smoke clouds, some vehicle dust, and low stratus clouds we would perform a helicopter to tank

line-of-sight calculation as follows:

1. Use LOWTRAN [4] (now replaced with MODTRAN[5]) to calculate the end-to-end transmission caused by the molecular extinction along the path.
2. Use XSCALE to calculate the end-to-end transmission due to extinction by fog and natural clouds.
3. Use COMBIC to calculate the end-to-end transmission due to smoke and dust clouds in the path.
4. Calculate the total end-to-end transmission as the product of these three terms.

If we are dealing with the effectiveness of a laser device instead of a broadband device, we replace the LOWTRAN/MODTRAN calculation with the EOSAEL LZTRAN model for laser transmission. the analyst would then typically compare this total transmission coefficient to a threshold value to determine if target acquisition or lock-on could occur.

Some radiance effects have been addressed in the EOSAEL, both for finite clouds as isolated effects and for the atmosphere as a whole as represented the sky-to-ground ratio calculation in FASCAT.

The EOSAEL included a climatology module, CLIMAT, providing weather driven climatology. Limited regions were originally available, though now North and South America; Europe; Southwest, Southeast, and Northeast Asia have been compiled. Missing from this collection are Central Asia, Africa, and Australia. Figure 1 shows the regions of the world that currently have climat summaries available. The CLIMAT statistics have been generated from one viewpoint, highly focused on aviation related ceilings and cloud cover, visibility, and precipitation. The use of these climatologies for electro-optic prediction has the drawback that the EO propagation statistics calculated from average values of weather variables is not the same as the average EO propagation calculated from complete weather observations. It is also difficult to understand the connection between extreme weather events and the resulting EO propagation expected.



Figure 1: Regions of the world for which CLIMAT abstracts have been built

After 20 years of support, the EOSAEL is now being commercialized[6]. ARL research is entering a new phase aimed at support of more sophisticated EO simulations.

A new paradigm is being started with the development of WAVES (Weather and Atmospheric Visualization Effects for Simulation) which is designed to support the same part of the battlespace, near earth (surface to 5-12 km AGL) tactical encounters (5-20 km on a side) area. WAVES has been developed from the ground up to represent inhomogeneous 3-D atmospheric effects calculations [7] for imaging sensors.

WAVES [8] has been developed to extend the problems that can be solved using traditional solutions such as MODTRAN.

This new suite of models must support imaging, through complex atmospheres including both complex natural clouds as well as through battlefield effects. WAVES produces 3-D fields of radiance that treat transmission and radiance as equal contributors to imagery. WAVES will modify computer generated visualizations and modify real images. We will of course draw from our past experience and models and interface to the best available supporting models.

Again, our audience is still diverse and trying to answer many different questions, we can not supply only a single answer. We need to develop a series of tools for systems designers and analysts to use. EOSAEL had and WAVES will inherit the army perspective of close to the ground, in the dirty battle-

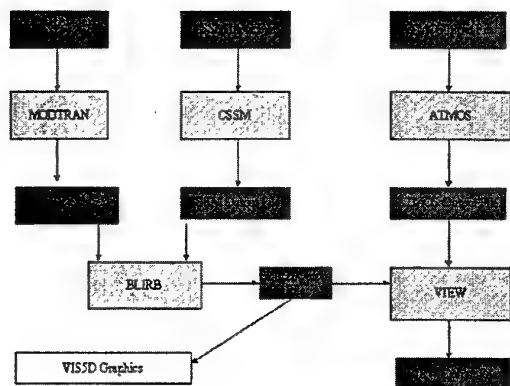


Figure 2: Organization of the WAVES components.

field. The 3-D grid of atmospheric illumination information computed by WAVES can be used for simulations supporting testing and evaluation, analysis, planning, training, and research.

## 2 WAVES

WAVES is a toolkit of several modules that will operate together. It tries to answer the question of what a sensor would see under given weather conditions, or how a sensor view would have been different if the weather had been different.

The ability to substitute different weather conditions and simulate effects allows testing and development to proceed at one location with confidence that we can predict operation at other locations with different weather. These capabilities also can be used to support mission rehearsal and contingency analysis.

It is integrated with other DoD modeling projects such as the US Air Force's MODTRAN[5] and Cloud Scene Simulation Model (CSSM)[9]. The relationship between the various components of WAVES is illustrated in figure 2.

The highest fidelity representations are photo-realistic image transformations. These can include both transformations of actual field data to repre-

sent other weather conditions or accurate rendering of computer generated images.

A lower fidelity level is represented by statistical sampling of measurements for grid based wargames and development of integrated Weapons-Sensor-Target-Weather (WSTW) effectiveness parameters. Representing the WSTW effectiveness as a decomposable factor problem, especially at the level required for accurate simulation based acquisition, remains an open problem. We hope that WAVES will give analysts some of the tools necessary to approach this problem from a fundamental physical understanding.

Finally, a simulation or engineering tool may want to look at the fundamental quantities such as the fluxes to integrate with other models.

### 2.1 Image Modification

Our most ambitious goal is modeling a sensor looking through the atmosphere seeing targets and backgrounds. When modifying an image to account for atmospheric effects we treat the pixels in the original image as sources that propagate to a detector. Along this journey some of the energy is removed before reaching the detector by extinction; molecular absorption and scattering, aerosol absorption and scattering. Also, energy in the atmosphere along the path joins in the journey to the detector; thermal emission, forward scattering by large aerosols, large angle scattering of fluxes in the atmosphere into detector.

The geometry used in WAVES for image modification is represented by a vector from observer to target,  $\vec{R}$ , for the pixel,  $(a, b)$ .

$$\vec{R} = \vec{R}_t - \vec{R}_o = \text{observer to target path vector} \quad (1)$$

The propagation of energy from the target pixels to the observer where it is represented as image pixels,  $I_{ab}$ , is described by,

$$L_{ab} \times T(\vec{R}) + P(\vec{R}) = I_{ab} \quad (2)$$

with,

$$L_{ab} = \text{source radiance} \quad (3)$$

from the scene element that is at range  $R$ . Where,

$$T = \text{transmission}, \quad (4)$$

and,

$$P = \text{path radiance}. \quad (5)$$

Each pixel in an image has a slightly different  $\theta$  and  $\phi$ , that are simply related to their location in the image. In addition, each pixel has a range from the observer that is a complex function of the details of the terrain and geometry of the objects in the scene.

The transmission and path radiance will be computed for a sparse sampling of  $\vec{R}_o$ ,  $\theta$ ,  $\phi$ , and  $R$ . The sampling of  $\theta$ ,  $\phi$ , and  $R$  represents an observer-centric sampling of target locations. Alternatively we could calculate all possible cell center to cell center lines-of-sight

## 2.2 Line-of-Sight Parameters

For a line-of-sight the range dependent transmission and path radiance values are calculated by the VIEW module of WAVES.

$$T(R) = e^{-\int_0^R \tau(\vec{R}) dR} \quad (6)$$

$$P(R) = \int_0^R T(\vec{R}) F(\vec{R}, \hat{\Omega}) dR \quad (7)$$

Within WAVES and VIEW these integrals are replaced by summations through the gridded volumes along the lines-of-sight and tabulated by range, and azimuth and elevation angles.

Thus we represent extinction by  $\tau(\vec{R}_{i,j,k})$  and compute fluxes as the directional quantities  $F(\vec{R}_{i,j,k}, \hat{\Omega}_n)$ . Our representation of space is a grid of 3 spatial dimensions, indexed by the values  $i, j, k$  augmented with discrete direction vectors indexed by  $n$ .

## 2.3 3 Dimensional Radiative Transfer

The 3-D Radiative Transport portion of WAVES is the Boundary Layer Illumination and Radiation Balance (BLIRB) model. Its task is to take a description of the inhomogeneous optical properties of a small region, use boundary conditions from MODTRAN, and

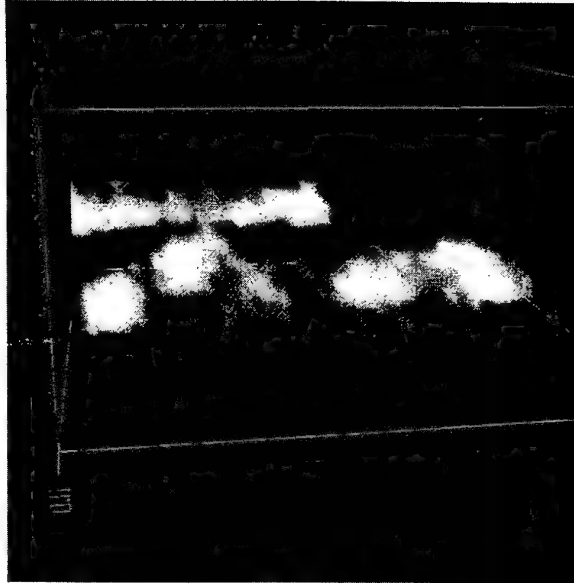


Figure 3: The CSSM cloud field.

then solve for the 3-D radiant fluxes at all locations and directions[7]. The model calculates local extinction coefficient, direct solar flux, and directional diffuse fluxes using a discrete ordinates approach to multiple scattering.

The local optical properties are derived from MODTRAN molecular extinctions, aerosol haze layers, 3-D cloud structures from CSSM, and will include in the future 3-D smoke effects from models such as COMBIC and STATBIC. Figure 3 shows a volumetric rendering of a CSSM cloud field for use in WAVES. Figure 4 shows the "surface" of the same cloud.

The result of running BLIRB is similar to a radiosity calculation from computer graphics, we know what the directional fluxes are everywhere, and we can embed small objects within this volume and calculate what light falls upon them. We can also perform calculations to determine the shadows these perturbing objects would cast.

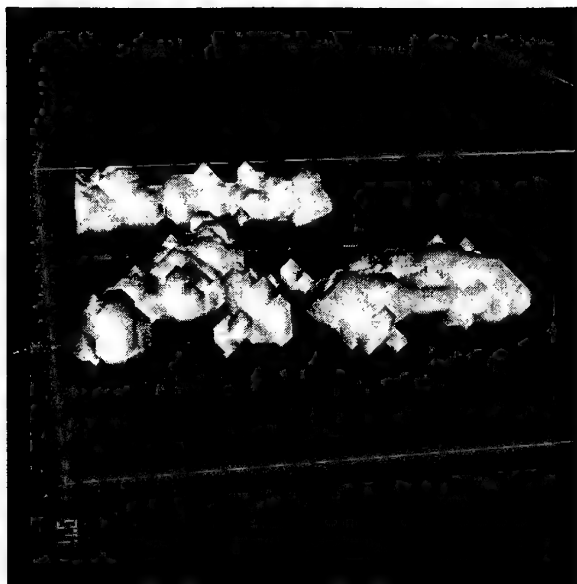


Figure 4: The cloud surface.

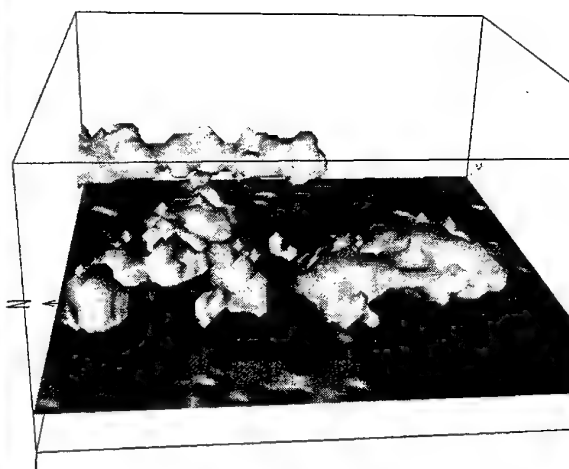


Figure 5: The direct solar surface illumination.

## 2.4 Illumination

In many cases we require knowledge of the energy illuminating a surface. For proper rendering of scene elements we need to know both the intensity of the direct solar component, that casts a shadow, and the diffuse fluxes, that fill in the shadows. Figure 5 shows the direct solar illumination beneath the cloud field. Figure 6 shows a vertical slice of the direct solar radiation and the complex structure of the cloud shadows. In most cases the magnitude of the diffuse component will vary based on both azimuth and elevation angle of the surface being illuminated. Figure 7 shows the downward diffuse flux under the cloud field created by reflection from the cloud. Figure 8 shows the downward diffuse flux under the cloud field created by transmission through the edges of the cloud. Figure 9 shows the upward diffuse flux above the cloud field created by reflection from the cloud.

In WAVES, these quantities are naturally calculated in the discrete ordinates methodology, and reported for the ground surface. This illumination at the surface (at all wavelengths) is also a quantity use-

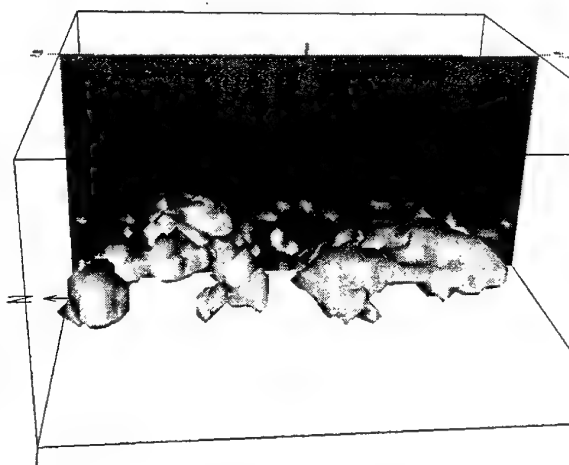


Figure 6: The direct solar illumination for a vertical slice.

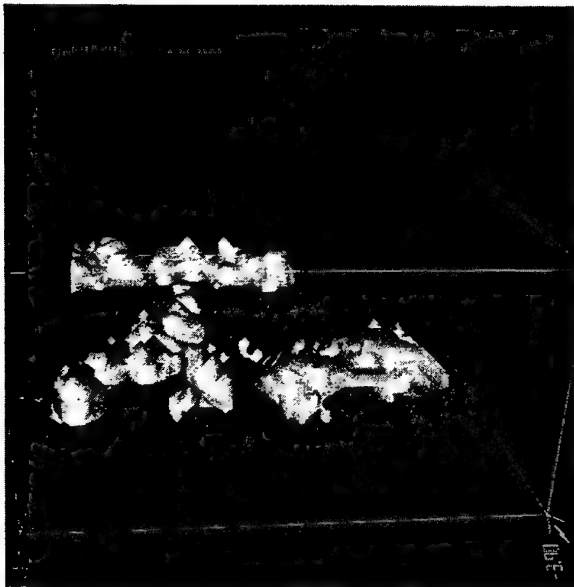


Figure 7: A volumetric rendering of the diffuse illumination in forward direction. Stream 1



Figure 8: A volumetric rendering of the diffuse illumination in forward direction. Stream 2

ful for thermal modeling of targets and backgrounds.

Proof of concept implementations for searchlights and flares have been implemented in BLIRB. If needed, other sources of artificial illumination can be incorporated.

## 2.5 Turbulence

ATMOS is used to calculate the vertical profile of the refractive index structure parameter,  $C_n^2$ , assuming horizontal homogeneity. This turbulence calculation is made using easily obtainable meteorological parameters[10] The refractive index structure parameter is used in a modulation transfer function (MTF) that is folded into the propagation calculations to give time-averaged effects, or blurring, from turbulence. Real time fluctuations due to turbulence are not computed using this model.

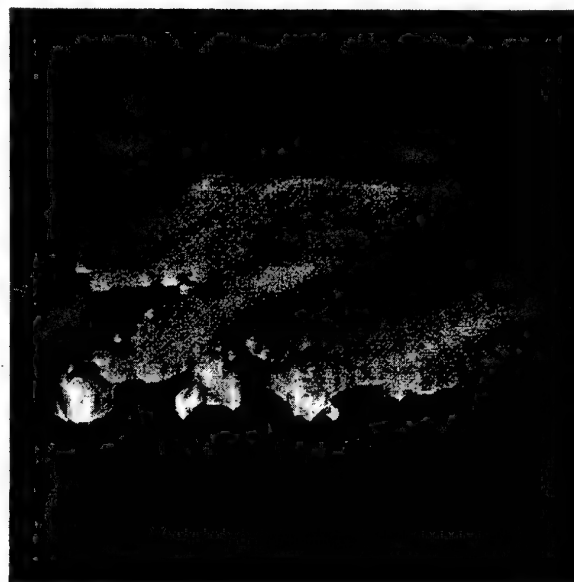


Figure 9: A volumetric rendering of the diffuse illumination in forward direction. Stream 5

### 3 Additional Capabilities

#### 3.1 COMBIC

COMBIC is an existing EOSAEL model that creates cloud skeletons and optical properties descriptions for artillery explosions, smoke munitions and vehicle dust[11, 12]. It has historically been used only to provide line-of-sight transmission calculations.

There are two fundamental ways we could treat smoke clouds in WAVES. The first uses superposition of optical properties from the COMBIC output with the existing optical properties describing our space. We then would solve the 3-d radiative transfer and obtain a full solution.

The second way is to perform the solution of the natural environment and treat the smoke as a perturbation of the natural state. In this case the smoke is treated much like a vehicle that doesn't have a major impact on the radiative properties of the space. We would then add the smoke, calculate the shadows cast by the smoke, and use an external model to add scattering from the smoke.

For one or two isolated smoke plumes the second method is appealing. When we consider what would happen in a major battle with hundreds or thousands of smoke plumes, we realize that the smoke could dominate the illumination near the ground and only the first modeling approach permits continuous and consistent change from no smoke, to all smoke.

#### 3.2 STATBIC

STATBIC[13] is a methodology for replacing the smooth Gaussian plumes used in the COMBIC model with volumetrically textured smoke density distributions that match the turbulent effects seen in actual smoke clouds. Our intention is to use STATBIC to produce realistic textures of smoke and dust plumes in our integrated 3-D simulation suite.

### 4 Other Models

In order for WAVES to be integrated with other parts of large simulations it must use weather data that is

consistent with the description used by other models in the simulation. There are several ways of doing this, the most useful is to integrate WAVES with other tools being used in the simulators. Examples are the Weather IN Distributed Simulations/Total Atmosphere Ocean Server (WINDS/TAOS) used in the JSIMS program, and the Distributed Environmental Effects Manager/Dynamic Information Architecture System (DEEM/DIAS) used in the JWARS program.

Also, the output of WAVES needs to be available for Object-Oriented simulators to extract and access. We are currently developing a toolkit that will include APIs to allow HLA simulations access to both the WAVES results and the individual WAVES tools.

### References

- [1] L. D. Duncan. Electro-optical systems atmospheric effects library. Technical Report ASL-TR-0047, U.S. Army Atmospheric Sciences Laboratory, White Sands Missile Range, NM 88002-5501, 1979.
- [2] Louis D. Duncan and Richard C. Shirkey. EOSAEL 82, executive summary. Technical Report ASL-TR-0122, U.S. Army Atmospheric Sciences Laboratory, White Sands Missile Range, NM 88002-5501, 1982.
- [3] Alan Wetmore. EOSAEL92. In *Proceedings of the Second Symposium on Measuring and Modeling the Battlefield Environment — NATO Panel IV, on Optics and Infrared, RSG-15 on Characterization of Battlefield Effects and Related Measurement Techniques*, volume 1B, Paris, France, June 1993.
- [4] F. X. Kneizys, E. P. Shettle, L. W. Abreu, G. P. Anderson, J. H. Chetwynd, W. O. Gallery, J. E. A. Selby, and S. A. Clough. Users guide to LOWTRAN 7. Technical Report AFGL-TR-88-0177, Air Force Geophysics Laboratory, Hanscom Air Force Base, MA 01731, 1989.
- [5] A. Berk, L. S. Bernstein, and D. C. Robertson. MODTRAN: A moderate resolution

model for LOWTRAN7. Technical Report GL-TR-89-0122, Air Force Geophysics Laboratory, Hanscom Air Force Base, MA 01731, 1989.

- [6] A. E. Wetmore, P. Gillespie, A. McCann, and J. Schroeder. EOSAEL — current work and future directions. In *Proceedings of the 1997 Battlefield Atmospheric Conference*, San Diego, CA, December 1997.
- [7] A. E. Wetmore and A. Zardecki. The boundary layer illumination and radiation balance model (BLIRB). In *Proceedings of the Cloud Impacts on DoD Operations and Systems 1993 Conference*, Fort Belvoir, VA, November 1993.
- [8] A. E. Wetmore, P. Gillespie, D. Ligon, M. Seablom, G. Seeley, and J. B. Mozer. Experimental evaluation of the integrated WAVES-CSSM models. In *Proceedings of the 1997 Battlefield Atmospheric Conference*, San Diego, CA, December 1997.
- [9] M. E. Cianciola, M. E. Raffensberger, E. O. Schmidt, and J. R. Stearns. Atmospheric scene simulation modeling and visualization. Technical Report PL-TR-96-2079, Air Force Phillips Laboratory, Hanscom Air Force Base, MA, 1996.
- [10] H. Rachele and A. Tunick. Energy balance model for imagery and electromagnetic propagation. *Journal of Applied Meteorology*, 33, 1994.
- [11] D. W. Hoock, R. A. Sutherland, and D. Clayton. EOSAEL 84, volume II, combined obscuration model for battlefield-induced contaminants, COMBIC. Technical Report ASL-TR-0160-11, U.S. Army Atmospheric Sciences Laboratory, White Sands Missile Range, NM 88002-5501, 1984.
- [12] S. D. Ayres and Maluka Munoz. Final statistical evaluation of the combic model.
- [13] Sean O'Brien. STATBIC users guide. Technical Report ARL-TR-1375, U.S. Army Research Laboratory, Adelphi, MD 20783, 1998.



## AUTOMATIC CORRECTION FOR ATMOSPHERIC DEGRADATION IN INFRARED IMAGES

D R EDMONDSON, L A WAINWRIGHT, E J PRICE, S A PARRISH, M GODFREY, N M FAULKNER, S P BROOKS

British Aerospace Systems and Equipment, Clifton Road, Plymouth, DEVON PL6 6DE

J P OAKLEY, M J ROBINSON

University of Manchester

### SUMMARY

This paper is concerned with methods to correct atmospheric degradation in thermal images in the 8-12 and 3-5 micron wavebands. Previous work [1], [2] has shown that a significant improvement in effective visibility may be achieved in the visible spectrum by using a simple model for atmospheric attenuation. The extension of this work into the infrared wavebands is reported here.

The method is based on a three-parameter model for the transmission of flux from the terrain to the imaging sensor. The measured flux is given by:

$$I = C_0 (1 + C_1 \exp(-\sigma R))$$

where  $R$  is the range and  $C_0$ ,  $C_1$  and  $\sigma$  are constants which depend on the atmospheric parameters and the terrain radiance  $\sigma$  is known as the extinction coefficient. The inverse problem is solved to obtain estimates for the three parameters using the actual image data. The values of sigma obtained in this way are in good agreement with those computed using MODTRAN.

A more interesting and useful feature of this approach is that, when the model is combined with a range map corresponding to the image, the atmospheric degradation may be reversed.

Results are presented using data from the visible, 3-5 micron and 8-12 micron wavelength image sequences in a maritime environment. The data was collected under conditions of moderate-to-poor visibility with extinction coefficients in the range 0.16 to 0.62 km<sup>-1</sup> for the IR wavebands. The enhanced images show a significant subjective improvement in clarity. This improvement is confirmed using three metrics based on contrast, SNR and segmentability. The method has been shown to offer worthwhile improvements over the full range of visibilities - improvements capable of translation into improved detection, identification and tracking.

### 1. INTRODUCTION

One important limitation in using a thermal imager for surveillance and tracking is its performance in adverse weather conditions. Any method which offers the possibility of increasing the range at which targets can be detected is well worth examining. The model-based contrast-enhancement method, the subject of this paper, falls very firmly into that category.

This paper describes an image-processing method for increasing the range at which targets can be detected, which is automatic in the sense that no parameters need be entered by the user.

This method [1], [2] was originally developed as a result of a collaboration between the University of Manchester and British Aerospace Military Aircraft and Aerostructures. The initial work was directed towards improving the visibility of terrain features captured by a forward-looking airborne Charge Coupled Device (CCD) camera.

Significant enhancement of images taken in conditions of haze and low-level fog was shown [1]. The work was later extended, by British Aerospace Systems and Equipment in collaboration with the University of Manchester, to the enhancement of infrared images in adverse weather conditions. The purpose of this paper is to report on recent experiments with the algorithm using infrared images from both the 3-5 micron and the 8-12 micron bands. Visible spectrum images of some of the scenes were also collected. The algorithm used is essentially that reported in [1]. However, a full description is given here for the convenience of the reader.

### 2. AIMS AND OBJECTIVES OF THE STUDY

The primary aim was to quantify both the absolute and the relative performance of the algorithm in three wavebands: visible light, 3-5 micron and 8-12 micron. The experimental arrangements are described below in Section 4.

Three metrics have been used to measure the improvement in image: one for image contrast, one for Signal-to-Noise Ratio (SNR) and one which quantifies the ease with which an image can be accurately segmented. These metrics, together with the results of their application, are described in Section 5 below.

One interesting feature of the Oakley algorithm is that, as a by-product of image processing, it generates an estimate for the overall extinction coefficient (across the whole band of interest). Thus one possible check that the algorithm is working correctly is to compare the figures for extinction coefficients with those produced by current MODTRAN codes for the corresponding atmospheric conditions. The results from this comparison are also presented in Section 5.

The overall aim is to establish whether this method *truly* offers advantages if applied in a real system.

### 3. EXPLANATION OF THE OAKLEY METHOD

The Oakley algorithm subtracts the extra radiance introduced by the atmosphere radiating in the infrared (the "airlight") from the total radiance detected at the camera. The remaining component is then the attenuated radiance from the terrain. This is scaled by a factor which compensates for degradation by scattering and absorption. Since the grey levels of the thermal image are directly related to the irradiance at the camera lens, an enhanced image using the compensated values can be generated.

In a vacuum there would be no attenuation of flux by the atmosphere and, if the solid angle corresponding to the  $k_{th}$  pixel was  $\Omega_k$  and the terrain radiance was  $M_k$ , then the irradiance at the sensor from a particular patch of terrain would be given by:

$$J_0 = \Omega_k M_k \quad (1)$$

The  $k_{th}$  pixel value,  $P_k$ , is then:

$$P_k = G\Omega_k M_k \quad (2)$$

where  $G$  is the conversion factor of the sensor.

The attenuation of the radiance from the terrain,  $J_r$ , due to scattering and absorption by the atmosphere is modelled by:

$$J_r = J_0 \exp(-\beta R_k) \quad (3)$$

where  $J_0$  is the irradiance that would theoretically come from the terrain if the intervening medium were a vacuum,  $\beta$  is the extinction coefficient and  $R_k$  is the distance of a terrain patch from the sensor.

The radiance introduced by the atmosphere (the "airlight"),  $J_b$ , is modelled by:

$$J_b = \frac{DP\Omega_k}{\beta} [1 - \exp(-\beta R_k)] \quad (4)$$

where  $D$  is the density of the particles in the aerosol and  $P$  is the radiant intensity of a single particle.

Therefore, the total irradiance at the camera is the sum of (3) and (4) ie:

$$J_{total} = J_b + J_r \quad (5)$$

Figure 1 shows the solid line representing equation (5) fitted to the actual irradiance and range values for individual pixels in the image.

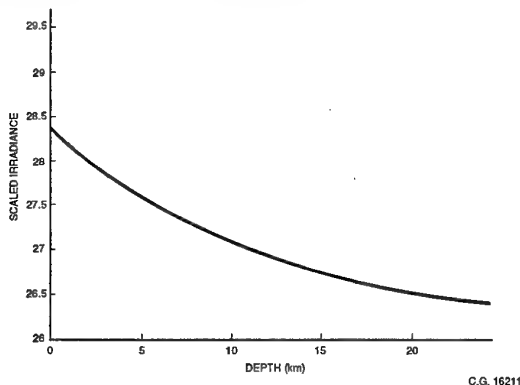


Figure 1 Solid Line Representing Equation (5)

Figure 2 shows how equation (5) comprises the two components - the attenuated terrain component decreasing with range (equation (3)) and the airlight increasing with range equation (4).

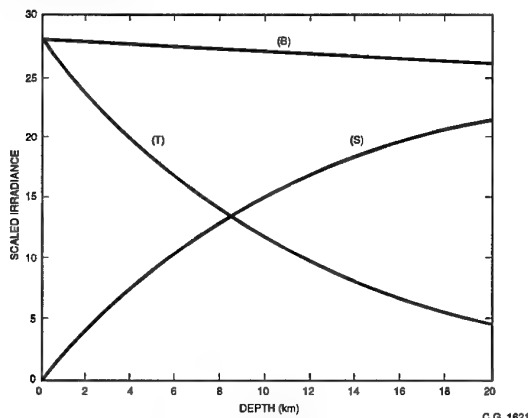


Figure 2 The Two Components of Equation (5)

The extinction coefficient  $\beta$  is, in general, a function of wavelength as is the radiance of the atmospheric particles.

However, for the purposes of image processing, the values

of  $\beta$  and the airlight term  $\left(\frac{DP}{\beta}\right)$  are assumed to be

constant. The relationship between the irradiance at the sensor and the range may then be described using the three-parameter model:

$$J_{total} = c_0 [1 + c_1 \exp(-\beta R)] \quad (6)$$

where  $c_0 = DP\Omega_k$  and  $c_1 = \frac{M\beta}{DP} - 1$

although estimates for  $c_0$ ,  $c_1$  and  $\beta$  are best obtained directly from the image data using a curve-fitting operation.

To do this, each pixel in the image is then assigned a range using knowledge of the scene and a range versus irradiance scatterplot generated which will exhibit a trend between received irradiance and distance from camera.

The curve fitted to the range versus irradiance data is a model which describes the theoretical relationship between the received flux  $P_k$  at the  $k_{th}$  pixel and its range  $R_k$ .

An example is shown in Figure 1. The solid line represents the model fit from (6). Note that typical sensors do not produce an output which corresponds directly to the irradiance. This is for two reasons. Firstly, they operate within a certain 'temperature' interval so that zero output does not, in general, correspond to zero flux. Secondly, the image data is Gamma-encoded for display on a video monitor. The relationship between the grey level  $P_k$  and the irradiance  $J_{total}$  may be described by the equation:

$$J_{total} = MP_k^{2.2} + c \quad (7)$$

where  $M$  and  $c$  are constants, which are usually determined by the settings of the sensor controls. The values of these constants may be determined using a radiometric calibration procedure (see Section 4).

Once values have been obtained for  $c_0$ ,  $c_1$  and  $\beta$ , the enhanced image is produced using a simple pixel-by-pixel transformation:

$$J_e = (J_{total} - J_b) \exp(+\beta R) \quad (8)$$

where  $J_b$  is given by  $c_0(1 - \exp(-\beta R))$ .

The range  $R$  will, in general, be different for each pixel and so  $J_b$  must be re-evaluated for each pixel.

$J_e$  is computed in this way for each pixel. Thus, the irradiance map is corrected for scattering and absorption by the atmosphere. The irradiance estimates thus produced are estimates for the irradiance values which would be measured if there were no degradation.

The corrected irradiance estimates may be suitably scaled and then Gamma-encoded for display on a conventional video monitor.

The different models corresponding to the various cases of  $c_1$  being positive, negative and zero have been negotiated.

## 4. DATA GATHERING

### 4.1 Trials Requirements

The main requirement for the trial was that there must be a sufficiently large, scattered radiation component for the method to subtract.

In order to guarantee a reasonable amount of atmospheric attenuation, the visibility must be either poor or the target must be at a long range. Since poor visibility was not a certain condition during the period of the trial, a site was chosen with a large available range.

The site selected at Jennycliff, just outside Plymouth, was 38m above sea-level and allowed a maximum range of 22km out to the horizon at sea. Figure 3 below shows the area of the field of view. Other major advantages of the site were:

- The Plymouth breakwater and the coastline from Kingsand to Penlee Point gave definite ranges.
- Within the area, commercial and pleasure marine activity would give a number of targets at different ranges within the images.
- The local weather station was virtually co-located with the trials site guaranteeing accurate meteorological data.
- The site was conveniently located only a few kilometres from British Aerospace.

The cameras used in these trials were:

- Inframetrics Thermacam (3 - 5 micron)
- Steinheil Nanoquest (8 - 12 micron)
- Panasonic NV - M40B VHS (visible)

It would have been desirable to ensure that each camera was set with the same field of view and also that the three cameras were synchronised. Neither of these was possible. The magnification was set such that the field of view of each camera was as similar as possible, if conditions indicated that a reasonably large extinction coefficient was likely.

Radiometric calibration of the data was catered for by collecting the temperature of the sea, in addition to the air temperature.

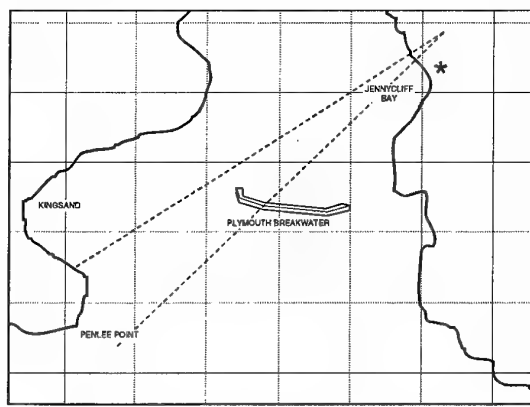


Figure 3 Schematic of Trials Site

#### 4.2 Trials Data

Data was collected on five days between 24th July 1997 and 7th August 1997. For once the British weather did not let us down. Although an anticyclone was firmly established over the area, a large amount of moisture had been trapped. This gave conditions of high humidity (plus very misty conditions) resulting in visibilities ranging from 3km to 16km. It would have been useful if data out to the full range of 22km had emerged. Full met. data was obtained from the Meteorological Office. Visibility was assessed by the trials engineers, using the range cues of the breakwater and the shoreline. Sea temperature measurements were supplied by the Plymouth Marine laboratory. This was used as an aid to the calibration of the images.

From the large volume of data collected, sequences from three runs were selected for further analysis.

The main criteria for selection were the presence of a number of targets within the sequence and the desire to cover a good range of extinction coefficients. Contrast enhanced images were produced for each run.

## 5. RESULTS

### 5.1 Qualitative Improvements

As in previous work (1) a good preliminary test is to establish if the images appear to have better contrast after enhancement. A sample of raw and enhanced images for all wavebands are shown in pairs below in Figures 4A and 4B, Figures 4C and 4D and Figures 4E and 4F. In all the runs digitised and selected for further analysis and at all wavebands, visual inspection confirmed the contrast had improved. For a number of these runs (eg 4A and 4B), the enhanced images show targets not visible before the process.

### 5.2 Extinction coefficient

The meteorological data associated with each run enabled the extinction coefficient to be calculated using MODTRAN3. This value is compared with the value obtained as part of the contrast enhancement process. The results are shown in Table 1.

Table 1 Comparison of Extinction Coefficients Obtained from the Oakley Method and MODTRAN3

Date	Run No	Waveband	$\beta_E$ Oakley	$\beta_M$ MODTRAN
6/8/97	1	VISIBLE	-	0.359
	1	3-5 micron	0.173	0.162
	1	8-12 micron	0.213	0.221
7/8/97	1	VISIBLE	0.848	1.085
	1	3-5 micron	0.157	0.323
	1	8-12 micron	0.292	0.314
7/8/97	2	VISIBLE	0.741	0.780
	2	3-5 micron	0.154	0.291
	2	8-12 micron	0.307	0.305

For both the visible and the 8-12 micron wavebands, the extinction coefficient obtained from the Oakley method ( $\beta_E$ ) and that obtained using MODTRAN3 ( $\beta_M$ ) show very good agreement.

The results for 3-5 micron are poor in two of the three runs considered. However, in the MODTRAN3 results, the value of the parameter ICSTL, which controls the degree of continental aerosol influence, has been set at various values between 5 and 9.

It is possible that a better choice of ICSTL will enable the agreement of the extinction coefficients at 3-5 micron to be improved without too much degradation in the visible and 8-12 micron bands.

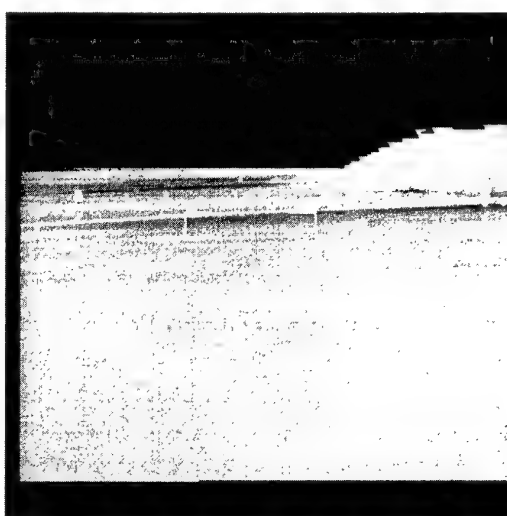
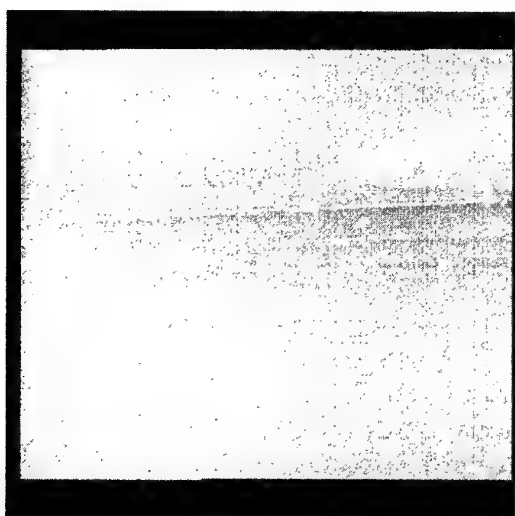
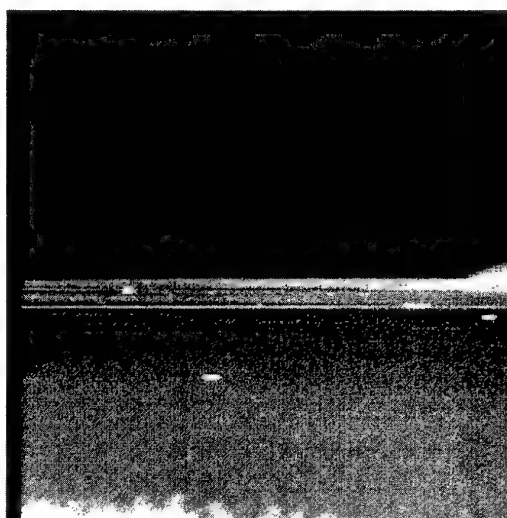
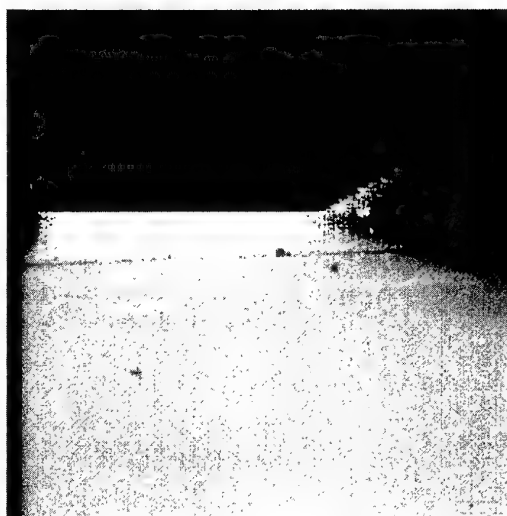
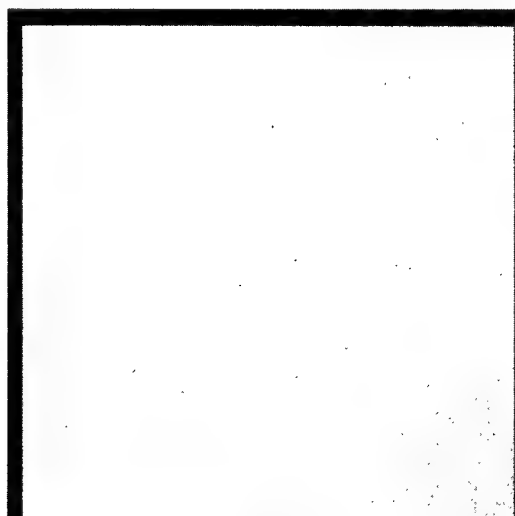


**Figure 4E Original - 8-12 micron**

**Figure 4F Enhanced - 8-12 micron**

**Before and After Images for the Same Run Covering the Three Wavebands**

### 5.3 Contrast Enhancement Metric

Since the aim of the Oakley algorithm is to improve contrast, it is an obvious choice to look at this metric first. The original form of the metric considered was very simple. Within the selected region, the maximum and minimum grey level values were determined for both the original image and the enhanced image. The contrast improvement (percent)  $C$  is given by:

$$C = \left( \left( \frac{E_{max} - E_{min}}{O_{max} - O_{min}} \right) - 1 \right) \times 100 \quad (9)$$

where  $E_{max}$  and  $E_{min}$  are the maximum and minimum grey levels respectively for the enhanced image and  $O_{max}$  and  $O_{min}$  the corresponding grey levels for the original image.

Though this metric should give a reasonable idea of the contrast improvement, it is rather crude. A better method is to sum the percentage improvement along each row in the defined region and then to average this over all the rows.

Thus, the average contrast improvement  $C_{av}$  is:

$$C_{av} = \frac{\sum_{r=1}^n C_r}{n} \quad (10)$$

where  $C_r$  is the percentage improvement for row  $r$  (found by applying equation [9] to row  $r$ ) and  $n$  is the total number of rows within the region. Results for  $C$  and  $C_{av}$  for a number of runs are given in Table 2.

The results obtained in Table 2 show the contrast improvement obtained over the whole image. The results show that, in general, the method gives significant improvements in contrast. For most cases, the contrast improvement measured over the whole picture shows a lower level of improvement. Two cases in the averaged case show an actual reduction in contrast. It is significant that they are both for the same run in the IR wavebands.

**Table 2 Contrast Metric Results - Overall Picture**

Date	Run No	Waveband	C	$C_{av}$
7/8/97	1	VISIBLE	392	377
	2	VISIBLE	49	70
6/8/97	1	3-5 micron	132	-12
7/8/97	1	3-5 micron	67	16
	2	3-5 micron	131	64
6/8/97	1	8-12 micron	44	-16
7/8/97	1	8-12 micron	95	30
	2	8-12 micron	49	70

In practice, the contrast improvement in the region of a target is of greater interest. To investigate this, one run was selected (7/8/97 Run 1) and the change in contrast improvement measured as the region of interest surrounding the target was increased.

During this process the box was kept centred on the target. It was also necessary to select targets which were well separated from other objects and also away from the border of the image. These results are shown in Table 3.

**Table 3 Change in Contrast Metric as the Region of Interest Surrounding a Target is Increased**

Waveband	Small Box	Medium Box	Large Box
VISIBLE	196	99	58
VISIBLE	115	105	94
3 - 5 micron	- 4	- 9	- 12
3 - 5 micron	137	105	104
8 - 12 micron	26	6	- 2
8 - 12 micron	203	165	119

These results show that, for individual targets, a similar pattern of contrast improvement results. This improvement is maximised when the bounding box around the target is small, ie the target dominates the area.

### 5.4 Signal-to-Noise Ratio

The signal to noise ratio (SNR) metric is the most commonly used measure of the quality of an image. The reason for this is that it is simple to implement and gives a result that is easy to interpret.

A high SNR is an intuitive indication of a clear image. The SNR formula used for this report is as follows:

$$SNR = \frac{\text{Average of Target} - \text{Average of Local Background}}{\sigma \text{ of Local Background}} \quad (11)$$

where 'average' and ' $\sigma$ ' refer to the mean and standard deviation of the pixel grey levels respectively.

This formula is implemented by defining a target within an image and then defining a local background area. The target is defined by hand picking pixels within an image which the user perceives as belonging to a target. The hand-picked target pixels are then assigned a bounding box which is defined as the rectangle which clips the extremes of the target in the horizontal and vertical directions. The local background area is then defined as the area between the target bounding box and another box which is a number of times larger than the bounding box of the target. For this project, the background box is scaled up by a factor of three on the target bounding box.

The results of the SNR calculation using the calculations described above are shown below in Table 4. The objects are taken from a single run but for the three wavebands. As expected, the process of contrast enhancement makes little difference to the SNR as defined in this paper. In the visible waveband, some improvement can be seen but, for the IR wavebands, little or no change is seen.

**Table 4 7th August 1997 Run 1 - SNR Results for Objects in the Three Wavebands**

Waveband	Original	Averaged	Enhanced
VISIBLE	6.29	8.07	11.51
VISIBLE	1.91	4.32	5.60
3-5 micron	12.60	13.44	12.41
3-5 micron	3.51	3.43	3.68
8-12 micron	8.58	8.64	8.51
8-12 micron	2.66	2.59	2.32

### 5.5 Automatic Segmentation

The most significant image processing application is that of Automatic Tracking and Recognition (ATR). Clearly, if the tracking of a particular target in an enhanced image is better than in the original, this suggests that the enhanced image is an improvement on the original. The automatic segmentation metric used here is a simple method of quantifying the trackability of an image.

The tracking system consists of two stages. The first stage is to segment the input image and the second stage (the tracking stage) attempts to follow targets in the segmented image. The latter process does not change, in the sense that the algorithms are identical, no matter what input is used. Therefore, the tracking quality is controlled entirely by the properties of the segmented image. The trick is to measure how useful the segmented image is to a tracking application.

The object of the segmentation process is to form an image in which possible targets are separated from the background. Usually the output is an image in which anything not considered as a target is black, ie zero brightness. Therefore, possible targets can be picked out easily by the tracker because they are simply the non-zero pixels. The quality of the segmented image can be measured by checking to see how well the automatically designated targets match up with real targets.

The problem of how to define the real targets remains. Fortunately, the human brain is extremely good at picking up targets within an image. On the whole, this is due to the huge target database that the brain contains which enables it to recognise objects within the image as targets. Further to recognising the objects, the brain can extrapolate to decide which pixels actually make up the target even though noise in the image may make it virtually impossible to see the edges of the object. This means that a target can be hand designated by eye with a great deal of accuracy.

The method used for this investigation is as follows. Firstly, a target in an image is designated by selecting individual pixels. The output from this process is a simple binary image in which the designated target pixels appear white and the rest of the image is black. The next step is to pass the image through an automatic segmentation process which will produce an image in which many targets can be identified. Finally, the hand picked or 'real' targets and the automatically selected targets can be compared.

The segmentation technique used in this project was the same as that used as part of many BASE tracking products.

A quality assessment is done by simply finding any automatically selected targets that coincide with the real target and calculating three values for each one in turn.

The three values calculated are as follows:

- The number of pixels designated as target pixels by both processes.
- The number of pixels designated as the real target but not selected by the automatic segmentation process.
- The number of pixels not designated as the real target but were nonetheless selected by the automatic process. This is known as the number of false alarms.

These three values are illustrated in Figure 6 below.

Table 5 below shows the results obtained for various targets in three of the runs.

**Table 5 Automatic Segmentation Before and After Contrast Enhancement**

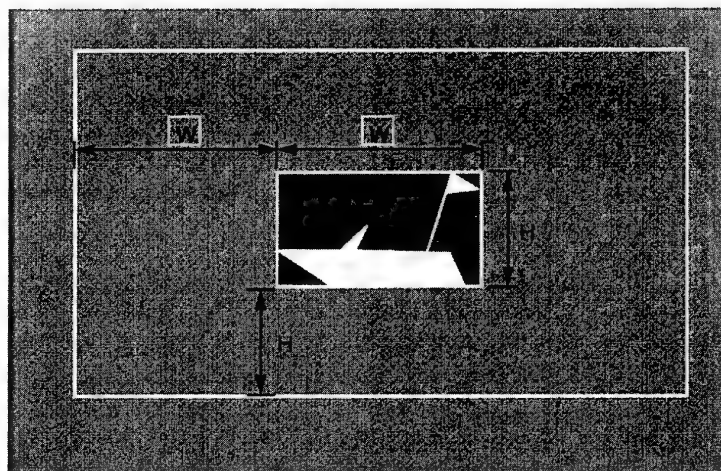
Raw Image			Enhanced Image		
Missed	Both	False Alarms	Missed	Both	False Alarms
2	170	54	0	172	25
0	103	102	0	103	14
0	87	68	0	87	34

The results shown in Table 5 are most encouraging. After enhancement, the 'false alarm' pixels for individual targets within an image are considerably reduced. This will enable better detection, identification and tracking to take place

### 6. DISCUSSION AND CONCLUSIONS

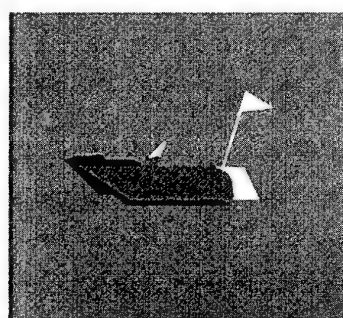
The aim of this work was to collect data and identify the improvement obtained by the Oakley method in a quantifiable manner. The main findings are these:

- In most cases the overall contrast of an image is improved in all wavebands. These improvements are large in a number of cases.
- SNR is relatively unaffected by contrast enhancement. This is to be expected as changes in contrast across the whole image will have little effect.
- Contrast enhancement tends to improve the performance of image segmentation. This is shown in the considerably lower number of 'false alarm' regions produced after enhancement.
- Contrast Enhancement is a valuable process and should aid the overall tracking process. It is particularly useful in adverse weather conditions. The estimation of the extinction coefficient is an interesting by-product of this algorithm.






C.G. 16218

Figure 5 The Target Bounding Box and Local Background Area used in the SNR Formula (11)



#### KEY:

-  = PIXELS SELECTED BY BOTH PROCESSES
-  = PIXELS MISSED BY AUTOMATIC PROCESS
-  = EXTRANEIOUS PIXELS SELECTED BY AUTOMATIC PROCESS

C.G. 16218

Figure 6 Parameters Used to Evaluate the Quality of the Segmented Image

## 7. FUTURE WORK

Four main activities are planned for the future:

- a) The current simulation is to be linked into a digital terrain database. This will enable the range of each pixel within the image to be calculated in a simple fashion.
- b) Work will be carried out to establish if this method aids in the classification of objects. The main features used in our current classification schemes will be examined and a suitable metric devised.
- c) The effect of frame averaging on the various metrics will be examined.
- d) The design and construction of a hardware demonstrator.

## 8. REFERENCES

1. J R Oakley and B L Satherly IEEE Transactions on Image Processing - Vol 7 No 2 February 1988 pp 167-179.
2. Patent Application PCT/GB96/01657 Image Enhancement.  
International Filing Date 12th July 1996.

## 9. ACKNOWLEDGEMENTS

The authors would like to thank Mike Everett and Dave Parker of British Aerospace Military Aircraft and Aerostructures for their help and encouragement.



# The infra-red signature of a hot scattering plume calculated by the SCATAX method

M. J. Caola,  
Sowerby Research Centre, British Aerospace,  
Filton, Bristol, BS12 7QW, England.

## Abstract

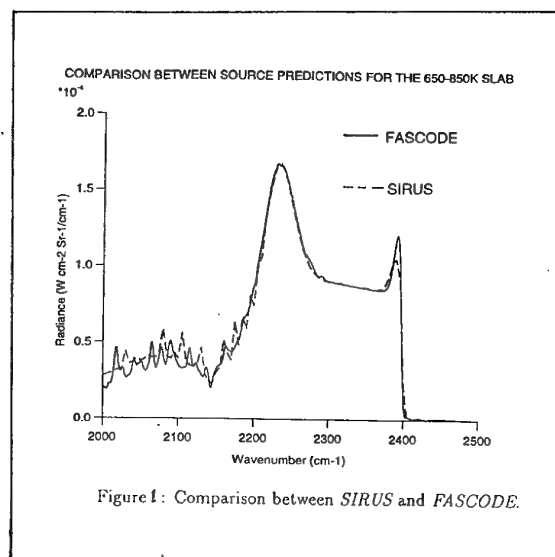
The Sowerby Research Centre of British Aerospace has developed an infrared predictive code, SIRUS, which models the signature of an air platform. We review briefly this code, and proceed to the calculation in code SCATAX of gas radiative transfer in a plume containing *scattering* particles.

An accurate radiative-transfer calculation of the signature of plume containing scattering particles is complex and costly: it is necessary for rocket engines, but may not be so for air-breathing engines (where only the properties along the single detector line-of-sight are involved).

We describe the physical basis of radiative-transfer with scattering, its implementation in the SCATAX code, present some quantitative results, and discuss the important 'searchlight' effect.

## 1. Introduction

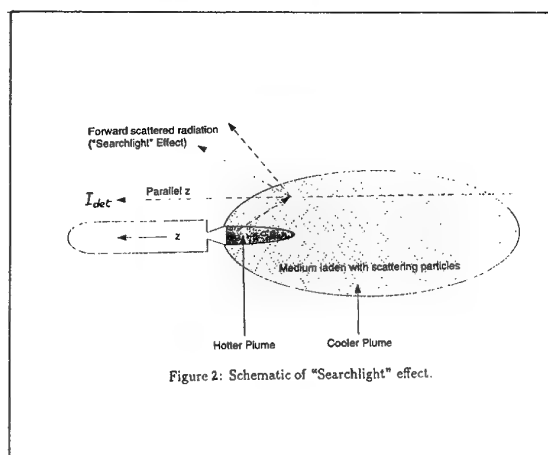
The infra-red signature of an air-platform is an important military parameter, and includes radiation from the plume, cavity and skin. British Aerospace (BAe) has developed a comprehensive I.R. signature code, SIRUS [1], for signature calculation. Fig.1 compares SIRUS and the exact FASCOD solution of a (non-scattering) plume signature through the atmosphere. In this paper we deal with the plume signature only, in particular a scattering plume.



If there are no scattering particles present only gas physical properties along a line-of-sight (l.o.s.) determine the radiance at a distant detector, but their presence means that the whole volume of the plume contributes to the radiance: thus accurate physical modelling and numerical calculation of a scattering-plume is a considerable task. We describe some features of a BAe (laboratory) code SCATAX which does this calculation. SCATAX is an 'exact' numerical implementation of a first-principles physical model of radiative transfer.

Solid rocket-motors have a high density of scattering particles and certainly need scattering-analysis for signature prediction, but liquid-motors and jet-engines may not, dependent on actual particle density: in any case, a preliminary scattering analysis is necessary to establish permissible approximations.

SIRRM (Standard Infrared Radiation Model) [2] is a realistic industry-standard code for scattering-signature prediction, which we believe is available only to the U.S. military. We have been able to compare SCATAX and SIRRM results via a SCORE collaboration, with excellent agreement: thus we feel that SCATAX is a solid basis for the incorporation into SIRUS as a n-flux band-model. We show results for the important case of the head-on signature of a missile, where the (cool) hard-body obscures the hot core of the plume. A non-scattering calculation then seriously underestimates the signature of the unobscured (cooler) outer plume, the true enhanced signature being due to scattering towards the detector of the intense core-radiance by the outer plume (Fig.2). This is often known as the 'searchlight effect'.





## 2. Analysis

The general exact radiative-scattering scattering equation [3] is ( $I$  is signature intensity,  $\alpha$  the absorption coefficient,  $\sigma$  the scattering coefficient,  $f$  the anisotropic phase function,  $I_B$  the Planck function,  $\mathbf{n}$  the direction of the l.o.s. and  $d\Omega$  a solid angle)

$$\frac{dI}{ds} = -\alpha I - \sigma I + I_B + \frac{\sigma}{4\pi} \int f(\mathbf{n}, \mathbf{n}') I(s, \mathbf{n}') d\Omega(\mathbf{n}')$$

and we will apply it to an axisymmetric plume specified by arbitrary distributions of temperature, concentration, gases and scattering particles.

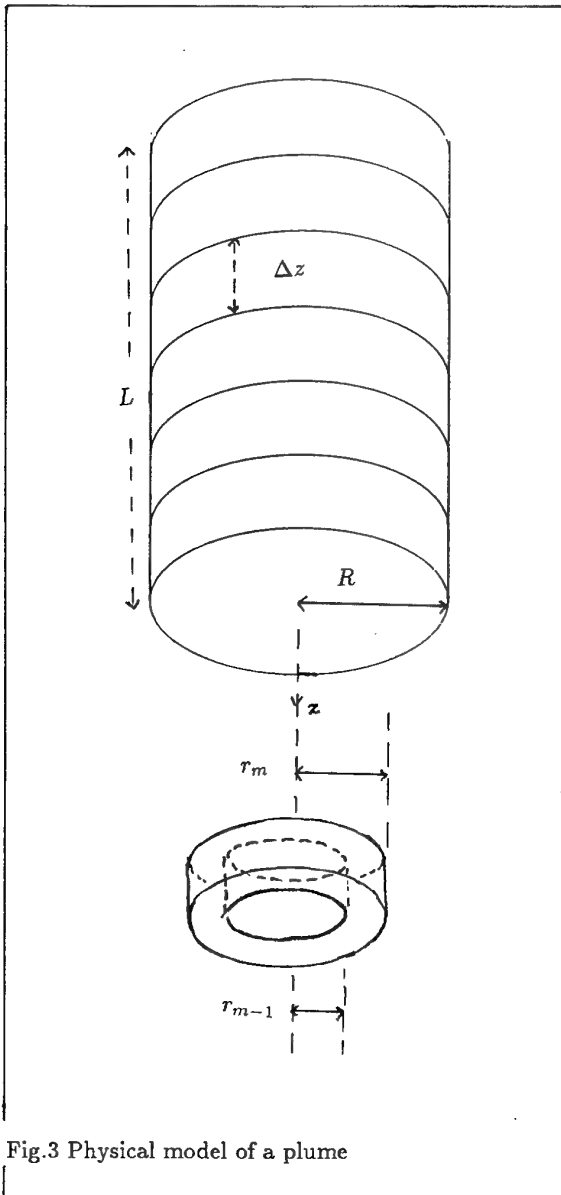


Fig.3 Physical model of a plume

Our physical model of a plume, Fig.3, is a set of interlocking rings which fill the plume volume. Each ring ( $m, n$ ) is of radius  $r_m$  to  $r_{m-1}$ , is of thickness  $\Delta z$ , is at position  $z_n$  on the axis, and has arbitrary (constant) temperature, gas and particle properties. This allows modelling of an arbitrary axisymmetric plume. The radiance of an arbitrary l.o.s. at axis angle  $\phi_p$  is specified by its ring intersection  $r_m$ , its axis intersection  $z_n$  and the distance  $s_j$  along it. These (many) radiances  $I_{m,p,n}^j$  obey the set of equations

$$I_{m,p,n}^j = g_{m,p,n}^j + \sum_{j',m',p',n'} K_{j'm',p',n'}^{j,m,p,n} I_{m',p',n'}^{j'}$$

where the process is driven by the ring temperature  $T_{mn}$  of the Planck source term  $g_{m,p,n}^j$ . The equations are suitable for numerical computer solution by matrix inversion, and are a discretization of the basic exact radiative transfer equation [3]. Code SCATAX gives the complete set of radiances  $\{I_{m,p,n}^j\}$ , which can then be used for the plume-atmosphere-detector problem being studied. The scattering kernel  $K$  contains the absorption coefficients of the plume gases ( $H_2O$ ,  $CO_2$ ,  $CO$ , ..), the albedo and phase of the scattering particles ( $C$ ,  $Al_2O_3$ ,  $MgO$ ,  $ZrO$ ), and determines the fraction of photons which are scattered from a l.o.s.  $\mathbf{n}'$  to the detector l.o.s.  $\mathbf{n}$ .

SIRUS presently treats scattering as a 2-flux model, which is a subset of the above solution, and is incorporated as a spectral band-model. The question of how best to band-model a scattering plume is an active one [4], and SCATAX is at present monochromatic: however, we have a proposed band-model solution which will be tested in SCATAX against the (exact) FASCODE solution. (A band-model approximation is one of practicality, since at present the exact 'line-by-line' monochromatic solution is computationally prohibitive.)

As a final technical point, SIRRM directly solves the integro-differential equations of radiative transfer whereas we in SCATAX convert the same equations to integral equations before solution. The SCATAX equations may (according to taste and experience) be said to give a more physical picture of scattering, and may also have numerical advantages.

## 3. Example, the searchlight effect

We will now discuss this effect in more detail and give some numerical results, recall Fig.2. In Fig.4 we model a plume with  $nn=6$  axis- $z$  sections,  $mm=5$  radial- $r$  sections and  $pp=6$   $\phi$ -angles. This is a relatively 'coarse' discretization, but it still means inversion of a matrix of dimension  $N \approx 2000$ , which gives some idea of the computational overhead.

The searchlight effect is illustrated in Fig.4. A detector sees a missile/platform head-on, and the missile body obscures the inner hot-core of its plume; the

outer cooler plume is thus the only l.o.s. seen by the detector.

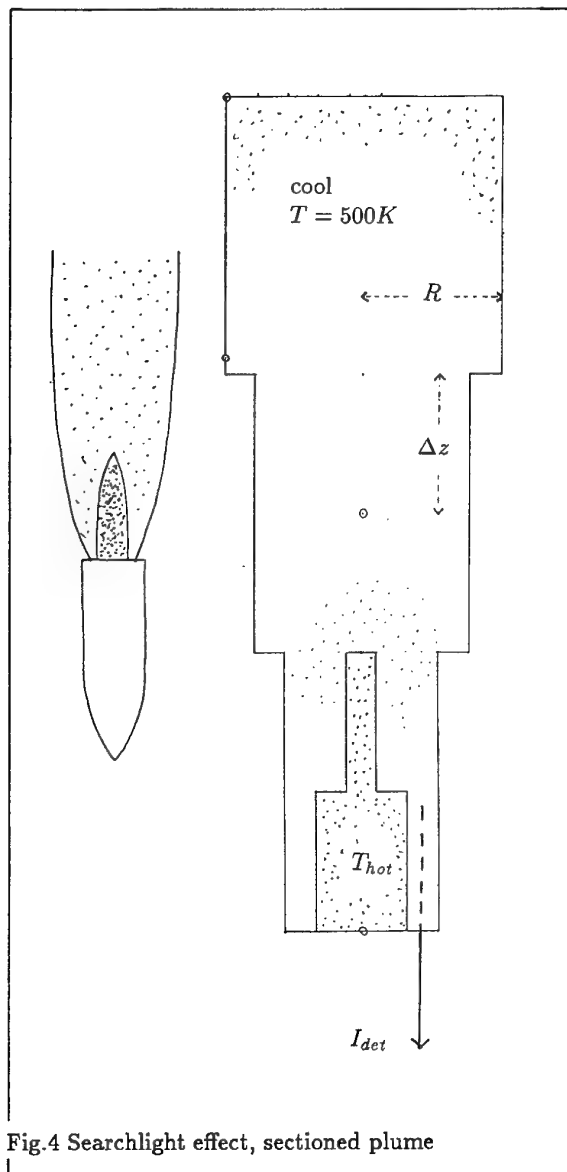


Fig.4 Searchlight effect, sectioned plume

The I.R. signature of the plume depends critically on whether the (outer, cooler) plume is scattering or not. Suppose for simplicity that the  $T_{hot}$  and  $T_{cool}$  temperatures of the plume are spatially uniform. Then,

- if the plume is non-scattering, the radiance at the detector cannot exceed the black-body radiance at  $T_{cool}$ , i.e.  $I_{det} \leq I_B(T_{cool})$
- if the plume is scattering, then the greater radiance  $I_B(T_{hot})$  of the hot-core propagates to the l.o.s. (with some attenuation), and is scattered along its way towards the detector.
- thus the signature  $I_{det}$  is increased by the presence of scattering in the plume. The increase can be significant, dependent on the

actual values of  $(T_{hot}, T_{cool}, \lambda)$  and the geometry of plume and l.o.s.

The above scenario is operationally important, since the head-on threat by a missile/platform is a common one, and the signature can be calculated only by considering radiative scattering.

Code SCATAX now allows analysis of the head-on searchlight signature for real plume geometry and gas properties. Some results are in fig.5, which shows how increasing the hot-core temperature increases the radiance  $I_{det}$  of a head-on l.o.s. which passes through only the cool outer-plume:  $I_{det}$  would be small and constant if the plume were non-scattering, and the error would increase with decreasing  $T_{cool}$ .

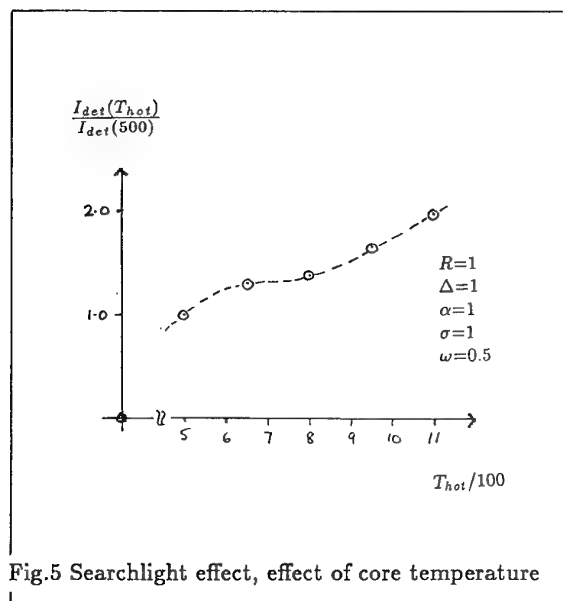


Fig.5 Searchlight effect, effect of core temperature

Fig.5 shows the relative error/enhancement of this searchlight effect (a searchlight is invisible unless it shines through a scattering atmosphere—or straight into one's eyes). We vary the core temperature  $T_{hot}$ , and the constant plume parameters are length  $L = 6$ , radius  $R=1$ ,  $T_{cool}=500K$ , gas-absorption coefficient  $\alpha = 1.0$ , particle scattering coefficient  $\sigma = 1.0$ , and wavelength  $\lambda = 3.0\mu m$ . The radiance  $I_{det}(T_{hot})$  is calculated by SCATAX and  $I_{det}(500)$  is the radiance of a non-scattering plume. The ratio of the two radiances is a measure of the need for a correct (scattering) calculation of plume radiance, here for purely illustrative parameters: this may be different for real cases of interest.

#### 4. Discussion

We have discussed role of scattering (particles) in the calculation of the infra-red signature of a plume, and

have shown how its neglect can lead to error, a serious underestimate in the important head-on case. We have described the BAe code SCATAX which, after comparison with the standard US code SIRRM, should provide realistic scattering signatures.

Plume radiation is but one part of the total signature calculation: what is ultimately wanted is the probability of detection of a platform through a given atmosphere and against a given background. This indeed is a complex, physically difficult, and computationally intensive calculation.

#### Acknowledgement

Development of the SCATAX code was supported by D.E.R.A., Farnborough, U.K.

#### References

- [1] 'SIRUS: a powerful infra-red prediction code', British Aerospace, Sowerby Research Centre, Technical Brochure 1996.
- [2] Freeman G. N., *et al.*, 'Development and validation of SIRRM', AFPR-TR-79-55 (1979)
- [3] Siegel R. and Howell J. R., 'Thermal Radiation Heat Transfer', 3e, Hemisphere (1992)
- [4] Reed, R. A., *et al.*, J. Thermophys. Heat. Transf., 40, 201, (1992)

PAPER No.: 11

DISCUSSOR'S NAME: W. Cornette

#### COMMENT/QUESTION:

1. How do you determine or predict the particle size distribution and states?
2. How do you include molecular absorption?

#### AUTHOR/PRESENTER'S REPLY:

The questions are partly addressed in the symposium paper.

1. Realistic signature calculations need good flowfield/CFD predictions and good data bases, e.g. latest HITEMP or similar for gases, IRMCOG or similar for particles.
2. Practical signal computation needs a band model for the plume gases, e.g.  $5\text{cm}^{-1}$  or  $1\text{cm}^{-1}$ . This is now standard for a non-scattering plume, but is not obvious for a scattering one, see [4].

# EFFECTS OF OBSCURANTS ON THE PERFORMANCE OF LASER RANGE FINDERS

A. Dimmeler, D. Clement  
Forschungsgesellschaft für Angewandte Naturwissenschaften e.V.  
Forschungsinstitut für Optik (FGAN-FfO)  
Schloss Kressbach  
D-72072 Tübingen, F. R. Germany  
Doc.: FGAN-FfO 1998/6

W. Büchtemann  
Dr. Büchtemann Optronik (dbo)  
Neckargasse 12  
D-72070 Tübingen, F. R. Germany

## SUMMARY

At the FGAN-FfO, the model COSMOS (Combined Optical/IR Sensor Modelling in the Presence of Obscurants and Smokes) is being formulated to predict and optimise the performance (i) of existing and future EO systems under the influence of measured and simulated battlefield effects in a variety of scenarios, and (ii) of smokes and obscurants in their role to neutralise EO sensors. EO Systems addressed in COSMOS include sensors, active and passive, imaging and non-imaging, in the visible, near infrared and in the short, medium and long wave infrared.

One part of COSMOS is related to laser range finders (LRF). The objective of the work presented here is to predict LRF range performance while accounting for effects such as multiple scattering and turbulence as well as target speckle effects (incorporating speckle averaging), in addition to system effects such as false alarm rate etc.

Initial model validation is based upon data measured at the US SMOKE WEEK XV. Size distributions of some selected, experimental smokes (brass, fog oil/graphite) are analysed, and are found to be lognormal. Based on this, Mie phase functions are computed.

Time resolved return signals of two laser range finders at different wavelengths, 1.54  $\mu\text{m}$  and 10.59  $\mu\text{m}$ , are compared with numerical predictions. Using the computed scattering functions, quantitative agreement with respect to temporal behaviour and absolute magnitude of LRF pulses back-scattered by the smoke clouds is obtained in most cases.

Good agreement is found when predicted statistics of LRF ranging results are compared with measured data. This includes cases where in the experiment the LRFs indicated multiple returns, the first echo being caused by the smoke screen, the second by the hard target behind the screen.

## 1. INTRODUCTION

There are well established models for predicting the performance of electro-optical (EO) devices such as the Thermal Range Model 3 of FGAN-FfO [1]. While they provide realistic representations of the systems modelled, their options for modelling atmospheric effects are often simplistic. On the other hand, there are models such as EOSAEL (Electro-Optical Systems Atmospheric Effects Library) [2] which describe the atmosphere, natural and battle induced, in a detailed manner but do not contain modules for predicting EO system performance. As an example, there is no model established in the defence community which would predict the performance of a laser range finder (LRF) while adequately accounting for ef-

fects such as multiple scattering in smokes, fire induced turbulence, and speckle.

Models which combine atmospheric effects with system engineering aspects with comparable level of sophistication are needed, however, if one wants to assess and optimise

- the performance of existing or future EO systems in real world applications, and
- the impact of obscurants on military EO systems.

To meet these goals, the model COSMOS (Combined Optical/IR Sensor Modelling in the presence of Obscurants and Smokes) [3] is being formulated at the FGAN-FfO.

The example given in this paper addresses the modelling of LRF systems. In Chapters 2 and 3, size distributions and Mie scattering phase functions of some smokes will be discussed. Related analysis results are presented in Chapter 4, and compared to experiment in Chapter 5. Finally, Chapter 6 serves the presentation of the basics of the COSMOS LRF model and the comparison of model predictions with experimental data. Model validation is based on data measured during US SMOKE WEEK XV (SW XV) [4, 5]. Participation in SW XV was possible through the former NATO AC/243 (Panel 4/RSG.15).

## 2. SIZE DISTRIBUTIONS OF BRASS AND FOG OIL/ GRAPHITE SMOKES

According to EOSAEL 92 [6], phase functions of inventory smokes can be calculated almost exactly because the particles are nearly spherical. Uncertainties do exist with respect to size distribution and complex index of refraction. With modern developmental smokes, like fog oil/graphite and brass, the situation is different. Considerations on particle size spectrum and shape are the subject of this chapter. For the index of refraction of fog oil, graphite and brass see Chapter 3.

While for fog oil and graphite the assumption of sphericity seems reasonable, this is probably not true for brass particles. Mie theory can be extended to conducting cylinders [7]. Major differences to spherical particles are found in the polarisation behaviour of the scattered radiation. If the particles are randomly oriented and if the detection of radiation is not polarisation sensitive, the major effect will be an enhanced cross section compared to an ensemble of spherical particles with equal mass concentration.

During SW XV, particle size distributions of both fog oil/graphite and brass smokes were measured with optical particle size analysers (FSSP-100 and ASASP-300) [4]. Re-

sults thus represent optically effective size distributions which can be described as the real size distributions multiplied with a size dependent enhancement factor. The signal reflects the average apparent *geometrical* cross section of the particles, in particular if the particles are large compared to wavelength. The near independence of transmission values on wavelength indicates that the particles are large indeed.

Particle size distributions of inventory smokes can be approximated by lognormal distributions [6]:

$$n(r) = \frac{dN}{dr} = y_0 + \frac{A}{r} \exp \left\{ -\frac{(\ln(r/r_c))^2}{2w^2} \right\} \quad (1)$$

$n(r)$ : number of particles of radius  $r$  per unit volume and size bin (increment,  $\text{m}^{-3}\mu\text{m}^{-1}$ ),

$N$ : total aerosol number density ( $N = \sqrt{(2\pi)} \cdot w \cdot A$ ,  $\text{m}^{-3}$ ),

$y_0$ : constant, usually  $y_0 = 0$ ,

$A$ : number density constant ( $\text{m}^{-3}$ ),

$r_c$ : distribution geometric mean,

$w$ : geometric mean standard deviation in log space ( $w = \ln 10 \cdot \sigma_{SF}$ ).

Fig. 1 shows average size distribution data obtained with brass smoke of SW XV, as communicated by U.S.ARL [4]. This data was fitted to the function of Eq. 1 by using a non-linear least square fitting algorithm based on the Levenberg-Marquardt algorithm. Two variants were employed, a 4-parameter fit and a 3-parameter fit were  $y_0 = 0$ .

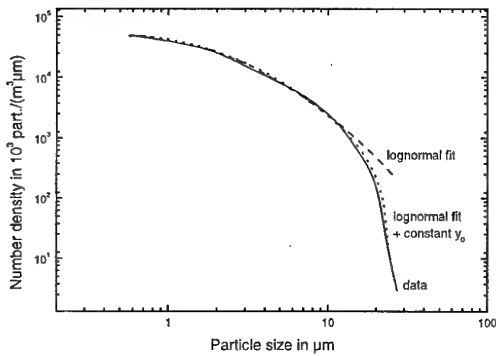


Fig. 1: Measured size distribution of brass smoke (solid line), compared to lognormal fit (dashed) and lognormal fit with additional constant  $y_0$  (dots).

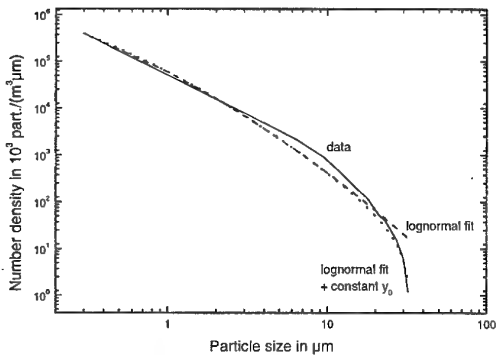


Fig. 2: Measured size distribution of fog oil/graphite smoke (solid line), compared to lognormal fit (dashed) and lognormal fit with additional constant  $y_0$  (dots).

While the 4-parameter fit is strikingly good throughout, the 3-parameter fit shows some discrepancy at large radii. The impact of this discrepancy on optical phenomena is minor yet

since it occurs only at radii where the number density falls two orders of magnitude below that at smaller particle radii. The similarity of constants  $A$ ,  $r_c$ , and  $w$  in Tab. 1 is an indication for this.

Smoke Parameter	Brass		Fog Oil / Graphite	
	4	3	4	3
$y_0 [\text{m}^{-3}]$	-361	-	-15	-
$A [\text{m}^{-3}]$	$5.47 \cdot 10^7$	$5.38 \cdot 10^7$	$1.46 \cdot 10^8$	$1.48 \cdot 10^8$
$r_c [\mu\text{m}]$	2.33	2.21	0.1	0.1
$w$	1.22	1.18	1.73	1.18

Tab. 1: Fit parameters for brass smoke and for fog oil/graphite smoke.

### 3. PHASE FUNCTIONS OF BRASS AND FOG OIL/GRAPHITE SMOKES

Smoke phase functions were computed using the Mie code PFCAL [8]. It computes phase functions for arbitrary size distributions and wavelengths. The size distributions used here are those of Tab. 1 (3-parameter fit). The wavelengths considered correspond to the two LRFs used in the experiments, with values  $1.54 \mu\text{m}$  and  $10.59 \mu\text{m}$ .

A further smoke specific input is the refractive index with real and imaginary part,  $n$  and  $k$ , respectively. For the experimental smokes, these were not known. For brass smoke it is not obvious to take the values of the bulk material: Dispersed as small particles, there will be a tendency of both, oxidation and aggregation of water [9]. Similarly it is not clear whether to treat the mixture of fog oil/graphite as two independent ensembles or as a mixture with unified properties.

Fortunately, scattering properties depend more on size distribution than on refractive index. To demonstrate this, various values for the brass smoke refractive index were chosen with the result that for fairly vast differences only marginal changes in the computed phase function occur. In Tab. 2 two sets of values are given. In one case values depend on wavelength. They were adapted from [9] and [10]. In the other case only one value for the complex index of refraction is given for both wavelengths.

The fog oil/graphite values in Tab. 2 were chosen to fall between the values of the constituents. Fig. 3 to 6 show the resulting phase functions.

	$n$	$k$
brass, adapted from [9, 10] for $1.54 \mu\text{m}$	1	12
brass, adapted from [9, 10] for $10.59 \mu\text{m}$	11	60
alternate brass for $1.54 \mu\text{m}$ and $10.59 \mu\text{m}$	4	20
Fog oil/graphite for $1.54 \mu\text{m}$	1.8	0.55
Fog oil/graphite for $10.59 \mu\text{m}$	2.25	0.8

Tab. 2: Real and imaginary part,  $n$  and  $k$ , of the refractive index used in the calculations.

Comparison of brass smoke phase functions in Fig. 3 (refractive index depends on wavelength) and Fig. 4 (only one value used) shows differences less than 4%, predominantly less than 1%.

Based upon data given in EOSAEL for the refractive index of inventory fog oil smoke (at  $1.06 \mu\text{m}$ ) a comparison between this type of smoke and the fog oil/graphite smoke can be made. Fig. 6 shows major differences in the phase functions.

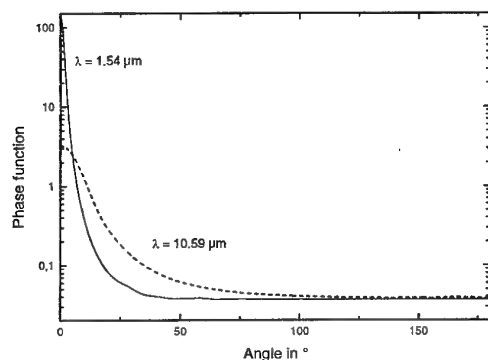


Fig. 3: Phase functions of brass smoke, computed with an index of refraction independent of wavelength.

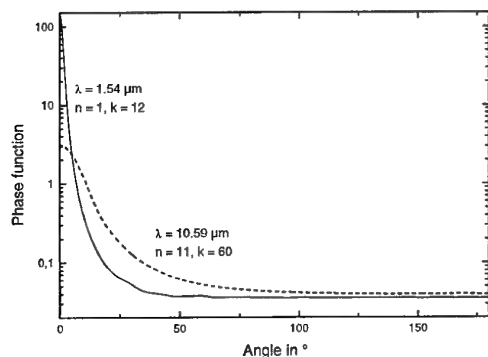


Fig. 4: Same as Fig. 3, but computed with a wavelength dependent refractive index.

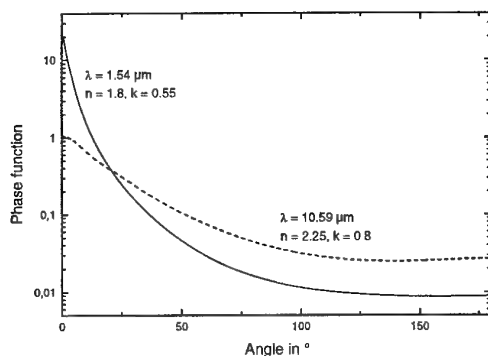


Fig. 5: Computed phase functions of fog oil/graphite smoke.

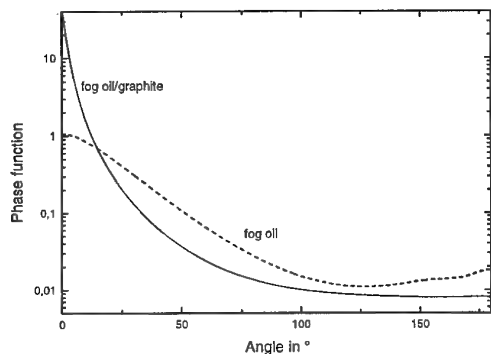


Fig. 6: Phase functions of inventory fog oil smoke (from EOSAEL) and fog oil/graphite at 1.06  $\mu\text{m}$ .

#### 4. LRF MEASUREMENTS DURING SW XV

The general set-up of the trials is described in [5]. Two LRFs were employed:

- Raman-shifted Nd:YAG LRF operating at 1.54  $\mu\text{m}$  and
- CO<sub>2</sub> LRF operating at 10.59  $\mu\text{m}$ .

Both LRFs were placed at a distance of 1780 m from the target. Smokes were deployed at a distance of about 1200 m.

Smoke cloud transmissions were recorded by the ARL multispectral transmissometer REVIRT. Wavelengths of interest here are 1.54  $\mu\text{m}$  and 8-14  $\mu\text{m}$  transmissions. Broadband 8-14  $\mu\text{m}$  transmission gives a good estimate for the narrow-band transmission at 10.59  $\mu\text{m}$  since transmission varies slowly with wavelength. Lines-of-sight (LOSs) between REVIRT and the LRFs did not coincide exactly. For the range of wind speeds, this introduced a delay of a few seconds in the time series of data.

For this investigation two smoke trials were selected. These are

- brass smoke, trial 7513 (FGAN-Ffo M713),
- fog oil/graphite, trial 8080 (FGAN-Ffo M718).

Fig. 7 shows transmission data at 1.54  $\mu\text{m}$  and 8-14  $\mu\text{m}$ , recorded during part of the brass smoke trial. Being almost identical, curves show the broadband effectiveness of the smoke.

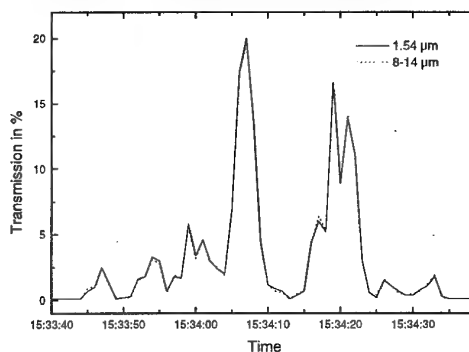


Fig. 7: Brass smoke transmission at 1.54  $\mu\text{m}$  and 8-14  $\mu\text{m}$ , showing the broadband effectiveness of the smoke.

Laser pulses were recorded prior to smoke deployment, see Fig. 8. The signal amplitude is limited to app. 0.7 V by the data recording equipment.

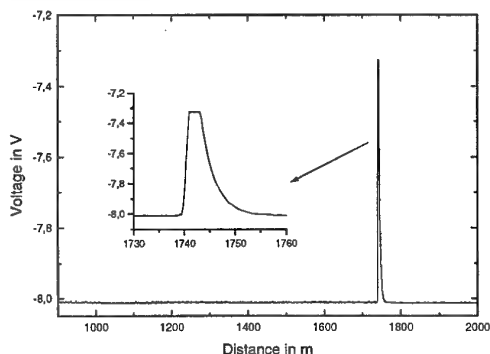


Fig. 8: Nd-Raman LRF return pulse prior to smoke deployment.

Fig. 9 displays the laser return signals during the brass smoke trial. Near the end of the set, two signals exhibit an appreciable return from the target. The second last pulse is displayed sepa-

ately in Fig. 10 with two insets displaying the data in an expanded distance scale.

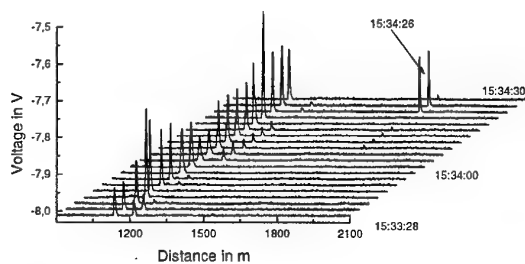


Fig. 9: Return signal of the Nd-Raman LRF ( $1.54 \mu\text{m}$ ) during the brass smoke trial.

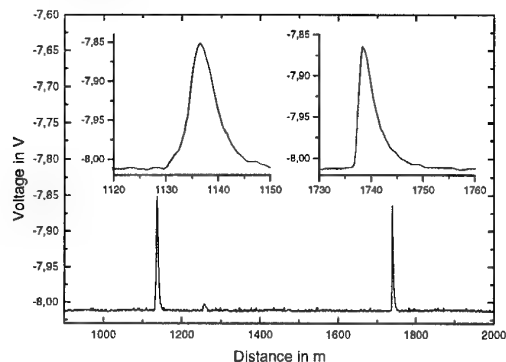


Fig. 10: Return signal of Nd-Raman LRF at 15:34:26. The two peaks (backscatter from cloud and reflection from target) are displayed with an expanded scale.

In Fig. 10 the peak-to-baseline voltage with the solid target return is about 150 mV which corresponds to about  $6 \mu\text{W}$  (assuming linearity of the LRF electronics). Compression starts at  $1 \mu\text{W}$ . A received power of 10-20  $\mu\text{W}$  is estimated. If this is compared to an expected clean air power of 1 mW a double pass transmission of about 1.5% and a single pass transmission of about 12% is concluded. This corresponds to the transmission measurement around 15:34:20 in Fig. 7 if one keeps in mind that the LOSs did not coincide exactly.

The HW of the target return pulse in Fig. 10 equals 25 to 30 ns (which corresponds to about 4 m). This reflects predominantly the bandwidth of the buffer amplifier (app. 25 MHz). The apparent HW of the backscattered radiation is slightly larger and equals about 5.5 m.

Fig. 11 shows the  $\text{CO}_2$  laser pulse recorded prior to smoke deployment. The target distance indicated was 1780 m. The slight difference in range as shown by Fig. 11 is due to the electronic processing (trigger, bandwidth) of the recording equipment. The HW of the pulse is about 80 ns which is equivalent to 12 m. This value reflects the large-signal behaviour of the electronic chain.

The baseline-to-peak voltage difference is app. 92 mV. With a target reflectivity of 65% [5] and the LRF parameters inserted into the laser radar equation, a received power of app. 200  $\mu\text{W}$  is calculated.

Fig. 12 shows the time resolved  $\text{CO}_2$  LRF returns during the brass smoke trial. As in Fig. 9 two smoke cloud returns can be observed here at around 15:34:00.

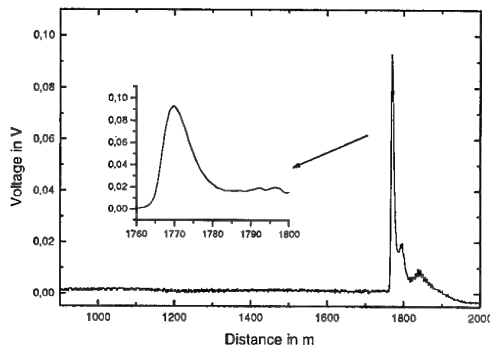


Fig. 11:  $\text{CO}_2$  LRF return pulse prior to smoke deployment, recorded at the same time as Fig. 8.

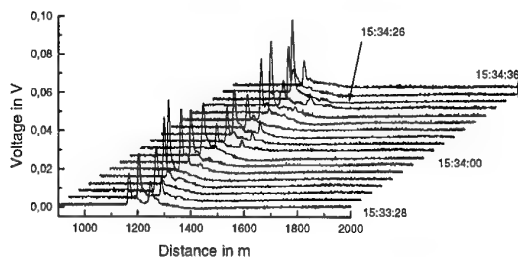


Fig. 12: Return signal of the  $\text{CO}_2$  LRF during the brass smoke trial.

Fig. 13 shows the  $\text{CO}_2$  LRF signal backscattered from the brass cloud. The double peak is probably due to a double discharge in the laser rather than a second real signal.

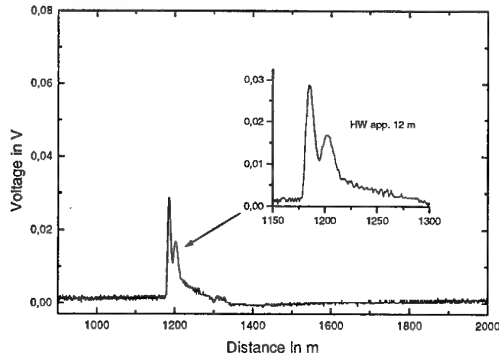


Fig. 13:  $\text{CO}_2$  LRF return signal backscattered from the brass cloud at 15:24:26.

The responsivity (V/W) of the  $\text{CO}_2$  LRF is not known. A rough estimate can be obtained as follows. The NEP is of the order of 10 nW. This is the same magnitude as for the Nd-Raman receiver using an avalanche detector which yields an SNR improvement of about 10 over a simple diode. At  $10.59 \mu\text{m}$  a diode has a responsivity (A/W) which is 7 times larger than for a diode at  $1.54 \mu\text{m}$  with the same quantum efficiency. This and the reduced bandwidth results in a NEP similar to the Nd-Raman avalanche diode. With an RMS noise of app.  $2 \cdot 10^{-4}$  V one obtains app. 20 kV/W for the linear region of the device. This yields a received power in Fig. 13 of app.  $1.5 \mu\text{W}$ .

## 5. CALCULATIONS USING NBMSCAT AND COMPARISON WITH MEASUREMENTS

Propagation of laser radiation through smokes is well described in the narrow-beam multiple-scattering module NBSCAT [11]. For a specific receiver geometry this EOSAEL module calculates the transmitted and backscattered irradiance profiles, the on-axis transmitted power and the lidar returns, while neglecting the slight offset between the LRF transmitter and receiver.

Calculations in this paper were performed using the program code NBMSCAT [12] which is functionally identical to NBSCAT but contains some corrections for lidar return predictions. This is of bearing here since it relates also to the signal obtained with the LRF from the smoke cloud.

The aim of the calculations is to compare the experimental results obtained in the smoke trials in conjunction with the two LRFs. Questions to be answered are e.g.:

- Is NBMSCAT able to describe the experimental data sufficiently good?
- Is there a simple approach to describe the data with the particular geometry of both LRF?

### Calculation with brass smoke

The parameters of the Nd-Raman LRF entering the model are given in Tab. 7.

Fig. 14 shows the return signals for an absorption coefficient of  $200 \text{ km}^{-1}$ . This value was chosen to yield a single pass transmission of app. 1% with a cloud thickness of 25 m. Such a value corresponds to a visual range of 20 m. The actual thickness however is not known.

A single pass transmission of app. 1% is compatible with the measured transmissometer readings. Due to the fact that LRF and transmissometer LOSs do not coincide exactly one cannot infer an absolute number directly from the transmissometer measurement. A value of 1%, however, is roughly compatible with Fig. 10 where returns from both, the cloud and the target, could be measured.

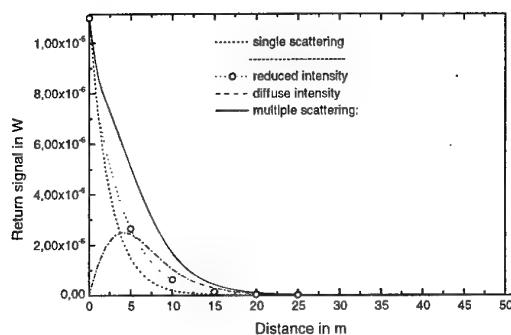


Fig. 14: Computed power backscattered from brass smoke as received by the  $1.54 \mu\text{m}$  LRF for an extinction coefficient of  $\alpha = 200 \text{ km}^{-1}$ .

Fig. 15 shows, in normalised form, the scatter signal and the system response due to laser width and receiver bandwidth. This width is essentially given by the electronics. The laser HW is app. 0.9 m. The computed pulse width equals apparently about 8.5 m (Tab. 3).

Parameter	Measured	Calculated
HW of backscattered pulse	5.5 m	8.5 m
Received backscattered power	10 - 20 $\mu\text{W}$	11 $\mu\text{W}$

Tab. 3: Measured vs. calculated parameters of Nd-Raman LRF returns ( $\alpha = 200 \text{ km}^{-1}$ ) through brass smoke.

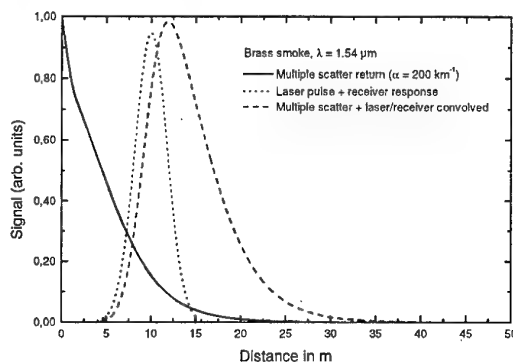


Fig. 15: Multiple scattering signal ( $\alpha = 200 \text{ km}^{-1}$ ), equivalent laser pulse and receiver electronics response function, and convolution of both (HW is app. 8.5 m).

For the  $\text{CO}_2$  LRF the parameters entering the model directly are given in Tab. 8. In addition, the same extinction coefficient as for the Nd-Raman LRF is used since the transmission showed the same behaviour at both wavelengths (Fig. 7).

The small-signal frequency response of the receiver system of app. 15 MHz, the laser pulse width of 40 ns and the calculated HWs in Fig. 16 lead to expected values of app. 10 m (for  $\alpha = 200 \text{ km}^{-1}$ ). This is compatible with the HW measured.

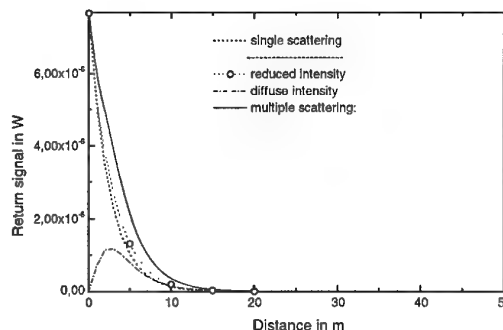


Fig. 16: Computed power backscattered from brass smoke as received by the  $\text{CO}_2$  LRF ( $\alpha = 200 \text{ km}^{-1}$ ).

Tab. 4 shows that there is a considerable difference between the calculated and observed power, unlike the Nd-Raman results.

Parameter	Measured	Calculated
HW of backscattered pulse	11 m	10 m
Received backscattered power	app. 2 $\mu\text{W}$	5 $\mu\text{W}$

Tab. 4: Measured vs. calculated parameters of  $\text{CO}_2$  LRF returns for a system frequency response of 15 MHz ( $\alpha = 200 \text{ km}^{-1}$ ) through brass smoke. Uncertainty in emitted laser power gives rise to a large uncertainty in the calculated power received.



### Calculation with fog oil/graphite

For the calculations the same values were used as in the previous chapters. Results are summarised in Tab. 5 and Tab. 6.

Parameter	Measured	Calculated
HW of backscattered pulse	7 m	7 m
Received backscattered power	5 - 10 $\mu$ W	14 $\mu$ W

Tab. 5: Measured vs. calculated parameters of Nd-Raman LRF returns ( $\alpha = 100 \text{ km}^{-1}$ ) through fog oil/graphite smoke.

Parameter	Measured	Calculated
HW of backscattered pulse	11 m	10 - 12 m
Received backscattered power	app. 1 $\mu$ W	1 - 3 $\mu$ W

Tab. 6: Measured vs. calculated parameters of CO<sub>2</sub> LRF returns for a system frequency response of 15 MHz ( $\alpha \approx 30\text{-}60 \text{ km}^{-1}$ ) through fog oil/graphite smoke. Uncertainty in emitted laser power gives rise to a large uncertainty in the calculated power received.

## 6. LASER RANGE FINDER MODELLING AND COMPARISON WITH SW XV MEASUREMENTS

The class of LRFs discussed here employs pulsed laser sources and incoherent detection. Pulsed LRFs offer the opportunity to record multiple echoes.

The required accuracy of the LRF is usually in the order of 5 m. This is equivalent to 33.4 ns. Laser pulse length and other parameters, see below, must be commensurate to this quantity.

Usually, when the laser fire command is initiated, a delay much longer than 33 ns occurs (exception: semiconductor lasers). Thus the emitted laser pulse itself is better used to start the range measurement (Fig. 17).

The laser pulse travels through the atmosphere experiencing some extinction. After being reflected by the target a small portion of the light will enter the detector. The range counter will either be stopped by a comparator or the corresponding value will be stored and the counter continues for one or more returns.

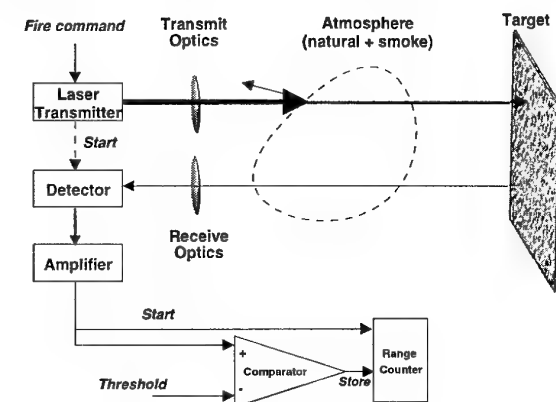


Fig. 17: Schematics of a laser range finder.

To describe and model LRF performance it is required to compute the pulse power which finally reaches the detector. This is done using the *laser radar equation*. This is where the effects e.g. of turbulence and aerosol extinction enter.

The detection process is furthermore described by the Noise Equivalent Power (NEP) of the detector/amplifier. The threshold of the comparator is set to a certain multiple of the detector/amplifier noise to prevent false alarms by noise only. The ratio is called Threshold-to-Noise Ratio (TNR).

If the average signal level reaches threshold, the detection probability is only 50% because the noise will move half the number of the pulses to higher, the other half to lower levels. To obtain a particular detection probability it is required to maintain a certain signal-to-noise-ratio (SNR) which is then a function of both threshold (false alarms) and detection probability.

The firing of the laser will cause in most cases strong transients which might leak through to the detector channel. Therefore, comparator action is held off for some time, corresponding to a minimum range. In addition, there might be strong returns from aerosols or solid objects, like branches of trees, in the near field (small  $R$ ). To avoid triggering one uses - if ever possible - not a coaxial - but a collinear arrangement as in Fig. 17 where the emitter and receiver fields of view only overlap at some distance. This establishes a minimum range  $r_{min}$ . In addition, one uses Time Programmed Gain (TPG) or Time Programmed Threshold (TPT). TPT has the advantage that for a strong near field return signal there is less overshoot and consequently less recovery time.

Systems known to the authors have full sensitivity after a few 100 meters, which is about ten percent of the design range. Those ranges are in most cases not of real interest to the user. In addition, the information about these values usually is difficult to obtain. Therefore, TPT or TPG is not included in the equations below. It should however be kept in mind when analysing experiments which might fall in that regime.

### 6.1 Laser radar equation

The signal received by a detector is described by the *laser radar equation*:

$$P_r = P_t \rho \frac{D^2}{4R^2} \tau_o \tau_A \quad (2)$$

- $P_r$ : power received by detector,
- $P_t$ : effectively transmitted power,
- $\rho$ : reflectivity of target  
(reflected angle = incident angle),
- $D$ : diameter of entrance optics,
- $R$ : range (distance),
- $\tau_o$ : transmission of optics (includes losses occurring due to reflections and absorption in the receiver as well as losses due to field stops (laser divergence larger than receiver field of view)),
- $\tau_A$ : atmospheric transmission (double pass).

Eq. 2 becomes the equation for determination of range if on the left side the undetermined  $P_r$  is replaced by the minimum power  $P_{min}$  which is required to achieve ranging with pre-set conditions, in practice with a certain probability of detection  $p_d$  and a certain false alarm probability  $p_f$  (see below).

Eq. 2 implies that the target is larger than the beam diameter. This leads to an  $R^2$ -dependence of the return signal. In cases, however, where the target diameter is less than the laser beam Eq. 2 must be modified.

## 6.2 False alarm and detection probability in Gaussian noise

The discussion follows [13], repeating some of the computational steps.

The noise current of the detector or the noise voltage after amplification is described with sufficient accuracy by Gaussian statistics. This includes noise from background, detector, and preamplifier. Depending on the noise sources, the current will change from positive to negative sign or - more frequently - will be positive or negative with respect to a constant dark or background current. In Fig. 18 and in the computation this constant current has been subtracted. The probability to find a particular value of current  $i$  is then

$$p(i) = \frac{1}{I_n \cdot \sqrt{2\pi}} \exp\left(-\frac{i^2}{2I_n^2}\right) \quad (3)$$

with

$$\int_{-\infty}^{\infty} p(i) di = 1$$

$I_n (= \sigma_i)$ : average noise current.

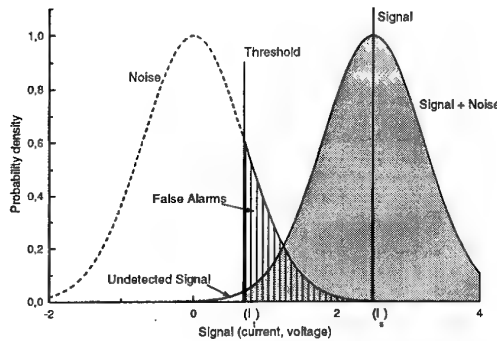


Fig. 18: Probability density of noise current, noise current plus signal and areas determined by threshold  $I_t$ .

In the presence of a signal, the signal current and the noise current are added. For practical applications, the distribution of noise plus signal is described by a Gaussian with the same width but shifted to the right by the amount of signal current  $I_s$ . (However, it has to be taken into account, if the signal contributes to the noise or if the signal varies - see below).

Now a threshold current  $I_t$  is introduced such that the signal is regarded as signal if  $i > I_t$  and as noise otherwise. This has consequences for false alarms and detection probability.

### False alarm probability and false alarm rate

The relation commonly used for the false alarm rate (FAR) is found in [13]

$$FAR = \frac{1}{\sqrt{3} \cdot 2\tau} \exp\left(-\frac{I_t^2}{2I_n^2}\right) \quad (4)$$

$I_t$ : threshold current.

Since these quantities appear as a ratio the units do not have to be currents. Frequently it is convenient to use NEP - noise equivalent power and TEP - threshold equivalent power.

This formulation uses a relation for the system bandwidth BW and the laser pulse length  $\tau$  ( $BW = 1/(2\tau)$ ). Re-installing the bandwidth yields

$$\begin{aligned} FAR &= \frac{BW}{\sqrt{3}} \exp\left(-\frac{I_t^2}{2I_n^2}\right) \\ &= \frac{BW}{\sqrt{3}} \exp\left(-\frac{TNR^2}{2}\right) \end{aligned} \quad (4a)$$

TNR: threshold-to-noise ratio.

An empirical relation exists between optimum bandwidth and pulse width (HW  $\tau_H$ )

$$BW \approx 1/(3\tau_H) \quad (5)$$

This value was found experimentally by developers at the company Eltro. This formula is used in subsequent computations and in the computer code.

The required quantity of LRFs is the false alarm probability  $p_{FI}$  during one ranging action. A conservative approach is to multiply the FAR with the time gate associated with the maximum range of the LRF  $\tau_m$ . Hence

$$p_{FI} = FAR \cdot \tau_m = FAR \cdot R_{max} \cdot c/2 \quad (6)$$

$R_{max}$ : maximum measuring range of the LRF,

$c$ : speed of light.

When specifying a LRF one will usually specify the false alarm probability  $p_{FI}$ . Eq. 6 and 4a give an implicit condition for the calculation of the associated TNR.

Eq. 6 is strictly valid if one takes the false alarm probability to be the value associated with the absence of a real target or when multiple pulses are counted. In a real situation with first pulse logic one would - of course - encounter a smaller false alarm probability, because  $\tau_m$  is cut short with the real return.

### Detection probability

Looking at Fig. 18 one recognises for the detection probability

$$\begin{aligned} p_d &= p(i_s + i_n > I_t) \\ &\equiv p(I_s + i_n > I_t) \\ &= p(i_n > I_t - I_s) \end{aligned} \quad (7)$$

$$\begin{aligned} p_d &= \frac{1}{I_n \cdot \sqrt{2\pi}} \int_{I_t - I_s}^{\infty} \exp\left(-\frac{i^2}{2I_n^2}\right) di \\ &= \frac{1}{\sqrt{\pi}} \int_{\frac{I_t - I_s}{\sqrt{2}I_n}}^{\infty} \exp\left(-\frac{i^2}{2I_n^2}\right) d\left(\frac{i}{\sqrt{2}I_n}\right) \\ &= \frac{1}{2} \left\{ 1 + \operatorname{erf}\left(\frac{I_s - I_t}{\sqrt{2}I_n}\right) \right\} \\ &= \frac{1}{2} \left\{ 1 + \operatorname{erf}\left(\frac{SNR - TNR}{\sqrt{2}}\right) \right\} \end{aligned} \quad (8)$$

with

$$\operatorname{erf}(x) = \int_0^x e^{-t^2} dt$$

SNR: signal-to-noise ratio,

TNR: threshold-to-noise ratio.

Fig. 19 shows the detection probability as function of the normalised signal-to-noise excess  $SNE = SNR - TNR$ .

To compute ranges it is not sufficient to assume the threshold signal of the LRF. One has rather to assume an excess SNR. To obtain, e.g. a 99% probability one needs

$$p_d = 0.99 \Rightarrow \text{SNR} - \text{TNR} = 2.33.$$

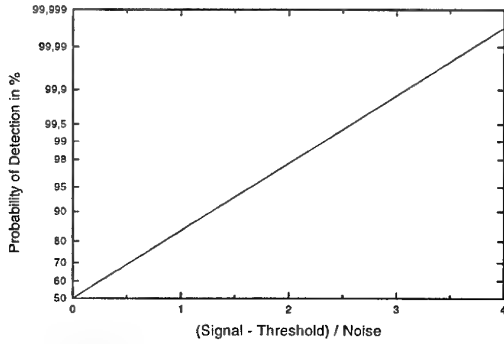


Fig. 19: Probability of detection as function of normalised signal-to-noise excess (SNE = SNR - TNR).

#### Pulse Peak Intensity Jitter of the Emitter

Laser pulses do vary - a relative variation of 5% around the mean is quite normal. For the assumption of a Gaussian distribution of the pulse peak intensity jitter with a standard deviation (STD)  $\sigma_j$  one describes the pulse peak intensity distribution at the detector as

$$p(i) = \frac{1}{\sqrt{I_n^2 + \sigma_j^2} \cdot \sqrt{2\pi}} \exp\left(-\frac{i^2}{2(I_n^2 + \sigma_j^2)}\right) \quad (9)$$

The detection probability is then [14]

$$p_d = \frac{1}{2} \left\{ 1 + \operatorname{erf} \left( \frac{\text{SNR} - \text{TNR}}{\sqrt{2(I_n^2 + \sigma_j^2)} \cdot (\text{SNR})^{0.5}} \right) \right\} \quad (10)$$

The corresponding definition of the signal-to-noise ratio SNR' is

$$\text{SNR}' - \text{TNR} = (\text{SNR} - \text{TNR}) / (1 + \sigma_j^2 \cdot \text{SNR}^2)^{0.5} \quad (11)$$

Assuming an SNR - TNR = 2.3, an SNR = 8 and a jitter STD  $\sigma_j = 0.1$ , Eq. 11 yields an increase to SNR' = 8.645.

#### 6.3 Turbulence effects

With regard to laser point-to-point transmission, atmospheric turbulence may cause severe fluctuations of the pulse peak intensity. In case of weak turbulence the variance of the "log-amplitude" - the logarithm of the amplitude - of a spherical wave is approximately

$$\sigma_x^2 = 1.058 \lambda^{-7/6} L^{1/6} C_n^2 \quad (12)$$

$\lambda$ : wavelength,

$L$ : path length,

$C_n^2$ : refractive-index structure constant ( $C_n^2$  may assume values up to about  $10^{-13} \text{ m}^{-2/3}$ ),

$\sigma_x^2$ : log-amplitude variance [15, p. 184ff].

Between the log-amplitude variance  $\sigma_x^2$  and the variance of the normalised intensity ( $\langle I \rangle = 1$ )  $\sigma_I^2$  one has the relation

$$\sigma_I^2 = \exp(4 \sigma_x^2) - 1 \quad (13)$$

with an approximation for weak turbulence

$$\sigma_I^2 \approx 4 \sigma_x^2 \quad (14)$$

Turbulence effects saturate at a value of app.  $\sigma_x^2 = 1$ . Saturation is reached with  $C_n^2 = 10^{-13} \text{ m}^{-2/3}$  for  $\lambda = 1.06 \mu\text{m}$  at a distance (total length) of 1.9 km. Variances of more than one are obtained even for moderate distances.

Applying this to the experiments with the Nd-Raman LRF, one has  $\lambda = 1.54 \mu\text{m}$  and  $L = 3400 \text{ m}$  ( $2 \cdot 1700 \text{ m}$ ) as input data for Eq. 12. The number taken for the length of the path as twice the single path assumes "uncorrelated paths".

Assuming a moderate turbulence of  $C_n^2 = 10^{-14} \text{ m}^{-2/3}$  - which is exceeded most of the time [16, 17] - one finds a standard deviation of

$$\sigma_I = 0.46.$$

#### Scintillation reduction due to averaging by a diffuse scatterer

Several laser pulses were recorded prior to the deployment of the smokes. It appears that the standard deviation is certainly less than 5% (including the laser pulse intensity jitter) and not the predicted 46% (see above).

This unexpected result is explained by scintillation averaging due to diffuse scattering from target.

At a distance  $L$  the appearance of the laser beam is determined by the Fresnel length  $(\lambda L)^{1/2}$ . The correlation length of intensity and phase equals approximately the Fresnel length. If the beam diameter  $D = 2\delta L$  ( $\delta$  being the divergence half angle) is larger than the Fresnel length, the beam is broken up in patches (or speckles) with an average length of  $(\lambda L)^{1/2}$ .

For example: The divergence of the Nd-Raman laser equals  $\delta = 0.25 \text{ mrad}$ , the distance is 1700 m. The beam diameter is then  $D = 0.85 \text{ m}$  and the Fresnel length is app. 0.05 m.

The number of these patches is approximately the area of the beam divided by the area of the average Fresnel patch. The number of the patches is then

$$n \approx (\delta L)^2 / (\lambda L) = \delta^2 L / \lambda \quad (15)$$

In the present example (Nd-Raman LRF) one finds  $n \approx 289$ .

After diffuse reflection the patches act as sources independent in intensity and phase. Adding these patches should give the reduction of scintillation usually found with statistical processes

$$\sigma_I^2 = \sigma_0^2 / n = \sigma_0^2 \lambda / (\delta^2 L) \quad (16)$$

$\sigma_I^2$ : average intensity variance,

$\sigma_0^2$ : variance seen by a point detector at  $L$ .

A more exact calculation [17] finds for the scintillation reduction factor

$$A = \sigma_I^2 / \sigma_0^2 \quad (17)$$

$$A = \frac{1}{1 + \{1.74 \delta (L / \lambda)^{1/2}\}^{7/3}} \quad (18)$$

For cases of interest the denominator of 18 is  $\gg 1$ . One has then

$$A \approx \left\{ 1.74 \delta (L/\lambda)^{1/2} \right\}^{-7/3} \quad (19)$$

The exponent 7/3 equals approximately 2 and therefore

$$A \approx 0.275 \lambda / (\delta^2 L) \quad (20)$$

Apart from the factor 0.275, the reduction factor in Eq. 20 is identical to the reduction factor of the intuitive solution (16).

One can integrate Eq. 20 directly into Eq. 12 and obtains for diffusely reflected beams

$$\sigma_{x,A}^2 = 2 \cdot 1.058 \cdot 0.275 \cdot \delta^{-2} \lambda^{-1/6} L^{5/6} C_n^2 \quad (21)$$

Here,  $L$  is the single path length assuming uncorrelated paths [17].

It is seen that for a given  $\delta$  the intensity fluctuation is virtually independent of the laser wavelength, indicating that the wavelength dependent change in intensity fluctuation is essentially compensated by the changing number of Fresnel patches.

For  $\lambda = 1.54 \mu\text{m}$ , a moderate turbulence of  $C_n^2 = 1 \cdot 10^{-14} \text{ m}^{-2/3}$  and a distance  $L = 1700 \text{ m}$ , Eq. 21 yields

$$\sigma_{x,A}^2 = 4.26 \cdot 10^{-4} \quad (22a)$$

and thus a *standard deviation* of the *intensity*

$$\sigma_{IA} = 0.04. \quad (22b)$$

This value is in much better agreement with experiment than the value obtained above.

This result is valid for *diffuse* reflection only - for *glint* reflection one has to use Eq. 12. The geometry of a non-coaxial LRF allows to assume *uncorrelated paths* for the direct and the return path. In this situation the total variance is computed as

$$\sigma_x^2 (\text{two way}) = 2 \cdot \sigma_x^2 (\text{one way}) \quad (23)$$

because the glint acts like a point source.

According to [14] one calculates the excess SNR factor which is required to obtain a certain detection probability  $p_d$  in the presence of turbulence with log-amplitude variance  $\sigma_x^2$

$$XFTURB = \exp\{\sqrt{2} \sigma_x \text{erf}^{-1}(2p_d - 1) + 0.5 \cdot \sigma_x^2\} \quad (24)$$

where  $\text{erf}^{-1}$  is the inverse of the error function.

For the averaged variance of Eq. 22a ( $\sigma_{x,A}^2 = 4.26 \cdot 10^{-4}$ ) one obtains (for *diffuse* reflection) and a  $p_d$  of 99%

$$XFTURB = 1.05.$$

For *glint* reflection Eq. 12 and 23 yield under the same conditions

$$XFTURB = 2.26.$$

#### Receiver aperture averaging

Eq. 12 is strictly valid - in its general range of validity - for point receivers. An extended receiver will average over the speckles which again have an average size of  $(\lambda L)^{1/2}$ . In the example given, the speckle size was app. 50 mm. Usually, the receiver apertures have similar size. Thus, receiver aperture averaging is not important for the cases considered and will thus not further be dealt with.

#### 6.4 Range determination of laser range finders

To determine the range of an LRF one uses Eq. 2, replacing the (undetermined) received power  $P_r$  by the *minimum power*  $P_{min} = P_{r,min}$  adequate for the desired detection attributes

$$P_{min} = P_t \rho \frac{D^2}{4R^2} \tau_o \exp\{-2(\beta \cdot R + \alpha \cdot CL)\} \quad (25)$$

$$P_{min} = NEP \cdot SNR \cdot XFTURB \\ = NEP \cdot (TNR + SNE) \cdot XFTURB$$

**NEP:** Noise Equivalent Power of the receiver for the actual bandwidth,

**SNR:** Signal-to-Noise Ratio,

**TNR:** Threshold-to-Noise Ratio associated with a particular false alarm probability (4a) and (6),

**SNE:** Signal-to-Noise Excess associated with a particular detection probability (10) and (11),

**XFTURB:** Excess factor required for detection with turbulence,

**$\beta$ :** volume extinction coefficient of the undisturbed atmosphere,

**$\alpha$ :** volume extinction coefficient of the smoke cloud,

**CL:** concentration-length product of the smoke cloud.

#### Nd-Raman LRF

The data of the Nd-Raman LRF is used to check the values, in particular of the TNR with the procedure given here. The complete set of data is displayed in Tab. 7.

Parameter	Value
<b>Transmitter</b>	
laser technology	Nd:YAG laser frequency shifted with a methane Raman cell
wavelength	1.54 $\mu\text{m}$
pulse energy	app. 12 mJ
pulse amplitude jitter	$\leq 5\%$
halfwidth of laser pulse	6 ns
pulse power	app. 2 MW, 1.5 MW with exit optic losses in 0.5 mrad
pulse repetition rate	app. 0.2 Hz sustained
transmitter divergence	0.5 mrad
transmitter aperture	40 mm
<b>Receiver</b>	
receiver field of view (FOV)	0.5 mrad
receiver aperture	60 mm
optical transmission	app. 0.7
noise equivalent power (NEP)	8 nW
threshold power	50 nW
false alarm probability	$\leq 0.001$
detection probability	$\geq 99\%$
bandwidth of buffer amplifier	100 kHz to 25 - 30 MHz
measuring range $R_{min} - R_{max}$	200 - 19900 m
target indication	first 3 targets displayed

Tab. 7: Data of the Nd-Raman LRF employed in the SW XV experiment.

The actual threshold-to-noise ratio  $TNR_{act}$  equals

$$TNR_{act} = 50 \text{ nW} / 8 \text{ nW} = 6.25.$$

With the pulse length of 6 ns, a measuring range of 19900 m

and a false alarm probability of 0.001, one computes

$$\text{TNR}_{\text{comp}} = 5.53.$$

This indicates that the actual value matches the theoretical value.

To achieve a 99% probability of detection, using Eq. 6 yields

$$\text{SNE} = 2.33.$$

### CO<sub>2</sub> LRF

The known data of the CO<sub>2</sub> LRF is summarised in Tab. 8. With this data one computes for a false alarm probability of 0.001

$$\text{TNR}_{\text{comp}} = 5.03.$$

The excess SNR for a 99% detection probability is the same as for the Nd-Raman LRF

$$\text{SNE} = 2.33.$$

Parameter	Value
<b>Transmitter</b>	
laser technology	CO <sub>2</sub> TEA (transversely excited atmospheric pressure)
wavelength	10.59 $\mu\text{m}$
pulse energy	app. 32 mJ
pulse amplitude jitter	$\leq 5\%$
halfwidth of laser pulse	40 ns
pulse power	app. 0.8 MW
pulse repetition rate	app. 1 Hz sustained
transmitter divergence	0.6 mrad
transmitter aperture	48 mm
<b>Receiver</b>	
receiver field of view (FOV)	0.6 mrad
receiver aperture	95 mm
optical transmission	app. 0.7
noise equivalent power (NEP)	app. 65 nW
threshold power	330 nW (computed)
false alarm probability	$\leq 0.001$
detection probability	$\geq 99\%$
bandwidth of buffer amplifier	50 kHz to 15 MHz
measuring range $R_{\text{min}} - R_{\text{max}}$	200 - 9900 m
target indication	first pulse/last pulse selectable

Tab. 8: Data of the CO<sub>2</sub> LRF used in the SW XV experiment.

### 6.5 Computations with SW XV data and comparison with measurements

Two principal subroutines were coded incorporating the theoretical analysis of the previous chapter. These routines were used for the subsequent analysis:

LRFRANGE (R): computes the LRF range  $R$  for a given set of parameters incl. preset detection probability,

LRFQUANT( $R, P_r, p_{d,act}$ ): computes received power  $P_r$ , detection probability  $p_{d,act}$  for a given range  $R$  and a given set of parameters.

With the distance of the LRF target (1775 m), the reflectivities of the target [5] and the derived threshold values ( $\text{TNR}_{\text{comp}} = 5.53$  for the Nd-Raman LRF,  $\text{TNR}_{\text{comp}} = 5.03$  for the CO<sub>2</sub> LRF) the detection probability as a function of the (one-way) smoke transmission was determined. The result is shown in Fig. 20. The probability scale is linear (other than the scale in Fig. 19). It can be seen that there is a narrow range only from marginal detection to unity probability of detection.

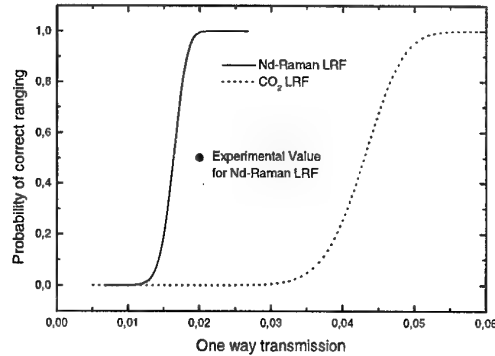


Fig. 20: Probability of detection for the Nd-Raman and the CO<sub>2</sub> LRFs as function of the one-way transmission through the brass smoke during SW XV.

The performance of the Nd-Raman LRF is about 2.5 times better than that of the CO<sub>2</sub> LRF. This result for identical transmission values is too optimistic for the CO<sub>2</sub> LRF since actual reflectivities - as compared to those of the laser target - are typically 3 times lower at wavelength 1.54  $\mu\text{m}$  but 20 times or more lower at 10.59  $\mu\text{m}$ . The CO<sub>2</sub> laser needs better transmission to match up with the Nd-Raman laser.

### Brass smoke

Figs. 21 and 22 show the time history for transmission measurements as well as actual and computed correct ranging events for the brass smoke trial.

For the threshold of the Nd-Raman LRF a transmission value of 2.5% was chosen which is 25% higher than the value suggested by Fig. 20. This takes into account transmission losses due to natural aerosol which were not measured.

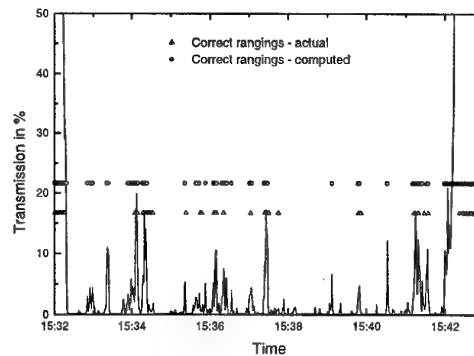


Fig. 21: Measured brass smoke transmission (solid line), overlayed by measured (triangles) and computed (circles) events of the Nd-Raman LRF correct ranging.

In the Nd-Raman LRF the "correct ranging" tag is displayed when the correct range is derived from the first, second or third

return. When smoke was present the first pulse always came from the cloud and sometimes a second return also.

The CO<sub>2</sub> LRF provides range reading for the first pulse only, and an indication of multiple returns. Correct ranging is assumed when the first pulse had the right value or when the return comes from the cloud and multiple returns are indicated.

When interpreting the results one has to realise that ranges were computed at the 1 s-intervals of the transmission measurements whilst the actual LRF ranging occurred only every 3 to 4 s.

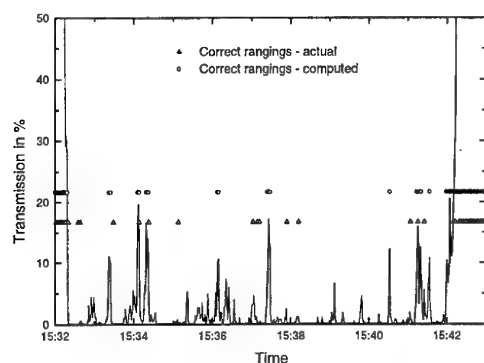


Fig. 22: Measured brass smoke transmission (solid line), overlayed by the actual (triangles) and computed (circles) events of the CO<sub>2</sub> LRF correct ranging.

When looking at the data of Figs. 21 and 22 one sees a partial individual correspondence of computed vs. actual correct ranging events. In about 50% of all cases, an individual correspondence is recognisable. There is a strong indication for the following explanation of this value: The LOSs of the LRFs and the transmissometer were some meters apart, and were inclined with respect to each other. Judging from the time history of the transmission data there are small-scale smoke density variations present. In addition, one has presumably not a "frozen" situation of the inhomogeneities transported by the wind. This explains why actual and computed ranging are loosely linked in time but not with a clear pattern which could be linked to wind speed.

Fig. 23 shows the statistics of experimental correct ranging as function of measured transmission in histogram form.

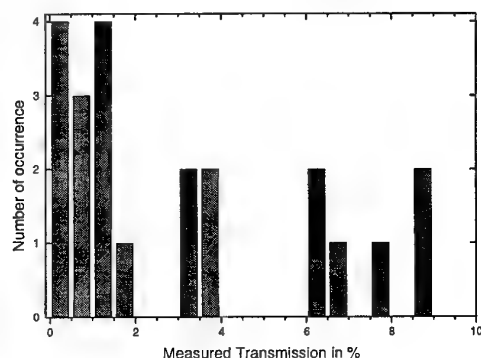


Fig. 23: Number of occurrence of correct ranging of the Nd-LRF as function of measured transmission of the brass smoke (bin width: 0.5%). 100% probability of correct ranging was app. at 10% transmission. The median value of transmission within that range is app. 2%.

The fact that actual and measured transmission did not coincide acts as an additional noise source broadening the distribution. Nearly 100% of the probability is reached only for transmission values beyond 10%. For *measured* transmission below 10% the median value of correct ranging is app. 2%, indicating that the *true* transmission value is app. 2%. This is in accordance with the computed value.

#### Fog oil/graphite smoke

While the brass smoke produced almost always transmission values near 0%, fog oil/graphite smoke gave rise to intermediate transmission values for most of the time. Consequently, the Nd-Raman LRF almost always worked. It seems more appropriate to compare events of failures rather than of correct ranging. This is done in Fig. 24 and in detail in Fig. 25.

The one-way transmission values which correspond to failures are close to 2% in accordance with the findings with brass smoke.

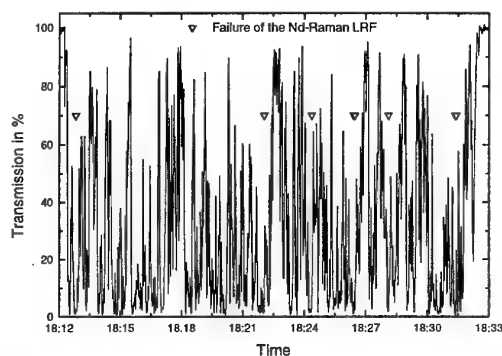


Fig. 24: Failures of the Nd-Raman LRF during fog oil/graphite smoke.

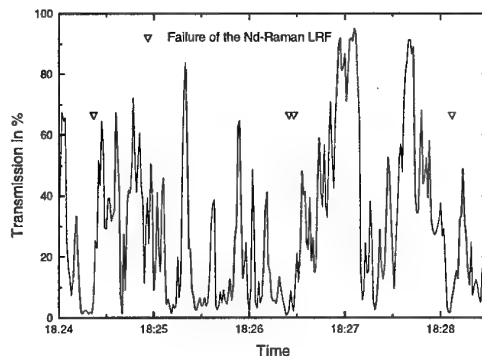


Fig. 25: Failures of the Nd-Raman LRF during fog oil/graphite smoke, detail of Fig. 24.

Fig. 26 shows the failure events of the CO<sub>2</sub> LRF. Also depicted are the expected failures derived from the measured transmission values assuming 10% and 12% transmission as the limit. Having in mind the caveats regarding actual and measured transmission, one concludes that an actual value of 10-12% is linked with the failures. Fig. 20 predicts rather a value of 4-5%. The discrepancy is most likely attributable to the degradation of the CO<sub>2</sub> laser which was diagnosed at the time of measurements.

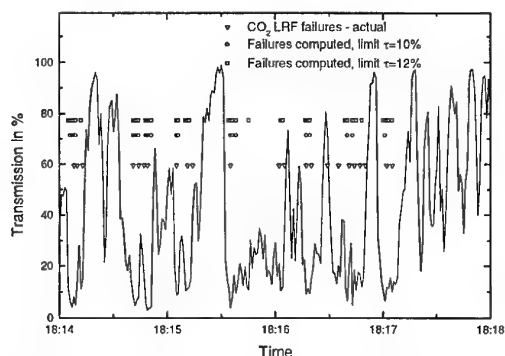


Fig. 26: Failure events of the CO<sub>2</sub> LRF during fog oil/graphite smoke. Actual failures (triangles), computed failures for a transmission limit of 10% (circles) and 12% (squares).

## 7. CONCLUSION

As part of an effort to establish the model COSMOS (Combined Optical/IR Sensor Modelling in the Presence of Obscurants and Smokes) which predicts the impact of smokes and battlefield effects on the performance of modern EO sensors, an in-depth description and analysis of the performance of laser range finders was carried out. In particular, multiscattering and turbulence effects are modelled in a realistic way. Scintillation averaging due to diffuse reflection is included. Quantitative agreement between computation and experiment was obtained.

Time resolved signals of two laser range finders were analysed, i. e. a Raman-shifted Nd:YAG LRF operating at 1.54  $\mu\text{m}$  and a CO<sub>2</sub> LRF at 10.59  $\mu\text{m}$ . Quantitative agreement of temporal behaviour and absolute magnitude of backscattered pulses could be obtained using scattering functions previously computed from size distributions of brass and fog oil/graphite smokes. Multiple scattering calculations were done using NBMSCAT.

Model validation was based on data of SMOKE WEEK XV. Of particular interest were two experimental broadband obscurants, i. e. brass smoke and fog oil/graphite smoke. No EO data are available for these smokes. Therefore, as a primary step, these smokes were analysed. Particle size distributions were found to be lognormal. Based on this, Mie phase functions were computed and used for the above calculations.

## References

- [1] Wittenstein, W., Schubert, W., "Analytisches Reichweitenmodell TRM3" in "FGAN-FfO Annual Report 1995", Report FGAN-FfO 1995/100.
- [2] Director, Battlefield Environment Directorate, Army Research Laboratory, "EOSAEL92" (references found with documents are still: US Army Science Laboratory, White Sands Missile Range, NM 88002).
- [3] Büchtemann, W., "COSMOS - Combined Optical/IR Sensor Modelling in the Presence of Obscurants and Smokes", Report FGAN-FfO 1998/08.
- [4] Communication U.S.ARL (Klimek, W.) to FGAN-FfO (Kleindienst, S.), SMOKE WEEK XV particle size distribution data, 17 June 96.
- [5] Kleindienst, S., Dimmeler, A., Clement, D., "Obscuration effects of smoke clouds", in "Targets and Backgrounds: Characterization and Representation II", Watkins, W. R., Clement, D., Ed., Proc. SPIE 2469, p. 440 - 451, 1995.
- [6] Davis, B.T., Wetmore, A.E., Tofsted, D.H., Shirkey, R.C., Sutherland, R.A., Seagraves, M.A., "EOSAEL92", Vol. 19, "Aerosol phase function data base PFNDAT", draft April 1994, U.S. Army Sciences Laboratory, White Sands Missile Range, NM.
- [7] Padmabandu, G.G., Abromson, D., Bickel, W.S., "Light scattering by micron-sized conducting fibers: an experimental determination", Appl. Optics, Vol.30, No.1, p. 139-144, 1991.
- [8] Bissonnette, L.R., FORTRAN code PFCAL, Defence Research Establishment Valcartier, Canada, 1996.
- [9] Gray, D.E., Ed., "American Institute of Physics Handbook", McGraw-Hill, New York, 1972.
- [10] Weast, R.C., Ed., "Handbook of Chemistry and Physics", CRC Press, Boca Raton, 1983/84.
- [11] Bissonnette, L.R., "EOSAEL 92", Vol. 17, "Narrow beam multiple scattering module NBSCAT", U.S. Army Sciences Laboratory, White Sands Missile Range, NM.
- [12] Bissonnette, L.R., "Computer code NBMSCAT - narrow beam multiple scattering module", Defence Research Establishment Valcartier (DREV), Canada, 1995.
- [13] "RCA Electro-Optics Handbook", Technical Series EOH-11, RCA Corporation, 1974 (Reprints available).
- [14] Accetta, J., Shumaker, D., Ed., "The Infrared and Electro-Optical Systems Handbook", Vol. 6, "Active Electro-Optical Systems", Environmental Research Institute of Michigan, Ann Arbor, 1993.
- [15] Accetta, J., Shumaker, D., Ed., "The Infrared and Electro-Optical Systems Handbook", Vol. 2, "Atmospheric Propagation of Radiation", Environmental Research Institute of Michigan, Ann Arbor, 1993.
- [16] Höhn, D.H., Ed., "FGAN-FfO Annual Report 1988", Report FGAN-FfO 1988/123.
- [17] Yura, H.T., Büchtemann, W., "Scintillation reduction factor for laser range finder performance calculations", Report FGAN-FfO 1985/51.

PAPER No. 12

DISCUSSORS'S NAME: G. Roy

COMMENT/QUESTION:

How important are the turbulence effects?

AUTHOR/PRESENTER'S REPLY:

Turbulence effects are very important for the performance of LRFs. This is the reason we included it into COSMOS. We have not yet considered the impact of turbulence on the problems discussed, one reason being that there was not enough variability in this parameter during the time the experimental data were taken. It will certainly be the subject of future investigations.



## Electrooptical Propagation Assessment in Coastal Environments (EOPACE)

Juergen H. Richter  
Propagation Division  
SPAWAR Systems Center, D88  
53560 Hull St.  
San Diego, CA 92152-5001  
USA

### SUMMARY

Several years ago the US Navy started an exploratory development program to measure and model atmospheric electrooptical properties in coastal environments. The initial measurement program was conducted in 1996 and 1997 in the southern California coastal region. Additional measurements are planned at US Atlantic coastal sites and other locations. Emphasis in EOPACE is on near-surface aerosols and transmission. The effort and findings so far are described and future plans outlined.

### 1. INTRODUCTION

All systems that rely on propagation of electromagnetic energy in the atmosphere are affected by atmospheric properties. In the case of radar and radio propagation in the troposphere, refractive layers are the primary cause for anomalous propagation conditions. Considerable effort in both propagation modeling and environmental sensing and modeling resulted in an operational assessment capability for radio waves (Craig, 1994). With the availability of electrooptical (EO) sensors and weapons, an EO propagation assessment capability was needed. EO propagation assessment is considerably more difficult because more atmospheric parameters play a role and the scales of interest are smaller than in radio propagation applications. Figure 1

<b>Primary Ranges of Interest and Environmental Parameters</b>	
<b>EM (Radio)</b>	<b>EO</b>
10 - 100s km	1- 10s km vis: 1 - 20 km
- refraction	- molecular absorption
- clutter, rough surface	- aerosol extinction
- turbulence	- turbulence
	- refraction
	- target/background radiances
	- sunglint/clutter

Figure 1. Atmospheric parameters and ranges for radio and EO propagation.

lists those parameters. For anomalous radio propagation, the primary atmospheric parameter is refraction and the ranges of interest are tens to hundreds of kilometers. In the EO case, molecular absorption, aerosol extinction, turbulence, and refraction are important as well as target/background contrast

and clutter for detection purposes. In the lower atmosphere, ranges of interest are generally in the 1-10 km range. Military conflicts are likely to involve coastal regions where EO propagation conditions are even more complex and variable. To improve EO systems performance assessment, a measurement and modeling program was started named EO Propagation Assessment in Coastal Environments (EOPACE).

### 2. EOPACE OBJECTIVES

Infrared (IR) passive surveillance systems performance predictions are of primary concern in EOPACE as illustrated in figure 2. Airborne Forward Looking IR (FLIR) systems are operational on several aircraft types. Key atmospheric parameters affecting FLIR performance are clouds and aerosols. Other parameters are contrast between the target

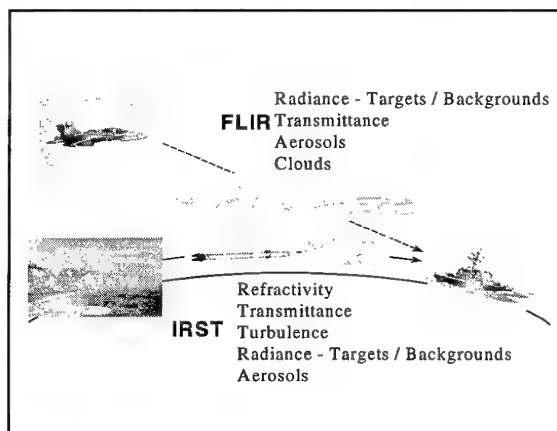


Figure 2. Atmospheric effects on passive surveillance systems.

and its background, path radiance, refraction, and atmospheric transmittance. The sea-skimmer missile threat is a serious concern for naval operations in coastal environments. To detect low-flying missiles, IR surveillance systems [such as IR search and track (IRST)] must look close to the ocean surface where large aerosols are important whose vertical distribution and properties are largely unknown. Aerosols in coastal environments can be a complex mixture between continental and marine aerosols and their extinction at IR wavelengths must be known for assessing the performance of passive surveillance systems. In addition,

meteorological mesoscale models capable of predicting EO propagation conditions are needed both for forecasting and, as a key component of data assimilation systems, for nowcasting. The development of such mesoscale models needs comprehensive measurements of appropriate EO atmospheric parameters for determining empirical parameters and for validation. Finally, IR surveillance sensors need to be tested in a well-described environment for accurate performance assessment. EOPACE was designed to address all of the above areas. Accordingly, the three primary objectives of EOPACE are:

- Quantify and model coastal aerosol effects on IR propagation.
- Provide input data for mesoscale data assimilation systems.
- Evaluate EO systems in coastal environments.

The southern California coastal area was chosen for the initial phase of EOPACE for the following reasons: first, the Navy controls excellent facilities and key participants' laboratories are located in this area. Second, the climatology of this region is similar to other important areas such as the Mediterranean. After an initial set of measurements in southern California, experiments in other geographic regions have been performed and are planned to provide inputs to models that are universally applicable.

Another important aspect in the planning and execution of EOPACE is teaming of US and foreign investigators. The great variety of complex measurements requires drawing on different expertise and backgrounds. U.S. participants include government laboratories, universities, and industry. Foreign countries participating in EOPACE include The Netherlands, Canada, the United Kingdom, and Australia.

### 3. EOPACE PROGRESS

Major emphasis in EOPACE has been on Intensive Observation Periods (IOPs) for coastal aerosols. Specifically, near-surface and surf-generated aerosols were measured either directly or through remote sensing techniques. In addition, techniques for characterizing coastal air mass properties were investigated. Finally, near-surface transmission measurements were performed. Seven IOPs in San Diego and Monterey were conducted during 1996-1997 and one exploratory field trial at Duck, North Carolina. Several data analysis workshops and special sessions (such as this one) have been conducted. Other examples are special sessions at the SPIE symposium in July 1997 in San Diego (Bissonnette and Dainty, 1997) and the Battlespace Atmospheric Conference 1997 (Anderson and Richter, 1998).

Gathman and Smith (1997) describe unique aerosol measurements in EOPACE. Two Particle Measuring Systems (PMS) aerosol counters were carefully calibrated to produce the same results when operated side by side. Subsequently, one was operated on a fixed shore site at the Naval Amphibious Base (NAB)[UK pms data], the other on a moving boat [NRaD boat pms] (NRaD is a previous name of SPAWAR Systems Center, San Diego). Figure 3 shows  $dN/dr$  measurements versus drop size radius  $r$  when the wind

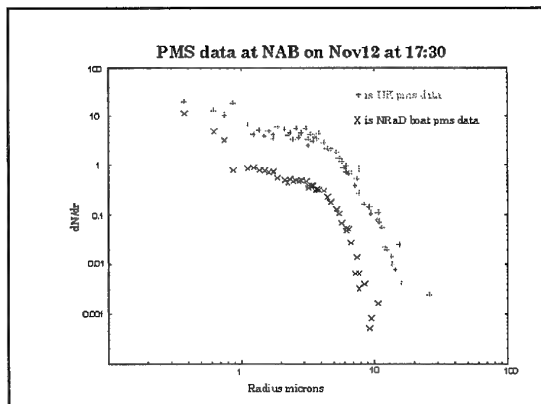


Figure 3. Aerosol size distribution measurements over water and on shore (onshore winds).

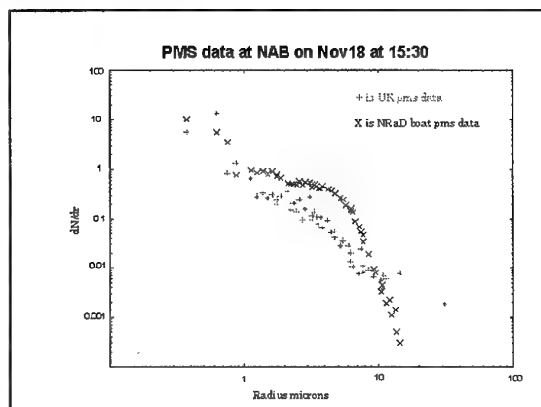


Figure 4. Aerosol size distribution measurements over water and on shore (offshore winds).

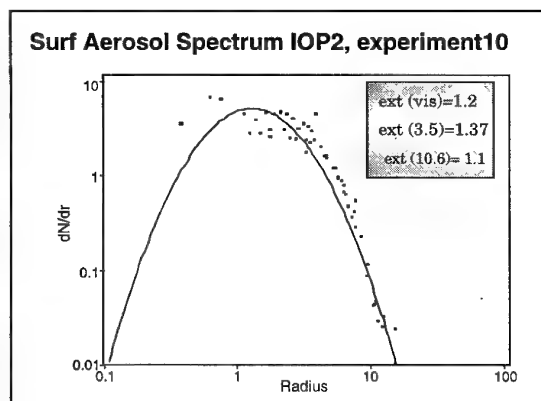


Figure 5. Surf-generated aerosol distribution.

blew from sea to land and figure 4 from land to sea ( $N$  is the number of particles per  $\text{cm}^3$ ). The difference of both curves in figures 3 and 4 is due to surf-generated aerosols. In figure 5,

this difference is plotted and fitted with a log-normal distribution which represents the surf-generated aerosol component. The contribution to extinction is calculated for three different wavelengths and is largest for 3.5 microns. Gathman and Smith (1997) were able to correlate extinction and swell height, thus permitting prediction of surf-generated aerosol extinction from swell height. Work is underway to investigate the horizontal transport of surf-generated aerosols using backscatter lidar measurements.

The Navy Aerosol Model [NAM] (Gathman, 1983) and the Navy Oceanic Vertical Aerosol Model [NOVAM] (Gathman et al., 1989) require a characterization of the background aerosol which involves a so-called air mass parameter (AMP). Various techniques have been investigated to determine the AMP. Among them are air trajectory analyses, measurements of atmospheric radon or condensation nuclei, sensing of optical depth from satellites, and nephelometer measurements. Battalino (1998) reviewed various techniques. Littfin et al. (1998) concluded that nephelometer measurements are the preferred technique for in-situ observations. Jensen et al. (1998) presented a remote sensing technique based on satellite measurements of upwelling radiance. Their approach opens the possibility of obtaining data in denied areas.

Finally, extensive near-surface transmission measurements conducted during EOPACE have demonstrated the importance of large aerosols on extinction and shown that atmospheric refraction may significantly affect transmission.

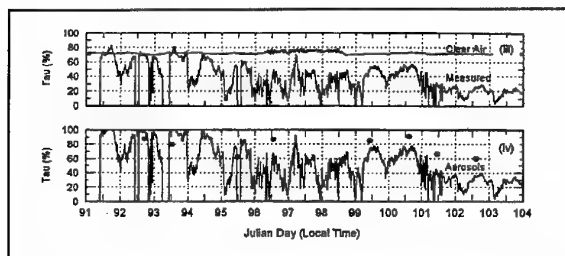


Figure 6. Transmission measurements in the mid-IR band (3.6-4.1 microns) over a 7 km path.

An example of transmission measurements in the mid-IR band (3.6-4.1 microns) is shown in figure 6 for a seven kilometer over-water transmission path (receiver/source heights were at 5 and 6 m). The upper graph shows measured transmission for a 13 day period in 1996. Also shown is calculated transmission due to molecular absorption (clear air) only. The lower part of figure 6 shows transmission with the clear air component removed, i.e., aerosol extinction only. The solid circles are transmission values calculated from drop size distribution measurements taken from a boat along the transmission path. There is good agreement (within the transmission measurement errors estimated to be  $\pm 30\%$ ) between the aerosol extinction inferred from the actual transmission data and those calculated from measured drop size distributions. The data clearly indicate the importance of aerosol extinction to near surface transmission. On occasion, measured transmission values exceed 100%. While some of

those instances may be due to experimental errors, there are periods where atmospheric refraction is responsible for signal enhancements (Zeisse et al., 1998). These brief periods are observed only occasionally but last longer than expected by scintillation. Refraction effects on longer paths can be even more pronounced and are an important factor to be considered in near-surface propagation assessment.

#### 4. EOPACE PLANS

With the California coastal measurements nearly completed, major emphasis is placed on thorough analysis of the data. This includes further analyses of measured transmission data with respect to molecular absorption, aerosol extinction, refraction, and scintillation; prediction of aerosol marine boundary layer effects from satellite optical depth measurements; derivation of empirical constants for aerosol models; and the use of advanced numerical models for prediction of near-surface aerosol size distributions. Additional measurements have already been performed at Duck, North Carolina and further IOPs are planned at Duck and also at Wallops Island, Virginia. Special attention will be given to horizontal transport of aerosol plumes using scanning lidar observations. In summer of 1998, additional measurements will be performed in the North Sea.

EOPACE results will be used to develop improved models for surf-aerosol production and transport. Near-surface transmission measurements will be further pursued to quantify effects of aerosols, refraction, and scintillation. These findings will lead to a better prediction capability of near surface transmission. The results from EOPACE will be incorporated into environmental decision aids such as the EOTDA (EO Tactical Decision Aid) and also be used to test and evaluate various existing propagation modeling codes. Dust particles and desert aerosols play an important role in potential conflict areas. EOPACE will address measurement, modeling and prediction of extinction properties of those aerosols in the near future. A description of EOPACE, including a list of publications, can be found at <http://sunspot.nosc.mil:80/543/eopace/eomain.html>.

EOPACE has been and will be assembling unique databases of simultaneously measured meteorological and EO data for development and testing of numerical mesoscale models. Such models are critical for development of data assimilation systems and for forecasting purposes. Future plans for EOPACE also include testing IRSTs under carefully described propagation conditions.

#### ACKNOWLEDGEMENT

This work is supported by the Office of Naval Research.

#### REFERENCES

- Anderson, K.D. and J.H. Richter, (Eds.), Proc. of the 1997 Battlespace Atmospherics Conference 2-4 Dec. 1997, SPAWAR Systems Center San Diego, TD 2989, March 1998
- Battalino, T., Air Mass Characterization for EO Propagation Assessment, NATO RTO CP 605 U, paper 17, 1998

Bissonnette, L.R. and C. Dainty, (Eds.), Propagation and Imaging through the Atmosphere, Proc. SPIE. Vol. 3125, 1997

Craig, K.H. (Ed.), Propagation Modelling and Decision Aids for Communication, Radar and Navigation Systems, AGARD LS 196, 1994

Gathman, S.G., Optical properties of the marine aerosol as predicted by the Navy Aerosol Model, Opt. Eng., 22, pp. 57-62, 1983

Gathman, S.G., G. de Leeuw, K.L. Davidson, and D.R. Jensen, The Navy Oceanic Vertical Aerosol Model, AGARD CP 454, pp. 17.1-17.11, 1989

Gathman, S.G. and M.H. Smith, On the Nature of Surf-Generated Aerosol and their Effect on EO Systems, Proc. SPIE, Vol. 3125, pp. 2-13, 1997

Jensen, D.R., C.H. Wash, and M.S. Jordan, Air Mass Parameterization and Coastal Aerosol Modeling, NATO RTO CP 605 U, paper 20, 1998

Littfin, K., S. Gathman, D. Jensen, and C. Zeisse, Analysis of Three Methods of Characterizing an Air Mass, NATO RTO CP 605 U, paper 21, 1998

Zeisse, C., S.G. Gathman, A. Barrios, W. Moision, K. Davidson, P. Frederickson, and B. Nener, Low altitude infrared transmission, Proc. of the 1997 Battlespace Atmospherics Conference 2-4 Dec. 1997, SPAWAR Systems Center San Diego, TD 2989, March 1998

## PAPER No. 13

DISCUSSOR'S NAME: C. Philbrick

COMMENT/QUESTION:

One of your viewgraphs listed SeaCluse. Could you explain what that is in relation to EOPACE?

AUTHOR/PRESENTER'S REPLY:

SeaCluse is described by Claverie et al. in paper #5 of this conference.

PAPER No. 13

DISCUSSOR'S NAME: J. Claverie

COMMENT/QUESTION:

What is the interest of using the parabolic equation for electrooptical propagation?

AUTHOR/PRESENTER'S REPLY:

The parabolic equation approximation to the wave equation allows for accurate modeling of propagation conditions even at caustics where ray tracing techniques break down.

DISCUSSOR'S NAME: H. Wittmann

COMMENT/QUESTION:

What is most important in characterization of aerosols

- droplet size distribution
- $DK$ , complex  $DK$ ?

I expect different EO behavior of aerosols depending on desert, high humidity (Amazon or Gulf of Mexico area) environments. As I see it, there is not a clear physics oriented definition of what is important in characterization of aerosol droplets ( $\rightarrow$  EO effects).

AUTHOR/PRESENTER'S REPLY:

IR propagation near the sea surface is influenced primarily by large aerosols. Since the chemical composition of marine aerosols is known, their size distribution is the important parameter. Also known is the growth factor of these hygroscopic aerosols which affects both size distribution and complex index of refraction. EO extinction effects are calculated by Mie theory using both size distribution and complex refractive index based on the ambient relative humidity.

# Electro-optical propagation just above wave tops as predicted by ANAM, the Advanced Navy Aerosol Model.

Stuart G. Gathman  
Propagation Division  
SPAWAR SYSTEM CENTER D883  
49170 Propagation Path  
San Diego, CA 92152-7385

Alexander M. J. van Eijk  
TNO-FEL, P.O. Box 96864  
2509 JG The Hague, The Netherlands

## 1. SUMMARY

An extension of the Navy aerosol model (NAM), intended to describe aerosol size distributions from 10 meters down to the wave tops is being developed. The preliminary version of the empirical Advanced Navy Aerosol Model (ANAM) is based on a series of meteorological and aerosol measurements taken during the Marine Aerosol Properties and Thermal Imager Performance (MAPTIP) experiment off the Dutch coast during 1993. The predicted aerosol size distributions of ANAM will be compared with direct aerosol measurements.

## 2. INTRODUCTION

The topic of this report is a preview of the Advanced Navy Aerosol Model, ANAM, which describes the aerosol size distribution found in the atmosphere from above shipboard level down to the tops of the highest waves. Mie theory then allows the calculation of electro-optical properties of the atmosphere with the assumption that these aerosols are spherical in shape and consist of solutions of sea salt and water. Unfortunately, there are not many measurements available on which to statistically base an empirical model. The lack of data becomes most prominent for high wind speeds and rough seas that produce effects of a serious nature on propagation.

The concentration of aerosol in the marine boundary layer results from an interplay of physical processes governing injection of aerosol by the bubble jet process from whitecaps, direct wave-tearing, vertical transport and deposition. In addition, the presence of waves has a distinct influence on the airflow. Only complex numerical models can address detailed pieces of this problem but these in turn are difficult to apply to real situations.

## 3. THE CONSTRUCTION OF ANAM

### 3.1 Methods for measuring giant aerosol

There are only a few ways to obtain in situ measurements in the region below 15 meters in extreme weather conditions and they all require some form of platform at sea on which to support the aerosol instrumentation. It is necessary that the measurements not disturb the air flow and the device should be cheap and/or waterproof (since it may get submerged by a wave or be sprayed by water). The small concentration of large sea salt particles requires large samples of air in order to get statistically significant results. In addition the inertia of these large droplets makes the sampling of these droplets difficult in that because of their mass, they simply will not follow an air stream around sharp turns in sampling tubes. The simple rotorod device (1) turns out to be the best method developed up to the present of obtaining the required data in this region but it is very labor intensive in its operation.

### 3.2 Overview of available rotorod data sets

The table below lists all rotorod data known by the authors to be available. The set spans a time period from 1983 to 1997 and contains data from 8 different locations. One location was in the North Atlantic, the others in coastal areas. The majority of data was recorded at platforms in the North Sea. The table also specifies the extent of individual data sets (number of profiles) and the maximum height in the profiles. The data can be available in two types: bins or images. The 'bins' data consists of aerosol concentrations (dN/dD values) in approximately 10 size bins in the diameter range 10-150 micron. The 'images' data consists of the original images as seen through the microscope at the time of the experiment. The image data can be distributed over any given set

of size bins and is therefore more flexible for analysis than the bin data.

With the exception of data sets 6, 8 and 15, all rotorod data has been obtained by TNO. Data set 10

was obtained upwind of the German FPN ("Forschungs Plattform Nordsee") platform located at 100 km northwest of the Elbe estuary in the North Sea (54° 42' N, 7° 10' W); see (2).

Table I

Set	Experiment	Location	Data type	Profiles	Up to
1	Asgamage A 1996	MPN, coastal platform	bins	27	12 m
2	Asgamage B 1996	MPN, coastal platform	images	13	12 m
3	Asgasex 1993	MPN, coastal platform	bins	8	12 m
4	Cumulus 1983	North Atlantic, ship	bins	25	11 m
5	Eopace IOP1 (TNO) 1996	Scripps pier, SIO, CA	bins	28	9 m
6	EOPACE IOP1 (SSC SD) 1996	Scripps pier, SIO, CA	images	10	10 m
7	Eopace IOP2 (TNO) 1996	Monterey Bay, CA, pier	bins	15	6 m
8	EOPACE IOP2 (SSC SD) 1996	Monterey Bay, CA, pier	images	9	6 m
9	Eopace IOP6 (TNO) 1997	Scripps pier, SIO, CA	images	27	7 m
10	FPN 1992	FPN, coastal platform	bins	17	27 m
11	Hexmax 1986	MPN, coastal platform	bins	43	12 m
12	Key 1990	Marathon, FL, ship	bins	35	4 m
13	Lolland A 1994	Denmark, mast	images	14	8 m
14	Lolland B 1995	Denmark, mast	bins	24	8 m
15	Maptip 1993 (SSC SD)	MPN, coastal platform	images	19	12 m
16	Maptip 1993 (TNO)	MPN, coastal platform	images	18	12 m
17	Sylt 1992	Sylt, coastal platform	bins	10	15 m

In the Sylt experiment (set 17); see (3) the measurements were made from a German jack-up barge ("Hubinsel Barbara") which was positioned 13.5 kilometers from the island of Sylt in the North Sea near the German-Danish border (54° 42' 09" N, 08° 11' 50" E). The Lolland experiments (sets 13 and 14) took place at a mast about 2 km northwest of Vindeby on the Danish island Lolland in the Store Bælt (4). The EOPACE rotorod data (sets 5, 6, 7, 8 and 9) was obtained at piers in La Jolla and Monterey (California) which extended from the beach into the ocean beyond the surf, see (5, 6). The Cumulus data (set 4) was obtained at the weather ship Ms. Cumulus at station Lima (57° N, 20° W) in the North Atlantic (7). The buoy measurements were made at a distance of about 6 m from the ship at the windward side, to reduce the influence of the hull. Measurements at higher elevations had to be made from the decks of the ship. The KEY90 experiment (set 12) took place near Marathon in the Florida Keys (8). The rotorod data were measured from a small boat (the Renegade) at a few kilometers from the island (roughly around 24° 1' N, 80° 3' W). The measurements were made while the boat was at station, and the waverider buoy was typically deployed at some 10-15 meters upwind of the boat.

### 3.3 Empirical data used in ANAM

The table shows that there now exists a reasonable number of rotorod spectra and profiles available for use as an empirical basis for ANAM. It seems useful to first select a set of data that contains the broadest size and height range of the measured aerosol spectrum and in which the weather provides a reasonable range of wind speeds and sea states. Algorithms can be developed with this set of data which relate the parameters of measured aerosol size distribution to the meteorological parameters which occurred during the measurement. Then once a full spectrum of the marine aerosol can be represented by an appropriate set of parameters, Mie calculations can be done on the spectra so that the electro-optical parameters can be determined.

We have chosen to start with the MAPTIP data since this set contains wide spectra profiles utilizing the combined data from the PMS (SSC SD) and rotorod (SSC SD and TNO) devices from close to the surface to 12 meters in height as well as an excellent set of meteorological measurement and conditions. There are some flaws in the data set recorded at the MPN tower and caused by the nearby land. For some of the

profiles, the wind direction was such that the nearby land induces fetch effects on the waves, which must eventually be taken into account. The relatively shallow depth of the water and its effects on wave development may be somewhat different from open ocean conditions. Nevertheless it is the best data set available at this time and will be used for the construction of the first version of the model. The philosophy here is to use the MAPTIP data set to construct an initial model that will then be tested and modified as necessary by utilization of the other data sets.

We are also aware that our assumptions of horizontal homogeneity with respect to all of these measurements do not hold close to the waves. This is obvious in that white caps do not uniformly cover a flat water surface but are located in areas that are related to wave structure. Streams of aerosol injected into the atmosphere probably also occur in discrete areas. Thus measurements from wave rider buoys and very low level fixed sensors may not be representative to the true average of aerosol concentration in these regions.

Concurrent with the testing of ANAM 1.0 with other field rotorod data, we feel that it is imperative to use the results of sophisticated numerical wind/wave models to extend the measured results above the waves down to the top of the highest wave.

### 3.4 An example of Aerosol data: MAPTIP

During the fall of 1993, a field experiment called MAPTIP (9) was planned and carried out by NATO AC/243 (Panel 04 / RSG.8), with the collaboration from AC/243 (Panel 04 / RSG.5). A major objective of this field experiment was to assess marine boundary layer effects on thermal imaging systems. The data collected from this experiment is used here to create models for the evaluation of the infrared propagation near the ocean surface related to marine-generated aerosols, turbulence and meteorological factors.

The key facility used in MAPTIP was the "Meetpost Noordwijk" (MPN), an oceanographic research tower (owned by the Dutch Department of Harbors and Public Works "Rijkswaterstaat") situated at approximately 9 km from the Dutch coast near the village of Katwijk (52° 11' 51.6" N, 04° 22' 57.6" E). On this tower were situated many types of instruments for the MAPTIP experiment and the data from these measurements are coordinated with other mobile platforms (aircraft, ship and buoys) and a shore location. The location of a stable platform situated in the North Sea where the high probability

of strong northerly winds and their associated waves makes this an ideal experiment location.

A useful feature of the MAPTIP experiment is the existence of a consensus meteorological data set which statistically combines and filters up to nine simultaneous measurements of the key meteorological parameters made by the various MAPTIP participants. The parameterization of this data is described in (10).

The portion of the aerosol spectrum from 0.3 to 50.0 micro meters radius was measured using both rotorod samplers and optical counters such as Particle Measurement Systems (PMS) instruments during MAPTIP. These devices were either mounted on movable platforms, which could be raised and lowered to the water surface, fixed on the tower, or mounted on a small wave rider buoy floating on the water.

An example of a combined MAPTIP data set is shown in figure 1. On this plot are shown the data from an experiment on 25 October 1993 in which simultaneous profiles were obtained at approximately (07:10 GMT) at the tower. The data shown in the figure were taken at an approximate altitude of 12 meters. It is obvious from placement of points in figure 1 that although the ranges of the devices differ from each other, there is sufficient overlap to allow for a much broader composite spectrum of the aerosol size distribution to be constructed than could be done with individual instruments. Of particular interest in the figure the "hump" of the aerosol size spectrum that was seen by the two rotorod devices but was beyond the useful range of the PMS probe.

The aerosol size distributions from MAPTIP were fitted by an analytical curve for parameterization purposes. These curves were analyzed for a maximum in  $dN/dr$  values and associated mode radii in the region between 5 and 20 microns in order to find the mode radius and mode amplitude represented by the large aerosol group (shown as the "hump" in figure 1).

The parameterization makes it now possible to look for relationships between the aerosol size distribution mode descriptors and some of the measured meteorological (e.g., wind speed) and geometrical (e.g., height) data that are available from the MAPTIP data set. The individual observations taken at different altitudes but close to each other in time were combined into profiles so that the average meteorological parameters during the period of the



profile would show the effect on the profiles themselves.

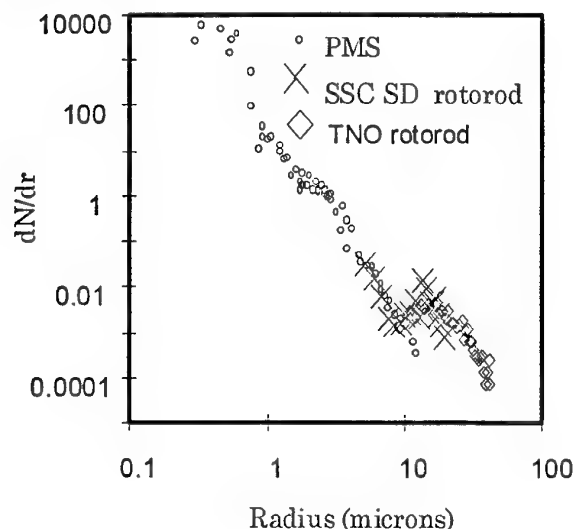


**Figure 1:** The extended aerosol size distribution from 25 October 1993 during MAPIP obtained from three independent and separately calibrated devices.

The conclusions from this analysis can be stated as:

- 1) There is a large size aerosol population produced by the white water process over the ocean and its concentration is related to wind speed.
- 2) The mode radius of this population seems to be independent of wind speed over the wind speeds and directions encountered in MAPIP.
- 3) The amplitude of the large aerosol mode is a function of wind speed, altitude and atmospheric stability.

#### 4. THE INITIAL STRUCTURE OF ANAM

The construction of version 1.0 of ANAM is based on an endeavor to empirically duplicate the aerosol size distribution at various altitudes just above the wave tops as measured in MAPIP. This is accomplished by constructing formulas based on the log normal parameters derived from the MAPIP data set. ANAM will be a multi-component model which includes an element to describe the very large aerosol in the region from about 15 meters down to the top of the highest wave. The description of this aerosol will be a lognormal function called the ANAM component or fourth mode. The total aerosol size distribution will then be the superposition of three lognormal functions from the Navy Aerosol Model, NAM (11) plus the ANAM component. From this

combined size distribution, the electrooptical properties can be calculated by the direct integration of the aerosol size distribution with Mie theory over the sizes of interest.

The large aerosols in the ANAM component are represented by a single lognormal size distribution:

$$\frac{dN_4}{dr} = \frac{A_4}{f_4} \cdot \exp \left( -C_4 \cdot \log \left( \frac{r}{r_{04} f_4} \right)^2 \right)$$

where  $C_4$  is related to the standard deviation of these large particles,  $f_4$  is the growth factor which is a function of relative humidity,  $r_{04}$  is the mode radius and  $A_4$  is the amplitude of this term and a function of wind speed, altitude, and mixing length.

In this simple model, the humidity effects of the droplet sizes are represented by a swelling factor,  $f$ . In ANAM each of the first three components use the appropriate swelling factor suggested by Gerber (12) and the  $f_4$  term is considered a sea salt droplet. The swelling factors are a strong function of relative humidity. The mode radius of the fourth term,  $r_{04}$ , was found to be independent of wind speed for the MAPIP experiment. The value of this parameter was determined by the use of the calibrated rotorod measurements to be 15 micrometers radius. The  $C_4$  term when parameterized with respect to the calibrated data set has a value of  $-5$ , whereas the  $C$  parameters for the other modes in NAM and NOVAM require the value of  $-1$ .

The  $A_4$  term is related to wind speed, the height above the mean water level and the Monin-Obhukov stability length  $L$ . At this stage of development, there is not enough data to determine any fetch effects on the function:

$$A_4(w, z, L) = U(w) \cdot p(z, L)$$

The mode average amplitude of the fourth component at 10 meters at a wind speed of  $w$  is represented as  $U(w)$ . ANAM version 1.0 first sets this term at the height of 10 meters using the MAPIP data. The scaling with respect to height above the water is done by multiplying with the profile function,  $p(z, L)$ .

The most complicated aspect of the fourth component is that of the altitude variation. The profile function used here must have several features so that it can mimic the features, which are observed in the MAPIP profiles. It must first of all have the value of 1 at 10 meters altitude so that the profile function can scale the whole range of altitudes to the empirical wind controlled value that was observed at MAPIP.

Secondly, there are no adequate measurements of these large aerosols at altitudes higher than the tower so that the actual function above 10 meters is not critical for the problem at hand. However, we assume that the function is zero at the inversion height which serves as a practical limit to this term. Below 10 meters, its behavior is a function of atmospheric stability, resulting in a straight profile (no vertical structure) for large negative  $L$  values.

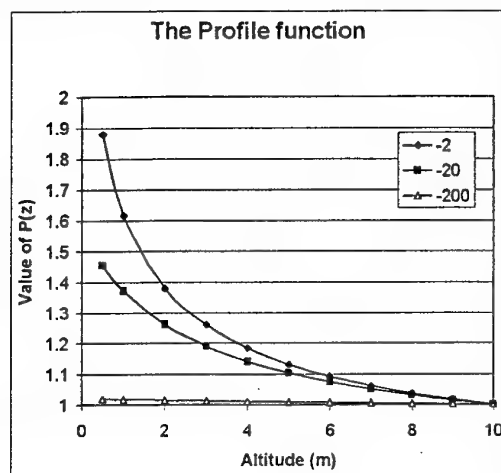


Figure 2: The profile function is plotted as a function of altitude for three values of the mixing length  $L$ .

The plot of the empirical profile function,  $p(z, L)$  between the wave tops and 10 meters is shown in figure 2 where  $p(z, L)$  is plotted as a function of  $z$  for three different values of  $L$ . The function  $p(z, L)$  is based in part on the classic non-dimensional profile function  $\phi(\psi)$  of Businger and Dyer (13). Only cases in which  $L$  is negative are allowed in this preliminary empirical model, as all of the data from MAPIP were done under unstable conditions.

#### 4.1 The electro-optical properties of ANAM

Once the aerosol size distribution,  $dN/dr$  is determined for a particular altitude above the mean water line, then Mie theory can be used to determine the interaction of the ensemble of spherical aerosol particles with electro-optical energy impinging on them. This requires an integration of the Mie scattering coefficient and the aerosol size distribution to be made over all appropriate sizes. The volume extinction coefficient is

$$\beta = \frac{\pi}{1000} \int Q \cdot \frac{dN}{dr} \cdot r^2 \cdot dr$$

where  $Q$  is the Mie efficiency factor,  $dN/dr$  the size distribution of the aerosol, and  $r$  is the aerosol size. The Mie scattering coefficient,  $Q$  is related to the

index of refraction of the droplets, the aerosol radius and the wavelength of the light. In the calculations here, the Mie coefficient,  $Q$  is calculated using the Dave program (14). The index of refraction of the white water produced droplets are assumed to be a solution of sea salt dissolved with water. The droplets are further assumed to be in equilibrium with the ambient relative humidity so that the dry size of the particle can be known through the swelling factor. Thus a volume mix of water and sea salt at any relative humidity is used to determine the index of refraction of the whole droplet solution.

Applying the four mode ANAM aerosol size distribution to the volume extinction coefficient integration from Mie theory described above we have:

$$\beta = \frac{\pi}{1000} \int Q \cdot \sum_{i=1}^4 \frac{A_i}{f_i} \cdot \exp \left( -C_i \cdot \log \left( \frac{r}{f_i \cdot r_{0i}} \right)^2 \right) \cdot r^2 \cdot dr$$

This equation is integrated over an appropriate range of sizes and with fine enough grid spacing directly. In the case of ANAM, the range of integration is  $0.001 \mu\text{m}$  to  $1 \text{ mm}$ . The integration is done for each of six decades using the Simpson rule.

#### 4.2 Optical characteristics near wave tops

The model ANAM 1.0 was written in FORTRAN and is capable of delivering an aerosol size distribution and a volume extinction coefficient for unstable environments given the input meteorological data, a wavelength, and an altitude.

ANAM version 1.0 is a simple model with inputs consisting of the regularly available meteorological parameters such as: air mass parameter (derived from either condensation nuclei concentration, visibility, radon, or nephelometer data), sea surface temperature, air temperature (at 10 m), relative humidity (at 10 m), current wind speed (at 10 m) and 24 hour average wind speed (at 10 m).

ANAM can now be used to investigate the optical properties in the regions below deck levels. ANAM has been constructed to represent the aerosol measurements of MAPIP. The first step of verification is to determine how well the model represents the measured aerosol data in MAPIP. The meteorological data for the measurements plotted in figure 1 were obtained and used as input to ANAM. The aerosol size distribution predicted by ANAM is shown plotted in figure 3 together with the measured data points from MAPIP for that time and place. This data shows that the model pretty well matches the measurement at least in this case.

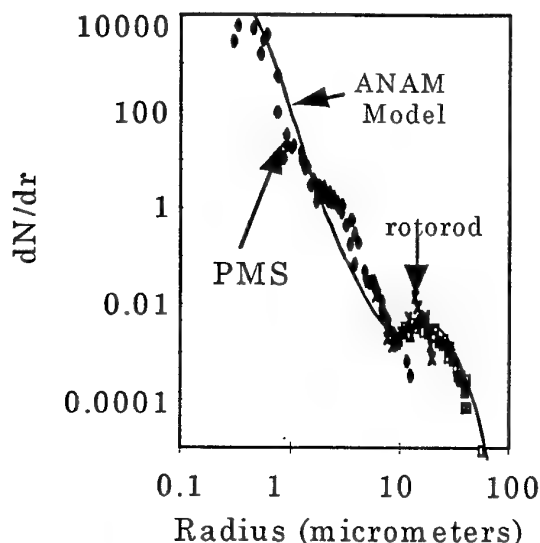


**Figure 3:** The  $dN/dr$  profile obtained during MAPTIP shown in figure 1 but with the modeled ANAM aerosol size distribution superimposed over that data as a line.

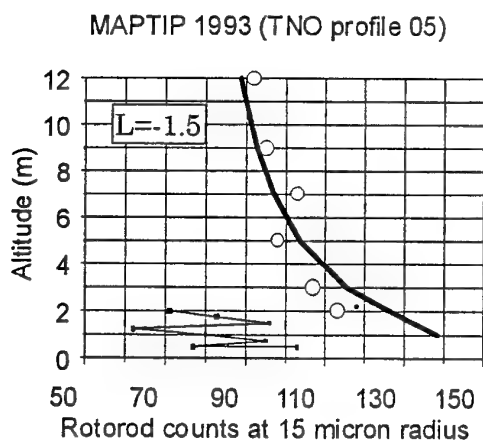


**Figure 4:** Profiles of TNO rotorod counts of 15 micron droplets and the ANAM prediction of these sizes for 24 October 1993 at 10:40 GMT. The stability for this case is represented by a mixing length,  $L = -1.5$  meters. The large circles are the measured rotorod data from devices on the tower mounted at fixed heights above the water. The small square symbols connected by a line are those measurements done at the same time from the wave follower buoy. The thick line is the ANAM prediction for this case.

A second test is to compare the vertical profile of the amplitude of the fourth mode with a typical multipoint rotorod profile obtained by TNO during MAPTIP with the model prediction. Such a plot is shown in figure 4. While the model and measurements seem to agree at the higher altitudes, there is a discrepancy between the moving wave rider data and the fixed tower data. It is important to note that the wave rider rotorod data (the small square markers connected by a line) have a different height reference than do the fixed data. The plane of reference of the height of these data is above the surface of the wave that is moving up and down and only has a mean value of zero. We would expect that the buoy values would be more comparable to the fixed data than they are. The discrepancy may be explained by the fact that the  $p(z,L)$  function in ANAM (1.0) is not yet fully adapted for the presence of waves. Efforts are currently underway to improve the  $p(z,L)$  function on an experimental and theoretical basis.

Finally after a cursory check of the operation of the model, we feel that ANAM could be used to investigate the optical properties of the atmosphere from 10 m down to the wave tops.

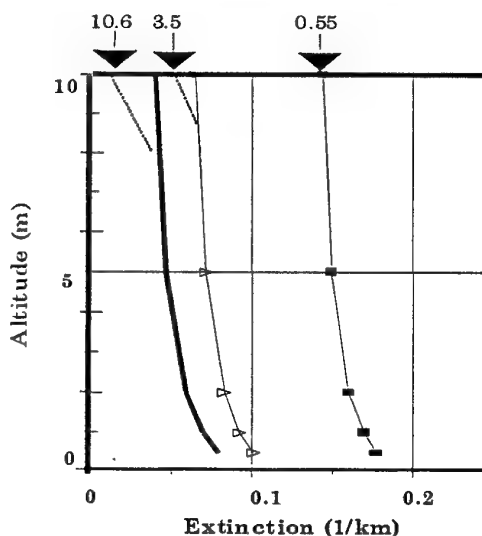


**Figure 5:** Extinction profiles calculations from ANAM for the visible (solid square markers), 3.5 micrometer IR (open triangles), and 10.6 micrometer IR (heavy solid line) wavelengths. The wind speed is set at 9 m/s, and the mixing length is  $-8.5$  meters. The arrows on top of the figure refer to the NAM predicted values for the same conditions. The dotted lines associate the NAM and the ANAM predictions.

Figure 5 shows the model results for a typical case with a Monin-Obukhov length of  $-8.5$  m and a wind speed of  $9$  m/s. In this figure are plotted the volume extinction coefficients for the visual wavelength (0.55 micrometers), the mid IR, (3.5 micrometers), and the far IR (10.6 micrometers) as they vary from 10 meters down to the wave tops. On the top side of the plot are three arrows which represent the values that NAM gives for these wavelengths. We see first of all that the additional ANAM component for the larger aerosols primarily affects the mid and far infrared extinction values. Compared to the NAM values, ANAM predicts an increase of the mid and far infrared extinction values at 10 m, thus reflecting the influence of the larger aerosols even at the height of 10 m.

The vertical variation of the extinction coefficient between 10 m and the wave crests is about 200% for the infrared wavelengths, whereas the variation for the visible wavelengths is about 25%.

As an indication of the effect of the vertical variation of the infrared extinction coefficient on the transmission over a 10 km path, we assume that molecular and aerosol extinction are of the same magnitude. In that case, the infrared transmission near the wave crests is only 36% of the transmission at 10 m height. This first example shows that the effect of large aerosols as represented by the ANAM component cannot be neglected when assessing the electro-optical propagation characteristics in the marine atmospheric surface layer.

## 6. ACKNOWLEDGEMENTS

The authors wish to acknowledge the support given this project by Dr. Scott Sandgathe and Dr. Ron Ferek of ONR and of Dr. Juergen Richter of SSC-SD. The authors acknowledge Dr. G. de Leeuw for making available the TNO-FEL rotorod data, and the dedication of the TNO-FEL personnel when making the rotorod measurements. The TNO participation in the development of ANAM is sponsored by the Royal Netherlands Navy (assignments A95KM729 and A96KM795).

## 7. REFERENCES

1. De Leeuw, G., "Vertical profiles of giant particles close above the sea surface", *Tellus* 38B, p51-61, 1986.
2. De Leeuw, G., Van Eijk, A.M.J. and Dekker, H., "Studies on aerosols in the marine atmospheric surface layer". EUROTRAC annual report, part 3

ASE, pp94-101. International Scientific Secretariat, IFU, Garmisch-Partenkirchen, Germany, 1992.

3. De Leeuw, G., Sittrop, H. and Heemskerck, H.J.M., "First impressions and some qualitative results from the SYLT92 experiment". TNO Physics and Electronics Laboratory Report FEL-92-A363, 1992.

4. Sorensen, L.L., Hertel, O., Pedersen, B., Wagner, M., Larsen, S.E., Hojstrup, J., Schultz, M., de Leeuw, G. and Geernaert, G.L., "Horizontal transport modeling and exchange of atmospheric nitrogen gases with the coastal ocean". *Proc. of the Second International Conference on Air-Sea Interaction and on Meteorology and Oceanography of the Coastal Zone*, September 22-27, Lisbon, Portugal, American Meteorological Society, p. 208-209, 1994.

5. Gathuman, S.G., "On the nature of surf generated aerosol and their effect on electrooptical systems", *Propagation and Imaging through the Atmosphere*, L. R. Bissonnette and C. Dainty editors, Proceedings of SPIE, 29-31 July 1997, San Diego, vol 3125, p2.

6. Gathuman, S.G. (1997), "Surf produced aerosol", *J. of Aerosol Science*, vol 28, supplement1, pS1.

7. De Leeuw, G., Parashar, S., Park, P.M., Perry, S.J., Roney, P.L. and Smith, M.H. "Aerosol study in the North Atlantic 1983". NATO AC/243 (Panel IV/RSG.8) Report 1986-01. (1986).

8. Gathuman, S.G., Jensen, D.R., Hooper, W.P., James, J.E., Gerber, H.E., Davidson, K.L., Smith, M.H., Consterdine, I.E., De Leeuw, G., Kunz, G.J. and Moerman, M.M., "NOVAM evaluation utilizing electro-optics and meteorological data from KEY-90". NRD Technical Report 1608, 1993.

9. Jensen, D. R., G. de Leeuw, and A. M. J. van Eijk, "Work Plan for the Marine Aerosol Properties and Thermal Imager Performance Trial (MAPTIP)", TD2573, NCCOSC, RDT&E Div, San Diego, CA 92152-5001, 1993.

10. Gathuman, S.G., "MAPTIP observations of large aerosol in the lowest 10 meters above waves", in *Image propagation through the Atmosphere*, J. Christopher Dainty and Luc R. Bissonnette eds. SPIE vol 2828, p 15, 1996.

11. Gathuman, S.G., "Optical properties of the marine aerosol as predicted by the Navy aerosol model", *Opt. Eng.*, 22(1), p 57, 1983.

12. Gerber, H.E., "Relative - Humidity Parameterization of the Navy Aerosol Model (NAM)", NRL report 8956, Dec 30, 1985.

13. Businger, J.A., "Transfer of heat and momentum in the atmospheric boundary layer", *Proc. Arctic Heat Budget and Atmospheric Circulation*, Santa Monica, Calif., RAND Corp., 305-332, 1966.

14. Dave, T. V., "Subroutines for Computing the Parameters of Electromagnetic Radiation Scattered by a Sphere", IBM Palo Alto Scientific Center Report #320-3237, 1968.

#### PAPER No. 14

DISCUSSORS'S NAME: A. Tooth

#### COMMENT/QUESTION:

When, do you estimate, will the results from your studies be included in the atmospheric prediction codes such as MODTRAN/FASCODE?

#### AUTHOR/PRESENTER'S REPLY:

The direct transition of ANAM into MODTRAN will not take place because of the small geometric scale of ANAM and the larger grid sizes of MODTRAN. However the MOSART model discussed in paper #3 is capable of incorporating the scale of a model such as ANAM into it. The ANAM model will not be released however until it has been adequately tested with independent data sets.

#### G. ANDERSON:

Comment on A. Tooth's suggestion that ANAM be ported to MODTRAN. Currently MODTRAN does not have an adequate refractive geometry to model transmission near the sea surface, including potential ducting and the impact of very large aerosols.

DISCUSSOR'S NAME: B. Mattiussi

Is air/water pollution taken into account in your model? What are the effects of sea state on your model?

#### AUTHOR/PRESENTER'S REPLY:

The quantity of air pollution is approximated in the A1 term of the model. Water pollution is not considered. Sea state is included in the model through its relationship with average and long term wind speed.

PAPER No. 14:

DISCUSSOR'S NAME: D. Dion

From modeled profiles of A4 shown in your presentation, we note that the increase of A4 with decreasing height would typically be of the order of 20-30%. Isn't it of the order of accuracy of A4 estimation at any height?

AUTHOR/PRESENTER'S REPLY:

It is true that the ANAM modeled profiles of A4 in the case presented have an increase of about 25% (for visible wavelengths) from 10 meters down to 1 meter. At other longer wavelengths this increase can be several hundred percent. There are other cases however (when the mixing length is very negative) that there is 0% variation for all wavelengths (that is there is no variation with altitude). On the other hand there are also cases with small negative values of the mixing length where all wavelengths have larger increases from 10 meters down to 1 meter. The empirical aspect of the model is built from a statistically significant number of observations. If the accuracy of the model were determined by these data alone, the order of accuracy of A4 would be much less than 25% and would be a very good indicator indeed that the model would be almost perfect. However the ultimate accuracy of the model must be determined by numerous verification experiments with independent data sets.

DISCUSSOR'S NAME: A. Tooth

Your studies will improve the prediction accuracy close to the sea surface. At what height above the sea surface do you consider the existing aerosol models to be valid?

AUTHOR/PRESENTER'S REPLY:

The initial version of ANAM under certain conditions shows that at 10 meters altitude there can be some differences between ANAM and NAM for larger wavelengths. Obviously the largest particles measured from MPN are not propagated to great heights. Although there are no rotorod measurements during MAPTIP above 15 meters, there are profiles of aircraft "Optical Aerosol Counters" measurements of the very large aerosol which show that there are very above 50 meters. I believe that somewhere between 15 and 50 meters the existing models would be adequate.

# Long-range transmission at low elevations over the ocean

A.N. de Jong, G. de Leeuw, P.J. Fritz, M.M. Moerman

TNO Physics and Electronics Laboratory

PO Box 96864

2509 JG The Hague

The Netherlands

## 1. SUMMARY

Results are presented from infrared transmission measurements over long ranges at low elevation in coastal waters. This work was part of the EOPACE programme, conducted at two locations along the US West Coast. In this programme data were collected for validation of atmospheric models, used to predict IR sensor performances.

Details are given on the transmissometer set-up and measurement methodology. The data concern midwave (3-5 $\mu$ m) and longwave (8-12  $\mu$ m) measurements, taken over the Monterey Bay (22 km) and San Diego Bay (15 km) in various periods of the year (March, April, August and November).

The results are compared with model predictions, including molecular extinction, aerosol scattering and refraction effects. The first two effects have been determined carefully and could be quantified to a certain extent with the help of simultaneously collected meteorological data. The refraction effects are of a more complicated nature due to the complex temperature profile structure over water, which is difficult to measure.

## 2. INTRODUCTION

The effects of water vapour and aerosols on infrared (IR) propagation through the atmosphere are well known and described in the literature [1]. As a result of the extinction due to these effects, the detection range of IR sensors is limited. For a point target, this detection range ( $R_d$ ) is directly related to the transmission by the following formula:

$$R_d = \sqrt{\frac{\Delta W * \tau(R_d)}{NEI * (S/N)_t}} \quad (1)$$

In this formula  $\Delta W$  is the target contrast (W/sr),  $\tau(R_d)$  the atmospheric transmission in the respective band over the range  $R_d$ , NEI the sensor's Noise Equivalent Irradiance (W/m<sup>2</sup>) and  $(S/N)_t$  the threshold signal to noise ratio.

For Infrared Search and Track sensors (IRST) interesting ranges are between 10 and 30 km, when detection of incoming missiles is envisaged. For these ranges the effect of water vapour and aerosols on transmission based upon Lowtran 7 predictions in the midwave and longwave IR is illustrated in figures 1, 2 and 3.

The effect of water vapour is shown in figure 1, where the transmission appears to decrease strongly with absolute humidity, as generally known the longwave IR much more rapidly than the midwave.

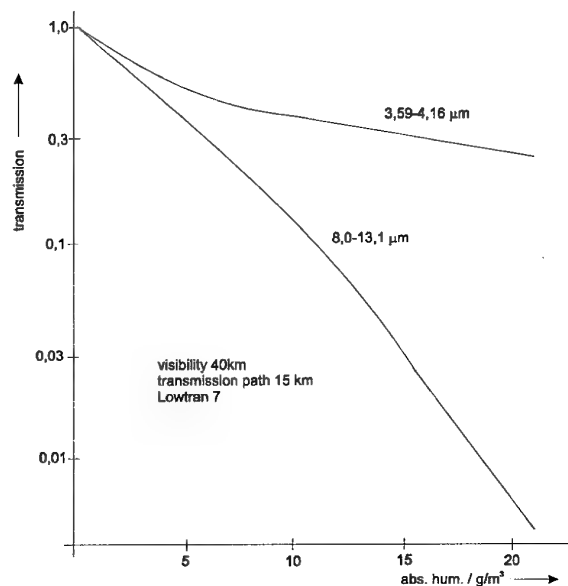


Fig. 1: Midwave and longwave IR transmission versus absolute humidity.

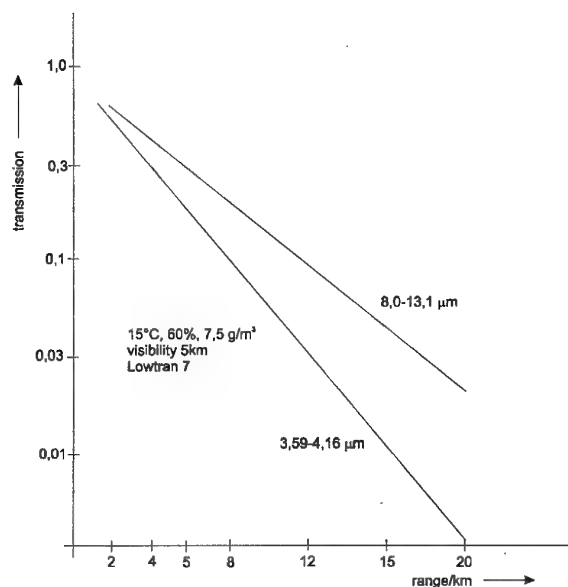


Fig. 2: Midwave and longwave IR transmission versus range.

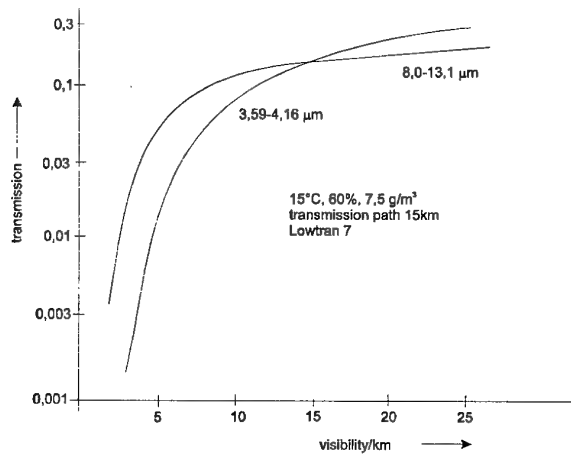


Fig. 3: Midwave and longwave IR transmission versus visibility.

The calculations were made for rather clear bands without CO<sub>2</sub> absorption and a visibility of 40 km. For ranges of about 15 km, we can write for the transmission values  $\tau_m$  and  $\tau_l$  for midwave and longwave as function of range R respectively

$$\tau_m = \exp(-\sigma_m R) \quad \tau_l = \exp(-\sigma_l R) \quad (2)$$

where  $\tau_m$  and  $\tau_l$  are the midwave respectively longwave extinction coefficients, approximately related to the absolute humidity  $h_a$  by

$$\tau_m = 0.0054 h_a \quad \tau_l = 0.0156 h_a \quad (3)$$

For  $h_a = 15 \text{ g/m}^3$  we find  $\tau_m = 0.08 \text{ km}^{-1}$  and  $\tau_l = 0.23 \text{ km}^{-1}$ . Figure 2 shows the transmission as function of R, for a visibility of 5 km. The midwave transmission decreases more rapidly than the longwave IR transmission. For an absolute humidity of  $7.5 \text{ g/m}^3$ , resulting in  $\tau_m$  and  $\tau_l$  values of about  $0.04 \text{ km}^{-1}$  resp  $0.12 \text{ km}^{-1}$  for water vapour, the total, combined extinction coefficients for a visibility of 5 km due to water vapour and aerosols are  $0.28 \text{ km}^{-1}$  resp  $0.19 \text{ km}^{-1}$ . The contributions of aerosols to these values are  $0.24 \text{ km}^{-1}$  resp  $0.07 \text{ km}^{-1}$  for midwave and longwave IR. Figure 3 shows an example of the variation of the transmission over a 15 km path with the visibility. For visibilities greater than 12 km, the effect of the visibility becomes almost negligible.

As an example we demonstrate the transmission effect on the detection range by substituting in formula (1) for NEI the midwave and longwave values of  $10^{-10} \text{ W/m}^3$  resp  $4 \cdot 10^{-10} \text{ W/m}^2$ , for  $\Delta W$ : 0.2 resp 1 W/ster (a low observable missile) and  $(S/N)_t = \bar{S}$ , an atmosphere of  $15 \text{ g/m}^3$  and visibility of 40 km.  $R_d$  is found to be 12.2 resp 8.4 km for the midwave resp longwave sensor.

So far theory and measurements are rather well in agreement for open ocean conditions with similar air and sea temperatures which are known along the path, known aerosol size distribution, and along paths that are not close to the sea surface.

In a coastal environment however, with high probability of inhomogeneities along the path and targets skimming the ocean at low altitude (for example 3 m), detection ranges are much more difficult to predict. Both the MAPTIP trials [2]

and other propagation measurements over long ranges over the North Sea [3] have shown strong anomalies in propagation effects.

In order to further investigate these anomalies, TNO-FEL, sponsored by the Netherlands Ministry of Defence and ONR, decided to participate in the EOPACE campaign (Electro Optical Propagation Assessment in Coastal Environment) organized at two locations along the US West Coast, well known for the atmospheric inhomogeneities, provided by generally cold water close to a desert-like land environment. Preliminary measurements by Bull [4] clearly showed the anomalies due to low level and along path gradients in temperature, humidity and particle size distribution. Unfortunately very few support data (e.g. aerosol and meteorological data) were taken during Bull's measurements. During the EOPACE campaign this was done much more carefully [5]. This provided a strong basis and data set for further validation of low level propagation models. The input from TNO-FEL in this programme consisted of transmissometry and collection of aerosol size distributions and meteorological data. Preliminary results on the transmissometry have been reported in [6] for the first phase of the project: the measurements in Monterey and San Diego in March and April 1996. Preliminary results on the second phase of the project, concerning transmission measurements in San Diego in November 1996 and August 1997 are reported in [7].

This paper contains an overview of the results of the transmissometry, the lessons learned and recommendations for the work to be carried out in the future.

### 3. DESCRIPTION OF SET-UP

Two locations have been chosen for the transmissometry: Monterey Bay with a 22 km path between Moss Landing Pier and Monterey Plaza hotel and San Diego Bay with a 15 km path between Imperial Beach Pier and the Naval Sub Base BOQ. Both paths are schematically shown in figures 4 and 5.

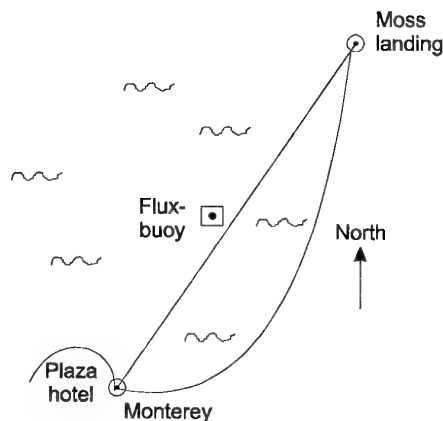


Fig. 4: Measurement path in Monterey.

The ranges are of operational interest concerning the detection of targets at an altitude of 3 m with a sensor at an altitude of 15 m. This causes the target to pop up over the horizon at a range of 19.4 km. For reasons of safety for the equipment we



mounted the transmissometer source at an altitude of 10 m above mean water level at Moss Landing and at 9 m altitude at Imperial Beach. The receivers were mounted at altitudes of 16.5 m resp 5.4 m in Monterey resp San Diego.

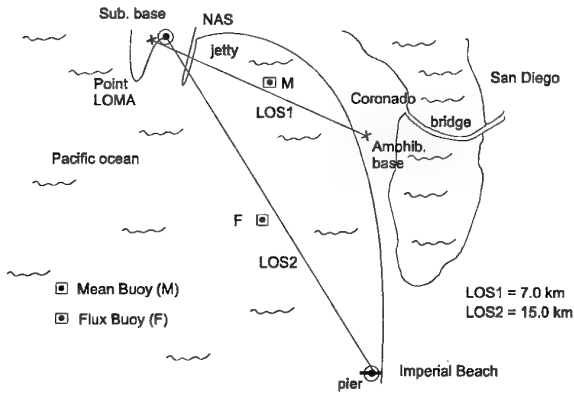


Fig. 5: Measurement path in San Diego.

Technical details on the transmissometer are presented in table 1. The transmissometer is basically similar to the one, used in earlier measurements over 18 km in the North Sea environment [8]. The transmitter and the receiver have identical Newtonian mirror optics with 230 cm<sup>2</sup> effective entrance pupil area.

Table 1: Technical parameters of TNO-FEL transmissometer.

Parameter	Value
Source collimator diameter	20 cm
Source focal length	40 cm
Source temperature	900 K phase 1; 1100 K phase 2
Beam divergence	10 mr phase 1; 6.25 mr phase 2
Chopping frequency	820 Hz
Useful source area	230 cm <sup>2</sup>
Receiver collimator diameter	20 cm
Receiver focal length	40 cm
Midwave detector type	HgCdTe phase 1; InSb phase 2
Midwave detector size	2x2 mm phase 1; 2 mm round phase 2
Midwave spectral bands	3.7-5.7 $\mu$ m phase 1; 3.60-4.04 $\mu$ m phase 2, Nov. 3.59-4.16 $\mu$ m phase 2 Aug.
Longwave detector size	2x2 mm
Longwave spectral band	8.0-13.1 $\mu$ m

A reference signal was transmitted by means of a radio link and used for synchronous detection of the 820 Hz modulated signal. The time constant was normally set at 3 sec and the signal was sampled with a frequency of 1 Hz. The signal to noise ratio for the 22 km range was about 600 resp 150 for the midwave resp longwave band for 100% transmission condition in phase 1 (March/April '96).

By averaging the signals over a period of 1 minute, the signal to noise ratio's improve a factor of 4.5. This means that a 1% longwave transmission level can be measured with an accuracy of 15%, which is acceptable (for the 1 minute integration time). The midwave transmission level is measured with a 4 times better accuracy.

It is noted that the set-up was slightly modified and improved during the campaigns. From phases 1 to 2, a new source with higher temperature was mounted to provide a higher signal to noise ratio. Also the HgCdTe midwave detector was replaced by an InSb one because of better homogeneity of the responsivity over the detector area.

The spectral bandfilter for the midwave band was changed to have better band correspondence with the SPAWAR transmissometer, simultaneously operating over a 7 km path in San Diego (see figure 5, [9]).

In the first three campaigns the transmissometer was operated with a midwave or longwave detector. In the fourth campaign 3 transmissometers were operated simultaneously; one midwave band in room 246 of the BOQ and two in room 146. The 2 lower receivers (midwave + longwave) in room 146 were at an altitude of 6.4 m above mean sea level; the receiver in room 246 at 9.4 m above mean sea level. This set-up provided an opportunity to investigate the dependence of transmission on height above the water.

The additional equipment, used in the various experiments consisted of:

- particle size distribution measurements (Knollenberg type) at Moss Landing Pier and Imperial Beach Pier
- meteorological equipment
- high resolution midwave imager in Monterey and San Diego during the first phase
- high resolution near IR camera
- near IR radiometer and 1000 Hz source for scintillation measurements in phase 1 and August '97 phase 2
- midwave camera for point source measurements in August '97, phase 2.

Results on the scintillation measurements have been reported in [10]. The near IR camera's were used to visually inspect the atmospheric behaviour. For this purpose, an alignment source was mounted near the transmitters. The transmitters in turn were aligned with a similar alignment source at the receiver side.

#### 4. CALIBRATION, SIGNAL HANDLING

As signal(s) we will consider here the signal from the Lock-In amplifier, which provides the time averaged (3 sec) RMS value of the 820 Hz signal, coming from the transmitter. As transmission along the path we measure by definition

$$\tau = \frac{\text{signal with atmosphere}}{\text{signal without atmosphere}} = \frac{\int_{\lambda_1}^{\lambda_2} e(\lambda) \tau(\lambda) \rho(\lambda) d\lambda}{\int_{\lambda_1}^{\lambda_2} e(\lambda) \rho(\lambda) d\lambda} \quad (2)$$

in which  $e(\lambda)$  is the source spectral emission,  $\rho(\lambda)$  the receiver spectral response and  $\tau(\lambda)$  the atmospheric spectral transmission.

It is important to note that all power received in the full instantaneous field of view, is taken into account. This means that possible contributions in the signal due to forward scattering by aerosols and refraction effects are included.

The determination of the 100% value from formula (2) is difficult because we cannot easily create a longwave vacuum path. In the meantime a zero range calibration (to make  $\tau(\lambda)=1$ ) causes a lot of optical problems, because it is questionable whether the transmitter and receiver can be aligned in such a way that no signal is lost by obscuration. Therefore we calibrated our transmissometer by measurement of the signals on two clear days over a path of 800 m and 2500 m near our laboratory in The Hague. For the atmospheric conditions at these days both integrals in formula (2) were calculated using Lowtran 7.

The signals for the 800 m and 2500 m ranges corresponded within a few percent, which gave us confidence in the method. Denoting the 5  $\mu\text{m}$  and 10  $\mu\text{m}$  signal over 2500 m by  $s_{2.5}(5)$  resp  $s_{2.5}(10)$  and the  $\tau$  values  $\tau_{2.5}(5)$  resp  $\tau_{2.5}(10)$ , we find for the transmission over the 22 km range:

$$\begin{aligned}\tau_{22}(5) &= \frac{s_{22}(5)}{s_{2.5}(5)} \cdot \frac{22^2}{2.5^2} \tau_{2.5}(5) \quad \text{resp} \\ \tau_{22}(10) &= \frac{s_{22}(10)}{s_{2.5}(10)} \cdot \frac{22^2}{2.5^2} \tau_{2.5}(10)\end{aligned}\quad (3)$$

where  $s_{22}(5)$  resp  $s_{22}(10)$  are the midwave resp longwave longrange (22 km) signals. For the 15 km range we take 15 instead of 22 in formula (3).

Before the calibration over 800 m resp 2500 m, we performed a number of laboratory measurements to check the components of the system:

- measurement of detector responsivities ( $D^*$ )
- measurement of spectral transmission of filters
- compare the 900 K source with a calibrated blackbody and measure its real temperature
- measure the source radiant intensity with detector and filter without optics
- measure the homogeneity of the emission/sensitivity over the pupil, test of optics transmittance/mirror reflectance
- test of the Lock-In amplifier, measure the noise histogram of the output signals
- test the homogeneity of the detector response over its surface with the 800 m outside experiment. Here we found the problem with the HgCdTe detector mentioned above.

Because in the first three campaigns we could measure with only one detector at a time (midwave or longwave), we frequently had to change the gain (and the phase!) of the Lock-In amplifier. Most of the times one detector was used in the receiver during between 3 and 6 hours.

In the fourth campaign (San Diego, August '97), the 'classic' receiver (room 246) was provided with a midwave detector, whereas the two receivers in room 146 had a midwave and longwave detector. The diameter resp focal length of these two receivers were 20 cm resp 50 cm. The 3 Lock-In amplifiers each had a different signal handling, which has been taken into account.

## 5. RESULTS

The general first impression of the results of the 4 transmission campaigns along the US West Coast is one of

great variability. The expected atmospheric inhomogeneities did occur, as well along the path as in altitude. Rapid variations of these conditions in time occurred and it became clear that transmittance values are very much dependent upon altitude of sources and receivers.

A visual impression of image distortion due to refraction is shown in figures 6 and 7, where the image of a point source is shown, as transmitted through the atmosphere over Monterey Bay. Striking is the fact that in figure 6, the source is just above an inversion layer, but in figure 7 just in the middle. The result is a vertically elongated line source. The pictures were taken in daytime.

Figure 8 shows a normal, frequently occurring mirage in San Diego. The mirage occurs when a cool air layer strikes over water. Sometimes the mirages occur in the middle of the night, sometimes in the early morning. Mostly these conditions lead to increased transmission values, as the intensity of both mirage components are similar and both fall on the detector. Figures 9-12 show results of transmission measurements in the four campaigns.

'Normal' transmission values for the 22 km range in Monterey for midwave (3.7-5.7  $\mu\text{m}$ ) and longwave (15°C, 70%) are about 7% resp 4%. Evident are the large increases by more than a factor 5 due to refraction effects, as visually illustrated in figure 7. The magnitude of this factor is difficult to predict when the temperature profile (at various locations) along the transmission path is not accurately known. It is clear that the knowledge of just one temperature at one altitude is insufficient.

Many authors have presented models to predict this refraction effect. Forand [11] and Dion [12] have integrated the effect in a complete atmospheric propagation model for marine boundary layers (IRBLEM). Church [13] presents the refraction effect as part of the IRST model IR Tool, developed by Areté associates. Besides these efforts, many authors have presented work, including attempts to retrieve the layering structure from sunset mirages [14, 15, 16, 17]. Unfortunately sunset and sunrise occur only once a day, so other methods are required to measure the temperature profile. Our own observation during EOPACE is that often strong gradients occur over a very short distance, so that the mirage seems to be a real reflection to a 'hard' surface.

An essential point is, that the transmissometer-receiver has such a large field of view (5 mrad) that all refraction effects are integrated. This means that the measured transmission value is of no direct significance for IRST's with an instantaneous field of view of circa 0.2 mrad. We can therefore not simply use for  $\tau(R_d)$  in formula (1) the measured value of  $\tau$ .

In this case, transmission as measured with a calibrated imager such as done in the LAPTEX experiments at Crete [18] is preferable and this value can directly be inserted in formula (1). The disadvantage is the increased uncertainty due to scintillation at long range.

During the campaign in Monterey some conditions occurred with fog and rain, most of the time only present along part of the path. The mirage conditions occurred frequently, nearly every day.

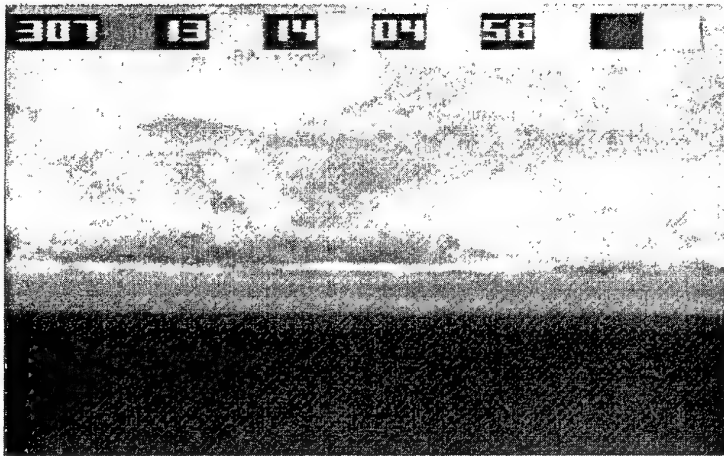


Fig. 6: Near IR picture of point source over Monterey Bay just above 'inversion' layer; 22 km; 7 March '96.

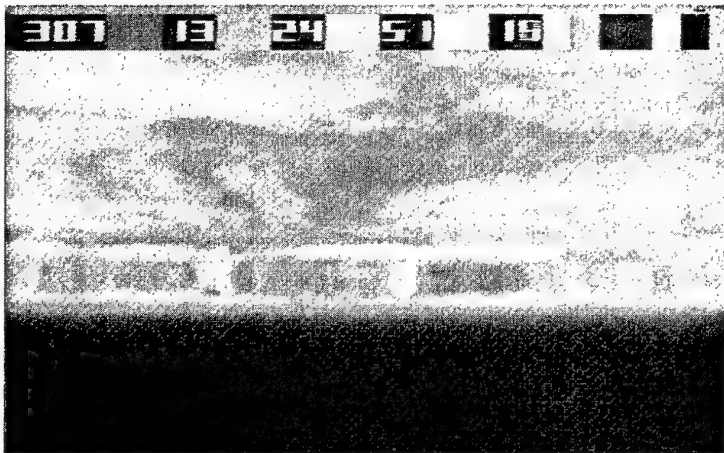


Fig. 7: Same picture as figure 6, 10 minutes later; point source in layer; strong refraction effect.

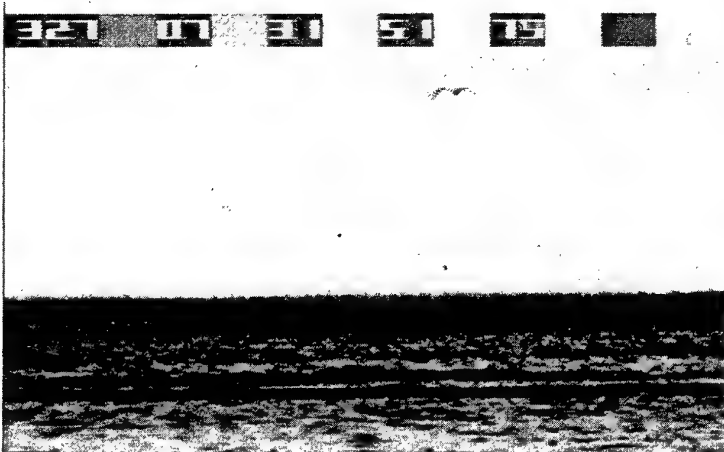


Fig. 8: Mirage condition 27 March '96 over San Diego Bay.

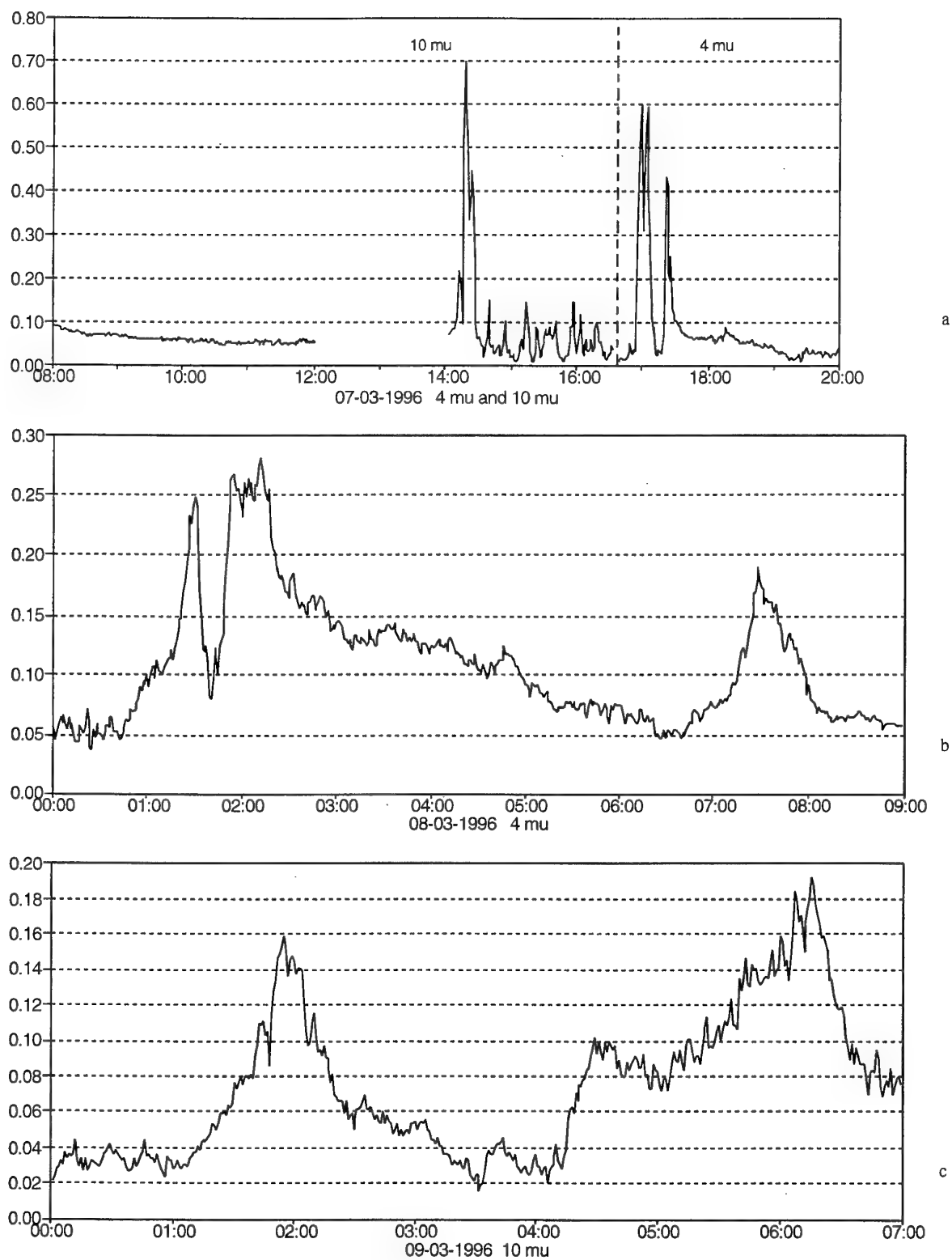


Fig. 9: Results of transmission measurements in Monterey, March '96.

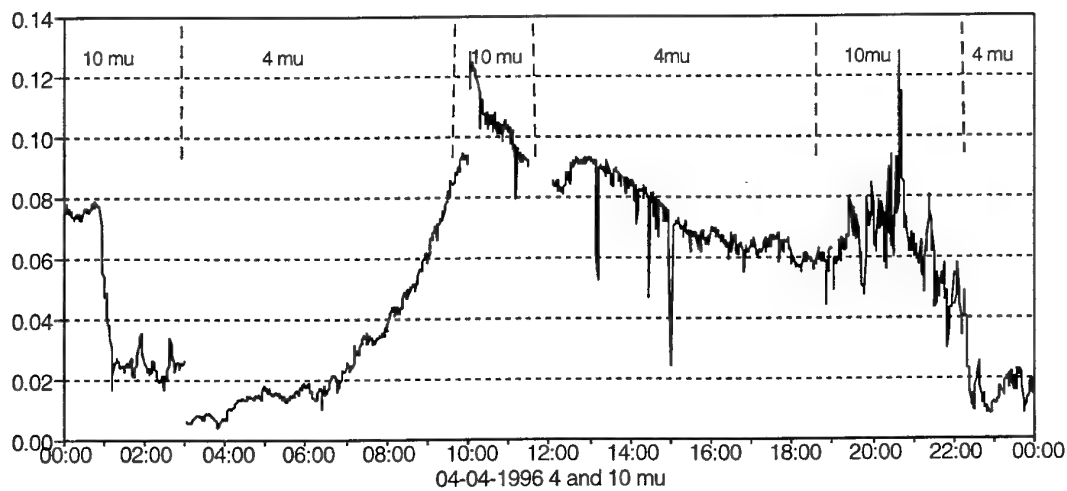
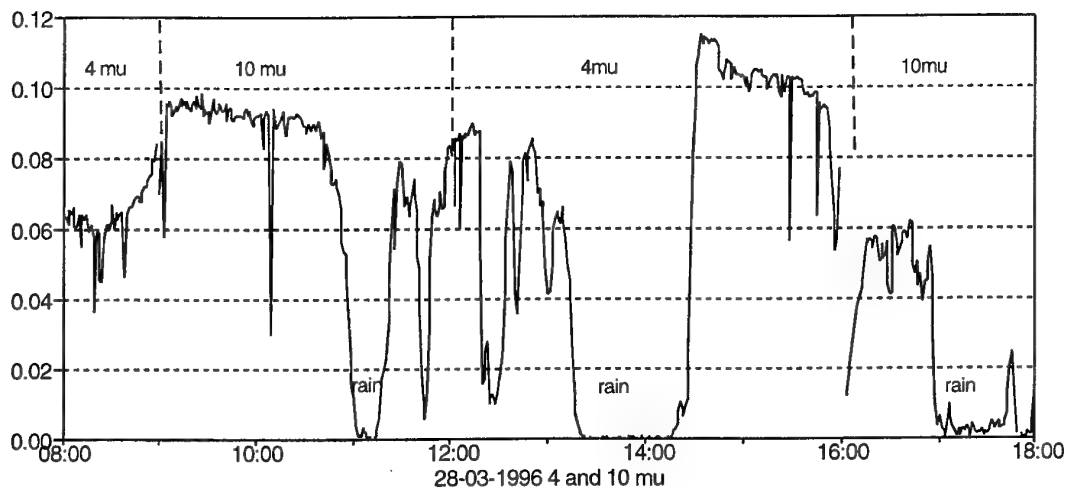
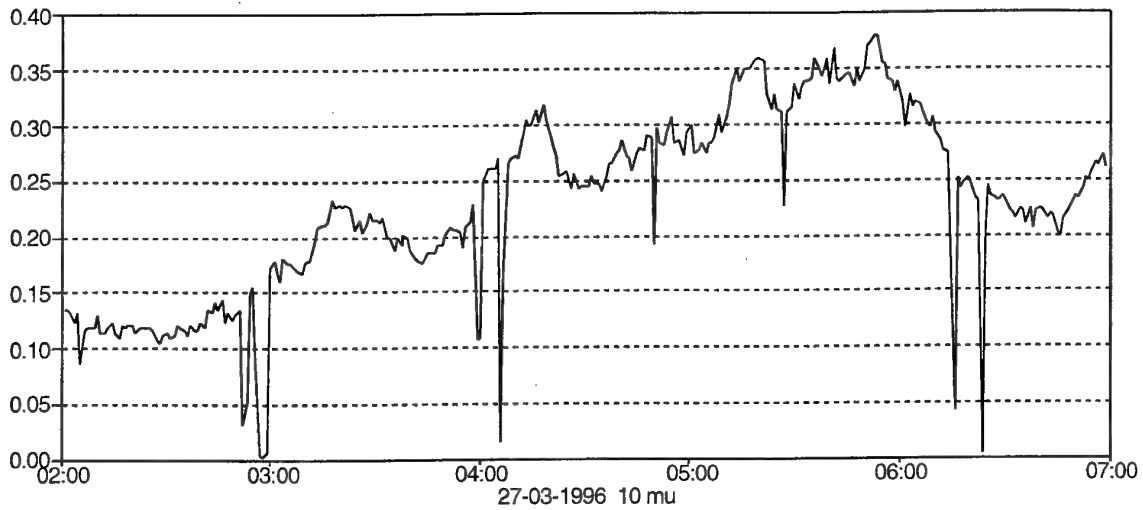


Fig. 10: Results of transmission measurements in San Diego, March/April '96.

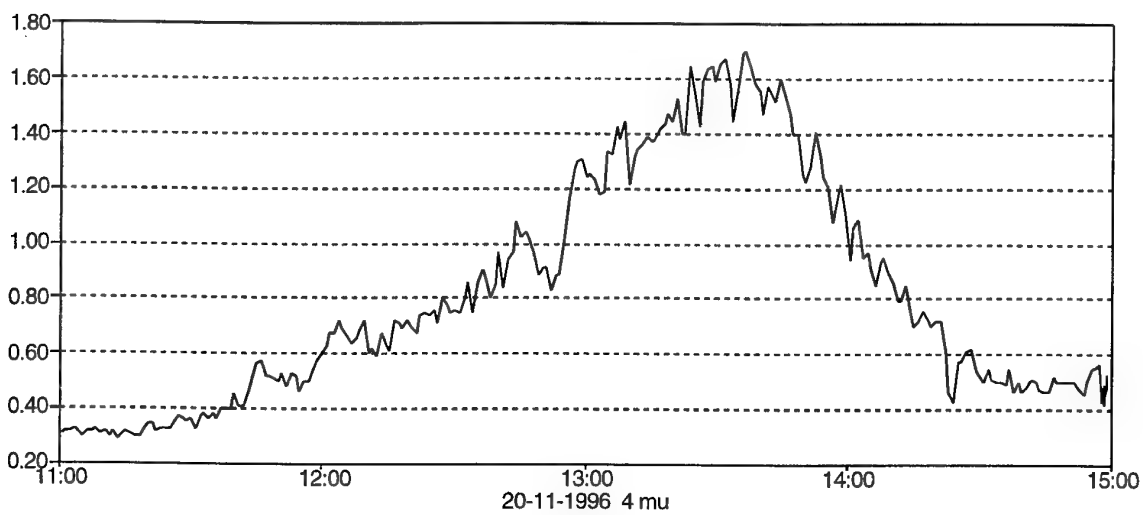
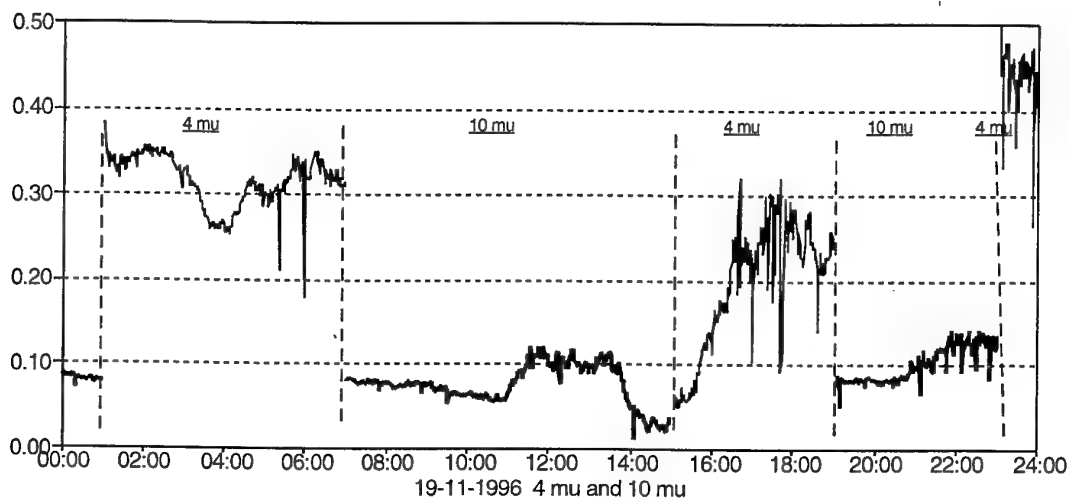
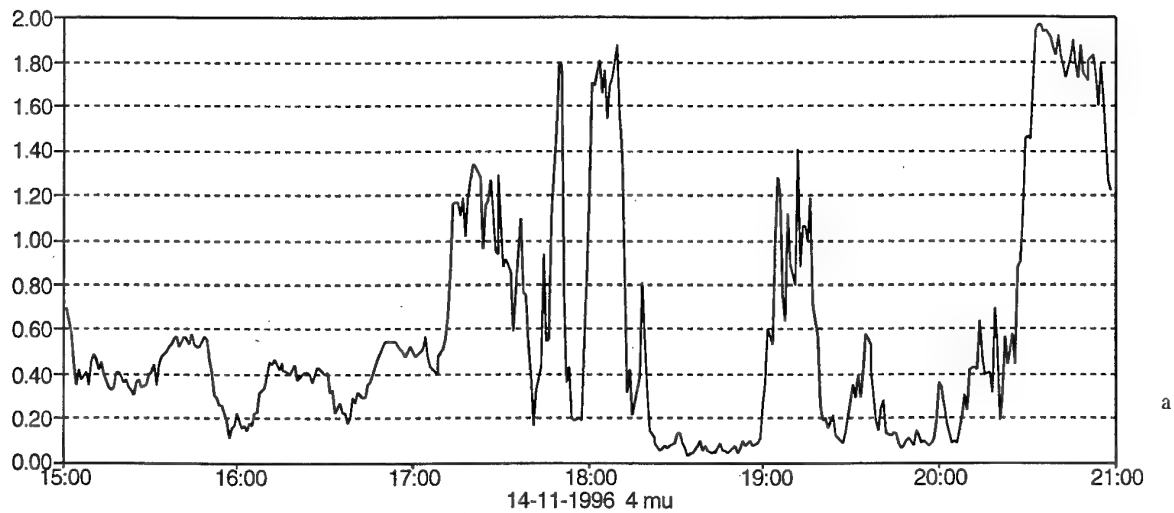
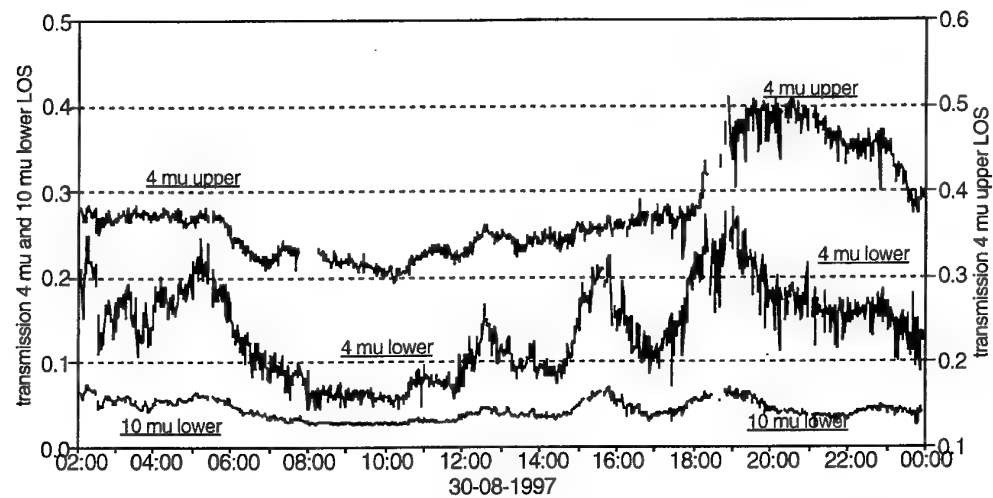
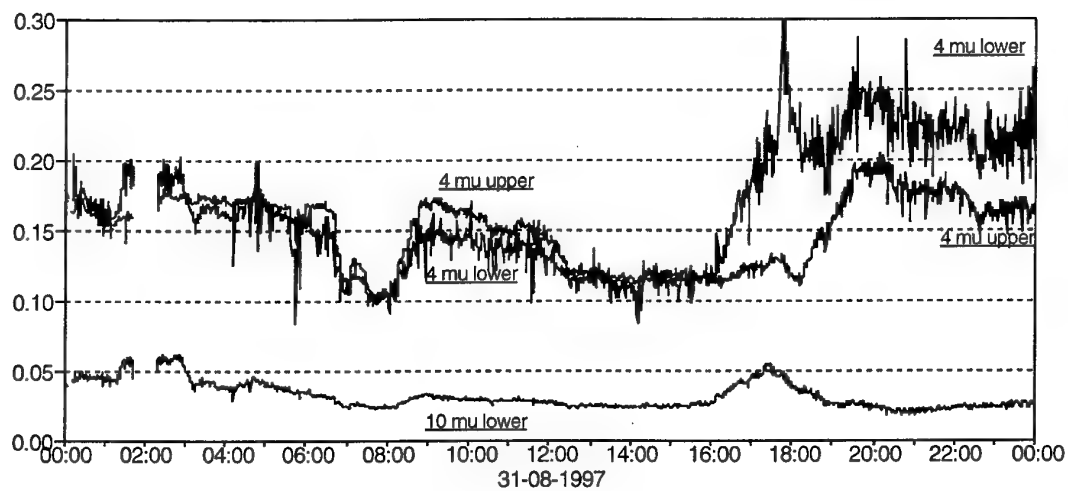


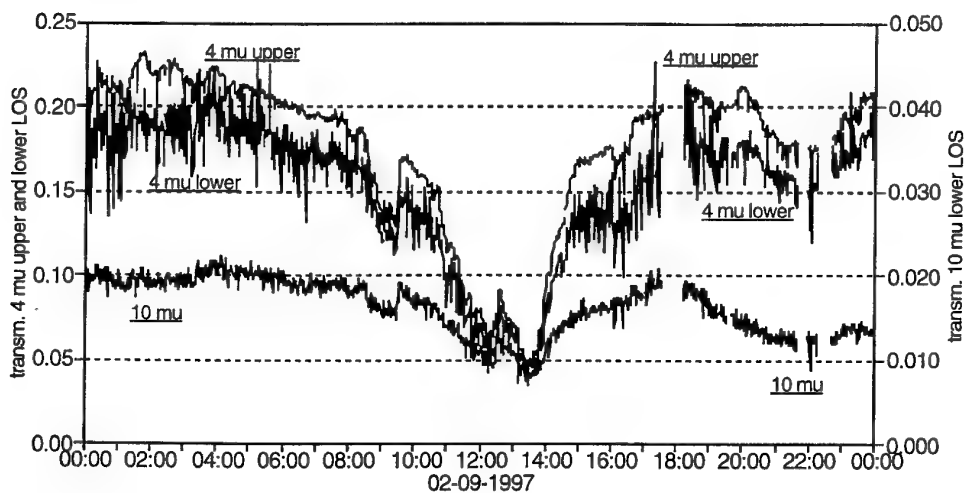
Fig. 11: Results of transmission measurements in San Diego, November '96.



a

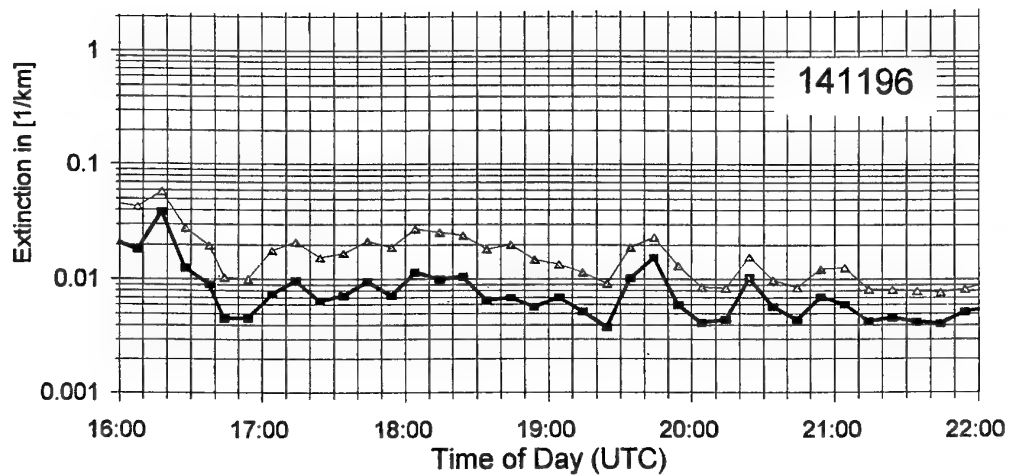


b

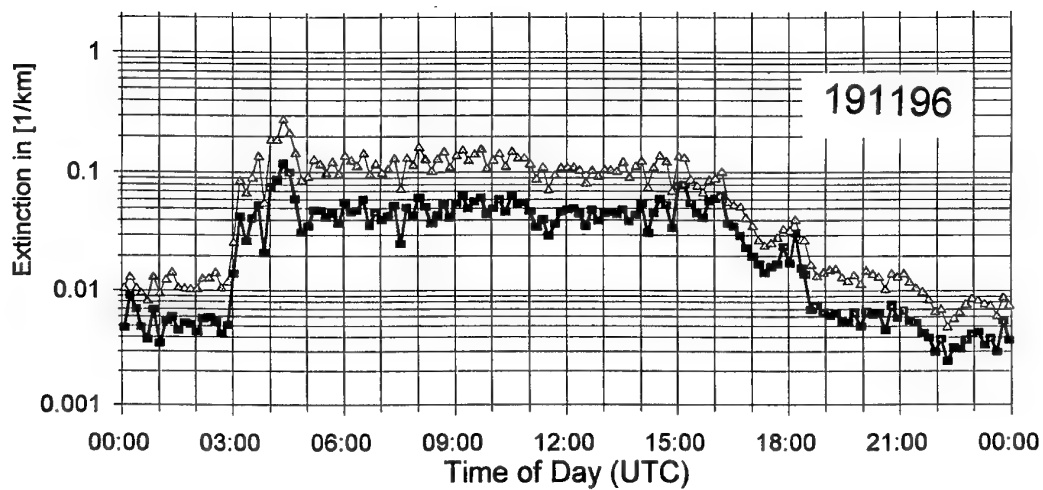


c

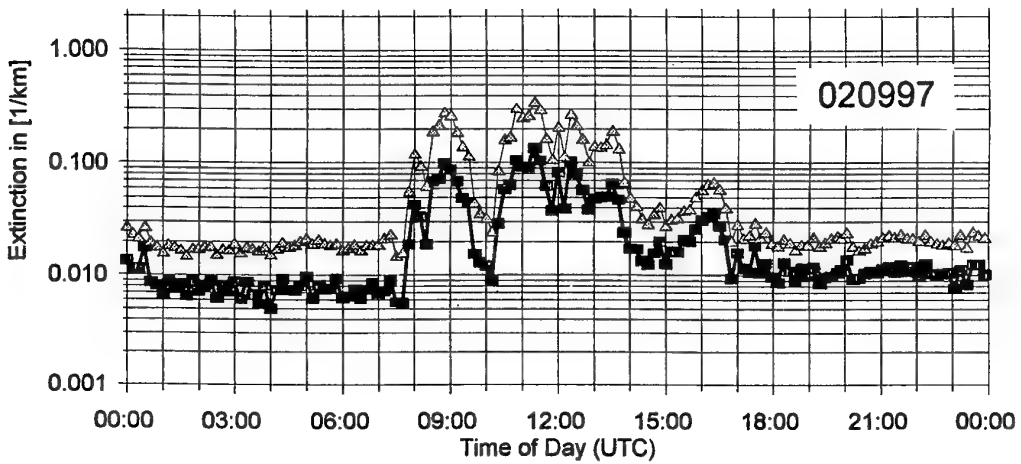
Fig. 12: Results of transmission measurements in San Diego, August/September '97.



a



b



c

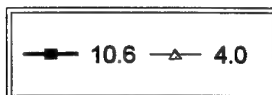


Fig. 13: Results of aerosol measurements in November '96 and August/September '97.



Results of the second campaign in San Diego, in March/April '96, are shown in figure 10. Again the subrefractive conditions occurred, resulting in excessive transmission values. While 'normal' transmission values for the local meteorological conditions are of the order of 10-15% for longwave, we observe a sudden increase to nearly 40% on the 27<sup>th</sup> of March near 6 a.m.

This phenomenon is illustrated by the image of the mirage in figure 8. The lower point source is the mirage, in this case just before being hidden behind the horizon. The angular separation between the real and mirage source is 0.87 mrad, which is typical for the 15 km range over the San Diego Bay. A similar separation was reproduced in many other occasions. Striking is the sharpness of the mirage point source, which can only be explained if the refraction effect is taking place in a thin layer of cold air, behaving as a reflector. The midwave transmission values are similar to those in the longwave band ( $\approx 10\%$ ). We have to realize here, that the 3.7-5.7  $\mu\text{m}$  band contains a lot of water vapour absorption lines, causing saturation in the 4.8-5.7  $\mu\text{m}$  wavelength region. In addition the  $\text{CO}_2$  band at 4.25  $\mu\text{m}$  also causes saturation. Taking into account only the spectral band 3.59-4.16  $\mu\text{m}$  (see figure 1), the transmission value would be close to 30%, for a visibility of 25 km.

Figure 10 shows also some periods with zero transmission due to rain somewhere in the path (figure 10.b). Figure 10.c shows a gradual increase in midwave transmission between 3 and 10 a.m. accompanied by a gradual change of visibility. The particle size distributions as measured at the Imperial Beach Pier, could not explain this behaviour quantitatively; apparently the aerosol was not homogeneously distributed along the path.

Figure 11 shows November '96 transmission data with the new midwave detector and filter. The time is given in GMT in these plots, which is identical to local time + 8 hours in winter. On average, the midwave transmission value is 35% and for longwave again around 10%. These values correspond well with the predictions from figures 1 and 3. Interesting is the result of the aerosol measurements; as shown in figure 13 the midwave/longwave extinction coefficients are about 0.02/0.01  $\text{km}^{-1}$  respectively, which for a range of 15 km corresponds to a transmission due only to aerosols of 0.75 resp 0.86.

Interesting again is the refraction effect in the morning on the 14<sup>th</sup> and during the night of the 20<sup>th</sup>. The midwave transmission went up to values of 200%! Similar to figure 9.a, the transmission values were fluctuating strongly with time. One factor could be the tide, which changes the altitude of the beam with respect to the air layers.

Interesting also is the aerosol effect on the 19<sup>th</sup>. The aerosol measurements (figure 13.b) show a midwave extinction coefficient of 0.1  $\text{km}^{-1}$  corresponding to an aerosol transmission of 0.22 over the 15 km path. The transmission data show transmission values (including molecular extinction) of 0.30 and more until 7 a.m. Apparently the particle size measurements were not representative for those along the whole transmission path, the location being higher at Imperial Beach than at other places. Another effect might be due to particles, produced in the surf zone or particles,

produced locally ashore. The wind direction was indeed between East to the North.

Around 13.30 the longwave transmission rapidly decreased to a few percent, which similar to the midwave transmission decreased to about 7%. After that period we observe a rapid increase of transmission to 25% midwave. Since no changes were observed in the extinction coefficients (figure 9.b) while during a short period around 14.00 the wind direction changed to North for about an hour, the observed variations must be due to local variation of aerosol and/or meteorological properties along the transmission path.

Refraction effects were observed on the 20<sup>th</sup> around 13.30 GMT (= 05.30 local time). The increase was about a factor 5.

Figure 12 shows results of the 4<sup>th</sup> campaign in August/September '97 in San Diego. Each of the figures shows 3 plots: one of the upper level midwave channel and two of the lower level midwave and longwave channels.

Figure 12.a shows clearly that the lower midwave channel transmission between 01.00 and 06.00 GMT (evening of 29<sup>th</sup> of August) has a transmission of about 30%, while the higher level has a transmission of 20%. The difference is probably due to sub-refraction for the lower level transmissometer. Later on that day (between 20.00 and 22.00) the midwave transmission at the higher elevation rises towards the midwave at the lower level, while the longwave level drops. This is probably due to a thin haze layer over the water surface. The average values of the transmission for this period were below those of previous campaigns. We measured about 20% for midwave and 4% for longwave. The main reason for this was the higher absolute humidity. With an air temperature of 20°C and a relative humidity of 80%, the absolute humidity is 14  $\text{g/m}^3$ .

From figure 1, midwave resp longwave transmissions taking into account only molecular absorption are 30% resp 4.6%. Looking more closely to the aerosol extinction, midwave resp longwave extinction coefficients are on the order of 0.03 resp 0.02, corresponding to aerosol transmissions of 0.64 resp 0.74. With these values, the total predicted transmission becomes 19% resp 3.4%, which corresponds well with the measured data.

Figure 12.b shows similar effects as figure 12.a. The higher elevation transmission is significantly and most of the time larger than the lower level transmission except for a short time around 17.00, when due to refraction the lower level transmissions increase by about a factor 2.

Figure 12.c shows the transmission plot for 2 September. The only effect of significance is a strong reduction in transmission around 12.00 GMT (4 a.m.) due to aerosols. In figure 13.c.a strong increase in extinction occurs from 08.00 GMT which explains the observed decrease in transmission. The wind direction was observed to change from East to North around 11.00 GMT. Apparently these Northerly winds carried the aerosols causing the drop in transmission. The extinction coefficient of 0.2 however predicts an aerosol transmission of 5% which is a much stronger effect than measured from the transmissometry. It is apparent that the midwave transmissions (both upper and lower level) are affected about 2× stronger than the longwave transmission.

## 6. CONCLUSIONS

The four transmission measurement campaigns, carried out in the framework of EOPACE along the US West Coast, have provided an interesting data set for investigation of the variability of atmospheric transmission behaviour due to instabilities and inhomogeneities in temperatures and their profiles, humidity and aerosol size distribution. For normal conditions Lowtran 7 predicts the transmission reasonably well. Refraction effects cause a strong deviation; one reason is that during transmission measurements the detector receives the sum of all mirage intensities in its field of view, being considerably larger than in operational IR sensors.

It is noted that the measured transmission values should not be used directly inIRST range performance formula due to the difference in Instantaneous Field of View of the transmissometer receiver and theIRST sensor.

It has been found that aerosol and meteorological measurements carried out only at the end of the measurement path, does not provide sufficient data for use as input for the propagation prediction models used to explain the observed transmission phenomena. Even the buoy in the middle and the sensor package on the boat do give a too local, insufficient set of input data. To fully predict the refraction effect, a very detailed profile in temperature is required.

During the four campaigns, carried out in various seasons the transmission behaviour was dominated by various phenomena and anomalies: strong refraction as well as haze conditions and high humidity.

## 7. ACKNOWLEDGEMENTS

All involved personnel from NRaD, now SPAWAR is greatly acknowledged for their support, especially Doug Jensen as great stimulator. Personnel from the BOQ at the Naval Subbase and the lifeguard station at Imperial Beach are greatly acknowledged for their help. At TNO-FEL Marco Roos, Hans Winkel and Ruud Kooijman are acknowledged for their technical support and data analysis.

The TNO participation in EOPACE is sponsored by the Netherlands MOD (assignment A95KM729) and the US Office of Naval Research ONR (grant N00014-96-1-0581).

## 8. REFERENCES

1. The IR and EO systems Handbook: Vol 2, SPIE Optical Engineering Press, 1993.
2. Session on MAPTIP at SPIE conference: Image propagation through the atmosphere, Denver, August 1996, SPIE Vol. 2828.
3. G. de Leeuw, 'Long-range IR propagation measurements over the North Sea', proceedings 55<sup>th</sup> AGARD-EPP specialists meeting, September 1994, Bremerhafen, Germany.
4. H.T. Bull, Near Surface Infrared Transmission Measurements, 1995, SPIE Vol. 2552, page 181-191.
5. Session on EOPACE at SPIE conference: Image propagation through the atmosphere, San Diego, July 1997, SPIE Vol. 3125.
6. A.N. de Jong, EOPACE Transmission Experiments Spring 1996, Preliminary Results, TNO report FEL-96-A090, March 1997.
7. A.N. de Jong, Transmission experiments during EOPACE, November 1996 and August/September 1997, Preliminary Results, TNO report FEL-97-A269, November 1997.
8. A.N. de Jong, Long Range Transmission Measurements over Sea Water, report PHL 1978-08.
9. C. Zeisse, Low Elevation Transmission Measurements at EOPACE, Part I: Molecular and Aerosol effects, SPIE Vol. 3125-11.
10. A.N. de Jong, Low Elevation Transmission Measurements at EOPACE, Part III Scintillation Effects, SPIE Vol. 3125-13.
11. J.L. Forand, The L(W)WKD Marine Boundary Layer Model, Report DREV R-9618, March 1997, Unclassified.
12. D. Dion, On the analysis of atmospheric effects on EO sensors in the Marine Surface Layer, 2<sup>nd</sup> NATO-IRIS conference, London, June 1996.
13. S. Church, Atmospheric mirage and distortion modelling for IR target injection simulations, SPIE Vol. 2742, Orlando, April 1996.
14. W.H. Lehn, Analysis of an infrared mirage sequence, Applied Optics, Vol. 36, N° 21, July 1997.
15. A.T. Young, Sunset science, I The mock mirage, Applied Optics, Vol. 36, N° 12, April 1997.
16. W.D. Bruton, Unique temperature profiles for the atmosphere below an observer from sunset image, Applied Optics, Vol. 36, N° 27, September 1997.
17. M.E. Thomas, Astronomical refraction, Johns Hopkins APL Technical Digest, Volume 17, N° 3 (1996).
18. A.N. de Jong, Point target extinction and scintillation as function of range at LAPTEX, Crete, SPIE Vol. 3125-17, July 1997, San Diego.

# Near-Surface Scintillation ( $C_n^2$ ) Estimates from a Buoy Using Bulk Methods during EOPACE

Paul Frederickson and Kenneth Davidson

*Department of Meteorology, Naval Postgraduate School  
589 Dyer Rd., Room 254, Monterey, CA 93943-5114, U. S. A.  
e-mail: frederic@met.nps.navy.mil*

Carl Zeisse and Ike Bendall

*Space and Naval Warfare Systems Center D883  
49170 Propagation Path, San Diego, CA 92152-7385, U. S. A.*

## 1. Summary

During the Electro-Optical Propagation Assessment in a Coastal Environment (EOPACE) experiment of August-September 1997, infrared transmission measurements were obtained along a 7 km path over San Diego Bay. Simultaneous meteorological measurements were obtained from a buoy located at the midpoint of the transmission path. In this study transmission-derived values of the refractive index structure parameter,  $C_n^2$ , are compared with bulk model-derived estimates obtained from the mean buoy data. The bulk  $C_n^2$  estimates agreed very well with the transmission measurements in unstable conditions. The bulk estimates were very poor in near-neutral conditions because of the great difficulty in accurately measuring the small air-sea temperature differences ( $\Delta T$ ) encountered, upon which  $C_n^2$  is highly dependent. The bulk  $C_n^2$  estimates agreed less well with the transmission measurements in stable conditions than unstable conditions. A theoretical sensitivity and error analysis shows that the bulk  $C_n^2$  estimates become extremely sensitive upon the measured value of  $\Delta T$  over a narrow Bowen ratio range and

under such conditions it is virtually impossible to accurately estimate  $C_n^2$  using bulk methods. The sensitivity analysis also indicates whether fluctuations in temperature, humidity or temperature-humidity correlation dominate the determination of  $C_n^2$  under various Bowen ratio ranges.

## 2. Introduction

Electro-optical (EO) imagery through the atmosphere near the ocean surface experiences rapid intensity fluctuations due to atmospheric turbulence, known as scintillation. Scintillation is closely related to the refractive index structure parameter,  $C_n^2$ . In an operational environment it would be useful to be able to evaluate and predict the effects of scintillation on EO imagery by estimating  $C_n^2$  from routinely measured air-sea parameters. Bulk models have been developed to estimate near-surface atmospheric turbulence properties from mean meteorological measurements. The relations between these atmospheric turbulence properties and  $C_n^2$  have also been established, thereby allowing  $C_n^2$  to be estimated from mean air-sea measurements. The purpose of

this study is to determine how accurately  $C_n^2$  can be estimated from routine meteorological measurements using bulk models under various conditions. This study is based on data obtained during the EOPACE experiment of August-September 1997. Bulk  $C_n^2$  estimates computed from mean measurements obtained on a buoy are compared with concurrent optical transmission-derived  $C_n^2$  measurements along an over-water propagation path to determine how closely the two methods agree under various air-sea conditions. In addition, a theoretical error analysis of the bulk  $C_n^2$  model is conducted.

### 3. Theory

The structure parameter for a quantity  $y$  is given by

$$C_y^2 = \frac{[\overline{y(x) - y(x+r)}]^2}{r^{2/3}}, \quad (1)$$

where  $y(x)$  and  $y(x+r)$  are the values of parameter  $y$  at two points separated by a distance  $r$  along the mean wind direction and the over-bar indicates an ensemble average. The refractive-index structure parameter,  $C_n^2$ , can be expressed according to the structure parameters for temperature,  $C_T^2$ , humidity,  $C_q^2$  and the temperature-humidity fluctuation correlation,  $C_{Tq}$ , as follows (Andreas [1]):

$$C_n^2 = A^2 C_T^2 + 2ABC_{Tq} + B^2 C_q^2, \quad (2)$$

where the coefficients  $A$  and  $B$  are known functions of the wavelength ( $\lambda$ ) and the mean atmospheric pressure ( $P$ ), temperature ( $T$ ), and specific humidity ( $q$ ). The first term on the right hand side of Eq. (2) represents temperature fluctuations and is always positive, the second term represents the correlation of temperature and humidity

fluctuations and can be positive or negative, while the third term represents humidity fluctuations and is always positive. For optical and infrared wavelengths the first term in Eq. (2) generally dominates, however, when the air-sea temperature difference is small the last two humidity-dependent terms can dominate.

### 4. The Bulk Surface-Layer Model

Monin-Obukhov similarity (MOS) theory is used to relate the structure parameters  $C_T^2$ ,  $C_q^2$  and  $C_{Tq}$  in Eq. (2) to the mean properties of the atmospheric surface layer. According to MOS theory, the fluxes of momentum, sensible heat and latent heat are assumed to be constant with height in the surface layer. In practice, the surface layer is regarded as the region near the surface where the fluxes vary by less than 10%, generally extending to a height of roughly 20 to 200 m. All dynamical properties in the surface layer are assumed to depend only upon the height above the surface,  $z$ , and upon certain scaling parameters, which are defined in terms of the assumed-constant fluxes, as follows:

$$u_* = (-\overline{w'u'})^{1/2}, \quad (3a)$$

$$T_* = -\frac{\overline{w'T'}}{u_*}, \quad (3b)$$

$$q_* = -\frac{\overline{w'q'}}{u_*}, \quad (3c)$$

where  $u_*$ ,  $T_*$  and  $q_*$  are the surface layer scaling parameters for wind speed, temperature and humidity, respectively, defined in terms of the kinematic fluxes of momentum ( $-\overline{w'u'}$ ), sensible heat ( $-\overline{w'T'}$ ), and latent heat ( $-\overline{w'q'}$ ), respectively. When a dynamical property is properly scaled by

these parameters, it can be expressed as a universal function of  $\xi$ , defined as:

$$\xi = \frac{z}{L} = \frac{zkg(T_* + 0.61Tq_*)}{Tu_*^2} \quad (4)$$

Here  $L$  is the Monin-Obukhov length scale,  $k$  is the von Karman constant ( $= 0.4$ ) and  $g$  is the acceleration due to gravity.  $\xi$  is often referred to simply as the 'stability', and is negative in unstable conditions, zero in neutral conditions, and positive in stable conditions.

According to MOS theory, the surface layer scaling parameters  $T_*$ ,  $q_*$  and  $u_*$  can be expressed in terms of the mean surface layer properties by the expression:

$$x_* = (\Delta x)k[\ln(z/z_{ox}) - \psi_x(\xi)]^{-1}, \quad (5)$$

where  $x$  represents wind speed ( $u$ ), temperature ( $T$ ) or specific humidity ( $q$ ) and the symbol  $\Delta$  denotes the mean air-sea difference. The  $\psi$  functions are the integrated dimensionless profile functions, defined by Paulson [2]. We have made the common assumption that  $\psi_T = \psi_q$ . The parameters  $z_{ou}$ ,  $z_{oT}$  and  $z_{oq}$  are known as the 'roughness lengths,' and were determined by the bulk surfaced-layer model formulated by Fairall et al. [3]. The reader is referred to this paper for further details on the bulk model employed in this study. We have assumed that the scalar roughness lengths are equal (i.e.  $z_{oT} = z_{oq}$ ).

When the structure parameters for temperature ( $C_T^2$ ), the temperature-humidity correlation ( $C_{Tq}$ ) and humidity ( $C_q^2$ ) are properly scaled according to MOS theory, they can be expressed as:

$$C_T^2 = T_*^2 z^{-2/3} g_T(\xi), \quad (6a)$$

$$C_{Tq} = T_* q_* z^{-2/3} g_{Tq}(\xi), \quad (6b)$$

$$C_q^2 = q_*^2 z^{-2/3} g_q(\xi), \quad (6c)$$

where  $g_T$ ,  $g_{Tq}$ , and  $g_q$  are dimensionless functions of  $\xi$  which must be determined empirically. Observations have not conclusively demonstrated that these functions are different from each other and MOS theory implies they should be similar [4]. Therefore, we have assumed that  $g_T = g_{Tq} = g_q \equiv g$ . Measurements of  $g$  for highly stable conditions ( $\xi > \sim 1$ ) are rare and exhibit much scatter. In this study we have used the function for  $g_T$  given by Andreas [1]:

$$g_T(\xi) = \begin{cases} 4.9(1 - 6.1\xi)^{-2/3}, & \xi \leq 0 \\ 4.9(1 + 2.2\xi^{2/3}), & \xi \geq 0 \end{cases} \quad (7)$$

Combining Eqs. (2), (5) and (6) results in:

$$C_n^2 = \frac{g(\xi)k^2 [A^2 \Delta T^2 + 2AB\Delta T\Delta q + B^2 \Delta q^2]}{z^{2/3} [\ln(z/z_{oT}) - \psi_T(\xi)]^2} \quad (8)$$

Combining Eqs. (4) and (5) results in:

$$\xi = \frac{zg(\Delta T + 0.61T\Delta q)[\ln(z/z_{ou}) - \psi_u(\xi)]^2}{T\Delta u^2 [\ln(z/z_{oT}) - \psi_T(\xi)]} \quad (9)$$

$C_n^2$  can now be estimated from mean air-sea measurements by solving Eqs. (7), (8) and (9) by an iterative process.

## 5. Experimental Setup

The EOPACE experiment of August-September 1997 took place in San Diego Bay. Infrared (IR) transmission measurements were obtained by SPAWAR System Center, San Diego (SSC-SD). The transmission path was 7 km in length over

San Diego Bay, with the IR source (transmitter) located at the Naval Amphibious Base and the IR receiver located near the Bachelor Officers Quarters at the Naval Submarine Base (see Figure 1). Meteorological data were obtained concurrently with the transmission data from an instrumented buoy deployed by the Naval Postgraduate School (NPS) at the mid-point of the transmission path.

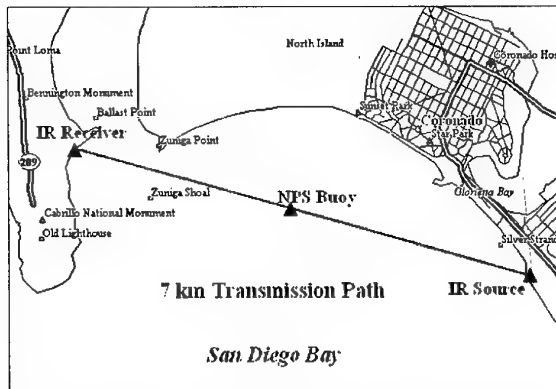


**Figure 1.** EOPACE experimental setup, August-September 1997.

## 6. Buoy Meteorological Measurements

The NPS buoy was deployed in San Diego Bay from 22 August to 8 September 1997. The following measurements were obtained on the NPS buoy: wind speed at a 4.9 m height above the surface, air temperature and humidity at 3.1 m, atmospheric pressure at 0.4 m, and sea temperature measured by a thermistor imbedded in the buoy hull 0.8 m below the surface. Only data obtained at night is included in this study, because it was discovered that solar radiation could penetrate the radiation shield and heat the temperature sensor, especially at low solar angles shortly after sunrise and before sunset. A fully enclosed, forced aspiration radiation shield could not be used on the buoy due to power constraints. The buoy measurements were averaged over 10 minute intervals and

bulk estimates of  $C_n^2$  were then computed from these mean values. The wavelength-dependent coefficients  $A$  and  $B$  in Eq. (8) were computed for a wavelength of  $3.8 \mu\text{m}$  using the formulas presented by Andreas [1]. Since  $C_n^2$  is height dependent (Eq. 8), the bulk  $C_n^2$  estimates were corrected for tidal sea level variations using tide data computed by the model 'Tides and Currents for Windows 95' by Nautical Software, Beaverton, OR.

## 7. Infrared Transmission Measurements

The SSC-SD transmission measurements were obtained from 23 August to 9 September 1997, using instruments and procedures similar to those described by Zeisse et al. [5]. The transmitter at the Amphibious Base was 6.2 m above mean sea level (MSL) and the receiver at the Submarine Base was 4.9 m above MSL. High-frequency mid-wave ( $3.5$  to  $4.1 \mu\text{m}$ ) IR transmission measurements were obtained hourly over a 41 second interval with a sampling frequency of 200 Hz. The lock-in time constant was 1 ms with a roll-off of 6 dB per octave (wait time 5 ms, equivalent noise bandwidth 250 Hz). The measured detector noise was less than 1 A/D level (0.1% of the free space signal) as compared to turbulent fluctuations between samples of about 50% of free space.  $C_n^2$  values were obtained by applying the normalized variance of the transmission data to the model formulated by Churnside et al. [6].

## 8. Bulk versus Transmission $C_n^2$ Comparison Results

A scatter plot of the NPS bulk and SSC-SD transmission  $C_n^2$  values is presented in Figure 2. A summary of the comparison statistics is presented in Table 1. The data have been

separated into air-sea temperature difference ( $\Delta T$ ) intervals, as measured on the NPS buoy. The linear correlation coefficient between the two populations is presented in the second column. The '% difference' is the average value of  $(C_n^2(\text{trans}) - C_n^2(\text{bulk}))/C_n^2(\text{trans})$ . The 'rms % difference' is the value of  $[(C_n^2(\text{trans}) - C_n^2(\text{bulk}))^2]^{1/2}$ , where the brackets denote an average, divided by the mean value of  $C_n^2(\text{trans})$ .

**Table 1.** Bulk versus transmission  $C_n^2$  comparison statistics.

$\Delta T$ Range	Corr Coeff	% Diff	rms % Diff
$\Delta T < -0.5^\circ\text{C}$	0.93	-16	35
$-0.5^\circ\text{C} < \Delta T < 0.5^\circ\text{C}$	-0.05	33	358
$0.5^\circ\text{C} < \Delta T < 1.5^\circ\text{C}$	-0.02	-45	86
$1.5^\circ\text{C} < \Delta T$	0.28	-293	228

The agreement between the bulk and transmission  $C_n^2$  values is very good for unstable conditions ( $\Delta T < -0.5^\circ\text{C}$ ). For these conditions the percentage difference between the two methods is -16% and the correlation coefficient is 0.93. The agreement between the two methods is very poor for near-neutral conditions ( $-0.5^\circ\text{C} < \Delta T < 0.5^\circ\text{C}$ ), exhibiting a very large degree of scatter (rms % difference of 358%), with the bulk  $C_n^2$  estimates being much lower than the transmission measurements in most cases. In weakly stable conditions ( $0.5^\circ\text{C} < \Delta T < 1.5^\circ\text{C}$ ), the comparison between the two methods exhibits much more scatter than for unstable cases (rms % difference of 86% as compared to a rms % difference of 35% for unstable conditions). For strongly stable

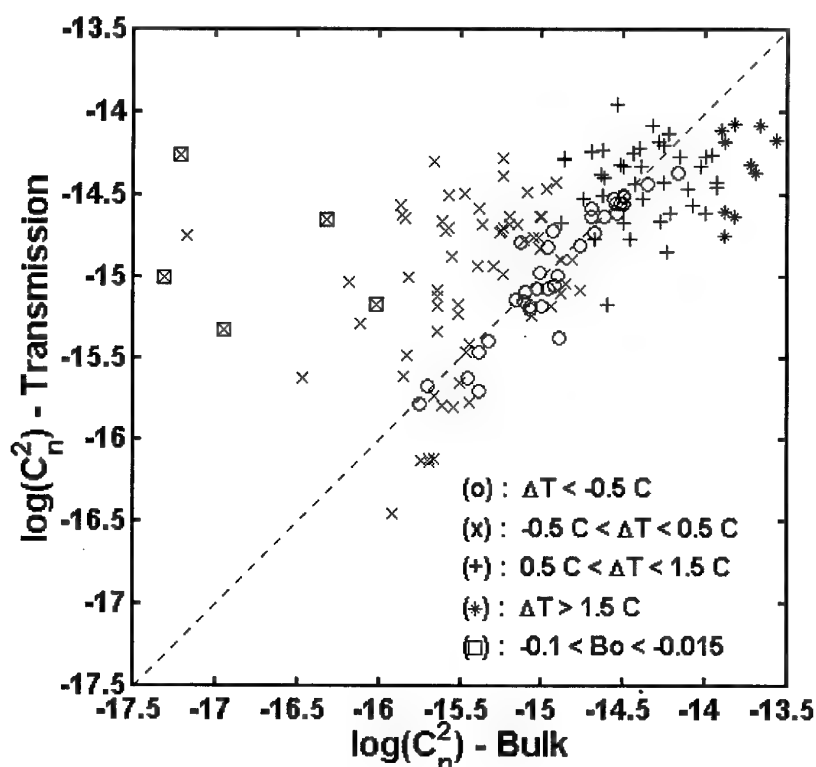


**Figure 2.** Scatter plot of transmission  $\log(C_n^2)$  measurements versus bulk  $\log(C_n^2)$  estimates separated into air-sea temperature difference ( $\Delta T$ ) intervals:  $\Delta T < -0.5^\circ\text{C}$  indicated by o's;  $-0.5^\circ\text{C} < \Delta T < 0.5^\circ\text{C}$  indicated by x's;  $0.5^\circ\text{C} < \Delta T < 1.5^\circ\text{C}$  indicated by +s;  $\Delta T > 1.5^\circ\text{C}$  indicated by \*s. Data points within the Bowen ratio ( $Bo$ ) interval  $-0.1 < Bo < -0.015$  indicated by squares.

conditions ( $\Delta T > 1.5^\circ\text{C}$ ) the transmission  $C_n^2$  measurements are systematically much lower than the bulk estimates, by 293% on average. It is possible that the optical transmission data were 'saturated' for these very stable conditions, thereby causing the transmission values to be much lower than the bulk estimates.

## 9. Bulk $C_n^2$ Model Sensitivity and Error Analysis

A theoretical sensitivity and error analysis was conducted for the bulk  $C_n^2$  model used in this study, using methods similar to those of Andreas [1]. The sensitivity coefficient for  $C_n^2$  upon a parameter  $x$ ,  $S_x$ , can be defined as:

$$S_x = \frac{x}{C_n^2} \left[ \frac{\partial C_n^2}{\partial x} + \frac{\partial C_n^2}{\partial \xi} \frac{\partial \xi}{\partial x} \right]. \quad (10)$$

A large value of  $S_x$  indicates that the bulk  $C_n^2$  estimates are highly sensitive to the measured value of  $x$ , while a small value of  $S_x$  indicates that the bulk  $C_n^2$  estimates are virtually independent of  $x$ . The relative error in the bulk  $C_n^2$  estimates is given by multiplying  $S_x$  by the assumed relative error in the measurement of  $x$ :

$$\frac{\delta C_n^2}{C_n^2} = S_x \frac{\delta x}{x}. \quad (11)$$

The  $C_n^2$  sensitivity coefficients for the air-sea temperature difference,  $S_{\Delta T}$ , and the air-sea humidity difference,  $S_{\Delta q}$ , are highly dependent upon the Bowen ratio. The Bowen ratio,  $Bo$ , is the ratio of the sensible heat flux over the latent heat flux, or  $Bo = c_p T^*/L_v q^*$ , where  $c_p$  is the specific heat of air at constant pressure and  $L_v$  is the latent heat of vaporization.  $S_{\Delta T}$  and  $S_{\Delta q}$  were computed for representative atmospheric conditions encountered during the experiment and for a

wavelength of  $3.8 \mu\text{m}$ , and are plotted versus  $Bo$  for different values of  $\xi$  in Figs. 3 and 4, respectively. Over a narrow Bowen ratio range (roughly  $-0.1 < Bo < -0.015$ ) the bulk  $C_n^2$  estimates become extremely sensitive upon the measured values of both  $\Delta T$  and  $\Delta q$ , making it virtually impossible to accurately estimate  $C_n^2$  by the bulk model in this  $Bo$  range. These small negative values of  $Bo$  generally only occur under near-neutral conditions (small  $T^*$  and, therefore,  $\Delta T$  values) and when the sensible and latent heat fluxes have opposite signs. In Figure 2 those data points with a Bowen ratio within the range  $-0.1 < Bo < -0.015$  are indicated by a square. It can be seen that all these data points occurred in near-neutral conditions (indicated by x's within squares) and that these bulk  $C_n^2$  estimates exhibited very large differences from the transmission  $C_n^2$  measurements, in agreement with the large predicted errors in the bulk  $C_n^2$  estimates within this  $Bo$  range.

From Figs. 3 and 4 it can be seen that, outside of the range  $-0.1 < Bo < -0.015$ , for a given value of  $Bo$  the absolute value of the sensitivity coefficients  $S_{\Delta T}$  and  $S_{\Delta q}$  are smallest for unstable conditions, larger for stable conditions and largest for neutral conditions. Therefore, for a given measurement accuracy the relative error in bulk  $C_n^2$  estimates will tend to be smallest for unstable conditions and largest for neutral conditions. This is in agreement with the bulk versus transmission  $C_n^2$  comparisons, with less scatter exhibited in unstable conditions (rms % difference of 35%) than in stable conditions (rms % difference of 86%) or near-neutral conditions. In near-neutral conditions the relative errors in  $C_n^2$  will tend to be very large on average because it is difficult to accurately measure the small  $|\Delta T|$  values encountered under such conditions, leading to large relative errors in  $\Delta T$ . This is reflected in the extremely large scatter in the



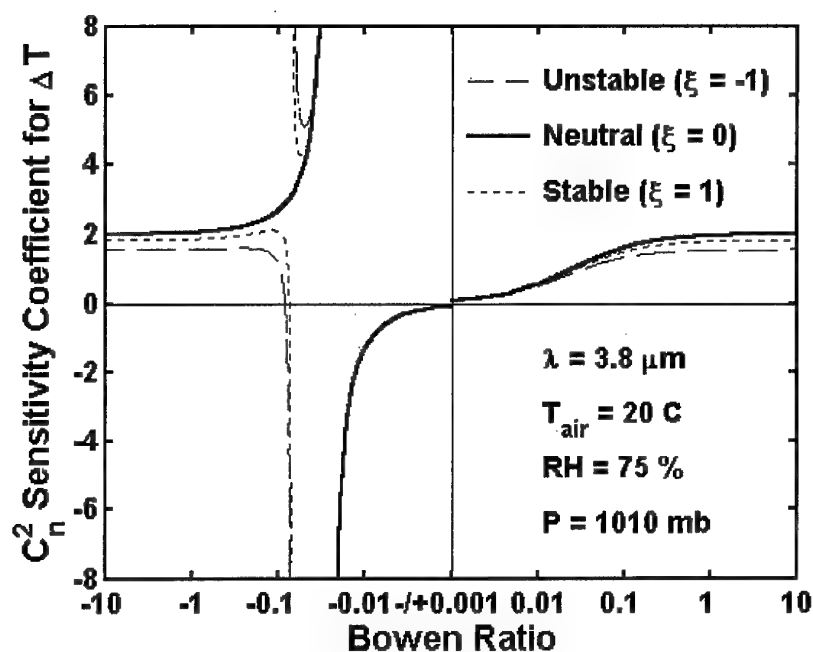


**Figure 3.**  $C_n^2$  sensitivity coefficient for the air-sea temperature difference,  $S_{\Delta T}$ , plotted versus the Bowen ratio. Unstable conditions ( $\xi = -1$ ) indicated by dashed line, neutral conditions ( $\xi = 0$ ) indicated by solid line and stable conditions ( $\xi = 1$ ) indicated by dotted line.

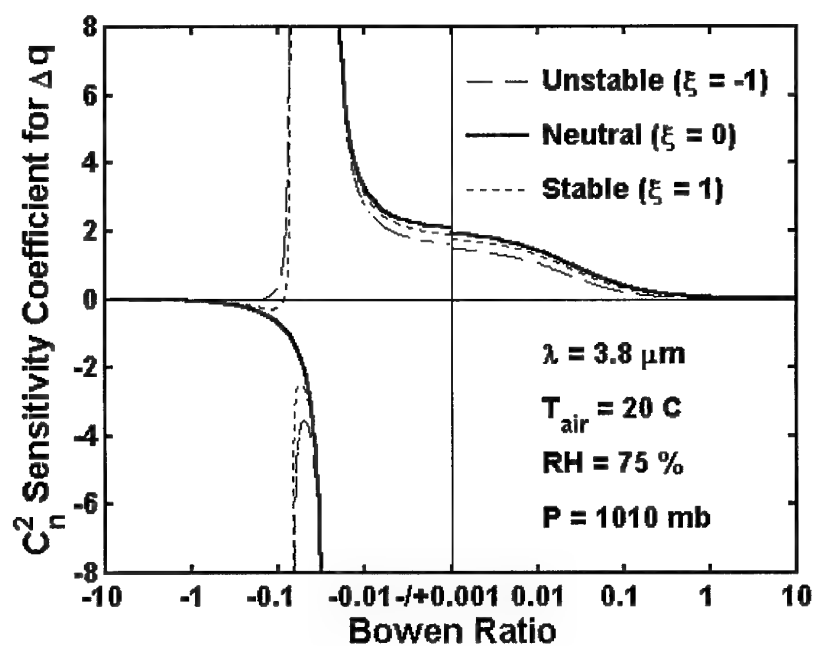


**Figure 4.**  $C_n^2$  sensitivity coefficient for the air-sea humidity difference,  $S_{\Delta q}$ , plotted versus the Bowen ratio. Unstable conditions ( $\xi = -1$ ) indicated by dashed line, neutral conditions ( $\xi = 0$ ) indicated by solid line and stable conditions ( $\xi = 1$ ) indicated by dotted line.

bulk versus transmission  $C_n^2$  comparison for near-neutral conditions (rms % difference of 358%).

The sensitivity coefficients  $S_{\Delta T}$  and  $S_{\Delta q}$  presented in Figs. 3 and 4 provide insight into the relative importance of temperature and humidity fluctuations in determining the resulting value of  $C_n^2$ . For  $Bo$  values less than  $-0.1$  and greater than  $0.1$ ,  $S_{\Delta T}$  is much greater than  $S_{\Delta q}$ , therefore temperature fluctuations, represented by the  $C_T^2$  term in Eq. (2), will dominate the resulting value of  $C_n^2$ . Within the range  $-0.01 < Bo < 0.01$ ,  $S_{\Delta q}$  is greater than  $S_{\Delta T}$ , therefore humidity fluctuations ( $C_q^2$ ) will dominate  $C_n^2$ . Within the range  $0.01 < Bo < 0.1$ ,  $S_{\Delta T}$  and  $S_{\Delta q}$  have similar magnitudes and are of the same sign, therefore the  $C_{Tq}$  term in Eq. (2) will dominate or be comparable in magnitude to  $C_T^2$  and  $C_q^2$ . Within the range  $-0.1 < Bo < -0.01$ ,  $S_{\Delta T}$  and  $S_{\Delta q}$  become very large and have opposite signs and it is impossible to accurately determine  $C_n^2$  or whether humidity or temperature fluctuations dominate.

## 10. Conclusions

This study has demonstrated that  $C_n^2$  can be accurately estimated in unstable conditions from routinely obtained meteorological measurements using bulk surface-layer models. The bulk  $C_n^2$  estimates were most accurate in unstable conditions because:

- 1) The bulk  $C_n^2$  estimates are the least sensitive to the measured values of  $\Delta T$  and  $\Delta q$  in unstable conditions.
- 2) The dimensionless structure function parameter,  $g(\xi)$ , upon which  $C_n^2$  is directly related, is better known in unstable conditions than in stable conditions.

Under neutral and stable stratification the use of bulk methods to estimate  $C_n^2$  was less successful. The poor accuracy observed in bulk  $C_n^2$  estimates in near-neutral conditions is due to three reasons:

- 1) The bulk  $C_n^2$  estimates are most sensitive to the measured values of  $\Delta T$  and  $\Delta q$  in neutral conditions.
- 2) The relative uncertainty in  $\Delta T$  measurements, which usually dominate the bulk  $C_n^2$  estimates, will tend to be largest in near-neutral conditions, when the values of  $|\Delta T|$  are smallest.
- 3) Over a narrow Bowen ratio range ( $-0.1 < Bo < -0.015$ ) which generally occurs only in near-neutral conditions, the bulk  $C_n^2$  values become extremely sensitive upon the measured values of  $\Delta T$  and  $\Delta q$ , making it impossible to accurately estimate  $C_n^2$ .

There are several probable reasons for the poor accuracy observed in bulk  $C_n^2$  estimates in stable conditions:

- 1) The bulk  $C_n^2$  estimates are more sensitive to the measured values of  $\Delta T$  and  $\Delta q$  in stable conditions than unstable conditions.
- 2) The dimensionless structure function parameter,  $g(\xi)$ , upon which  $C_n^2$  is directly related, is poorly known in stable conditions and the function in use may be greatly in error.
- 3) In very stable conditions turbulence is suppressed by the atmospheric stratification, which can allow the atmosphere to become de-coupled from the surface, thereby invalidating MOS theory and the bulk  $C_n^2$  model used in this study.

## Acknowledgments

This work was funded by the U. S. Office of Naval Research, program managers Dr. Scott Sandgathe and Dr. Ronald Ferek. The authors thank Mr. Keith Jones and Mr. Doug McKinney (McKinney Technology) for their efforts in deploying the NPS buoy and Mr. Bill Moision and Dr. Brett Nener for their assistance in acquiring the transmission data. A special thanks is due to Dr. Douglas Jensen for his able organizational skills during EOPACE and for providing the tide data used in this study.

*Atmospherics Conference*, San Diego, CA, 2-4 December 1997.

## References

1. Andreas, E. L., "Estimating  $C_n^2$  Over Snow and Ice From Meteorological Data", *J. Opt. Soc. Am.*, 5A, 481-495, 1988.
2. Paulson, C. A., "The Mathematical Representation of Wind Speed and Temperature Profiles in the Unstable Atmospheric Surface Layer", *J. Appl. Meteorol.*, 9, 857-861, 1970.
3. Fairall, C. W., E. F. Bradley, D. P. Rogers, J. B. Edson and G. S. Young, "Bulk Parameterization of Air-Sea Fluxes for Tropical Ocean-Global Atmosphere Coupled-Ocean Atmosphere Response Experiment", *J. Geophys. Res.*, 101, 3747-3764, 1996.
4. Hill, R. J., "Implications of Monin-Obukhov Similarity Theory for Scalar Quantities", *J. Atmos. Sci.*, 46, 2236-2244, 1989.
5. Zeisse, C., S. Gathman, A. Barrios, B. Moision, K. Davidson, and P. Frederickson, "Low Altitude Infrared Transmission", *Proceedings, Battlespace*
6. Churnside, J. H., R. J. Latatits and J. J. Wilson, "Two-color Correlation of Atmospheric Scintillation", *Appl. Optics*, 31, 4285-4290, 1992.

# Air Mass Characterization for EO Propagation Assessment

Terry E. Battalino  
Geophysics Branch, Code 521420E  
Naval Air Warfare Center Weapons Division  
Point Mugu, CA 93042-5001  
USA

## SUMMARY

The US Navy effort to measure and model air mass influences upon atmospheric optical and infrared transmission is reviewed. Two decades ago, air mass analysis experiments were initiated to supplement the development of real-time aerosol assessment models for open ocean environments. Air mass histories were determined from air trajectories, satellite derived cloud motion vectors, atmospheric radon gas concentrations, measurements of condensation nuclei (CN), and model iteration procedures. Subsequently, a unique air mass parameter concept was incorporated into the Navy Aerosol Model. Recently, the US Navy has expanded its program of electrooptical propagation to include coastal and near-surface aerosol environments, which are often frequented by diverse air mass changes. Additional air mass characterization techniques have recently been developed based on the foundation established earlier. Future plans and recommendations are outlined.

## LIST OF SYMBOLS

$P$	Air mass parameter (dimensionless)
$Rn$	Atmospheric radon concentration (pCi/m <sup>3</sup> ).
$Rn_i$	Radon count for $i^{\text{th}}$ trajectory at terminus.
$Rn_0$	Initial radon count before arrival at terminus.
$\Delta t$	Time between trajectory observations.
$C_j$	Radon accumulation rate for $j^{\text{th}}$ location.
$\beta$	Disintegration constant ( $\beta = 0.6931$ ).
$t_{ijk}$	Time between $k^{\text{th}}$ occurrence of $i^{\text{th}}$ trajectory at $j^{\text{th}}$ location and arrival at terminus.
$T$	Radon half-life ( $T = 3.83$ days).
$L_{ij}$	Occurrences of $i^{\text{th}}$ trajectory at $j^{\text{th}}$ location.
$n(r)$	Radius-number distribution (cm <sup>-3</sup> $\mu\text{m}^{-1}$ ).
$N$	Cumulative size distribution (particles cm <sup>-3</sup> ).
$r$	Aerosol particle radius.
$k$	Visibility scaling ratio.
$f$	Aerosol growth factor (depends on humidity).
$A_i$	Amplitude $i$ of the NAM.
$r_i$	Modal radius $i$ of the NAM.
$a$	CN parameter regression constant (0.0855677)
$\gamma_{\text{ext}}$	Aerosol extinction coefficient
$\lambda$	Wavelength
$m$	Complex index of refraction
$Q_{\text{ext}}$	Mie efficiency factor
$b$	Regression constant ( $b = 5.2928$ )
$c$	Regression constant ( $c = 0.3185$ )
$d$	Regression constant ( $d = 0.5395$ )

## 1. INTRODUCTION

As tropospheric air is transported over the planetary boundary layer, it often remains in contact with the surface of the earth for a sufficient time to acquire meteorological properties, such as temperature, moisture, and aerosol content, that typifies the underlying surface. In this way, a body of air is modified and becomes characterized as a distinct air mass. The precise location over which the air mass frequents can have unique attributes that identify the area as a specific air mass source region; for instance, a rough sea surface may generate large salt particles and an industrial complex may produce small combustion nuclei. In general, for characterizing the moisture content and aerosol size distribution, air masses are distinguished as continental and maritime source regions. Although additional classifications of air mass source regions that incorporate thermal properties and atmospheric stability are possible (Ref 1), the continental and maritime air mass designations are the most widely adopted in applications involving atmospheric optical and infrared transmission.

Aerosols generated over the continents and suspended in the atmosphere may be broadly classified into two categories; silicate aerosols ( $r > 0.5 \mu\text{m}$ ), which are produced by natural erosion and dispersed by the wind, and condensation aerosols ( $r < 0.5 \mu\text{m}$ ), which are produced by other natural and anthropogenic processes (Ref 2, 3). Condensation aerosols were first measured in the atmosphere by Aitken (Ref 4) and are often referred to as Aitken or condensation nuclei. The typical Aitken counter will draw air into a small chamber and saturate it by contact with water or wet blotting paper, and then force it to undergo a nearly adiabatic expansion that rapidly cools the chamber and produces considerable supersaturation. This causes droplets to grow on the microscopic nuclei to an appreciable drop size that can be detected and counted by a variety of methods (Ref 2). These nuclei, which often number in the several tens of thousands per cm<sup>3</sup> in city air, originate primarily at the earth's surface and are transported aloft by convection currents. The typically large number densities and small particle sizes of condensation nuclei principally impact upon the short wavelength region ( $< 1 \mu\text{m}$ ) of the electrooptical (EO) spectrum.

Marine aerosols are comprised of larger size sea spray particles that are produced by bursting bubbles at the sea surface. They are predominately sodium chloride and are injected into the atmosphere from the breaking of air bubbles in the sea foam and spray (Ref 5). In general, air engulfed and trapped under a breaking wave rises to the sea surface in bubbles, which measure approximately 500  $\mu\text{m}$  in diameter, where upon the bubbles burst and eject water jet drops and bubble caps. This gives rise to a bimodal particle size distribution (Ref 3), in which the jet drops form the super-micron mode and the bubble caps form the sub-micron mode. The bimodal generation mechanisms, which are strongly dependent upon wind speed (Ref 6,7), have been incorporated into the Navy Aerosol Model (Ref 8,9,10,11,12) along with a background continental aerosol mode, to represent marine aerosol size distributions as a tri-modal superimposition. Although relatively few in number, the larger size marine aerosols play an important role in the attenuation of infrared wavelengths.

Taking into consideration the diverse influences of aerosol source regions and corresponding particle concentrations, the chemical compositions, and the meteorological factors driving the transport mechanisms, permits the bulk resolution of the aerosol size distribution and the ensuing optical properties. The purpose of this paper is to review in brief outline past and present efforts to characterize the air mass component affecting EO propagation in the marine coastal atmosphere.

## 2. AIR MASS ANALYSIS

In a concerted effort to determine the effects of a marine atmosphere on EO propagation, the U.S. Navy established a Marine Environment Test Range on the northwestern end of San Nicolas Island (SNI), California. Simultaneous meteorological and optical transmission measurements were initiated in May 1978 under the Cooperative Experiment of West Coast Oceanography and Meteorology (CEWOM-78), sponsored by the U.S. Navy's Electro Optical Meteorology (EOMET) and Optical Signatures Programs (OSP).

One of the major objectives of the EOMET program was to characterize, for a variety of atmospheric conditions, the marine boundary layer meteorological parameters that influence EO propagation (Ref 13). An approach initiated (Ref 8,9) in this endeavor was to develop a model representative of the atmospheric aerosol size distribution based upon measurable meteorological variables. Since the particle size distribution and aerosol refractive index are required in Mie computations (Ref 14) of extinction, and because they are distinguishable between different air mass

regimes, CEWCOM-78 included a study of air mass histories.

### 2.1 Cloud Motion Vectors

The motions of low clouds as observed in film loops constructed from photographs by the geo-stationary environmental satellite (GOES) were used to derive provisional histories of low-level winds for data sparse regions in the vicinity of SNI during CEWCOM-78 (Ref 15,16).

The GOES photo in Fig. 1 illustrates an example of an interesting and fairly common weather phenomenon off the southern California coast. A well-defined "Catalina eddy" became established in the southern California bight in the wake of a "Santa Ana" (offshore flow) condition during the CEWCOM-78 period. The marine stratus cloud formations are suggestive of a cyclonic circulation pattern in the vicinity of SNI. The suspected flow pattern was confirmed by analysis (Ref 15) of GOES film loops and is diagrammed in Fig. 2 along with other air mass movements derived by tracking cloud features at that time.



Figure 1. GOES Satellite Imagery at 1845 GMT (1045 PST) on May 14, 1978, showing a well defined "Catalina eddy" circulation engulfing SNI and vicinity in a layer of marine stratus clouds.

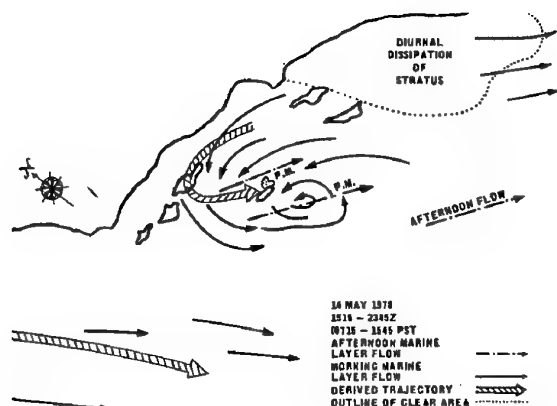


Figure 2. Marine layer flow patterns derived from GOES film loops for the period 1515-2345 GMT (0715-1545 PST) during May 14, 1978. The air mass history at SNI is influenced by cyclonic circulation.

Catalina marine layer eddies span about 200 km and are formed in response to larger scale synoptic events (Ref 15). They typically result in the rapid spread of stratus cloud cover accompanied by a deepening marine layer. The cloud spiral depicted in Fig. 1 is a classic feature of the Catalina eddy. The synoptic conditions leading to this eddy circulation consisted of an advancing cold front and retreating high-pressure system that spawned a southwesterly flow in the marine surface layer. During this episode the southwest wind direction observed at SNI would have indicated a strictly marine air mass condition. However, the cloud motion vectors of Fig. 2 and other indices of aerosol concentration implied a recent overland air mass history.

Cloud motion vectors of low-level clouds are useful air mass tracers in coastal areas, especially in data void regions, but some caveats are in order. The air parcel paths derived by cloud vectors are usually of short duration, perhaps less than 12-hours, and will vary depending upon the life span of the distinctive cloud trait being tracked. The winds at cloud levels are generally unknown and may not accurately represent near-surface conditions (Ref 16). Also, the method can only be applied when a sufficient amount of the cloud element is discernable. Since low-level clouds are not always present, this technique has limited application and other procedures must be investigated.

## 2.2 Air Trajectories

During the CEWCOM-78 period, surface wind data for southern California and off shore island stations were plotted on local area synoptic charts and used to construct streamlines (Ref 17). Trajectories were computed from the streamline charts in conjunction with isotach analyses, and hand constructed backward

in one hour increments from SNI for periods up to 24-hours. The trajectory analysis coinciding with the time frame of Fig. 1 and Fig. 2 revealed a southwesterly pattern (Ref 15), suggesting innocuous marine air mass predominance at SNI.

In an effort to improve the trajectory methodology, the procedure was computer automated (Ref 18) to provide analyses of the same data for 24-hour duration periods. The computerized trajectories also detected a southwesterly flow arriving at SNI, and this too was identified as a maritime influence (Ref 19).

However, further examination of the air trajectories for duration up to 5 days (Ref 20), show air parcels caught in a spiral path before terminating at SNI. This is consistent with a cyclonic eddy circulation accompanied with a continental mainland air mass influence. Hence, short duration trajectories can be deceiving as to the air mass origin or recent history. In marine coastal areas or in regions near landmasses that provide a source of continental aerosols, the selection of the proper air mass influence is an important factor for EO model assessment.

## 2.3 Atmospheric Radon

Atmospheric radon 222 is a product of the uranium 238 decay series. It is an inert radioactive gas (half-life 3.82 days) produced by the decay of radium 226 (half-life 1622 years) which is found in various quantities in the soils and rocks of the earth's crust. Most of the rare gas emanates from continental areas, with less than 2% originating in the oceans (Ref 21). After formation in the ground, radon diffuses into the atmosphere where its short lived daughter products become attached to aerosol particles that are transported with the prevailing winds. The majority of the radon burden collected by an air mass depends upon its duration over land regions and the radon emissions rate from those regions; radioactive decay, diffusion, and turbulent mixing (Ref 22) govern the removal processes. Because radon is produced mainly on landmasses and has a reasonably long half-life, it has been widely used as an air mass tracer (Ref 18,23,24,25,26) over oceanic areas.

Since radon exhalation depends upon the variable conditions of soil moisture, atmospheric pressure, crustal radium deposits, and the strength of the radium source, relative changes in radon concentrations are more meaningful as an air mass tracer than absolute concentrations. Radon levels of a few pCi/m<sup>3</sup> are typical over oceanic air, while concentrations of several tens of pCi/m<sup>3</sup> are found over land. A relative increase in radon concentration over the ocean, for example, may indicate that the air has a recent overland history; thus, monitoring radon fluctuations can provide a means to determine whether a given location is experiencing an intrusion of continental or maritime air.

Radon levels measured at SNI and around the offshore vicinity during CEWCOM-78 show a large variability in the air mass behavior (Ref 26). The radon concentration time coincident with the Catalina eddy ranged from 27 to 41 pCi/m<sup>3</sup> dropping to less than 2 pCi/m<sup>3</sup> as the eddy dissipated. This suggests that SNI experienced an influx of continental aerosols during this period.

Subsequent comparisons between air trajectories and radon measurements at SNI, categorized trajectories into low (<10 pCi/m<sup>3</sup>), medium (≥10, <30 pCi/m<sup>3</sup>), and high (≥30 pCi/m<sup>3</sup>) radon levels (Ref 18,27,28).

In order to quantify air mass effects on EO propagation an air mass factor (Ref 8,9,10,11) is introduced as an input parameter to the Navy Aerosol Model (NAM). The air mass parameter (P) is determined from Eq. (1) and is indexed to the atmospheric radon concentration (Rn) measured at the surface.

$$P = 1 + \frac{Rn}{4} \quad (1)$$

Equation (1) uses absolute radon values because it was established for the Eastern Pacific Ocean or, more specifically, for San Nicolas Island. The factor of four in Eq (1) should be adjusted for applications to other geographical regions in which the background radon emission is significantly dissimilar to SNI. Unfortunately, to determine the appropriate empirical factor for various geographical locations requires an extensive knowledge of global radon variability, so it is unlikely that Equation (1) will have broad utilization. In addition, other constraints such as the high cost, maintenance, and inadequate commercial availability of radon instrumentation have encouraged investigators to explore alternate methods for determining the air mass parameter.

## 2.4 Trajectory Radon Parameterization

Air mass parameterization techniques (Ref 29,30,31,32) using a combination of trajectory and radon information have been developed for SNI. The procedures estimate radon as the sum of an initial background level, and as an accumulation of the changing radon exhalation rates of the surface along a trajectory path. The radon emission rates are derived for specific grid areas near SNI using the prior trajectory and radon information. The approach is formulated by a system of  $m$  linear equations, one equation for each trajectory and simultaneous radon measurement, and  $n+1$  variables:

$$Rn_i = Rn_0 + \Delta t \sum_{j=1}^n C_j \sum_{k=1}^{L_{ij}} \exp \left[ \frac{-\beta t_{ijk}}{T} \right] \quad (2)$$

where  $Rn_i$  is the radon concentration measured at the terminus of the  $i^{\text{th}}$  trajectory,  $Rn_0$  is the initial background radon level, and  $C_j$  is the effective radon accumulation rate for the  $j^{\text{th}}$  grid area traversed. It is assumed that the rate at which an air parcel accumulates radon is equal to the radon exhalation rate of the underlying surface, and that the time,  $\Delta t$ , an air parcel dwells in a grid area is one hour. The exponential term takes into consideration the time decay factor where  $\beta$  is the disintegration constant,  $T$  is the radon half life, and  $t$  is the time between the  $k^{\text{th}}$  occurrence of the  $i^{\text{th}}$  trajectory at the  $j^{\text{th}}$  location, and arrival to the terminus.

The effective radon indices or radon accumulation rates, which are the constant  $C_j$ 's in Eq. (2), were derived using a total of 256 48-hour duration trajectories terminating at SNI simultaneous with radon observations. A 15-grid domain centered on SNI and extending throughout southern California was used for this investigation. The derived indices illustrated a very general tendency for higher accumulation rates over or near land as opposed to over the open sea. The method of least squares was used to solve Eq. (2). The results showed excellent agreement between the measured radon and the radon predicted by Eq. (2) using the previously determined indices and trajectory information. A correlation coefficient of 0.82 between the observed and predicted radon levels revealed no systematic deviations from the linear assumptions.

Although this approach produced favorable results for SNI and could be adapted to other locations, their remains several issues that should be further studied (Ref 16,20,33). Some of the indices show high rates of accumulation over the southern California bight that are physically unrealistic, suggesting that other factors such as vertical and horizontal mixing, and trajectories of greater duration must be incorporated. Nevertheless, the trajectory radon parameterization scheme provides an objective means by which trajectory information may be utilized in lieu of radon. The radon estimate obtained from Eq. (2) can be substituted into Eq. (1) to determine the air mass parameter input for the NAM.

## 2.5 Condensation Nuclei

Measurements of condensation nuclei (CN) during the CEWCOM-78 (Ref 34) show a strong similarity with the time series history of radon (Ref 20). CN levels peaked at 6209 particles per cm<sup>3</sup> during the Catalina eddy and dropped to 333 particles per cm<sup>3</sup> thereafter. Prior to the eddy, the CN concentration was about 1500 particles per cm<sup>3</sup>. Since CN are a direct measure of the atmospheric aerosol load, it is apparent that the eddy circulation pattern transported continental aerosols to SNI. Unlike radon, which only provides a relative indication of air mass change, the CN measurement is absolute. One does not have to guess or provide an estimate of the atmospheric aerosol content when a direct and absolute measure, like CN, is available.

The size distribution for the NAM kernel is given by

$$n(r) = \frac{dN}{dr} = \sum_{i=1}^3 \frac{k}{f} A_i \exp \left[ - \left( \ln \left\{ \frac{r}{f r_i} \right\} \right)^2 \right] \quad (3)$$

where the  $A_1$  amplitude is scaled to the air mass parameter expressed in Eq. (4).

$$A_1 = 2000 P^2 \quad (4)$$

It has been demonstrated (Ref 33,35,36,37) that the NAM distribution of Eq. (3) can be integrated to provide a calculated aerosol number density, which can be equated to a measured CN count, thereby allowing for a direct solution of the  $A_1$  amplitude. The air mass parameter,  $P$ , is then determined from Eq. (4). The integrated number density,  $N$ , is computed for specific limits of integration that correspond to the size range measured by CN instrumentation.

$$N = \int_{r_a}^{r_b} n(r) dr \quad (5)$$

In practice (Ref 12,33,36,37,38), the lower integration limit,  $r_a$ , in Eq. (5) is set to 0.001  $\mu\text{m}$  while the upper limit,  $r_b$ , is fixed at 5  $\mu\text{m}$ . It is important to choose a CN monitor such that  $r_a < r_1$  where  $r_1$  is the modal radius for the  $A_1$  amplitude ( $r_1 = 0.03 \mu\text{m}$ ), so that the integration of Eq. (5) will incorporate  $A_1$ . Conversely, if  $r_a$  is too small this procedure may break down due to the presence of another mode of higher number density (small size) aerosols (Ref 39). In this case, the CN monitor will detect the higher number density in addition to the contribution from the  $A_1$  term, and should not be equated to Eq. (5).

Likewise, the upper integration limit,  $r_b$ , must satisfy the condition  $r_b > r_1$  in order to capture the  $A_1$  amplitude. There is no ill consequence caused by a very large upper limit. Ideally, the choice of  $r_a$  and  $r_b$  need only bridge across  $r_1$  by some small amount,  $\Delta r$ , such that  $r_a = r_1 - \Delta r$  and  $r_b = r_1 + \Delta r$ . However, only manually operated CN monitors are available for measurements over narrow size ranges. The apparent advantage of an aerosol measurement over a restricted particle size range is the exclusion of contributions from the  $A_2$  and  $A_3$  wind speed driven amplitudes. Although this may seem to be quite important, in actuality the impact is very limited and inconsequential.

Although analytical and numerical solutions have been developed for  $A_1$  (Ref 33,36,37), which permit  $P$  to be

determined from Eq. (4), they are elaborate and some simplification is in order. The cumulative number density or equivalent CN concentration of Eq. (5) can be calculated for a range of  $P$ , and then a regression relationship can be established for  $P$  as a function of  $N$ . This concept is illustrated in Fig. 3 and is expressed in Eq. (6) as a single term regression equation, where  $a$  is the CN air mass parameter regression constant.

$$P = a \sqrt{N} \quad (6)$$

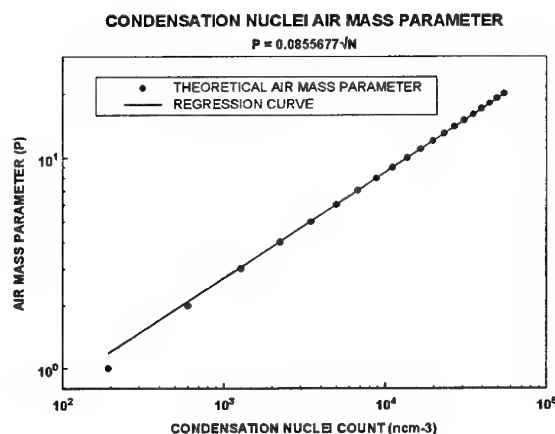


Figure 3. Air mass parameter plotted against the theoretical CN count calculated from Eq. (5) for the maximum wind speed (20  $\text{msec}^{-1}$ ) and for  $P = 1$  to 20.

Since  $n(r)$  is dependent upon relative humidity through the aerosol growth factor,  $f$ , in Eq. (3), and since  $n(r)$  also depends upon the wind speed through the  $A_2$  and  $A_3$  amplitudes, the computed  $N$  might also be expected to show similar dependence. Notwithstanding, it has been established (Ref 36,37) that no dependence on relative humidity exists because the NAM is normalized to the growth factor. The size distribution shifts towards larger particle sizes as the humidity increases. This enhances the number density of larger size particles while reducing the number of smaller size particles, such that the total aerosol count remains constant or nearly so. In effect, introducing relative humidity results in growth of the larger size particles at the expense of the smaller size particles.

The calculated CN was found to be strongly dependent on the air mass parameter and only slightly dependent on the wind speed (Ref 36,37). These results occur because the  $A_2$  and  $A_3$  wind speed driven amplitudes are associated with far fewer particles than the  $A_1$  air mass driven amplitude. Because the  $A_2$  and  $A_3$  amplitudes increase the production of larger size aerosol particles



with increasing wind speed, the computed CN count is greater during high wind speed events. The  $A_1$  amplitude through the air mass parameter modifies the significance of this wind speed effect, by virtue of its dominance in CN over the other amplitudes. The difference in CN between the highest and lowest wind speeds supported by the NAM is 42% for  $P = 1$  and 10% for  $P = 2$ . No significant differences are observed for  $P > 2$ . The calculated CN concentration for  $P = 1$  is 194 particles per  $\text{cm}^3$  for the highest wind speed, and 137 particles per  $\text{cm}^3$  for the lowest wind speed. CN levels less than 200 particles per  $\text{cm}^3$  are rare, and the percent measurement error at these levels will be large.

Although the CN air mass parameter as expressed in Eq. (6) is simple and easy to use, provides a direct and absolute measure of the air mass property, has no dependence on the relative humidity, and no practical dependence on wind speed, it has some imperfections. While the CN technique has undergone limited but favorable evaluations (Ref 12,38) on shipboard, the issue of instrument maintenance and its sensitivity to detection of smoke aerosol contaminants has been raised.

## 2.6 Model Iteration Techniques

Measurements of aerosol extinction or transmission also afford an opportunity to determine the air mass parameter. The assumption is that the air mass parameter is the only unknown of the model-input and output variables. The methodology requires several calculations, preferably at two or more wavelengths with an atmospheric transmission model such as LOWTRAN (Ref 40), to reiterate over all air mass parameter possibilities. The model calculated results for each air mass parameter are compared to the measurement(s) for the optimum fitting.

Simultaneous multiple wavelength measurements of atmospheric transmission and meteorological input parameters during the EOMET and OSP experiments were used as a database to test this concept (Ref 41). The mean deviation, which is a measure of the model bias, is plotted against the air mass parameter in Fig. 4 for each of five different wavelengths.

The 0.51-0.61  $\mu\text{m}$  visibility band in Fig. 4 shows no deviation because it was used as the scaling factor,  $k$ , in Eq. (3). The visibility-scaling factor is the ratio of the observed to the calculated aerosol extinction for this band. In effect, the model calculated extinction at 0.51-0.61  $\mu\text{m}$  is adjusted to the observed value so no deviation is expected.

The other wavelength bands are negatively biased for low values of the air mass parameter and positively biased for higher values, except for the 10.54-10.77  $\mu\text{m}$  band that always remains negatively biased. A positive

LOWTRAN 6 MODEL

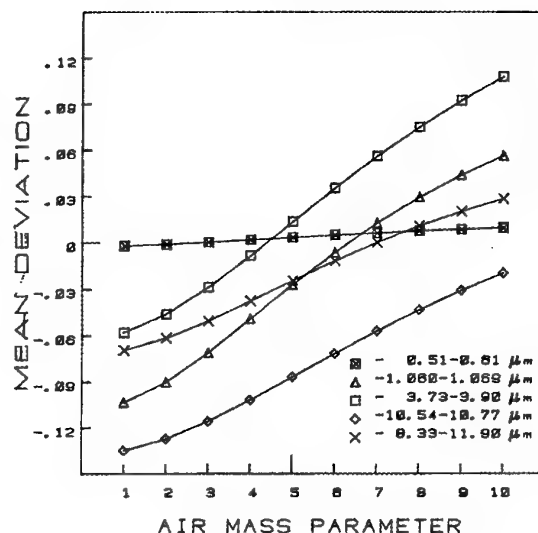


Figure 4. LOWTRAN 6 atmospheric transmission model mean deviation computed for air mass parameter  $P = 1$  to 10. The mean deviation is computed as the average of the differences between the model calculated broad band transmission and observations.

bias means that the model calculated transmission is greater than the measured transmission. The 3.73-3.90  $\mu\text{m}$  band crosses the zero bias line (mean deviation) near  $P = 4.5$ , while the 1.060-1.069  $\mu\text{m}$  intersects near  $P = 6.5$ , and the 8.33-11.90  $\mu\text{m}$  at about  $P = 7.5$ . Ideally, all of these curves should intersect at one point on the zero deviation line and this point would correspond to the optimum air mass parameter.

The varied result in Fig. 4 proves that it is hazardous to extract the air mass parameter by this method. It is likely that the model, measurements, or meteorological representativeness along the 4.06 km transmission path are in question. The equal weighting that the visibility scaling parameter applies to each of the NAM amplitudes must also be questioned, and may be physically unrealistic. In addition, the expectation that the optimum air mass parameter will fall on the zero deviation line may not be valid. A more realistic expectation is that all of the transmission curves (not the mean deviation) will intersect at a common point. Variations of the basic model iteration technique have met with more favorable results by other investigators (Ref 42,43), but in these instances no more than two wavelengths were employed with satellite remote sensing, and the application is limited to clear skies.

## 2.7 Visibility Air Mass Parameter

The air mass parameter,  $P$ , can be calculated from Mie theory using the NAM size distribution given by Eq. (3) and a measurement of the visual extinction coefficient (Ref 11,44,45). The aerosol extinction coefficient,  $\gamma_{\text{ext}}$ , is formulated from Mie theory as

$$\gamma_{\text{ext}}(\lambda) = \int_0^{\infty} \pi r^2 Q(\lambda, r, m) n(r) dr \quad (7)$$

where  $\lambda$  is the wavelength,  $m$  is the complex refractive index and  $Q_{\text{ext}}$  is extinction efficiency factor (Ref 46). In this approach, all quantities in Eq. (7) are assumed known and one solves for the air mass parameter.

This procedure is similar to the visibility scaling parameter, except it is more plausible because it exerts weighting only on the first amplitude. The difficulty with this approach is that the visibility air mass parameter will be dependent upon the wind speed and relative humidity through  $n(r)$  in Eq. (3). It is the integral of  $n(r)$  in Eq. (5) that can be taken as independent of the NAM parameters. Additionally, any adjustment to or determination of a NAM amplitude based upon extinction measurements will conceal potential errors in the amplitude parameterizations. For example, determining the  $A_1$  amplitude via extinction could compensate for a deficiency in  $A_3$  that might have been detected if the  $A_1$  parameter was independent. Different mechanisms that are, in essence, independent of each other, generate the three modes of the NAM. Making adjustments to one mode to force the computed extinction to match the measurement, obscures any potential difficulties with the other modes, and makes the model evaluation process more complicated. The visibility air mass parameter is appealing, however, and variations on the basic technique have been evaluated favorably (Ref 38,47,48,49).

## 3. NAM SENSITIVITY TO AIR MASS INDEX

The sensitivity of the NAM to the air mass parameter has been investigated with a QUICK BASIC adaptation (Ref 50) of the original model (Ref 9), which does not include the relative humidity parameterization (Ref 51). The adapted model accepts CN as input for the air mass parameter as expressed in Eq. (6). The variation of the model calculated extinction versus the range of wavelengths supported by the NAM, is shown in Fig. 5 for a series of air mass parameters. In this example, the relative humidity and wind speed are held constant at 80% and 10 msec<sup>-1</sup>, respectively. The characteristic curves show that the shortest wavelengths are most impacted by the air mass parameter.

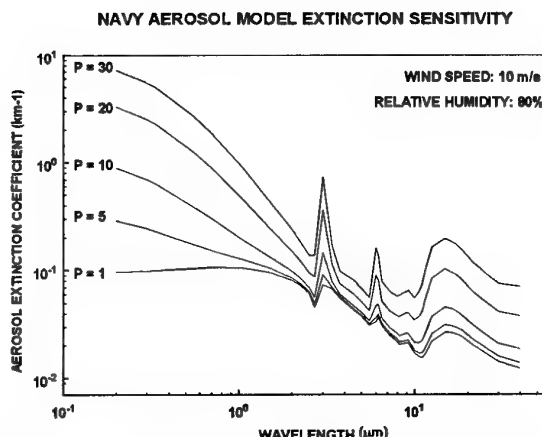


Figure 5. Aerosol model extinction coefficients versus wavelength for air mass parameters 1, 5, 10, 20 & 30. The wind speed and relative humidity are held constant at 10 msec<sup>-1</sup> and 80%, respectively.

Short path length optical instruments used during the EOPACE program measure the aerosol extinction at wavelengths in the 0.55 μm, 3.5 μm, and the 10.59 μm regions. Fig. 6 illustrates the variation in extinction at these wavelengths for the air mass parameter under the same relative humidity and wind speed constraints as in Fig. 5. The results in Fig. 6 illustrate that an increase of approximately 1-20 in the air mass parameter will increase the extinction by an order of magnitude at 0.55 μm. The air mass parameter has little impact on the model-computed extinction at 3.5 μm and some influence on the 10.59 μm extinction.

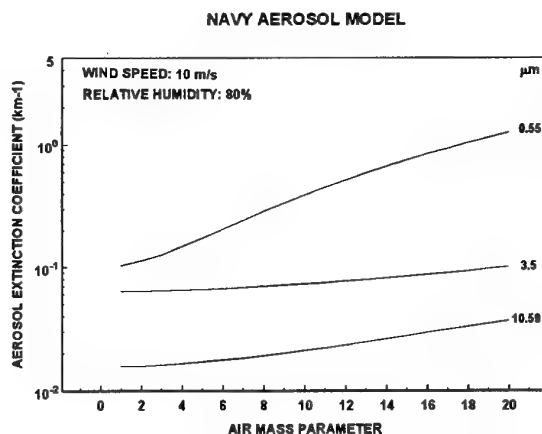


Figure 6. Aerosol model extinction coefficients versus air mass parameter for the selected wavelengths of 0.55 μm, 3.5 μm, and the 10.59 μm. The wind speed and relative humidity are held constant at 10 msec<sup>-1</sup> and 80%, respectively.

In reference to Fig 5, the majority of the extinction contribution occurs near the visible wavelength, as would be predicted by Mie theory (Ref 46), and this justifies the interest in a visibility based air mass index.

The results in Fig. 5 and Fig. 6 will be modified for different cases of wind speed and relative humidity. Fig. 7 shows a family of relative humidity curves for 0.55  $\mu\text{m}$  extinction sensitivity to air mass parameter. A similar example is provided in Fig. 8 for the 10.59  $\mu\text{m}$  case.

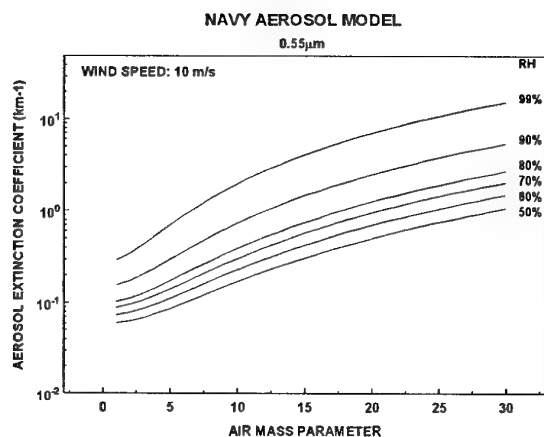


Figure 7. Aerosol model extinction coefficients at 0.55  $\mu\text{m}$  versus air mass parameter for different relative humidity conditions ranging from 50-99%.

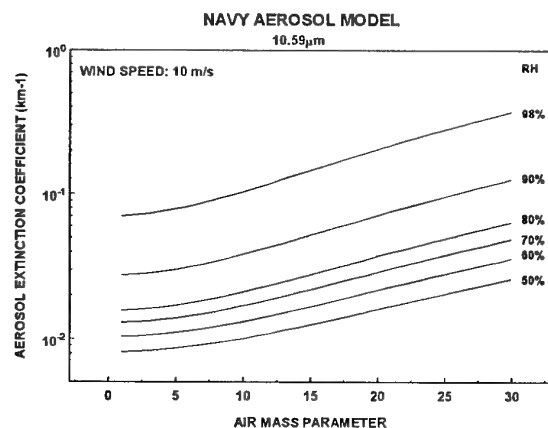


Figure 8. Aerosol model extinction coefficients at 10.59  $\mu\text{m}$  versus air mass parameter for different relative humidity conditions ranging from 50-99%.

#### 4. AIR MASS PARAMETER COMPARISON

The measurements of radon and CN during the CEWCOM-78 experiment have been reexamined with the intention of indexing radon to CN. The CEWCOM-78 period exhibited the large variability in air mass conditions that are required in order to perform a good comparison. Since radon gas concentrations depend upon the geographically varying crustal radium deposits, and despite the fact that CN concentrations are intrinsic to the air mass, any empirical relationship derived will most likely be valid only for SNI and vicinity.

The scatter plot in Fig. 9 shows the CN count plotted as a function of the radon level. The data scatter is fitted to a combined exponential and power law relation given in Eq. (8).

$$N = \exp(b + cRn^d) \quad (8)$$

$Rn$  is the radon concentration level and  $N$  is the CN count and  $b$ ,  $c$ , and  $d$  are regression constants.

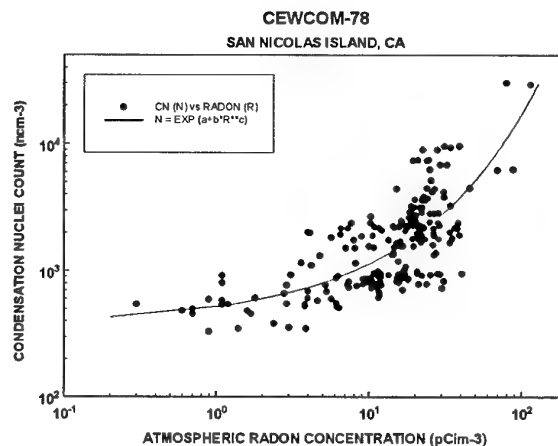


Figure 9. Scatter plot of simultaneous measurements of CN and radon during CEWCOM-78. Regression curve is superimposed on the data scatter.

The original radon air mass parameter, as computed in Eq. (1), can be calculated from this data and compared to the CN air mass parameter established in Eq. (6). The results are provided in the scatter plot of Fig. 10 along with a reference line. The radon air mass parameter has a tendency to over estimate the CN, except during clean air episodes in which it is found to underestimate the CN.

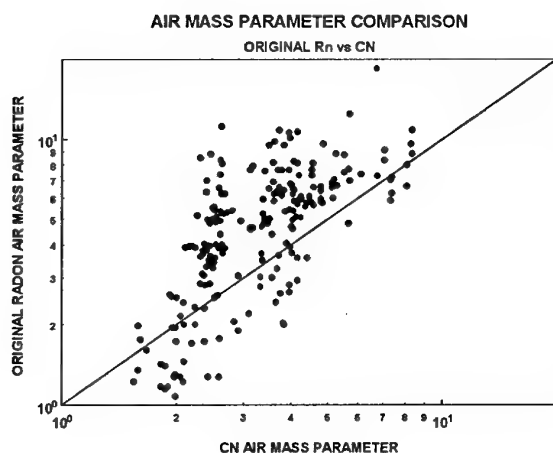


Figure 10. Scatter plot of original radon air mass parameter computed from Eq. (1) compared to the CN air mass parameter of Eq. (6). The reference line is the locus of points at which both parameters are identical.

If Eq. (8) is used to convert radon to an equivalent CN count, then the CN air mass parameter or Eq. (6) can be applied to the converted radon data. This results in a derived radon air mass parameter shown in the Fig. 11 comparison.

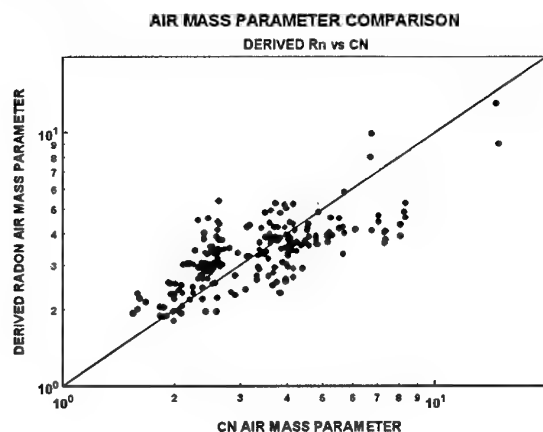


Figure 11. Scatter plot of derived radon air mass parameter computed by substituting Eq. (8) into Eq. (6). Comparison is made to the CN air mass parameter. The reference line is the locus of points at which both parameters are identical.

## 5. CONCLUSIONS

Various methods for air mass analysis for EO propagation assessment have been discussed. They include: cloud motion vectors derived from satellite film loops, air mass trajectories, atmospheric radon

concentration, trajectory radon parameterization, condensation nuclei concentration, model iteration technique, and the visibility method. Each approach has its own unique set of advantages and disadvantages. Not explicitly discussed were the nephelometer system and the satellite aerosol optical depth retrieval procedure. Several of these methods are currently being evaluated in the EOPACE program.

The NAM has incorporated a unique air mass parameter. Sensitivity studies of the NAM extinction to the air mass parameter show that the shorter wavelengths are influenced most by variations in the air mass parameter.

All of the NAM input variables, such as visibility, wind speed, and relative humidity, are clearly defined quantities except the air mass parameter. The various air mass parameter options that have been studied are indications of how complex it is to characterize an air mass for its optical properties. The criteria for establishing an air mass parameter must include a definition of  $P$  that is consistent with the independent aerosol mode it is to represent. Thus it is highly desirable that  $P$  be a model independent parameter, i.e. independent of wind speed, relative humidity, and Mie theory calculations. A standard or reference for  $P$  must be established for calibration purposes. The air mass parameter should be a universal index and, therefore, not limited to specific geographical areas or weather scenarios. It should be easy to measure and apply. Any equipment or instrumentation used to assess the air mass parameter should be easy to maintain.

As the analysis of EOPACE data proceeds, it may be concluded that one type of measurement would best define or provide an absolute measure or calibration of the air mass parameter, while another type of instrument may provide a more desirable operational capability. In this case, the operational instrument would be calibrated to the standard instrument, in a similar way that radon has been calibrated to CN.

A narrow band size distribution integration spanning equally across the  $A_1$  amplitude is the only direct and independent assessment of the air mass parameter. This type of measurement is not available. The next best substitute is the CN count, which could be used as the standard measurement, but it remains to be determined whether CN will be a viable operational measure of the air mass parameter.

It is noteworthy that the concept of an input parameter, as applied to the air mass parameter, has evolved away from the original premise or objective. Specifically, that input parameters for aerosol extinction models are derived from basic meteorological variables. Virtually all of the air mass characterization techniques discussed here cannot be classified as a basic meteorological

variable, with the possible exception of air trajectories, which are constructed from measurements of wind speed and direction. In the future, a movement away from real-time assessment models will be replaced with dynamic aerosol models that will forecast the modal amplitudes from wind fields, with procedures not unlike air trajectory analysis.

## ACKNOWLEDGEMENTS

The assistance of A. Ortiz and M. McGovern with model calculations, and C. Fisk on the use of Table Curve software for curve regression is appreciated. This report has also benefited from discussions with R. Helvey and J. Rosenthal. This work was supported by the SPAWAR Systems Center, San Diego, CA (formally NCCOSC, RDTE DIV 883). Funding was provided by Dr. Juergen H. Richter under the Office of Naval Research Exploratory Development Program.

## REFERENCES

- Huschke, R.E., "Glossary of Meteorology", American Meteorology Society, Boston, MA, 2<sup>nd</sup> ed, 1970, pp. 18-20.
- Fletcher, N.H., "The Physics of Rain Clouds", Cambridge University Press, Cambridge, UK, 2<sup>nd</sup> ed., 1966, pp. 64-102.
- Patterson, E.M. "Size distributions, concentrations, and composition of continental and marine aerosols", *Proceedings of the Workshop on Atmospheric Aerosols: Their Formation Optical Properties and Effects*, Ed. by A. Deepak, Spectrum Press Baltimore, MD, 1982, pp. 1-38.
- Aitken, J., "On the number of dust particles in the atmosphere", *Trans Roy.Soc.Edinb.*, 35, 1887, pp.1.
- Fleagle, R.G. and J.A. Businger, "An Introduction to Atmospheric Physics", Academic Press, New York, NY, 1963, pp. 87.
- Woodcock, A.H., "Salt nuclei in marine air as a function of altitude and wind force", *J. Meteorol.*, 1953, pp. 362-371.
- Patterson, E.M., Kiang, C.S., Delany, A.C., Wartburg, A.F., Leslie, A.C.D., and Huebert, B.J., "Global measurements of aerosols in remote continental and marine regions: Concentrations, size distributions and optical properties, *J. Geophys. Res.* 85, 1980, pp. 7361-7376.
- Gathman, S.G., "Optical properties of the marine aerosol as predicted by the Navy aerosol model", *Opt. Eng.*, 22, 1983, pp.57-62.
- Gathman, S.G., "Optical Properties of the Marine Aerosol as Predicted by a BASIC Version of the Navy Aerosol Model", NRL Memorandum Report No. 5157, Naval Research Laboratory, Washington, D.C., 1983, pp. 31.
- Gathman, S.G. and B. Ulfers, "On the Accuracy of IR Extinction Predictions Made by the Navy Aerosol Model", *Proceedings of the Ninth Conference on Aerospace and Aeronautical Meteorology*, American Meteorology Society, Omaha, NB, 1993, pp. 194-198.
- Gathman, S.G. and K.L. Davidson, "The Navy Oceanic Vertical Aerosol Model", NRaD Technical Report No. 1634, Naval Command, Control and Ocean Surveillance Center, RDT&E Division, San Diego, CA, 1993, pp. 107.
- Gathman, S.G., "Assessment of NAM, the Navy aerosol model, for visibility determinations in inland seas such as the Persian Gulf", *AGARD Conference Proceedings 582*, Remote Sensing: A Valuable Source of Information, Paper no. 33, Toulouse, France, 1996, pp. 5.
- Richter, J.H. and H.G. Hughes, "Electro-optical atmospheric transmission effort in the marine environment", NOSC Technical Report No. 696, Naval Ocean Systems Center, San Diego, CA, 1981, pp. 51.
- Dave, J.V., "Subroutines for computing the parameters of electromagnetic radiation scattered by a sphere", Technical Report No 320-3237, IBM Scientific Center, Palo Alto, CA, 1968, pp. 67.
- Rosenthal, J., T.E. Battalino, H. Hendon, and V.R. Noonkester, "Marine/Continental History of Aerosols at San Nicolas Island During CEWCOM-78 and OSP III", PMTC Technical Publication TP-79-33, Pacific Missile Test Center Technical, Point Mugu, CA, 1980, pp. 285.
- Rosenthal, J., T. Battalino, L. Eddington, R. Helvey, C. Fisk, and D. Lea, "Aerosol Transport and Origin", *Proceedings of the NATO Research and Technology Agency Conference*, (This Volume), EO Propagation, Signature, and Systems Performance Under Adverse Meteorological Conditions Out-of-Area Operations, Paper no. 18, Naples, Italy, 1998, pp. 15.
- Rosenthal, J., T.E. Battalino, H. Hendon, and V.R. Noonkester, "Marine/continental history of aerosols at San Nicolas Island During CEWCOM-78 and OSP III", *Proceedings of the Second Conference on Coastal Meteorology*, Amer. Meteor. Soc., Los Angeles, CA, 1980, pp. 84-93.
- Battalino, T.E. and R.A. Helvey, "Air mass trajectories and atmospheric radon measurements during the EOMET/OSP experiments on San Nicolas Island (1978-1980)", PMTC Technical Publication TP000001, Pacific Missile Test Center, Point Mugu, CA, 1982, pp.23.
- Battalino, T.E., R.A. Helvey, C. J. Walcek, J. Rosenthal, and J. Gottschalk, "Air mass trajectory analysis as an aid in distinguishing marine from continental aerosol distributions at San Nicolas Island.", *Proceedings of the Workshop on Atmospheric Aerosols: Their Formation Optical Properties and Effects*, , Ed. by A. Deepak, by Spectrum Press Baltimore, MD, 1982, pp. 125-134.

20. Helvey, R.A., "Air Trajectories and Air Mass Characteristics in the Southern California Coastal Region", *Proceedings of the NATO Research and Technology Agency Conference*, (This Volume), EO Propagation, Signature, and Systems Performance Under Adverse Meteorological Conditions Out-of-Area Operations, Paper no. 19, Naples, Italy, 1998, pp.14.
21. Wilkening, M.H. and W.E. Clements, "Radon 222 from the ocean surface", *J. Geophys. Res.*, 80, 1975, pp. 3828-3830.
22. Larson, R.E., D.J. Bressan, K.W. Marlow, T.A. Wojciechowski, and J.L. Heffter, "A comparison of concentrations of fission products, Radon 222, and cloud condensation nuclei over the North Atlantic", *Pageoph.*, 117, 1979, pp. 874-882
23. Fontan, J., D. Blanc, and A. Bouville, "Meteorological conditions dependence of radon concentrations in the air above the Arctic", *Nature*, 197, 1963, pp. 583-584.
24. Rama, K., "Using natural radon for delineating monsoon circulation", *J. Geophys. Res.*, 75, 1970, pp. 2227-2229.
25. Prospero, J.M., and T.N. Carlson, "Radon-222 in the North Atlantic Trade Winds: its relationship to dust transport from Africa", *Science*, 167, 1970, pp. 974-977.
26. Larson, R.E., and D.J. Bressan, "Air mass characteristics over coastal areas as determined by radon measurements", *Proceedings of the Second Conference on Coastal Meteorology*, Amer. Meteor. Soc., Los Angeles, CA, 1980, pp. 94-100.
27. Battalino, T.E. and R.A. Helvey, "Comparison of Air Trajectories and Atmospheric Radon at San Nicolas Island", *Geophysical Sciences Technical Note No. 74*, Pacific Missile Test Center, Point Mugu, CA, 1982, pp. 18.
28. Battalino, T.E. and R.A. Helvey, "Comparison of Air Trajectories and Atmospheric Radon at San Nicolas Island", *Proceedings of the Fifth Conference on Atmospheric Transmission Models*, Air Force Geophysics Laboratory, Hanscom AFB, MA, 1982, pp. 18.
29. Battalino, T.E. and R.A. Helvey, "Air Trajectory Parameterization Technique for use in the Navy Aerosol Model", *Geophysical Sciences Technical Note No. 82*, Pacific Missile Test Center, Point Mugu, CA, 1983, pp. 19.
30. Battalino, T.E. and R.A. Helvey, "Air Trajectory Index for Electro-Optical Propagation Assessment at San Nicolas Island", *Geophysical Sciences Technical Note No. 93*, Pacific Missile Test Center, Point Mugu, CA, 1985, pp. 14.
31. Battalino, T.E. and R.A. Helvey, "Air Mass Parameterization in the Navy Aerosol Model", *Geophysical Sciences Technical Note No. 103*, Pacific Missile Test Center, Point Mugu, CA, 1985, pp. 25.
32. Battalino, T.E. and R.A. Helvey, "Air Mass Parameterization in the Navy Aerosol Model", *Proceedings of the Eighth Conference on Atmospheric Transmission Models*, Air Force Geophysics Laboratory, Hanscom AFB, MA, 1985, pp. 18.
33. Battalino, T.E., "Air mass characterization for optical propagation modeling in the coastal marine atmosphere", *Proceedings of the International Society for Optical Engineering (SPIE)*, Vol. 3125 *Propagation and Imaging through the Atmosphere*, San Diego, CA, 1997, pp. 47-58.
34. Mack, E.J., C.K. Akers, and T.A. Niziol, "Aerosols in the marine boundary layer", *Proceedings of the Second Conference on Coastal Meteorology*, Amer. Meteor. Soc., Los Angeles, CA, 1980, pp. 105-112.
35. Battalino, T.E., "Condensation nuclei air mass parameter", *Proceedings of the Environmental Support Technology 6.2 Spring Technical Review*, Office of Naval Technology Conference, Naval Ocean Systems Center San Diego, CA, 1990.
36. Battalino, T.E., "Numerical and Analytical Solutions of the Small Particle Amplitude in the Navy Aerosol Model", *Geophysics Technical Note No. 199*, Naval Air Warfare Center Weapons Division, Point Mugu, CA., 1996, pp. 20.
37. Battalino, T.E., "Numerical and Analytical Solutions of the Small Particle Amplitude in the Navy Aerosol Model", *Proceedings of the 19<sup>th</sup> Annual Review Conference on Atmospheric Transmission Models*, Phillips Laboratory, Hanscom AFB, MA, 1996, pp. 20.
38. Littfin, K.M., A. K. Goroch and T.E. Battalino, "Comparison of three methods of characterizing an air mass", *Proceedings of the 1997 Battlespace Atmospherics Conference*, Space and Naval Warfare Systems Center (SPAWAR), Technical Document No. 2989, San Diego, CA, 1997, pp. 10.
39. Smith, M.H., Personal communication, 1996.
40. Kneizys, F.X., E.P. Shettle, W.O. Gallery, J.H. Chetwynd Jr., L.W. Abreu, J.E.A. Selby, S.A. Clough and R.W. Fenn, "Atmospheric transmittance/radiance computer code LOWTRAN 6", AFGL-TR-83-0187, Air Force Geophysics Laboratory, Hanscom AFB, MA, 1983, pp. 200.
41. Battalino, T.E., "Measurements and Model Comparisons of Atmospheric Transmission at San Nicolas Island", *Proceedings of the Ninth Conference on Atmospheric Transmission Models*, Air Force Geophysics Laboratory, Hanscom AFB, MA, 1986, pp. 27.
42. Hughes, H.G., "Technique for Selecting An Aerosol Model Useful for Infrared Atmospheric Transmittance calculations", *NOSC Technical report No. 1282*, Naval Ocean Systems Center, San Diego, CA, 1989, pp. 16.
43. Jensen, D.R., C.R. Zeisse, K.M. Littfin and S.G. Gathman, "EOPACE (Electrooptical Propagation

- Assessment in Coastal Environments) Overview and Initial Accomplishments", *Proceedings of the International Society for Optical Engineering (SPIE)*, Vol. 3125 Propagation and Imaging through the Atmosphere, San Diego, CA, 1997, pp. 98-108.
44. Hutt, D.L., D. Dion, and J. Gilbert, "Comparison of marine aerosol model predictions with extinction and size distribution measurements", *Proceedings of the International Society for Optical Engineering (SPIE)*, Vol. 3125 Propagation and Imaging through the Atmosphere, San Diego, CA, 1997, pp. 37-46.
  45. Dion, D., D. Hutt, L. Gardenal, and J. Gilbert, "Accounting for vertical variation of turbulence and aerosol extinction in the marine surface layer", *Proceedings of the International Society for Optical Engineering (SPIE)*, Vol. 3125 Propagation and Imaging through the Atmosphere, San Diego, CA, 1997, pp. 157-166.
  46. van de Hulst, H.C., *Light Scattering by Small Particles*, Dover Publications, Inc., New York, NY, 1981, pp. 470.
  47. Littfin, K.M. and A. K. Goroch, "Determination of an air mass using nephelometer measurements and the Navy Aerosol Model", *Proceedings of the International Society for Optical Engineering (SPIE)*, Vol. 3125 Propagation and Imaging through the Atmosphere, San Diego, CA, 1997, pp. 59-65.
  48. Goroch, A.K., "Retrieval of size distribution information from nephelometer measurements" Naval Research Laboratory Technical Report (in press), Monterey, CA, 1997.
  49. Goroch, A.K., "Air mass parameter retrieval from nephelometer data in the Sea of Japan", *Proceedings of the 1997 Battlespace Atmospheric Conference*, Space and Naval Warfare Systems Center, Technical Document No. 2989, San Diego, CA, 1997.
  50. Ortiz, A.R. and T.E. Battalino, "QUICK BASIC Adaptation and Air Mass Parameter Modification of the Navy Aerosol Model", Geophysics Technical Note No. 209, Naval Air Warfare Center Weapons Division, Point Mugu, CA, 1998.
  51. Gerber, H.E., "Relative Humidity Parameterization of the Navy Aerosol Model (NAM)", NRL Report No. 8956, Naval Research Laboratory, Washington, D.C., 1985, pp. 13.

## PAPER No. 17

DISCUSSOR'S NAME: G. de Leeuw

## COMMENT/QUESTION:

The most important influence on the extinction in coastal areas is often the anthropogenic aerosol e.g., in the North Sea and Mediterranean. Is a natural tracer like Radon useful in this respect or would visibility be better? Could you give a recommendation of what to use?

Dr. Smith (CMAS, UK) used a volatility system to determine several anthropogenic contributions for the chemical composition. Do you expect this a promising road for future applications?

## AUTHOR/PRESENTER'S REPLY:

Radon has been used as an effective air mass tracer in the North Sea and over the Mediterranean area as well. It has a half-life of about 3.8 days. The relative changes in Radon concentration are more useful than the absolute Radon levels because Radon will vary with crustal radium deposits, which vary from location to location. Measurements of visibility would be better because it is not a relative measurement like Radon. It depends upon your application. If you want to know where the air mass came from then air trajectories would be best. If you want a general idea as to whether the air mass has a recent history over the sea or land, then Radon would suffice. If you want more quantitative information, then you must consider visibility and condensation nuclei. No one measurement of an air mass property can provide all the information required to fully characterize the air mass. If you have air trajectory information you may know something about the recent history or origin of the air mass, but you have little direct knowledge about the aerosol content. You would infer the aerosol content from the trajectory history. If you had condensation nuclei measurements you would have direct information about the aerosol content and infer the air mass history. The various methods of air mass analysis complement each other. If you must make a choice of one method over the others, then the specific application intended will dictate that choice.

Yes, sensitivity studies of the Navy Aerosol Model extinction to the air mass parameter reveal that the shorter wavelengths are most sensitive. The visual extinction coefficient responds to changes in the air mass parameter, which has been shown to be related to the condensation nuclei concentration, and should provide information about anthropogenic aerosols.



## AEROSOL TRANSPORT AND ORIGINS

J. Rosenthal  
T. Battalino  
L. Eddington  
R. Helvey  
C. Fisk  
D. Lea

Geophysics Branch (Code 521400E)  
Naval Air Warfare Center Weapons Division  
Point Mugu, California 93042-5001 USA

### SUMMARY

Electrooptical propagation assessments and air pollution studies both share a need to detect and measure the nature of aerosols. To forecast and model the effects of these aerosols requires the ability to trace particles to their origins, and to recognize and understand the processes whereby they're transported from source to impacted area. Since the transport may take place in the vertical as well as hundreds of miles in the horizontal, a detailed 3-dimensional view of transport mechanisms including vertical sampling over short time intervals is necessary. Two complimentary studies in coastal Southern California during summer 1997 contributed an unprecedented amount of data to better understand the process of aerosol transport. During the EOPACE Intensive Operation Period (IOP) during August 1997, aerosol and atmospheric properties were measured by Navy participants at the coast on islands, at sea on ships, in the air by both instrumented aircraft and various sounding techniques as well as by satellite. Simultaneously, the multi-agency Southern California Ozone Study (SCOS-97)/North American Research Strategy for Tropospheric Ozone (NARSTO) also conducted an intensive monitoring period extending from north of Point Conception to south of the Mexican border, and from west of San Nicolas Island to the Mojave Desert. During this study, a total of 6 aircraft, 26 radar-wind profilers, 11 radiosonde sites, 6 ozonesonde sites, lidars and about 150 surface observation sites monitored ozone, precursors, aerosols, tracers, and a wide range of meteorological parameters.

Data from the two overlapping data sets plus prior studies reveals complex circulation patterns whereby aerosols are transported from urban areas out to sea on diurnal land breezes only to return on the same or subsequent days to different locations on the mainland. Although the mixed layer is generally assumed to exhibit uniform conditions, evidence is available which show sharp wind shears within this region such that pollutants at the surface are sometimes transported in an opposite direction than at altitudes of only about 500 meters. A description of, and evidence for the complex transport processes observed are discussed.

### 1. INTRODUCTION

Prediction and assessment of electrooptical system performance as well as air quality both share a heavy dependence on the presence of aerosols. Their type, chemistry, size distribution and origins are critical in determining impacts on both the military and general public. This paper will focus mainly on the issue of determining aerosol origins, and on the meteorological complexity that is responsible for making source detection a non-trivial problem.

### 2. LARGE SCALE TRANSPORT MECHANISMS

It is well known that marine aerosols generated by wave action and bubble-burst [1] over ocean areas cover a large portion of the global atmosphere. Even though generated at sea or along coastlines, salt particles injected into the air from plumes [2] and through vertical mixing,

extend the particles through a deep layer where they serve as condensation nuclei. The larger particles settle out through gravitational forces, impact on surfaces, and precipitation, and their numbers are generally a maximum on the windward sides of coastlines. Horizontal winds also transport these particles of marine origin hundreds to sometimes thousands of miles inland, but their numbers are considerably reduced with increasing distance from the coast as well as vertical extent, and where precipitation systems are active.

Soil and dust particles from arid lands also are transported by the atmosphere, not only to other regions over land, but also over ocean areas. In particular, dust and sand from the African Sahara is frequently mixed through a deep layer of the atmosphere and transported westward across the Atlantic Ocean by the Trade Winds where the material is deposited through the Caribbean area and continental U. S. [3, 4]. Depending on the season and synoptic weather pattern, the dust offshore may also be incorporated into vortices and frontal systems with transport to Europe, as is suggested may be the case in figure 1.

Other sources of aerosol include material injected into the atmosphere during volcanic eruptions, combustion particles from wildfires (figure 2), and various types of anthropogenic sources of air pollution [5].

It is obvious that as aerosols travel higher into the atmosphere, their subsequent paths become more variable and complex.

In general, most studies on aerosol transport tend to depict transport as if it occurred all at one level. Some of this assumed simplicity is due to the relatively dense network of surface wind observations (where we perceive the effects of aerosols) and the general paucity of wind observations aloft. The fact that air pollution in general is a low-level phenomenon, make trajectories based on surface wind data especially useful.

On the other hand, an examination of water vapor satellite imagery (figure 3) reveals an interglobal and sometimes cross-hemispheric continuity of flow patterns at levels above 15,000 feet (> 5,000 meters) that is not revealed by simple examination of the few upper air stations that do exist. It is obvious that for aerosols that reach vertically well into the atmosphere, the impact of these upper winds also need to be taken into account.

### 3. SOURCE ATTRIBUTION TECHNIQUES

A number of methods are available to infer the source regions of aerosols. In all of these, a measurement of the gas or particulate of interest, or at least a surrogate indicator, is necessary as ground truth for the more indirect techniques; or as direct evidence of the displaced aerosol or pollutant.

Examples of direct techniques would be sampling of ozone, nitrogen oxides, large or fine particles, radon, condensation nuclei and hydrocarbons using chemical or lidar-based systems and particle counters. Examples of indirect methods would include air trajectory studies, satellite remote sensing techniques, nephelometers, and standard airfield visibility observations.

Among the indirect techniques, Wash & Davidson et al [6] at the U. S. Naval Postgraduate School in Monterey have demonstrated the ability of using multi-spectral satellite data to detect seaward plumes of continental aerosols revealed as anomalies in the optical depth. Additional indirect techniques are discussed in reference [7]; also, Littfin and Goroch [8] have demonstrated use of nephelometers as another promising tool for detecting time changes of aerosol conditions by obtaining an integrated measurement of backscatter.

Among the older techniques which are gaining renewed interest with the adoption of new air pollution standards in the U. S., analysis of visibility data permits tracking of low-visibility

air due to aerosols transported from one region to another. Rosenthal [9] demonstrated in 1967 how even widely-available airfield visibility reports can be analyzed over airport-dense areas like southern California to map the diurnal movement of smog during pollution-prone periods when temperature and humidity conditions precluded confusion between fog and pollution.

Of all the indirect techniques used in tracking aerosols and pollutants, the one that is best tied to the underlying meteorological causes that result in the transport is the use of air trajectories.

Individual trajectories can be constructed from successive positions of detected tracers at known locations in time [10]. Air trajectories can also be constructed, either forward or backward in time, based on a sufficient number of wind reports. Backward trajectories are most useful in tracing the possible "sources" or beginning points for a parcel of air that ends up at a known location. Forward trajectories are most useful in determining where a parcel will (or would have) moved to if the assumed forecasts of wind direction and speed were correct.

During the multi-agency Southern California Ozone Study (SCOS-97)/North American Research Strategy for Tropospheric Ozone (NARSTO), a forecast team was set up to predict when various pre-determined pollution transport scenarios would occur, and thus serve as a basis for mobilizing federal, state and local agencies to support a high intensive operating period. As part of this forecast effort, algorithms developed to construct moving point-to-point trajectories emanating from a single location, in one-hour time steps, using the predicted (one-hour) wind field produced by the Navy's Coupled Ocean-Atmosphere Mesoscale Prediction System (COAMPS) developed by the Naval Research Laboratory (NRL), Monterey, California [11]

An example of these trajectories, plotted at the validation time for a COAMPS 36-hour surface

wind forecast is shown in (figure 4). Of particular interest is how the local changes in wind in coastal regions result in the transport (of aerosols) from land to sea, and then back to land, over widely differing paths and locations, all emanating from a single point. Two important mechanisms are demonstrated from this simple example. One is the role of coastal eddies in the lower atmosphere, and the second is the regular diurnal turning of the wind near shorelines in response to land/seabreeze regimes.

#### 4. LOCAL WIND CIRCULATIONS AND METEOROLOGICAL COMPLEXITIES

It is readily evident that individual clouds, smoke and pollutants tend to be carried with the wind at that level [12]. So it should be no surprise that varying, but recurring wind features would be prime mechanisms in transporting aerosols to regions different from what might otherwise be expected from consideration of such simplistic features as the prevailing wind.

Along the coast of Southern California, the combination of large scale (synoptic) forcing plus topographic mountain barriers along the coastline result in mesoscale eddies over the adjacent offshore waters (figure 5). Usually termed the "Catalina Eddy" due to their proximity to Catalina Island, [13, 14] these features result in low level southeasterly flow over coastal regions contrary to the usually assumed prevailing northwesterly winds. The result is that smoggy aerosols from the Los Angeles Basin are transported northwestward (both due to overland and over water routes) to adjacent basins in different counties where their origin is a surprise to some.

Lea et al [15, 16, 17, 18] described how southeast winds along the coast form a principal route for smog transport to areas north and west of Los Angeles. Southeast winds are not limited to coastal eddies; they are typical pre-frontal winds during the cool season (and in spite of the lower sun angle which limits photochemical formation of ozone, are still effective in

transporting aerosols), and also following Santa Ana (offshore wind) conditions [18, 19, 20, 21, 22].

Importantly, the southeast flow may not always be in evidence at the surface itself. Sometimes, within a deep southeast, transport current, a very shallow westerly sea breeze may develop at ground-level within the polluted air mass making the source of the pollution more difficult to identify. Under these conditions however, the southeast wind responsible for the transport is almost always in evidence at all levels of about 1,000 to 2,000 feet or above. Thus, upper air winds, or measurements made on higher terrain are important clues to where the transport is actually coming from.

An excellent example of transport under this situation was developed using data compiled during SCOS-97. Figures 6a through 6c are surface wind analyses selected at 12-hour intervals from a series of 6-hourly charts, during a smoggy episode. At Point Mugu and adjacent Laguna Peak (1500 ft elevation) at the coast, the 3 analyses indicate southwest winds at 00Z on 6 August 1997, light southerlies at 12Z, and westerly winds at 00Z on 7 August. On Laguna Peak, under generally hazy conditions, measurements of ozone continued to increase during the day reaching a peak value of about 142 parts per billion at about 03Z on 7 August (figure 7). Surface winds were difficult to use to explain the source region. At this time, winds at the surface were northwest at 3 knots as measured at the airfield. However, examination of the winds measured on Laguna Peak near the ozone monitor revealed a steady period of southeast winds during the late afternoon and evening from about 18Z on the 6th to about 5Z on August 7th (figure 8). At the same time that the surface winds were northwest at 3 knots, the winds on Laguna Peak were southeast at 10 kts. This was a clear example of aerosol and smog transport riding on a current of air blowing at low levels from the Los Angeles Basin, but not extending down to the surface itself where a shallow sea breeze prevailed. Similar episodes were documented over 30 years ago by Lea [19].

Even though trajectory analyses at the surface can be used successfully to reveal aerosol transport, a much clearer picture is obtainable when upper air (and/or higher terrain) measurements are also available. In some cases, they may be essential to reveal the true 3-dimensional structure of aerosol transport.

## 5. DIURNAL VARIATIONS

While diurnal variations of the wind are common, these cyclic reversals under otherwise persistent weather conditions are most noteworthy along coastlines where the wind switches back and forth between onshore and offshore, depending on the time of day. During the afternoon sea breezes, marine aerosols make their way landward. At night and early morning, offshore breezes bring continental aerosols out to sea. In shifting from one regime to the other, there is often a period of along-shore winds which are effective in transporting polluted urban aerosols from one locality to another. This diurnal sloshing about of dirty continental air was described by Rosenthal [9] during a smoggy heat wave in October 1965. Airfield visibility observations from throughout southern California were analyzed each hour with contours of visibility values (in miles) interpolated both forward and backwards in time for consistency. The high temperatures that prevailed during the period precluded fog as a complicating factor in ascribing low visibility air to smoggy aerosols from land areas. Figures 9a through 9d show the successive location of the smoggy air at 0800, 1400, 1700 and 0200 the following day, local time. At night, under the influence of land breezes, the smoggy aerosols are displaced largely towards the coast and out to sea. In mid-morning, as the winds veer, the continental aerosols are transported in part, up the coast to Ventura County. Afternoon sea breezes bring this transported portion in to inland valleys, while the bulk of the dirty air over the sea is returned to progressively further inland areas. At night, the cycle resumes. In this manner, electrooptical systems operating in a littoral environment will be influenced by an alternating mix of air mass factors and IR extinction [7, 20].

Figure 9e shows the approximate maximum seaward extent of the smoggy air during this episode. Figure 10 shows a period of transport "down" the coast to San Diego during a period of northerly winds during this episode.

## 6. AEROSOLS IN THE INVERSION LAYER

While the horizontal winds are primarily responsible for aerosol transport over long distances, several mechanisms are also underway which facilitate displacing the aerosols from one horizontal current to another. One of these mechanisms involves aerosols being vented up the heated slopes of mountains in the daytime from where it may be re-directed seaward by the returning arm of the sea breeze aloft.

Another mechanism results in continental aerosols being injected into the inversion layer when radiational cooling within a clear polluted layer results in formation of a shallow inversion. Increased intrusion of marine air results in a deeper and deeper mixed layer while the new polluted air aloft remains in the strengthened inversion from where it is transported by winds at that level. Smoggy air transported in this manner may come back to the surface when it intersects higher terrain, or when mixed downward by fumigation.

## 7. COINCIDENT WIND AND AEROSOL MEASUREMENT

Virtually every method employed for detecting and tracking aerosol transport requires a detailed description of the local wind field in time, whether that be in 2 or 3 dimensions. Such coincident measurements of wind and pollutants are typically maintained over relatively small spatial domains as part of air pollution monitoring networks established in local districts. Since transport involves wind circulations that transgress both the meso and synoptic scale, accurate understanding of the significance of transport requires coincident measurements of winds and pollutants over a much larger domain.

Field data collection programs which marshal the needed resources to accomplish such undertakings are infrequent. In 1978 the Navy's Cooperative Experiment for West Coast Oceanography and Meteorology (CEWCOM) directed by Naval Oceans System Center under the sponsorship of Naval Air Systems Command resulted in a large amount of valuable data [23]. In summer 1997, two additional significant and independent efforts occurred simultaneously, and the synergistic benefits of the data collection efforts provides an unprecedented opportunity for examining the role of transport. One effort was the Electro-optical Propagation Assessment in Coastal Environments (EOPACE) managed by the Propagation Division, SPAWAR Systems Center, San Diego under the sponsorship of the Office of Naval Research (ONR) [24, 25]. The other program, in which the Navy was an active participant under the sponsorship of the Chief of Naval Operations (N457) was the Southern California Ozone Study (SCOS-97) and the North American Research Strategy for Tropospheric Ozone (NARSTO). Under EOPACE and SCOS-97, both programs completely characterized the volume in which transport takes place with a multitude of surface, upper air (rawinsonde), aircraft, lidar, nephelometer, condensation nuclei, ship, satellite and networks of monitoring stations. Under SCOS alone, managed by the State of California Air Resources Board (CARB), a total of 26 radar profilers, 6 aircraft, 14 radiosonde stations, 6 ozonesonde stations, lidars, about 250 surface stations and various analytic tools were employed from north of Point Conception in California to south of the Mexican border, and from the open sea east to the deserts. Since aerosol transport obeys no political or jurisdictional boundaries, the large domain ensures that adequate data is available to detect and understand the transport that occurred during several differing episodes. The following paper by Helvey [26], will discuss transport of air mass characteristics during CEWCOM, using trajectory analysis.

## 8. CONCLUSIONS

Meteorological features and complexities transport pollution and continental aerosols far out to sea, and the resulting changes in air mass parameters can significantly impact electro-optical system performance in the littoral zone. Aerosol transport is both episodic (synoptic and mesoscale events), and diurnal in nature, with long-shore transport occurring in addition to reversals between offshore and onshore components. Accurate observation, assessment and prediction of aerosol transport requires a coincident set of wind and particulate / precursor / aerosol data. Importantly, winds just above the surface may be substantially different than at the surface itself which can be critical in tracing the origins of aerosols. Field measurement programs like CEWCOM, EOPACE and SCOS-97, which derived 3-dimensional characterizations of the lower atmosphere may provide the data needed for accurate trajectory and modeling studies, and together with remote sensing data may permit a full understanding of the transport problem.

## ACKNOWLEDGMENTS

This work was supported in parts by the SPAWAR Systems Center, San Diego, Division 88, EOPACE Program (Dr. Juergen Richter) under the ONR Exploratory Development Program, and by the Shore Compliance Branch (Mr. Ron Tickle) of the Chief of Naval Operations (N457).

## REFERENCES

1. Hidy, George N, "Aerosols" Academic Press, Inc. (1984)
2. Philbrick, C. R., "Atmospheric Optical Extinction Measured by Lidar", Penn State University, NATO AGARD/RTA Sensors & Electronics Technology Panel Meeting, Naples, Italy, March 1998
3. Westphal, D., O. B. Toon and T. N. Carlson, 1988, "A Case Study of Mobilization and Transport of Saharan Dust", J. Atmos. Sci., vol 45
4. Karyampudi, V. Mohan and Toby N. Carlson, "Analysis and Numerical Simulations of the Saharan Air Layer and Its Effect on Easterly Wave Disturbances", Journal Atmospheric Sciences, vol. 45 No. 21, 1988
5. Limaye Sanjay, Patrick M. Fry and Steven A. Ackerman, "PC-McIdas in Satellite Monitoring of Oil-Fires in Kuwait Expedition (Smoke)", Space & Science & Engineering Center, 6th conference on Satellite Meteorology and Oceanography Jan 5-10, 1992
6. Wash, C., G. deLeeun, M. Jordan and K. Davidson, "Satellite and Ship Based Lidar Measurements of Optical Depth During EOPACE", Proceedings the 1997 Battlespace Atmospheric Conference, 2-4 Dec 1997
7. Battlino, Terry, "Air Mass Characterization For EO Propagation Assessment", NATO AGARD/RTA Sensor & Electronics Technology Panel Meeting, Naples, Italy March 1998
8. Littfin, Kathleen, A. Goroch, "Determination of the Origin of an Air Mass using Nephelometer Measurements and the Navy Aerosol Model", SPIE Proceedings of the Conference on Propagation and Imaging through the Atmosphere", vol. 3125, pp 59-65, 29-31 Jul 1997
9. Rosenthal, Jay, "Diurnal and Synoptic Changes in Visibility Patterns During a Heat Wave Over Southern California", American Meteorological Society at the Conference on Fair-Weather Meteorology", Santa Barbara, CA, Feb 1967
10. Battalino, T. E. and R. A. Helvey, "Air Mass Trajectories and Atmosphere Radon Measurements During the EOMET/OSP Experiments on San Nicolas Island (1978-1980), Pacific Missile Test Center, Technical Publication TP 1, Point Mugu, CA 1982

11. Hodur, R., "The Naval Research Laboratory's Coupled Ocean/Atmosphere Mesoscale Prediction System (COAMPS), Monthly Weather Review, vol. 125, 1997, pp. 1414
12. Rao, S. T., I. G. Zurbenko, R. Neagu, P. S. Porter, J. Y. Ku, and R. F. Henry, "Space and Time Scales in Ambient Ozone Data", Bulletin American Meteorological society, 1997, pp 2153-2166
13. Thompson, William T., Stephen D. Burk, and J. Rosenthal, "An Investigation of the Catalina Eddy", Monthly Weather Review, vol. 125, No. 6, June 1997
14. Rosenthal, Jay, "Picture of the Month, -A Catalina Eddy", Monthly Weather Review, vol 96, No. 10, Oct 1968
15. Lea, Duane, Roger A. Helvey, Jay Rosenthal, Lee Eddington, Charles Fisk, "A Review of Air Pollution Transport Mechanisms Affecting Ventura County", Geophysics Technical Note No. 192, Naval Air Warfare Center, Point Mugu, Feb. 1995
16. Eddington, Lee, Jay Rosenthal, Roger Helvey, Chuck Fisk, Terry Battalino, "A Review of Meteorological Studies Pertaining to Southern California Offshore Ship Emissions and Their Effect on The Mainland", Geophysical Sciences Technical Note No. 200, Naval Air Warfare Center, Point Mugu, CA, Feb. 1997
17. Helvey, Roger A., "A Smog Transport Mechanism in Coastal Southern California", video tape, Geophysics Branch, Naval Air Warfare Center, Point Mugu, CA, 1995
18. Rosenthal, Jay, "Point Mugu Forecasters Handbook" Pacific Missile Range, PMR-TP-72-1, Point Mugu, CA, 1 Apr 1972
19. Lea, Duane A., "Vertical Ozone Distribution in the Lower Troposphere Near an Urban Pollution Complex", J. Applied Meteorology, vol. 7, pp 252-267, 1968
20. Dorman, Clive, "Winds Between San Diego and San Clemente Island", Journal of Geophysical Research, vol. 87 No. C12, 1982 pp 9636-9646
21. California Air Resources Board, "Air Analysis Comments", California Air Quality Data, vol. 1X, No. 3, 1977
22. Lea, Duane, "Easterly Winds in the Lower Troposphere Over Coastal Southern California" (Draft Report) Geophysics Branch, Naval Air Warfare Center, Point Mugu (1997)
23. Rosenthal, Jay, T. Battalino, and V. R. Noonkester, "Marine/Continental History of Aerosols at San Nicolas Island during CEWCOM-78 and OSP III", Pacific Missile Test Center Technical Publication TP-79-33, Point Mugu, CA, 1979
24. Richter, Juergen, "Electrooptical Propagation Assessment in Coastal Environments (EOPACE), NATO AGARD/RTA Sensors & Electronics Technology Panel Meeting, Naples, Italy, March 1998
25. Jensen, Doug, "Air Mass Parameterization and Coastal Aerosol Modeling", NATO AGARD/RTA Sensors & Electronics Technology Panel Meeting, Naples, Italy, March 1998
26. Helvey, Roger and T. Battalino, "Air Trajectories and Airmass Characteristics in the Southern California Coastal Region", NATO AGARD/RTA Sensors & Electronics Technology Panel Meeting, Naples, Italy March 1998



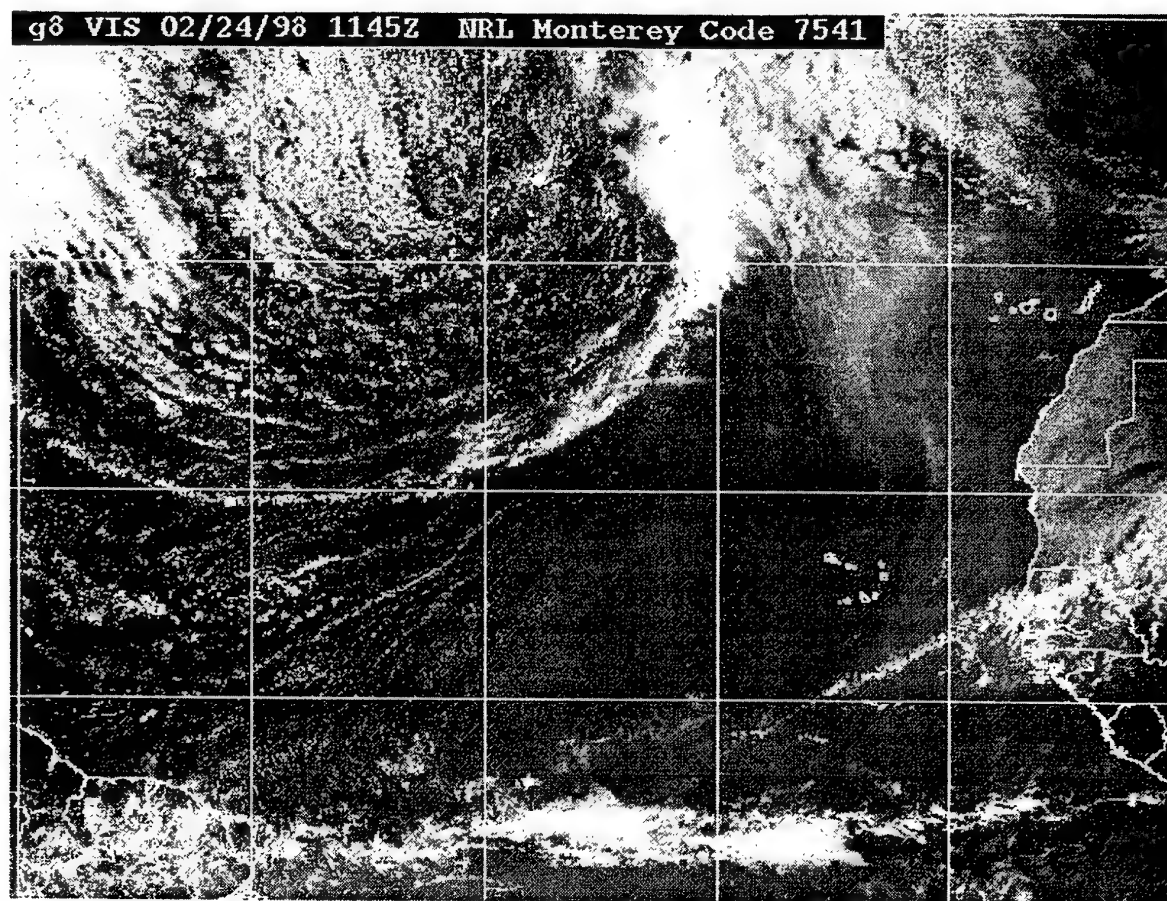


Figure 1. GOES 8 visual satellite image showing widespread African dust cloud offshore ready to be entrained into frontal systems moving towards Europe. (Image provided by courtesy of Doug Westphal, NRL, 25 Feb 98)





Figure 2. Combustion particles from wildfires blown out to sea

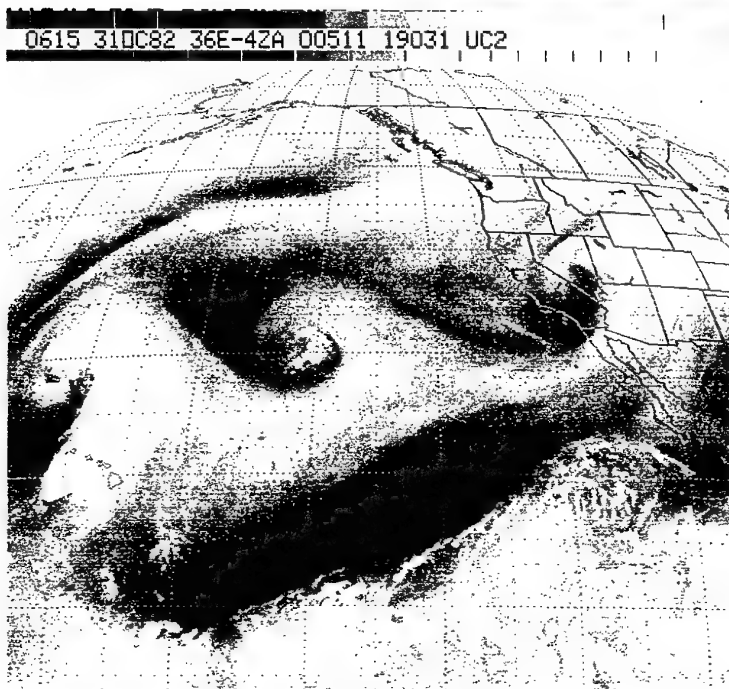


Figure 3. Large-scale circulation patterns in middle troposphere (as seen on water vapor Imagery) capable of transporting aerosols between land and ocean areas.

COAMPS 12.5 m Streamline/Transport 36 HR FCST (knots)  
12Z 15 Apr '97

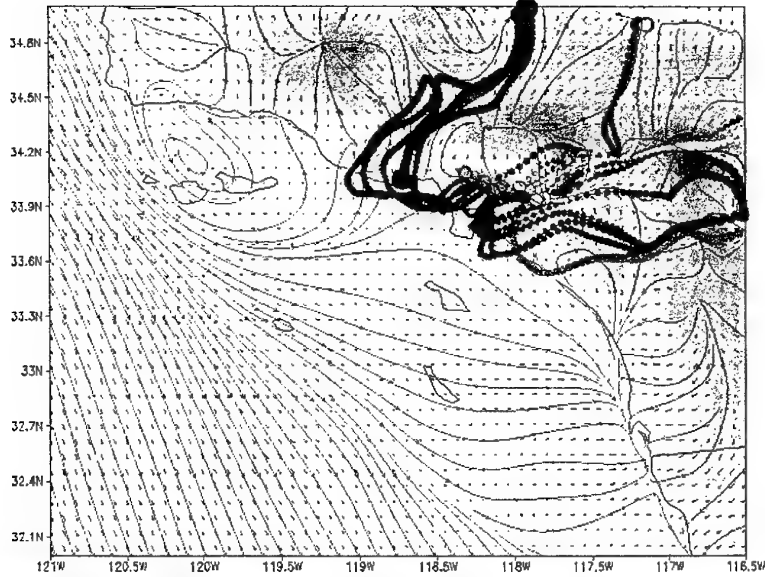
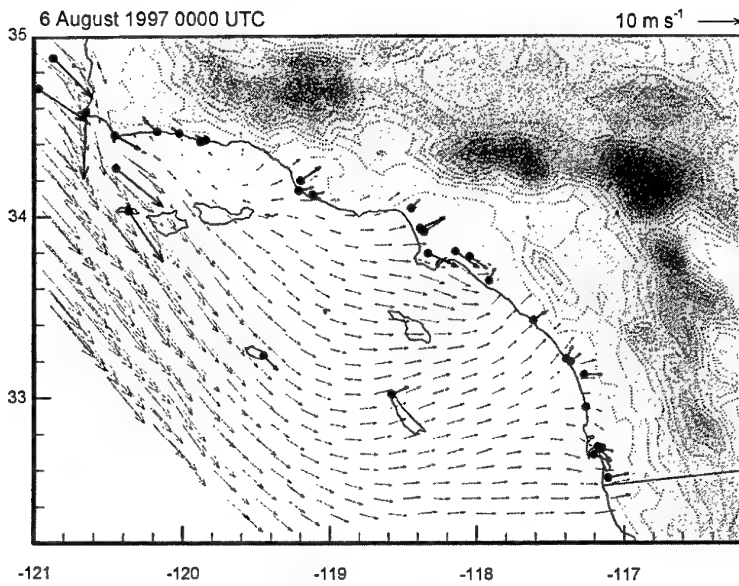


Figure 4.  
Hour-by-hour surface trajectories from  
single point in Los Angeles Basin based on  
hour-by-hour COAMPS wind predictions  
(plotted on 36-hour forecast). Used in  
predicting transport conditions during  
SCOS-97



Figure 5. Satellite view of 'Catalina Eddy' off (and  
over ) coastal Southern California.



## SURFACE WIND VECTORS

Figure 6a. Surface wind analysis during SCOS-97 on 6 Aug 1997 at 0000 UTC

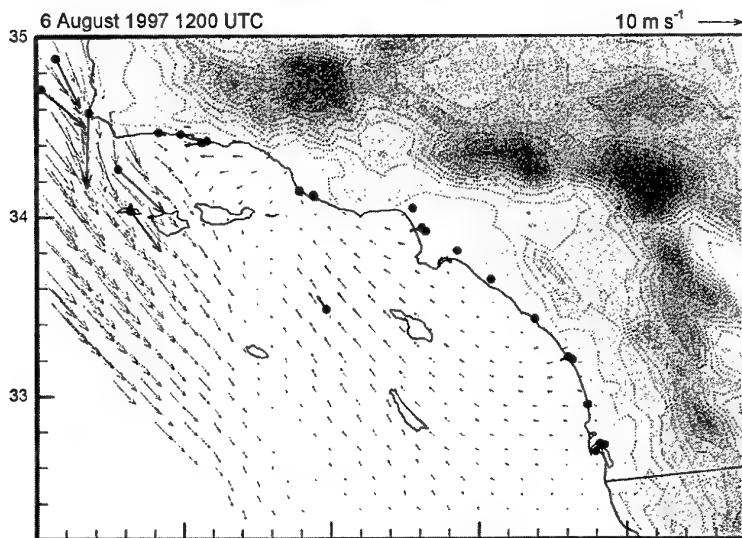


Figure 6b. Surface wind analysis during SCOS-97 on 6 Aug 1997 at 1200 UTC

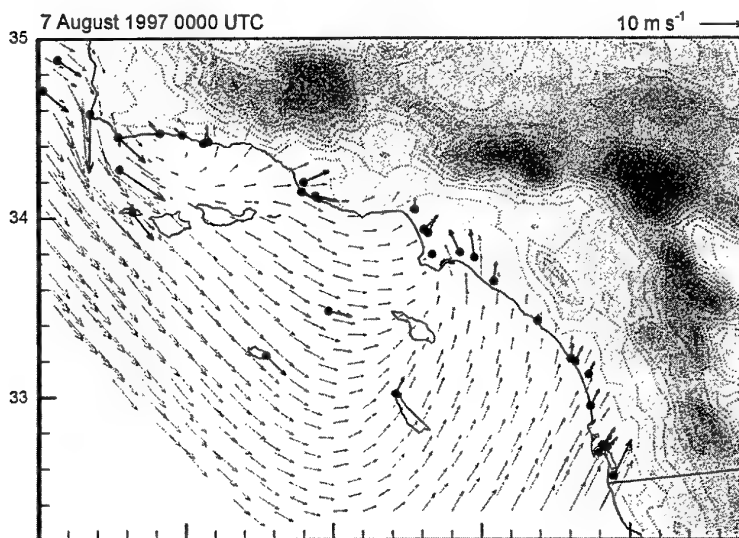


Figure 6c. Surface wind analysis during SCOS-97 on 7 Aug 1997 at 0000 UTC

## 1997 Laguna Peak Ozone

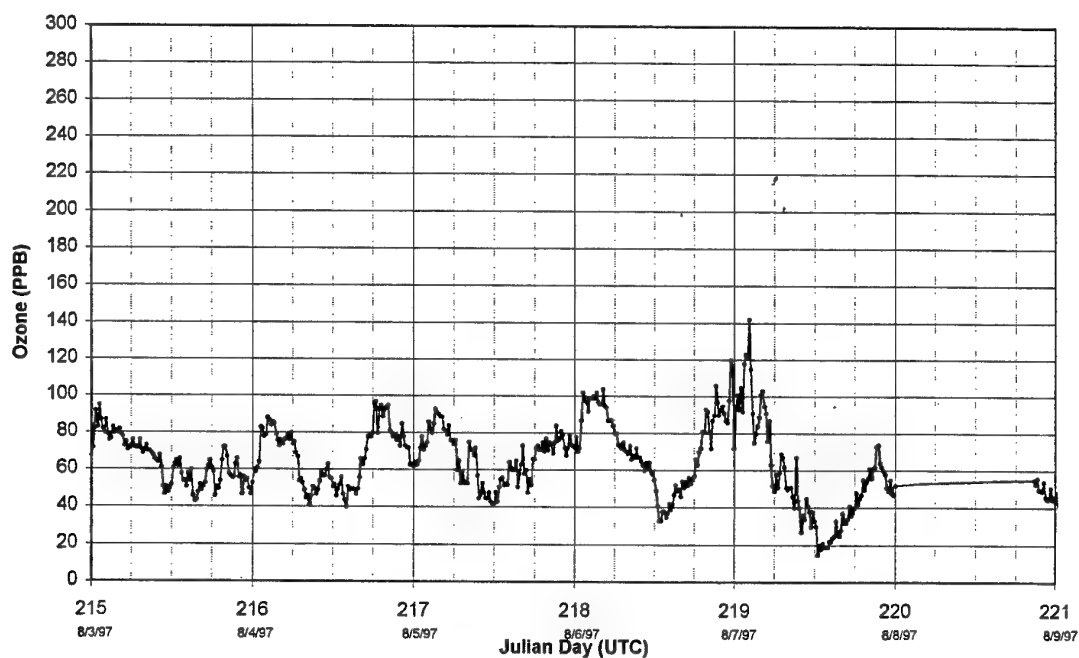


Figure 7. Time section of Laguna Peak ozone during SCOS-97

## Laguna Peak Wind Speed and Direction

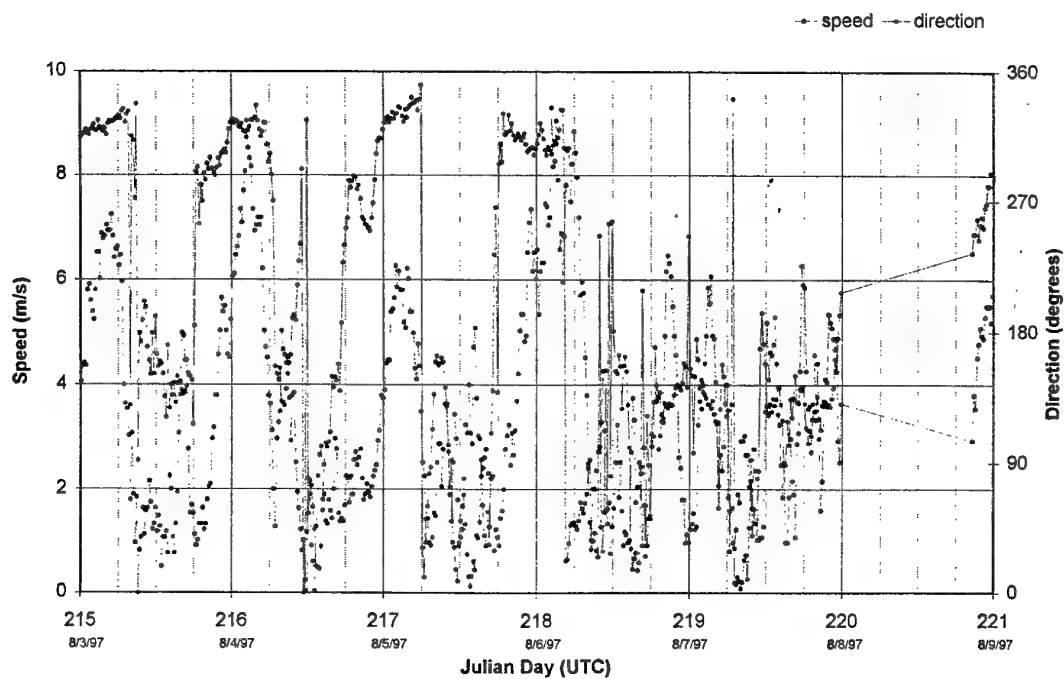


Figure 8. Time section of Laguna Peak wind speed and direction during SCOS-97

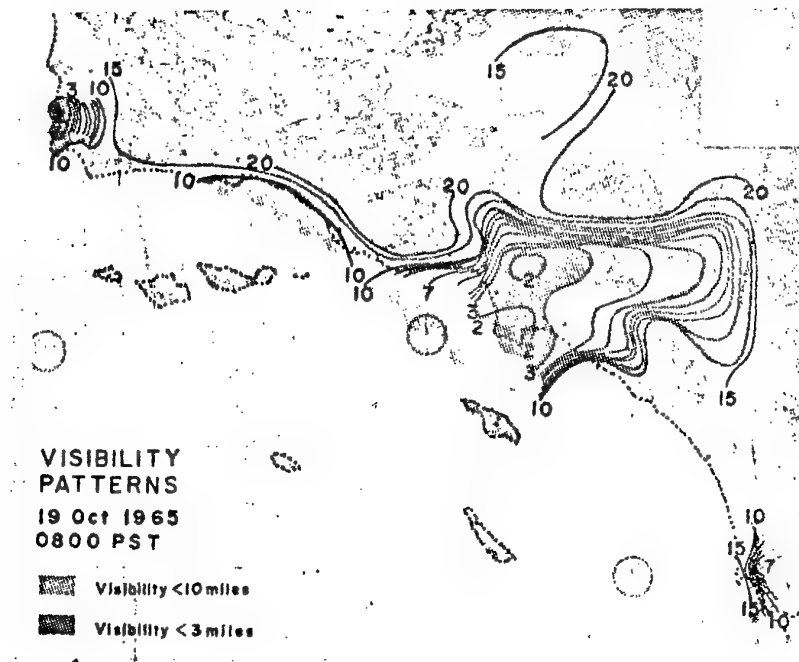


Figure 9a. Isopeths of visibility (miles), 08 PST, 19 October 1965. Heavier shading indicates regions in which reported visibilities are 3 miles or less.

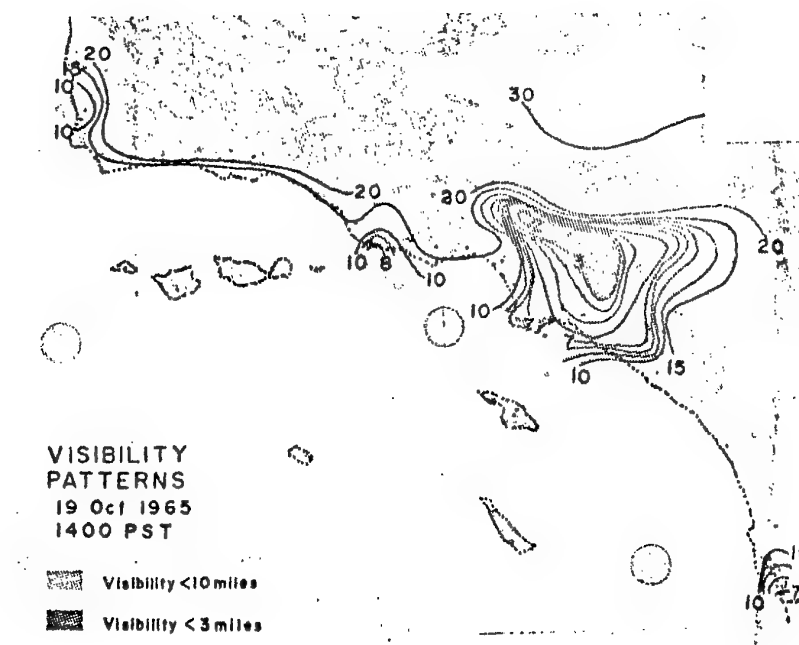


Figure 9b. Same as figure 9a except at 14 PST, 19 October 1965.

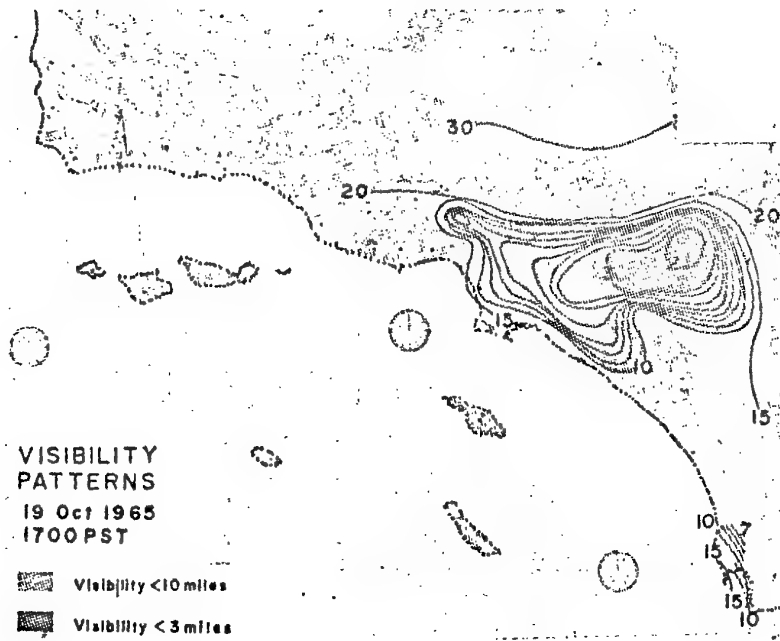


Figure 9c. Same as figure 9a except at 17 PST,  
19 October 1965.

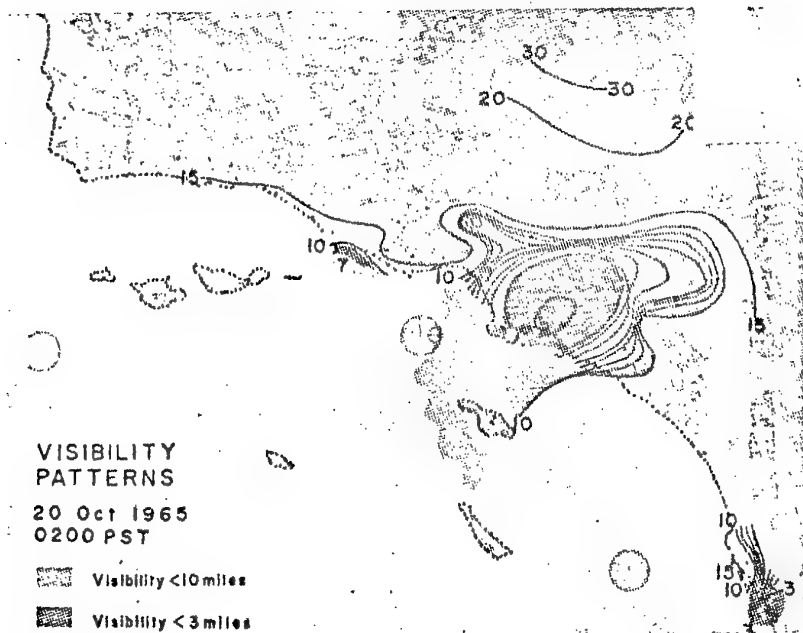


Figure 9d. Same as figure 9a except at 02 PST,  
20 October 1965.

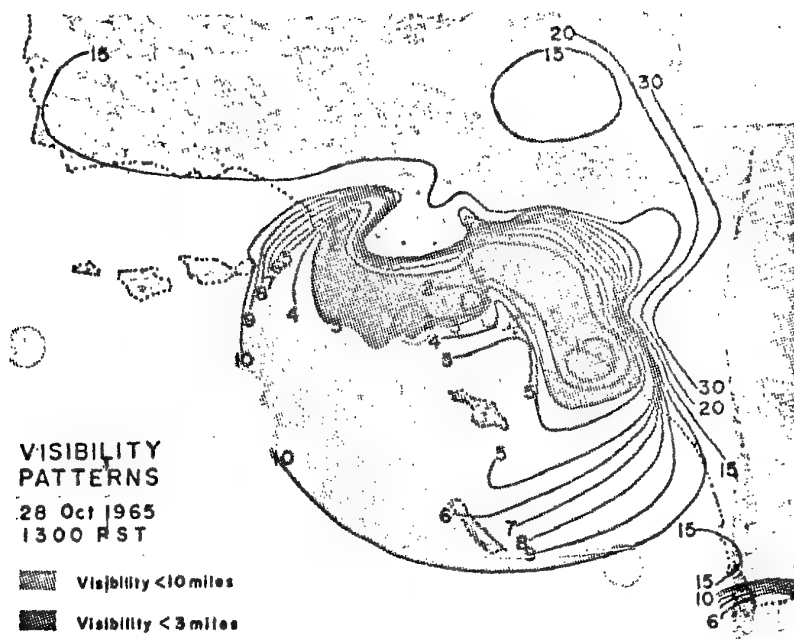


Figure 9e. Same as figure 9a except at 1300 PST,  
28 October 1965.

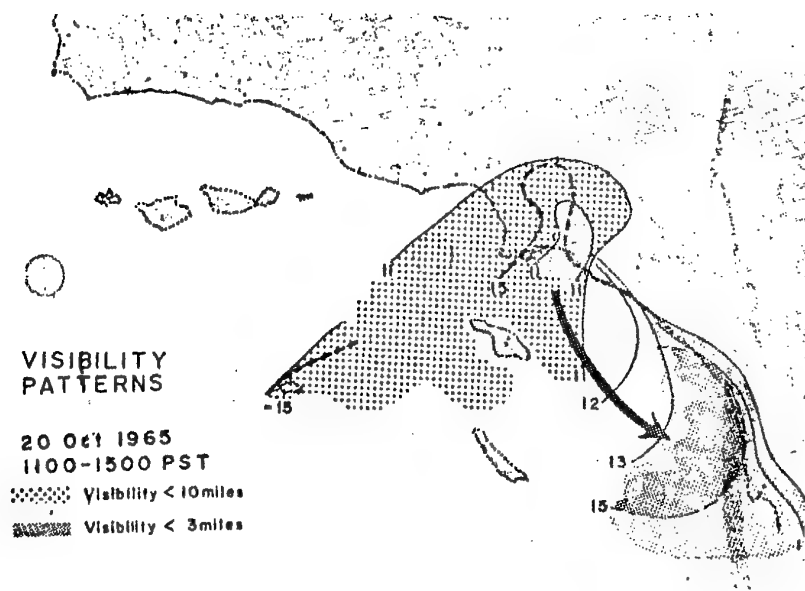


Figure 10. Transport to San Diego in northerly flow.  
Isochrones of 10-mile visibility, 11-15  
PST, 20 October 1965. Overlapping  
portion of 15 PST isochrone is dashed for  
improved demarcation. Regions in which  
reported visibilities are 10 miles or less are  
indicated by bold stippling at 11 PST and  
by cross-hatching at 15 PST. Regions in  
which reported visibilities are 3 miles or  
less are indicated by fine stippling at 11  
PST and by overlapped cross-hatching at  
15 PST. Arrow indicates suggested  
direction of movement of 3-mile visibility  
air.

## Air Trajectories and Air Mass Characteristics in the Southern California Coastal Region

Roger A. Helvey  
Terry E. Battalino  
Geophysics Branch (Code 521400E)  
Naval Air Warfare Center Weapons Division  
Point Mugu, California 93042-5001 USA

### 1. SUMMARY

In this paper certain techniques are described which support analysis and prediction of meteorological conditions in the natural environment affecting electrooptical propagation. The techniques, utilizing computed air trajectories, have been initially applied by us to data from the CEWCOM program [1] conducted from 1978 to 1980 at San Nicolas Island, and will be exercised in subsequent work with additional data sets from several more recent electrooptical and air pollution measurement programs. Evidence for effects of transport and related weather factors on aerosol variations and electrooptical extinction computed from the Navy Aerosol Model (NAM) is presented.

### 2. INTRODUCTION

The contribution of aerosols to extinction of electrooptical energy has been expressed in terms of several parameters in the Navy Aerosol Model [1]. The smaller particles, denoted "A1" in the NAM, produced largely by anthropogenic sources especially important in populated and industrial areas, are very persistent once introduced into the atmosphere. Hence concentrations accumulated in these areas can be transported downwind for considerable distances over periods of several days, as opposed to larger aerosol components which are more dependent on local factors and conditions for shorter time scales. Computed air trajectories, using a Lagrangian technique based on wind analyses from observations or numerical models provide a means of tracing atmospheric contaminants forward and backward in time once they have been observed, but prediction of visibility variations additionally depends upon adequate specification of particulate production in source locations, and the spatial distribution of the contaminants at an initial time. The methods described here may be useful for both of these problems.

An intermediate-sized component, denoted "A2" in the NAM, originates from wind action on the sea, and although somewhat less persistent than the A1 mode aerosols still requires specification of wind conditions for a substantial period preceding the desired electrooptical propagation assessment. In the NAM this is provided in the form of 24-hour mean winds observed at the location of interest. An alternative approach will be suggested which should constitute a more realistic basis for calculation of the A2 aerosol, especially in coastal areas.

### 3. MEASURED INDICATORS

Radon, a radioactive gas emitted from the soil has been found to be a useful indicator for estimation of the A1 aerosol component. This is due to two essential considerations: it originates almost entirely over land areas as do the relatively small A1 mode aerosols, and it together with its daughter products has an intrinsic half-life (3.8 days) which roughly approximates the longevity in the lower atmosphere of the small

particulates of interest. However, the association is indirect, and radon measurement instrumentation for this application is not widely available and can be somewhat troublesome to operate reliably. Condensation nuclei (CN) concentration has been under investigation as a possible replacement because it is directly related to the aerosol content of the air. An example of both types of data obtained concurrently is given in Figure 1, from measurements at the sea level site at the northwest tip of San Nicolas Island during 7 to 25 May, 1978. Radon was also measured from the research ship Acania, which was in the southern California coastal region most of the period, even if not always in close proximity to the Island site. The radon and CN

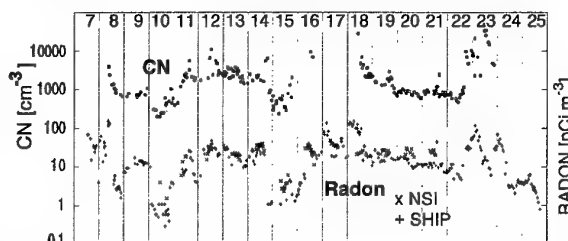


Figure 1. Condensation nuclei (CN, upper points) and radon (lower) measured at northwest tip of San Nicolas Island, for 7 to 25 May 1978. Also plotted is radon observed from a research vessel which was near the Island much of this period. The three sets of data vary in concert, all reflecting basically the same changes in air mass history.

vary in a similar manner. This is demonstrated more clearly in Figure 2, where both have been converted into an equivalent Air Mass Parameter (AMP), using established relationships [2,3]. The AMP governs the level of the A1 aerosol component and resulting extinction predicted by the Navy Aerosol Model. For reference, on the right side of the graph is an extinction scale, determined by holding NAM input parameters which control other aerosol size modes, to specified values (instantaneous and mean wind speeds of 5 m/s, relative humidity 80%).

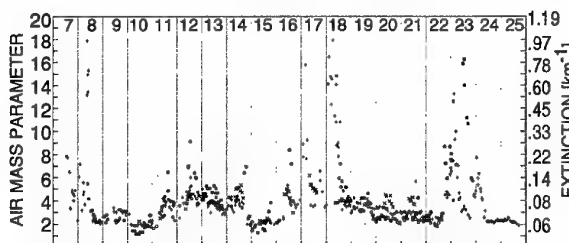


Figure 2. Air Mass Parameter (AMP) computed from CN and radon measurements, 7 to 25 May 1978. AMP scale is at left. Extinction coefficient scale at right is for corresponding A1 magnitude from the Navy Aerosol Model, with instantaneous and mean speeds of 5 m/s and relative humidity 80%.



#### 4. TRAJECTORY APPLICATIONS

In-situ measurements such as those described above are necessarily diagnostic in that they can only represent conditions for a limited region of time and space around the point of observation. Over wider areas, and for conditions at a future time, in addition to the predicted wind field and mixing depth it will be necessary to have knowledge of the location and strength of aerosol sources over an extended region, and the distribution of aerosol concentrations at an initial time. Remote sensing from satellites is one possible way information on the spatial distribution can be obtained. Another is by construction of air trajectories to estimate spatial variations of relatively conservative properties of an air parcel, such as A1 aerosol or related long-lived indicators in either an upstream or downstream direction with respect to one or more measurement sites. (These sites can themselves be moving, as in the case of ships). If the aerosol sources and initial spatial concentration are known, then construction of forward trajectories from observed winds or numerical model fields furnishes a basis for prediction of future spatial patterns and concentrations at points of interest.

##### 4.1 Streaklines

Atmospheric trajectories are the track of an air parcel in a forward or backward sense, from a specified fixed point. A single parcel of air is represented, at different positions in time. *Streaklines* are a related but different kind of track; they show the positions of different parcels of air at some specified time; these parcels are related in that they have passed over the reference site at some past time (a forward-streak, or plume), or will pass over the site at some future time (a backward streak). This characteristic suggests the use of streaks as an aid in analysis of air mass properties which change slowly during the movement of an air parcel, since the time series data at a particular site can be extrapolated forward or backward spatially along such lines.

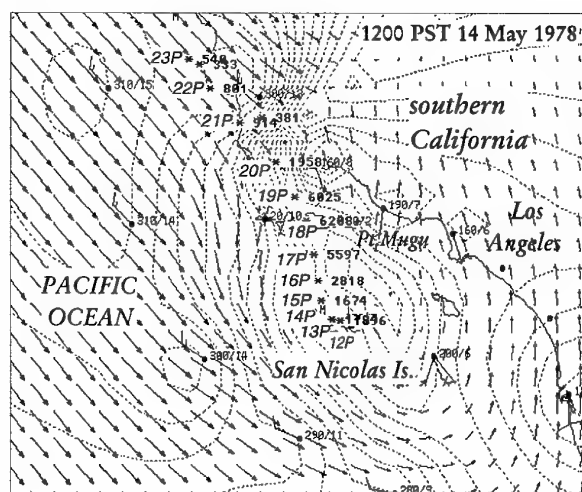


Figure 3. Wind observations and analyzed wind vectors, with hourly backstreak positions from 1200 PST 14 May 1978. Dotted lines are isotachs at 1-knot intervals. Hour is indicated to left of backstreak positions and CN concentration on subsequent arrival at terminus (San Nicolas Island) given on the right. Parcel positions are based on air trajectory calculations using a sequence of this and previous hourly gridded wind fields. For properties of the air parcel which are conserved during this period, the measured values upon arrival at San Nicolas Island can be extrapolated along the backstreak line to provide an estimate of the spatial distribution of the observed parameter.

Figure 3 shows wind observations and gridded wind vectors obtained by interpolation over coastal southern California, for 1200 PST 14 May 1978. Wind speeds are contoured at 1-knot intervals. A backstreak line emanating from the site at the northwest tip of San Nicolas Island has been constructed using an hourly sequence of such data, by computing back-trajectories for each of the parcels separated by one hour along the line (in terms of their individual arrival times at the Island). The times indicated are progressively later with distance upstream of the Island. Values of condensation nuclei concentration are plotted alongside the hourly points, under the assumption that those persist to reach the Island as observed subsequently. It can be noted that values first increase, then decrease with distance northwest along the line. This strongly suggests a real spatial variation, with the highest values over the Santa Barbara Channel (6025 particles per cubic cm) at 1200 PST, and much cleaner air over the ocean to the northwest. Although the backstreaks for a single site will generally be insufficient for a two-dimensional spatial interpretation, consideration of trajectories and backstreaks for earlier times do permit such a construction in this case because of special meteorological conditions.

During 13-14 May 1978 the southern California bight was occupied by a cyclonic (counter-clockwise) wind pattern in the marine layer known locally as a "Catalina Eddy". On the 13th winds at San Nicolas Island were from the southwest, around the base of this eddy pattern, during which time CN concentrations from 1600 to 3800 particles per cm were measured. Subsequently this air proceeded northward just off the coast near Los Angeles, then turned west and southward to reach the Island late on the 14th with CN concentrations over 6000 particles per cubic cm, an increase of about 4000. Figure 4 compares CN concentrations before and after this increase took place. Ordinarily this change would invalidate the use of values along the backstreak line for spatial analysis, but the earlier pass by the Island established the amount of change, which could then be

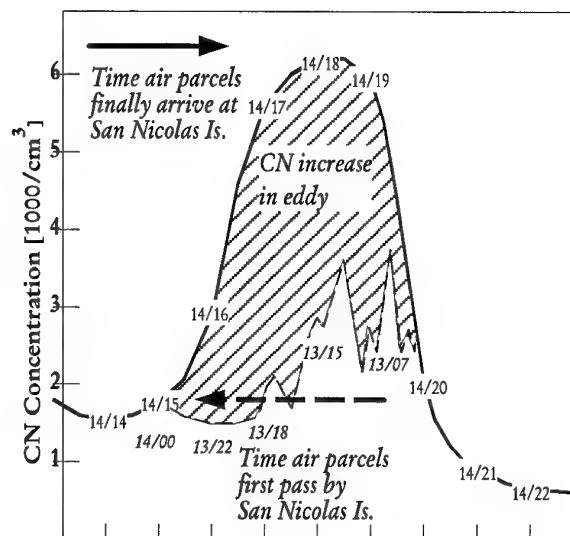


Figure 4. Condensation nuclei (CN) increase in eddy circulation off southern California coast, 13-14 May 1978. The concentration increased by approximately 4000 particles per cc during the period, as indicated by trajectory analysis showing values around 1500 to 3800 when the air initially passes over or near San Nicolas Island on the 13th, rising to 6200 on subsequent arrival at the Island measurement site on the 14th.

considered in the analysis. A probable reconstruction of the spatial pattern is shown in Figures 5a and 5b, at 0600 and 1800 PST 14 May 1978 respectively. The reason for the increase in concentration is strongly suggested by a temporary period of winds from the east, presumably carrying air pollution offshore from the Los Angeles area around 0600 PST. At this time, winds (not shown) were similarly easterly atop Laguna Peak at 1500 feet altitude near Point Mugu, so that mixing down of polluted air aloft may also have contributed to the region of high concentrations shown. The heavy lines are isopleths which outline the probable region of highest concentrations indicated by values along the backstreak line, an area about 20km across, which enveloped the Island at 1800 PST before being replaced by much cleaner air from the northwest a few hours later (as seen in Figure 3).

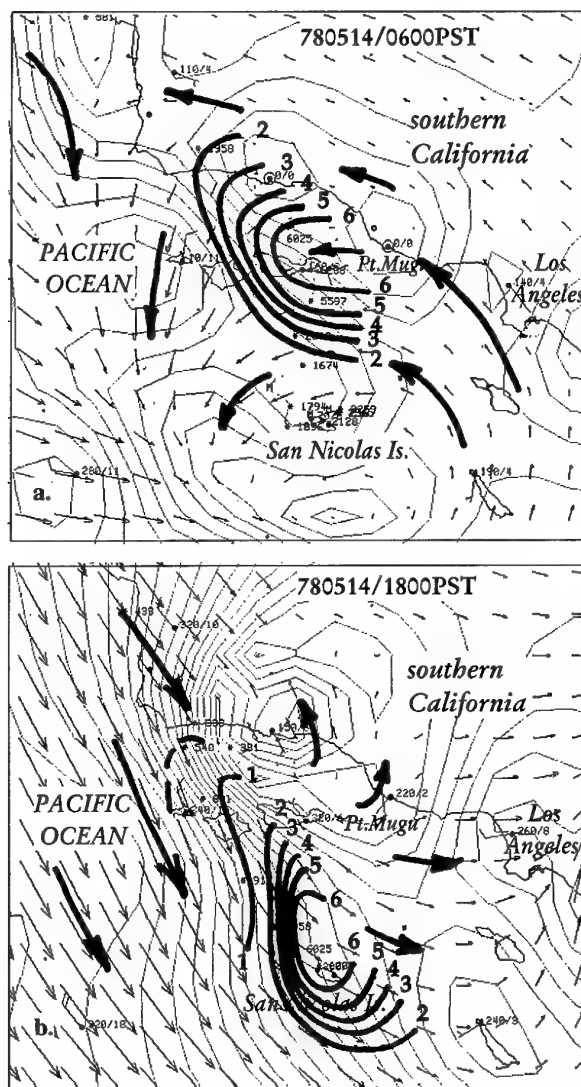


Figure 5. Condensation nuclei and gridded winds at 0600 and 1800 PST on 14 May 1978 are shown. The CN contours are implied by backstreak analysis of parcel CN values at upstream locations from the San Nicolas Island site. An area of large CN values developed in air which had previously passed over and near the Island from the southwest. This increase appeared to result from offshore flow of polluted air from the Los Angeles urban complex on the morning of the 14th, eventually reaching the Island later that afternoon.

#### 4.2 Back-Trajectory Tomography

We have previously described an inverse technique [4,5] whereby a rough estimate of the average distribution and strength of sources of the A1 component aerosols may be possible. This technique, which we shall refer to as back-trajectory tomography (BTT), requires radon or CN data measured at one or more sites over a fairly lengthy period, and construction of a large number of back-trajectories terminating at the measurement site (not necessarily stationary). The underlying concept is similar to a mathematical-statistical technique employed in medicine (computerized axial tomography), oceanography, solar atmospheric dynamics, seismology and other fields, where analysis of data obtained outside the region of interest is used to infer the distribution of properties inside the region. In these applications the attenuation or refraction of some form of electromagnetic, acoustic, seismic or other energy propagating through the subject volume is analyzed. For our purpose, the region of interest is traversed by air trajectories, which carry information in the form of accumulated concentrations of a tracer constituent such as radon or CN to an exterior measurement site. The BTT technique yields coefficients which are taken to be an estimate of the average rate of release of radon or small-particle loading of a parcel of air, presumably determined by properties specific to the locations traversed. In the case of CN, this would include anthropogenic sources of air pollution arising from activities such as combustion of fuels or use of volatile materials in urban areas. For civilian air pollution applications, compilation of an emission inventory of all important sources in a region would be a standard procedure in preparation of a control strategy; for obvious reasons this is not likely to be practical for operational military electrooptical applications.

Radon rather than CN was employed as an air mass tracer for this application of the BTT, since it was measured throughout the CEWCOM himode periods which provided the source of wind data for this study, whereas CN was gathered for a much more limited period of time. A number of improvements were made in the BTT procedure since earlier applications to this data set. A somewhat larger domain was used, and trajectories followed back for 72 hours if possible, instead of the 48 hours previously employed. By interpolation from irregularly timed measurements to regular hourly intervals, an increase from 273 to almost 400 essentially concurrent radon observations and trajectories was obtained from the five CEWCOM data collection periods in 1978, 1979 and 1980. Singular Value Decomposition, a more robust method than the Normal Equation approach, was applied for solution of the simultaneous equations representing the radon versus trajectory relationship. Finally, the BTT was modified to permit designation of arbitrarily-shaped zones rather than rectangular cells for the determination of best-fit coefficients. The assigned source areas can thus be laid out according to geographical regions likely to possess similar meteorological characteristics, in an attempt to improve the efficiency and reliability of the solution.

Figure 6 displays zones used for the present analysis, defined in terms of an underlying, higher resolution grid pattern. Computed coefficients in the basis equation are shown. Highest coefficient values are generally over the mainland, as would be expected due to radon emission from the soil. The irregular and sometimes large values along the periphery may occur because trajectories were not constructed beyond the map boundaries (or 72 hours maximum, whichever came first). The computations will also be affected to the extent that winds vary with height, by unresolved wind features and turbulent diffusion of properties so that computed surface-based trajectories are not fully representative of radon or aerosol transport.

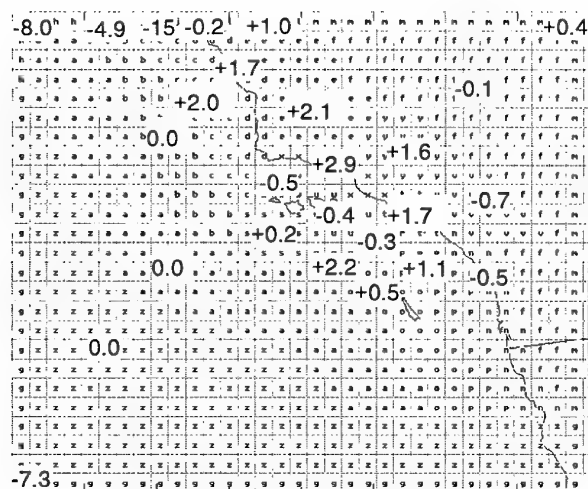


Figure 6. Radon effective source coefficients computed from Back-Trajectory Tomography for CEWCOM periods. Coefficients apply to zones defined in terms of an underlying, higher resolution grid pattern (identified by letters in cells). Highest values are generally over the mainland, as would be expected due to radon exhalation from the soil.

Application of the BTT coefficients to the individual trajectories gives results presented in Figure 7, showing the sequence of observed radon concentrations at the Island (plotted as small circles) and corresponding computed values. The agreement is generally good. This suggests but does not prove the potential value of the BTT; testing of the coefficients on an independent data set will be required. The correlation coefficient between observed and computed radon is 0.82, confirming the ability of the technique to explain a large portion of the variability in measured radon for this data set.

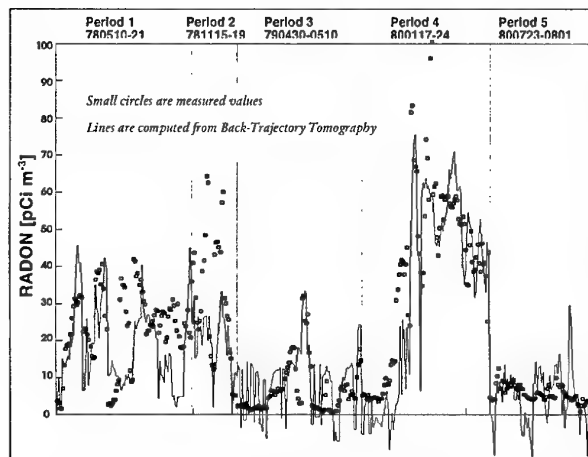


Figure 7. Radon at San Nicolas Island during Periods 1-5 of CEWCOM program. Data are plotted sequentially but because of missing hourly points are not on a strictly chronological scale. Observed values are shown as small circular symbols; the line connects points computed using Back-Trajectory Tomography coefficients and the appropriate air parcel history from individual trajectories.

#### 4.3 Parcel Mean Wind Speed

The possible utility of trajectory-based techniques has been discussed above for the A1 aerosol component. Another application is in improvement of wind speed required for estimation of the A2 component in the Navy Aerosol Model.

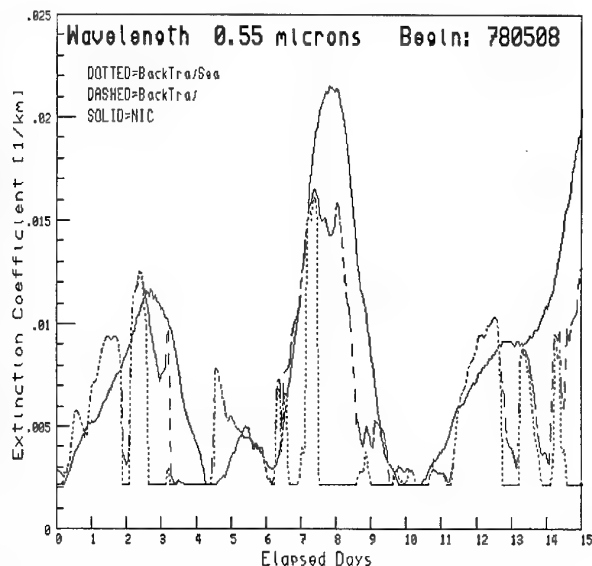


Figure 8. Extinction coefficient at 0.55 microns computed from the Navy Aerosol Model, for three different methods of obtaining 24-hour mean speeds required for the A2 aerosol component. Wind data for 8-23 May 1978 were used. Instantaneous speed was fixed at 5 m/s and relative humidity at 80%. The solid line represents the conventional approach, computing mean speeds for winds observed at San Nicolas Island for preceding 24-hour periods. The dashed line is 24-hour mean speed along the air parcel back-trajectories. The dotted line shows extinction using mean speeds from the recommended procedure, based on the overwater portion of the 24-hour back-trajectory winds.

The aerosol size for this component is larger than the A1 and therefore less persistent, but assessment still requires wind data for a substantial period of time, which in the NAM is taken to be 24 hours. The standard approach is to compute mean wind speed at the measurement site. But the generation of A2 aerosols occurs along the moving parcel; therefore it would seem more realistic to compute the mean speeds accordingly, for each 24-hour period up to arrival of the parcel at the measurement site (or any location for which an extinction prediction is needed). In Figure 8 we show the effect of different methods of computing 24-hour mean speed on extinction at 0.55 microns using the NAM. This is the wavelength most likely to have the greatest sensitivity to the A2 aerosol. To isolate the mean wind effect, other input parameters were held constant (relative humidity = 80%, instantaneous winds = 5 m/s, Air Mass Parameter = 3). The solid line represents results from the conventional method using mean speed computed for the site at San Nicolas Island. The dashed line is computed for air parcels arriving at the site, using speeds computed along the parcel 24-hour upstream trajectory. Since many of the trajectories are over land during that period, however, the appropriate values are shown by the dotted line, where parcel mean speeds are adjusted to reflect overwater fetch (the mechanism for A2 aerosol generation represented in the NAM is limited to overwater conditions). Large differences in computed extinction are evident, especially around 8 May.

#### 5. CONCLUSIONS

Techniques for using computed air trajectories to support analysis and prediction of A1 and A2 aerosol components used in the Navy Aerosol Model have been presented which are consistent with the relative persistence of these components. The BTT may be potentially useful, when sufficient data can be

compiled, to derive a rough estimate of average source strength and distribution, subject to factors affecting representativeness of the computed trajectories. Back- and forward-streak analysis can be used in extrapolation of data, especially valuable in data-sparse regions for estimating spatial patterns in aerosol distribution. Computed air trajectories provide a basis for prediction of aerosol variations by estimating displacement and evolution of spatial aerosol patterns. Finally, a more appropriate assessment of mean wind speeds for estimation of the A2 mode aerosol can be obtained by the use of trajectory analysis.

## 6. ACKNOWLEDGEMENTS

Support for this effort was provided by the SPAWAR Systems Center, San Diego, Division 88, EOPACE Program (Dr. Juergen Richter) under the ONR Exploratory Development Program. Mr. Chuck Fisk assisted in the preparation of illustrations, and Art Ortiz and Matt McGovern in data processing.

## 7. REFERENCES

1. Gathman, S.G., "Optical properties of the marine aerosol as predicted by the Navy Aerosol Model", *Opt. Eng.*, 22, 1983, pp. 57-62
2. Battalino, T.E. and R. A. Helvey, "Air mass parameterization in the Navy Aerosol Model", *Proceedings of the Eighth Conference on Atmospheric Transmission Models*, Air Force Geophysics Laboratory, Hanscom AFB, MA, 1985.
3. Battalino, T.E., "Air mass characterization for optical propagation modeling in the coastal marine atmosphere", *Proceedings of the International Society for Optical Engineering (SPIE)*, Vol. 3125, Propagation and Imaging through the Atmosphere, San Diego, CA, 1997, pp 47-58.
4. Battalino, T.E. and R.A. Helvey, "Air trajectory parameterization technique for use in the Navy Aerosol Model", *Geophysical Sciences Technical Note No. 82*, Pacific Missile Test Center, Point Mugu, CA, 1983.
5. Battalino, T.E. and R.A. Helvey, "Air trajectory index for electro-optical propagation assessment at San Nicolas Island", *Geophysical Sciences Technical Note No. 93*, Pacific Missile Test Center, Point Mugu, CA, 1985.

PAPER No.: 19

DISCUSSOR'S NAME: J. O'Connor

To what extent does the half-life of Radon lead to problems in computing back-trajectory paths since these will in some cases leave the map area for which data and meteorological measurements exist? Could this explain discrepancies between CN and Radon based measurements?

AUTHOR/PRESENTER'S REPLY:

Although I neglected to mention it, we did correct for Radon decay (half-life = 3.8 days) in computing the coefficients representing effective Radon sources from the tomographic technique. The trajectories were computed back 72 hours or to the edge of the analysis domain; for Radon, CN or some other slowly-changing property of an air mass, the trajectories should really be determined for a longer period and distance back. In any event, Radon and CN accumulate as a result of completely different physical mechanisms so will not always vary in the same manner.

## PAPER No. 19

DISCUSSOR'S NAME: G. de Leeuw

## COMMENT/QUESTION:

In the back streak analysis CN are used as passive or inert traces. However, CN are formed through a number of chemical and physical processes involving SO<sub>2</sub>, NO<sub>8</sub>, etc., produced by e.g., combustion processes, which render CN not a good tracer in the first hours, especially since e.g., SO<sub>2</sub> is removed only slowly (some % per hour).

## AUTHOR/PRESENTER'S REPLY:

Streak analysis is a method for extrapolating measurements of some air mass property made at a point, into the special domain upstream and downstream. The simplest possible circumstance is that the property is strictly conserved, so that the local change is entirely due to advection (the so-called individual change within the traveling air parcels is zero). Of course, there are many complications that can cause departures from this ideal in the real atmosphere. If the individual change due to chemical or other processes is substantial then such effects should be included. Nevertheless, even if they are ignored, the application of streak analysis still furnishes information on the probable spatial distribution of the measured property and related parameters (at least the spatial pattern may be inferred even if not the actual amplitudes, as long as the individual changes do not greatly exceed the advection.).

## Air Mass Parameterization and Coastal Aerosol Modeling

D. R. Jensen  
Propagation Division  
SPAWARSYSCEN SAN DIEGO D883  
49170 Propagation Path  
San Diego, CA 92152-7385  
U.S.A.

C. H. Wash  
M. S. Jordan  
Meteorology Department  
NAVAL POSTGRADUATE SCHOOL CODE MR/WX  
589 Dyer Road  
Monterey, CA 93943-5114  
U.S.A.

### SUMMARY

A technique has been developed by which satellite upwelling radiance measurements, MODTRAN, and the NOVAM (Navy Oceanic Vertical Aerosol Model) aerosol model can be used to infer surface boundary layer extinction coefficients as a function of wavelength. This technique utilizes: 1) satellite upwelling radiance measurements for determining the total aerosol optical depth for a specific geographic location and time, 2) MODTRAN to calculate the optical depth associated with tropospheric aerosol scatter above the boundary layer (assuming that no aerosols are being entrained into the troposphere from other sources), and 3) NOVAM for modeling the optical depth of the marine boundary layer (determined by subtracting the MODTRAN aerosol tropospheric optical depth from the satellite derived total optical depth) as a function of air mass parameter (AMP). By adjusting the air mass parameter in NOVAM so that the calculated optical depth matches that required for the marine boundary layer, the air mass parameter for the marine boundary layer can be inferred from remote satellite radiance measurements. Initial results using the EOPACE (Electrooptical Propagation Assessment in Coastal Environments), (Refs 1 & 2), database appear promising for inferring surface boundary layer extinction coefficients as a function of wavelength from remote satellite radiance measurements. It also shows promise for the initial development of a coastal aerosol model.

### 1. INTRODUCTION

Atmospheric aerosol extinction, refraction, turbulence and infrared sea and terrain background models in MODTRAN are presently inadequate for representing infrared (IR) propagation close to the ocean surface and in coastal environments. This requires accurate models to be developed and incorporated into MODTRAN for determining the predicted performance of electrooptical (EO) systems used for detecting low-altitude targets.

Not much is known concerning the coastal air mass characteristics required for advanced aerosol modeling. Since the diverse air mass transitions that frequent coastal environments may have profound effects on the aerosol properties and EO propagation, a good assessment of the

Navy Aerosol Model and the Navy Oceanic Vertical Aerosol Model (NAM & NOVAM, respectively) air mass parameter for coastal applications is essential. When using NAM/NOVAM for calculating extinction coefficients and optical depths in the marine boundary layer (MBL), the AMP is the most critical input parameter and is, of course, the most difficult to obtain. Several techniques are being evaluated or utilized to obtain this parameter including air mass trajectory analysis, radon, condensation nuclei, and multiple wavelength nephelometer measurements. All of these techniques are in-situ measurements for a given geographic location. When considering the complexity and variability of the air mass characteristics within a coastal environment, an alternate remote sensing technique for determining the AMP must be determined for NAM/NOVAM to be applicable for coastal application. This paper presents an alternative approach for determining the surface AMP from satellite upwelling radiance measurements, MODTRAN, and the NOVAM aerosol model. In this paper two case studies (5 & 7 April 1996) are presented for the evaluation of this technique for remotely inferring surface boundary layer



Figure 1. Aerosol optical depth in the marine atmospheric boundary layer off the coast of southern California inferred from visible and near infrared data provided by the NOAA AVHRR satellite.

extinction coefficients as a function of wavelength. Initial results appear promising.

## 2. PROCEDURE

Figure 1 is a NOAA-14 AVHRR satellite image of upwelling radiance showing the complexity of the aerosol optical depth structure in the southern California coastal zone, stretching from San Diego in the lower right hand corner through the Los Angeles basin to Santa Barbara in the upper left hand corner. Land regions, including the islands off the California coast, are blacked out.

The gray shading superimposed on the water of the California bight represents the different coastal aerosol optical depths given by

$$OD_{\lambda}(L) = \int_0^L \beta_p(x, \lambda) dx \quad (1)$$

where the extinction coefficient  $\beta_p(x, \lambda)$  is calculated from Mie theory using

$$\beta_p(x, \lambda) = \int_0^{\infty} \pi^2 Q_p(r, \lambda) \frac{dN(x)}{dr} dr \quad (2)$$

$Q_p(r, \lambda)$  is the mean scatter efficiency and  $\frac{dN(x)}{dr}$  is the aerosol size distribution.

Considering this complexity, no single coastal aerosol model can be developed that will be representative of this coastal environment. Therefore, in order to utilize existing aerosol models for predicting the performance of EO systems within a coastal region, it needs to be determined if the air mass parameter for various coastal locations can be derived from remotely sensed satellite imagery.

An initial approach for determining the surface air mass parameter from satellite upwelling radiance measurements, MODTRAN, and NOVAM is shown in Figure 2.

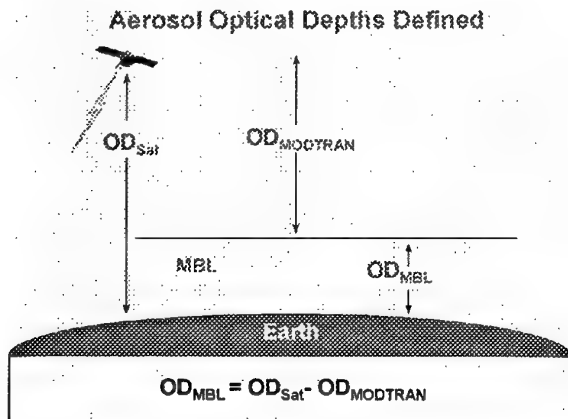


Figure 2. Aerosol optical depths defined.

The defined total optical depth ( $OD_{Sat}$ ) is that determined using satellite radiometric measurements (Refs 3 & 4). Utilizing MODTRAN and the tropospheric aerosol model, the optical depth associated with the tropospheric scatter above the boundary layer can be calculated ( $OD_{MODTRAN}$ ) using equations (1) and (2). This assumes that no aerosols are being entrained into the troposphere from other sources and that no clouds are present. The difference between these two optical depths is that required in the marine boundary layer ( $OD_{MBL}$ ). The relationship is expressed as

$$OD_{MBL} = OD_{Sat} - OD_{MODTRAN} \quad (3)$$

Utilizing NOVAM, the optical depth of the marine boundary layer can be modeled as a function of air mass parameter using equations (1) and (2). The mathematical expression showing the AMP functional relationship is given by

$$\frac{dN_i}{dr} = A_i \frac{\exp\{-1 * [\log \frac{r}{C_i f}]^2\}}{f} \quad i=1, 2, 3 \quad (4)$$

where

$$A_1 = 2000 * AMP^2$$

$$A_2 = \text{Max}[5.866(w_a - 2.2), 0.5]$$

$$A_3 = 10^{(0.06w_i - 2.8)}$$

and  $C_i = 0.03, 0.24$ , and  $2.0$  respectively.  $f$  is the humidity scaling factor.

The magnitude of the  $A_i$  component of the three log normal NOVAM aerosol size distribution is proportional to the square of the AMP. By adjusting the AMP in equation (4) so that the calculated optical depth using the NOVAM distribution and equations (1) and (2)

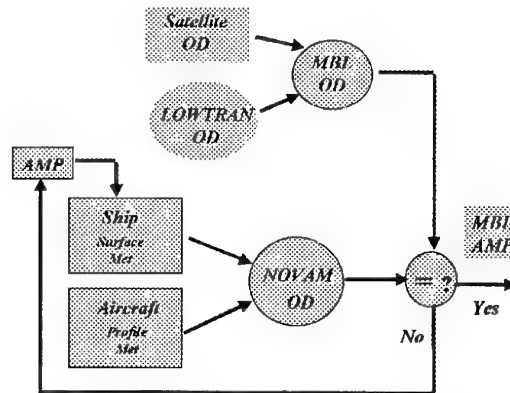


Figure 3. AMP iteration procedure for inferring MBL optical depths.



( $OD_{NOVAM}$ ) matches that required for the marine boundary optical depth ( $OD_{MBL}$ ) of equation (3), it appears that the AMP for the MBL can be inferred from remote satellite radiance measurements. Figure 3 summarizes the AMP iteration procedure for inferring the MBL AMP from remote satellite observations.

Following the iteration procedure of Figure 3, the required marine boundary layer optical depth ( $OD_{MBL}$ ) is determined by subtracting the MODTRAN optical depth ( $OD_{NOVAM}$ ) from the satellite optical depth ( $OD_{Sat}$ ). NOVAM is then exercised as a function of AMP. When the  $OD_{MBL}$  determined from satellite and MODTRAN calculations does not match that calculated using NOVAM, the AMP in NOVAM is iterated until the  $OD_{NOVAM}$  does match the MBL value. This AMP is then the input parameter for the dynamic aerosol model that can be used to predict the performance of EO systems in that geographic area corresponding to the satellite overpass.

### 3. ANALYSIS

Seven different data points, corresponding to different

geographic locations for 5 April 1996, 1814 through 2159 GMT, and 7 April 1996, 1714 GMT, have been analyzed from the EOPACE database. The NOAA-14 AVHRR satellite images, calibrated for optical depth, for these two periods are shown in Figures 4 & 5, respectively. The gray shading that is superimposed on the water of the California bight represents the inferred aerosol optical depth (equations 1 and 2) and are given by the shading code inset on the left side of the figures. The inferred aerosol optical depths were derived from radiometric measurements according to the Durkee retrieval technique (Refs 3, 4, & 5). This technique depends on three assumptions: 1) that the boundary layer is well mixed, 2) that optical depth is completely determined by aerosol extinction, and 3) that the amount of water vapor in the boundary layer is known by other techniques. The optical depths do not include the effects of molecular absorption, but they do include aerosol scattering in the troposphere and the marine atmospheric boundary layer. It is also assumed that the aerosols in the marine boundary layer provide the major contribution to these data. The solid shading near and seaward of the channel islands in Figure 5 is the result of clouds and should not be interpreted as optical depth.

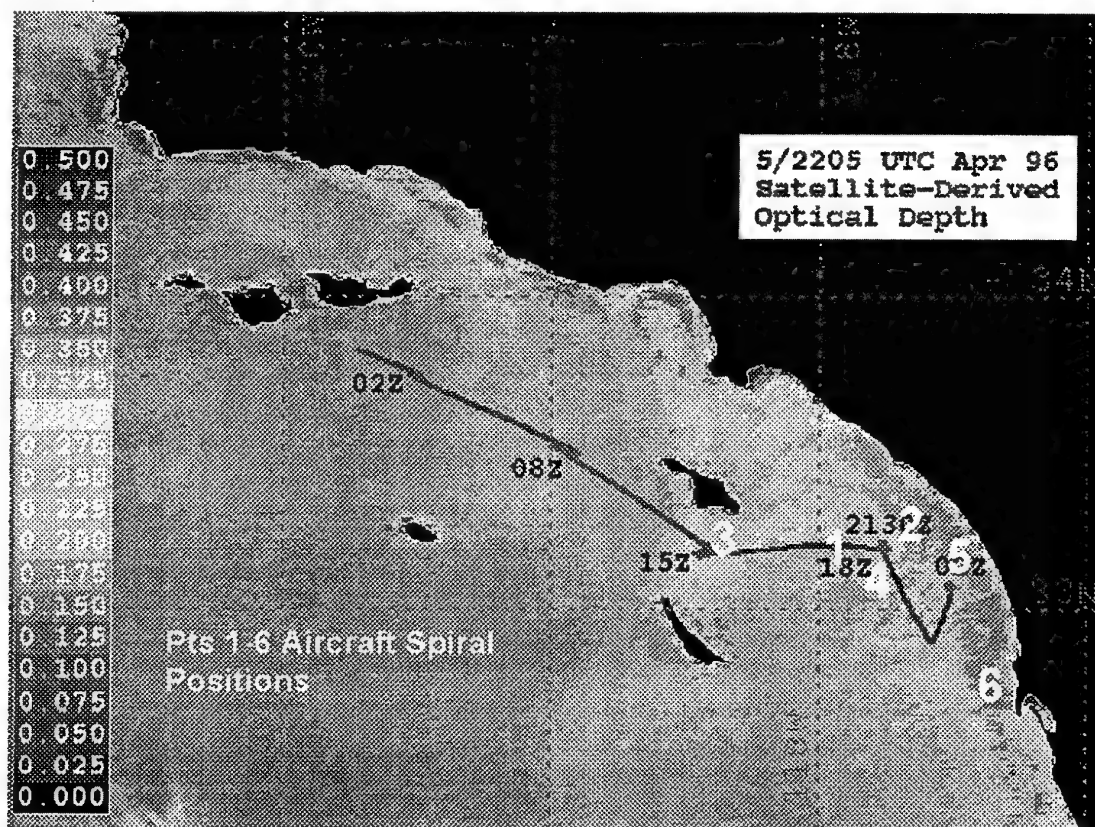


Figure 4. Aerosol optical depth inferred from visible and near infrared data provided by the NOAA AVHRR satellite for 5 April 1996.

Superimposed on the satellite image is the Pt. Sur ship track showing where surface meteorological data was taken. During each of the data periods, a twin engine Piper Navajo aircraft carrying aerosol spectrometer

probes (Ref 6) executed vertical spiral patterns near the Pt. Sur for meteorological and aerosol profile information. Spiral locations for the 5 April data period are given by the large numerals in Figure 4. Aircraft



spirals on 7 April were in the vicinity of the Pt. Sur and are not shown on the figure. A shallow surface layer

existed for both these data periods.

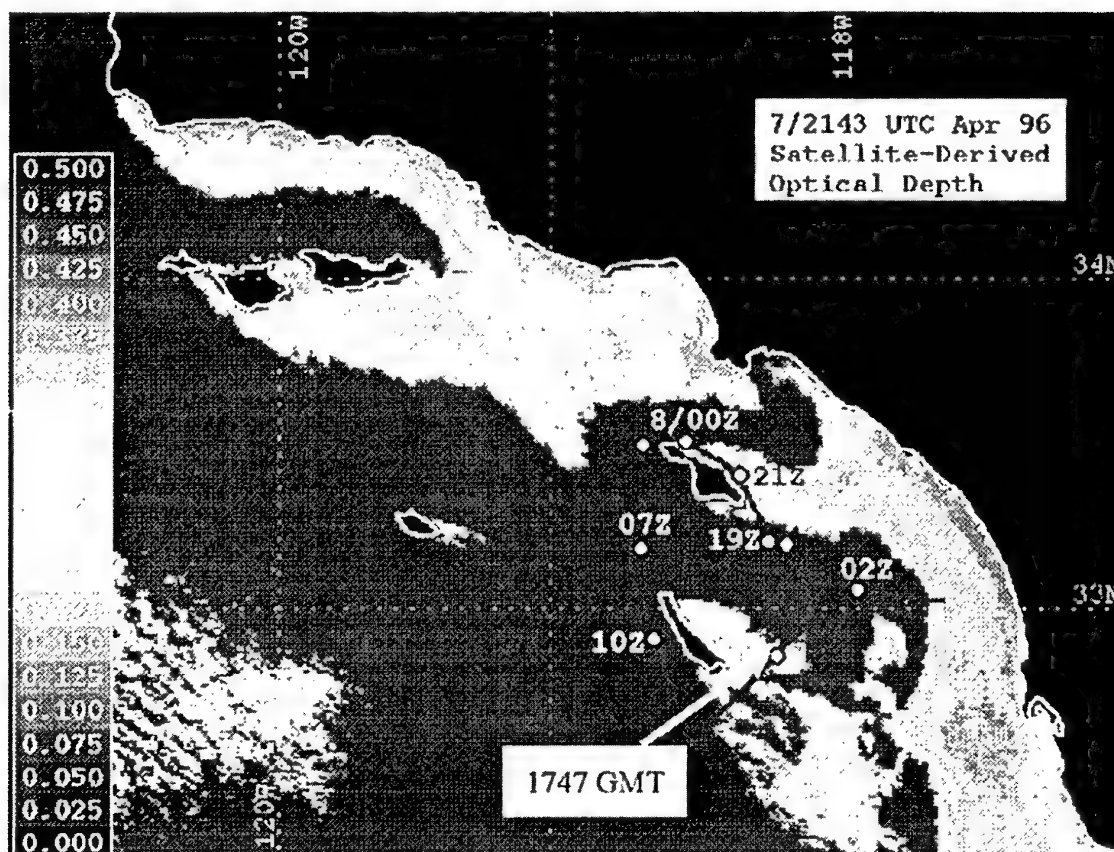


Figure 5. Aerosol optical depth inferred from visible and near infrared data provided by the NOAA AVHRR satellite for 7 April 1996.

Table 1 summarizes the derived  $OD_{Sat}$ , the  $OD_{MODTRAN}$ , the corresponding optical depth required for the boundary layer ( $OD_{MBL}$ ), and the value of the AMP required to match the  $OD_{NOVAM}$  with that required for the boundary layer, e.g., for 5 April 96, 1814 GMT, the required AMP to satisfy the required  $OD_{MBL} = 0.106$  is between 5 and 6 (NOVAM calculated ODs are 0.097 and 0.115, respectively). For all cases the satellite optical depth exceeded the tropospheric optical depths and the AMPs determined from NOVAM provided ODs that satisfied the required optical depth of the boundary layer and were within the range of 1 to 10.

These AMPs, inferred from satellite imagery for a given time and geographic location, can now be used in NOVAM and the propagation codes to infer the surface boundary layer extinction coefficients as a function of wavelength.

#### 4. CONCLUSIONS

A technique has been developed by which satellite upwelling radiance measurements, MODTRAN, and the NOVAM aerosol model can be used for inferring surface boundary layer extinction coefficients as a function of wavelength. Initial results using the EOPACE database

appear promising. These results also show promise for the initial development of a coastal aerosol model.

#### 5. ACKNOWLEDGEMENTS

We thank the participants of EOPACE for their efforts in making this analysis possible. This work was supported by the Office of Naval Research.

#### 6. REFERENCES

1. K. M. Littfin and D. R. Jensen, "An overview of EOPACE (Electrooptical Propagation Assessment in Coastal Environments), including in situ and remote sensing techniques." Paper 10 in Proceedings CP-582 of the AGARD SPP Symposium on "Remote Sensing: A valuable Source of Information," Toulouse, France, 22-25 April, 1996.
2. C. R. Zeisse, D. R. Jensen, and K.M. Littfin, "EOPACE (Electrooptical Propagation Assessment in Coastal Environments) overview and initial accomplishments," Proceedings of the 1996 Battlespace Atmospherics Conference, NRaD TD 2938, pg 203, December 1996.

Date/ Time (GMT)	Satellite OD	MODTRAN OD	MBL OD	NOVAM MBL OPTICAL DEPTH									
				AMP									
				1	2	3	4	5	6	7	8	9	10
5 Apr 96 1814	0.18	0.074	0.106					0.097	0.115				
1907	0.15	0.075	0.075		0.064	0.082							
2048	0.21	0.072	0.138										0.130
2117	0.20	0.073	0.127			0.122	0.131						
2137	0.17	0.073	0.097	0.075	0.110								
2159	0.16	0.063	0.097	0.072	0.108								
7 Apr 96 1747	0.13	0.073	0.058					0.056	0.088				

Table 1. AMP characterization summary.

3. Rouault, M. and P. A. Durkee, "Characterization of Aerosols from Satellite Remote Sensing," Nucleation and Atmospheric Aerosols, N. Fukuta and P. E. Wagner, eds., 1992, p. 357.

4. Davidson, K. L., C. H. Wash and M. S. Jordan, "Remote Sensing of Coastal Atmospheric EM/EO Conditions," Proceedings of the 1996 Battlespace Atmospherics Conference, NRD TD 2938, pg 217, December 1996.

5. Wash, C. H., K. L. Davidson, and M. S. Jordan, "Multispectral Remote Sensing of the Coastal Atmospheric Boundary Layer," paper 45 in Proceedings CP-582 of the AGARD SPP Symposium on "Remote Sensing: A Valuable Source of Information." Toulouse, France, 22-25 April, 1996.

6. Models FSSP-100 and OAP-200X, Particle Measuring Systems Incorporated, 5475 Airport Boulevard, Boulder, CO 80301-2339.

PAPER No: 20

DISCUSSOR'S NAME: C. Philbrick

The data points which you showed correspond to relatively low values of optical depth (extinction). What is the dynamic range of the technique? Are there any difficulties at higher extinction values?

AUTHOR'S REPLY:

The satellite technique is limited to cloud-free conditions and optical depths of less than approximately 0.4.

PAPER No. 20

DISCUSSOR'S NAME: D. Clement

In order to find an AMP set which is coherent with the satellite OD data, you are using an iterative procedure (the "loop"). Is this procedure mathematically well-behaved? Did you encounter convergence problems?

AUTHOR/PRESENTER'S REPLY:

The procedure involves iterating the AMP, an input to NOVAM, until the NOVAM optical depth agrees with that required for the marine boundary layer inferred from satellite radiance measurements and MODTRAN tropospheric aerosol scattering. Mathematically iterating the AMP in NOVAM to find a range of optical depths is no problem. Convergence of the NOVAM optical depth to that required for the boundary layer is critically dependent upon having the proper meteorological input parameters. Specifically, when the visibility is not known, MODTRAN assumes a default visibility and this creates convergence problems. Having the proper input parameters for NOVAM/MODTRAN is critical for this iteration procedure.

DISCUSSOR'S NAME: B. Rosier

Are the airplanes or in-situ measurements simultaneous with the NOAA-14 measurement? If not, what is the time difference between the two data sets?

AUTHOR/PRESENTER'S REPLY:

On 5 April 1996, support aircraft and in-situ measurements were made during a four hour time period prior to the NOAA-14 satellite overpass (1814 – 2159 GMT). The overpass was at 2205 GMT. The last data point for the 5 April (2159 GMT) occurred just 6 minutes prior to the overpass. The one data point for 7 April 1996 was at 1747 GMT, four hours prior to the overpass. In order for this technique to be valid you have to assume that only small changes in the air mass characteristics will result over a four to six hour period.

DISCUSSOR'S NAME: G. Anderson

Was there any input from the spiraling aircraft data employed in the MODTRAN optical depth calculation – or did you use a "default" MODTRAN model atmosphere for this segment of your calculation?

AUTHOR/PRESENTER'S REPLY:

The default MODTRAN atmosphere and tropospheric aerosol scattering models were used to calculate the optical depth above the height where the aircraft stopped making measurements. The only inputs that were used for the MODTRAN optical depth calculations were surface visibility. No aircraft data was used.

PAPER No: 20

DISCUSSOR'S NAME: G. de Leeuw

Lidar measurements during EOPACE show that most of the AOD is due to aerosol above the MBL, and that in the MBL the aerosol concentrations are very low. This has also been observed during TARFOX off the U.S. East coast. Yet the general consensus is that most of the aerosol is in the BL. From the available databases, is there information available on the occurrence of aerosol above the MBL, rather than in the MBL?

AUTHOR/PRESENTER'S REPLY:

This technique assumes, for the present, that no aerosols are being entrained into the troposphere from either the boundary layer or horizontal transport from other sources. This must be addressed in the future but is not accounted for in this paper. One problem we are encountering here is the term "marine boundary layer". As per the classical definition, the depth of the boundary layer for 5 April 1996 was approximately 100-200 m. Aircraft and lidar measurements both showed significant aerosol structure above this level. The calculations for the MODTRAN optical depths were made for heights greater than 600 meters, the height where the aircraft spirals ended. For this paper, most of the aerosol structure is assumed to be contained within this 600 m layer, not the actual marine boundary layer. Also, it is understood that the aerosols within this 600 m layer are not uniformly distributed. The calculated NOVAM optical depth is an integrated optical depth over the 600 m layer and does not assume any vertical aerosol profile. The vertical variability and entrainment of aerosols, both within the boundary layer and troposphere, must be considered at some point.

## ANALYSIS OF THREE METHODS OF CHARACTERIZING AN AIR MASS

Kathleen Littfin  
Stuart Gathman  
Douglas Jensen  
Carl Zeisse

Space and Naval Warfare Systems Center San Diego  
Propagation Division Code D883  
49170 Propagation Path  
San Diego, CA 92152-7385

### Summary

The origin of an air mass is an important factor in predicting performance of electrooptical systems. The aerosol content varies significantly depending upon whether the air mass is anthropogenic or natural, marine or continental, rural or urban. Most areas of military interest today are in coastal environments, where there can be a wide variety and rapid changes of atmospheric conditions. Atmospheric models need a reliable and easily obtainable indication of air mass characteristics in order to accurately predict aerosol extinction and detection ranges. This paper compares three methods of determining the gross characteristics of small background aerosol in an air mass: radon concentration, condensation nuclei concentration, and scattering from aerosol. These measurements, along with a full complement of meteorological and aerosol data, were obtained during two EOPACE (Electrooptical Propagation Assessment in Coastal Environments) experiments conducted in San Diego, California in November 1996 and August/September 1997.

### 1. Introduction

When trying to predict the behavior of electrooptical (EO) systems, a major unknown is aerosol extinction. In determining aerosol extinction, a primary unknown is the composition of the air mass through which the electrooptical system is sensing. In the Navy Aerosol Model (NAM), Gathman (Ref 1) introduced a quantity called the air mass parameter (AMP) which quantifies the amount of small aerosol in an air mass as a number between 1 (entirely marine in origin) and 10

(heavily continental in origin). NAM is included in the present version of MODTRAN 4.

Characterizing an air mass is essential to accurately predicting EO systems behavior, but AMP is a difficult parameter to measure. The aerosol extinction can vary significantly depending on whether the origin of the air mass is marine or continental, anthropogenic or natural, rural or urban.

Figure 1 shows the aerosol size distribution equations for NAM. The  $A_1$ ,  $A_2$ , and  $A_3$  coefficients of the three lognormal distributions depend directly on air mass, 24-hour average wind speed, and current wind speed, respectively, as described by Gathman (Ref 1 & 2). The  $A_1$  coefficient of the largest lognormal function represents the smallest particles, the background aerosols that are usually advected to the area rather than being locally generated. This largest component is a function of the air mass; in fact, the  $A_1$  coefficient is proportional to the square of the AMP, as shown in figure 1. The air mass parameter has the most significant effect on the aerosol extinction in the shorter wavelengths.

### 2. The Radon Method

A traditional and reliable method of determining the AMP is to measure the beta radioactivity of radon daughter products (Ref 3 & 4). This method has the advantage that its measurements are not affected by local contaminants such as smoke, smog, or exhaust. It is not dependent on the aerosol or on visibility itself but is actually a tracer reflecting how long an air mass has been at sea, since various natural processes clear out

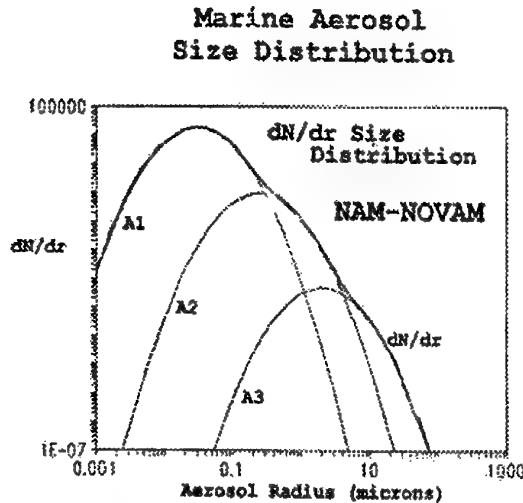


Figure 1. Note that the  $A_1$  component (the largest curve) is dependent of the square of the air mass parameter. The AMP has a significant effect on the aerosol size distribution.

small aerosol over time. Radon, which is produced over land, but not over water, is in a much higher concentration when the air mass has just traveled over land.

Radon devices used to test communities for the presence of radon are not sensitive enough; the sensors we use are three orders of magnitude more sensitive than those devices. Instrumentation used to measure radon is not readily available for shipboard or aircraft use, and is no longer commercially available. Although measuring radon may be an accurate method for tracing an air mass, a more practical and readily available method has been sought.

### 3. The Nephelometer Method

In a method recently developed, Goroch (Ref 5) calculates the AMP by using scattering measurements from a three wavelength integrating nephelometer and the aerosol size distribution equations of the Navy Aerosol Model. In the nephelometer method (Ref 6), the extinction at wavelength  $\lambda$  resulting from the presence of the aerosol distribution in an air parcel is proportional to the Mie scattering efficiency integrated over the particle concentration:

$$\sigma(m, \lambda) = \int \pi^2 Q(m, r, \lambda) \frac{dN}{dr} dr \quad (1)$$

where  $Q$  is the Mie scattering efficiency,  $m$  is the complex index of refraction,  $r$  is the particle

$$\frac{dN}{dr} = A_i \frac{\exp\{-1[\log(r / C_i f)]^2\}}{f}$$

( $i=1,2,3$ )

where  $r$  = radius

$f$  = particle swelling factor  
(based on RH)

$$A_1 = 2000 \cdot \text{AMP}^2$$

$$A_2 = \max[(5.866 \cdot \text{avg wind} - 2.2), 0.5]$$

$$A_3 = 10^{(0.06 \cdot (\text{instantaneous wind} - 2.8))}$$

$$C_i = 0.03, 0.24, 2.0, \text{ respectively}$$

radius, and  $dN/dr$  is the aerosol size distribution. The integral is dependent on the relative humidity and the aerosol size distribution as shown in figure 1.

The NAM model extinction can be evaluated at the three measured nephelometer wavelengths: blue (450 nm), green (550 nm), and red (700 nm). From that, the AMP needed to satisfy the model is calculated (Ref 5).

### 4. The Condensation Nuclei Method

Battalino (Ref 7) developed another method of determining AMP by using condensation nuclei (CN) measurements. CN monitors measure submicron sized particles present in a specific volume of air. They count the total number of particles; there is no size distinction.

In the CN method of determining the AMP, Battalino also uses the Navy Aerosol Model. The CN method equates the measured CN count to the CN count obtained by integration of the NAM size distribution spectrum over radius limits specified by the particle size measurement range of the CN monitor. This leads to determination of the  $A_1$  coefficient, which is proportional to the square of the AMP.

Battalino developed a table with fixed ranges of CN particles per cubic meter corresponding to the 1 - 10 range of the AMP in the NAM. This

method is independent of relative humidity and almost completely independent of wind speed. CN is an intrinsic property of the air mass, but since the measurement depends directly on the number of particles present in the sample, contamination of the sample by smoke or exhaust from local sources is a problem. In order to obtain accurate background aerosol information, it is important to locate the CN monitor away from particle-producing sources such as generators, smokestacks, or car exhaust.

### 5. Comparison of Measurements

Characterization of the coastal air mass is one of the major objectives of the international effort called Electrooptical Propagation Assessment in Coastal Environments (EOPACE) (Ref 8). Several intensive operational periods were conducted in the San Diego Bay in 1996 and 1997. Figure 2 shows the location of those experiments.

In the Aug/Sept 1997 experiment, radon and CN monitors were co-located at the receiver end of two infrared transmission paths (labeled "IR receiver" in figure 2) at the Naval Submarine Base San Diego. A nephelometer and CN monitor were located on an instrumented boat, which traveled along both the 7 km and 15 km transmission paths. A third CN monitor was located at the Naval Amphibious Base (marked IR Source in figure 2). All three platforms were instrumented with meteorological and aerosol equipment. Instrumented buoys were located at the midpoints of both paths.

AMPs were calculated using each of the three methods: radon, nephelometer, and CN. Figure 3 shows three time series graphs. The vertical axis is the AMP and the horizontal axis is the Julian Day of the experiment. All three graphs show the radon AMP from the Naval Submarine

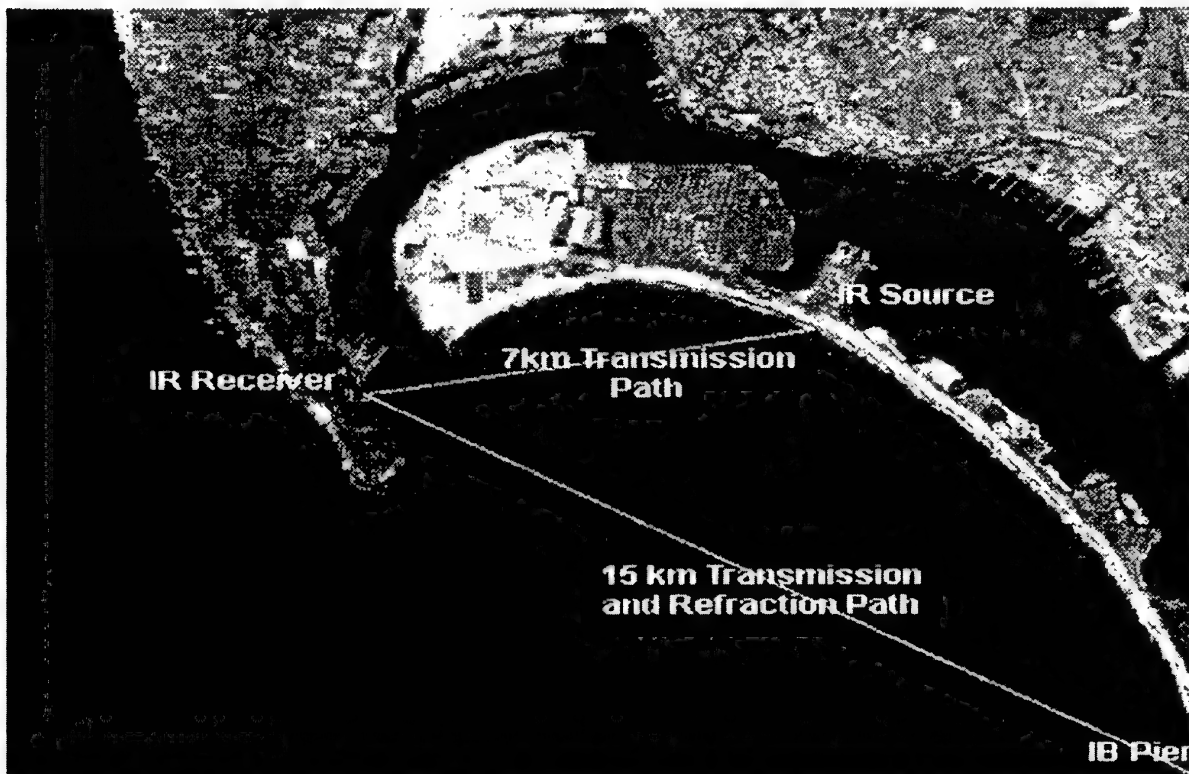


**Figure 2.** The San Diego Bay. The transmission paths set up during the November 1996 and Aug/Sept 1997 EOPACE experiments were instrumented at each end, and at midpoint buoys. The ends marked "IR Receiver" and "IR Source" show the locations of meteorological equipment at the Naval Submarine Base and Naval Amphibious Base, respectively. An instrumented boat also traveled along both paths, and midpoint buoys were also equipped with meteorological sensors.

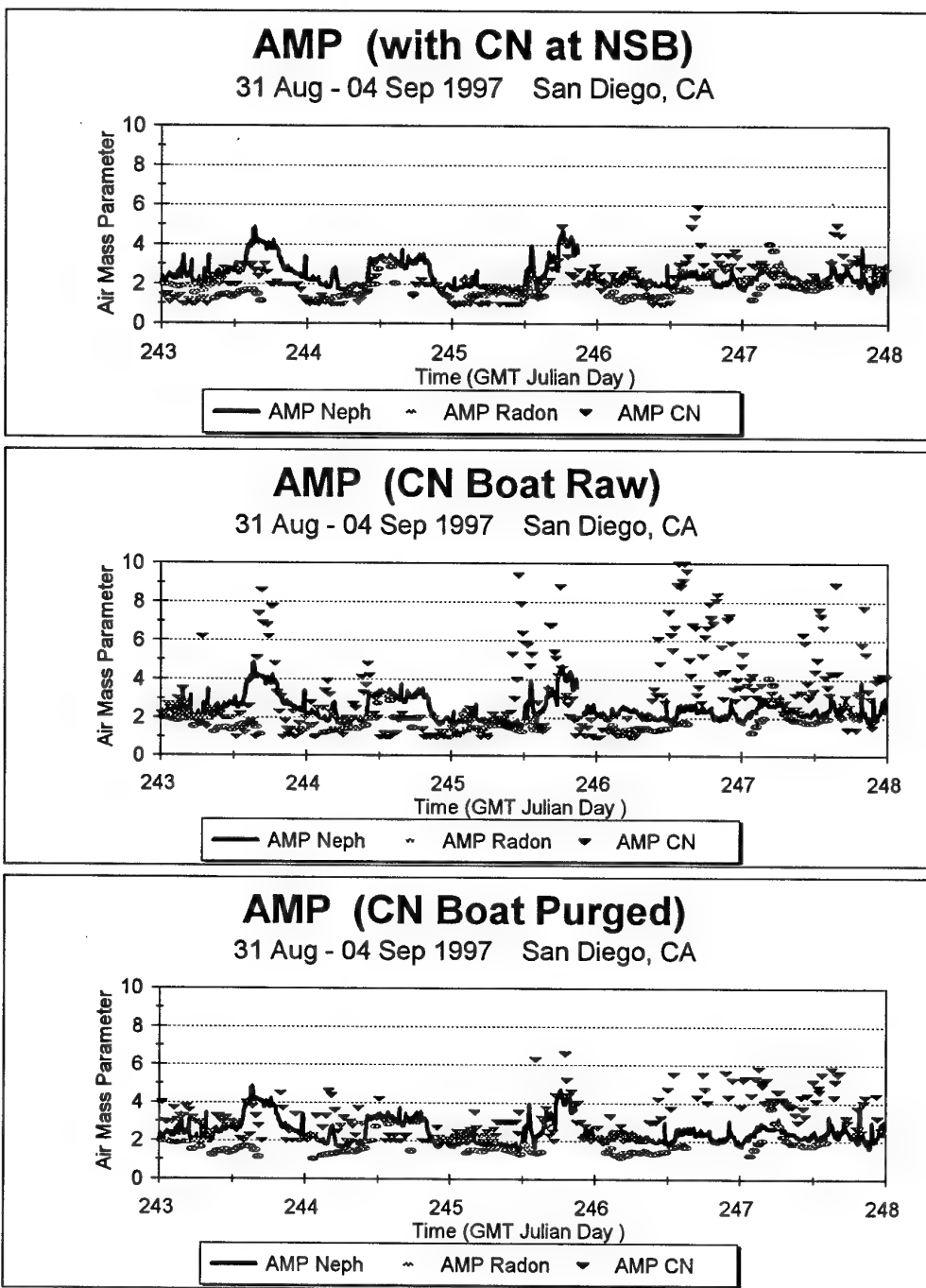


**Figure 3.** Three time series graphs of 5 days. All three graphs show the radon AMP from the Naval Submarine Base (circle) and the nephelometer AMP from the boat (line). The top graph shows the CN AMP (triangle) from the Sub Base and the middle graph shows the CN AMP from the boat. Contamination from generators and boat exhaust can be seen in the boat graph. This was anticipated, and a relative wind monitor was located on board to assure we used only those readings made when the relative wind was within plus or minus 30° of blowing exhaust directly behind the boat, away from our sensors on the bow.



Base and the nephelometer AMP from the boat. The only difference in the graphs is the CN AMP. The top graph shows the CN at the Sub Base and the middle graph shows the CN from the boat. The readings from the boat were contaminated by generators located on the boat, and by the boat exhaust itself. We therefore used a relative wind monitor on board to assure that we only used readings made when the relative wind was within plus or minus 30° of blowing exhaust directly behind the boat, avoiding our sensors located on the bow.

The bottom graph in figure 3 shows this purged CN AMP data from the boat. Even with this precaution, the CN values are still higher than those at the Sub Base where there was less contamination. The nephelometer was not as affected by this problem, as can be seen by its closer agreement to radon measurements, which are independent of exhaust.

None of the methods can be called "truth" since AMP is not a directly measurable parameter. Since there is no absolute AMP measurement, we will consider an average of all three methods at a given time to be our best estimate of the true air mass parameter. To assure not weighing one method more heavily than another, we used only those times where we had readings for all three methods. Figure 4 shows the best estimate for the 11 day period from August 25 - Sept 4, 1997. The graph is a frequency distribution; the horizontal axis is the unitless air mass parameter. The lower values indicate a marine air mass, and the higher numbers indicate more continental influence. The vertical axis is the number of observations of a particular AMP during the period. As would be expected in a coastal environment with a predominately onshore flow, the AMP was generally marine in nature, with some continental influence. The average AMP for the 11 day period was 2.5 with a standard deviation of 0.89.

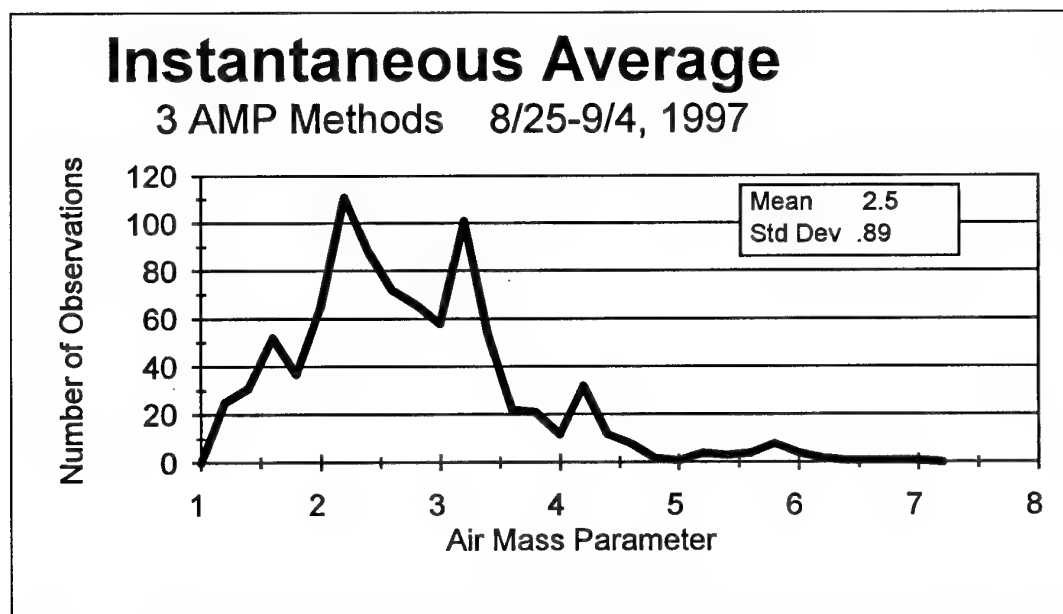


**Figure 4.** Frequency distribution showing the best estimate of the AMP for an 11-day period from August 25 – September 5, 1997. Since no one method is known to be any better than the others are, we used an average of all three AMP methods for our best estimate. The low numbers of AMP indicate a marine air mass and the higher numbers indicate more continental influence. As would be expected in a coastal environment with a mostly onshore flow, the AMP for this period was generally marine in nature, with some continental influence.

We then calculated how far each method differed from our best estimate at each point. Figure 5 shows the distribution about the instantaneous average for CN AMPs for the three CN monitors located at the Naval Submarine Base, the Amphibious Base, and the boat. There is a large spread, even though the boat data was purged as previously described. The large spread for CN could be due to exhaust

from other craft in the bay, or the fact that CN measures very small aerosol (down to 3 nm) and therefore sees more particles than the other methods. Figures 6 and 7 show the distributions about instantaneous averages for the radon AMP and nephelometer AMP, respectively. The nephelometer method was closest to the best estimate.

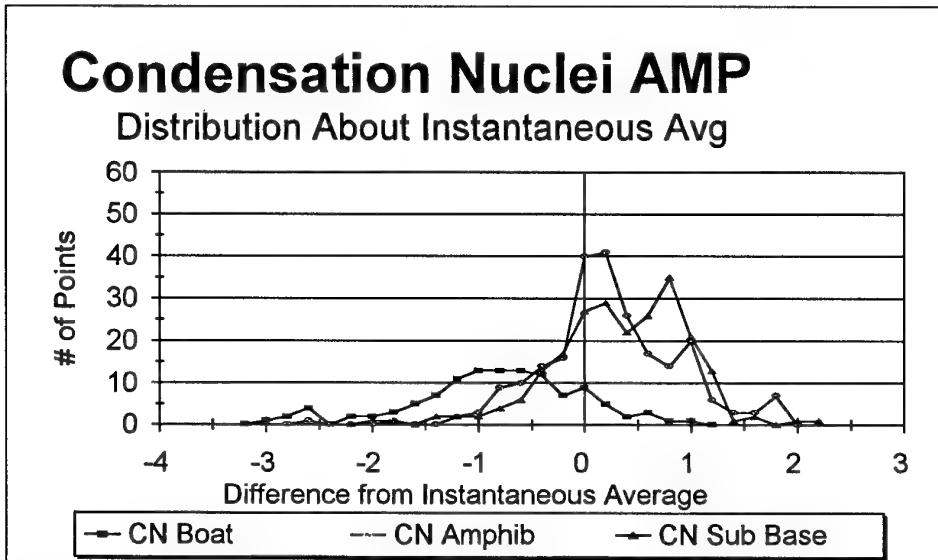


Figure 5. The differences between the instantaneous average and AMP for each of the three CN monitors.

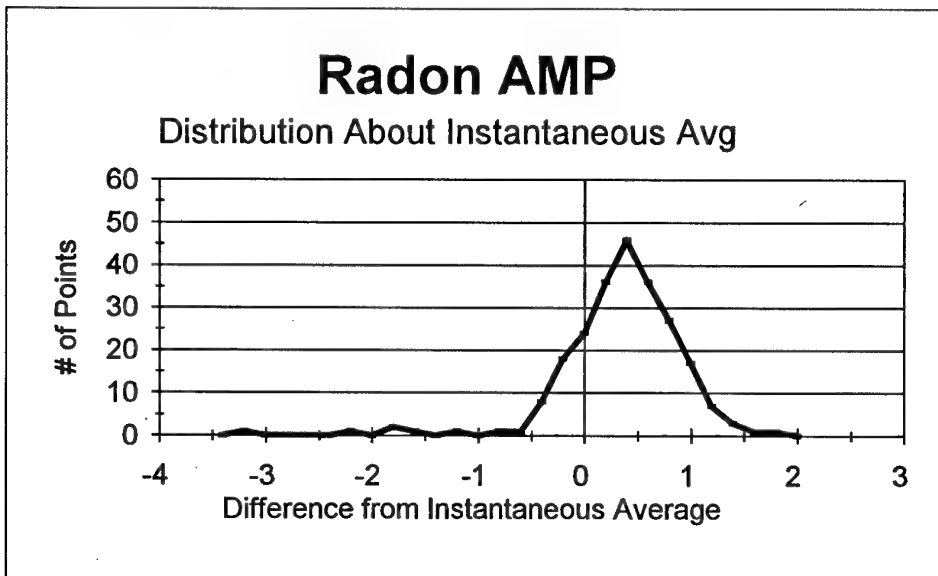
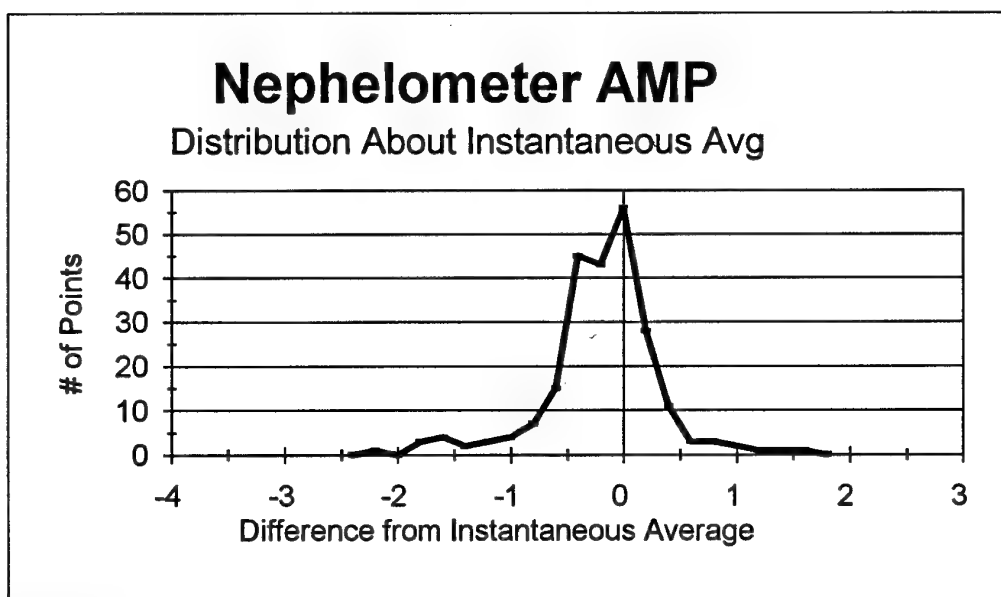


Figure 6. The difference between the instantaneous average and the radon AMP.



**Figure 7.** The difference between the instantaneous average and the nephelometer AMP.

The primary question, of course, is how does this affect aerosol extinction? This can be answered by using the Navy Aerosol Model to calculate extinction at four wavelengths:  $0.55\mu$ ,  $1.06\mu$ ,  $3.5\mu$ , and  $10.6\mu$ . Meteorological values from August 30 were typical for the period, and values were used from that day: wind speed of 4.1 m/s, relative humidity of 85%, air temperature of 21°C, and visibility of 25 km. Extinction was calculated using our AMP mean of 2.5, then recalculated using one standard

deviation above and below the mean. Figure 8 shows that for infrared wavelengths, there is virtually no change in the extinction, with little change in extinction in the visible. All three methods give a reasonable estimate of the air mass parameter, but it appears the best method would be the nephelometer. Scattering is an intrinsic property of the aerosol itself, and nephelometers are readily available instruments. Radon monitors are scarce and CN monitors are highly affected by local contaminants.

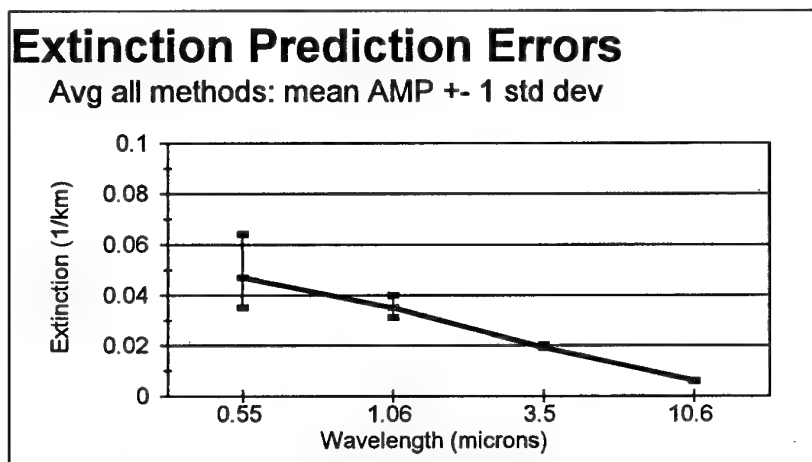


**Figure 8.** Extinction prediction errors for the mean AMP and plus or minus one standard deviation. For infrared wavelengths, there is virtually no change in extinction, and very little change in the visible.

Figure 9 shows a scatter diagram of the three methods used in another EOPACE experiment in November 1996. The radon monitor, CN monitor and nephelometer were co-located at the Naval Submarine Base in San Diego. The nephelometer and radon methods show a high correlation, while the CN again shows more spread.

## 6. Conclusion

While all three methods give a reasonable estimate of the air mass parameter, for this particular data and location the nephelometer method proves to be the most reliable. Scattering is an intrinsic property of the aerosol itself, and nephelometers are readily available instruments. Radon monitors with the required

sensitivity are scarce and no longer commercially available, and CN monitors are highly affected by local contaminants.

An air mass parameter gives quick, valid information on whether an air mass is marine or continental in origin, and that aids researchers in determining aerosol extinction. Real-time models depend upon speed and a valid approximation may prove more useful than an exact answer, which takes hours of computing time.

## Acknowledgements

This work was sponsored by the United States Office of Naval Research, ONR-322.

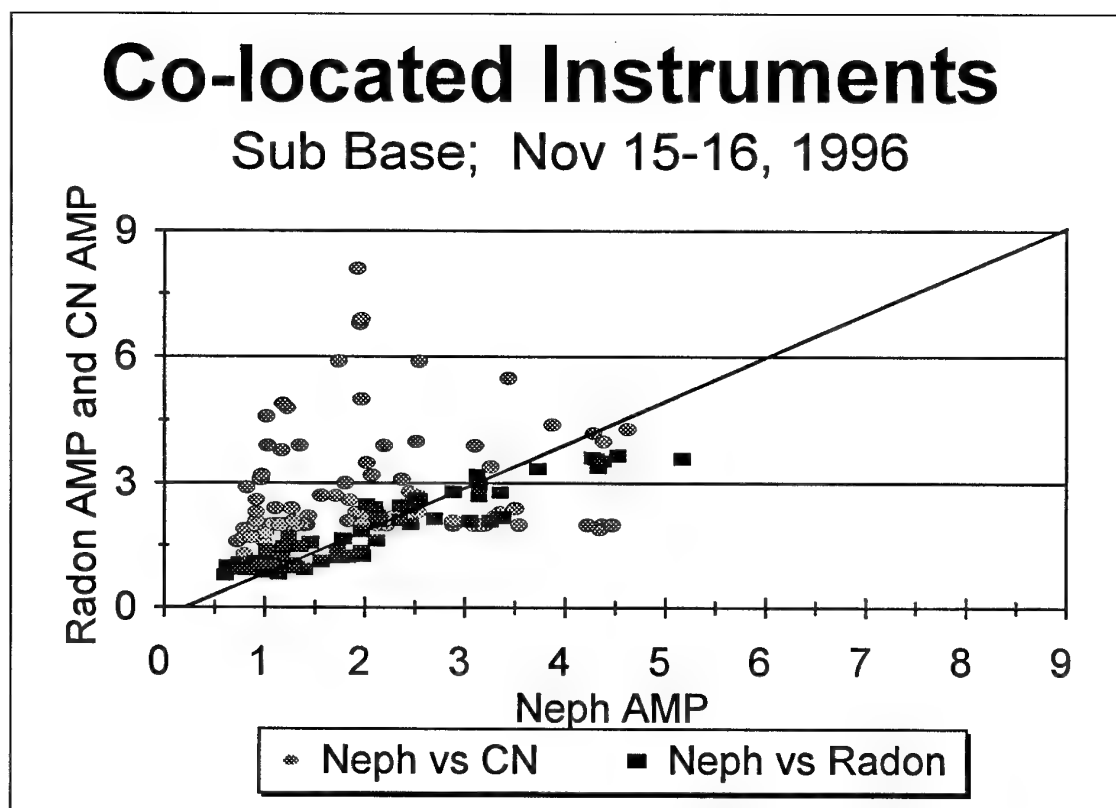


**Figure 9.** Correlation of the nephelometer AMP & CN AMP and nephelometer AMP & Radon AMP where all three instruments were co-located at the Naval Submarine Base San Diego.

## References

1. Gathman, S. G. "Optical properties of the marine aerosol as predicted by the Navy aerosol model," *Optical Engineering*, 22 (1) p. 57, 1983.
2. Gathman, S. G., and K. L. Davidson, "The Navy Oceanic Vertical Aerosol Model," Technical Report 1634, Naval Command, Control and Ocean Surveillance Center, 1993.
3. Larson, R. E., and D. J. Bressan, "Automatic radon counter for continual unattended operation," *Rev. Sci. Instrumen.*, 49(7), pp. 965-969, 1978.
4. Larson, R. E., and W. Kasemir, "Measurements of Atmospheric  $^{222}\text{Rn}$  at San Nicolas Island and Over Nearby California Coastal Areas During CEWCOM-78," Naval Research Lab Memorandum Report 3941, 1979.
5. Goroch, Andreas K., "Retrieval of size distribution information from nephelometer measurements," Naval Research Laboratory report, November 1996.
6. Littfin, K., and A. Goroch., "Determination of an air mass using nephelometer measurements and the Navy Aerosol Model," *SPIE Conf. Proceedings* July 1997, Vol 3125, pp. 59-65.
7. Battalino, T. E., "Numerical and Analytical Solutions of the Small Particle Amplitude in the Navy Aerosol Model," Naval Air Warfare Center Weapons Division Geophysics Technical Note No. 199, June, 1996.
8. Littfin, K. M. and D. R. Jensen, "An Overview of EOPACE (Electrooptical Propagation Assessment in Coastal Environments), Including In Situ and Remote Sensing Techniques, *AGARD Conference Proceedings* 582, paper #10, 1996.

PAPER NO: 21

DISCUSSOR'S NAME: D. Dion

You showed how variable the CN count could be, especially on board ship. Have you assessed contamination by ship of nephelometer measurements, for instance, correlation between readings and ship motion/speed?

AUTHOR/PRESENTER'S REPLY:

Having only one nephelometer during these experiments, we could not do a concurrent comparison as we could with CN. However, our data shows the nephelometer measurements were not as sensitive to the ship contamination as were the CN measurements. This is probably due to the fact that CN monitors count smaller particles (as low as 3 nanometers), which do not actually affect extinction at the visible wavelengths of the nephelometer.

PAPER No. 21

DISCUSSOR'S NAME: G. de Leeuw

The nephelometer seems a good instrument, but:

Why is the nephelometer not sensitive to locally produced contaminants?

The AMP is determined from the nephelometer data using NAM. Can the AMP then still be considered as an independent parameter that can be used in NAM?

AUTHOR/PRESENTER'S REPLY:

Any contaminant that are large enough to affect the scattering at visible wavelengths will show up in the nephelometer readings. But this instrument is relatively insensitive to the smallest aerosol. It is our hypothesis that the exhaust from the boat has a wide particle size distribution and that while the CN measures all of these particles, the nephelometer only measures the larger, more significant particles.

We are assuming that NAM describes the aerosol size distribution. We then need three independent observations to determine the 3 amplitudes. In this case, the three independent observations are nephelometer scattering AMP, average winds, and instantaneous wind speed. The nephelometer we used produces three scattering values at three visible wavelengths. Even one of these values, along with the two wind parameters, would be sufficient to determine the unknowns of NAM. However, we are using some of the additional data available from this instrument to decrease the error in the determination of A1. Our method does not use nephelometer readings to determine A2 or A3, but relies on the supporting data including wind statistics.

DISCUSSOR'S NAME: C. Wash

Can you explain the diurnal variation of the AMP in your 31 August - 4 September time series?

AUTHOR'S REPLY:

The diurnal variation of the AMP is the usual case in the southern California coastal area. There is a pattern of diurnal shift of wind direction from onshore to offshore almost every evening. So the air mass will be primarily marine during the day and continental at night.

## Analysis of Nephelometer Observations during EOPACE IOP-7

Andreas K. Goroch  
Marine Meteorology Division  
Naval Research Laboratory  
VOX: 408-656-4889  
FAX: 408-656-4769  
E-mail: [goroch@nrlmry.navy.mil](mailto:goroch@nrlmry.navy.mil)

Kathleen Littfin  
Space and Naval Warfare Systems Center San Diego  
Propagation Division Code D883  
49170 Propagation Path  
San Diego, CA 92152-7385

### Summary

Aerosol scattering measurements were conducted aboard a small boat during EOPACE IOP-7 from 25 August 1997 to 4 September 1997. Measurements were taken with a three wavelength integrating nephelometer, providing total scattering (from 7° to 170° scattering angle) and backscattering (from 90° to 170° scattering angle) at three wavelengths: blue (450 nm), green (550 nm), and red (700 nm) (Anderson et al, 1996). The measurements were obtained two meters from the surface at the bow of the boat transiting the IOP-7 propagation path. A preliminary analysis of the scattering relates the scattering to characteristics of the size distribution (Smirnov et al, 1995) and the degree of continental versus maritime influence of the mesoscale atmospheric environment. The Angstrom coefficient was observed to vary from 1.3 to 2, corresponding to a relatively broad size distribution. The Angstrom parameter is compared to that calculated from observed size distributions simultaneously measured aboard the boat. The nephelometer data are analyzed with empirical orthogonal functions to evaluate the independence of the six data channels, and to determine the utility and sufficiency of the several selected channels.

### 1. Introduction

Aerosol scattering is the dominant extinction mechanism in the visible wavelengths, and as such is critical to the analysis and prediction of atmospheric effects on electrooptical (EO) sensor systems. The applications of these systems are manifold in the military context, from surveillance systems required for ship safety and target identification to automated target detection and tracking subsystems of a weapon. These systems are a component of the naval commander's suite of sensors, including acoustic and electromagnetic systems. While the EO systems often have significant advantages (being a passive sensor

significantly reduces the sensor vulnerability), the effects of the environment can be significant and lead to the choice of other options.

Aerosol scattering information is often extended to several wavelengths corresponding to the wavelengths of the sensors of interest. The wavelength dependence of the scattering and the size distribution of the aerosols are related, although in general, not uniquely. Various measures of the relation have been used from the very simplest such as the Angstrom coefficient (the power law dependence of the scattering on wavelength) to various modes of an assumed size distribution. A particularly successful method has been the modeling of the distribution as a combination of simpler distributions (Whitby, 1973), with coefficients relating to instantaneous wind, average wind speed, and empirical air mass characteristics as described by Gathman in the Navy Aerosol Model (NAM) (Gathman, 1983, Gathman and Davidson, 1993). This parameterization has been directly related to parameters related to Navy tactical decision aids (Goroch, 1997).

This work examines the nephelometer measurements as part of comprehensive measurements of coastal aerosol characteristics. The work described here analyzes the nephelometer data in the context of the local meteorology, and points out information available in the measurements conducted.

### 2. Measurements

This program measured detailed environmental and aerosol conditions in the coastal region near the shore of San Diego. The TSI three wavelength integrating nephelometer (Anderson et al., 1996) was mounted below the deck of an 11 meter boat, with a 3 meter plastic sampling tube extending to the life line at the bow. The sampling intake was

located approximately 2 meters above the average water line. Nephelometer data included total (integrated from 7° to 170° scattering angle) and backward (integrated from 90° to 170° scattering angle) collected at 450 (blue), 550 (green), and 700 (red) nm wavelengths. The measurements were collected using the standard TSI data collection software. Meteorological measurements were collected on the bridge, approximately 3.5 meters above the surface. The met data were averaged over 1 minute intervals and saved on a laptop computer.

### 3. Analysis

The nephelometer data were analyzed using several techniques. The change of the size distribution can be described with the Angstrom parameter, which relates to the power law dependence of the scattering coefficient on wavelength,

$$\sigma_1 = \sigma_0 \left( \frac{\lambda_1}{\lambda_0} \right)^{-\alpha}$$

where  $\sigma$  is the scattering coefficient,  $\lambda$  is wavelength, subscripts 0 and 1 correspond to different wavelengths, and  $\alpha$  is the Angstrom coefficient (Trakovsky and Shettle, 1987). In the case of a Junge power law particle size distribution, the Angstrom coefficient can easily be shown to be the Junge coefficient minus one. This parameter is commonly related to atmospheric turbidity, since as the coefficient increases, the ratio of large to small particles decreases.

With scattering measurements at three wavelengths, three Angstrom coefficients can be obtained for each pair of wavelengths. The similarity of these pairs indicates how closely the particle distribution adheres to the power law distribution.

A combination of log normal distributions provides a somewhat more realistic assessment of the size distribution (Fitzgerald, 1991; Pruppacher and Klett, 1980). The Navy Aerosol Model (NAM), has been successfully used to describe marine aerosols as a combination of log normal distributions (Gathman, 1983; Gathman and Davidson, 1993). The coefficient of the smallest radius aerosol mode is physically related to the maritime or continental characteristic of the air mass, and is generally termed the air mass parameter (AMP). Nephelometer measurements have been used to retrieve the air mass parameter (Goroch, 1997; Littfin and Goroch, 1997).

It has been proposed that large particles (>1 micron diameter) can dominate the nephelometer measurements. Since most of the large particle scattering contribution is in the forward direction, the ratio of total scattering to backscattering provides some information on the potential for such contamination.

### 4. Variation of nephelometer observations

The preliminary analysis of the EOPACE IOP-7 nephelometer data has been conducted for the first 5 days of the experiment. The data sets were selected from the periods during which the boat was on the IOP-7 propagation path, offshore from the Coronado strand. The scattering coefficients for two days, 26 and 27 August, 1997 were found to demonstrate an interesting contrast in observations. Both days were characterized by negligible wind and calm seas. Meteorological observations reported elsewhere show the two days to be quite similar in terms of stability and mesoscale features.

The nephelometer total and backward scattering cross sections are shown in Figures 1 and 2. Both runs were conducted at approximately the same time of day, from 0500 to 0700 local. The scattering increases during this interval for both days. Each day has a maximum toward the end of the day. The scattering on the 27<sup>th</sup> however is significantly greater than that on the 26<sup>th</sup>. An examination of the two figures also shows there are differences in the relationships both between the scattering and backscattering, and among the different colors.

The most evident feature of both days is the large peak occurring toward the end of the data collection event. Figures 3 and 4 show the scattering and the ship track, with several locations identified on both the ship track and the backscatter plots. On both days, the ship changed from an outbound to an inbound track at the same time as the scattering showed an anomalous peak. It is expected that this peak corresponds to local contamination when the vessel is either stopped or changing course.

The air mass parameter (AMP) was retrieved using the procedure described earlier (Goroch, 1997). The air mass parameter is shown in figures 5 and 6 for retrieval techniques using each of three pairs of total scattering values, and from the combination of all three values. The AMP is consistently greater on the 27<sup>th</sup> than on the 26<sup>th</sup>, consistent with the observed increased scattering. Since the AMP retrieval artificially removes the large mode aerosol, this may indicate a problem with the scaling of the



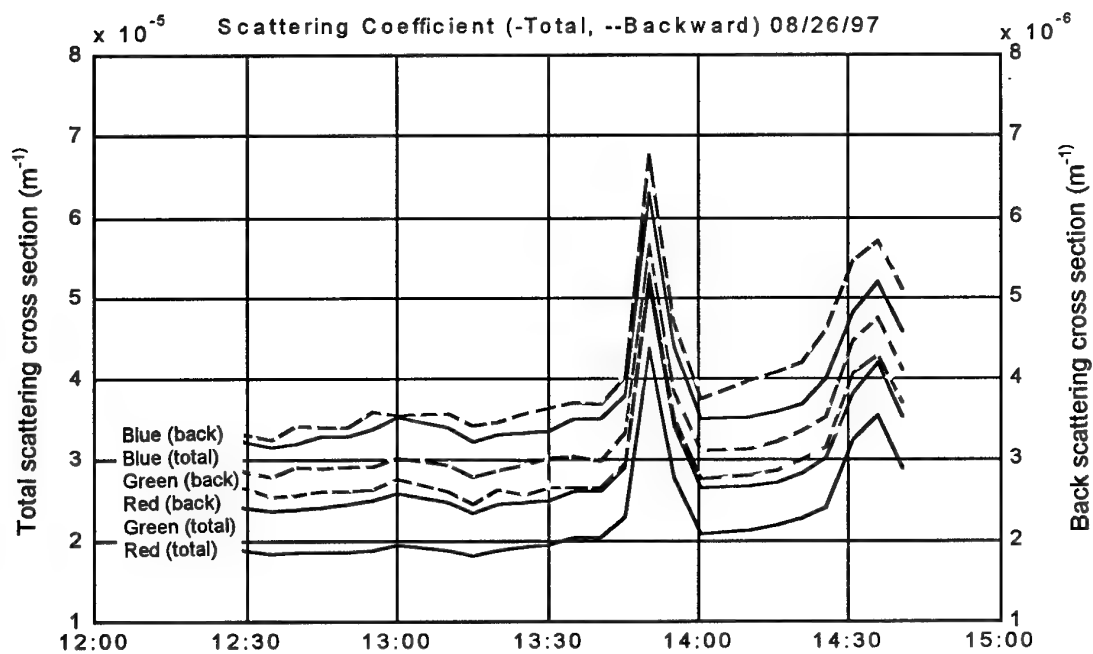


Figure 1. Nephelometer total and backward scattering cross sections during 26 Aug 98 ship event. Note the backscattering cross section scale is on the right.

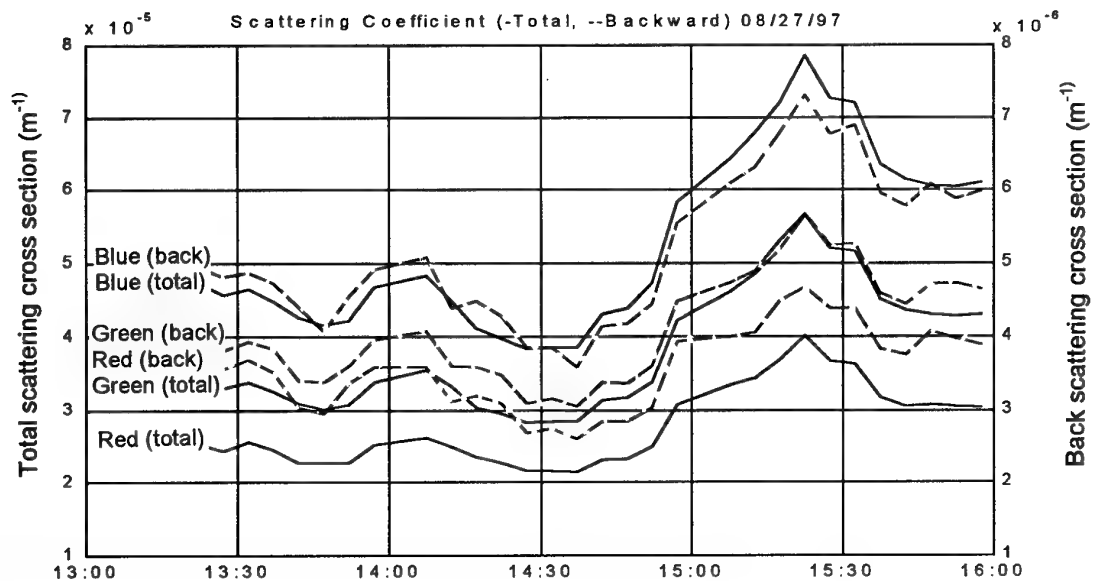


Figure 2. Nephelometer total and backward scattering cross sections during 27 Aug 98 ship event

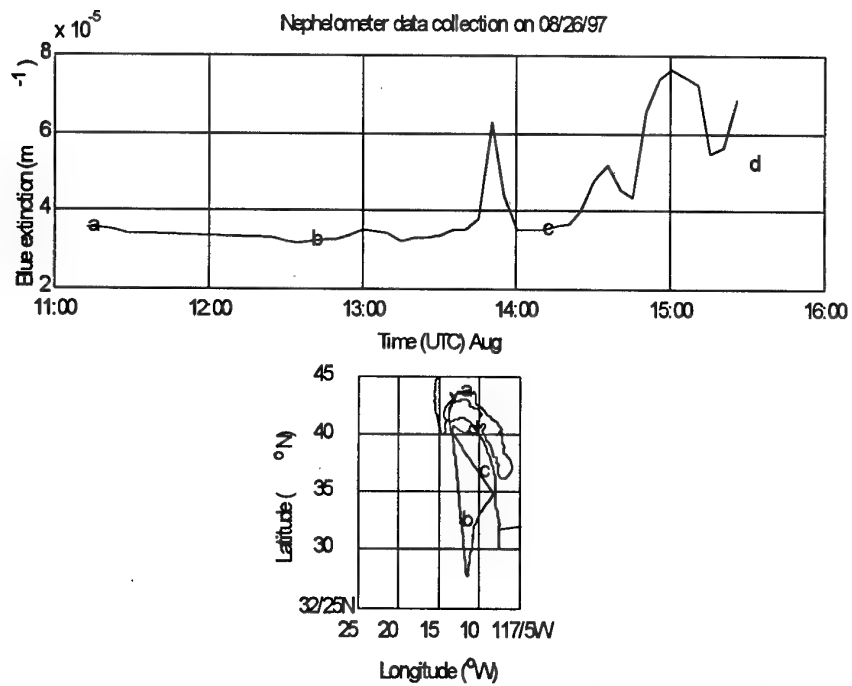


Figure 3. Ship track during 26 Aug 98 event. Ship locations are correlated to nephelometer observations above.

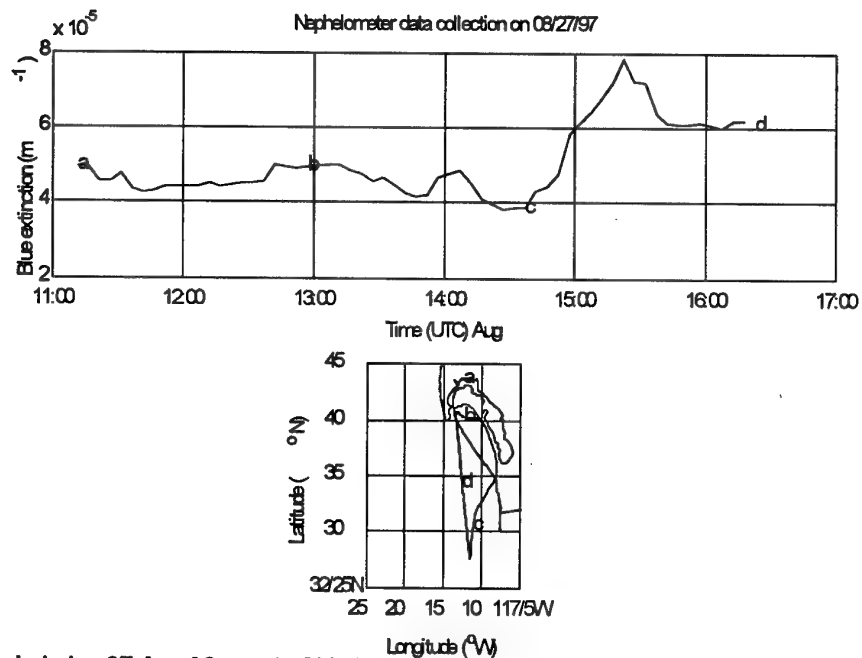


Figure 4. Ship track during 27 Aug 98 event. Ship locations are again correlated to the nephelometer observations.

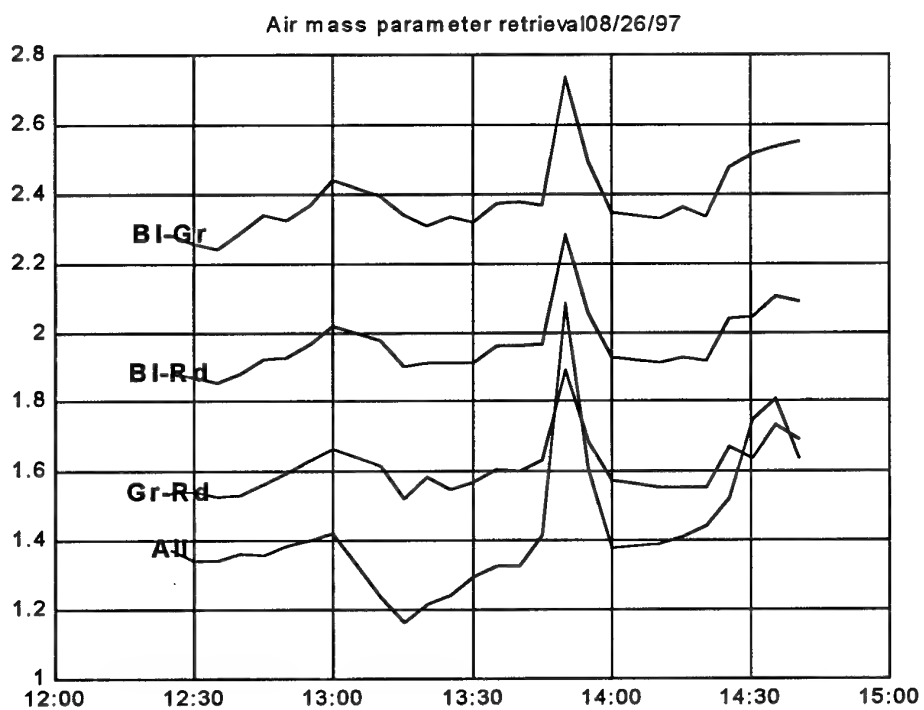


Figure 5. Air mass parameter retrieval using pairs of channels and all channels in least squares retrieval.

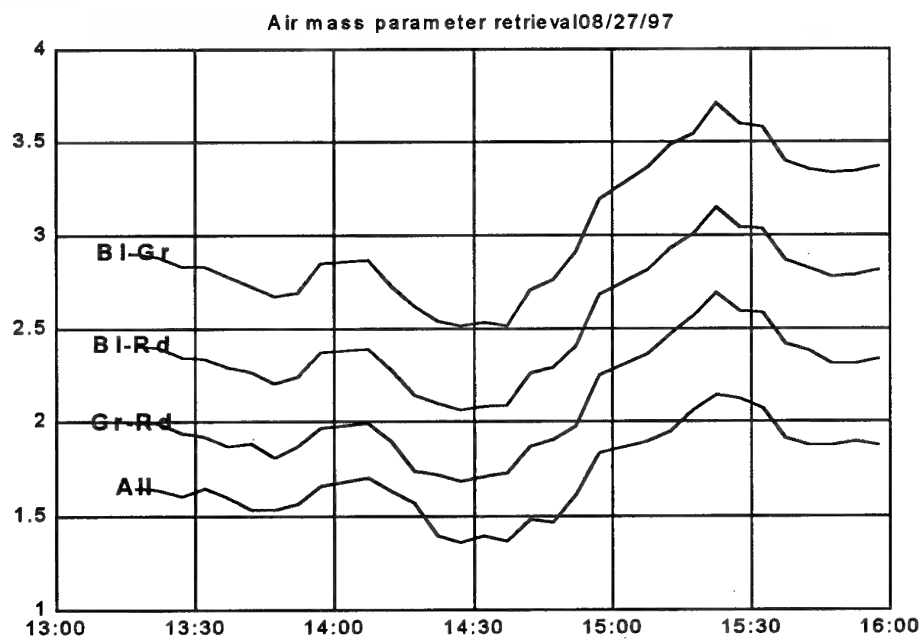


Figure 6. Air mass parameter retrieval for 27 Aug 98.

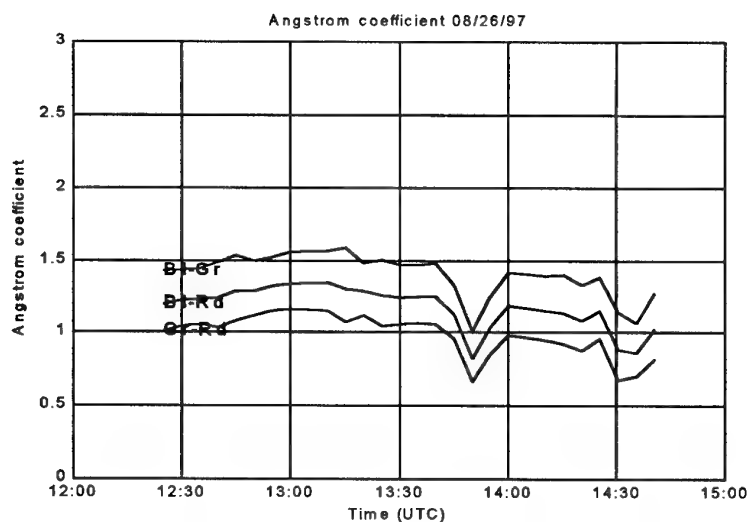


Figure 7. Angstrom coefficients calculated from pairs of scattering observations on 26 Aug 98.

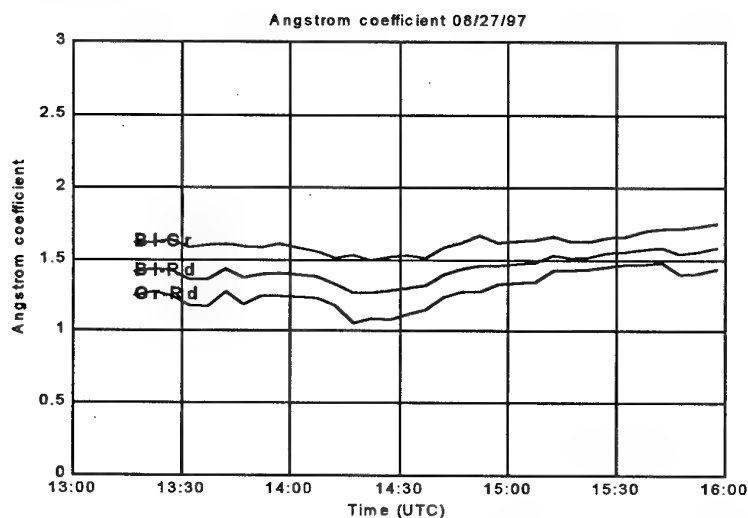


Figure 8. Angstrom coefficients calculated from pairs of nephelometer measurements on 27 Aug 97.

large aerosol component at very low wind speed. This conjecture must await analysis and comparison to detailed aerosol spectra.

Angstrom coefficients were calculated from the three pairs of scattering values (figures 7 and 8). The Angstrom coefficients were similar to values expected in clean marine regions (Smirnov et al., 1995). The values on the second day were somewhat larger than the first, consistent with the increasing relative concentration of larger particles.

## 5. Conclusions

Aerosol scattering measurements were conducted off the Southern California coast during August 1997. Comparison of two subsequent days indicates a moderate change in aerosol conditions although

the wind speeds were quite low, and temperature and humidity were similar. The scattering was related to the air mass parameter and the coefficient corresponding to the smallest particle mode was retrieved. Although the AMPs were low, consistent with a clear marine air mass, the differences between the two days were significant. The differences in the AMP were consistent with the differences in the Angstrom parameter. The Angstrom parameter was similar to the value expected from a strongly maritime environment.

## Acknowledgments

The support of the Space and Naval Warfare Command (PMW-185) and the U.S. Navy Office of Naval Research is gratefully acknowledged.

## References

- Anderson, T.L. et al., 1996. Performance characteristics of a high-sensitivity, three-wavelength total scatter/backscatter nephelometer. *Journal of Atmospheric and Ocean Technology*, 13: 967-986.
- Fitzgerald, J.W., 1991. Marine Aerosols: A Review. *Atmospheric Environment, Part A*, 25: 533-546.
- Gathman, S.G., 1983. Optical properties of the marine aerosol as predicted by the Navy aerosol model. *Optical Engineering*, 22(1): 57-63.
- Gathman, S.G. and Davidson, K.L., 1993. The Navy Oceanic Vertical Aerosol Model. 1634, Naval Command, Control, and Ocean Surveillance Center, RDT&E Div., San Diego.
- Goroch, A.K., 1997. Air mass parameter retrieval from nephelometer data in the Sea of Japan. In: K.M. Anderson and J.H. Richter (Editors), *Battlespace Atmospheric Conference, NRD - San Diego, CA*, pp. 47-51.
- Littfin, K. and Goroch, A.K., 1997. Determination of the origin of an air mass using nephelometer measurements and the Navy aerosol model, SPIE Annual Meeting, *Propagation and Imaging through the Atmosphere*, San Diego, CA, pp. 06.
- Pruppacher, H.R. and Klett, J.D., 1980. *Microphysics of Clouds and Precipitation*. Reidel, London.
- Smirnov, A., Villevalde, Y., O'Neill, N.T., Royer, A. and Tarussov, A., 1995. Aerosol Optical Depth Over the Oceans: Analysis in Terms of Synoptic Air Mass Types. *Journal of Geophysical Research*, 100(D8): 16639-16650.
- Trakhovsky, E. and Shettle, E.P., 1987. Wavelength scaling of atmospheric aerosol scattering and extinction. *Applied Optics*, 26: 5148-5153.
- Whitby, K.T., 1973. Modeling of multimodal size distributions., *Jahreskongress GAF*, Vienna, Austria, pp. 136-142.

PAPER No. 22

DISCUSSOR'S NAME: G. de Leeuw

Has the AMP also been retrieved from the nephelometer data for higher AMPs? And is the error then still <1?

AUTHOR/PRESENTER'S REPLY:

In this experiment, the AMPs were all rather low. But if you refer to my reference number 6 from the SPIE 1997 Conference proceedings, you will see comparisons of AMPs as high as 9, which indicates a strong continental influence. The agreement in the November 1996 experiment shown indicates agreement within plus or minus 2 AMP units. While not quite as good as the plus or minus one for marine AMPs, it is certainly good enough agreement to use accurately for IR predictions using the Navy Aerosol Model.

## Satellite and Ship-based Lidar Estimates of Optical Depth during EOPACE

**Carlyle H. Wash, Mary S. Jordan and Phillip A. Durkee**

Department of Meteorology  
Naval Postgraduate School  
589 Dyer Rd., Room 254  
Monterey, CA 93943-5114, USA  
Phone: 408-656-2516 Fax: 408-656-3061  
wash@nps.navy.mil

**Pepijn Veeffkind and Gerrit de Leeuw**

TNO Physics and Electronics Laboratory  
The Hague, The Netherlands

### SUMMARY

Coastal Marine Atmospheric Boundary Layer (MABL) aerosol optical depth is estimated from satellite data and compared with ship-based aerosol and lidar backscatter measurements, aircraft-measured aerosol, and rawinsonde data during the EO Propagation Assessment in Coastal Environments (EOPACE) Intense Observing Period (IOP) during April 1996. In the examined cases, satellite retrievals of aerosol optical depth and the ship and aircraft measurements were in good qualitative agreement. The ratio of visible and near-infrared NOAA AVHRR channels successfully depicted regions of maritime aerosol during the beginning and later parts of the IOP and the period of continental aerosol associated with the strong offshore flow of the Santa Ana event.

### 1. INTRODUCTION

Knowledge of the coastal MABL for the entire battlespace is critical for modern Navy operations. To support modern weapon and sensor systems, quantitative assessment of a number of MABL properties are needed. They include: optical depth, boundary layer depth, sea surface temperature, and surface layer temperature and moisture. These needs are even more critical in the coastal zone with the sparse surface observations away from the coast and the high temporal and spatial variability of littoral circulation systems. Satellite remote sensing is the only data source that can measure MABL properties in the coastal zone with the needed high spatial resolution. However, many of the uses of satellite data are qualitative. Quantitative satellite remote sensing methods need to be tested to provide these needed littoral data.

The EOPACE program focuses on the characterization of aerosol and boundary layer properties in the coastal zone and the determination if air mass parameters in various coastal locations can be derived, to a practical degree, from satellite imagery. In support of this project, several IOPs have been conducted. The combination of satellite data with several in situ surface and aircraft data sets offers an excellent opportunity to monitor significant optical depth and aerosol changes and in the coastal zone. In addition, quantitative comparisons can be made. The objective of this paper is to evaluate satellite-derived aerosol optical depths estimates using aircraft and ship-based aerosol measurements, a ship-based lidar and rawinsonde profiles of the MABL. Results from the April 1996 experiment will be presented in this paper with additional results from the March 1997 experiment expected to be available at the conference.

### 2. SATELLITE OPTICAL DEPTH RETRIEVALS

Radiative transfer theory provides the basis for methods used to characterize aerosol properties from satellite remote measurements. In a cloud-free, marine environment, the shortwave, solar radiation measured by a satellite radiometer is primarily the result of scattering by both molecular constituents of the atmosphere (Rayleigh scattering) and larger suspended aerosol (Mie scattering). Corrections to solar irradiance of less than 5% for ozone absorption are applied and aerosols are assumed to be non-absorbing. In the absence of sun glint, reflectance from the ocean surface is also small and contributions to the satellite-measured radiance due to surface foam and subsurface reflection are accounted by empirical measurements.

For atmospheres with small optical depths such as the clear, marine atmosphere, contributions by multiple scattering can be neglected. After accounting for Rayleigh scatter, the satellite-measured radiance can be related to optical depth, as illustrated in Equation 1.

$$L_a = \frac{\omega_o F_o}{4\mu} p(\psi_s) \delta_a \quad (1)$$

where  $L_a$  is the measured radiance at the satellite due to aerosol scattering at a given wavelength,  $\omega_o$  is the single scattering albedo,  $F_o$  is the incoming solar radiance at the top of the atmosphere,  $P$  is the scattering phase function,  $\psi_s$  is the scattering angle,  $\delta_a$  is aerosol optical depth, and  $\mu$  is the cosine of the satellite zenith angle (Ref. 1).

Durkee et al (Ref. 1) and Rouault and Durkee (Ref. 2) proposed a method of parameterizing the scattering phase function,  $P$ , based on the ratio of the aerosol radiance measured in channel 1 (visible) and channel 2 (near-IR) of the NOAA AVHRR satellite sensor. Other recent multi-channel aerosol estimates have been presented by Veefkind, et al (Ref. 3). Because the scattering efficiency of an aerosol distribution is wavelength dependent, scattering for a specific aerosol population peaks when the radius of the aerosol is nearly equal to the radiation wavelength. Subsequently, radiance counts measured by the AVHRR visible and near-IR channels will change with aerosol size distribution changes such that the ratio of channel radiances will be larger for smaller size particle distributions and smaller for larger size particle distributions. Durkee et al (Ref. 1) called the ratio of the channel aerosol radiances the particle size parameter, S12. Since S12 varies pixel by pixel over the entire image, the scattering phase functions can be parameterized pixel-by-pixel allowing variations in aerosol distributions to be properly factored into the optical depth retrieval. In addition, the S12 permits characterization of the aerosol size properties for the clear air in the image.

### 3. EOPACE IOP

This paper will report on the EOPACE IOP that was conducted from 2-12 April 1996 off the Southern California coast. During this IOP the R/V Point Sur traversed the coastal zone with a vertical pointing 1.06 micrometer LIDAR (provided by TNO), frequent rawinsonde temperature and moisture measurements (provided by NPS) and surface layer aerosol measurements. In addition, an instrumented aircraft measured aerosols and basic meteorological parameters

in the region. Polar orbiting NOAA satellite data was received and processed at NPS for the period. This IOP was of particular interest in that significant changes in MABL properties and aerosols occurred during the measurement period.

### 4. RESULTS

After leaving port on 2 April, the R/V Point Sur moved southward along the coast on 3 April. During this day, low and mid tropospheric flow was from the northwest and maritime aerosols spectra dominated the MABL. The MABL was very deep with a thickness of approximately 1100 m. NOAA satellite pass (not shown) from 2227 GMT 3 April showed clear conditions along the coast. The retrieved optical depth in this region was .25 associated with the larger-size marine aerosol size distribution and deep MABL. The S12 ratio for this area shows small values ranging between 1.7 and 1.9. These values indicate the larger, maritime aerosols dominate the MABL. This is consistent with ship-based data and air trajectories for this day.

Significant changes occurred in the low-level flow during the next 24 hours. Strong offshore northeasterly flow developed as illustrated in the 1000 mb streamline analysis for 0000 GMT 5 April in Figure 1. Doppler wind profilers in the region also show the development of a Santa Ana wind regime. The profiler at the Ontario airport measured NE winds in excess of 30 knots during the afternoon of 4 April while the coastal profiler at Los Angeles (LAX) airport measured north and NE winds of 10-20 knots above 700 m.

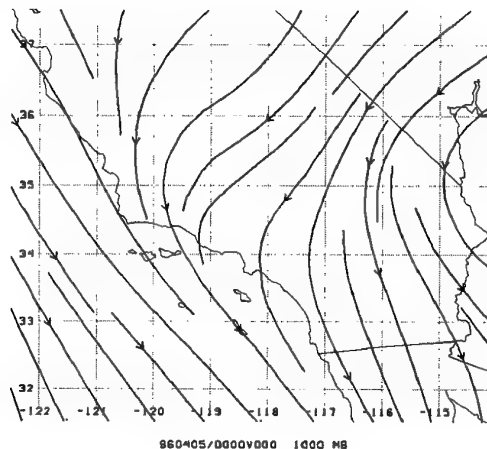


Fig. 1. 1000 mb streamlines for 0000 GMT 5 April 1996. Wind flow in the coastal region of the Southern California bight is offshore, bringing continental aerosols over the water.

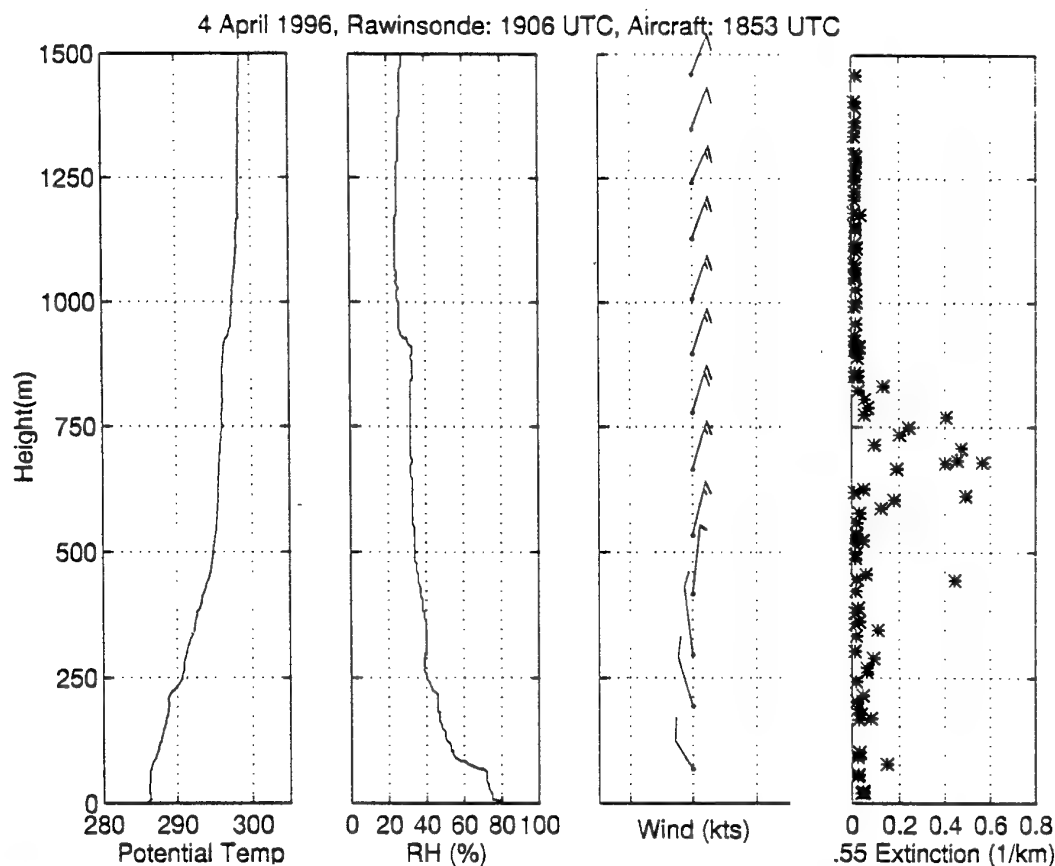


Fig. 2. Rawinsonde for 1906 GMT and aircraft aerosol extinction data for 1853 GMT 4 April 1996. Rawinsonde was launched from the R/V Pt. Sur and the aircraft concurrently flew a spiral vertical profile over the Pt. Sur. Plotted from left to right is rawinsonde measured potential temperature (C), relative humidity (%), winds (kts), and aircraft measured aerosol extinction at 0.55 microns.

Associated with this flow, an elevated layer of continental aerosols was observed by ship, aircraft and satellite sensors. Figure 2 presents an aircraft profile at 1853 GMT 4 April showing a distinct layer of aerosol extinction at 600-800 meters. Rawinsonde temperature, moisture, and wind data, collocated with the aircraft extinction data, are also included in this figure. These winds show NE winds in this layer of 15 to 20 knots. Figure 3 presents a time section of backscatter from the TNO mini lidar aboard the R/V Point Sur. The emitter is a 60 mJoule Nd/YAG laser and lidar returns are averaged over 10 minute periods. Data from 4 April shows strong backscatter return in a layer from 400 to 700 m. The layer of strong backscatter is in agreement with the high extinction values from the aircraft.

The NOAA satellite data from 2216 GMT 4 April is presented in Figure 4. High values of optical depth are

estimated over the entire Southern California coastal area. Values range from .17 to .38. There is a distinct plume of aerosols leaving the coast between Los Angeles and San Diego. The S12 ratio from this pass indicates a much higher ratio than 24 hours earlier. Values range from 2.9 to 3.1 indicating small aerosol sizes, typical of continental sources, are dominating the region. This is consistent with the lidar and aircraft data discussed earlier.

On April 5 the R/V Point Sur moved southeastward toward the plume observed by the NOAA satellite on 4 April. Subsidence associated with the offshore flow was quite intense this day and the MABL depths were very shallow, less than 100 m. Aircraft profiles and ship-based lidar (Fig. 3) continue to show aerosols in the lowest 1000 km. The aircraft data does not show a distinct layer of elevated extinction, but small values of aerosol extinction are present throughout the lowest



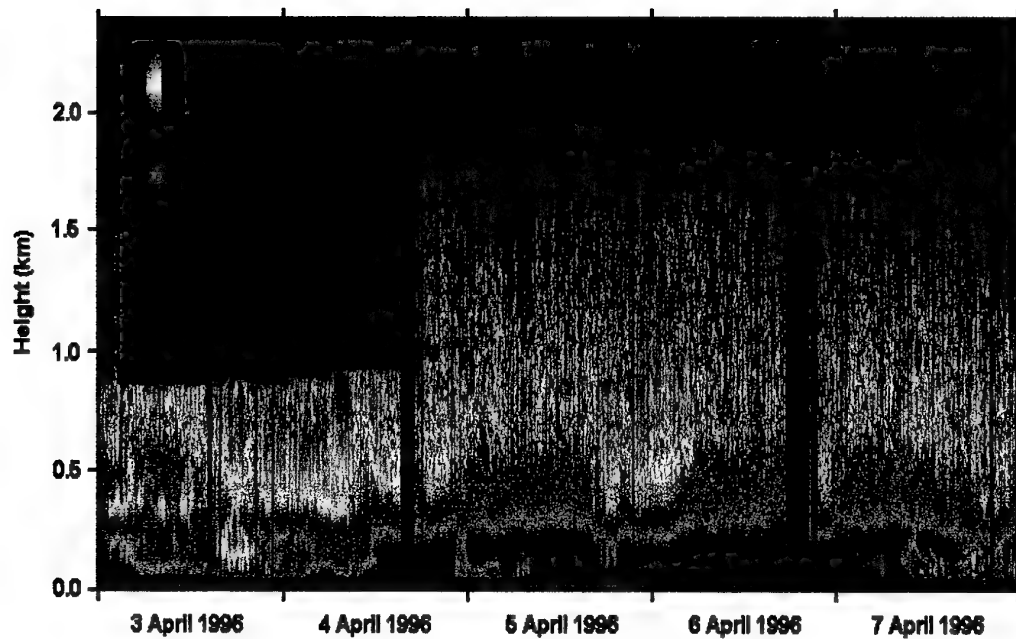


Fig. 3. Backscatter from the TNO mini lidar aboard the R/V Point Sur for 00 GMT 3 April - 00 GMT 8 April 1996. The emitter is a 60 mJoule Nd/YAG laser and returns are averaged over 10 min periods.



Fig. 4. Optical depth estimated from NOAA AVHRR data for 2216 GMT 4 April 1996. The R/V Point Sur ship track is indicated by the blue line. Rawinsonde launch locations are denoted by the red dots.

1 km. Satellite data for 2205 GMT 5 April (not shown) indicated lower values of optical depth (.15 to .25) but the remnant of the plume is still detectable.

The ship steamed through the plume location between 15 and 24 GMT 5 April. The stronger lidar backscatter values at that time (Fig. 3) are consistent with the satellite data. The S12 ratio continues to be high indicating smaller, continental aerosols over the coastal zone. In addition, Doppler wind profilers in the region also show the strengthening of this Santa Ana regime. The profiler at Ontario airport showed NE winds between 25 and 40 knots in the lowest 500 m during the afternoon of the 5 April while the coastal profiler at LAX airport showed N wind of 20 knots below 700 m.

On 6 April, the Point Sur traversed along the coast, 20 miles offshore, between Oceanside and Long Beach, which was the area of the plume on 4-5 April. The MABL continued to be quite shallow, less than 100m, due to subsidence and strong offshore flow. By 2100 GMT, rawinsonde data indicates that 10-15 knot westerly flow was reestablished below 1200m, and the strong NE winds continued above that level. The lidar (Fig. 3) for 6 April measured strong backscatter off the aerosol early in the day, but the significant decrease in backscatter at the end of the day is consistent with the return of westerly flow and a marine air mass.

On 7-8 April, the Point Sur traversed around San Clemente and Santa Catalina Islands and then returned near the coast, south of Long Beach, on its way to San Diego. During this period the offshore flow ceased, the MABL deepened to 300 m, with NW low-level winds. This was accompanied by more low-level cloudiness in the MABL. In the clear areas, optical depth values decreased to .10 to .15 and the S12 ratio decreased indicating the return of maritime aerosols in the MABL. This was confirmed by in situ measurements aboard the R/V Point Sur.

## 5. CONCLUSIONS

During this IOP satellite retrievals of aerosol optical depth and the ship and aircraft measurements were in good qualitative agreement. The NOAA satellite S12 ratio successfully depicted regions of maritime aerosol during the beginning and later parts of the IOP and the period of continental aerosol associated with the strong offshore flow of the Santa Ana event.

At this time, quantitative data from the lidar of aerosol extinction are not available. Therefore, a more quantitative assessment of satellite versus in situ data is not available. This will be a major priority in future studies with this and other IOP data sets.

The new generation of geostationary satellite, GOES-9, was operating over the West Coast at this time. The higher radiometric resolution from GOES-9 sensors provide the opportunity to retrieve aerosol depth. GOES-9 data from this period will be used to add to the temporal resolution of the satellite data for this period. In particular, GOES data should be able to monitor the development of the aerosol plume on 4 April.

## 6. ACKNOWLEDGMENTS

The NPS work is supported by SPAWAR Systems Center, San Diego through Office of Naval Research funding. The Netherlands Ministry of Defense, assignment A95KM729, and the US Office of Naval Research, Grant N00014-96-1-0581, support the participation of TNO-FEL in EOPACE. Aerosol retrieval work at TNO-FEL is supported by SRON EO/008. The authors would be to thank Kenneth Davidson, NPS, Michael H. Smith and Martin K. Hill, Centre for Marine Atmospheric Sciences, University of Sunderland, Sunderland, United Kingdom, and Kathleen Littfin, SPAWAR Systems Center, San Diego, CA, for sharing data and their expertise. EOPACE coordination and direction is provided by Dr. D. R. Jensen for the SPAWAR Systems Center, San Diego, CA.

## 7. REFERENCES

1. Durkee, P. A., F. Pfeil, E. Frost, and R. Shema, 1991. Global analysis of aerosol particle characteristics. *Atmos. Env.*, **25A**, 2457-2471.
2. Rouault, M. and P. A. Durkee, 1992. Characterization of aerosols from satellite remote sensing. In *Nucleation and Atmospheric Aerosols*, 357-360, N. Fukuta and P. E. Wagoner (Eds), A. Deepak Publishing.
3. Veefkind, J. P., G. de Leeuw, and P. A. Durkee, 1997. American Geophysical Union Fall Meeting, December 1997, San Francisco, CA.

## Aerosol production in the surf zone and effects on IR extinction

F.P. Neele<sup>1</sup>

G. de Leeuw<sup>1</sup>

A.M.J. van Eijk<sup>1</sup>

E. Vignati<sup>2,3,4</sup>

M.K. Hill<sup>5</sup>

M.H. Smith<sup>5</sup>

<sup>1</sup>TNO Physics and Electronics Laboratory, P.O. Box 96864, 2509 JG The Hague, The Netherlands

<sup>2</sup>Risø National Laboratory, Roskilde, Denmark

<sup>3</sup>National Environmental Research Institute, Roskilde, Denmark

<sup>4</sup>Joint Research Centre, Environment Institute, Ispra, Italy

<sup>5</sup>Centre for Marine and Atmospheric Sciences, University of Sunderland, Sunderland, UK

### SUMMARY

The aerosol production in the surf zone, as determined from measurements, at two sites along the California coast is presented. The data used were collected during three EOPACE (Electro-Optical Propagation Assessment in Coastal Environments) measurement campaigns in 1996 and 1997. Particle counters were deployed at both the end and the base of two piers which extended into the ocean, beyond the surf zone. For winds from the sea, a clear increase in aerosol concentration was measured, between the particle counters at the end and the base of the piers. Aerosol concentrations were measured at the base of the piers at three heights, which allowed for the estimation of the aerosol production in the surf zone. Taking into account the different whitecap ratios, the surf zone aerosol source function derived from the data compares well with previously reported open-ocean source functions, in agreement with the common bubble (film and jet drops) origin. Wind speeds measured during the experiments were up to about 9 m/s; therefore, the source function presented here applies to the bubble part of the source spectrum only. Infra-red extinction coefficients were computed from the aerosol concentrations, using a Mie scattering code. Extinction values may be up to two orders of magnitude larger than in the unperturbed oceanic air mass; the vertical gradients in extinction are also much stronger than those reported for open-ocean conditions. A simple aerosol dispersion model, using observed surf zone aerosol production rates, predicts that air masses up to several km from the surf zone may be significantly affected by the surf-produced aerosol. For winds from land, this proves the importance of the surf zone in assessing the performance of electro-optical systems in coastal areas.

### 1. INTRODUCTION

Aerosols in the marine atmospheric boundary layer and their effects on a variety of processes have been investigated in the past decades by various research groups. One of the effects of the maritime aerosol that has attracted attention was their influence on the propagation of electro-magnetic radiation at wavelengths in the atmospheric transmission windows in the IR<sup>1</sup>, both for military applications and, more recently, also for climate. Until the 1990's, the open ocean was considered most important. However, many experiments were conducted with the instrumentation ashore. The effect of the nearby surf zone was considered negligible. Experiments where aerosols

were measured both ashore and on a ship to assess the influence of the surf on the aerosol concentrations close to the shoreline indicated that the surf was unimportant<sup>2</sup>.

However, during the ONR (Office of Naval Research) aerosol workshop in Monterey, in May 1994, a simple calculation by Monahan (UCONN), showed the possible impact of the aerosol produced in the surf zone<sup>3</sup>. This calculation was based on aerosol production by a whitecap, and a realistic assumption as regards the equivalent whitecap coverage of the surf zone and its horizontal extent. The importance of this (then hypothetical) effect was recognised and included as an applied research topic into EOPACE (Electro-Optical Propagation Assessment in Coastal Environment), the work programme of which was formulated in the following year<sup>4</sup>. EOPACE started in October 1995. Three Surf experiments (Surf-1, 2 and 3) were conducted as part of EOPACE to determine the production of aerosol over the surf, in a variety of environmental conditions at coastal sites in California: La Jolla, near San Diego, in January/February 1996 (Surf-1) and in March 1997 (Surf-3), and in Moss Landing, Monterey Bay (March 1996, Surf-2). The final goal of these experiments was to provide an assessment of the effect of the surf on electro-optical propagation in a coastal environment. It was a common effort of several research groups from the USA, the UK and The Netherlands involving measurements of aerosols, bubbles and meteorological parameters including turbulence and visibility, as well as laser visualisation of the aerosol plumes over the surf and spectral transmission measurements<sup>4</sup>.

In this paper, results are presented from the analysis of data collected by TNO Physics and Electronics Laboratory (TNO-FEL) and the University of Sunderland (CMAS) in the three EOPACE Surf experiments, extending the work presented by de Leeuw et al.<sup>5</sup>. Other results were presented by Gathman & Smith<sup>6</sup>.

The present analysis shows that, over the surf, the aerosol concentrations may increase by up to two orders of magnitude, depending on the height above sea level and aerosol size. The largest increase is observed for aerosols with diameters of about 10 µm (the largest aerosol in the present, corrected data set).

The vertical aerosol concentration gradients observed during the surf experiments provided the necessary data to measure the aerosol production in the surf zone. A clear dependence

on wind speed was observed, with higher fluxes observed at higher wind speeds, probably resulting from more efficient upward turbulent transport. Taking into account the different whitecap area between the surf zone and the open ocean, the aerosol source function derived here agrees well with previously reported source functions for open-ocean conditions, for aerosol sizes up to about 10  $\mu\text{m}$ , in agreement with the common origin, i.e., breaking waves. The present data set does not cover the spume domain, as the wind speeds did not exceed 9 m/s.

The infrared (IR) extinction coefficients calculated from the aerosol size distributions similarly show an increase of up to two orders of magnitude over the surf zone. Extinction gradients are presented and compared with results for open-ocean conditions. Estimates of the effect of the increased extinction on transmission across the surf are presented for on-shore winds. For off-shore winds, an extensive study, involving advection of the surf-produced aerosol and size-dependent dispersion and deposition, is necessary for the assessment of the surf effect on the performance of EO systems, along lines of sight that intersect the surf zone. Estimates of the horizontal extent of the surf produced aerosol in off-shore winds are derived with a simple dispersion model. In future work, a more comprehensive model will be applied to this problem.

## 2. EXPERIMENTAL SETUP

### 2.1 Experiment sites

The measurements were performed at the piers of the Scripps Institute of Oceanography (SIO), La Jolla, San Diego (Surf-1 and Surf-3) and Moss Landing, Monterey (Surf-2). At both locations, sea breeze conditions govern the wind pattern: winds from land during the night and early morning, light winds from sea during the afternoon. Aerosol probes were installed at both ends of the piers to exploit these conditions. For winds from sea, data from one of three particle counters at the end of the piers provided background size distribution in the well-mixed air mass before it entered the surf zone. At the base of the piers, three particle counters measured the increase in aerosol concentration due to production in the surf zone, at different heights above sea level. The production in the surf zone can be estimated from the vertical gradient measured by the three counters. Standard meteorological parameters (temperature, humidity, pressure, wind speed and direction) were recorded at various positions on the piers. Table 1 lists the most important instruments and their locations.

Instrument	Type	Position	Average height above mean sea surface	Parameter measured
PMS1	ASAS-300A and CSAS-100-HV	Base of Pier	12 m (Surf-1,3) 7 m (Surf-2)	Aerosol size distribution 0.16-32 $\mu\text{m}$
PMS2	CSASP-200	Base of Pier	15 m (Surf-1,3) 11.2 m (Surf-2)	Aerosol size distribution 0.2-20 $\mu\text{m}$
PMS3	CSASP-100-HV	Base of Pier	7 m (Surf-1,3) 5 m (Surf-2)	Aerosol size distribution 0.5-47 $\mu\text{m}$
PMS4	FSSP-100	End of Pier	11 m (Surf-1,3) 6 m (Surf-2)	Aerosol size distribution 0.5-47 $\mu\text{m}$
Rotorod	-	Variable	1-9 m (Surf-1,3) 1-6 m (Surf-2)	Aerosol size distribution $D > 13 \mu\text{m}$
BMS	-	Variable	-0.36 m	Bubble size distribution $D > 30 \mu\text{m}$
Sonic anemometer	Solent research type	various	various	Wind speed and direction (20 Hz) & turbulence; Turbulence profiles & wave effects on air flow
Cup anemometer	Thies	Base of Pier	12.5 m (Surf-1,3) 11.5 m (Surf-2)	Wind speed
Wind vane	Thies	Base of Pier	12.8 m (Surf-1,3) 11.5 m (Surf-2)	Wind direction
Rotronic	MP440	Base of Pier	12 m (Surf-1,3) 7 m (Surf-2)	Air temperature & RH
Rotronic	MP440	Base of Pier	13.2 m (Surf-1,3) 11.2 m (Surf-2)	Air temperature & RH
Nephelometer	-	Base of Pier	12 m (Surf-1,3) 7 m (Surf-2)	Aerosol scattering
Pyranometer	Kipp	Base of Pier	12 m (Surf-1,3) 6.6 m (Surf-2)	Irradiation
Rain detector	-	Base of Pier		Rain occurrence
Barometer	Honeywell 142PC30A	Base of Pier	11 m	Atmospheric pressure

Table 1. Instrumentation used during the Surf experiments. Aerosol sizes refer to the diameters measured.

## 2.2 Particle counter (inter)calibration

All particle counters were size calibrated with particles with well-defined diameters. To remove any remaining differences among the instruments, a instrument comparison test was performed prior to the Surf-1 and Surf-3 experiments. During the test, all particle counters were operated for several days at the same location. The size distributions measured during this period were averaged to obtain a common mean, and inter-instrument correction curves were defined as the deviation of each instrument from this common mean. These correction curves were applied to the data of the subsequent experiments.

Unfortunately, there was no such instrument comparison period prior to the Surf-2 experiment. Instead, correction curves were obtained from the Surf-2 data directly. It was assumed that the data from the counters at the base of Moss Landing represent the true size distributions (these counters had been calibrated at the laboratory with aerosol of known size distributions). The difference between the data from pms4 (at the end of the pier) and pms1 (at the pier base, at comparable height) is then equal to the pms4 instrument correction *minus* the surf effect for onshore winds, while for winds from land this difference equals the instrument correction *plus* the surf effect. Hence, the instrument correction factor for pms4 can be obtained from the average difference between pms1 and pms4, for both onshore and offshore winds. Correction curves for pms4 that were obtained in this way showed a smooth dependence on aerosol size.

## 3. AEROSOL CONCENTRATIONS

Figure 1 presents part of the data set, showing clearly the effect of the surf zone on the aerosol concentrations. The lower part in figure 1 shows concentrations of particles with a diameter of 5  $\mu\text{m}$ , during the first four days of the Surf-1 experiment (January 24 through 27, 1996). These concentrations are relative to the concentrations measured by the particle counter at the pier end which, for westerly (onshore) winds, represent the background aerosol. Also presented in figure 1 are meteorological parameters such as air temperature, relative humidity, wind speed, wind direction and wave height and period.

Wind speed was generally low, usually less than 2 m/s with occasional short periods of higher wind speeds of up to 4 m/s. These wind speeds are still too small to cause significant production of sea spray aerosol over the open ocean. The wind direction followed the general sea breeze pattern, with offshore winds (easterly wind directions) during the night and morning, quite suddenly changing to onshore flow late in the morning and back to offshore before sunset. Relative humidity varied between 70% and 100%, while air temperatures were between 8  $^{\circ}\text{C}$  and 17  $^{\circ}\text{C}$ . Significant wave height varied between 0.5 and 1.5 m, and the wave period slowly decreased from 11 s in the first few days, to 5 s around day 28 (after which it increased to more than 15 s).

As expected, an obvious correlation is observed between the aerosol concentration and wind direction. During westerly winds, a strong increase in aerosol content with respect to the background was observed. The concentrations varied significantly among the three probes, the highest concentrations measured by pms3 which was situated closest to the sea surface. When the wind was from land, the three probes at the

pier base measured similar aerosol concentrations (as expected) and the surf generation was visible as an enhancement of the concentrations measured with pms4.

No clear dependence of the aerosol concentration on meteorological parameters other than wind direction and wind speed are apparent from figure 1. It is expected that significant wave height and wave period are key elements in the aerosol production, but no clear correlation has been found. Although variations in these parameters were relatively small during the experiments, significant variations in the width and activity in the wave breaking zone were observed. The text in the middle panel in figure 1 gives a rough indication of the rigour or activity in the surf zone. The first two days of the Surf-1 experiment a 'normal' surf zone was observed of about 100 m wide. During day 26 the surf zone gradually narrowed and whitecapping decreased, but, due to a simultaneous increase in wind speed and concurrent enhanced transport, this is not readily visible in the aerosol concentrations at the pier's base.

The aerosol gradients, as derived from the data presented in figure 1, show a peculiar feature. The concentrations are highest at the lowest sampling point of about 7 m above sea level (pms3), and then decrease with height. However, in onshore winds, the concentrations at 12 m were often observed to be somewhat lower than at 15 m. The particle counters at 12 m were mounted above the deck of the pier (pms1). In contrast, the more detailed profiles of giant particles ( $D > 13 \mu\text{m}$ ), measured with the Rotorod rotating impaction samplers, do not show a decrease in aerosol concentration near the pier deck. The Rotorod samples were taken at height intervals of 1 m, requiring about 20 minutes for a complete profile. It is noted that the Rotorod profiles were measured at some distance from the Pier (upwind), whereas the data presented in figure 1 for the 12 m level were measured with pms1 mounted at about 1.5 m above the pier deck on a wooden box, near the railing.

It is presumed that heating of the Pier deck by solar radiation resulted in the observed reduction in relative humidities, which in turn induced a shift in the particle size distribution to smaller diameters. Hence, the observed concentrations will have been smaller, thus causing the dip in the concentration profile at 12 m. This view is supported by the observation that during offshore winds the concentrations showed the expected decrease with height (cf. figure 1, usually between 8 p.m. and 11 a.m.). The kink was observed only during the afternoon, when the Pier deck was warm. Indeed, the humidity and temperature sensors mounted close to the box at heights of 12 and 13.2 m above sea level, showed significant differences (in fact the relatively low humidities and high temperatures near the box were the reason for having a second sensor somewhat further away from the pier surface).

## 4. SURF ZONE AEROSOL SOURCE FUNCTION

The data presented in the previous section can be used to estimate the aerosol production in the surf zone. Combining the data from the three surf experiments, wind speeds up to about 9 m/s are covered.

An example of the effect of the surf on the aerosol size distributions is presented in figure 2, showing aerosol size distributions measured simultaneously with all four aerosol counters in on-shore wind. The difference between the data from pms4 (representing the background concentration) and the data from the counters downwind from the surf can be

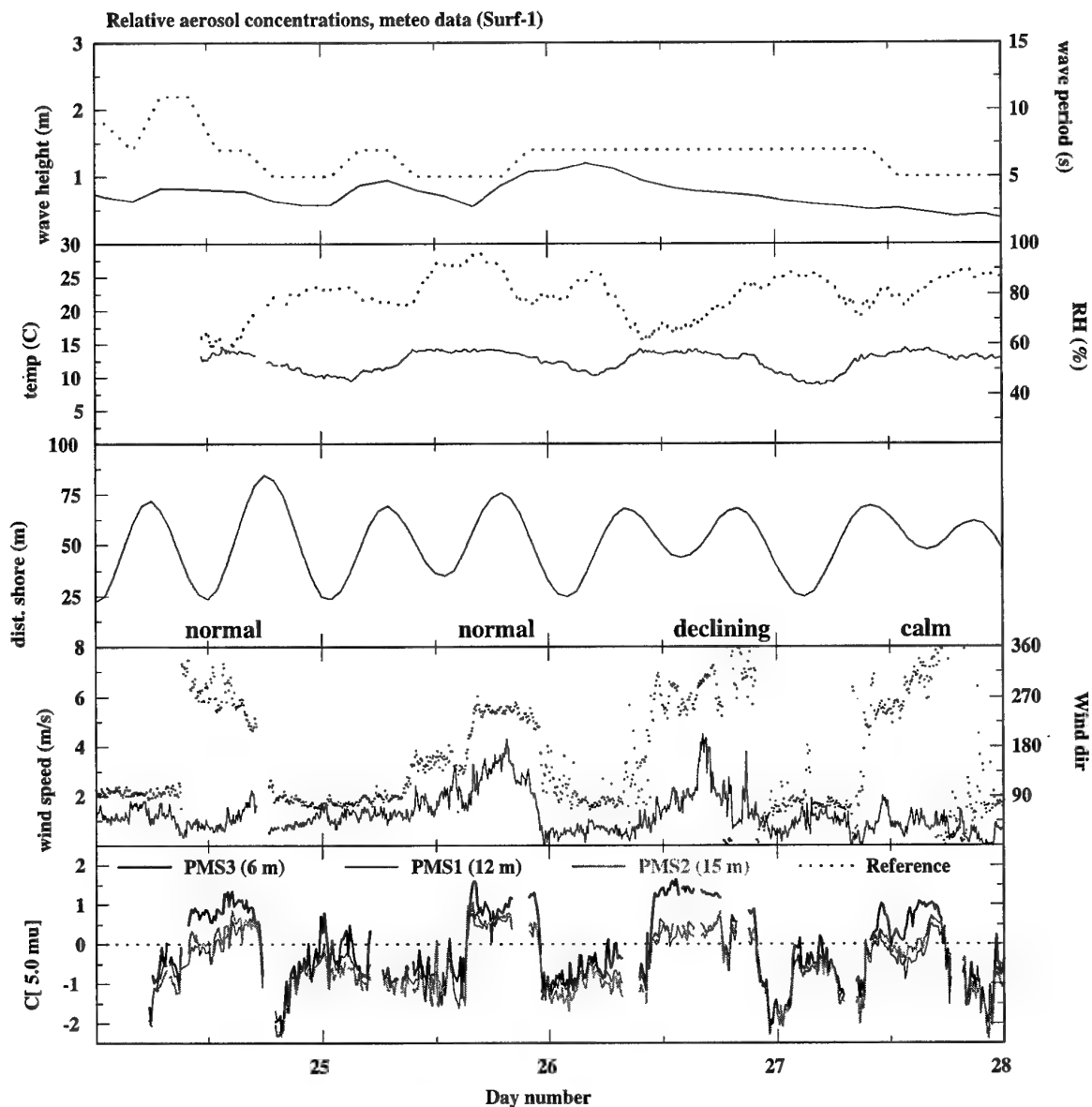


Figure 1. Relative aerosol concentrations (diameter  $5 \mu\text{m}$ ) and relevant meteorological parameters during the first four days of the Surf-1 experiment. The bottom panel shows aerosol concentrations (in  $^{10}\log$  format) at the base of the Scripps Pier relative to those from the particle counter at the end of the Pier (pms4):  $^{10}\log(\text{pms1,2,3}) - ^{10}\log(\text{pms4})$ . For onshore winds (westerly winds, during the afternoons), pms4 measured the aerosol concentration in the well-mixed air mass before it enters the surf zone. The upper panels show the various meteorological and wave parameters measured during the campaign. Parameters plotted on the left hand side axes are plotted as solid lines, those on the right hand side axes are plotted as dotted lines. There is a strong correlation of aerosol concentration with wind direction. During winds from sea, aerosol concentration may be up to 100 times higher than in the air mass unaffected by the surf zone. In the middle panel (showing tide, or distance to the water line) the rigour of the surf is indicated. The declining activity in the surf zone on day 26 cannot be readily correlated with a decrease in aerosol concentrations at the pier's base, due to a simultaneous increase in wind speed.

attributed entirely to generation in the surf zone. The surf effect on the aerosol content is largest for large diameters, as can be seen in figure 2.

To obtain an estimate of the overall production in the surf, the surf contributions to the aerosol concentrations were averaged for all periods of on-shore winds during three surf experiments. The results for the Surf-1 and Surf-3 experiments are shown in figure 3, for diameters of 1, 5 and  $10 \mu\text{m}$  and wind

speeds up to 2 m/s. The data clearly show the variation of the aerosol concentration with height, with gradients increasing with particle size. The concentrations near 12 m are not shown, for reasons discussed above. The results in figure 3 suggest that at the base of the pier the surf-produced aerosol extends to heights of about 30 m. This height compares well with lidar observations of the surf-produced aerosol plumes (R. Philbrick, unpublished results). It should be stressed that

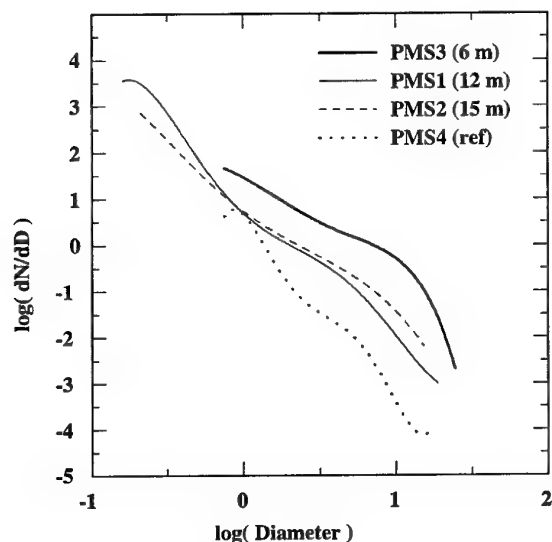


Figure 2. Typical aerosol size distribution ( $\text{cm}^{-3}/\mu\text{m}$ ) measured during onshore winds. The surf-produced aerosol causes higher concentrations at pms1-3. This effect is larger for larger diameters.

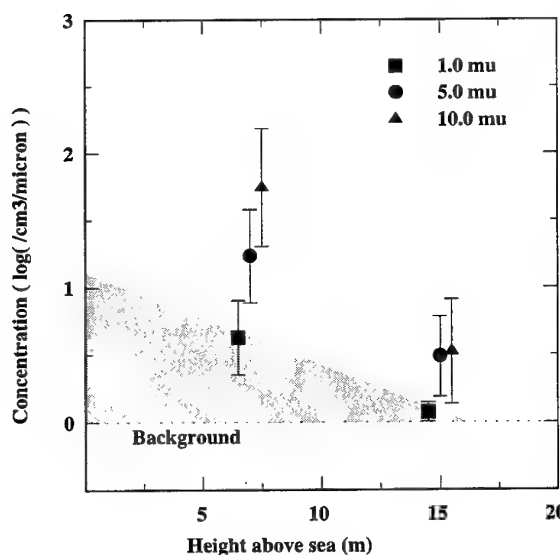


Figure 3. Average increase in aerosol concentrations, for wind speeds up to 2 m/s during the Surf-1 and Surf-3 experiments. Shown are averages of concentrations at two heights at the base of the Scripps pier, relative to the background concentration. Aerosol concentration increases sharply towards sea level, with gradients increasing with particle size. The shaded area corresponds with the number of  $1\mu\text{m}$  particles generated in the surf zone. Data shown are from pms2 (7 m height) and pms3 (15 m height).

figure 3 shows the enhancement of the aerosol concentrations downwind from the surf zone.

Data like those in figure 3 are used to estimate the total number of aerosol produced by the surf, as a function of aerosol size. It is assumed that the aerosol height profile is logarithmic,

which is expected for an equilibrium situation<sup>7</sup>. Obviously, close to the source there will be no equilibrium between production and removal. However, the limited data that are presently available do not allow for a more sophisticated approach.

The horizontal aerosol flux downwind from the surf zone  $dF/dD$  is given by the expression

$$\frac{dF}{dD}(D) = \frac{u}{L} \int_0^{z_{\max}} \left( \frac{dN}{dD}(z, D) - \frac{dN}{dD}_{bg}(D) \right) dz$$

where  $dN/dD$  is the aerosol concentration as a function of height  $z$  and aerosol diameter  $D$ ,  $dN/dD_{bg}$  the concentration in the well-mixed air before it enters the surf zone,  $u$  the wind speed at the base of the pier and  $L$  the width of the wave breaking zone. The background concentration, for onshore winds, is measured with the particle counter at the pier's end, pms4.  $dN/dD(z, Z)$  is obtained by fitting a logarithmic profile to the data measured at the base of the pier, as explained above. The aerosol numbers are integrated between sea level and the height at which the concentrations have returned to the background value ( $z_{\max}$ ). In figure 3 the area over which the  $1\mu\text{m}$  particles are integrated is indicated by the shaded area. The horizontal flux over the beach near the base of the pier is obtained by multiplying the aerosol number by the wind speed  $u$ . The additional assumption is made that this flux is due completely to production in the surf zone, and, therefore, that the vertically integrated horizontal flux over the beach equals the vertical flux integrated over the whole surf zone. Thus, particle deposition between the surf zone and the pier base is ignored. A division by the width of the surf zone  $L$  normalises the surface flux to a value independent of  $L$  (units  $\text{m}^{-2}\text{s}^{-1}\mu\text{m}^{-1}$ ).

Figure 4 shows the aerosol number and volume fluxes, obtained from data from the Surf-1 and Surf-3 experiments at wind speeds up to about 9 m/s. The aerosol sizes represent the size upon formation derived from the relation between  $r_{80}$  (radius at 80% humidity) and  $r_0$  (radius upon formation),  $2r_{80} = r_0$  (Ref. 8). The humidity during the Surf experiments was never significantly different from 80% during onshore winds.

Figure 4 shows that the surface flux of particles of  $0.8\mu\text{m}$  in diameter increases by about a factor of 10 between the lowest and the highest wind speeds. For larger particles the wind speed effect appears to be smaller. Since the suspension is more efficient at higher wind speeds, i.e. larger particles remain airborne longer<sup>9</sup>, this finding suggests that fewer larger particles would be produced at higher winds. This suggestion seems unlikely and hence the observed wind speed effect on the surface flux of the largest particles is probably an artefact which may be caused by the statistics in the measurements of the largest particles. Wave height (and, hence, surf activity) is assumed independent of wind speed, which is a reasonable assumption for the relatively low wind speeds encountered during the experiments and the sea-breeze conditions at La Jolla.

The volume flux shows a clear maximum at a diameter of just over  $10\mu\text{m}$ . This finding is consistent with the bubble origin of the aerosol since the peak concentration of jet drops is expected near  $10\mu\text{m}$ <sup>10</sup>. The data in figure 4 (top) do not show a clear wind speed dependence of the position of this



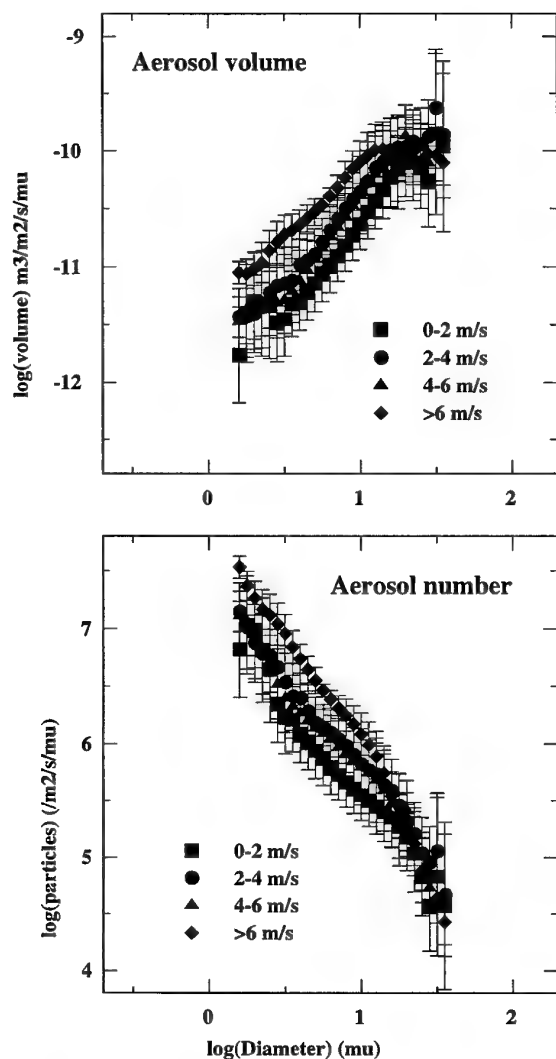


Figure 4. Aerosol fluxes  $dF/dD(D)$  from Surf-1 and Surf-3 data. Top: aerosol volume ( $\text{m}^3/\text{m}^2/\text{s}/\mu\text{m}$ ); bottom: aerosol number ( $\text{m}^2/\text{s}/\mu\text{m}$ ) produced in the surf zone. The data have been arranged as a function of wind speed. The diameter refers to the diameter upon production.

maximum, in accordance with the assumed bubble origin of the aerosol.

The aerosol source function as presented in figure 4 is valid for the surf conditions near the SIO Pier. Extrapolation to other locations requires knowledge on the physical mechanisms determining the surf characteristics and their effects on the production of sea spray aerosol. Efforts are underway to describe these effects (see below).

Assuming a 100% whitecap cover in the surf zone<sup>11</sup>, the surf data can be related to open ocean conditions and compared with published results on the surface source function. Such data were compiled by Andreas et al.<sup>12</sup>. These data are reproduced in figure 5. All source functions in figure 5 apply to a wind speed of 20 m/s; comparison with the surf aerosol source function in Figure 4 requires a correction for the difference in whitecap coverage between the surf and open ocean at a wind speed of 20 m/s. Monahan &

O'Muircheartaigh<sup>11</sup> give an empirical relation between the open-ocean whitecap coverage and wind speed

$$A(W) = 3.84 \cdot 10^{-6} U_{10}^{3.41}$$

with  $A(W)$  the fraction of sea surface covered by whitecaps, and  $U_{10}$  the wind speed at 10 m height. According to this relation, the whitecap coverage at 20 m/s wind speed is about 10%. For a proper comparison between the open-ocean and surf aerosol source functions, the source function found in this study is divided by a factor of 10. The results are shown in figure 5, together with the aerosol source function obtained from the Surf-2 (Monterey) data. For the Surf-2 experiment, a surf width of 30 m was assumed. Error bars for the Surf-2 source function are larger, due to the smaller data set.

The two surf source functions obtained in the present study compare well with the open-ocean source of Miller<sup>13</sup>. The bubble part of the Monahan et al.<sup>14</sup> source function also agrees well with the Surf-1,2,3 source functions. The sharp increase in the source function of Monahan et al.<sup>14</sup> near a diameter of 20  $\mu\text{m}$  is due to spume drops. The fluxes predicted by the source function of Smith et al.<sup>15</sup>, also shown in figure 5, are too low in the size range considered here.

Recent studies by Petelski & Chomka<sup>16</sup> and Chomka & Petelski<sup>17</sup> provide a comparison with aerosol production in the surf zone at a location on the Baltic coast; their fluxes (several

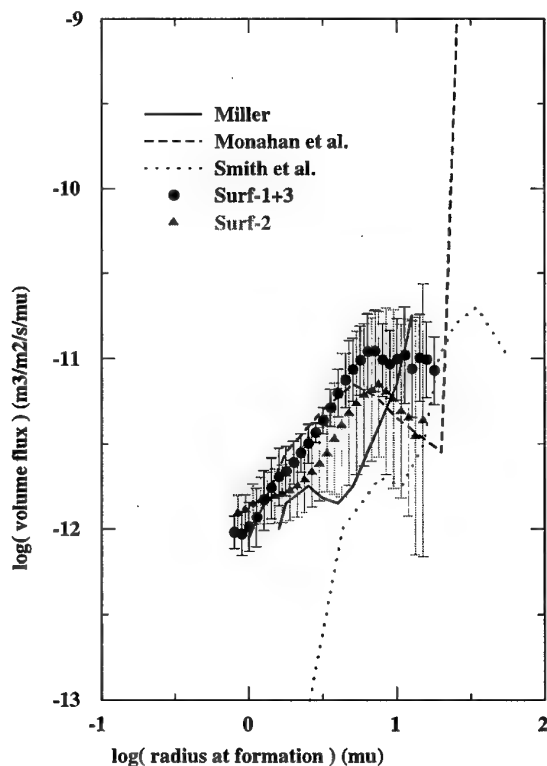


Figure 5. Aerosol source functions. The surf zone aerosol source function, corrected for whitecap ratio of 10% (wind speed 20 m/s), as derived from the Surf-1,3 and Surf-2 experiments have been inserted. There is good agreement with the source function of Miller<sup>13</sup> and Monahan et al.<sup>14</sup>. Also shown is the source function of Smith et al.<sup>15</sup>.



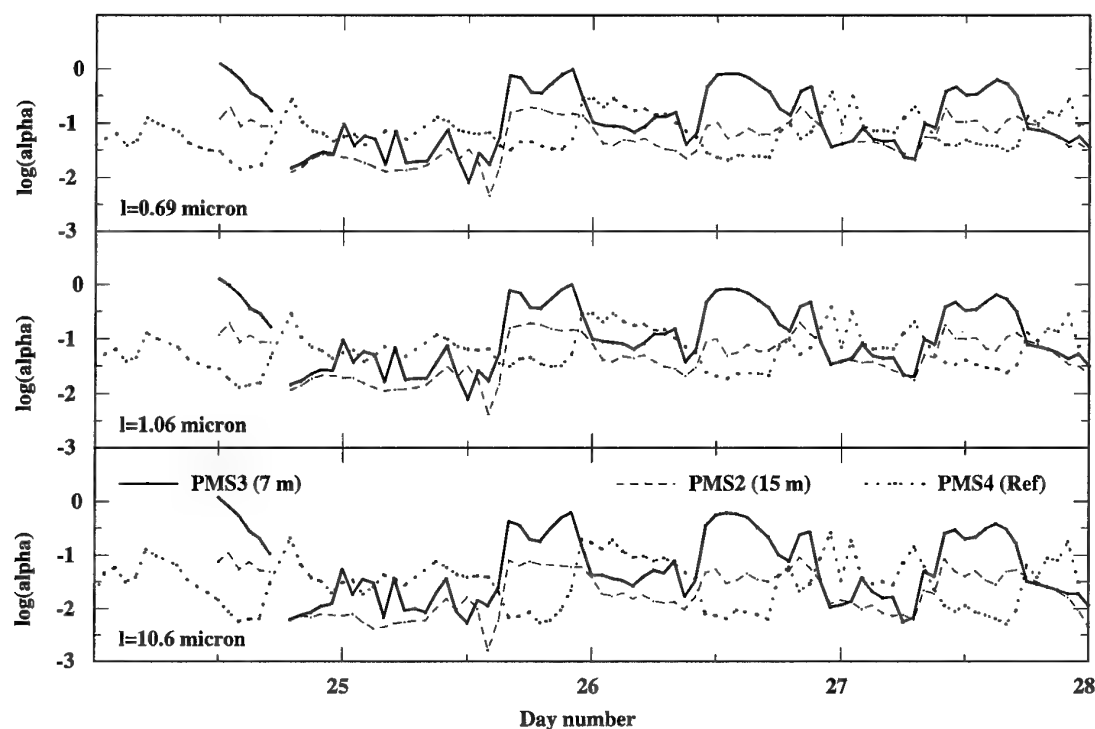


Figure 6. Extinction coefficients ( $\alpha$  in  $\text{km}^{-1}$ ) computed from the aerosol data in figure 1, for wavelengths 0.69, 1.06 and 10.6  $\mu\text{m}$ . Not shown are data from pms1, for reasons discussed in the text.

hundreds of  $\mu\text{g}/\text{m}^2/\text{s}$ ) are of the same order of magnitude as those presented here, integrated over the size range in the figures.

### 5. IR EXTINCTION PROFILES

Extinction coefficients at five wavelengths in the visible and infra-red (IR) atmospheric transmission windows were computed from the aerosol size distributions using a Mie<sup>18</sup> code. Results for wavelengths of 10.6, 1.064 and 0.69  $\mu\text{m}$  are shown in figure 6, for the same period as in figure 1. The data from pms1 are not shown, because they were affected by the hot pier surface. The surf effect is obvious in figure 6, with significant vertical gradients during the afternoons, when the extinction behind the surf zone was up to two orders of magnitude larger than over the open ocean. This effect is most pronounced for the longer wavelengths. Note that the effect of the surf on the extinction is present not only for winds from sea (during the afternoons), but also for winds from land. During the nights and mornings, the extinction at 7 and 15 m above sea level was similar, but the extinction at the end of the pier (pms4) was consistently higher. Effects of water vapour are not included in these calculations. Due to evaporation, the water vapour concentrations may also have been enhanced over the surf, thus increasing the IR absorption. Extinction profiles for open-ocean conditions, show an (expected) increase of extinction coefficients towards the sea surface<sup>19</sup>. Whereas at the open-ocean almost zero gradients were observed for the lowest wind speeds, stronger gradients occurred for moderate (4-7 m/s) winds, while at high winds the aerosols were well-mixed throughout the surface layer, resulting in negligible extinction gradients. Data such as those shown in figure 6 allow the estimation of the average extinc-

tion gradient in the surf zone, as a function of both wavelength and wind speed.

Figure 7 shows the mean extinction profiles derived from the Surf-1 and Surf-3 data, as a function of wind speed. The extinction profiles in figure 7 are shown up to the height where the background extinction is attained (between 20 - 40 m above mean sea level). The background extinction coefficients vary between 0.1 and 0.01  $\text{km}^{-1}$ . The profiles do not show that this background extinction value increases with increasing wind speed, as would be expected.

In contrast with the open ocean, where aerosol production is more directly related to wind speed, surf zone production may be high, even for low wind speeds, resulting in significant extinction gradients to heights of 20 to 40 m above sea level. Whereas Gathman<sup>19</sup> found a ratio between the extinction at 10 m and 1 m above mean sea level of only about a factor of 1.5, in these data this ratio ranges from 2 (6-8 m/s wind speed) to almost 10 (0-2 m/s wind speed) just downwind from the surf zone. At 5 m above mean sea level, the extinction coefficient in the air just downwind from the surf zone is about a factor of 60 (0-2 m/s winds) to 6 (6-8 m/s winds) higher than just upwind from the surf zone (derived from the data from pms4). The data show little dependence of the extinction gradient on wavelength. The strong correlation with wind speed is further emphasised in figure 8, which presents the average extinction gradient versus wind speed. The values show the behaviour expected for the case of a strong, nearby surface source of aerosol, with increasing dilution for higher wind speeds.

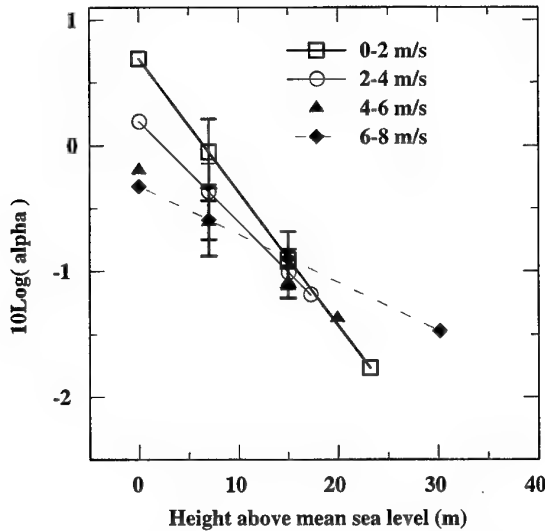


Figure 7. Profiles of  $\log(\text{extinction})$  versus height above mean sea level; the unit of extinction is  $\text{km}^{-1}$ . Curves are shown for four wind speed intervals; the wavelength is  $4.0 \mu\text{m}$ . Data used are from the Surf-1 and Surf-3 experiments, for winds from sea only.

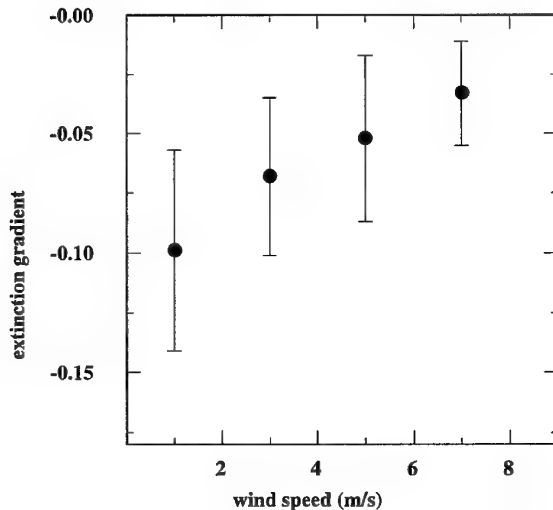


Figure 8. Extinction profile slope as function of wind speed. Shown are the slopes of the profiles from figure 7.

## 6. AEROSOL DISPERSION

The extinction coefficients in figures 6, 7 and 8 apply only to the base of the pier. For an assessment of the effect of surf-generated aerosol on the performance of electro-optical systems for lines of sight intersecting the surf zone, path-integrated (and range-dependent) extinction or transmission needs to be taken into account.

Two examples are presented which show the effect of the surf-produced aerosol on the transmission for both on-shore winds and winds from land.

### 6.1 Winds from sea

In this case, only the aerosol produced in the surf zone and transported across the shoreline up to the point where the electro-optical sensor system is situated needs to be taken into account. Consider a transmission path of 10 km length, crossing a surf zone with an effective width of 300 m obliquely. Assume that the background extinction coefficient is  $0.05 \text{ km}^{-1}$  (the average background value in figure 7), while the extinction over the effective surf is enhanced by a factor that varies between 3 and 300. Transmission losses, relative to the situation where the surf has no influence of the extinction, were calculated as a function of the angle of incidence of the path through the surf zone. The results are shown in figure 9. The curves are labelled with the enhancement factor of the extinction coefficient in the surf zone: '10' corresponds to a surf zone in which the extinction is 10 times higher than in the unperturbed air mass. The figure shows that the increase of the aerosol extinction over only the surf zone, by realistic values of about 2 orders of magnitude (see figure 6), causes rather dramatic losses in transmission.

### 6.2 Off-shore winds

In off-shore winds, the effect of the surf on the transmission may be much more serious, as the surf-produced aerosol may be transported over considerable distances. Hence they may influence the extinction along the entire transmission path. In the following, a simple aerosol model is applied in a first attempt to estimate the down-wind dispersion of the surf-produced aerosol and the resulting effect on extinction.

As a first approximation of the dispersion of aerosol produced in the surf zone, the diffusion equation for a line source in a simplified atmosphere is solved analytically. The application of a line source model is justified by considering the surf as a source with a relatively small vertical extent (maximum 30 m, as derived from data as displayed in figure 7, situated along the coast line. With this hypothesis, the model was formulated for aerosols emitted from a continuous crosswind line source located at the land-sea transition. The mean concentration downwind from a line source at a height  $h$  is given by

$$\langle c(x, z) \rangle = \frac{q(zh)^{1/2}}{\sigma_z^2 u} \exp \left[ -\frac{(z^2 + h^2)}{2\sigma_z^2} \right] I_{-1/2} \left[ \frac{zh}{\sigma_z^2} \right]$$

where  $x$  is the downwind distance from the source,  $z$  the measuring height,  $u$  the mean wind speed,  $q$  the source strength,  $I_{-1/2}$  is the modified Bessel function of the first kind of order  $-1/2$ .  $\sigma_z^2 = 2K_{zz} x/u$ , where  $\sigma_z$  is the vertical dispersion coefficient and  $K_{zz}$  is the vertical turbulence coefficient. The wind speed and the vertical turbulence coefficient are assumed constant with height<sup>20</sup>.

Particle deposition is taken into account by modifying the source strength  $q(x)$  with a reduction term which is dependent on the distance from the source<sup>21</sup>

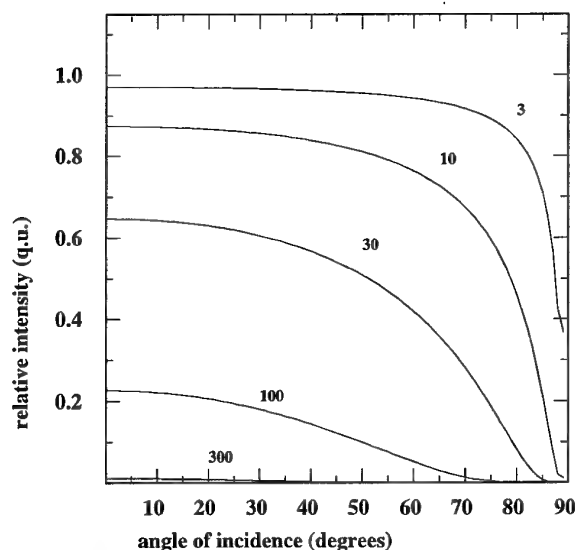


Figure 9. Path-integrated extinction losses in on-shore wind, plotted as function of the angle between the transmission path and the normal to the shore line. The total length of the transmission path is 10 km, the effective width of the surf zone is 300 m. The labels indicate the extinction in the surf zone: '10' represents a surf zone in which the extinction is 10 times higher than the background value. Background extinction is set to  $0.05 \text{ km}^{-1}$ .

$$\frac{q(x)}{q(0)} = \left[ \exp \int_0^x \frac{dz}{\sigma_z \exp\left(h^2 / 2\sigma_z^2\right)} \right]^{-\left(\frac{2}{\pi}\right)^{1/2} \left(\frac{v_d}{u}\right)}$$

where  $v_d$  is the wind speed dependent particle deposition velocity. The model applies only in neutral conditions. Deposition velocities were calculated using the expression of Slinn and Slinn<sup>22</sup>.

The average concentrations derived from the Surf-1 data were used as input to the model. To account for the vertical extent of the surf, these concentrations were extrapolated to heights of 1-30 m, and the model was applied for a series of release heights, with the receptor point fixed at a single level of 10 m. The concentrations arriving at the receptor point from the various release heights were then integrated to obtain the actual concentrations of the surf-produced aerosol at the receptor point. The distance between the source and the receptor point was varied from 10 m up to 25 km. The calculations were made for aerosols with diameters of 1-10  $\mu\text{m}$ , and wind speeds of 2 and 10 m/s. An example of the results for wind speed of 2 m/s is shown in figure 10. Close to the source the concentrations increase somewhat due to mixing of the particles from several heights to the receptor height, then a gradual decrease is observed. Even at 25 km from the source, the concentrations are decreased only by about one order of magnitude. This implies that the surf-induced enhancement of the aerosol concentrations in off-shore winds may have serious consequences for the transmission over sea.

It may be argued, that in off-shore winds the surf production of aerosol may be much lower than in on-shore winds. However, in this calculation concentrations were used which were

measured at an average distance of 50 m downwind from the surf, in wind speeds that usually did not exceed 2 m/s. Hence, the surf was mainly due to swell. Also, the data in figure 1 show that, in off-shore winds, the concentrations of the aerosols at the end of the pier are appreciably enhanced over those measured at the base of the pier, which in fact is due to the enhancement of the concentrations by the surf production.

The model was derived with the assumption that the wind speed and the vertical turbulence coefficient are constant with height. Although this leads to errors only at short distances (up to about 500 m) from the source<sup>23</sup>, this calculation should only be regarded as a first attempt to estimate the influence of surf-produced aerosol. In the future, more comprehensive models will be applied to take into account the vertical extent of the aerosol, the wind profile and associated vertical mixing, as well as other potential processes in the marine boundary layer that may affect the aerosol, other than advection, dispersion and deposition.

The effect on extinction can be found with this model, as the concentrations as a function of height and distance from the surf zone can be computed. In general, it can be expected that the strong extinction gradients observed near the surf zone gradually disappear as the air mass moves away from the surf zone and becomes better mixed. Figure 10 shows that at a distance of 25 km, concentrations may be as high as 10% of the concentrations measured just downwind from the surf zone.

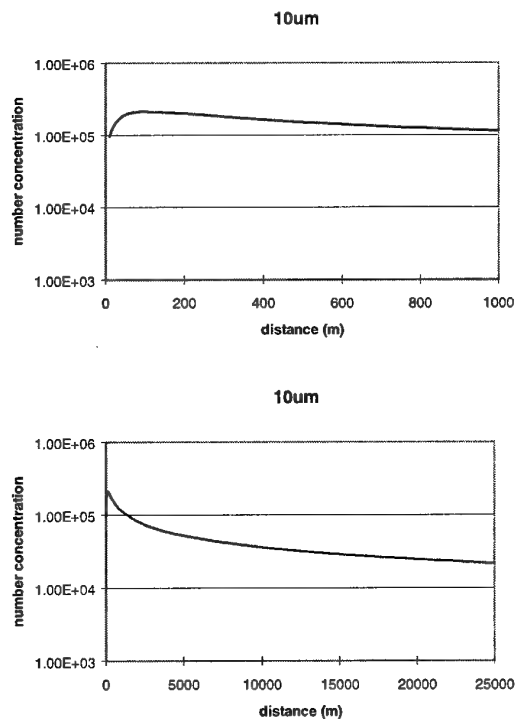


Figure 10. Aerosol concentrations for particles of  $10 \mu\text{m}$  in diameter, calculated as a function of distance from the surf using the aerosol transport model described in the text.

## 7. DISCUSSION AND CONCLUSIONS

The analysis of the aerosol measurements obtained during the EOPACE Surf experiments show that, in the diameter range between 0.5 and 10  $\mu\text{m}$ , the aerosol concentrations increase by up to two orders of magnitude due to production in the surf zone. A clear correlation is observed between wind speed and the aerosol flux downwind from the surf zone. The data from the three particle counters that were used in the height interval between about 7 and 15 m above mean sea level suggest that at an average distance of 50 m from the surf the maximum height attained by the surf produced aerosol is between 20 and 30 m.

The aerosol source functions which were derived from the three data sets not only agree well between the La Jolla and Monterey sites, but also compare well with surface fluxes previously reported for open-ocean conditions. All source functions used in the comparison apply to aerosol produced from bubbles (film and jet drops). Prior to the comparison with open-ocean aerosol surface fluxes, the only scaling applied to the surf source functions is a correction for whitecap ratio, which is considerably higher in the surf zone than at the open ocean, even at wind speeds of 20 m/s. The good agreement among the surf and open-ocean aerosol source functions suggests the existence of a single, well-defined bubble source function, expressed in aerosol produced per unit white cap. This result indicates that the whitecap ratio is an important parameter controlling the aerosol flux from the sea surface. Application to different conditions and locations is then a matter of measuring the local whitecap ratio. On the open ocean, wind speed is most likely to control the whitecapping ratio, while in surf zones the swell is probably more important than the local wind speed and direction. This is especially true for the sites of the Surf experiments, where winds follow a sea breeze pattern and are generally too low to significantly affect wave breaking.

This study is continuing to derive a model describing the effect of the surf on the aerosol production. The relation between the incoming wave field (direction of arrival, spectral content) and the rigour of the surf zone will be considered. Currently available software predicts the wave energy dissipation in the surf zone, which is the key parameter controlling aerosol production<sup>17</sup>. Preliminary results suggest that such an approach is viable, as the aerosol production is similar at very different surf zones, for comparable levels of wave energy dissipation.

The effect of surf-produced aerosol on IR extinction has been shown to be considerable. Not only do the data suggest a large effective width of the surf zone, but they also show that the extinction coefficients over the surf may be two or three orders of magnitude larger than in the unperturbed oceanic air. A more complete description of the surf effect on IR propagation requires detailed modelling of the size-dependent aerosol dispersion. Examples of the first attempts to apply such an aerosol transport model were presented. It is realised that this model may be an oversimplification of the real situation with developing wind and wave fields in off-shore winds, as well as temperature and humidity gradients that will affect the aerosol physics. For future application, more comprehensive models will be developed.

## Acknowledgements.

The participation of TNO-FEL in EOPACE is supported by the Netherlands Ministry of Defence, assignment A95KM729,

and the US Office of Naval Research, Grant N00014-96-1-0581. CMAS is supported by ONR, Grant No N00014-96-1-0321, and MoD DERA Portsmouth Contract No.

SSDH300037. Scripps Institute for Oceanography granted us permission to use the Pier in La Jolla. EOPACE was organised by Dr. D.R. Jensen from NRaD. Without Leo Cohen the measurements in La Jolla would not have been possible.

## References.

- [1] Fairall, C.W., Davidson, K.L. and Schacher, G.E., "Meteorological models for optical properties in the marine atmospheric boundary layer", *Opt. Eng.* **21**, pp. 847-857, 1982.
- [2] Kohnle, A. and J.H. Richter, "Result of the Fall 1981 North Sea measurements", *NATO AC/243 (Panel IV/RSG.8) Report 1983-01*, 1983.
- [3] Goroch, A.K. and Geernaert G.L. (Editors), "Coastal Aerosol Workshop Proceedings", *Naval Research Laboratory, Report Number NRL/MR/7542--95-7219*, 138pp, NRL Monterey, Monterey, CA, 93943, June 1995.
- [4] Jensen, D.R., "EO propagation assessment in coastal environments (EOPACE)", NCCOSC RDTE DIV, Code 543, San Diego, CA 92152-7385, USA, May 1995.
- [5] de Leeuw, G., Neele, F.P., van Eijk, A.M.J., Vignati, E., Hill, M.K. and Smith, M.H., "Aerosol production in the surf zone and effects on IR extinction", *SPIE proceedings volume 3125*, 14-27, 1997.
- [6] Gathman, S.G., and Smith, M.H., "On the nature of surf-produced aerosol and their effect on electro-optical systems", *SPIE Proceedings Volume 3125*, 2-12, 1997.
- [7] Goroch, A.K., Burke, S. and Davidson, K.L., "Stability effects on aerosol size and height distributions", *Tellus*, **32**, 245-250, 1980.
- [8] Andreas, E., "Sea spray and the turbulent air-sea heat fluxes", *J. Geophys. Res.*, **97**, 11429-11441, 1992.
- [9] de Leeuw, G., "Modeling of extinction and backscatter profiles in the marine mixed layer", *Appl. Optics*, **28**, 1356-1359, 1989.
- [10] Cipriano, R.J., and Blanchard, D.C., "Bubble and aerosol spectra produced by a laboratory 'breaking wave'", *J. Geophys. Res.*, **86**, 8085-8092, 1981.
- [11] Monahan, E.C., and O'Muircheartaigh, I.G., "Optical power-law description of oceanic whitecap coverage dependence on wind speed", *J. Phys. Oceanogr.*, **10**, 2094, 1980.
- [12] Andreas, E.L., Edson, J.B., Monahan, E.C., Rouault, M.P. and Smith, S.D., "The spray contribution to net evaporation from the sea: a review of recent progress", *Boundary Layer Meteorol.*, **72**, 3-52, 1995.
- [13] Miller, M.A., "An investigation of aerosol generation in the marine planetary boundary layer", M.S. thesis, 142 pp., Dep. of Meteorol., Pa. State Univ., University Park 1987.
- [14] Monahan, E.C., D.E. Spiel and K.L. Davidson, "A model of marine aerosol generation via whitecaps and wave disruption", in "Oceanic whitecaps", edited by E.C. Monahan and G. Mac Niocaill, pp. 167-193, Reidel, 1986.
- [15] Smith, M.H., Park, P.M. and Consterdine, I.E., "Marine aerosol concentrations and estimated fluxes over the

- sea", *Quart. J. Roy. Meteorol. Soc.*, **119**, 809-824, 1993.
- [16] Petelski, T. and Chomka, M., "Marine aerosol fluxes in the coastal zone - BAEX experimental data", *Oceanologia*, **38**, 469-484, 1996.
  - [17] Chomka, M. and Petelski, T., "Modelling the sea aerosol emission in the coastal zone", *Oceanologia*, **39**, 211-225, 1997.
  - [18] Mie, G., "Beiträge zur Optik trüber Medien, speziell kolloidaler Metallösungen", *Ann. Phys.* **25**, pp. 377-445, 1908.
  - [19] Gathman, S.G., "Aerosol profiles near the sea surface during MAPTIP", in "Propagation assessment in coastal environments", AGARD CP **567**, paper 20, 1995.
  - [20] Seinfeld, J.H., "Atmospheric Chemistry and Physics of Air Pollution", Wiley, 1986.
  - [21] Hanna, S.R., Briggs, G.A. and Hosker, R.P. Jr., *Handbook on Atmospheric Diffusion*, Published by U.S. Department of Energy, DOE/TIC-11223 (DE82002045), 1982.
  - [22] Slinn, S.A., and Slinn, W.G.N., "Predictions for particle deposition on natural waters", *Atmospheric Environment*, **14**, pp. 1013-1016, 1980.
  - [23] Smith, F.B., "The problem of deposition in atmospheric diffusion of particulate matter", *Journal of the Atmospheric Sciences* **19**, pp. 429-434, 1962.

## OPTIMIZING INFRARED AND NIGHT VISION GOGGLE SENSOR PERFORMANCE BY EXPLOITING WEATHER EFFECTS

Paul Tattelman  
Dana M. Madsen  
Joel B. Mozer  
Timothy C. Hiett  
Air Force Research Laboratory  
29 Randolph Road  
Hanscom AFB, MA 01731

### 1. Abstract

The Air Force Research Laboratory is developing software to predict the influence of the weather and other environmental parameters on the operational performance of Electro-Optical (EO) sensors used in air-to-ground munitions, navigation systems, and Night Vision Goggles (NVGs). Products under development include Infrared (IR) Target-scene Simulation Software (IRTSS) to provide target area scenes for pilot situational awareness prior to a mission, Night Vision Goggle (NVG) Operations Weather Software (NOWS) for NVG environmental performance impacts, Target Acquisition Weather Software (TAWS) to provide an EO targeting replacement for the currently operational EO Tactical Decision Aid, and Weather Automated Mission Planning Software (WAMPS) for automating weather impacts into the mission planning process.

Unique measurement facilities have been established to develop and evaluate EO target and background signature models in the infrared (IR, 3-5 and 8-12 micron) and near-infrared (.7-.9 micron) NVG wavelengths. IR data and imagery along with supporting meteorological and geophysical data are collected for systematic model validation. Experiments have been conducted at a fixed site at Hanscom AFB for three years. A mobile van has been equipped to conduct IR and NVG experiments at several sites on Otis ANGB, Cape Cod, MA. Data from both of these facilities are used for model development and an extensive validation of model performance under a variety of target/background types and weather conditions. In addition, IRTSS predicted IR scenes are being compared against actual weapon video.

This presentation will describe products being developed, data collection facilities and model

validation efforts, and mission planning techniques for optimizing weather related sensor performance.

### 2. Background

The Weather Impact Decision Aid (WIDA) program at the Air Force Research Laboratory is developing new products that provide performance predictions for EO Systems. The current focus is on IR and night vision systems. WIDA efforts translate conventional weather data into information needed by the warfighter to exploit the battlespace environment. WIDA products provide warfighters with predictions and visualizations of the influence of weather and other environmental parameters on Electro-Optical (EO) Sensors (infrared, laser, visible) used in air-to-ground munitions, navigation systems, and night vision goggles (NVGs). These products allow mission planners to factor weather into key decisions such as mission time, target approach heading, tactics, and weapons selection. They provide combat aircrews with detection/lock-on range predictions and/or target scene predictions, facilitating target location and positive identification.

The current WIDA program is divided into the following four projects:

- a. Infrared Target-scene Simulation Software (IRTSS) - Simulated "through-the-sensor" target scene visualizations for pre-flight situational awareness that include the effects of weather and time of day.
- b. Night Vision Goggle (NVG) Operations Weather Software (NOWS) - NVG performance predictions based on forecast weather, and natural and cultural illumination, including detection ranges (e.g. for landing zones and air refueling), on a laptop Windows 95 computer.

- c. Target Acquisition Weather Software (TAWS) - EOTDA replacement providing predicted detection/lockon ranges for IR/TV/NVG/laser weapons and target scene visualizations, in a Windows 95 environment.
- d. Weather Automated Mission Planning Software (WAMPS) - Automated EO weather-impact support in force-level mission planning systems.

The above components are discussed in more detail in the following sections.

### 3. IR Target-scene Simulation Software (IRTSS)

IRTSS provides an IR visualization of the target scene (currently 8-12  $\mu\text{m}$ , but 3-5  $\mu\text{m}$  will be added). The visualization capability includes terrain shadowing, realistic vegetation graphics and animated fly throughs that allow for 3-dimensional positioning of the sensor to view the scene from any angle. IRTSS is primarily being developed for incorporation into the AF Mission Support System (AFMSS) that will support aircrew mission planning and execution. IRTSS development includes the following components:

- a. Thermal Models - Physics models are used to calculate IR radiances of elements of the targets and surrounding terrain. The currently operational Electro-Optical Tactical Decision Aid (EOTDA) uses a Thermal Contrast Model (TCM2) for targets and backgrounds. IRTSS is upgrading TCM2 for targets. For backgrounds, IRTSS uses radiance models developed by the Smart Weapons Operability Enhancement (SWOE) Program. Current modeling is for 8-12  $\mu\text{m}$ ; a 3-5  $\mu\text{m}$  model will be added in the future.
- b. Atmospheric Transmission Model - Atmospheric transmission is calculated using MODTRAN, but calculation time is minimized using a spatial interpolation scheme developed for IRTSS.
- c. Sensor Performance Model - Sensor performance modeling characterizes the ability of specific IR sensors to distinguish targets and backgrounds. IRTSS is developing an improved sensor performance model to overcome limitations in the models currently used in the EOTDA.

In addition, IRTSS is developing automated data management techniques to drive the above models. Geographic data sets are generated using ARC/INFO, a commercial Geographic Information System (GIS). Geographic data sets are generated from a variety of sources, including National Imagery and Mapping

Agency (NIMA, formerly DMA), USGS, commercial satellites, and national imagery, and can support large areas (e.g. 40 km x 40 km at 10m resolution). The GIS is being programmed to fully automate this process. IRTSS models are also driven using real-time weather derived from the AF Automated Weather Distribution System (AWDS).

### 4. Night Vision Goggle (NVG) Operations Weather Software (NOWS)

The NOWS effort began with a deficiency in Air Force Special Operations Command (AFSOC) weather support to covert night-time helicopter air refueling using NVGs. After meeting with pilots of the 9th Special Operations Squadron and AFSOC weather personnel in March, 1991, AFRL initiated an R&D effort to predict weather impacts on the performance of NVGs. A contractual effort began in FY92. The prototype NOWS was delivered in FY94 and demonstrated to AF Weather. This led to a greatly expanded list of requirements for NOWS from AFSOC and Air Combat Command (ACC) to support differing scenarios, targets, backgrounds and hazards for NVG operations. NOWS Version 1.0 was delivered in FY95 for evaluation by AFSOC weather (16th OSS). The NOWS Graphical User Interface (GUI) and products were developed in close coordination with AFSOC and ACC.

NOWS Version 4.0 was delivered in Dec 97 to ACC and AFSOC for evaluation at more than 50 operational weather units worldwide. The current version offers distinct advantages over other NVG support products including:

- a. Physics-based models incorporating relevant weather for target/background detection range,
- b. Upward and downward lines-of-sight,
- c. Atmospheric attenuation and path radiance effects,
- d. NVG sensor modeling

NOWS provides worldwide map backgrounds for displaying, choosing, and tracking missions. It provides alerts to NVG operations hazards such as loss of horizon and towers, and provides NVG ranges as a function of user-selected probabilities. It also depicts optimum azimuth to approach a target or background. Weather-data input is automated with manual override capability. Upgrades include terrain elevation and features, full sensor bandpass spectral computations, an urban illumination model, and map-based color-coded output products. Future plans call for modeling individual light sources,

terrain shadowing and masking effects, and incorporation of additional customer requirements.

#### 5. Target Acquisition Weather Software (TAWS)

TAWS is currently planned as a replacement for the EOTDA. EOTDA Version 3.1 was delivered in 1994, and is currently being used operationally by the AF and Navy. This product was developed during a period of relatively primitive PC and workstation capabilities, limiting its utility. Furthermore, the EOTDA had only limited validation, is tedious to run, and often requires subjective manipulation by forecasters to adjust for discrepancies or bias in the core physics models. Also, it doesn't support MWIR sensors.

IRTSS and NOWS models will provide the IR and NVG portions of TAWS, which will also include an upgraded TV model and a laser model. TAWS will be developed as a joint AF/Navy program with the AF Research Laboratory as the lead agency in cooperation with the Navy SPAWAR Systems Center, San Diego CA and the Naval Research Lab, Monterey CA. As a minimum, TAWS would provide more accurate acquisition and lock-on ranges, improved guidance on tactics, far superior visualizations, probability outputs, ability to support multiple taskings, and guidance on weather sensitivities.

TAWS will be developed over a four-year period that began in August 1997 and will include five major software releases culminating in the final version in August 2001. Development will incorporate customer/user feedback (e.g. pilots, mission planners).

#### 6. Weather Automated Mission Planning Software

Currently, weather impacts on systems and operations are not included in force-level automated mission planning systems. In order to support the appropriate selection of weapon and navigation sensors for hundreds, or even thousands of sorties, it is imperative that mission planners have WIDAs that automatically assess weather impacts for specific sensors against selected targets and backgrounds.

A survey of EO requirements was conducted for the WIDA program. This study acknowledged the importance of understanding and exploiting weather effects on EO systems. The survey of planners and pilots pointed out numerous WIDA requirements

including the need for simultaneous guidance for multiple targets, guidance for weapon selection, target-area visualization, and more wavelengths than the current EOTDA.

Whereas TAWS is primarily a tool to support mission execution, WAMPS is envisioned as a force-level (24-72 hrs) stoplight weather impact mission planning capability. By providing red/yellow/green (unfavorable/marginal/favorable) guidance for each weapon/target combination, planners can better select weapons or alternatives or modify times-over-target. WAMPS will integrate new technologies developed in the AFRL WIDA program with other decision aids available in the EOTDA and elsewhere. The goal here is to demonstrate how weather decision aids can greatly enhance mission planning by exploiting both offensive and defensive weather sensitivities.

#### 7. WIDA Model Validation

An integral part of the AFRL WIDA program is product validation. Two separate facilities are used to make comprehensive meteorological and sensor measurements. A fixed site at Hanscom AFB, MA., (about 15 miles north of Boston) is used to collect all meteorological and EO data required by the IRTSS thermal models. Hiatt (1995) provides a complete description of this facility. In addition to comprehensive meteorological and EO-related measurements, imagery is collected using a FLIR 2000 (8-12  $\mu\text{m}$ ), a FLIR PRISM (3-5  $\mu\text{m}$ ), and a TV camera (visible) observing two simple test targets. Currently, only the 8-12  $\mu\text{m}$  data are being used for thermal-model validation and improvement.

A mobile platform has also been instrumented for IRTSS and NOWS validation measurements. Data collection using the mobile (trailer) facility will be primarily at the Camp Edwards range at Otis ANGB, Cape Cod, MA. For NOWS, the mobile facility includes measurements utilizing three laboratory-grade spectroradiometers, NVGs, and tailored bar targets. The fixed and mobile facilities are referred to as WIDA Lab, and data collected ensure that WIDA products will be thoroughly evaluated during their development.

In addition, IRTSS is being evaluated by the 46th Test Wing and 46th Weather Squadron at Eglin AFB, FL and the Naval Strike and Air Warfare Center, Fallon NAS, NV. Pilots are briefed using IRTSS, and cockpit video and meteorological validation data are returned for analysis and product upgrade.



## 8. Optimizing Sensor Performance

The objectives of the WIDA program are focused into the following two areas:

- a. Mission Planning - Inject weather and its impact on sensor performance into key decisions such as mission time, weapon choice, and tactics.
- b. Mission Execution - Provide aircrews with target-scene visualizations, optimum attack headings, and detection/lock-on range predictions in a chosen wavelength for situational awareness and tactical planning.

Knowledge on the interaction of the natural environment and time of day with sensor performance allows the mission planner to improve the odds that an aircrew will arrive at the target with the right weapons and tactics to get the job done. For navigation considerations, optimum routes and sensors can be employed. The level of success in employing this strategy is dependent on the accuracy of the models that predict how the weather will impact sensor performance, and the accuracy of the input data to these models (primarily weather forecast data). Results from analysis of the 8-12 micron data collected at our Hanscom AFB site indicate that 84% of the time the TCM2 and SWOE models, used for calculating the temperature difference between a test target and its background, respectively, correctly predict when the contrast between a target and its background is less than 1K. Thus, if a thermal contrast of at least 1K is required for a sensor to see the target, we can predict that there is insufficient contrast quite well. These data were collected under a variety of weather conditions, and the model predictions are for observed weather conditions that are fed into the models.

The sensor depiction in the cockpit is also dependent on the atmospheric transmission of the thermal signal and the ability of the sensor to resolve the signal. Our comparison of cockpit video versus model predictions of the scene components indicate that if you are doing a good job predicting the thermal values of the components in the scene, the hot and cold parts of the scene hold up quite well in the sensor depiction. This leads us to a high confidence level in our ability to do a good job modeling the IR scene using the component models for thermal contrast, atmospheric transmission, and sensor performance.

The accuracy of the weather forecast and other required WIDA model inputs is another issue.

However, it is very important to stress that bad weather (e.g. rain, snow, fog, and even low clouds) is a showstopper for most IR and NVG sensors. The greatest ability to exploit these sensors is under relatively benign weather conditions during which target/background contrast are the deciding factors in sensor performance. Also, the diurnal cycle has a profound effect on IR target/background temperatures. Selection of the best time of day for a mission can greatly improve the likelihood of success even if the forecast is imperfect. Targets and backgrounds heat up and cool down at different rates depending on the solar radiation, thermal mass of the target back-ground type and characteristics, and many other environmental variables. Under most weather scenarios, the solar radiation and nighttime outgoing radiation components will have the greatest impact on target/background heating and cooling rates. The key to improving sensor performance is to plan their use for times when the target/background contrast is large enough to be resolved by the sensor (i.e. avoid times of thermal crossover).

A simulation experiment was devised to address the impacts of considering the diurnal cycle and weather forecast accuracy. A one-week set of target and background temperature measurements was chosen at random from data taken at the Hanscom validation site. These measurements were made at one-minute intervals and contained typical variability due to solar diurnal effects as well as weather influences such as wind, rain and clouds passing over the target. For this experiment, 1000 aircraft sorties were simulated using the target/background thermal contrast data as the sole measure of the ability of a hypothetical IR weapon system to dispatch a typical target.

Three separate cases of mission simulations were performed using different levels of forecast planning in the sortie scheduling process. For the first case, weather and diurnal effects were ignored completely. These sorties were scheduled to occur at random times evenly distributed throughout the one-week period with no consideration of predicted contrast. The second case included time-of-day effects by scheduling sorties only when the target/background thermal contrast was greater than a given threshold as predicted by a simple thermal model. In the third case, the actual thermal contrast data were used to determine whether or not to schedule a sortie at a given time. Various magnitudes of random Gaussian noise were added to the raw temperatures in order to simulate the inaccuracy of weather forecasts and thermal predictions. In all three cases, mission

success was indicated when the actual target/background temperature contrast was greater than 5°F (an arbitrary threshold chosen to represent a hypothetical IR sensor). The mission was tagged a failure when this criterion was not met.

Table 1 shows the results of these simulations. Case I resulted in the lowest percentage of successful missions. This is not surprising since no consideration of weather or time-of-day was included in this scenario. For Case II it is apparent that a significant improvement in the sortie success rate is achieved by considering the solar effects. It is important to note, however, that this case assumes a perfect knowledge of the thermal properties of the target and background and that a proper model of the appropriate heating and cooling rates is known. This is not usually the case in a real-world scenario.

Experiment	Success rate (%)
Case I No effects	30
Case II Time-of-day effects	64
Case III Forecast accuracy:	
50%	44
75%	81
90%	92
100%	100

Table 1 - Weather in mission panning simulation experiment results

Finally, Case III reveals mixed results depending on the quality of the forecast. For the case of a 50% forecast accuracy the sortie success rate is 44%, significantly less than the 64% success rate from Case II. This is evidence that climatological information coupled with a good thermal model is more beneficial than a poor weather forecast for planning missions. When better forecasts are made, on the other hand, the success rate is much better with 92% mission success indicated for a 90%

weather forecast. In the limit where the weather forecast and the thermal model are perfect, all missions are successful. Based on the analyses of our WIDA models presented above, we believe most of the error described by Case III results from weather forecast inaccuracy.

## 9. Closing Remarks and Summary

The Department of Defense has spent considerable sums of money trying to engineer "all-weather" systems that are not impacted by the environment. A recent study by the GAO found that smart weapons were overrated. The study found that "all-weather" effectiveness was overstated by DoD, that precision guided munitions functioned effectively only in optimum conditions, and that IR, EO, and laser systems were seriously degraded by weather. Considerable improvement could be obtained by tailoring weapon choice, time of attack, and tactics to the weather. The use of validated environmental decision aids in mission execution and the automated mission planning process would bring current "smart systems" closer to the desired "all-weather" capability than trying to engineer-out the weather and at a small fraction of the cost.

The WIDA program is developing products that translate conventional weather data into information that the warfighter needs to exploit the battlespace environment. This article presented an overview on projects that support air-to-ground IR targeting and operations using NVGs. Future efforts will incorporate weather sensitivities of other EO sensors into decision aids that will enhance all levels mission planning and execution.

## References

1. Hiatt, T. (1995) A User's Guide to the ACT/EOS Validation Experiment Level-2 Data Set, PL-TR-95-2136, Environmental Research Papers No. 1181, October 1995.

PAPER No. 25

DISCUSSOR'S NAME: UNIDENTIFIED

Do the models (NOWS, IRTSS) consider differences in "cultural" areas, i.e., wood/coal burning, in their calculations. PSO environmental factors differ from 1st world factors?

AUTHOR'S REPLY:

Our models do not include effects of industrial or other man-made effluents. Consideration is given only to natural environments.

DISCUSSOR'S NAME: D. Clement

Can you comment on the various models you have included for describing:

- target behavior,
- backgrounds,
- systems performance.

AUTHOR/PRESENTER'S REPLY:

For targets and backgrounds we are using the models in the currently operational EOTDA. In addition, we are evaluating the U.S. Army Smart Weapon Operability Enhancement (SWOE) data collected by the Cold Regions Research and Engineering Laboratory for backgrounds. We are also developing generic target builders that will allow users to build targets that are not already included in the IR products (i.e., IRTSS, TAWS). For system performance, we are improving the sensor performance models that are in the EOTDA.

DISCUSSOR'S NAME: D. CLEMENT

What type of climatic regions is included in your work? Specifically, do you also consider operations in desert-like zones? If yes, how do you treat aerosol-driven atmospheric extinction in arid zones?

AUTHOR/PRESENTER'S REPLY:

Data for IR and NVG model validation is collected in Massachusetts year-round. Thus, the mid-latitude data include hot, dry, and humid conditions, as well as fairly extreme winter weather. We do have a cooperative effort with the Navy at Fallon Naval Air Station, Nevada, which is providing desert-type data for our IR models. For atmospheric transmission, we use MODTRAN.

## Performance Assessment of an Active Imaging System in Degraded Weather Conditions

Vincent Larochelle, Deni Bonnier, Gilles Roy and Pierre Mathieu  
 Defence Research Establishment Valcartier  
 2459 Pic-XI Blvd. North  
 Val-Bélair, Québec, Canada, G3J 1X5  
 Tel: 418-844-4360; FAX: 418-844-4511  
 E-mail: vincent.larochelle@drev.dnd.ca

### Abstract

All systems operating in the visible and infrared bands of the spectrum are subject to a severe performance degradation when used in adverse weather conditions like fog, snow or rain. This is particularly true for active systems as rangefinders, laser designators, lidars and active imaging sensors where the laser beam will suffer attenuation, turbulence and scattering from the aerosols present in the atmospheric path. This paper presents the ALBEDOS active imaging performance in fog which was determined by observing reference targets through a 22-m controlled-environmental chamber, where fogs with various densities and droplet sizes were generated in a calibrated manner. ALBEDOS is an acronym for Airborne Laser-Based Enhanced Detection and Observation System and is based on a compact, powerful laser diode illuminator and a range-gated intensified CCD camera. It is capable of detecting and identifying people or objects in complete darkness and, to some extent, in adverse weather conditions. In this paper, we compare the efficiency of the range-gated active imager in fog with those of a far-infrared thermal imager and of a low-light level camera operating in a continuous mode.

### Subject Matter Keywords

ALBEDOS  
 Active imager  
 Fog  
 Optical depth  
 Extinction coefficient  
 Thermal imager  
 FLIR  
 Illuminator  
 Range-gated  
 Intensifier  
 CCD camera

### 1 INTRODUCTION

In the last decade, the number of electro-optical sensors through all military services around the world has increased significantly. The overwhelming advantages enjoyed by a force that owns devices like laser rangefinders, designators, night-vision goggles, day and night cameras and thermal imagers were evident during the 90-91 Gulf war, when the United States with their coalition members employed such technology extensively. Armed forces during conflicts or peacekeeping missions have discovered the short-to-medium range capabilities of these optronic devices and their complementary roles to radars. Today, almost all surveillance platforms, being either light armored vehicles,

aircraft or vessels, are equipped with some electro-optical (E-O) sensors and, in a near future, active imaging systems will add to the list. Active imagers are capable of detecting and identifying targets in complete darkness and, to some extent, in adverse weather conditions. Before integrating any surveillance system in a platform, a good understanding of his weaknesses and of the parameters that affect its performance is required in order to provide to the operator the maximum capability of the sensor. In the optical band of the spectrum, the atmosphere has always played an important role to determine the performance of a system. Absorption, scattering and turbulence are the main atmospheric features that limit a sensor range of operation.

Between a thermal imager that will assure a long-range detection of objects based on their emissivity and an active intensified near-infrared imager that will allow a positive identification of targets based on their reflectivity, a factor of ten in wavelength, with completely different atmospheric transmission windows, exists and yields comparison between them that is not straightforward. In addition, the performance of the thermal imager is affected only by a one-way path absorption and scattering as the active imager, because of its illuminating beam, will have to count on a two-way (back and forth) atmospheric propagation. Therefore, a trial was organized to compare adequately the performance of both surveillance sensors in fog. A far-infrared (FIR) thermal imager from Agema operating in the 8 to 12- $\mu$ m spectral band was boresighted to the near-infrared (NIR) range-gated active imager ALBEDOS. The tests were conducted at the Defence Research Establishment Valcartier (DREV) in a 22-m long environment chamber where fog of various densities can be simulated. This facility is located at mid-distance of a 200-m outdoor range where a test van or trailer can be installed at one extremity with targets at various ranges along the path. The site is fully instrumented and can provide the one-way total transmission with a large dynamic range. The NIR and FIR imagers had their field of view adjusted to cover approximately the same angular field. Comparisons by low-contrast detection were carried out by the same operator, assuming the human perception equivalent for both types of imagery. Corresponding transmission data were recorded for all experiments. Among the targets selected, there are a large bar pattern canvas, a black body (for some tests only), a man, a lifejacket with retroreflective tapes and a vehicle.

### 2 THE AEROSOL CHAMBER

The aerosol chamber is 22 m long, 2.4 m high, and 2.4 m wide. It is located on DREV's site and is shown in Figure 1.

It was built of black painted plywood panels (outside being painted white). The opening of the doors, at both ends of the chamber, is electrically triggered and the doors collapse simultaneously under gravity within 0.5 s. Six small mixing fans located on the chamber floor are operated during materials dissemination as well as data acquisition [1]. The dissemination of water droplets is carried out by 15 air-atomizing nozzles distributed along the chamber ceiling (Fig. 2). Prior to generating the water droplets, all the chamber walls are watered to create a quasi-saturated atmosphere. Most measurements were conducted with water droplets (to create fogs of various initial densities); however, two were achieved with Dualite MS3™ and talcum powders. The two doors are usually opened 30 s after completion of dissemination.

Two transmissometers were used at a small off-axis angle with the ALBEDOS trailer. They operated at the same wavelength of 0.9  $\mu\text{m}$  but with different field of views (FOVs), namely 1 and 10 mrad. This wavelength is relatively closed to the 0.81  $\mu\text{m}$  of the ALBEDOS active imager. The sensors and the transmissometers were located 100 m from the chamber. The targets (canvas, truck, etc) were installed approximately 80 m away from the back end of the chamber. The average size of water particles, measured with a Malvern Particle Sizer prior to the opening of the doors, was 30  $\mu\text{m}$  with a size distribution covering 10 to 60  $\mu\text{m}$  approximately. The dualite MS3 particles have the shape of hollow spheres with an average diameter of 25  $\mu\text{m}$ . Concerning the talcum powder, the average size is less than 1  $\mu\text{m}$ .

### 3 SENSORS DESCRIPTION

The sensor suite included the ALBEDOS range-gated active imaging system, a far-infrared thermal imager and, for comparison with the active imager, a GEN III low-light level TV camera operating in a continuous mode. A view of the installation is shown in Figure 3 with the step van containing the transmissometers and the 8-m long ALBEDOS trailer. The three imaging sensors were fixed outside the trailer (Figure 4) on two large tripods equipped with a kinematic head. The recording instrumentation along with the monitors and controllers were located inside the trailer. The field of views (FOVs) of the three sensors were relatively matched. The following subsections present a more detailed description of the sensor suite.

#### 3.1 Far infrared thermal imager

The 8 to 12- $\mu\text{m}$  infrared thermal imager is the Model Thermovision 1000 from Agema Infrared Systems. Figure 5 is a picture of the device. It is built around a common module Sprite mercury-cadmium-telluride (HgCdTe) scanning detector (5 elements in parallel) cooled to 77 K with an integral Stirling closed-cycle microcooler. The camera is equipped with a dual-field of view lens providing either 20° (H) x 13.3° (V) or 5° (H) x 3.3° (V) total FOV. This corresponds to instantaneous FOVs (IFVOs) of 0.6 (wide FOV) or 0.15 mrad (narrow FOV) respectively. Table I outlines the most important characteristics of the Agema camera.

Table I: Characteristics of the Thermovision 1000

<b>Detector:</b>	
Detector type:	Sprite, 700- $\mu\text{m}$ length 5 elements in parallel
Overscan factor:	1.67
<b>Scanned image:</b>	
Frame frequency:	30 Hz
Line frequency:	3000 Hz
Interlace:	None
Number of IFOV/line:	565
<b>Presented image:</b>	
Sampling raster (H/V):	798/400
Magnification (electronic zoom):	8X
Aspect ratio:	3:2
<b>Lens dual FOV:</b>	
Instantaneous FOV:	0.6 mrad wide 0.15 mrad narrow
Field of view (H x V):	20° x 13.3° wide 5° x 3.3° narrow
<b>Minimum resolvable temperature:</b>	
MRT:	0.1°K

#### 3.2 ALBEDOS Active Imager

The Airborne Laser-Based Enhanced Detection and Observation System (ALBEDOS) is an active imaging system based on a range-gated low-light level TV camera and a compact powerful laser diode array illuminator.

The ALBEDOS project was initiated at DREV in March 1993 under the sponsorship of the National Search and Rescue Secretariat (NSS). It was intended to enhance the search capability of Search and Rescue (SAR) teams during their missions. Similarly, its surveillance capability has been investigated through various scenarios. The system was mounted into a Wescam 24-inch diameter stabilized platform for airborne operations. Figure 6 shows a picture of the internal components of the unit with one-half of the spherical enclosure removed.

ALBEDOS is a range-gated active unit capable of imaging a scene in total darkness and/or in the presence of rain, snow, haze or fog [2 to 7]. The principle of operation of a range-gated system is illustrated in Figure 7. A laser pulse is emitted at time  $T_0$ , while the intensifier gate is closed. As the laser pulse travels through the atmosphere, it encounters various aerosols and a portion of the energy is reflected back or backscattered to the camera but the gate is still closed and no signal is detected as shown in  $T_1$ . Eventually, the laser pulse reaches the target area at time  $T_2$ , and some energy is reflected back toward the receiver while the gate is still closed. Part of this energy, after travelling again through the atmosphere, reaches the sensor at time  $T_4$  which corresponds to the predetermined time selected by the operator to activate the gate on the intensifier in order to collect the incoming energy.

Because the gate is off during the laser pulse round trip, the amount of backscattered and/or background recorded is null. The only contribution comes from the reflected and the background energy after gate activation. This increases significantly the signal-to-noise ratio (S/N) of the intensified-camera unit and therefore enhances substantially

the detection, recognition and identification capabilities of the system. Moreover, another increase in the S/N ratio and consequently in the system performance is obtained by triggering the laser 525 times per frame for a time-integration of the energy received by the sensor.

Without range-gating, a pulsed laser imaging system would collect all the backscattered energy from the aerosols in the illuminated field of view which would increase the noise level and consequently reduce the detection range. So, it is paramount to judiciously select the timing for the gate activation if the operator wants to improve or maximize the system performance for a given scenario or mission.

Figure 8 shows a schematic of ALBEDOS basic operational components. These are a pulsed laser source, a CCD camera, a GEN-III gated image intensifier, a 48X motorized-zoom lens, a video display, a Super-VHS recorder and associated electronics. One of the main functions of the electronic components is the synchronization of the two prominent elements of the system: the laser source and the range-gated intensified camera. The time or range-gating electronic unit provides a wide selection of gate widths, pulse widths and delays for a very effective enhanced detection and observation system.

The illuminator used in ALBEDOS is based on a Laser Diode Array (LDA) source and an optical collimator to correct for the large natural divergence of the laser beam emitted by the diode array. The illuminator operates in the near-infrared at a wavelength of 810 nm. Two different laser beam divergences, 2 and 10 degrees, are available and can be selected by the operator. The maximum average power is around 13 W for a repetition rate of 15.75 kHz. Table II presents the main operational characteristics of the integrated illuminator. The safe operational range for this laser device, according to the nominal ocular hazard distance (NOHD) calculations, is 28 m for the naked eye and some 200 m if a 7 x 50 pair of binoculars is used.

Table II: Laser illuminator characteristics

Average power@15 kHz:	12.8 W
Minimum pulse length:	100 ns
Maximum pulse length:	2.0 $\mu$ s
Minimum beam divergence:	1.9 x 3.2 degrees
Maximum beam divergence:	9.6 x 10.6 degrees
Wavelength (20°C):	810 nm
Wavelength shift:	0.4 nm/°C
Power consumption:	<150 W

The spectral response of the imaging sensor, made of the 48X-zoom lens, the GEN-III intensifier tube and the CCD camera, peaks around 800 nanometers and its variable gating time, from 100 ns to 2  $\mu$ s, gives a possible window or range depth of 30 to 600 m with a trigger delay adjustable between 0 and 47  $\mu$ s corresponding to a maximum operational range of 7 km. This camera, whose main characteristics appear in Table III, was built by Ball Aerospace. If the laser illuminator is turned off, this camera can be used in a passive mode of operation as a high-performance low-light level (LLL) TV camera. In the active mode of operation, an operator can make covert observations of scenes at large ranges unless someone uses night-vision goggles (NVG) to

look in his direction. Furthermore, this camera is quite immune to dazzling by external coherent and/or incoherent light sources since it has an integrated narrow-band optical filter and is gated at a high-repetition rate with a very low duty cycle.

Table III: Gated-intensified camera characteristics

Intensifier gain:	30000-50000
CCD size:	750 x 480 pixels
Luminance range:	$10^{-7}$ - 100 lux
Output video format:	RS-170, CCIR
Resolution:	520 TV Lines @ $2 \times 10^{-4}$ fc
Zoom lens:	32-800 mm focal length

The payload normally installed in the stabilized platform consists of the laser illuminator, the time-gated intensified CCD camera and the gyroscopes. For the purpose of the present tests, the sensor was installed outside its platform, on a large tripod (see Figure 4). The equipment in the trailer comprises a system interface unit, a power conditioner, a control console, a super-VHS video recorder, a 9-inch monochrome TV monitor, a time code generator/reader and a 28 V power supply.

### 3.3 The low-light level TV camera

In conjunction with ALBEDOS and the thermal imager, an intensified CCD camera equipped with a GEN III micro-channel plate (MCP) was used. The camera is Model ISG-350-Y-Q from Xybion Electronics Corp. (Figure 9) and was operated in its continuous mode (no range gating). A 70 to 210 -mm zoom lens (F-number from 1.4 to 5.6) was used in front of the low-light level camera and was adjusted such as to match the field of view of the two other sensors. Its important characteristics are summarized in Table IV.

Table IV: Characteristics of the low-light level camera

#### Camera System

Horizontal resolution:	$\geq 440$ TV lines
Vertical resolution:	485 lines
Optical input format:	1-in (12.7 x 9.52 mm)
Minimum face plate illumination:	$\leq 10^{-6}$ lux
Signal-to-noise ratio:	35 dB

#### MCP Intensifier

Type:	GEN III
Spectral response:	600 to 900 nm
Resolution:	40 line pairs/mm
Size:	18-mm diameter
Luminance gain:	$> 16,000$ at $10^{-6}$ lux input
Gain range:	0 to 18,000

#### CCD Imager

Type:	Interline transfer
Picture elements:	768 (H) x 493 (V)
Sensing area:	8.8 mm x 6.6 mm

## 4 THE TRIAL

The trial was conducted during three separate nights, one in October 1996 and the two others in October 1997. For the night in 1996, the sky was overcast with a temperature of 6°C, a relative humidity close to 100% and a visibility approaching 10 km. In October 1997, it was an overcast sky for both nights with a temperature close to 0°C and a visibility superior to 20 km. The vehicle used as a target was a small pickup truck. A large white-on-black bar pattern canvas was suspended at the end of the range, that is 80 m beyond the extremity of the environmental chamber (i.e. 200 m from the sensor suite). The canvas is a calibrated optical resolution target Model RST-7601 with a contrast ratio of 20:1 manufactured by Tracor Aerospace (Figure 10). The lifejacket is a commercial device equipped with retroreflective tapes (Figure 11).

### 4.1 Contrast

An object can be detected if its contrast is above a certain threshold. No two individuals have exactly the same threshold but statistical laboratory and many field experiments have been performed to determine an average value. Experts proposed thresholds from 0.02 for objects of reasonable size in daylight to a more conservative estimate of 0.05 [8]. For the present tests, at the beginning of each experiment when the doors collapsed under gravity, the targets were most of the times hidden behind a fog of high density. As the fog slowly dissipated and its density was decreasing, targets started to appear as more and more bright and defined objects against a dark background and the observer determined the exact moment of positive detection. It was estimated that this moment happened when the contrast was between 5 and 10%. This was valid for the thermal imager, the low-light level camera and the range-gated active imager.

### 4.2 Optical Depth

The transmissometers provide the transmission data through the 22-m long chamber for each run. Typically the tests lasted 120 s during which the transmittance varied from  $\sim 10^{-5}$  to  $\sim 1$ , and the visibility through the environmental chamber from totally obscured to fully unhindered. Quantitatively, we use the observer cue to determine the transmittance at which the targets were detected or identified. For convenience and because the term "optical depth" is more usual in the scientific community who studies the atmospheric propagation, the transmittance values directly measured by both transmissometers were converted into optical depth using the well-known exponential law:

$$OD = -\ln T \quad [1]$$

where  $T$  is the transmittance. The optical depth is in fact the extinction coefficient  $\alpha$  multiplied by a range  $R$ .

### 4.3 Man and Lifejacket

Tests were conducted simultaneously on a man and a lifejacket commercially equipped with flexible retroreflective tapes. Two more strips of Polarflex retroreflector tape Model AM300T from Reflexite Canada

have been added on the lifejacket sleeves as shown in Figure 11. The Polarflex tape is based on microprisms as the tape already sewed on the lifejacket are built with microspheres. The man was standing besides a support on which the lifejacket was suspended. Both the man and the lifejacket were located approximately 50 m at the back the environmental chamber, i.e. between the chamber and the canvas. Figure 12 illustrates an example of a run test where the time plot of the measured transmittance  $T$  is given. The two curves represent the data from the two transmissometers (1 and 10 mrad) for a total time interval of 120 s following the chamber doors opening. Because the computer started to record transmittance data 5 s prior the doors opening, these data depicted by the first 5 s in the graph are obviously not valid. The transmittance time plot shown in Figure 12 is the one from run #20 measured in October 1997.

Along with the transmittance graph, a sequence of three video images for each sensor (ALBEDOS active imager, Agema thermal imager and Xybion intensified camera) illustrates three particular moments of the experiment (Figures 13 to 15): a) few seconds following the doors opening; b) few seconds following detection of the lifejacket or the man by the observer; c) the time at which either target (man or lifejacket) is fully visible. The reproductions of the video images are not faithful representations, the actual images show much better resolution. Moreover, when watching images unrolling at 60 Hz on a monitor, human brain performs some sort of integration which increases the apparent contrast of the target to the background. In static images, this integration does not occur. Because the detection principle of the active imager and the low-light level camera is based on the reflectivity contrast between an object and the background, the lifejacket with its retroreflective tapes is obviously the target of choice. On the other hand, a thermal imager detects the heat produced by a warm body and the man, not the lifejacket, becomes the preferred target. It is of interest to note from Figure 13 that the Polarflex microprisms retroreflector tapes are more effective than their counterparts based on microspheres.

Table V tabulates the results from a series of runs conducted during the three days of the trial. The scenario consisted of detecting either the man or the lifejacket in the presence of artificially created dense fogs. In this Table, the optical depth (OD) is calculated from the transmittance value measured at the exact time the detection occurred after the opening of the chamber doors. It is important to note that for the cases of ALBEDOS and the low-light level Xybion camera, the light beam must travel twice through the fog, contrary to the thermal imager where the infrared light goes through it only once.

In Figures 13 to 15, the observer using ALBEDOS declared detection of the lifejacket at  $t = 8$  s, which gives a transmittance of 0.0042, i.e. an optical depth OD of 5.5. The same observer using the Agema thermal imager stated that he detected the man 21 s after the opening of the doors, corresponding to a transmittance of 0.014 and an OD of 4.3. For the Xybion camera, the time delay for detection was 83 s, giving a transmittance of 0.029 and an OD of 3.5. These numbers appear under run #20 in the Table. An immediate conclusion points at the optical depths measured for the ALBEDOS sensor which exceed those of the thermal imager



and low-light camera by a factor of 1.5 approximately. This means that, in general, an active imager of ALBEDOS type will have a better penetration in fog than an Agema far-infrared thermal imager, at the condition that the man searched by the two sensors wears a lifejacket with retroreflector tapes. This scenario is likely to happen in search and rescue operations for which ALBEDOS has been primarily developed. Also, these tests demonstrate that the range-gating option for active imaging in degraded weather conditions is highly efficient. This is proven by the difference in optical depth between ALBEDOS (range-gated) and the Xybion camera (continuous mode) where both used the ALBEDOS illuminating source. Finally, it is shown that without lifejacket (runs #22 and #23), the performance of the thermal imager when detecting a man is better than that of ALBEDOS with its range gating feature. However, without range gating as it is the case for the Xybion camera, the performance is seriously limited when compared to the two other sensors. Note that run #17 has been carried out with talcum powder for which the thermal imager is the most efficient sensor.

Bissonnette et al. [8] in a recent publication have determined that the maximum enhancement you can expect in visual-contact range in daytime fog provided by a lighting system versus no lighting system is approximately 4.2. This corresponds to a maximum optical depth of 12.6 for a one-way path. The present scenario is similar to their case in that the lighting system is replaced by a retroreflector and that our range-gated low-light level camera from ALBEDOS for nighttime operations is equivalent to their daytime visible camera. Looking at Table V, the optical depth for ALBEDOS averages 5.0 for a two-way path which, when multiply by two, is relatively close to the fundamental 12.6 mentioned above.

Table V: Man/lifejacket detection

Run #	Fog Type	Optical Depth		
		ALBEDOS	Agema	Xybion
5	water	7.1	3.0	---
6	water	5.0	2.9	---
9	water	---	3.4	---
15	water	3.4	---	3.6
16	water	5.2	3.7	2.7
17	talcum	2.6	9.2	2.5
18	Dualite MS3	4.8	5.9	4.0
19	water	6.3	4.3	3.5
20	water	5.5	4.3	3.5
21	water	5.0	4.1	3.2
22	water	2.0 (man)	3.2	0.21 (man)
23	water	1.8 (man)	4.1	0.30 (man)

#### 4.4 Truck Detection and Classification

Two runs have specially been conducted on a small pickup truck located between the canvas and the environmental chamber (~170 m from the sensor suite). For the thermal imager, the engine of the truck was idling for some time. Table VI summarizes the results. Both the detection and the classification of the target were considered. Detection occurred as soon as the contrast between the vehicle and the background was sufficient for the observer to certify the presence of a target. Once the observer recognized the detected object as a vehicle, classification was considered as

being achieved. The time after doors collapsing by gravity for which detection and classification occurred was recorded and from curves similar to Figure 12, the transmittance was calculated. From the table, it is clearly seen that the thermal imager has a better penetration in fog than ALBEDOS and the Xybion camera. This is also true for the ALBEDOS when compared to the low-light level camera. For the thermal imager, the detection is achieved through the heat generated by the vehicle's engine. Regarding ALBEDOS and the Xybion camera, both operate in active mode and the detection of the vehicle is mainly based on the weak retroreflection effect from the headlamps. Finally, the data measured for both runs are in good agreement.

Table VI: Truck detection and classification

Run #	Fog Type	Optical Depth					
		ALBEDOS		Agema		Xybion	
		det.	Class.	Det.	Class.	Det.	Class.
26	water	3.1	2.7	4.4	2.7	1.0	0.22
27	water	3.3	2.2	5.3	3.4	1.5	0.22

#### 4.5 Bar Pattern Canvas

As mentioned previously, a large optical resolution canvas with a 20:1 contrast ratio and white bar patterns of various sizes was used as a calibrated target (Figure 10). Two sets of bars were selected by the observer. Each set consisted of three vertical and three horizontal bars. The larger set had bars of 7.6 cm x 38.1 cm. The bar sizes of the smaller set were 4.8 cm x 23.8 cm. One spatial period for these bars (a white bar followed by a black space equivalent in dimensions) corresponds to subtended angles of  $0.152/200 = 0.76$  mrad and  $0.096/200 = 0.48$  mrad at 200 m. These values are well over the resolution limit of the three sensors. Only two sensors, ALBEDOS and the Xybion camera, were used during these tests. The Agema thermal imager could not resolve the bar pattern because there is no temperature difference at night between the white bars and the black canvas. Figures 16 and 17 present a sequence of three video images for each sensor, illustrating three particular moments of the experiment. The time mentioned under the images is the time delay after the doors opening. These images were extracted from run #13 and recorded either shortly after the opening of the chamber doors, after detection of the bar patterns by the observer or after the fog had completely dissipated. The bright light seen in the last two images of the Xybion camera is the light source for the two transmissometers and could not be removed. The blooming effect caused by this light affected the automatic gain of the camera (by decreasing it); this explains the reason why the canvas and the bar patterns do not appear as sharp as in the last image of ALBEDOS. The light is dim in ALBEDOS images not because of the range gating feature which normally allows the intensified camera to observe only a certain depth in space (the gate was too large here), but because of the low duty cycle of the sensor. Table VII summarizes the results obtained during the trial. It outlines the fact that ALBEDOS again, performed better with its range-gating feature than the continuous-mode Xybion camera. Also, it is of interest to note that the observer often detected the large and small bars simultaneously.



Table VII: Canvas bar pattern detection

Run #	Fog Type	Optical Depth			
		ALBEDOS		Xybion	
		large bars	small bars	large bars	small bars
11	water	3.4	3.3	0.02	---
12	water	2.8	2.8	0.02	0
13	water	3.5	3.5	0.62	0.45
15	water	2.8	1.9	0.51	0.22
16	water	2.6	2.4	0.01	0
17	talcum	2.3	2.0	1.7	---
18	Dualite MS3	1.3	1.3	0.74	0.22
19	water	2.3	2.3	0.70	0.43
20	water	2.5	2.5	0.74	0.57
21	water	1.8	1.5	0.31	0.01
22	water	1.9	1.8	0.30	0.02
23	water	1.9	1.8	0.60	0.13
24	water	2.7	2.3	0.94	0.52
25	water	2.7	2.3	0.83	0.30

#### 4.6 Canvas

Tests have also been conducted on detecting the canvas itself. Here, the bar patterns are not important, but only the piece of tissue suspended at 200 m from the sensor suite. Table VIII tabulates the results and demonstrates again the efficiency of range-gated active imagery. However, the thermal imager had to detect an object with practically no temperature contrast against the surrounding background. A black body heated at 100°F (37.°C) was installed for some runs (#2,3,6) between the chamber and the canvas. The optical depth measured with the Agema imager for this warm object (comparable to the human body temperature) was determined to be 4.3, 4. 2 and 4.3. These relatively high values confirm that a thermal imager can also be efficient for detecting objects in fog when a minimum of temperature contrast exists.

Table VIII: Canvas detection

Run #	Fog Type	Optical Depth		
		ALBEDOS	Agema	Xybion
11	water	3.4	3.0	0.46
13	water	3.5	2.7	0.66
15	water	2.8	3.1	0.51
16	water	2.6	3.4	0.02
17	talcum	2.3	7.9	1.7
18	Dualite MS3	1.3	3.1	0.95
19	water	2.3	0.83	0.83
20	water	2.5	0.65	1.0
21	water	1.8	1.0	0.42
22	water	2.0	1.0	0.48
23	water	1.9	0.77	0.77
24	water	2.7	1.3	1.0
25	water	2.7	1.1	1.0
26	water	2.5	1.3	1.0
27	water	2.2	2.2	1.3

## 5 CONCLUSION

Performance of medium-to-long range surveillance systems, particularly those operating in the optical band of the spectrum, have always been affected by either the absorption, the scattering or the turbulence of the atmosphere. These effects are especially strong in the presence of rain, snow or fog. The Defence Research Establishment Valcartier or DREV has organized a trial to

determine and compare the performance of three optical sensors in fog. They were a thermal imager which operates in the far-infrared (8 to 12  $\mu\text{m}$ ), an active imager called ALBEDOS and a low-light level camera, the last two working in the near-infrared. The thermal imager assures a medium range detection of objects based on their emissivity as the active imager allows a positive identification of targets based on the reflectivity contrast with the background. Because the active imager provides its own illumination and because its intensified camera can be gated, it can operate in complete darkness and, to some extent, in degraded weather conditions. However, the active imager performance is affected by the atmosphere twice as much as that of the thermal imager, since the illuminating beam must travel back and forth in a two-way path. The third sensor is a low-light level camera which operates in a continuous mode and allows comparison with the range-gated ALBEDOS. Because the capability of active imaging systems in fog is still relatively unknown and because efficiency comparison in fog between them and thermal imagers is not straightforward since they operate in completely different atmospheric windows, it was decided to go ahead with a trial.

The tests were conducted on a 200-m range where a 22-m long environmental chamber is located. Fog of various initial densities were artificially generated and transmissometers were providing transmittance data as a function of time. The field of views of the three sensors were similar in size and coaligned. In general, range-gated active imagers have a better penetration in fog than thermal imagers, particularly when targets exhibit a retroreflection asset. Also, it was shown that active imagers efficiency to distinguish details of a scene through fog exceeds that of thermal imagers. However, the latter devices present a high figure-of-merit on warm objects where the contrast with the background is sufficient. The potential of range-gating have been demonstrated by comparing ALBEDOS with a low-light level camera operating in a continuous mode. Finally, one of the key finding of the present investigation is the demonstration that performance in fog of active imagers on cooperative targets is relatively close to the fundamental limit. This conclusion can be quite significant in search and rescue (SAR) operations where crews could benefit of this technology.

#### Acknowledgements

The authors would like to thank Messrs. D. Dubé, G. Tardif and C. Bastille for their technical assistance during the course of the project.

#### References

- [1] G. Roy, L.R. Bissonnette, C. Bastille and G. Vallée, "Estimation of Cloud Droplet Size Density Distribution from Multiple-Field-of-View Lidar Returns", Opt. Engineering, Vol. 36, No. 12, pp. 3404 to 3415, December 1997.
- [2] "Active-Gated TV for Search and Rescue Operations", International Defense Review, No. 5, 1996.

- [3] D. Bonnier, V. Larochelle, D. Dubé, G. Tardif, and G. Ralph, "ALBEDOS Fall 1995 Flight Trial Overview", DREV TM-9521, February 1996, UNCLASSIFIED
- [4] D. Bonnier, and V. Larochelle, "A Range-Gated Active Imaging System for Search and Rescue and Surveillance Operations", SPIE Vol. 2744: Infrared Technology and Applications XXII, 8-12 April 1996, Orlando.
- [5] A. Jenkins, M. Vandenburg, S. Tritchew, D. Bonnier and V. Larochelle, "An Airborne Laser-Based Enhanced Detection and Observation System for Coast Guard and Maritime Patrol Application", SPIE Proceedings, Vol. 2269, July 1994.
- [6] A. Jenkins, M. Vandenburg, S. Tritchew, D. Bonnier and V. Larochelle, "An Airborne Laser-Based Enhanced Detection and Observation System for Coast Guard and Maritime Patrol Application", Night Operations Symposium XII, San Francisco, October 3-5, 1995.
- [7] D. Bonnier, V. Larochelle, P. Mammoliti, B. MacKean, S. Tritchew and A. Jenkins, "ALBEDOS: An Active Imaging System for Search and Rescue and Surveillance Operations", Proceedings of the NATO/IRIS Conference on Active Systems, NATO Panel IV RSG-13, Monterey, California, May 3-25, 1995.
- [8] L.R. Bissonnette, G. Roy, C. Bastille and G. Vallée, "Visibility of Lighting Systems for Helicopter Landing in Fog", DREV - TM-9705, October 1997, UNCLASSIFIED.

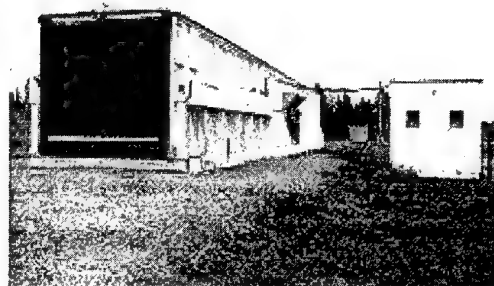


Figure 1: The 22-m long aerosol chamber.

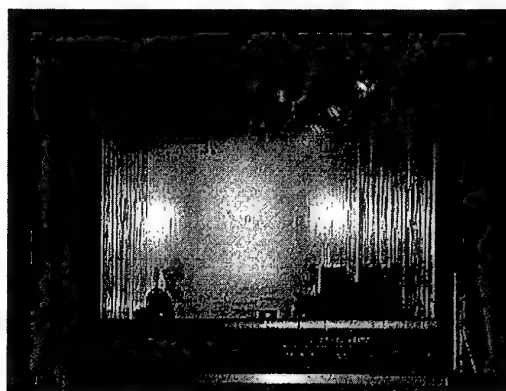


Figure 2: Fog created inside the chamber.



Figure 3: Transmissometers and sensors installation 100-m from the aerosol chamber.

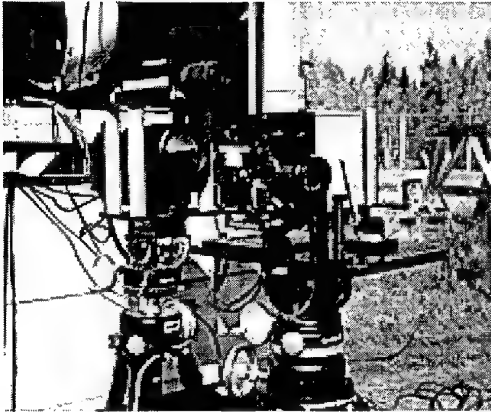


Figure 4: Sensors on tripods.

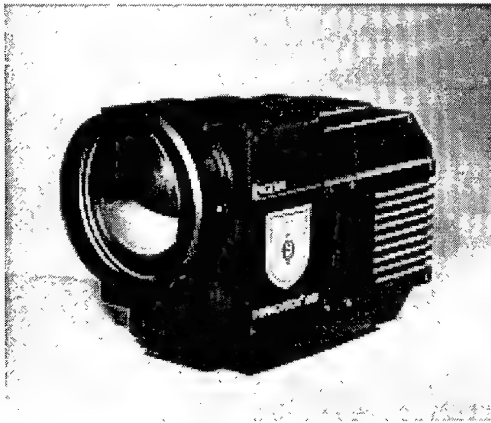


Figure 5: The Thermovision 1000 FLIR from Agema Infrared Industries.

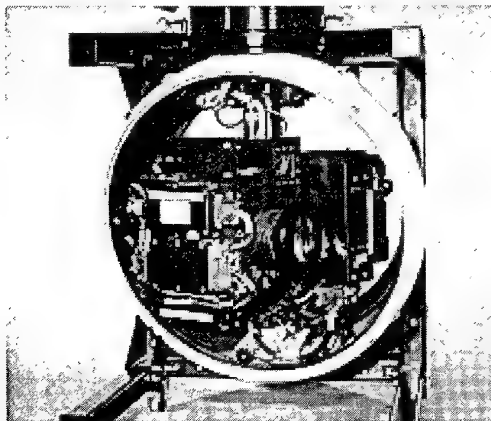


Figure 6: ALBEDOS active imager inside its 24-inch diameter airborne stabilized platform.

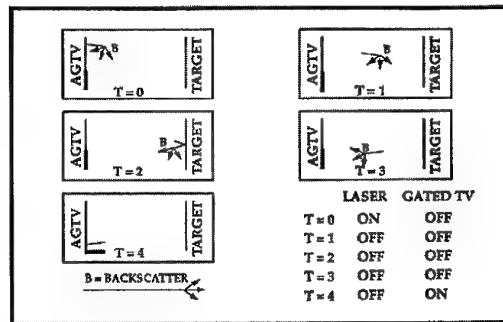


Figure 7: Principle of range gating.

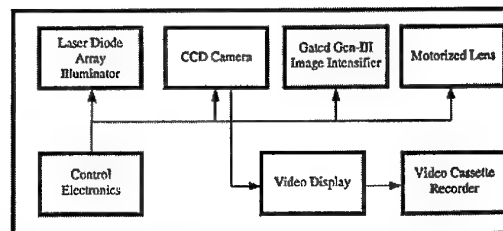


Figure 8: ALBEDOS basic schematic diagram.



Figure 9: The Xyberion intensified camera.



Figure 10: The optical resolution target or bar pattern canvas from Tracor Aerospace.



Figure 11: The lifejacket with flexible retroreflective tapes.

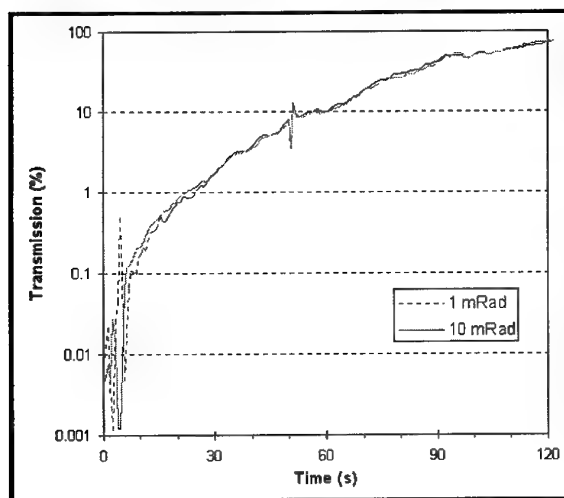
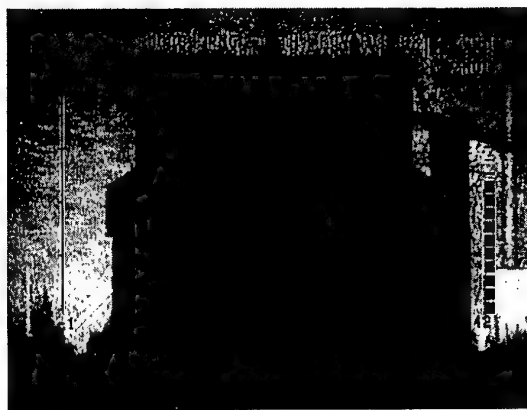
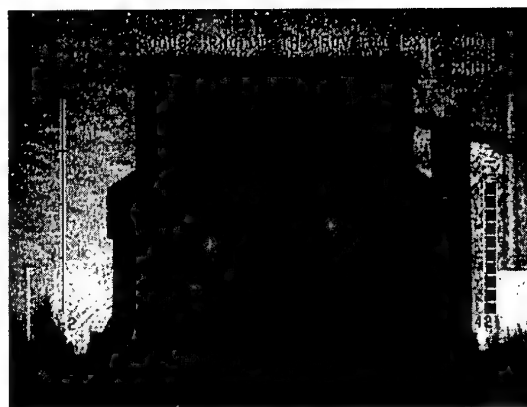


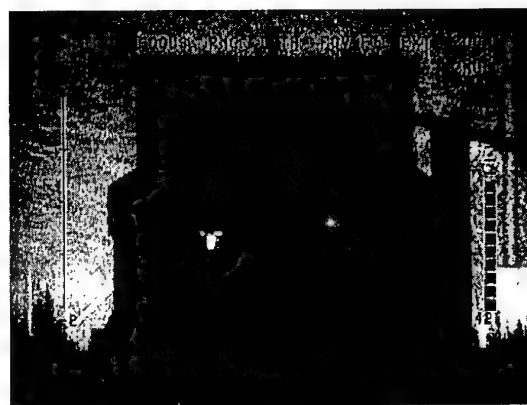
Figure 12: Transmittance as a function of time for run # 20.



a) 6 s.



b) 13 s. ( 5 s. after detection )



c) 38 s.

Figure 13: Detection of the lifejacket (at left) using the range-gated ALBEDOS active imager. The time mentioned below each figure is the time after the opening of the doors at which the frame image was recorded. This is valid for the following figures.



a) 6 s.

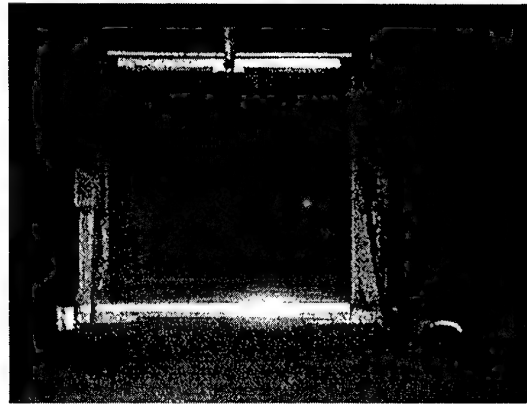


b) 22 s. ( 7 s. after detection )

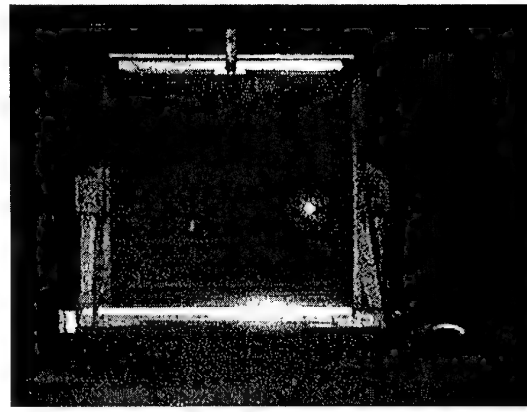


c) 90 s.

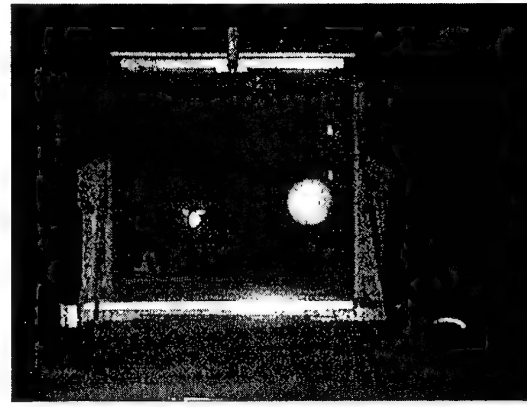
Figure 14: Detection of a man using the far-infrared thermal imager from Agema Infrared Industries



a) 6 s.

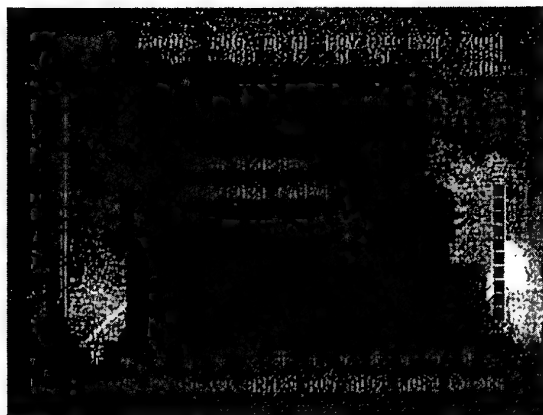


b) 36 s. ( 6s. after detection )

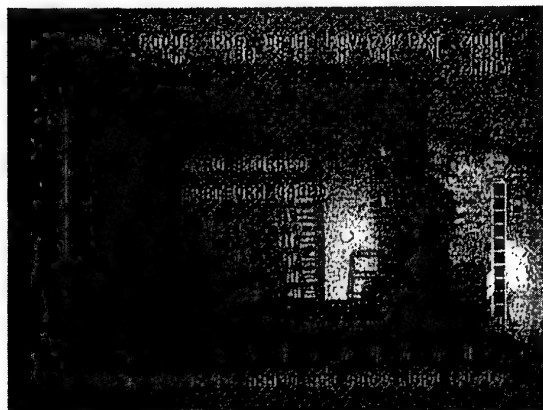


c) 80 s.

Figure 15: Detection of the lifejacket ( at left ) by the Xybion low-light level camera operating in a continuous mode. Note the blooming effect at right produced by the light source of the transmitters.



a) 10 s.

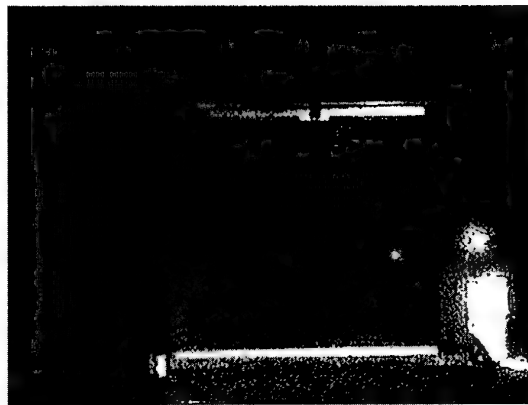


b) 60 s. ( 8 s. after detection )

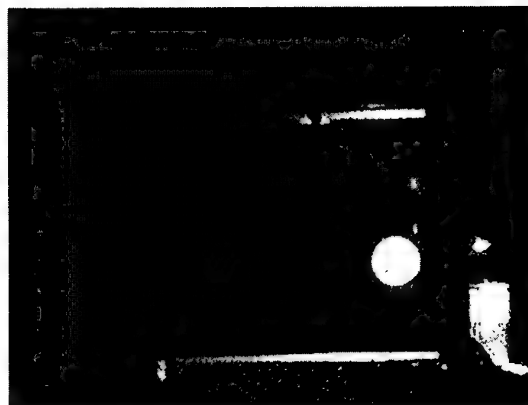


c) 86 s.

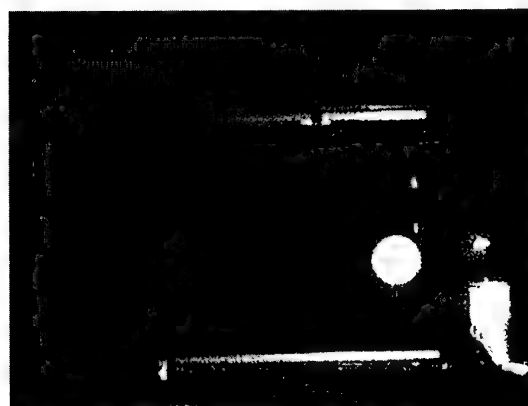
Figure 16: Detection of the bar pattern ( at right, top and 5 th sets ) with the ALBEDOS active imager.



a) 10 s.



b) 101 s. ( 35 s. after detection )



c) 146 s.

Figure 17: Detection of the bar pattern with the Xybion intensified camera.

PAPER No. 28      D. Clement

COMMENT/QUESTION:

The performance of the system does not depend on transmission through fog but also on back-scatter from fog particles. The latter may depend on particle size distribution. How do you make sure that there is a correlation between size distribution of fogs you generate in the test chambers with those of naturally occurring fogs?

AUTHOR/PRESENTER'S REPLY:

Air atomizing spray nozzles are used. The particle size is measured with a Malvern Particle Sizer. The mean volume diameter is around 25 $\mu$ m. This is a slightly larger value than the main volume diameter of a C2 type cloud.

DISCUSSOR'S NAME:      D. Clement

COMMENT/QUESTION:

I assume that the laser wavelength you exploit is around 1 $\mu$ m. Do you foresee a problem with eye safety?

AUTHOR/PRESENTER'S REPLY:

The eye safe distance is 30m.

# TACTICAL LASER SYSTEMS PERFORMANCE ANALYSIS IN VARIOUS WEATHER CONDITIONS

Capt. R. Sabatini

Italian Air Force Research and Flight Test Division (DASRS) - Official Test Centre (RSV)  
Technical Group (GT) - Avionics and Armament Evaluation Service (SSAA)  
Pratica di Mare Airport  
Pomezia 00040 (Rome), ITALY

## SUMMARY

A method for evaluating the performance of laser systems operating in the infra-red is presented in this paper. Particularly, state-of-the-art Nd :YAG target designators (LTD) performance are investigated in realistic operational scenarios, taking into account laser beam atmospheric propagation and target reflection characteristics, in different operational and environmental conditions. Various standard atmospheric propagation models have been used for the 1.064  $\mu\text{m}$  wavelength of Nd :YAG and their results compared. Furthermore, a simplified laser beam propagation model has been developed taking into account both absorption and scattering effects, in various weather conditions (visibility, humidity, etc.). Particularly, the model for dry-air conditions has been derived from the studies and experiments conducted by Elder and Strong on infrared laser propagation at various wavelengths, while for rain propagation the basic model has been integrated with the equations developed by Middleton.

Moreover, an appropriate reflection model has been used and different geometric conditions taken into account, in order to evaluate the performance of laser systems in realistic operational scenarios. The number of parameters in the models has been reduced in order to make the overall algorithm manageable in a PC mission planning program to be delivered at a Flying Squadron level, preserving an acceptable level of reliability for the operational and atmospheric conditions of practical interest. All conclusions drawn here are referred to laser target designators, but they apply to most non-coherent detection laser systems including range finders and beam riders operating at 1.064  $\mu\text{m}$ .

## LIST OF SYMBOLS

$H_t$	MSL altitude of transmitter
$H_r$	MSL altitude of receiver
$H_g$	MSL altitude of target
$R_T$	range transmitter-target
$R_R$	range target-receiver
$\alpha$	aircraft angle of incidence
$\gamma$	aircraft ramp angle
$\gamma_r$	angle between the LOS target-receiver and the perpendicular to the aperture

$Q_d$	laser depression angle
$\varepsilon$	receiver depression angle
$\eta$	target inclination over the horizon
$Q_t$	angle between the LOS transmitter-target and the perpendicular to the target surface
$Q_r$	angle between LOS receiver-target and the perpendicular to the target surface
$MDP$	seeker minimum detectable power density
$\rho_T$	target reflectivity
$\Phi_o$	transmitter pick power
$D_R$	diameter of receiving aperture
$A$	illuminated area of target
$A_t$	area of target surface
$A_b$	beam area at a distance $R_T$
$V$	visibility
$w$	water vapour content
$w_t$	water vapour in the trans. path
$w_r$	water vapour content in the rec. path
$\rho$	relative humidity
$\tau_{at}$	absorptive transmittance
$\tau_{asi}$	transmittance due to scattering
$\beta$	scattering coefficient
$\tau_{atm}$	atmospheric transmittance
$D_L$	beam diameter at transmitter
$\alpha_T$	beam divergence
$F$	energy density at target
$G$	irradiance of target surface
$U$	transmitted energy
$\sigma_w$	sea-level atmospheric attenuation coeff.
$\alpha_{HT}$	$\sigma_w$ fractional decrease from $H_t$ to sea level
$A_R$	receiver aperture area
$A_M$	projected spot area in the plane normal to the receiver sight line
$\beta_{HR}$	$\sigma_w$ fractional decrease from sea level to $H_r$

## INTRODUCTION

Technological development in the realm of optronics have led to innovative concepts in the mission management of current and next generation ground attack aircraft. Particularly, tactical laser systems including LIDAR, rangefinders (LRF) and target designators (LTD) are being used extensively today by most air forces in the world and new promising laser technologies are being explored. Most laser systems are active devices that operate in a manner very similar to microwave radars but at much higher frequency (e.g., LIDARS, LRF).



Other devices (e.g., LTD, Beam-riders) are simply used to precisely direct laser guided bombs (LGB) or other airborne weapons against ground targets. A combination of both functions is often encountered in modern integrated airborne navigation-attack systems.

Compared to similar microwave devices, the higher frequency of laser systems has the beneficial effect of smaller components and remarkable angular resolution values. On the other hand, laser systems performance are much more sensitive to the vagaries of the atmosphere and are thus generally restricted to shorter ranges in the lower atmosphere than microwave radar.

Because of the existence of atmospheric windows and the availability of suitable components (laser sources), laser systems are built at specific wavelengths. Most tactical laser systems are constructed at 1.064  $\mu\text{m}$  (Nd:YAG), 1.54  $\mu\text{m}$  (Er:glass and Raman-shifted Nd:YAG), and 10.6  $\mu\text{m}$  ( $\text{CO}_2$ ) wavelengths. Laser systems can be grouped according to the detection technique (i.e., coherent or non-coherent), the signal modulation technique, the type of measurement (if any), the wavelength of operation or the function performed. Generally, the term LIDAR (or LADAR) is referred to active devices belonging to the family of coherent detection laser systems. This paper, however, will concentrate on LTD/LGB combinations, which are typically included (together with most LRF) in the group of non-coherent detection laser systems. Since most state-of-the-art LTD/LGB combinations operate at 1.064  $\mu\text{m}$  wavelength (Nd:YAG), the laser beam atmospheric propagation and target reflection models have been optimised for this wavelength, taking also into account other characteristics of existing systems.

The theory of operation of laser weapon systems is simple. The LTD is an accurate pointing system which provides the laser source, the precision optics and stabilisation required to accurately shine the laser beam on the target. The LGB detector generate an electric signal when light is received at the wavelength of the laser, consequently the laser light reflecting off of the target is "visible" to the weapon. This provides signals on which the weapon can "home" toward the target by actuating its aerodynamic surfaces. Obviously, the pointing accuracy of the laser is most important, as any laser error will degrade the accuracy of the weapon.

Over the last decade, the Italian Air Force Research and Flight Test Establishment (DASRS-RSV) has been involved in various activities related with laser systems for airborne applications. Particularly, a Laser Designation Pod (LDP) with both TV and IR

capability has been integrated on the TORNADO aircraft, together LGB of various characteristics.

Since the beginning of the activities, it appeared essential to define the most appropriate methods of LDP/LGB performance evaluation, in a representative part of the aircraft envelope and in realistic operational scenarios. This was important not only for experimental purposes, but also considering the remarkable advantage that the introduction of these methodologies could determine in the refinement of the tactics of employment of laser systems, in both training and attack missions.

Unfortunately, the available scientific and technical literature was not sufficient alone to allow such a deep investigation. Moreover, the majority of required technical data about the LTD/LGB systems were not made available by the manufacturers.

Therefore, the ItAF preceded autonomously, using the experience gained in flight test activities conducted at RSV and performing some laboratory measurements at DASRS in order to determine the LDP/LGB characteristics.

These activities permitted to obtain all information required for a PC mission planning program, that is now being implemented for delivery at an operational level. In perspective, developing an adequate display format, a similar program may even be used on the aircraft for real-time mission management.

The paper begins with a review of the underlying theory behind the algorithms used in the program. Particularly, a discussion about the laser range equation is presented, followed by a description of the atmospheric propagation/reflection models and of the relevant geometric elements of a typical attack mission. Successively, the practical applications of the study are discussed and the results of some calculations are presented relative to an example of LTD/LGB combination.

The paper closes with some concluding remarks. Three appendixes present more details about the mathematical derivation of the various equations and the curves describing in a graphic form the range performance of the particular LTD/LGB combination considered, in various weather conditions.

### LASER RANGE EQUATION

A fundamental problem in laser systems analysis is the determination of the total optical power density that is present at the receiver aperture (case of LIDAR and LRF) or laser guided bomb (LGB) seeker and, consequently, the total optical power incident on the photosensitive element of the receiver (i.e., the detector).

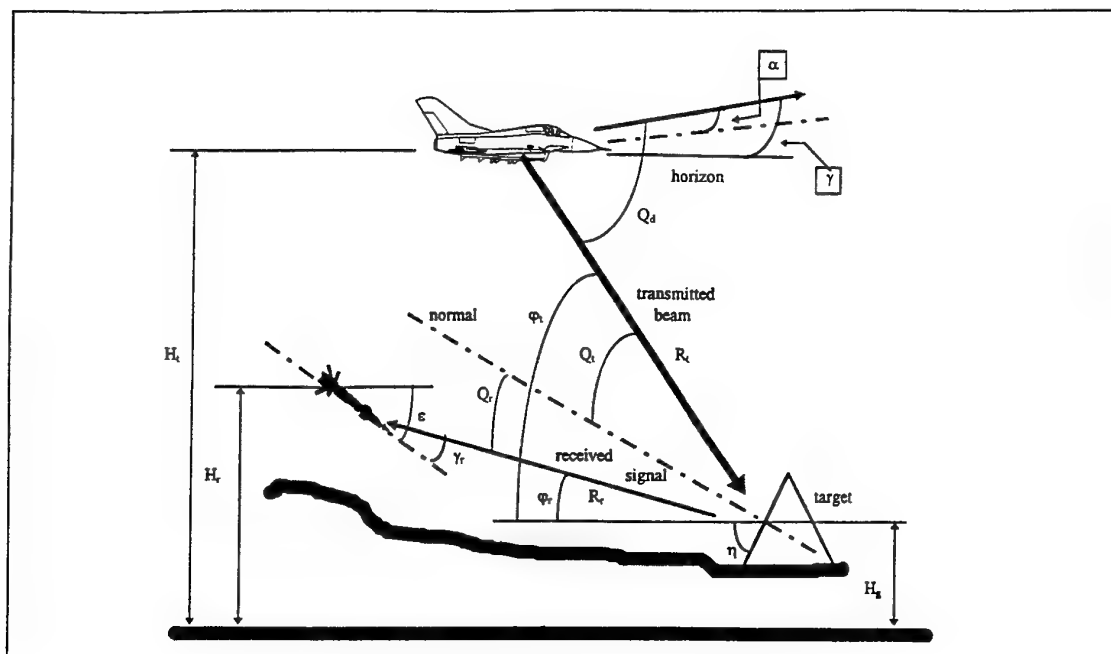


Figure 1. Typical mission geometry (vertical profile).

The laser range equation is commonly used to determine the power received under specific conditions and against a particular target.

Depending on the detection technique (i.e., coherent or non-coherent) and other system/target characteristics, there are various forms of the laser range equation [1], [2]. Due to the aim of the present paper, only the range equation valid for non-coherent detection laser systems (LRF and LTD) will be discussed.

With reference to the geometry of a typical ground attack mission with laser guided bombs (fig. 1), the maximum range performance of an LTD system can be estimated using the following equation:

$$MDP = \frac{4\rho_r\Phi_s A \cos Q_t \cos Q_r \cos \gamma_r \tau_m}{\pi^2 (D_s + \alpha_r R_r)^2 R_s^2} \quad (1)$$

( $R_r = R_s$  for a LRF)

whose simplified form, assuming a circular aperture and an extended target (i.e., a target larger than the beam spot), is the following:

$$MDP = \frac{\rho_r \Phi_s D_s^2 \cos Q_t \cos Q_r \cos \gamma_r \tau_m}{4R_s^4} \quad (2)$$

The theory behind both equations is presented at Appendix A.

From a "user" point of view, the difficulties of this approach are represented by the calculation of  $\tau_m$  (a function of  $R_r$ ,  $R_s$ ,  $V$ ,  $w$ , etc.), the knowledge of the target characteristics (i.e., shape, reflectivity, etc.) and, very often, the unavailability of technical

data on the seeker-head detector and active laser system.

However, since the physical characteristics of the target are generally known before performing an attack and the target is generally extended at ranges of practical interest, it is sufficient to use the diffuse reflectivity of the surface that will be illuminated, at the wavelength considered (i.e., 1.06  $\mu\text{m}$ ). Moreover, since the characteristics of LTD signals are standardised within NATO countries by the STANAG 3733, there is no much the system designer can do in order to enhance the performance of an LTD, except than increasing the output power of the system. On the other hand, some laboratory experiments have shown that a reliable measurement of the seeker minimum detectable energy is possible, directly using the seeker and a relatively simple instrumentation [2].

It is therefore possible to calculate the performance of a LRF/LTD system as long as the atmospheric propagation of the laser beam can be adequately modelled.

This is not an easy task, especially taking into account the considerable variation that the atmospheric parameters may experience during a mission and for a propagation path that may exceed 10-15 km.

### ATMOSPHERIC PROPAGATION

Various standard atmospheric propagation models have been used for the 1.064  $\mu\text{m}$  wavelength of Nd:YAG and their results compared in various weather conditions. Furthermore, a simplified laser

beam propagation model has been developed for the 1.064  $\mu\text{m}$  wavelength of Nd:YAG laser. The model takes into account absorption and scattering effects and is valid for dry-air and rain conditions for any value of visibility and relative humidity. Particularly, the model for dry-air conditions has been derived from the studies and experiments conducted by Elder, Strong [3] and Langer [4] on infrared laser propagation at various wavelengths, while for rain propagation the basic model has been integrated with the equations developed by Middleton [5].

In the following, only a brief outline of the relevant equations is presented. More details are given at Appendix B.

The simplified equations for dry-air conditions, referred to the four cases of practical interest, are the following :

Visibility  $\geq 6 \text{ km}$ ,  $w_i > w_j$ ,  $w_i > w_j$

$$\tau_{\text{atm}} = k_i^2 \left( \frac{w_i^2}{w_s w_r} \right)^{\beta} \cdot \left\{ \exp \left[ -\frac{391}{V} \cdot \left( \frac{\lambda_i}{0.55} \right)^{-(0.002 \cdot V + 1.029)} \cdot (R_i + R_s) \right] \right\} \quad (3)$$

Visibility  $\geq 6 \text{ km}$ ,  $w_i > w_j$ ,  $w_r < w_j$

$$\tau_{\text{atm}} = k_i^2 \left( \frac{w_i}{w_r} \right)^{\beta} \cdot \left\{ \exp \left[ -A w_r^{1/2} - \frac{391}{V} \cdot \left( \frac{\lambda_i}{0.55} \right)^{-(0.002 \cdot V + 1.029)} \cdot (R_i + R_s) \right] \right\} \quad (4)$$

Visibility  $< 6 \text{ km}$ ,  $w_i > w_j$ ,  $w_r < w_j$

$$\tau_{\text{atm}} = k_i^2 \left( \frac{w_i}{w_r} \right)^{\beta} \cdot \left\{ \exp \left[ -A w_r^{1/2} - \frac{391}{V} \cdot \left( \frac{\lambda_i}{0.55} \right)^{-(0.002 \cdot V + 1.029)} \cdot (R_i + R_s) \right] \right\} \quad (5)$$

Visibility  $< 6 \text{ km}$ ,  $w_i > w_j$ ,  $w_r > w_j$

$$\tau_{\text{atm}} = k_i^2 \left( \frac{w_i^2}{w_s w_r} \right)^{\beta} \cdot \left\{ \exp \left[ -\frac{391}{V} \cdot \left( \frac{\lambda_i}{0.55} \right)^{-(0.002 \cdot V + 1.029)} \cdot (R_i + R_s) \right] \right\} \quad (6)$$

The equation for rain conditions, is the following :

$$\tau_{\text{atm-LTD}} = k_i^2 \left( \frac{w_i^2}{w_s w_r} \right)^{\beta} \cdot \left\{ \exp \left[ -\beta_{\text{rain}} (R_i + R_s) \right] \right\} \quad (7)$$

where the scattering coefficient with rain ( $\beta_{\text{rain}}$ ) is a function of the rainfall-rate ( $\Delta x/\Delta t$ ) and the dimension of the rain drops ( $a$ ), as described at Appendix B.

## GEOMETRIC CONSIDERATIONS

There are three cosine factors in equations (1) and (2). They are related to the assumption of a "Lambertian" reflector (i.e., diffuse reflection of the laser signal incident on the target surface). It is essential, in order to determine the performance of an LTD/LGB combination during an attack, to take into account the variation of the angles  $\gamma_r$ ,  $Q_i$  and  $Q_r$  (Fig. 1).

On the other hand, in order to calculate the maximum range for effective illumination (MIR), it is important to determine the maximum values of these angles during an attack. Moreover, the angles  $\gamma_r$ ,  $Q_i$  and  $Q_r$  should be expressed as functions of other physical or geometrical parameters that are known prior the mission (e.g., seeker FOV, angle  $\eta$ , etc.).

From Eq. (2), the maximum theoretical value of the angle  $\gamma_r$  is :

$$\gamma_{r(MDP)} = \arccos \left( \frac{MDP \cdot \pi R_s^2}{\rho_r \Phi \cdot \cos \theta_i \cos \theta_r \tau_{\text{atm}}} \right) \quad (8)$$

However, we must consider that the seeker of the LGB must always intercept a portion of the reflected signal sufficient to activate the detector in order to guide the weapon against the target by appropriate motion of its control surfaces. In other words, as we can see in Fig. 2, the theoretical cone given by rotation of the angle  $\gamma_{r(MDP)}$  around the normal to the aperture, should always encompass the FOV of the seeker.

Therefore, since after the first laser pulse sequence is received  $\gamma_r$  should never exceed the FOV, we can reasonably assume that the maximum value of the angle  $\gamma_r$  is equivalent to the seeker FOV.

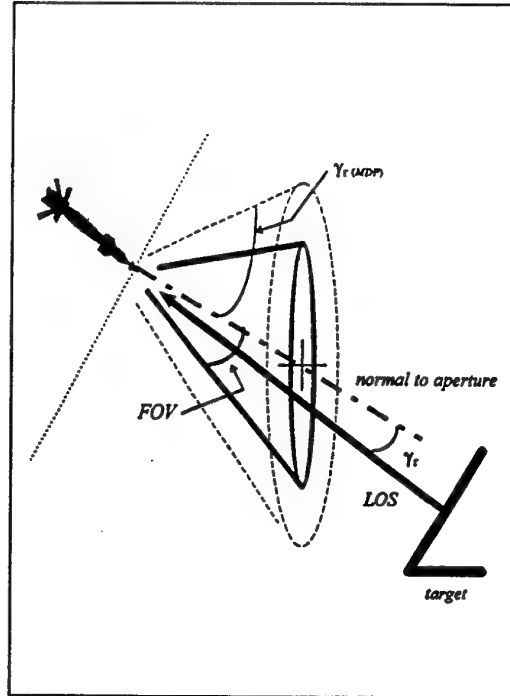


Figure 2. LGB-Target Geometry.

Considering the geometry of typical ground attack missions with LGB, also the angles  $Q_i$  (angle between the LOS transmitter-target and the normal to the target surface) and  $Q_r$  (angle between the LOS receiver-target and the normal to the target surface), can be determined.

With reference to Fig. 1, the angles  $Q_i$  and  $Q_r$  can be expressed as :

$$Q_i = \eta + \varphi_i - 90^\circ \quad (9)$$

$$Q_r = 90^\circ - \eta - \varphi_r \quad (10)$$

where  $\eta$  is the target inclination,  $\varphi_i$  is the angle between the transmitted beam axis and the horizon ( $\varphi_i = Q_d - \gamma + \alpha$ ) and  $\varphi_r$  is the angle between the LGB-target LOS and the horizon ( $\varphi_r = \varphi_i - Q_i - Q_r$ ). Knowing  $Q_d$  (laser depression angle),  $\alpha$  and  $\gamma$ , it is possible to determine the value of the angle  $Q_i$  during the attack, solving the equation :

$$Q_i = \eta + Q_d - \gamma + \alpha - 90^\circ \quad (11)$$

More difficult is the determination of  $Q_r$ , since the angle  $\varphi_r$  can not be determined without knowing continuously the position assumed by the line of sight LGB-target (i.e., the guidance algorithms and accurate ballistics of the LGB). However, knowing the angle  $\beta$  at the beginning of the designation (from the ballistics of the unguided weapon) and taking  $\gamma$ , equivalent to the seeker FOV, we have that :

$$\varphi_r = \beta \pm \gamma_{r(\text{MAX})} = \beta \pm \text{FOV} \quad (12)$$

Since, it is reasonable to assume that after the designation is initiated, the angle  $\gamma$ , will be kept as low as possible by a PG-LGB, we can assume that  $\varphi_r = \beta$  in this case. Therefore, the approximate value of the angle  $Q_r$  during an attack with PG-LGB and BTB-LGB, can be determined solving the equations :

$$Q_r = 90 - \eta - \beta \quad \text{for PG-LGB} \quad (13)$$

$$Q_r = 90 - \eta - \beta + \text{FOV} \quad \text{for BTB-LGB} \quad (14)$$

For the purpose of determining the maximum values that the angles  $Q_i$  and  $Q_r$  can reach during an attack, which determine the absolute minimum performance of a particular LTD/LGB combination (worst case), it is meaningful to take into account the horizontal profile of a typical self-designation attack mission illustrated in Figure 3.

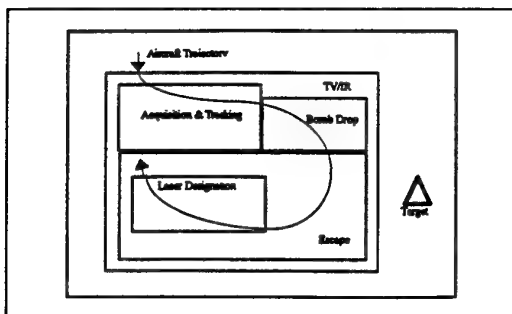


Figure 3. Mission horizontal profile (self-designation).

Since the designation is initiated in the final portion of the bomb drop trajectory, it is generally performed at a considerable range from the target (comparable to the visual range). This means that, normally, the angles  $Q_i$  and  $Q_r$  never reach values close to  $90^\circ$  during an attack, even in the worst case when  $\eta = 90^\circ$ . On the other hand, in the case of horizontal target ( $\eta = 0^\circ$ ), the cases where  $Q_i$  and  $Q_r$  get close to  $90^\circ$  are not of practical interest.

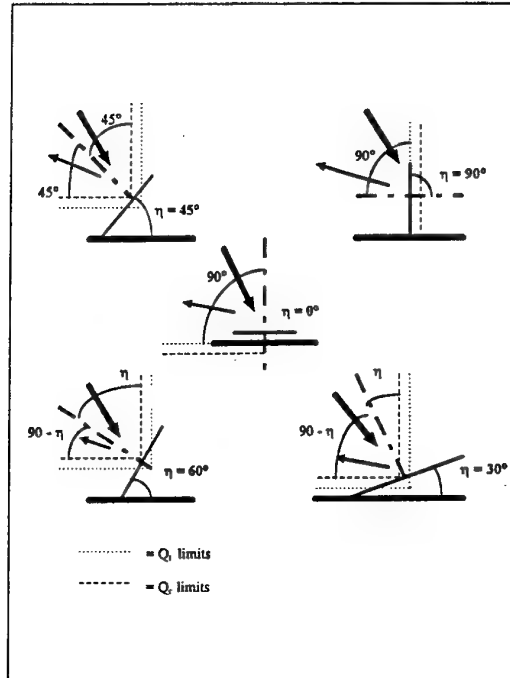


Figure 4.  $Q_i$  and  $Q_r$  limits.

Looking at Figure 4, it appears evident that the angle  $Q_i$  is smaller than  $\eta$  when  $\eta > 45^\circ$ , while it is generally smaller than the complementary of  $\eta$  when  $\eta < 45^\circ$ . Similar considerations apply for  $Q_r$ . Therefore, with these assumptions, the worst case conditions for  $Q_i$  and  $Q_r$  are the following :

$$\begin{cases} Q_{i(\text{MAX})} = 90 - \eta \\ Q_{r(\text{MAX})} = 90 - \eta \end{cases} \quad \text{for } \eta < 45^\circ$$

$$\begin{cases} Q_{i(\text{MAX})} = \eta \\ Q_{r(\text{MAX})} = \eta \end{cases} \quad \text{for } \eta \geq 45^\circ$$

### REFLECTIVITY CONSIDERATIONS

A surface that is a perfect diffuser scatters incident light equally in all directions. For such "ideal" surfaces, the intensity ( $\text{W/m}^2$ ) of diffuse reflected light is given by :

$$I_d = I_i k_d \cos \theta \quad 0 \leq \theta \leq \pi/2 \quad (15)$$

where  $I_i$  is the intensity of the light source at the target,  $\theta$  is the angle between the surface normal

and a line from the surface point to the light source (considered as a point source). The constant  $k_d$  is an approximation of the diffuse reflectivity, which depends on the nature of the material and the wavelength of the incident light.

Equation (15) can be written as the dot product of two unit vectors :

$$I_s = I_i k_d (L \cdot N) \quad (16)$$

where  $N$  is the surface normal and  $L$  the direction vector from the light source to the point on the surface.

The approximate diffuse reflectivity of various target materials ( $\lambda=1.064 \mu\text{m}$ ), are listed in Table 1.

Target	Material	Reflectivity
Shelter	Concrete (Aged)	40%
Metal Roof	Aluminum (Oxidized)	50%
Building Roof	Terra Cota	25%
Tanker	Steel (Painted)	30%
Aircraft	Painted Alum. Alloy	25%
Road	Asphalt	20%

TABLE 1. Diffuse Reflectivity of various targets.

In actuality, any reflection from a practical surface should be considered as the sum of a specular component and a diffuse component. The existence of these two components has been shown experimentally and is not a consequence of the choice of a particular model.

A surface attribute that is important to model is the surface roughness. A perfectly smooth surface reflects incident radiation in a single direction. A rough surface tends to scatter incident radiation in every direction, although certain directions may contain more reflected energy than others. This behaviour is obviously also dependent on the wavelength of radiation; a surface that is smooth for certain wavelengths may be rough for others. For example, oxidised or unpolished metal is smooth for radio waves (say  $\lambda=10^{-2}$  m) and very rough for radiation in the near-infrared (NIR) part of the spectrum. In general, metals can be prevalently diffuse or specular reflectors in the NIR depending on whether they are polished or not. So reflection is not predominantly dependent on the material but also on its surface properties. Another factor in reflection is the grazing angle of the incident laser source. This can in fact determine the entity of the reflected signal and which component of reflection (i.e., diffuse or specular) is prevailing.

Therefore, a "realistic" reflection model should at least represent the target surface as some combination of a perfect diffuse reflector and a perfect specular surface. One such a model is described at Appendix C.

## CALCULATIONS

We can not attempt to calculate the range performance of a particular LTD/LGB combination, using the data given in Table 2. These data are referred to generic LTD and LGB systems operating at a wavelength of  $1.064 \mu\text{m}$ .

Using the equations described above, we can now calculate the range performance of this particular LTD/LGB combination in a certain operational scenario, with different atmospheric conditions (i.e., visibility, humidity, etc.).

LTD	
Beam Diameter	50 mm
Beam Divergence	0.5 mrad
Wavelength	$1.064 \mu\text{m}$
Pick Energy	120 mJ
Pulse Duration	20 nsec
LGB	
FOV	$20^\circ$
MDP	$3 \mu\text{W}/\text{m}^2$

TABLE 2. LTD/LGB Characteristics

Moreover, with the same atmospheric conditions, we can calculate the performance of the systems when used against different targets (i.e., reflectivity, inclination), and the maximum distance of the illuminating aircraft for an effective designation.

The curves shown at Appendix C describe in a graphic form the range performance of the considered LTD/LGB combination, with different values of visibility (i.e., all other parameters have been set to the "worst case" value). Particularly, the range LTD-target is given as a function of the range LGB-target. The curves have been traced for different inclinations of the target over the horizon (i.e., different values of the angles  $Q_{i(\text{MAX})}$  and  $Q_{r(\text{MAX})}$ ).

Using these curves it is also possible to determine whether or not the attack can be performed with a certain estimated minimum illumination time.

Given the bomb initial conditions (i.e., velocity and trajectory, from the unguided weapon ballistics) before designation is initiated, it is possible to estimate the designation time, taking into account the time required by the LGB from those initial conditions to stabilise towards the target (i.e., guided weapon ballistics).

If the guidance algorithms are unknown it is possible to roughly estimate the designation time by assuming a straight trajectory of the bomb towards the target and a velocity in the final portion of its drop correspondent to the maximum theoretical velocity of the weapon. With these assumptions, the minimum theoretical range LGB-target before designation can be plotted in the graphs given at Appendix D and consequently the maximum range of the aircraft at the beginning of the designation is determined. Obviously, when this range is less than the Target Lethal Range (TLR), the attack can not be performed successfully.

For instance, assuming a maximum theoretical velocity of the LGB in the order of 800 fts/sec and a minimum designation time of 12 sec, the distance LGB-target before designation should not exceed 3 km, for an effective guidance. Plotting this value in the graphs D-1 and D-2, we notice that in the worst geometric conditions (i.e.,  $\eta$  close to  $0^\circ$  and  $90^\circ$ ) the range aircraft-target at the beginning of the designation is below the visual range (i.e., less than 1 km for a 2 km visibility and about 3 km for a 4 km visibility). In all other cases (i.e.,  $V > 4$  km) the illumination can be performed from a distance comparable to (or, theoretically, even greater than) the visual range.

#### APPLICATIONS OF THE STUDY

The equations presented in this paper can be used for estimation of LRF and LTD/LGB performance in different operational scenarios. Particularly, they can be the basis of a PC program for mission planning and optimisation, allowing validation and refinement of the operational tactics (for both self-designation and co-operative attacks). Moreover, adopting an adequate display format, they can be even used to implement a software for real-time mission management in the aircraft.

A possible display format for the PC Mission Planning Program (MPP) is shown in Figure 5.

The Maximum Illumination Range (MIR) circles should always encompass the Target Lethal Range (TLR) circle. The MIR at the beginning ( $MIR_1$ ) and at the end ( $MIR_2$ ) of the designation can be displayed (all other MIR circles are included between these two).

Knowing the target surface orientation, reflectivity and inclination, it is also possible to determine the optimal illumination sector (OIS) and the optimal bomb direction (OBD).

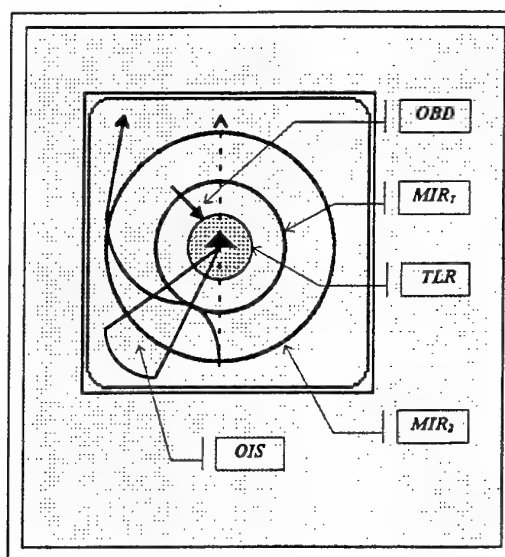


Figure 5. Possible MPP Display Format.

In order to obtain this kind of presentation, the operator should insert the following information :

- LDP characteristics
- LGB seeker MDP ;
- LGB seeker FOV
- Target surface reflectivity ;
- Target surface inclination ;
- Target surface orientation
- Visibility ;
- Relative humidity ;
- Temperature
- Expected bomb direction ;
- Desired Escape Direction.

A pictorial representation of a possible cockpit display format is shown in Figure 6.

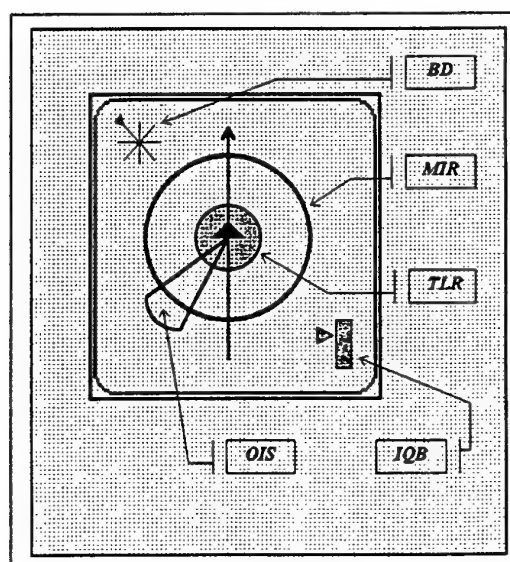


Figure 6. Possible Cockpit Display Format.

An indication of the MIR associated with current direction and position can be provided in real-time, together with an Illumination Quality Bar (IQB). Moreover, knowing the Bomb Direction (BD), it is possible to provide an indication of the OIS, including the MIR relative to it. In order to obtain this kind of presentation, assuming that all information required on relevant LDP and LGB types are available to the aircraft computer (together with aircraft-target relative position information), the pilot should insert prior the attack (e.g., through a dedicated data entry format), the following information :

- Type of LDP/LGB combination ;
- Target surface reflectivity ;
- Target inclination ;
- Visibility ;
- Relative humidity ;
- Temperature ;
- Expected bomb direction ;
- Target surface orientation.

The atmospheric parameters (i.e., visibility and humidity) should be obviously referred to the target location. If the relative humidity is unknown, it can be set to 100% (i.e., worst case). Similarly, if the target inclination is unknown or the target is a curve surface (e.g., a shelter) the inclination can be set to the worst case value (i.e., 90° or 0°).

#### FINAL REMARKS

In this paper we have illustrated the results of a study conducted by the Italian Air Force Research and Flight Test Establishment (DASRS-RSV) in order to define a method for predicting the performance of laser systems operating in the infrared, with different operational and environmental conditions.

The study was mainly addressed to airborne laser systems for target designation (LTD), used to precisely direct laser guided bombs (LGB) against ground targets. However, most of the results presented in this paper are applicable to all non-coherent detection laser systems (e.g., range finders, beam-riders, etc.).

An atmospheric laser beam propagation model has been implemented taking into account both absorption and scattering effects, in different weather conditions (visibility, humidity, etc.). The number of parameters in the model has been reduced as much as possible, in order to make the model manageable at an operational level, notwithstanding the model reliability for the atmospheric propagation window of interest. Moreover, an appropriate reflection model has been used and different geometric conditions taken into account, in order to evaluate the performance of the laser systems in realistic operational scenarios.

The results of the study are very encouraging, giving the opportunity to improve the tactics of employment of the laser guided weapons and to determine the range of possible uses of particular combinations LTD/LGB in favourable and adverse weather conditions.

An activity now ongoing is the implementation of a MPP, based on the algorithms developed in the study, for laser attack mission planning and optimisation at a Squadron level. It is expected that the software will also be able to assist in the definition of laser safety criteria for both test range and training operations.

Moreover, adopting an adequate display format, the algorithms developed can be even used to implement a software for real-time mission management in the aircraft.

#### ACKNOWLEDGMENT

The author gracefully acknowledge the valuable advice given by Lt.Col G Arpaia, Maj P Cuppone and Maj F Guercio of DASRS-RSV and the conversations held with Mr F Fouchard of Thomson Avionique (Paris).

#### REFERENCES

1. A. V. Jelalian. "Infrared laser radar system". AGARD CP482. Dec 1990.
2. R. D. Hudson. "Laser and low light television". Hughes Aircraft Company, CA, 1980.
3. T. Elder, J. Strong. "The infrared transmission of atmospheric windows". J. Franklin Ins., 1953.
4. R. M. Langer. Signal Corps Report No. DA-36-039-SC-72351. May 1957.
5. W. E. K. Middleton. "Vision through the atmosphere". Univ. of Toronto Press. 1952.
6. B. T. Phong. "An empirical model of light reflection". Journal of Applied Physics. 1975.

#### APPENDIX A

The beam area at a distance  $R_T$  is given by :

$$A_t = \frac{\pi(D_t + \alpha_r R_T)^2}{4} \quad (\text{A-1})$$

The energy density ( $\text{J/m}^2$ ) at the target as a function of transmitted energy is given by :

$$F = \frac{U}{A_t} e^{-(\alpha_a + \alpha_s) R_T} \quad (\text{A-2})$$

This energy density is measured normally to the transmitter line of sight (LOS).



Using equation (A-1), the equation (A-2) can be written in the form :

$$F = \frac{4U}{\pi(D_i + \alpha_r R_r)^2} e^{-(\sigma_r \alpha_r R_r)} \quad (A-3)$$

The energy (G) of a laser spot that will irradiate a given target surface (A) is that portion passing through the projected area ( $A_N$ ) in the plane orthogonal to the sight line. The irradiance of the target surface can be calculated using the equation :

$$G = F \frac{A_N}{A} \quad (A-4)$$

therefore :

$$G = \frac{4UA_N}{A\pi(D_i + \alpha_r R_r)^2} e^{-(\sigma_r \alpha_r R_r)} \quad (A-5)$$

Assuming that the target surface ( $A_N$ ) is greater than the laser spot on target, we have :

$$A_N = A \cos \theta_i \quad (A-6)$$

Therefore, in this case:

$$G = \cos \theta_i \frac{4UA_i}{A\pi(D_i + \alpha_r R_r)^2} e^{-(\sigma_r \alpha_r R_r)} \quad (A-7)$$

A rigorous approach requires that all possible target-spot relative dimensions are taken into account (i.e., "extended" target, target smaller than laser spot and "wire" target). However, considering the aim of this paper, only the extended target case will be considered. In fact, for a typical airborne LTD the illuminated area of the target is smaller than 3 m<sup>2</sup> when the system is operated from a distance of 10 km. However, since the other cases are applicable to LRF (and other systems), a detailed explanation of them can be found in the literature [1], [2].

The brightness of the irradiated target is determined by the irradiance level and by the reflectance characteristics of the target surface with respect to wavelength. Assuming a Lambertian target (i.e., diffuse reflector), the brightness (B) is given by :

$$B = \frac{\rho_r G}{\pi} \quad (A-8)$$

where  $\rho_r$  is the target diffuse reflectivity.

The energy ( $E_R$ ) collected by a receiving aperture observing this target is obtained from :

$$E_R = \frac{BA_R A_N}{R_r^2} e^{-(\sigma_r \alpha_r R_r)} \quad (A-9)$$

$A_M$  is related to the target laser spot area by :

$$A_M = A \cos \theta_i \quad (A-10)$$

Therefore, the final expression for energy intensity (I) at the receiver aperture for the Lambertian target

is, by substitution :

$$I = \frac{E_R}{A_R} = \frac{4\rho_r UA \cos \theta_i \cos \theta_r e^{-(\sigma_r (\alpha_m R_m + \alpha_r R_r))}}{\pi^2 (D_i + \alpha_r R_r)^2 R_r^2} \quad (A-11)$$

Since  $A = A_b$  for an extended target (i.e., provided the entire spot is on the target), we have :

$$I = \frac{\rho_r U \cos \theta_i \cos \theta_r e^{-(\sigma_r (\alpha_m R_m + \alpha_r R_r))}}{\pi R_r^2} \quad (A-12)$$

If the seeker of the "smart bomb" is not turned towards the target, an additional cosine factor would be introduced reducing the effective receiving aperture as a function of the angle between the line of sight and normal to the aperture ( $\gamma_R$ ). Therefore :

$$I = \frac{\rho_r U \cos \theta_i \cos \theta_r \cos \gamma_R e^{-(\sigma_r (\alpha_m R_m + \alpha_r R_r))}}{\pi R_r^2} \quad (A-13)$$

If the transmitter and receiver are collocated (case of LRF), the equations can be simplified by setting :

$$\begin{aligned} H_r &= H_t & \beta_{HR} &= \beta_{HT} & \gamma_r &= 0 \\ R_r &= R_t = R_o & \theta_r &= \theta_i \end{aligned}$$

Therefore :

$$I = \frac{\rho_r U \cos^2 \theta_i e^{-(2\sigma_r \alpha_m R_m)}}{\pi R_o^2} \quad (A-14)$$

## APPENDIX B

Attenuation of laser radiation in the atmosphere is described by the Beer's law :

$$\tau = I(z) / I_o = \exp(-\alpha z) \quad (B-1)$$

where  $\tau$  is the transmittance,  $I_o$  is the transmitted energy,  $I(z)$  is the energy received at a distance  $z$  from the laser source and  $\sigma$  is the attenuation coefficient. If the attenuation coefficient is a function of the path, then Eq. (B-1) becomes :

$$\tau = \exp \left[ - \int_0^z \sigma(z) dz \right] \quad (B-2)$$

The attenuation coefficient is determined by four individual processes: molecular absorption, molecular scattering, aerosol absorption and aerosol scattering. Therefore, the atmospheric attenuation coefficient ( $\sigma$ ) is given by :

$$\sigma = \alpha + \beta \quad (B-3)$$

where  $\alpha = \alpha_m + \alpha_a$  is the absorption coefficient and  $\beta = \beta_m + \beta_a$  is the scattering coefficient (the subscripts  $m$  and  $a$  designate the molecular and aerosol processes respectively). Each coefficient depends on the wavelength of the laser radiation. A simple approach, yielding approximate values of the absorption coefficient has been suggested by Elder and Strong [3] and modified by Langer [4]. Their approach is particularly useful because it



provides a means of relating the atmospheric absorption of the  $i$ th window to the relative humidity (a readily measurable parameter).

The empirical expressions developed by Langer are:

$$\tau_a = \exp(-A_i \cdot w^{1/2}), \quad \text{for } w < w_i \quad (\text{B-4})$$

$$\tau_a = k_i \left( \frac{w_i}{w} \right)^{\beta_i} \exp(-A_i \cdot w^{1/2}), \quad \text{for } w > w_i \quad (\text{B-5})$$

where  $A_i$ ,  $k_i$ ,  $\beta_i$  and  $w_i$  are constants whose values are the listed in Tab. B-1,  $w$  (the total precipitable water in mm), is given by:

$$w = 10^{-3} z \rho_a \quad (\text{B-6})$$

and  $\rho_a$  is the absolute humidity in  $\text{g/m}^3$ .

Window	$\Delta\lambda$ ( $\mu\text{m}$ )	$A_i$	$k_i$	$\beta_i$	$w_i$
I	0.72-0.94	0.0305	0.800	0.112	54
II	0.94-1.13	0.0363	0.765	0.124	54
III	1.13-1.38	0.1303	0.830	0.093	2.0
IV	1.38-1.90	0.211	0.802	0.111	1.1
V	1.90-2.70	0.350	0.814	0.1035	0.35
VI	2.70-4.30	0.373	0.827	0.095	0.26
VII	4.30-6.0	0.598	0.784	0.122	0.163

TABLE B-1. Constants for equations (B-4) and (B-5).

The value of  $\rho_a$ , the density of water vapour, can be found by multiplying the appropriate number in Table B-2 by the relative humidity.

Temperature										
$^{\circ}\text{C}$	0	1	2	3	4	5	6	7	8	9
-20	0.89	0.81	0.74	0.67	0.61	0.56				
-10	2.15	1.98	1.81	1.66	1.52	1.40	1.28	1.18	1.08	0.98
0	4.84	4.47	4.13	3.81	3.52	3.24	2.99	2.75	2.54	2.34
10	4.84	5.18	5.54	5.92	6.33	6.76	7.22	7.70	8.22	8.76
20	9.33	9.94	10.57	11.23	11.96	12.71	13.50	14.34	15.22	16.14
30	17.22	18.14	19.22	20.36	21.55	22.80	24.11	25.49	27.00	28.45
40	30.04	31.70	33.45	35.28	37.19	39.19				

TABLE B-2. Mass of water vapour in saturated air ( $\text{g/m}^3$ )

For instance, if the temperature is  $24^{\circ}\text{C}$  and the relative humidity is 75%, the absolute humidity is  $16.2 \text{ g/m}^3$  and the precipitable water content is  $1.62 \times 10^{-2} \text{ mm}$  per meter of path length.

Approximate values of the transmittance due to scattering ( $\tau_{si}$ ) can be obtained with the expression:

$$\tau_{si} = \exp \left[ -\frac{391}{V} \cdot \left( \frac{\lambda_i}{0.55} \right)^{-2} \cdot z \right] \quad (\text{B-7})$$

where  $\lambda_i$  must be expressed in microns.

For ranges between 6 and 100 km, the following linear regression can be used to calculate the

approximate values of  $\delta$ :

$$\delta = 0.0057 \times V + 1.025 \quad (\text{B-8})$$

If, because of haze, the visual range is less than 6 km, the exponent  $\delta$  is related to the visual range by the following empirical formula:

$$\delta = 0.585 \times V^{1/3} \quad (\text{B-9})$$

where  $V$  is in kilometres. For exceptionally good visibility  $\delta = 1.6$ , and for average visibility  $\delta \approx 1.3$ .

The scattering coefficient with rain ( $\beta_{rain}$ ) is strongly dependent on the size of the drops. Middleton [5] has shown that  $\beta_{rain}$  is:

$$\beta_{rain} (\text{cm}^{-1}) = 1.25 \times 10^{-4} \times \frac{(\Delta x / \Delta t)}{a^3} \quad (\text{B-10})$$

where  $\Delta x / \Delta t$  is the rainfall rate in  $\text{cm/sec}$  and  $a$  is the radius of the drops in  $\text{cm}$ .

Rainfall rates for four different rain conditions and the corresponding transmittance due to scattering of a 1.8 km path are shown in Table B-3.

Condition	Rainfall-rate ( $\text{cm/hr}$ )	$\tau_{si}$ for $z=1.8 \text{ km}$
Light Rain	0.25	0.88
Medium Rain	1.25	0.74
Heavy Rain	2.5	0.65
Cloudburst	10.0	0.38

TABLE B-3.  $\tau_{si}$  of a 1.8 km path through rain.

## APPENDIX C

A reflection model commonly used in engineering applications where light/object interactions have to be described, is the Phong's model. This divides the reflectivity into a diffuse component and a specular component. The bi-directional spectral reflectivity is given by:

$$\rho_i(\lambda, \theta_i, \phi_i, \theta_r, \phi_r) = k_{diffuse} + k_{specular} \cos^n \Phi \quad (\text{C-1})$$

where  $k_{diffuse}$  is the fraction of energy diffusely reflected,  $k_{specular}$  is the fraction specularly reflected and  $\Phi$  is the angle between the mirror direction  $R$  and the viewing direction  $V$  (Figure 5).

In his original paper [6], Phong gives:

$$k_{specular} = W(i) \quad (\text{C-2})$$

implying a dependence on the incidence angle  $i$ . However, no details are given on the nature of  $W(i)$  and most implementations now ignore this and reduce the bidirectional reflectivity to a reflectivity that depends only on the outgoing angle of interest:

$$\rho_i(\lambda, \theta_i, \phi_i, \theta_r, \phi_r) = \rho_i(\lambda, \phi) \quad (\text{C-3})$$

where the material is assumed to be isotropic.

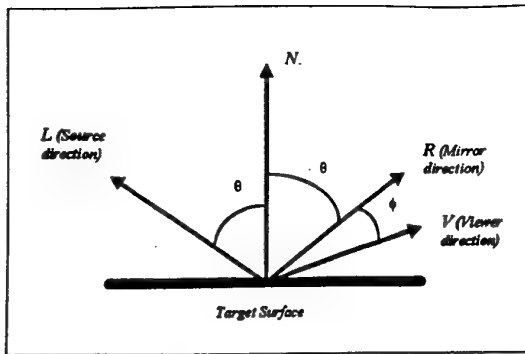


Figure 5. Vectors used in Phong reflection model.

Although there is nothing to prevent an anisotropic dependence of reflectivity on both the outgoing angles the Phong model is most often implemented as above. The empirical spread of the highlight about the mirror direction was Phong's important innovation, giving a cheap but effective way of calculating the geometry of the specular highlight. The Phong's model can be given in terms of the unit vectors associated with the geometry of the point under consideration. Therefore, for the reflected light intensity, we have :

$$I = I_i [k_s (\cos \theta) + k_r (\cos^* \phi)] \quad (C-4)$$

or :

$$I = I_i [k_s (L \cdot N) + k_r (R \cdot V)^n] \quad (C-5)$$

where  $k_s$  is the specular reflection coefficient, usually taken to be a material dependent constant,  $n$  is the index that controls the "tightness" of the highlight.

Figure 6 shows the variation in light intensity at a point  $P$  on a surface calculated using equation (C-5). The intensity variation is shown as a profile (i.e., a function of the orientation of  $V$ ). The intensity at  $P$  is given by the length of  $V$  from  $P$  to its intersection with the profile. The semicircular part of the profile is the contribution from the diffuse and ambient terms. The specular part of the profile is shown for different values of  $n$ . Note that large values of  $n$  are required for a tight highlight to be obtained.

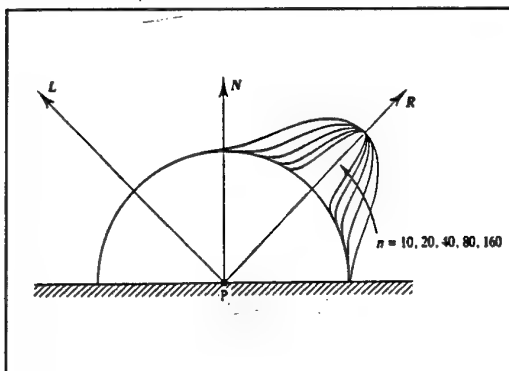


Figure 6. Intensity at  $P$  as a function of  $V$  orientation.

Another important factor, to be accounted for during daytime operation, is the sunlight reflected from the target. Particularly, the solar irradiance of the target ( $I_s$ ) at the operation wavelength plays an important role, since it adds to the  $I$  term in equation (C-4) to determine the amount of energy effectively received, after propagation, at the observer location.

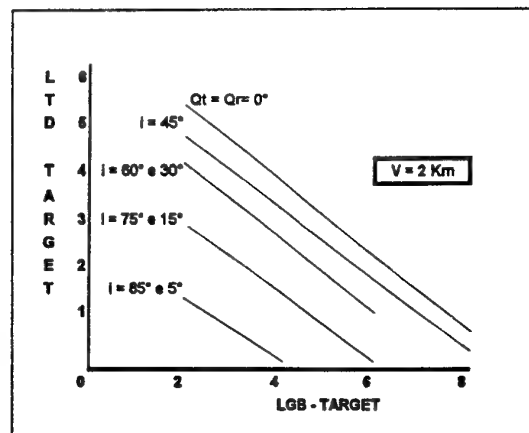
According to the Phong model (i.e., assuming a point source, a point observer and a point target), the intensity of reflected solar light at the wavelength considered can be approximated by :

$$I_s = E_s [k_s (\cos \theta') + k_r (\cos^* \phi')] \quad (C-6)$$

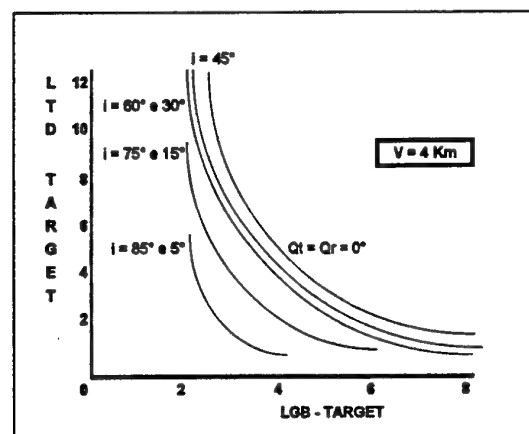
where  $E_s$  is the solar spectral irradiance at the target ( $W/m^2$ ) at the operating wavelength of the laser and  $\theta'$  is the angle between the solar illumination and the normal to the reflecting surface of the target.

#### APPENDIX D

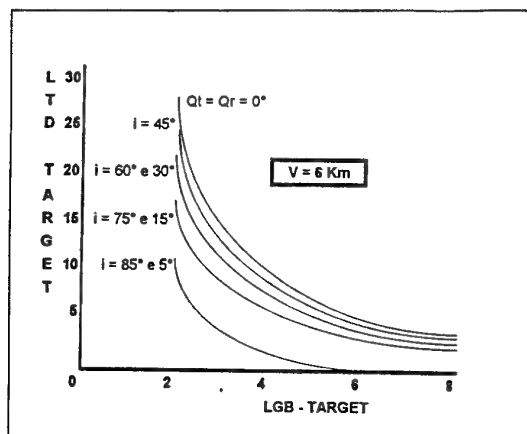
D-1



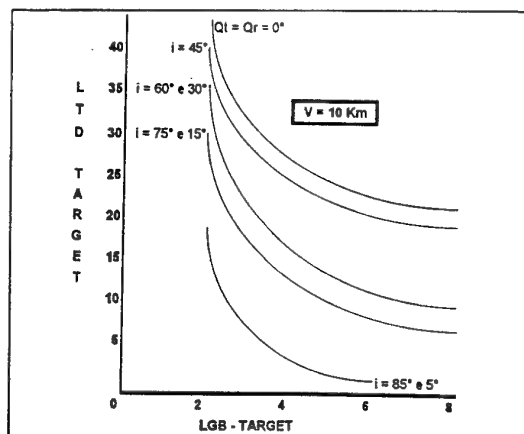
D-2



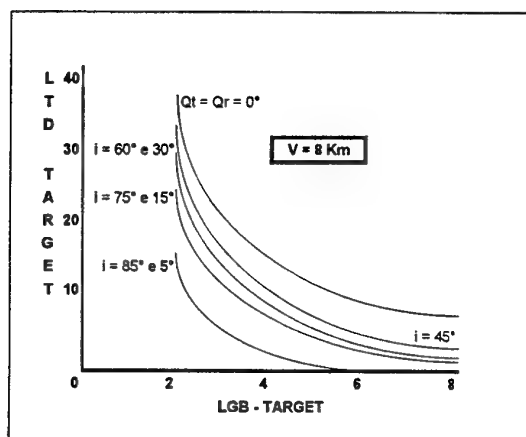
D-3



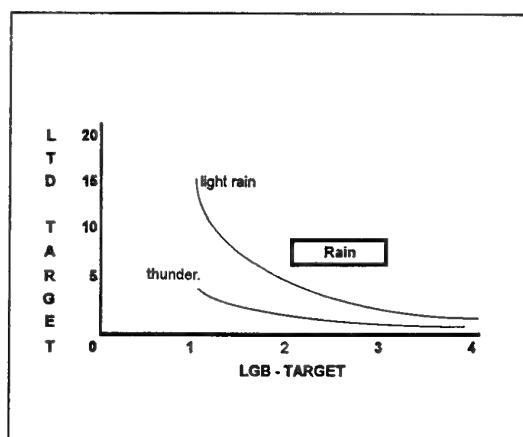
D-5



D-4



D-6



PAPER No.: 29

DISCUSSOR'S NAME: A.M. Bouchardy

COMMENT/QUESTION:

What type of accuracy do you need for input meteorological data to make good performance predictions?

AUTHOR/PRESENTER'S REPLY:

The model needs flying squadron level accuracy data (visibility and humidity provided by the airport meteorological office). Since the program is used for mission planning/optimisation a "worst case" approach is often acceptable.

PAPER No. 29

DISCUSSOR'S NAME: E. Schweicher

COMMENT/QUESTION:

1. Is the YAG laser diode-pumped or flash lamp pumped?
2. I found your value of 0.5 mrad a little bit too high for the laser divergence. Your comments?
3. How do you cope with the boresight problem between observation channel and designation channel?

AUTHOR/PRESENTER'S REPLY:

1. Flash lamp pumping.
2. The actual value is much smaller.
3. With a pilot/navigator commanded boresight facility. In single-seat aircraft (e.g. EF2000, AMX) an automatic boresight capability is highly desirable.

Midcourse Space Experiment (MSX): Overview of Mid-Wave Infrared Atmospheric Gravity Waves  
in Earth Limb and Terrestrial Backgrounds

R.R. O'Neil  
H.A.B. Gardiner  
J.J. Gibson

Air Force Research Laboratory  
Hanscom AFB  
Bedford MA 01731, USA

A. T. Stair  
Visidyne Inc.  
Burlington, MA 01803, USA

## SUMMARY

The first space-based observations of atmospheric gravity waves (GW) in the mid-wave infrared (MWIR) region have been measured by the SPIRIT III radiometer on the Midcourse Space Experiment (MSX) during the period from launch, April 24, 1996, to the end of cryogenic operations, February 25, 1997. During this time approximately 230 data collection events were performed to measure infrared backgrounds in earth limb and terrestrial scenes. Of these, 80 data collection events of 20 minutes average duration were completed to characterize MWIR background clutter in a wide variety of measurement conditions for two spectral bands, B1 (4.22 - 4.36  $\mu\text{m}$ ) and B2 (4.24 - 4.45  $\mu\text{m}$ ) in lines-of-sight both below the horizon (BTH) and up to 50 km tangent altitude above the horizon (ATH). Atmospheric gravity or buoyancy waves were a frequent feature in the BTH and low altitude ATH MWIR backgrounds. The present paper presents preliminary results summarizing the frequency of occurrence and latitudinal and monthly distribution for fifty data collection events of this category. The wave structures are found to introduce perturbations of up to a few percent of the measured radiance, have their own spatial frequency signature distinct from clouds, and, because of the large optical density in the central regions of the  $\text{CO}_2$ ,  $\Delta\nu_3=1$  band, are observed at altitudes above approximately 30 km altitude on a line of sight. In some scenes the waves appear as superposed circular features, while in others they show more complex patterns. Specific examples of thunderstorms creating circular GW patterns have been identified in these MSX measurements, and it is believed that other sources may also contribute to the formation of these waves, such as atmospheric winds and tides, interactions with orographic features and volcanic eruptions, etc. In this paper images of the waves and supporting data are presented along with statistical parameters of waves (mean radiance, the ratio of the standard deviation to mean radiance, noise to mean, clutter to mean, correlation length, PSD slope and radiance gradient) for a representative MWIR BTH measurement of atmospheric waves. In addition, the monthly latitudinal distribution for selected parameters

indicative of atmospheric gravity waves are presented within the limits of the MSX sampling.

## 1.0 INTRODUCTION

During the ten month period of cryogenic operations from April 24, 1996 to February 25, 1997, the SPIRIT III infrared radiometer<sup>2</sup> aboard the Midcourse Space Experiment (MSX)<sup>1</sup> obtained measurements of a wide variety of terrestrial, earth limb and celestial backgrounds, including the first observations of atmospheric gravity waves in the mid-wave infrared (MWIR) region (Bands B1: 4.22 - 4.36  $\mu\text{m}$  and B2: 4.24 - 4.45  $\mu\text{m}$ , FWHM) in scenes both below-the-horizon (BTH) and above-the-horizon (ATH). Because these waves have 1.0 to 100 km scale sizes (as measured by MSX), are frequently present in both day and night scenes and will be a background clutter component in any nominal MWIR system spectral band, characterization of the wave's spatial properties, frequency of occurrence and global distribution is of significant interest to the surveillance systems community. This paper addresses the questions of frequency of occurrence and latitudinal distribution of atmospheric waves in the Band B1 (4.24 - 4.36  $\mu\text{m}$ ) MWIR region as observed by MSX and the influence of spectral filter selection on the spatial frequencies perceived by a space-based sensor.

## 2.0 MWIR ATMOSPHERIC GRAVITY WAVES

Most of the MSX SPIRIT III observations of atmospheric gravity waves reported here were made in the pushbroom scan mode in which the boresight was held at a fixed nadir angle mode (an experiment designated EL09), usually in a plane perpendicular to the MSX direction of motion, in which each of two staggered columns of 192 detectors per focal plane column traced out a time sequence of radiance data at a 72 Hz sampling rate, with scan motion created by the orbital movement of the MSX platform. A total of 50 such EL09 data collection events were made during the cryogen period and their global distribution is shown in Figure 1, along with whether night or day conditions held at the target point. Note the preponderance of data collection events taken over the region from Central to South-Eastern Asia and the paucity of data in the Western

Hemisphere and over Africa. Measurements in some regions, such as the South Atlantic Anomaly (SAA) region, were precluded or limited by operational and instrument constraints and these stand as limitations to the development of a complete global distribution of the observed parameters.

Figures 2 and 3 show images of MWIR atmospheric gravity waves captured by the SPIRIT III radiometer. Details of geometries of the observations are given in Table 1. In Figure 2 a nearly circular wave pattern is presented for a high BTH/low ATH event (bore sight nadir angle is 60.5 km) which extends from 40 km below the horizon to 20 km above the horizon. The pattern continues across both bands B1 (lower portion of image) and B2 (upper portion of image). To date two scenes with

circular wave patterns have been identified in the 50 EL09 data collection events. Much more common is the complex wave pattern seen in Figure 3, for a BTH image bore sight of 57 degrees above the nadir position. Again, waves are present in both bands B1 (lower portion of figure) and B2 (upper portion of figure), but band B2 also contains apparent cloud structures, while band B1 does not. The explanation for this difference between bands B1 and B2 is that B2, being a somewhat broader filter than B1 (B2: 4.24 - 4.45  $\mu\text{m}$ , B1 4.22 - 4.36  $\mu\text{m}$ ), observes lower altitudes at wavelengths on the red side of its bandpass, whereas the spectral region in which the two filters overlap lies in the very optically thick  $\text{CO}_2$   $\nu_3$  region that limits a space-based sensor to altitudes above 30 km.

## MSX BTH DATA SUMMARY 4/24/96 - 2/25/97

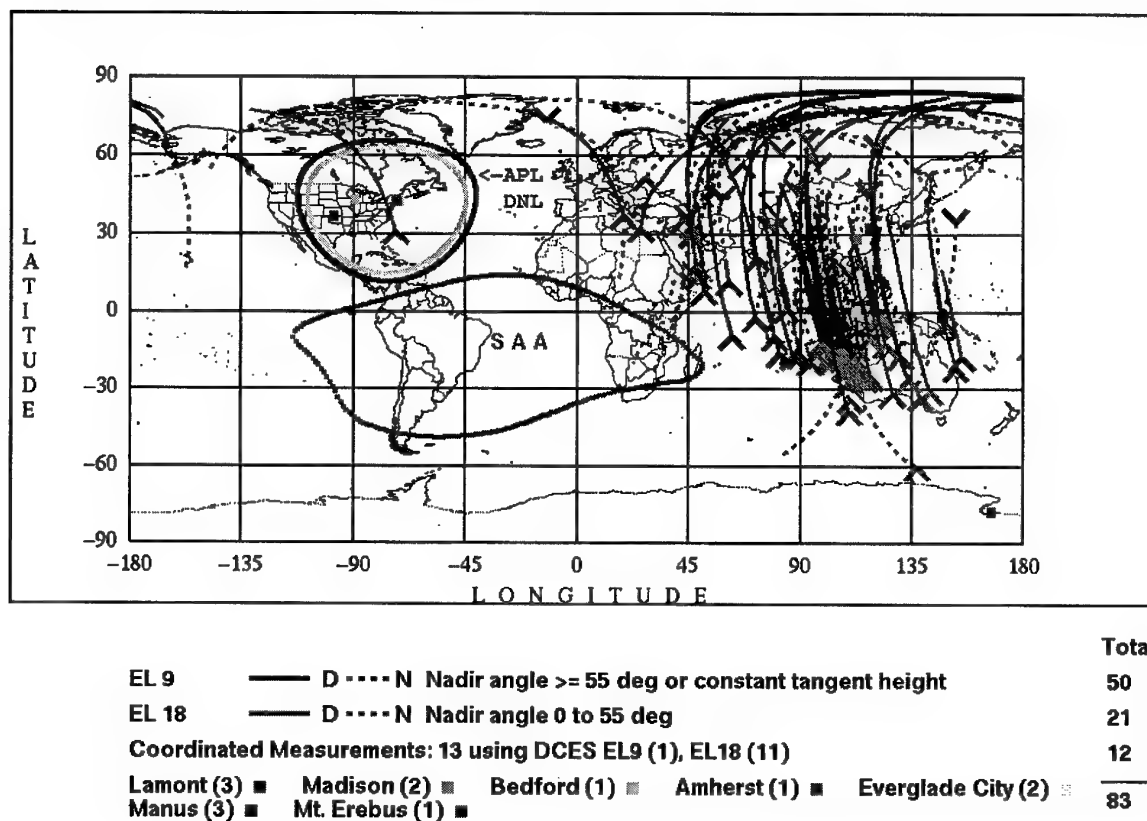


Figure 1. The global distribution of 83 below the horizon (BTH) and low altitude above the horizon (ATH) data collection events performed to measure MWIR background clutter including the 50 EL09 events discussed in this paper. The solid lines, labeled D, indicate day conditions at the line of sight target region. The broken lines, labeled N, indicate night. Operational constraints precluded measurements while the spacecraft was within the South Atlantic anomaly (SAA) and data down linking requirements limited the number when the spacecraft was within view of the telemetry receiving station at the Applied Physics Laboratory in Laurel, Maryland.

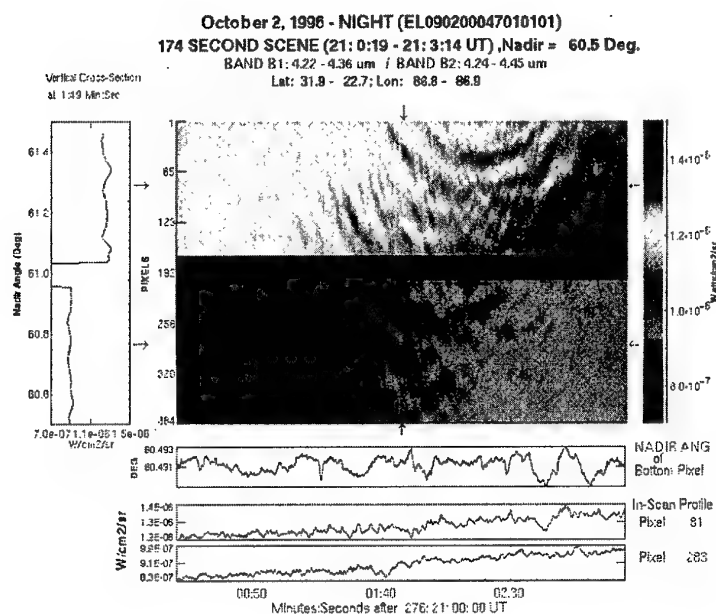


Figure 2. This circular atmospheric gravity wave image has been analyzed and the source identified as an high altitude thunderstorm that was isolated from other clouds. The image includes both the narrow B1 band (lower section) and the wider B2 band (upper section).

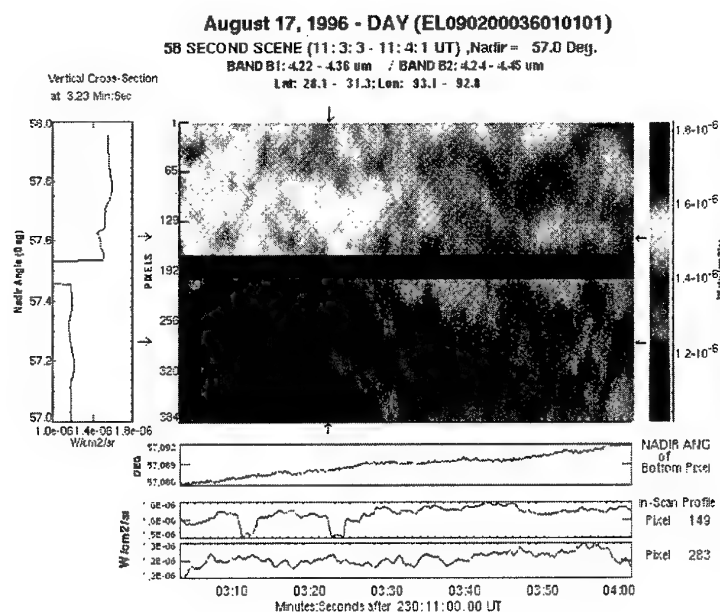


Figure 3. Atmospheric gravity waves are present in both MWIR bands in this image recorded at an angle 57 degrees from the nadir position. Clouds are evident in the B2 section (upper panel) as indicated in the lower portion of the figure by the in-scan profile for pixel 149 at times near 03m:10s and in the interval from 03m:20s to 03m:30s.

Table I. Geometries of MSX MWIR Wave Images

EVENT:	EL090200047 (Figure 2)	EL090200036 (Figure 3)
COMMENTS	nearly circular wave pattern, upper portion of B2 is above the horizon, image extends to altitude of 20 km	shows waves with apparent clouds in B2, and waves but no apparent cloud effects in B1
DATE:	2 Oct 1996	17 Aug 1996
NADIR ANGLE (DEGREES)	60.5	57
IMAGE START TIME (UT)	21:00:19	11:03:03
STOP TIME (UT)	21:03:14	11:04:01
IMAGE DIMENSIONS		
WIDTH (SECONDS)	174	58
(DEGREES)	10.1	3.4
(km)	1039	361
HEIGHT (DEGREES)	1	1
LATITUDE START (DEGREES)	31.9N	28.1N
STOP (DEGREES)	22.7N	31.3 N
LONGITUDE START (DEGREES)	86.8	93.1
STOP (DEGREES)	86.9	92.8

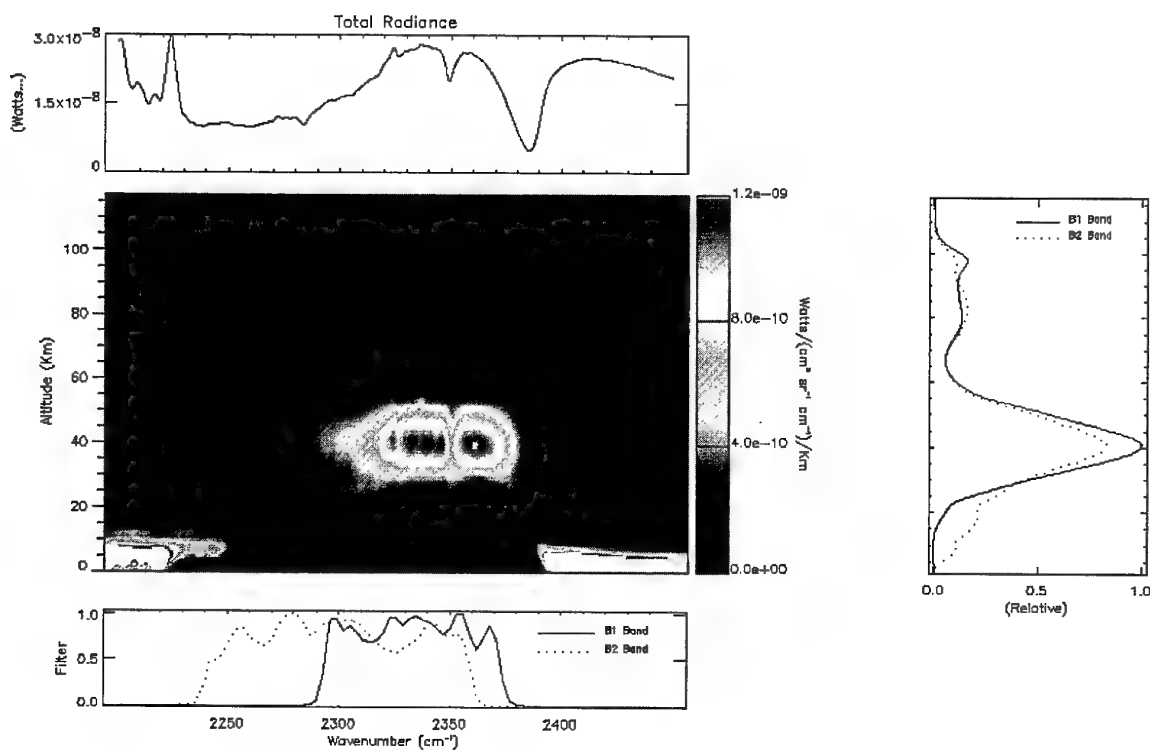


Figure 4. The weighting or contribution function in the spectral region from 2200  $\text{cm}^{-1}$  ( $4.55 \mu\text{m}$ ) to 2450  $\text{cm}^{-1}$  ( $4.08 \mu\text{m}$ ) calculated for a daytime atmosphere for a satellite at 900 km (MSX) with a BTH viewing aspect  $57^\circ$  from nadir.

This optical thickness influences the viewing of atmospheric gravity waves in the MWIR. This is seen with the aid of the weighting or contribution function

shown in Figure 4 in which the relative contributions to the radiance received at the SPIRIT III sensor from various altitudes along the line of sight are shown for the  $57^\circ$



degree nadir case of Figure 3. It is seen that for this case the main peak for both the B1 and B2 filters occurs around 40 km altitude with a full width of approximately 20 km, with weak contributions from near 80 km altitude produced in daylight atmospheres by solar induced fluorescence. In addition band B2 has a third prominent tropospheric peak largely due to the less abundant isotopic  $^{13}\text{CO}_2$  which is not as optically dense as the main isotopic form,  $^{12}\text{CO}_2$ . The region about the 40 km peak on the line of sight then is where the waves seen in the MWIR by MSX are being sensed. It can be shown that as the nadir angle is varied from low BTH to low ATH, the prime weighting function layer width diminishes with a very slight change in the altitude of the layer (40 km), and the tropospheric contribution to B2 decreases. For ATH lines of sight, the 40 km layer width continues to decrease as contributions from higher altitudes become more prominent. For optically thick limb cases, this means that the dominant contribution region is at a higher altitude than the tangent point and on the side of the tangent point closest to the sensor<sup>3</sup>.

The weighting function acts as a low pass filter, attenuating waves with wavelengths much less than the width of the weighting function layer. This means that for infrared systems applications the weighting function associated with the selected spectral filter will be a factor in determining what wave spatial frequencies are perceived by the sensor.

Recently, Dewan, et al.<sup>4</sup> have traced the source of the circular atmospheric gravity wave pattern, observed by MSX in the MWIR spectral region and shown in Figure 2, to an isolated thunderstorm. Two such circular wave patterns have been identified in the 50 data collection events discussed in this paper. In both instances the source has been identified as isolated thunderstorm. Brown, et al.<sup>5</sup> have shown that radiance fluctuations attributable to atmospheric gravity waves in MSX MWIR observations, have a  $k^{-5/3}$  fall-off in the power spectral density (PSD) function with horizontal wave number and  $k^{-3}$  vertical wave number fall-off. These exponents are found to be one greater than the corresponding exponents for temperature fluctuation PSD fall-offs and are consistent with the saturated cascade theory of atmospheric gravity waves.

### 3.0 ONE-MINUTE STATISTICAL DATA

For purposes of generating statistical parameters characterizing the spatial-temporal variations of the radiance backgrounds and determining the global distribution of atmospheric gravity waves, one minute segments of data for selected Band B pixels were taken as the basic time interval from which products could be generated to form elements of a statistical ensemble. Such radiance statistical products as the mean, standard deviation, noise and clutter, maximum radiance, minimum radiance, correlation length, power spectral density (PSD) slope and radiance gradient were generated for each one minute segment. The process is illustrated in Figure 5, in which a one minute segment from a 25 minute data collection event (EL090200036 on 17 Aug 1996) is highlighted and selected statistical products are indicated which were calculated for that one data minute segment.

The measurement times in Figure 5 are in minutes after 10h:00min:00sec UT on 17 Aug 1996 (day 230).

### 4.0 APPROACH TO DETERMINING STATISTICS OF MWIR ATMOSPHERIC GRAVITY WAVES

In order to determine the distribution of gravity waves as a function of latitude, longitude, time of day, season, etc., the ratio of standard deviation to mean radiance was taken as the prime statistical indicator. On average, the useable period of data from an individual data collection event was approximately 15 minutes. Only data from EL09 data collection events are included here. This means that 50 different data collection events were included in this study with nadir angles restricted to the range of 45 to 62.2 degrees covered by the EL09 experiments. This nadir angle range includes the high BTH/low ATH region, with the horizon, depending on the radius of the earth, lying in a small region around 61.2° for the MSX platform (space craft altitude approximately 900 km). Additional MSX SPIRIT III MWIR data exist and will be included in a more complete study.

The measurements obtained by the SPIRIT III sensor in the narrow MWIR band, B1 (4.22 - 4.36  $\mu\text{m}$ ), were taken to be most indicative of the presence of atmospheric gravity waves. This is because nearly all the radiance sensed in band B1 originates from altitudes above 30 km, thus eliminating the effects of clouds and terrestrial influences, and allowing atmospheric gravity waves to be the dominant source of background structure.

The approach in this preliminary statistical study has been to use only the data from four band B1 pixels. These detectors are evenly separated across the focal plane column of band B1 and include detectors 121, 141, 161 and 181, which cover regions in object space separated by distances of about 6 km (vertical projection) between detectors in the limb and distances of 4.3 km, 13.4 km and 115.1 km for MSX nadir angles of 45, 57 and 61 degrees, respectively, in BTH cases (horizontal projection along surface of earth).

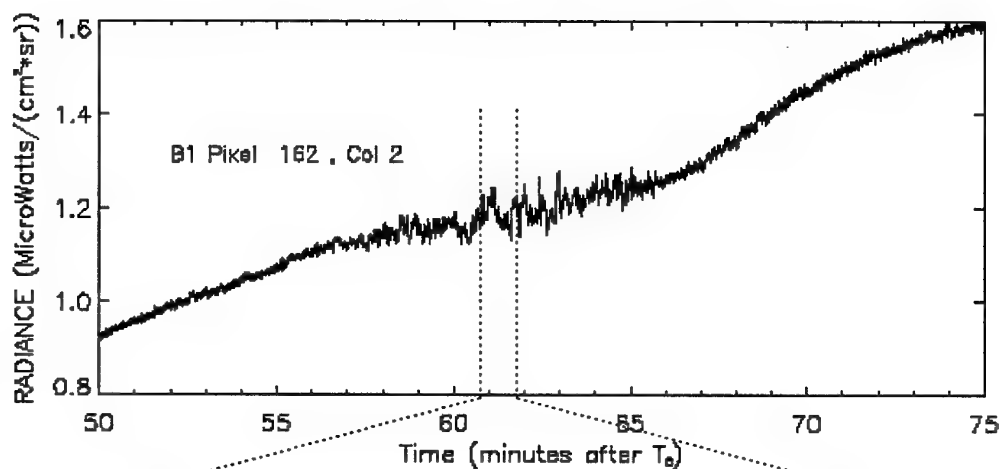
The approximate size then of the statistical population is of the order of 3000 samples (50 events x 4 detectors x 15 minutes). To determine the global distribution, the samples in the population were assigned to bins of 10° of latitude x 10° of longitude. The data was then binned by month, integrating over longitude, so the latitudinal distribution could be presented as a function of month to determine seasonal behavior.

From calibration information and the magnitude of the high frequency component of power spectral density in the one minute segments, the noise level in each one minute sample could be established. It was determined that in cases where the standard deviation to mean (STDM) ratio was less than 0.5% the observation was dominated by the sensor noise and when the STDM was between 0.5% and 1.0% the observation contained a mix of noise and signal from waves. However when the STDM was above 1.0%, the observed fluctuations in the narrow MWIR band were induced by and a measure of atmospheric gravity waves.

# TIME SERIES: ONE-MINUTE SAMPLES

EL090200036 17 Aug 1996 Day Band B1 (4.22- 4.36 $\mu$ m) Detector 162, Col 2

Reference Time  $T_0 = 230^d: 10^h: 00^m: 00^s$



## SELECTED ONE-MINUTE STATISTICS

Time Interval 61-62 minutes after  $T_0$

Mean: $1.19 \times 10^{-6}$ W/cm <sup>2</sup> -sr	Max. St. Dev./Mean (in 0.5 sec window): $7.73 \times 10^{-3}$
St. Dev./Mean: $2.17 \times 10^{-2}$	Correlation Length: 21.4 km
Noise/Mean: $3.01 \times 10^{-3}$	PSD Slope: -2.87
Clutter/Mean: $2.15 \times 10^{-3}$	Radiance Gradient: $8.92 \times 10^{-8}$ W/cm <sup>2</sup> -sr-km
	(99th Percentile for 1.38 km Footprint)

Figure 5. A representative sample of the radiance profile measured by a B1 pixel from the data collection event also illustrated in Figure 3. Selected time series analysis products for a one minute data sample are shown.

## 5.0 RESULTS

Figure 6 shows the latitudinal and monthly distribution of samples which were made in the period from 23 May 1996 to 24 February 1997 having a standard deviation to mean ratio equal to or greater than 1.0%, as well as the total number of samples in each 10° latitude bin. The gray scale coding indicates the relative frequency of occurrence which is simply the ratio of these values in each monthly latitude bin. The total number of sample in this population is 2854. For the May to September period, the greatest frequency of occurrence is in the Southern Hemisphere for latitudes from approximately 20 to 50 degrees and in the sub-tropical region between 10° and 30° North latitude.

In the period from September 1996 to February 1997, Figure 6 shows the greatest frequency of occurrence is in the polar vortex region at high latitudes (above 60° North) In addition the southern sub-tropical region (10° to 30° South latitude) shows a high frequency of occurrence.

It is seen that the frequency of occurrence has a definite seasonal dependence. During the Spring and Summer, the Southern Winter latitudes and the sub-tropical Summer region from 10° to 20° North latitude have the highest frequency of occurrence for wave activity in the areas sampled. October seems to be the period of least wave activity, and during the Late Fall-Winter period, the activity in the Polar Vortex is evident as is the increased activity in the Southern sub-tropical region.

These results are in excellent accord with the data reported by the Microwave Limb Sounder (MLS) on board the Upper Atmosphere Research Satellite (UARS)<sup>6</sup> using a similar weighting function as that for the MSX SPIRIT III band B1.

Recent modeling efforts<sup>7</sup> indicate that the MSX and the UARS MLS results can be explained by the coupling of the spaced-based observer's weighting function with the filtering of such waves by atmospheric background winds through Doppler shifting and refraction. This, along with

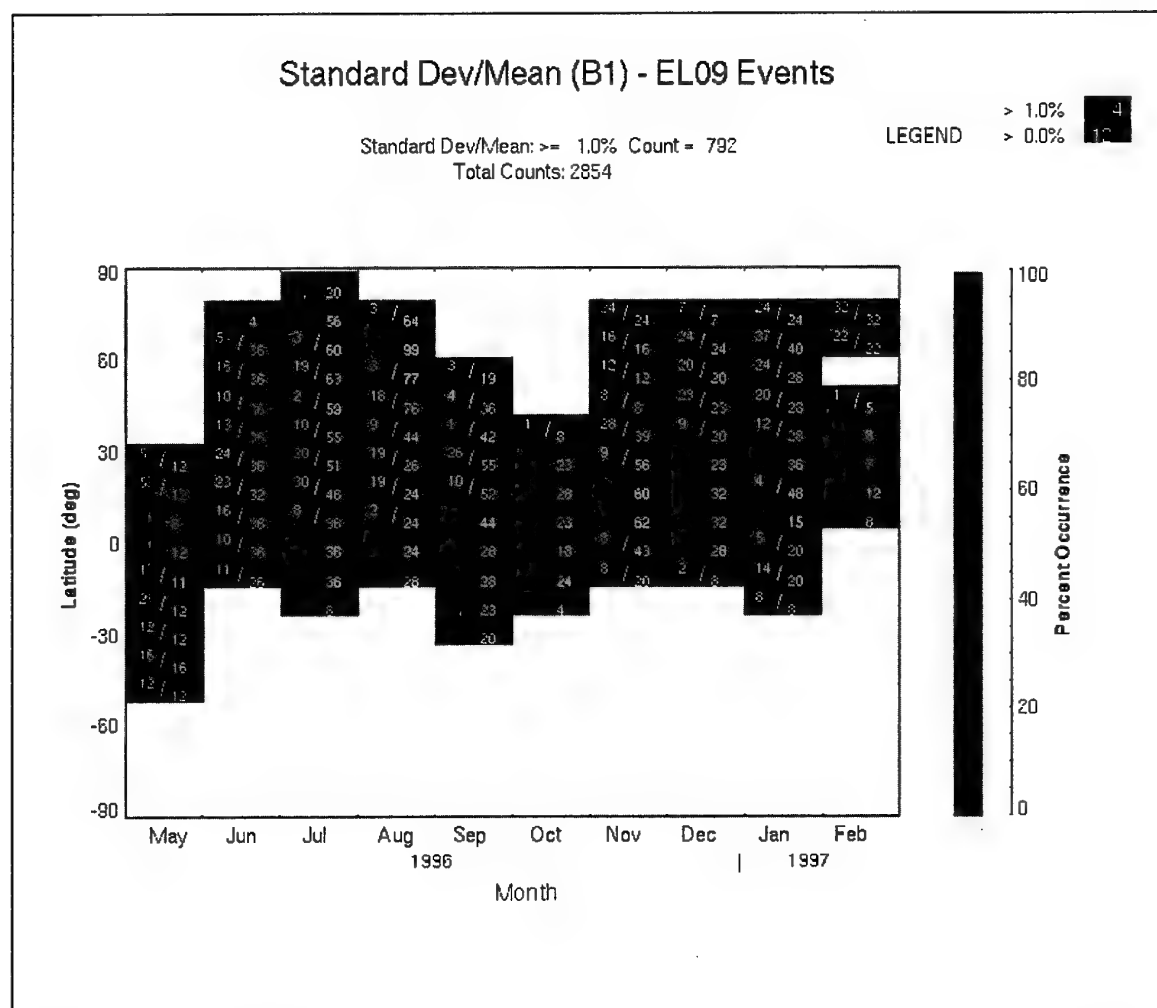


Figure 6. The monthly latitudinal distribution of one minute samples of MSX MWIR B1 band radiance with a standard deviation to mean radiance of 1 percent or more. The numerical entries in each monthly latitude bin are the total number of one minute samples (the value in the lower right quadrant) and the number of samples with a ratio of standard deviation to mean radiance of 1% or more (upper left quadrant). No entry in the upper left quadrant in the shaded regions where data was taken indicates a value of zero for the number of samples with a ratio of standard deviation to mean radiance of one percent or more.

source amplitude variations and distributions, such as thunderstorms, orographic features, etc., are thought to give rise to the geographical, and seasonal variations in gravity wave observations.

## 6.0 CONCLUSIONS

The recent discovery from MSX SPIRIT III observations that MWIR atmospheric backgrounds contain clutter contributions from gravity waves is a major new finding with implications for surveillance system applications.

First it is noted that the waves can take a variety of patterns, ranging from the circular to superposition of elliptical forms and more complicated patterns. The presence of these MWIR waves has been observed from low nadir angles up to the earth's horizon and into the limb, at least to an tangent altitude of 50 km. The wave phenomena appear as the dominant source of MWIR

structure in the narrow MSX MWIR band in radiance seen in both day and night conditions.

Second, the spatial character of the waves as perceived by a space-based sensor is influenced by the spectral filter characteristics it uses. In the heart of the  $4.3\mu\text{m}$   $\text{CO}_2$  band, such as in the case of the SPIRIT III band B1 filter ( $4.22 - 4.36\mu\text{m}$ ), the weighting function peaks at an altitude of approximately 40 km, has a peak layer width of about 20 km for a nadir angle of  $57^\circ$  and excludes significant contributions from altitudes below 30 km. This limits the minimum vertical and horizontal spatial wavelength detectable at the space-based sensor to roughly the thickness of the weighting function layer. However at higher nadir angles, the weighting function width narrows while still keeping the peak altitude in the vicinity of 40

km. This allows smaller wavelength features to be observed. As the filter spectral extent is opened up, such as in the case of the band B2 filter (4.24 - 4.45  $\mu\text{m}$ ), additional weighting function layers are added, especially at lower altitudes, which permit space-based viewing to lower altitudes, clouds and perhaps the perception of different size wave phenomena.

Third, the MWIR radiance variations associated with atmospheric gravity waves have standard deviation to mean ratios predominantly in the range of 1 to 2 %, with some extending as high as 9 percent.

Fourth, a standard deviation to mean radiance of 1% or more was found in 792 of the 2854 one minute samples. Thus, in this data set recorded in selected global regions and using the gravity wave detection criteria of a ratio of standard deviation to mean radiance of 1 % or more, stratospheric atmospheric gravity waves were observed with an occurrence frequency of 28 percent.

Finally, the global distribution of atmospheric gravity waves are in accord with the temperature variance distribution seen by the UARS Microwave Limb Sounder<sup>6</sup>. The MSX results based on MWIR radiance measurements show that the frequency of occurrence of the wave phenomena is highest in the winter polar vortex period (November - February in Northern hemisphere) and in the sub-tropical region (10 to 30 degree latitudes ) during local late-Spring and Summer.

Recent modeling efforts<sup>7</sup> indicate that the MSX and the UARS MLS results can be explained by the coupling of the spaced-based sensor's weighting function with the filtering of such waves by atmospheric background winds through Doppler shifting and refraction. This, along with source amplitude variations and distributions, such as thunderstorms, orographic features, etc., are thought to give rise to the geographical, and seasonal variations in gravity wave observations.

## 7.0 ACKNOWLEDGMENTS

The MSX program is sponsored by the Ballistic Missile Defense Organization. and their support is gratefully acknowledged. The superb engineering teams at Utah State University and the Applied Physics Laboratory provided infrared sensors and a spacecraft with unique measurement and performance capabilities. Dr. John D. Mill, the MSX project scientist, provided steady management, guidance, expertise and encouragement for the duration of the program.

## 8.0 REFERENCES

1. J.D. Mill, R.R. O'Neil, S. Price, G.J. Romick, O.M. Uy, E.M. Gaposchkin, G.C. Light, W.W. Moore Jr, T.L. Murdock and A.T. Stair Jr, "Midcourse Space Experiment: Introduction to the Spacecraft, Instruments and Scientific Objective", Journal of Spacecraft and Rockets, Vol 31 (5), pp 900-907, 1994.
2. "SPIRIT III User's Guide", Revision 5, May 1995, SDL 92/-041, Space Dynamics Laboratory, Utah State University, Logan, Utah.

3. R.H. Picard, R.R. O'Neil, H.A. Gardiner, J. Gibson, J.R. Winick, W.O. Gallery, P.P. Wintersteiner, E.R. Hegblom and E. Richards, "Remote Sensing of Discrete Stratospheric Gravity-Wave Structure in 4.3  $\mu\text{m}$  CO<sub>2</sub> Emission from the MSX Satellite", to be published

4. E.M. Dewan, R.H. Picard, R.R. O'Neil, H.A. Gardiner, J. Gibson, E.R. Hegblom, E. Richards, M. Kendra and W. Gallery, "Thunderstorm Generated Waves as Seen in 4.3  $\mu\text{m}$  Images From the MSX Satellite", to be published.

5. James H. Brown, R.R. O'Neil, H.A. Gardiner, J.H. Gruninger, N.A. Grossbard, E.R. Hegblom and E. Richards, "Continuous Gravity Wave Infrared Power Spectra Observed From the MSX Satellite: Evidence for a k-(n+1) Dependence of the Temperature Structure", to be published.

6. D.L. Wu and J.W. Waters, Satellite Observations of Atmospheric Variances: A possible Indication of Gravity Waves", Geophys. Res. Letters, Vol 23 (24), pp 3631-3634, 1 Dec 1996.

7. M.J. Alexander, "Interpretations of Observed Climatological Patterns in Stratospheric Gravity Wave Variance", J. Geophys. Res. (in press).

PAPER No. 33

DISCUSSOR'S NAME: C.R. Philbrick

COMMENT/QUESTION:

The seasonal variation of mid-latitude gravity wave occurrence, that your measurements clearly show, would be explained by the cut-off of wave propagation from tropospheric wave sources by the zonal wind circulation. This process was described by Dick Linzen in a classic paper around 1970.

AUTHOR/PRESENTER'S REPLY:

Recent analysis by J. Alexander (private communication) suggests the vertical scale sizes described in this MWIR band (approximately 15-20 km full width half maximum weighting function centered near an altitude of 40 km) are produced by filtering effects of winds at this altitude. Thus the global distribution of these observations should be correlated with the global and seasonal presence of high velocity winds. This appears to be the case.

## AN INVESTIGATION OF METHODS TO IMPROVE THE ESTIMATION OF BATTLEFIELD GROUND CONDITIONS

Alan Whitelaw, Sally Howes, John Brownscombe, Oliver Greening (ESYS Limited)  
Jon Turton, David Bennetts (UK MoD, Meteorological Support Group)  
ESYS Limited, 1 Stoke Road, Guildford, Surrey, GU1 4HW  
tel: +44 1483 304545, fax: +44 1483 303878, email awhitelaw@esys.co.uk

### SUMMARY

The principal objective of this work, which is being undertaken for the UK MoD Meteorological Support Group, is to improve the estimation of ground conditions in order to allow factors such as vehicle trafficability to be determined. Surface vegetation and soil moisture conditions are also important factors when considering the performance of electro-optic systems. These factors also influence the thermal characteristics of the ground and so affect its appearance in thermal imagery. Soil moisture affects the lofting of dust into the air from vehicle movements, where the presence of dust can adversely impact the ability of electro-optic sensors to 'see' targets. Thus, this work can be applied to the problem of determining those ground conditions which can affect electro-optic systems. The work has focused on two approaches, the use of satellite remote sensing techniques and meteorological/hydrological modelling, both of which are applicable to out-of-area (OOA) scenarios.

This paper reviews the ability of different satellite based sensors to measure ground conditions, in particular soil moisture. The sensors considered are Synthetic Aperture Radar (SAR), infrared (concentrating on thermal) and passive microwave. The potential of SAR data to provide this information is considered in more detail. Meteorological modelling developments are also discussed and, as the spatial resolution of meteorological models increases they will need

to simulate of surface moisture exchanges more accurately. In the longer term, it is expected that such models will become capable of predicting soil moisture conditions, and that these models would benefit from the use of SAR data for verification or initialisation of the soil moisture predictions.

Work is currently in progress to assess the capabilities of SAR data in more detail by using a known test site. A preliminary description of this work is also given.

### 1. INTRODUCTION

This paper considers how to provide battlefield soil state information, concentrating on satellite data and modelling techniques. The emphasis is on developing a practical short term solution, although longer term options are considered in parallel. The methodology for the study is given in Figure 1.

The structure of the paper is as follows:

- requirements;
- satellite data sources;
- modelling methods;
- analysis;
- conclusions and recommendations; and a
- preliminary review of follow-on work to explore the potential for using satellite based SAR for soil state determination.

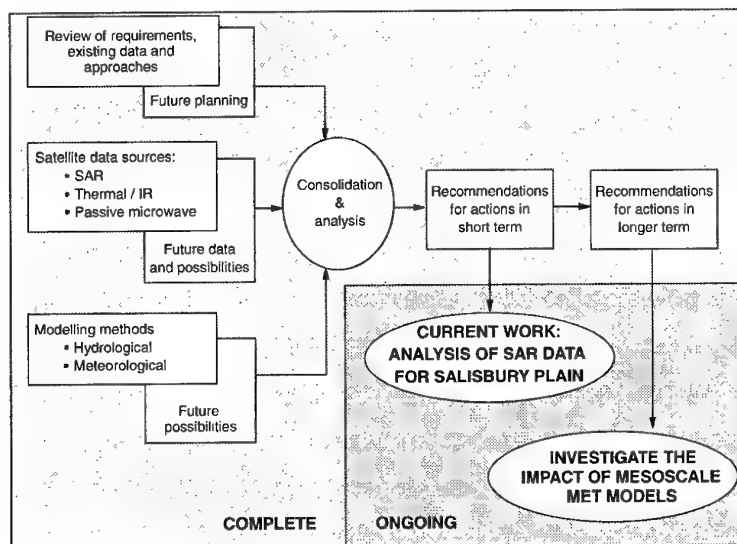


Figure 1: Study methodology

## 2. REQUIREMENTS

### 2.1. The military requirement

Military applications requiring soil state information include the following:

- predicting off-road vehicle trafficability (or 'going');
- predicting the performance of electro-optic systems (which can be affected by atmospheric dust and the thermal properties of the ground);
- making river level and flood predictions;
- military engineering.

This study was conducted with the emphasis on vehicle trafficability, although improved predictions of surface conditions and soil moisture will benefit those other applications mentioned above.

### 2.2. Measurement requirements

Figure 2 shows how different variables can be combined to provide soil state and trafficability assessments.

This study has concentrated on the soil moisture component of soil state because it is a key input to trafficability models and can also be used as a trafficability indicator in its own right. Soils can also be highly variable in terms of organic content, mineral composition, texture, layering and depth; these factors also influence the way moisture changes affect the soil.

The most important region of the soil for measurement is the top 30 cm of the soil for trafficability and the top few cm for dust emission, although these will vary with surface roughness.

## 3. SATELLITE DATA SOURCES

### 3.1. Background

The range of satellite data sources which can provide information on soil moisture is given in Figure 3.

Three sensor types are considered in more detail. These are shown in Figure 4, which is a summary overlay to Figure 3. The key point to note is that SAR data are high resolution but relatively infrequent, while the reverse is true for the other data sources. A tabular summary is given in Table 1.

### 3.2. Synthetic Aperture Radar (SAR)

A SAR is a radar which uses data processing techniques to enhance the effective spatial resolution of measurements available from a limited antenna size. As a result, it is a particularly useful sensor for remote sensing from airborne and spaceborne platforms.

The backscattering from each SAR pulse is affected by the dielectric properties of water close to the soil surface and thus provides information on:

- soil moisture (usually in the top 5 to 10 cm of the soil)
- snow cover (penetration depth depends on snow wetness)
- vegetation cover

The spatial resolution of spaceborne SARs which offers sufficient radiometric resolution for these applications is generally of the order of 30 m to 100 m.

The technique most commonly used is to correlate SAR backscatter with soil moisture for a specific land cover classification. The correlation coefficients between point measurements of soil moisture and radar backscatter are

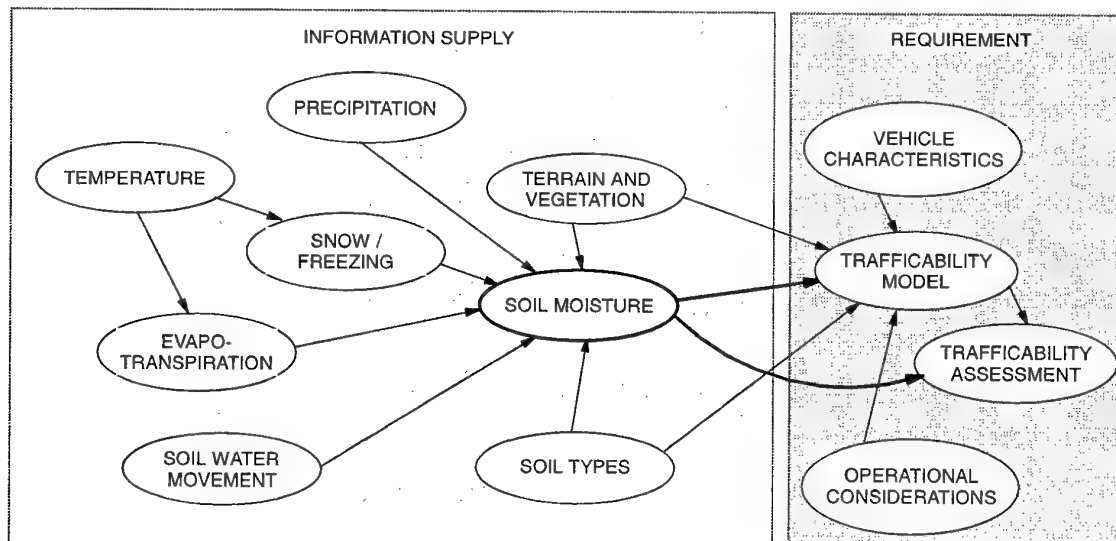


Figure 2: Context for the study

Infrequent	Local area analysis	SAR	Topography and land cover	Large area dynamic updates
Frequent		Regional area dynamic updates	Thermal IR	Passive Microwave
	Detailed			Averaged

vegetation on the backscatter, since these effects are considerably greater during the summer growing season. The effects of roughness and vegetation can be corrected for by developing and applying different soil moisture to backscatter relationships for different land cover classes. These classes are often determined using other satellite data sources such as



AVHRR (for vegetation change) or SPOT/Landsat (for cover types).

Future satellite SARs with multiple frequency and multiple polarity will offer the ability to reduce the problems of vegetation and roughness. However, difficulties will always remain with dense vegetation, but such areas are inherently less accessible to vehicles, so this is not a major problem for trafficability.

Used in isolation, SARs are currently best at monitoring relative moisture changes on a stable surface. However, SAR data can offer a useful contribution to the determination of soil moisture, in particular providing information on its spatial distribution. Future developments are likely to enhance this.

### 3.3. Passive microwave

Passive microwave measurements are a function of surface emissivity and temperature, the product of which gives the Brightness Temperature, which can be related to soil moisture.

Passive microwave data are currently available from the US DMSP satellite which carries the SSM/I instrument. The most suitable channel is that with the lowest frequency, ie. 19 GHz. This provides data at very low resolution (about 50 km), making the data difficult to relate to field situations despite the fact that the information is available at least daily.

The problem of spatial resolution with passive microwaves is difficult to overcome. The reason is that very low frequencies are needed for soil moisture and lower frequencies require

larger antennas. This is a major limitation for satellite-based instruments.

One way to alleviate the resolution problem for a passive microwave instrument is to use an aperture synthesis approach, similar to that used for the active microwave SAR. This has been achieved in an airborne instrument known as ESTAR (Electronically Scanned Thinned Array Radiometer), which operates at about 1.4 GHz and achieves resolutions in the region of 100 m. However, this capability is not yet available on satellite platforms.

### 3.4. Thermal IR

Given a realistic surface temperature model, it is possible to estimate soil moisture through the evolution of the near surface temperature and relative humidity. This method can only be used on clear sky days when the diurnal evolution of the near surface values provides information on the properties of the surface. The technique is better for correcting errors in the deep soil reservoir than in surface layers and is better with vegetation covered surfaces. It is also less sensitive to moisture variability close to saturation than SAR.

Whilst this approach may complement the strengths and weaknesses of SAR, it is limited by cloud cover and is also dependent on surface modelling. Therefore, it was not considered to be a practical approach.

VARIABLE TO BE MEASURED OR CORRECTED	RADAR (SAR)	PASSIVE MICROWAVE	OPTICAL NEAR / IR	THERMAL IR
ATMOSPHERIC EFFECTS	Not significant at normal radar frequencies	Ice and precipitation can affect results	Must be corrected for accurate classification	Water vapour corrections required
CANOPY MOISTURE	Recent rainfall may cause overestimate of profile moisture	May influence surface soil moisture estimates	Internal canopy moisture via vegetation colour	From difference between sat & ground measured temperature
VEGETATION TYPE / COVER / CONDITION	Dense vegetation precludes moisture measurement	Effects greater at shorter wavelengths	Major application of this type of observation	Affects surface / atmosphere temperature differences
SURFACE SLOPE	Steep slopes must be processed out, need a DEM.	Resolution too low to require correction	Affects local solar incidence angle	Effects of aspect on surface temperature
SURFACE ROUGHNESS	Needs to be extracted for optimum results	Needs to be extracted for optimum results	No	Affects surface / atmosphere temperature differences
SNOW COVER	Snow area and some indications of wetness.	Snow cover and snow water equivalent possible	Has been used successfully	Effective measurements of snow cover
SOIL MOISTURE PROFILE	Sensitivity via dielectric constant	Longer wavelengths better, but give lower spatial resolution	Not directly	Can give estimates of bulk soil moisture
SOIL TYPE / TEXTURE	Preferably specified a priori	Needs to be extracted for optimum results	Bare soil colour	Bare soil temperature variability

Table 1: Summary of the capabilities of different satellite sensor types (including visible / near IR)

## 4. MODELLING METHODS

### 4.1. Hydrological models

Hydrological models simulate a subset of the hydrological cycle, generally within a river basin. This usually includes taking precipitation as an input and evapotranspiration and river discharge as output. Modelling soil moisture is an important component of these models. Spatially distributed hydrological models would be essential for soil state predictions, but these are not yet developed to operational status.

The availability of Geographic Information Systems (GIS) in the military environment provides a potential framework for the use of hydrological models. Hydrological models could also incorporate important 'local' factors if these are known such as topography and soil variability. Such models could provide a basis for extrapolating satellite observations of soil moisture in the following ways:

- modelling the changes in moisture content which occur between satellite passes;
- modelling changes within the soil from the surface downwards, when only near surface measurements are available.

Work is in progress to develop this integration at hydrological research institutes.

### 4.2. Meteorological models

Numerical Weather Prediction (NWP) models operate at scales ranging from the global to the mesoscale. The resolution of NWP models is increasing as greater computing power becomes available and as the physics in the models is improved. For example, in the UK, the UK Met Office operational mesoscale model is planned to reduce to a 12 km grid by May 1998, and is expected to reduce to below 5 km within the next 5 years. The mesoscale model is currently run operationally for the UK area and also for the Gulf and Bosnia regions to support military operations.

Such models are now using increasingly sophisticated schemes for calculating surface fluxes and are demonstrating realistic relationships between soil moisture and surface temperature and humidity. Three areas of development are likely to further enhance the capabilities of UK meteorological models in this area before the year 2000:

- ECMWF surface physics scheme - this currently uses optimal interpolation but is progressing firstly towards a separate variational analysis using atmospheric analysis as

a driver and then to a coupled variational analysis. This would forecast soil moisture and/or use satellite moisture measurements as inputs.

- The UK Met Office will be implementing a new surface exchanges scheme (MOSES) in its mesoscale model and is developing an improved MOSES 2 scheme with soil moisture data inputs and forecasts.
- A 1-D Site Specific Forecast Model (SSFM) is also being developed by the UK Met Office. This will be linked to mesoscale model output, but will have a finer vertical resolution and a more detailed description of the local surface characteristics. The SSFM is currently being run for 15 sites and tested against soil moisture and micro-meteorological measurements made at Cardington, and should become operational within a year or so.

## 5. ANALYSIS

### 5.1. Summary of satellite sensor capabilities

Table 1 summarises the capabilities of the main satellite sensor types considered in Section 3. Of the types considered, SAR data are considered to provide the most scope for future development because they offer a resolution which can benefit tactical and operational applications. Passive microwave data, such as SSM/I which are currently available can complement SAR by offering much more frequent coverage, but their resolution limits their applicability for tactical applications. Higher resolution passive microwave systems are unlikely to be available in the near future. Thermal IR methods are not considered to be practical in the short term.

### 5.2. Modelling methods

Meteorological models are not just a direct alternative to satellite data, but offer a means of extending the information available from sources such as SAR. The main limitation of current operational models is their state of development, as they are not yet capable of predicting soil state conditions to the accuracy and resolution required. This is expected to change in the medium term.

## 6. CONCLUSIONS AND RECOMMENDATIONS

Figure 5 summarises the current status of the different methods. The most effective approach in the short term is the use of SAR data. As meteorological models develop these are likely to become the preferred method, using data sources such as SAR for input and/or validation.

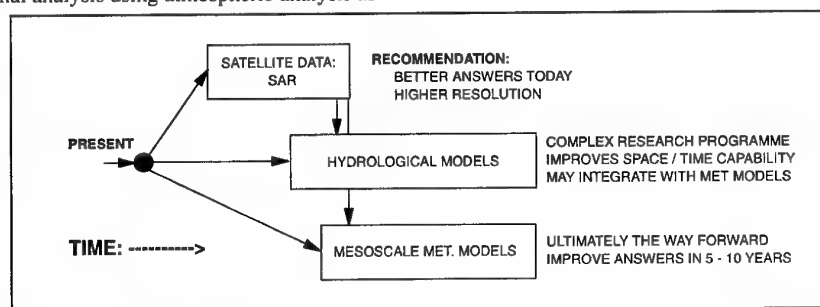


Figure 5: Summary of ways forward in the short and long term

### 6.1. Short term

Figure 6 summarises the approach for the short term. The output of this approach would be digital soil moisture maps which could be used directly as part of the decision making process, or as input to more established techniques for determining vehicle trafficability.

- these models will include increasingly sophisticated treatments of hydrological processes, and hence should produce more realistic predictions of soil moisture.

In addition, a higher resolution battlefield scale model CMETS (Computerised METeorological System) is being developed for the British Army. CMETS will utilise a high

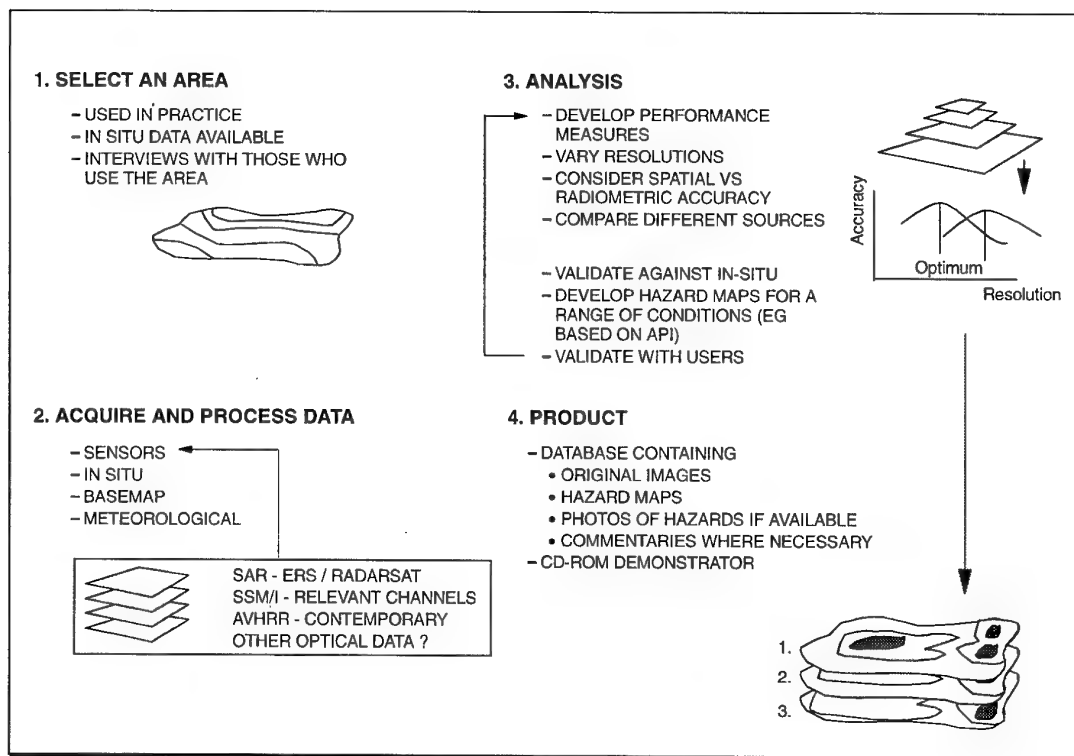


Figure 6: Summary of proposed short term approach

The benefits of this approach are:

- greater spatial resolution than existing methods (eg. climatology or visual assessments);
- it complements existing methods and could be used to support the use of trafficability models (eg. SMSP/NRMM), or to provide a visual overlay to guide manual assessments;
- the approach could be extended to provide support to OOA operations;
- it would provide a verification/initialisation capability to support the longer term meteorological modelling methods.

### 6.2. Long term

The study has suggested that mesoscale meteorological models are likely to become capable of providing useful soil state information. In particular:

- these models are already being run to support OOA military operations (eg. in the Gulf and Bosnia).
- the resolution of the UK mesoscale models used to support such operations will shortly fall to 12 km and probably below 5 km over the next 5 years;

resolution topographic/terrain database and assimilate mesoscale model predictions and local in-situ data, and will provide more detailed meteorological predictions to support a wide range of military applications, including artillery fire, trafficability and the use of electro-optic sensors. CMETS is likely to include an embedded hydrological model, which would be driven by the meteorological forecast, to enable soil moisture conditions to be predicted on a finer scale

As a consequence, meteorological predictions from mesoscale and battlefield scale meteorological models are likely to become increasingly important for the support of OOA field operations over the next 5 to 10 years.

## **7. PRELIMINARY REVIEW OF FOLLOW-ON WORK**

The methodology proposed in Figure 6 is the basis for an evaluation of the capability of SAR to provide soil state information. This work is still in progress, but the main elements are described in this section.

### **7.1. Area for analysis**

The area chosen is the Salisbury Plain Training Area in the UK. This area is used extensively for training with military vehicles including tanks and artillery. It also has the advantage that it is covered with relatively uniform grassland vegetation which does not vary greatly throughout the year. The area has a typical chalkland rendzina soil which is relatively thin and transmits water rapidly. This makes some of the analysis atypical, but this will be countered by applying the analysis to some of the heavier brown earth soils surrounding the Plain. It should also be noted that in areas where erosion has occurred, or on some of the improved tracks, dust emissions can be considerable in the summer months when conditions are dry.

### **7.2. Acquisition and processing of data**

The following data are being used for the analysis:

- 34 SAR subscenes from the ERS-1 and 2 satellites (25 km x 25 km) of which 2 cover the entire training area from East to West;
- a recent land cover classification based on the use of a CASI (Compact Airborne Spectrographic Imager) survey;
- a digital elevation map at 20m resolution;
- a 1:25,000 digital basemap;
- a digital map of made up tank tracks.

In addition to these, the following meteorological data are being used:

- raingauge data from various locations in and around the training area (recording at least hourly);
- rainfall radar data to provide estimates of the spatial distribution of rainfall.

### **7.3. Analysis**

At this stage only a preliminary analysis has been undertaken. The full analysis still awaits the proper correction of the data. The two major elements of the analysis are:

- visual analysis of the data using multi-temporal composites;
- calculation of the normalised backscatter.

The calculation of normalised backscatter effectively averages the data to reduce the effects of speckle, thereby improving the radiometric resolution. The effect is similar to increasing the number of looks. In addition, the calibration constants are applied to the sensors at this stage, ensuring that SAR data from the ERS-1 and ERS-2 satellites can be used interchangeably.

The result of performing the analysis on two dates from the Tandem Mission (when ERS-1 and 2 were flown together in coordinated orbits) separated by 24 hours shows a significant

change in backscatter in response to changes in the rainfall patterns and corresponding soil moisture. However, it should be noted that the data used are not yet fully terrain corrected and thus any conclusions drawn are tentative.

The next stages of the analysis will be as follows:

Preparation of the SAR data:

- precise location onto the digital base map;
- terrain correction using the digital elevation map.

Analysis:

- use the normalised backscatter analysis and the land cover classification to determine the optimum locations and scales at which to determine normalised backscatter for the corrected images;
- produce plots to summarise the results, relating these to the rainfall histories for each of the images;
- refine the analysis by repeating at different scales and using different filtering methods;
- support the analysis with more multitemporal plots based on the fully corrected images, and by theoretical analysis.

Verification:

- compare the information derived against knowledge about the key 'trouble spots' and through discussions with operational users.

## **8. SUMMARY**

This programme of work has evaluated options for the provision of soil state information from existing and future sources. The most suitable satellite sensor for most applications is considered to be SAR on the basis of its high spatial resolution. The provision of soil moisture information for the near surface makes the technique applicable to trafficability, but also relevant to other missions or systems which can be affected by the surface moisture conditions (eg. predicting the lofting of dust which can affect electro-optic sensors).

A number of methods could be developed to exploit SAR data, but one approach which is being investigated is to build up a library of SAR images for areas of potential interest and to use these to assess the characteristics of the surface under different meteorological conditions.

This work is still in progress, where the aim of the project is to produce a technical demonstrator which will show the capability of using SAR data for soil moisture prediction and surface characterisation, and its applicability for supporting trafficability assessments.

PAPER No. 34

DISCUSSOR'S NAME: G. Anderson

COMMENT/QUESTION:

Do you envision data synthesis/fusion between VIS/NIR imaging sensors on SAR to achieve more immediate assessment of surface water, subject to limitations of "clear"-sky conditions?

AUTHOR/PRESENTER'S REPLY:

(I assume the question relates to soil moisture rather than free standing water areas).

Yes, especially in the longer term. So far we have used VIS/NIR data in a "static" mode, to provide a land cover classification within which we analyse the SAR information. The next stage may be to make the VIS/IR classification dynamic (i.e. update regularly to take account of seasonal growth patterns). We have not used inversion models which combine the SAR and VIS/NIR data directly. It will be interesting to see what can be done with MODIS/MERIS data as well as future very high resolution sensors (i.e. 1m pan, 4m multispectral).

DISCUSSOR'S NAME: D. Edmondson

COMMENT/QUESTION:

At what time will more frequent/accurate satellite data be available?

AUTHOR/PRESENTER'S REPLY:

In terms of SAR data, the next two launches will be ENVISAT and Radarsat 2, both early next century. The SAR on ENVISAT offers vertical and horizontal polarisation, which should help the accuracy of retrievals. Radarsat 2 will offer higher resolution. Improvements in the frequency of observation may be possible if effective methods can be developed to extract soil moisture information from the variable beam modes offered by these future missions.

PAPER No. 34

DISCUSSOR'S NAME: D. Edmondson

COMMENT/QUESTION:

What was the size of the area covered for moisture content in Salisbury Plain?

AUTHOR/PRESENTER'S REPLY:

We used 2 SAR subscenes to provide coverage of the Plain, each of which was just over 25km x 25km giving 1250 Km<sup>2</sup>. The area of interest within this was 380 km<sup>2</sup>.

# EVALUATION OF CONCURRENT THERMAL IR ATMOSPHERIC PROPAGATION AND AEROSOL PARTICLE SIZE DISTRIBUTION MEASUREMENTS AT GOTLAND, SWEDEN

R. Carlson  
R. Tong  
SPAWAR Systems Center, San Diego, D743  
San Diego, CA 92152-5000, USA

G. de Leeuw  
P. Fritz  
TNO Physics and Electronics Laboratory  
P.O. Box 96864  
2509 JG, The Hague, The Netherlands

H. Garner  
San Diego State University  
Department of Astronomy  
San Diego, CA, USA

E. Vignati  
Joint Research Center, Environment Institute  
TP 460, 21020 Ispra, Italy

## SUMMARY

Measurements of spectrally resolved (2-14  $\mu\text{m}$ ) thermal infrared atmospheric transmission were made at the Swedish island of Östergarnsholm in the Baltic. The 908 meter horizontal path was located a few meters above the ocean surface. Concurrent measurements of meteorological parameters and aerosol particle size distribution were also made. The site on the island provides fetches ranging from about 3 km up to several hundreds of km, while very short fetches are provided when the wind is over the island. A variety of meteorological conditions were encountered during the experiments.

A preliminary comparison of the transmission measurements with the bulk meteorological parameters showed some of the expected dependence upon relative humidity, mainly in the 3-5  $\mu\text{m}$  region. A preliminary analysis of the data shows qualitatively a good agreement with both the variation in the meteorological conditions and the variation of the aerosol concentrations for 6 out of 7 of the measurement periods.

provided measurements of aerosol particle size distributions and meteorological parameters at both ends of the 908 meter transmission path. A range of meteorological conditions were encountered during the measurement period, including high wind speed, long sea fetch conditions which created high sea spray conditions. In this paper, temporal correlations are described between the atmospheric transmission measurements, meteorological parameters, and aerosol particle size distributions.

## 2 SITE DESCRIPTION

The measurements were made on the island of Östergarnsholm, a low-lying uninhabited island in the Baltic, located 3 km off the East coast of Gotland, Sweden. A 30 meter meteorological mast maintained by the University of Uppsala is located at the southern tip of the island. This site provided a variety of conditions including long fetch (>100 km) open ocean conditions and short fetch with land effects.

## 1 INTRODUCTION

The imaging geometries of submarine and surface vessel sensors in the littoral zone are not adequately presented in atmospheric propagation models such as LOWTRAN 7 and MODTRAN. As a result, the SPAWARSYSCEN, San Diego, Atmospheric Propagation Analysis (APA) program initiated a series of atmospheric propagation measurements in the coastal atmospheric marine boundary layer (Ref 1,2,3). The most recent of these measurements were made in the Baltic off the east coast of Gotland, Sweden in May 1997. These atmospheric transmission measurements were coordinated with the European Air Sea Exchange Process Studies (ASEPS) program (Ref 4). This program is organized to measure and evaluate processes near the air-sea interface involving air-sea exchange of gaseous species and aerosols as well as the physical and chemical interactions between gasses and aerosols (Ref 5). In particular, TNO-FEL (The Hague)

The measurement towers at the south end of the transmission path are shown in Figure 1. A view of the transmission path looking south is shown in Figure 2.

The Östergarnsholm site was evaluated for its similarity to U.S. Navy submarine and surface ship operational areas. A study of historical meteorological data for this area was performed and it was found that Östergarnsholm provides conditions similar to typical U.S. Navy operational areas above 50° North.

## 3 MEASUREMENT TECHNIQUE

Atmospheric propagation measurements were made along a horizontal over-water path from 3 to 13 May, 1997. These measurements were made in the thermal infrared region from 2 to 15  $\mu\text{m}$ . The path length was 908 meters and at a height of approximately 2 meters above the sea surface. The

measurement path extended across the southwest facing side of the crescent moon shaped island.

The APA technique for measuring transmittance involves measurement of the signal across a long path then quickly realigning the detector to measure the signal along a short path. Atmospheric transmission is then calculated from measurement of the infrared signal received over both a short path and a long path using the definition of transmittance (T) derived from Beers Law.

$$T = e^{-\sigma(R_2-R_1)} = \frac{S_{\text{long}} \text{ at } R_2/\Omega_2}{S_{\text{short}} \text{ at } R_1/\Omega_1} \quad (1)$$

$\sigma$  = attenuation coefficient

$S_{\text{short}}$  = Signal Response from the short path source

$R_1$  = short path length

$S_{\text{long}}$  = signal response from the long path source

$R_2$  = long path length

$\Omega_1$  = solid angle of long path source

$\Omega_2$  = solid angle of short path source

The above calculation includes the ratio of the long path signal to a reference short path. The reference short path (50.4 m) signal was made during a period of low wind speed ( $5 \text{ m s}^{-1}$  from the north and low relative and absolute humidity (50% and  $3.7 \text{ g m}^{-3}$ ) on 4 May.

Due to errors caused by this technique, some transmission measurements are greater than one. A short path laboratory measurement is under investigation which will allow a more accurate calculation of transmittance. In the data presented here, all transmittances will simply be relative to the short path measurement made at the lower humidity. Although this is only a relative technique, it is still useful for finding relative trends over the measurement periods until an adequate laboratory short path measurement can be made.

A CI Systems Model SR-5000 infrared spectrometer is used to measure the signal from the IR source. The spectral resolution of the measurements is an average of  $0.0152 \mu\text{m}$  from 1.3 to  $5 \mu\text{m}$  and an average of  $0.061 \mu\text{m}$  from 8 to  $14.5 \mu\text{m}$  with the use of a circular variable filter wheel. A complete spectral scan is accomplished in approximately 13 seconds. Five spectral scans were taken every eight to ten minutes and then averaged.

The IR source includes a CI Systems Model SR-9 5-inch diameter, clear-aperture collimator with a 38-inch focal length optical system. This collimator system incorporates a two-optical element Newtonian telescope system with a 5-inch diameter, off-axis, parabolic mirror and a 1.5-inch focusing secondary mirror. The CI Systems Model SR-2-33 Blackbody Source is operated at  $1000^\circ\text{C}$  ( $\pm 1.5^\circ\text{C}$ ). Emissivity of the source is 0.99.

Aerosol particle size distributions were continuously measured with optical particle counters from Particle Measuring Systems (PMS, Boulder, Colorado). A PMS type CSAS-100-HV probe (PMS3) measuring particles in the diameter range from  $0.5\text{--}47 \mu\text{m}$  was placed in a box at a height of about 3 meters above sea level at the south end of the transmission path. This box automatically aligned itself with the prevailing wind. A PMS type CSASP-200 (PMS2) was located in the scaffolding shown in Figure 1 at the south

end of transmission path at a height of 10m above sea level. Another PMS type CSASP-200 (PMS4) was placed at the North end of the transmission path, also at a height of about 3 meters above the sea surface. PMS2 and PMS4 measured particles in the diameter range from  $0.2\text{--}20 \mu\text{m}$ . The PMS2 and PMS4 were manually rotated into the wind during transmission measurement periods.

Meteorological parameters were measured using automatic recording weather stations placed at the south end of the island at about 13m above sea level and at the north end of the transmission path at about 4 m above sea level. Data on wind speed and direction, relative humidity, air temperature and solar radiation were continuously recorded.

#### 4 RESULTS AND DISCUSSION

Concurrent transmission, aerosol and meteorological measurements were made under a wide range of conditions during the campaign. The transmittance data was evaluated for correlation with meteorological parameters and aerosol particle size distributions.

Examples of transmittance and aerosol data are shown in Figures 3, 4 and 5 for the 10 May measurement period. Figure 2 shows a photograph of the waves in the transmission path during the 10 May measurement period. This particular day shows the sensitivity of the transmittance to sudden changes in meteorological conditions and aerosol concentrations.

Figure 3 shows the spectral transmittance data collected during the measurement period. Figure 4 shows a temporal plot of the transmittance data averaged over the three dominant transmission bands including  $2.8$  to  $4.3 \mu\text{m}$ ,  $4.3$  to  $5.5 \mu\text{m}$  and  $7.3$  to  $13.5 \mu\text{m}$ . Trends in the transmittance will now be described along with associated meteorological and aerosol parameters.

Figure 4 shows a sudden drop in transmittance at 11:00. The effect was more prominent in the shorter wavelengths. This decrease in transmittance correlates with the sharp increase in particle concentrations (Figure 5) due to the appearance of marine haze and increased humidity at this time.

Transmittance then increases again during the next 1.5 hours. Around 1330 another decrease is observed after which the transmission fluctuates around a more constant value.

The above observations can be qualitatively understood from the meteorological conditions and the aerosol concentrations. Variations in relative humidity and atmospheric pressure (not shown) indicate passage of a low pressure front before noon. The wind speed increased to a value of more than  $10 \text{ m s}^{-1}$  with a long sea fetch (which still must be confirmed by air mass trajectories).

The data in Figure 5 shows an increase of the particle concentrations in both the large and giant aerosols during the high wind speed periods. The increase in the concentrations of the large particles is likely due to the advection of polluted air from industrialized areas in Western or Central Europe (which again has to be confirmed by air mass trajectories). The increase in the concentrations of the giant particles is conjectured to be caused, at least in part, by surface generation



of sea spray due to the interaction between wind and waves at wind speed of around  $10 \text{ m s}^{-1}$  and occasionally higher. The increase in wind speed may give rise to the formation of young waves which break easier than in a well-developed wave field, while the frontal activity may have caused a confused wave field with waves coming from different directions and thus interfering and breaking.

It can also be seen in Figure 5 that the maximum concentration of giant particles was reached before noon and then decreased. The concentration of the large particles continued to increase. With a slightly decreasing relative humidity, the larger particles may be shrinking due to evaporation, thus causing a shift in the size distribution to the smaller particles.

Limitations on paper length preclude including such detailed analysis of all data sets. However, general trends in all the data sets may be found in Tables 1 through 3. A comparison of transmittance in each of the three prominent transmission bands is compared to LOWTRAN 7 predictions and the trends in relative and absolute humidity, wind speed and direction, and the concentration of large ( $2.2$  to  $2 \mu\text{m}$  diameter) and giant ( $>2 \mu\text{m}$  diameter) aerosols.

There are a few preliminary trends worth noting. Transmittance in all bands was highest on 3 May when the lowest relative and absolute humidities were measured, as well as the lowest concentrations of both large and giant aerosols. Although the wind speed of  $6\text{--}14 \text{ m s}^{-1}$  is quite high, the NNW wind direction caused the transmission path to be sheltered from the wind by the bulk of the island of Östergarnsholm. This sheltering effect reduced the amount of white caps and sea spray which would be expected at this range of wind speeds. LOWTRAN 7 predictions are also the highest for this date even though the model cannot take into consideration the sheltering effect of the topography.

All data measured and modeled during periods of long sea fetch (S to SSE) show lower transmittance than the sheltered fetch on 3 May. Transmittance does not seem to correlate with any single meteorological or aerosol parameter. For example, transmittance was lowest in all bands on 8 May. However, the relative and absolute humidities were not the highest encountered, the wind speed was very low, and the concentration of aerosols was relatively low. Under these conditions, a relatively high transmittance would be expected compared to other measurement periods.

## 5 DISCUSSION

Spectrally resolved transmission, measured over a path of 908 m across the bay of Östergarnsholm, was averaged to obtain the transmission in the three dominant transmission bands in the mid- and far IR windows. The trends in the band-averaged transmission has been qualitatively explained in terms of the local meteorological situation and the resulting aerosol particle size distributions. In general, the transmission follows the trends in the relative humidity and aerosol size distributions, with some exceptions. LOWTRAN 7 predictions are also somewhat consistent with measured data.

The observed discrepancies between the aerosol particle size distributions and the observed transmission may be due to effects that cannot be caught in a simple model based on only meteorological parameters. This is illustrated with the example presented in Figure 6 which shows the wind speed dependence of the fine aerosol fraction (particle concentrations integrated over sizes smaller than  $1 \mu\text{m}$ ), for wind directions between  $110$  and  $180$  degrees (long sea fetch). Clearly, two groups appear with quite different concentrations. In spite of the common meteorological conditions, the air masses are quite different, possibly with different origins. Indeed, the weather maps indicate two different air masses, one originating in clean arctic regions, the other coming from more polluted areas in Europe.

Consideration of the history of the air masses involved and chemical composition will further help to identify the aerosol behavior. This example clearly illustrates that consideration of only the local situation is not sufficient to explain the observed aerosol and transmittance behavior.

Finally, it is emphasized that the measured transmission is relative to signal measured over a 50 m path in clear weather. Hence the transmission values are not absolute, although it is not expected that they will change significantly with laboratory calibration. A final qualitative analysis will be made once the transmission values have been calibrated based on a short-path transmission measurement in the laboratory (in preparation).

## 6 ACKNOWLEDGMENTS

Funding for SPAWARSYSSEN, San Diego was provided by Office of Naval Research 322. Dr. Steve Ackleson and Dr. Scott Sandgathe. Funding for TNO/FEL was provided by the ONR Europe NICOP program (contract N68171-97-M-5442), the European Commission BASYS program (contract MAS3-CT96-0058), and the Netherlands Ministry of Defense (A95KM784).

## 7 REFERENCES

1. Law, D.B., Tong, R., Hintz, R., Terpening, L., Edwards, G., Csanadi, C., Tessmer, S., Johnson, C., "Atmospheric propagation analysis program", Technical Report 1577, Naval Command, Control and Ocean Surveillance Center RDT&E Division, San Diego, January 1993.
2. R. Carlson, D.B. Law, C. Csanadi, G. Edwards, and R. Tong, "Thermal infrared transmission through the marine atmospheric boundary layer and LOWTRAN 7 predictions", *Proc. SPIE*, vol 2828, pp. 532-541, August 1996.
3. Carlson, R., Law, D.B., Csanadi, C., Edwards, G., Tong, R., "Thermal Infrared Propagation Across the Surf Influenced Marine Atmospheric Boundary Layer", *Proc. SPIE*, vol 3125, pp 192-202, July 1997.

4. L.L.S. Geernaert, H. Bergstrom, A.M.J. van Eijk, T. Ellermann, P. Fritz, G.L. Geernaert, J. Hojstrup, B. Jensen, G. de Leeuw, J. Nielsen, B. Pedersen, and A.-S. Smedmann, "Micrometeorological Process Study of Gaseous Reactive N-Compounds, BASYS-Workshop, Warnemunde, (Ge), 29-31 Sept., 1997
5. G. de Leeuw, A. van Eijk, and E. Vignati. Aerosol Particle Size Distributions on Östergarnsholm (Sweden). Proc. Nordic Aerosol Symposium NOSA 97, Chalmers University of Technology, Göteborg, Sweden, 23-24 October 1997.

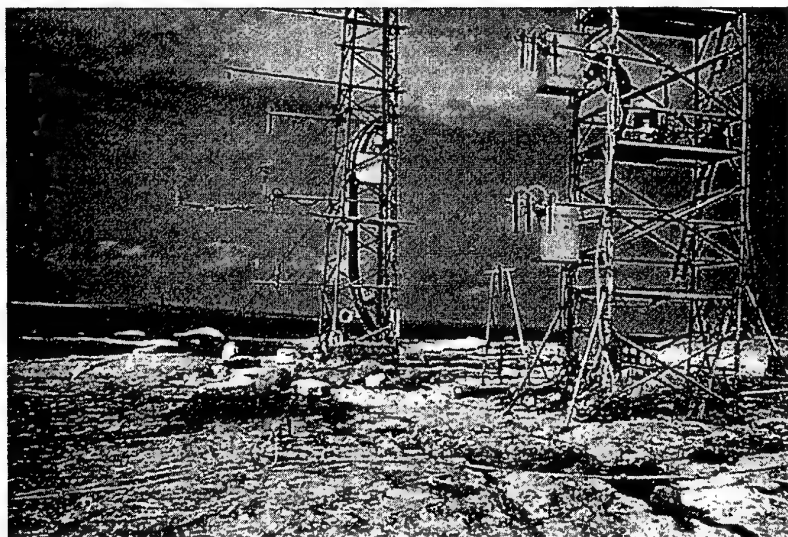


Figure 1. Instrument towers and south end of transmission path on Östergarnsholm, Sweden, 10 May 1997.

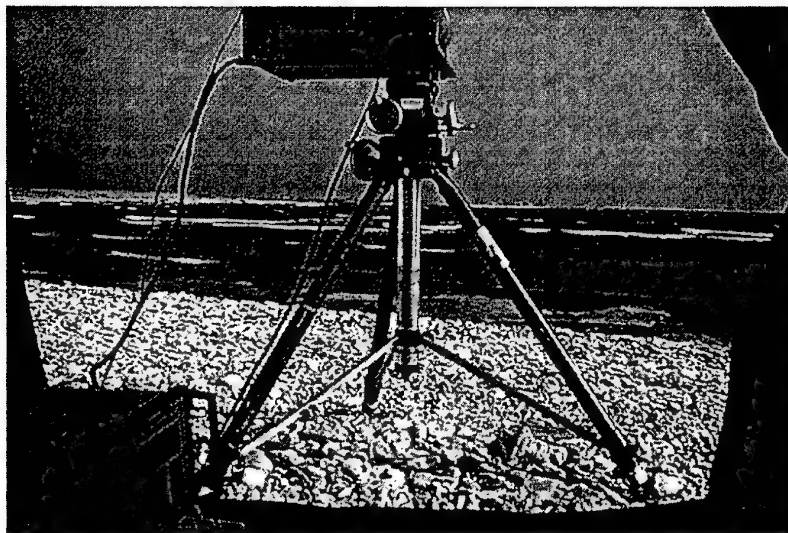


Figure 2. Whitecaps and waves in transmission path under high wind conditions on 10 May 1997. Looking south from IR source.

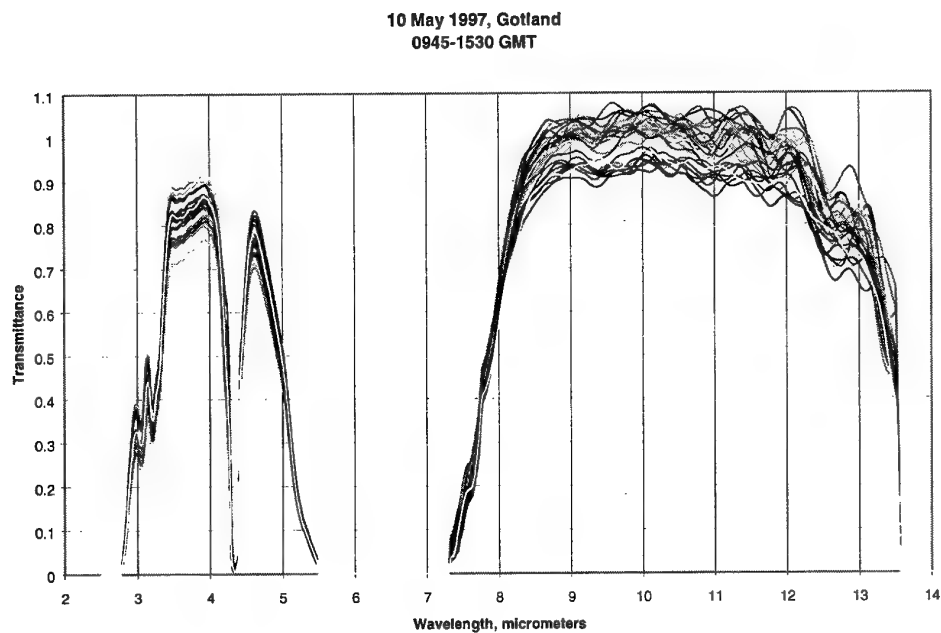


Figure 3. Spectral transmittance measured on 10 May 1997.

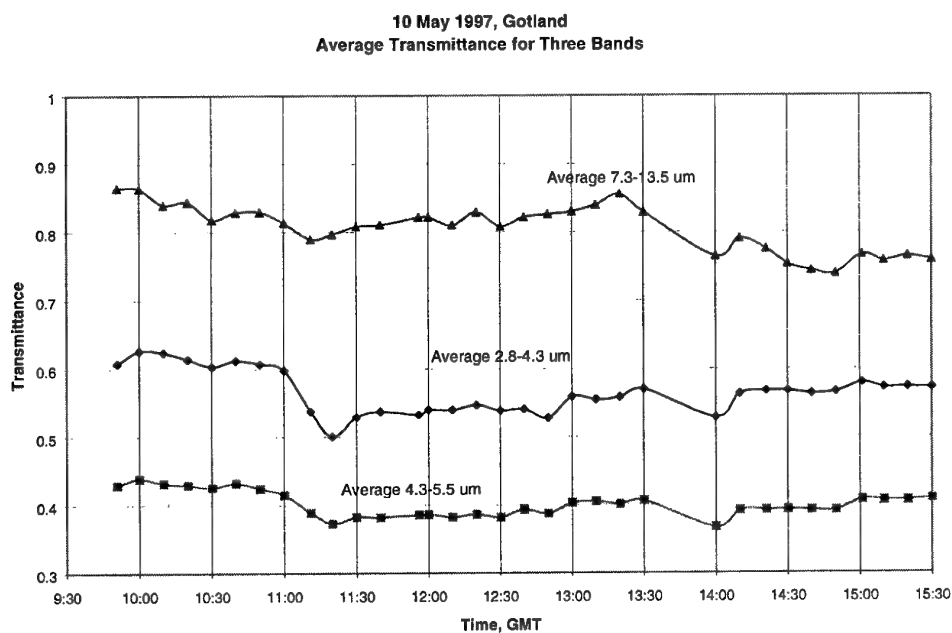


Figure 4. Average transmittance for three prominent band passes plotted over time for 10 May 1997. Note drop in transmittance due to marine haze at 1100.

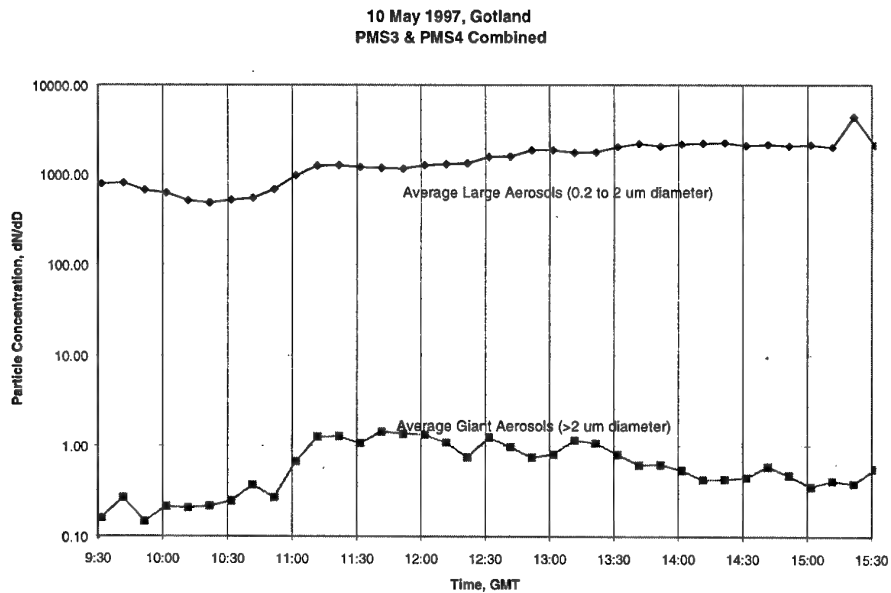


Figure 5. Large and Giant aerosols plotted over time for 10 May 1997. Note the increase in aerosol concentrations due to marine haze at 1100.

Date 1997	RH% avg.	Absolute Humidity gm m <sup>-3</sup>	Wind Speed m s <sup>-1</sup>	Wind Direction	% Trans., 2.8-4.3 μm average	PC-TRAN 7 Avg. % Trans., 2.8-4.3 μm	Large Aerosols 2.2-2 μm diameter dN/dD	Giant Aerosols >2 μm diameter dN/dD
8 May	65-80	5-6	2-5	SSE	50	57	200	0.1
10 May	85+	6.5	10-15	S	55	53	1000	1
13 May	80	10	2-5	S to SE	55	53	1000	0.1-1.0
11 May	85+	6.3	6-10	S	60	53	900	0.2
12 May	80+	6	2-8	SSE	60	56	1000	0.15
4 May	55-75	4-5	3-7	SSE	65	61	30	<0.1
3 May	35-40	3.5	6-14	NNW	75	63	30	<0.1

Table 1. Transmittance in 2.8-4.3 μm region sorted in ascending order and compared to LOWTRAN 7 predictions and measured meteorological and aerosol parameters.

Date 1997	RH% avg.	Absolute Humidity gm m <sup>-3</sup>	Wind Speed m s <sup>-1</sup>	Wind Direction	% Trans., 4.3-5.5 μm average	PC-TRAN 7 Avg. % Trans., 4.3-5.5 μm	Large Aerosols 2.2-2 μm diameter dN/dD	Giant Aerosols >2 μm diameter dN/dD
8 May	65-80	5-6	2-5	SSE	35	36	200	0.1
13 May	80	10	2-5	S to SE	35	32	1000	0.1-1.0
10 May	85+	6.5	10-15	S	40	34	1000	1
11 May	85+	6.3	6-10	S	40	34	900	0.2
12 May	80+	6	2-8	SSE	40	34	1000	0.15
4 May	55-75	4-5	3-7	SSE	45	39	30	<0.1
3 May	35-40	3.5	6-14	NNW	55	41	30	<0.1

Table 2. Transmittance in 4.3-5.5 μm region sorted in ascending order and compared to LOWTRAN 7 predictions and measured meteorological and aerosol parameters.

Date 1997	RH% avg.	Absolute Humidity gm m <sup>-3</sup>	Wind Speed m s <sup>-1</sup>	Wind Direction	% Trans., 7.3-13.5 $\mu$ m average	PC-TRAN 7 Avg. % Trans., 7.3-13.5 $\mu$ m	Large Aerosols 2.2-2 $\mu$ m diameter dN/dD	Giant Aerosols >2 $\mu$ m diameter dN/dD
8 May	65-80	5-6	2-5	SSE	60	74	200	0.1
13 May	80	10	2-5	S to SE	65	69	1000	0.1-1.0
4 May	55-75	4-5	3-7	SSE	75	77	30	<0.1
11 May	85+	6.3	6-10	S	75	72	900	0.2
12 May	80+	6	2-8	SSE	75	72	1000	0.15
10 May	85+	6.5	10-15	S	80	71	1000	1
3 May	35-40	3.5	6-14	NNW	90	79	30	<0.1

Table 3. Transmittance in 7.3-13.5  $\mu$ m region sorted in ascending order and compared to LOWTRAN 7 predictions and measured meteorological and aerosol parameters.

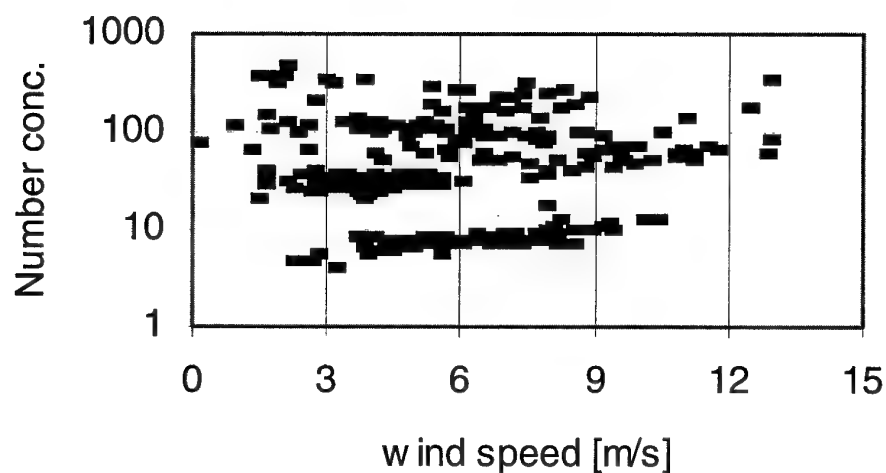


Figure 6. Number concentration of aerosols < 1  $\mu$ m diameter as a function of wind speed, for wind directions between 110 and 180 degrees (long sea fetch).

PAPER No. 35

DISCUSSOR'S NAME: G. Anderson

COMMENT/QUESTION:

MODTRAN should have full prior capabilities of LOWTRAN aerosols. We will assure that any problems will or have been corrected.

AUTHOR/PRESENTER'S REPLY:

The remark that MODTRAN did not accept the wind speed input referred to the pc version.

PAPER No. 35

DISCUSSOR'S NAME: D. Dion

COMMENT/QUESTION:

In your Mic scattering calculations have you considered a different refractive index for the different air mass origins?

AUTHOR/PRESENTER'S REPLY:

In our Mic calculations we take into account a continental component and a marine component with a different refractive index.

## Low-Altitude Point-Target EXperiment (LAPTEX): Analysis of horizon target detection

**Denis Dion**

Defence Research Establishment Valcartier, 2459 Pie-XI Blvd. North,  
Val-Belair, Qc, G3J 1X5, Canada, denis.dion@drev.dnd.ca

**Piet Schwering**

TNO Physics and Electronics Laboratory, P.O. Box 96864, 2509 JG The Hague,  
The Netherlands, Schwering@fel.tno.nl

**Karin Stein**

FGAN-FfO, Schloss Kressbach, D-72072 Tübingen, Germany, stein@ffo.fgan.de

**Arie de Jong**

TNO Physics and Electronics Laboratory, P.O. Box 96864, 2509 JG The Hague,  
The Netherlands, anjn7@fel.tno.nl

**Hans Winkel**

TNO Physics and Electronics Laboratory, P.O. Box 96864, 2509 JG The Hague,  
The Netherlands, Winkel@fel.tno.nl

### SUMMARY

During the Low-Altitude Point-Target EXperiment (LAPTEX), conducted in Summer 1996 in Crete (Greece), tracking of low-level targets up to horizon ranges were performed in the IR to assess near-sea surface effects on IR surveillance system performance. This paper presents the analysis of two measurement sessions which are deemed representative of conditions in mid-latitude inner-sea littoral environments. During one session, atmospheric refraction permits beyond-the-horizon tracking, while during the other session, refraction is responsible for producing mirages and reducing slightly the maximum detection range. Received signal versus range is compared with model calculations using MODTRAN, the IR Boundary Layer Effects Model (IRBLEM) and the Thermal Range model for Point target detection (TRP). For the selected conditions, in which aerosol extinction does not play a major role, models are shown to provide an appreciably accurate description of transmission and received signal-to-noise ratio versus range.

### 1. INTRODUCTION

In July 96, the NATO AC/243 Panel 4 Research Study Group 5 conducted a measurement campaign, the Low-Altitude Point-Target EXperiment (LAPTEX), in the Mediterranean Sea with sensors and equipment installed on the island of Crete, in Greece. The objective was to assess performance of IR surveillance systems in mid-latitude inner-sea littoral environment and to collect data for supporting on-going development of models aimed at:

- i - describing environmental effects on near-sea surface electro-optical detection;
- ii - predicting performance ofIRST systems;
- iii - characterizing sea and sky background near the horizon, and
- iv - describing ship signature.

Low-flying aircraft detection and identification experiments were also conducted. During the 3 week campaign, Canada, Denmark, Germany, Italy, the Netherlands, the United Kingdom and the United States performed measurements while Greece provided logistic and technical support along with ships and aircrafts. A description of the experiment is given in Ref. 1.

To fulfill objectives i. and ii., ship-mounted IR targets were tracked using on-shore sensors during ship outbound and inbound runs. The analysis presented in this paper focuses on two specific sessions, for which observations are compared with model calculations. TNO-FEL in the Netherlands [2] and FfO in Germany [3] have already reported on some of their respective observations.

This paper combines measurements of Canada, Germany and the Netherlands teams together with revised model calculations, incorporating near-sea surface effects with a close look at refraction effects. For the analysis we use two propagation models, MODTRAN developed by Phillips Laboratory in the US and the IR Boundary Layer Effects Model (IRBLEM) which is currently under development at DREV, and one system model, the Thermal Range model for Point target detection (TRP), developed in Germany. The experimental setup and equipment are briefly presented in section 2.0, section 3.0 gives details on the atmospheric conditions during the selected sessions, section 4.0 presents models used for the analysis and section 5.0 presents and discusses observations made during the two sessions together with model calculations. Finally, section 6.0 summarizes lessons learned and draws conclusions.

## 2. EXPERIMENTAL SETUP

LAPTEX was conducted at the NATO Forces Accuracy Check Site (FORACS) near Chania and Souda Bay in Crete (Greece). For the near-sea surface target tracking sessions, IR targets provided by TNO-FEL were mounted on the Greek Research vessel Strabon (A 476). Targets were mounted 13.6 m above the water surface using a tower installed on the ship; one target heading forward and the other one heading backward, so to perform target tracking during both out- and in-bound ship runs. During a session, the Strabon sailed away up to a certain range beyond the horizon and then returned, following a 60 degree North trajectory, as shown in Fig. 1.

### 2.1 Sensors

TNO-FEL and FfO performed measurements in the 3-5 and 8-12 micron IR windows. However, data analysis in this paper is limited to the 3-5 band only, since long range tracking ( $R > 15$  km) was not possible in the 8-12 with the sensors used due to the high absolute humidity in this maritime region [2]. TNO-FEL and FfO sensors were located about 100 m apart along the coast line, 20.4 and 19.7 m above the sea surface, respectively. Note that the latter are relevant heights for IR surveillance systems on a ship. Simultaneously, DREV performed high-resolution imaging in the visible to capture the fine refraction-induced phenomena using cameras located 10 and 20 m above the sea surface. Specifications of sensors used by the three nations are summarized in Table 1.

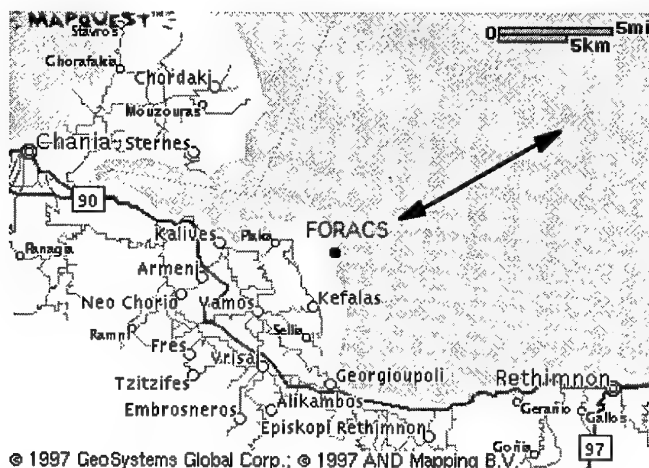


Fig. 1 LAPTEX at FORACS (Crete); the double-head arrow shows Strabon trajectory

Table 1 - Sensors

	MODEL	Band (microns)	IFOV (mrad)	NEI ( $10^{-14}$ W/cm <sup>2</sup> )	Height (m)
TNO-FEL	Cincinnati-IRC160	3.7-4.6	0.1	1.0	20.4
FfO	Cincinnati-IRRIS 256-LN	3.0-5.0	0.1	1.4	19.7
DREV	Sony AVC-D5 (2)	> 0.8	0.01	-	20.3 & 10.4

### 2.2 Meteorological measurements

Extensive meteorological measurements were performed at sea and on land. A wave-rider buoy and a buoy made at TNO-FEL were moored 1.1 km from FORACS. They together provide the basic parameters needed for model computations: pressure, air and sea temperature, humidity, wind speed and direction, and wave height. The wave rider buoy also gives wave spectra and direction, which can be useful to investigate the impact of sea roughness on calculations, and to conduct sea

background studies. Furthermore, standard meteorological measurements were performed continuously on the Strabon by both TNO-FEL and DREV during tracking sessions.

Moreover, onboard Strabon were collected data on aerosol extinction, using two different techniques: (1) using a Particle Measurement Systems (PMS) put in place and operated by TNO-FEL, which gives the distribution of the particle size from which the



extinction coefficient can be derived through Mie scattering calculation; (2) using a Particle Volume Monitor (PVM) or extinctionmeter, which gives a signal proportional to the forward scattering coefficient at 3.8 microns.

### 3. CASE STUDY

In this paper we analyze 2 experimental sessions conducted on the 16 and 22 July respectively. Continuous meteorological recording at various locations and redundancy of measurements are suitable

to reliably characterize the prevailing conditions. From a global analysis of meteorological data considering all sources of information, we came up with the sets of data shown in Table 2 to describe the conditions that prevailed on the 16 and 22 July at LAPTEX. These sets mostly correspond to the buoy data, as in many instances ship meteorological measurements are suspected to be contaminated by ship structure and motion; in particular, for most runs, the measured wind speed and humidity appear to be highly correlated with the ship speed.

Table 2 - Meteorological data for the 16 and 22 July

	16 July 96 9-12 hrs* super-refraction	22 July 96 19-22 hrs* sub-refraction
<i>Air temperature (C)</i>	27.4	24.2
<i>ASTD (C)</i>	+ 2.0	- 0.5
<i>Humidity (% / g/m3)</i>	57 / 14.3	64 / 14.1
<i>Wind speed (m/sec)</i>	4.5	3.0
<i>Wind direction (dg North)</i>	320 - 340	300 - 325
<i>24-hr avg. wspd (m/sec)</i>	5.1	4.1
<i>Wave height (m)</i>	0.3	0.7
<i>Visible range** (km)</i>	> GOS + 6	GOS - 1
<i>Meas. Extc. coef. (km-1)</i>	0.020	0.019
<i>NAM Extc. coef. (km-1)</i>	0.018	0.010

\* Local time

\*\* GOS: geometrical optical sight (km)

The two selected runs were conducted under good weather conditions, with very good visibility and moderate wind. The absolute humidity was relatively high, as expected in this maritime mid-latitude area. The North-West wind, which blew perpendicular to the ship trajectory, brought in a mixture of sea and land air. These coastal conditions are thought to be typical in this area in Summer. They are definitely representative of conditions that prevailed during the 3 week campaign, except for 3 or 4 days when the sea got very rough and prevented ship tracking sessions.

What differentiates the conditions is the air-sea temperature difference (ASTD), leading to different kinds of refraction conditions. On 16 July, super-refraction prevailed near the surface, permitting beyond-the-horizon detection. On 22 July, sub-refraction prevailed, which is known to limit the maximum inter-vision range (MIVR) between target and sensor, compared with the geometrical optical sight (range limitation imposed by earth curvature in the absence of refraction effect) [4]. These refraction effects on detection

range were confirmed by observations in the visible. Table 2 gives the maximum detection range observed by Canada in the visible using a camera 10 m above the sea surface and a target onboard ship 7 m above the surface. The ASTDs for the 16 and 22 July were common values at LAPTEX, and at the same time among the maximum and minimum values recorded. The 16 and 22 July were selected to consider the cases where refraction effects were among the strongest observed.

The last two rows of Table 2 give, in the 3-5 band, the measured aerosol extinction coefficients onboard Strabon and the calculated values using NAM (in MODTRAN), respectively. For the NAM calculations, an air mass parameter (AMP) of 3 was chosen as it was found to lead to calculated visibilities greater than 50 km, which was judged in agreement with observed visibilities. Greater values of AMP would give visibilities which are less than likely, considering observations made in the visible. For the 16 and 22 July sessions, the average PMS and PVM extinction

coefficients agree very well. Note that for 16 July, very good agreement is obtained between calculation and measurement while, for 22 July, the calculation is about half the measured value.

#### 4. MODELS

To support the analysis of the 16 and 22 July observations, calculations were performed using 3 computational models, two propagation models and one system detection model: The MODerate resolution TRANsmission (MODTRAN v3.5), the IR Boundary Layer Effect Model (IRBLEM v2.7.5) and the Thermal Range model for Point target detection (TRP). MODTRAN [5] is a widely used radiative transfer model which was developed by Phillips Laboratory as a successor to LOWTRAN 7. Details on MODTRAN are given in several dedicated papers included as part of these Proceedings.

IRBLEM is a propagation software package which is being developed in the framework of a joint Canada-Netherlands program with the aim of complementing MODTRAN for dealing with near-sea surface propagation effects [6]. The model combines effects of molecular absorption, aerosol extinction and refraction, taking into account the rapid change of refractivity and aerosol content with respect to the elevation near the sea surface. In IRBLEM, vertical profiles of refractivity,  $C_n^2$  (turbulence) and aerosol extinction coefficient are calculated and fed into a ray-tracing module, together with molecular transmittance obtained using MODTRAN, to compute what is hereafter called *effective transmittance*. The effective transmittance is the product of the molecular transmittance, the aerosol transmittance and the refractance, the latter being a refraction-dependent gain factor expressed in transmittance units. This new quantity was introduced several years ago [7]. The analysis presented in this paper shows some experimental validation of refractance calculation. IRBLEM is made modular. It is composed of modules that can be readily substituted. In the following analysis of LAPTEX data, computation of aerosol extinction was substituted by measurements made onboard Strabon.

The Thermal Range model for Point target detection (TRP), developed in Germany, has been designed to perform a complete IR system detection calculation [8]. Thus, as opposed to MODTRAN and IRBLEM, which are propagation models exclusively, TRP is a system model from which system performance can be assessed. TRP performs target-background contrast radiance computation, takes into account atmospheric transmission along with turbulence-induced blurring, and finally, it contains a sensor model which takes into account the sensor optics, detector sensitivity and size, and platform jitters. For the TRP calculations shown in this paper, sensor and target were assumed to be fully stabilized. Furthermore, IRBLEM is used to provide the effective transmittance and  $C_n^2$ ; the latter is required to estimate blurring effect on detectability.

#### 5. OBSERVATIONS AND CALCULATIONS FOR THE SELECTED CASES

##### 5.1 - 16 July

Figure 2 shows TNO-FEL measurements for 16 July together with MODTRAN and IRBLEM\* calculations for 16 July, wherein the TNO-FEL average received signal is converted to effective in-band transmittance. Outbound and inbound run data are shown. The average signal is calculated considering 50 frames and the range is given by a GPS system onboard. The star (\*) in IRBLEM\* means that, in IRBLEM, measurement of aerosol extinction is used instead of any prediction. For the TNO-FEL sensor, the geometric optical sight of the IR source is 29.3 km. As predicted under positive ASTD conditions, tracking is performed beyond the horizon, up to 32 km. At this range, the received signal was strong enough to keep tracking much further away. Unfortunately, the ship stopped at 32 km and returned in accordance to the plan.

From close range to 20 km, MODTRAN and IRBLEM\* calculations are very close to each other. At these ranges, the refraction effect on transmission is negligible (i.e. refractance=1) and, since in IRBLEM the molecular absorption is given by MODTRAN, the difference between the two calculations turns out to be dependent upon the aerosol extinction only. As mentioned above, for 16 July the NAM prediction of aerosol extinction is very close to the measurement.

From 20 km and further, one notices that IRBLEM\* transmittance decreases slightly more rapidly than MODTRAN transmittance, leading to a better agreement with observations. This is due to refractance, unaccounted for in MODTRAN, which decreases with range under positive ASTD conditions. For this run, transmission is dominated by molecular transmittance, and near the horizon, refractance gets as significant as the aerosol transmittance. According to IRBLEM\*, at 30 km, the molecular transmittance is 0.14, aerosol transmittance is 0.55 and refractance is 0.54.

Figure 3 shows the FFO measurements with the SNR calculations obtained from the TRP-IRBLEM\* combination. For selected ranges, 3 seconds of signal were analyzed. Each dot in the Figure shows the result for one camera frame. For the German setup, the geometric optical sight is 28.8 km. The calculated BEST and WORST case curves correspond respectively to the optimistic and pessimistic situations where the target peak received signal always falls in the middle of a detector (optimistic) or always falls between detectors (pessimistic), taking into account turbulence-induced blurring. In particular, at 30 km, TRP-IRBLEM\* calculations show that, because of turbulence, only 66 % of the available energy hits the detector even in the BEST case, whereas some 34 % of target energy reaches a detector in the WORST scenario.

## 5.2 - 22 July

Figure 4 shows signal received with the TNO-FEL IRC160 system during the outbound run of 22 July, converted again to transmittance, together with MODTRAN calculation. The solid line marked with squares shows the average received signal, and the x's and \*'s denote the average-plus-standard deviation and average-minus-standard deviation, respectively. This allows one to appreciate the level of signal fluctuations along the path. It is noteworthy that MODTRAN calculation, which includes NAM calculation, gives a relatively good description of the signal variation with range. This is obtained even though the calculated aerosol extinction coefficient differs significantly from the measured one (as shown in Table 2), as the aerosol contribution remains small compared with molecular absorption.

Figure 5 shows the same graphic, except that a modified IRBLEM\*, hereafter referred to as IRBLEM\*\*, is used instead of MODTRAN for the calculations. The Monin-Obukhov theory used to describe the vertical refractivity profile ceases to apply when the stability length,  $L$  (which is an indicator of the level of atmospheric stability), is too low. To obtain a reliable result, one shall ensure, as a rule of thumb, that  $L$  is greater or equal to the sensor height. This was not the case for the 22 July run because of the prevailing low wind speed. It was then decided to present calculations considering the closest conditions where the theory applies. IRBLEM\*\* calculation means that IRBLEM\* is used considering a slightly increased wind speed (to 4 m/sec) so to have the stability length just greater than sensor height. It is noteworthy that, in the case of 16 July,  $L$  was sufficiently high for the model to apply.

Note that with IRBLEM\*\*, the increase of signal just before target loss is pretty well described. This steep increase of signal is due to a refraction-induced mirage. The calculated maximum inter-vision range (MIVR), 28 km, is however slightly less than observed, 28.4 km. Let us recall that in this case the geometric optical sight is 29.3 km. The calculated transmittance variation with range agrees very well with the measurement trend, except near 20 km where significantly more signal is received. The cause of this signal increase has yet to be investigated.

Figure 6 shows the FFO SNR measurements and TRP calculations for the 22 July. In this case, the predicted turbulence is much less than for 16 July; calculations show that more than 90% of the available energy falls on the detector in the BEST case (defined above). Near MIVR, one observes a tremendously large SNR variation; large variation of signal was also observed from TNO-FEL measurements. Because of the ship motion, due to the waves, for one frame the target may be beyond the horizon, while for subsequent frames the target signal is magnified due to the presence of a mirage. For the German sensor, the geometric optical sight is 28.8 km, the observed MIVR is about 27.5 km and the predicted MIVR is 27.8 km.

In summary, for the 22 July, molecular absorption is the principal source of attenuation along the path. Refraction is responsible for abruptly limiting detection range about 1 km less than the geometric optical sight but, nonetheless, the mirage increases detectability at MIVR.

## 6. LESSONS LEARNED AND CONCLUSIONS

Experiments were conducted by the NATO Research Study Group 5 in the Mediterranean Sea in Summer 1996 to assess performance of IR systems under typical mid-latitude littoral inner-sea conditions. In this paper, we presented analysis of tracking of low-level targets in the 3-5 micron band, with targets getting near and crossing the horizon.

For most of the 3 week campaign, the visibility was good and the wind was moderate and blew along the coast. Under these conditions, IR transmission versus range was shown to be dominated by molecular absorption, because of the characteristically high absolute humidity in this region. When the air-sea temperature difference (ASTD) is negative, refraction is likely to be the second factor of importance (so it was on 22 July). Under this condition, the maximum detection range is reduced vis-à-vis the geometric optical sight but the signal intensity is significantly increased at detection range due to mirage formation. Since occurrence of large negative ASTD leading to significant range limitation is improbable in this region, especially in Summer, because of mirage, refraction can be said to globally produce a positive effect on detection. Furthermore, positive ASTD (16 July) makes possible detection beyond-the-horizon, even for small ASTDs. Under these conditions, however, refraction losses, described by refractance in the calculations, reduces transmittance - and thereby detectability - at horizon ranges and further. Tracking beyond the horizon in the IR was achieved more than once at LAPTEX. For the cases considered in our analysis, aerosol extinction did not play a critical role, being of the order of refractance under positive ASTD conditions. Aerosol extinction becomes more significant when the sea gets rough.

In our analysis, MODTRAN calculation globally gave a relatively good description of the transmittance variation versus range. NAM calculation of aerosol extinction was shown to be less than satisfactory, producing however no major impact on total transmittance because of the limited significance of this factor in the selected cases. For the selected cases, very good description of the received signal variation with range is obtained when using IRBLEM with measured aerosol extinction. This leads us to conclude that MODTRAN calculation of molecular transmittance (used in IRBLEM) and the IRBLEM description of refraction effects are valid and of appreciable accuracy. The main source of inaccuracy in the propagation models would then reside in the estimation of aerosol

extinction. Finally, the TRP model developed in Germany proves valid and efficient for carrying out system study in marine conditions when combined with IRBLEM calculations to account for near-sea surface atmospheric effects.

## 7. REFERENCES

1. De Jong, A.N., "LAPTEX, Low Altitude Point Target Experiment, July 96, A Summarized Trials Description", TNO report, FEL-96-1196, 1996
2. De Jong, A.N. and Winkel, J., "LAPTEX point target data analysis", TNO Report FEL-97-A067, 1997
3. Stein, K., "Characteristics of Shipborne Targets in Warm Coastal Environment in Mid and Long Wave IR", Proceedings of SPIE EUROPTO Series, Optics in Atmospheric Propagation and Adaptive Systems, Volume 3219, 1997
4. Dion, D. and Leclerc, B., "Investigation of the Air Refractivity Effects on IR Sensors in the Marine Boundary Layer", DREV-Report-4570/89, 1989
5. Beck, A., Berstein, L.S., Robertson, D.C., "MODTRAN: A Moderate Resolution Model for LOWTRAN 7", Final Report, Spectral Sciences, Inc., Burlington, MA, 1989
6. Dion, D. and Schwering, P., "On the Analysis of Atmospheric Effects on Electro-Optical Sensors in the Marine Surface Layer", (invited paper) IRIS Conference, UK, June 1996
7. Dion, D., "Refraction Effects on EO System Detection Ranges in Coastal Environments", AGARD Conf. Proc. on Propagation Assessment in Coastal Environments, AGARD-CP-567, 1995
8. Schuberth, W., "TRP", FfO Report-1992/20, 1992

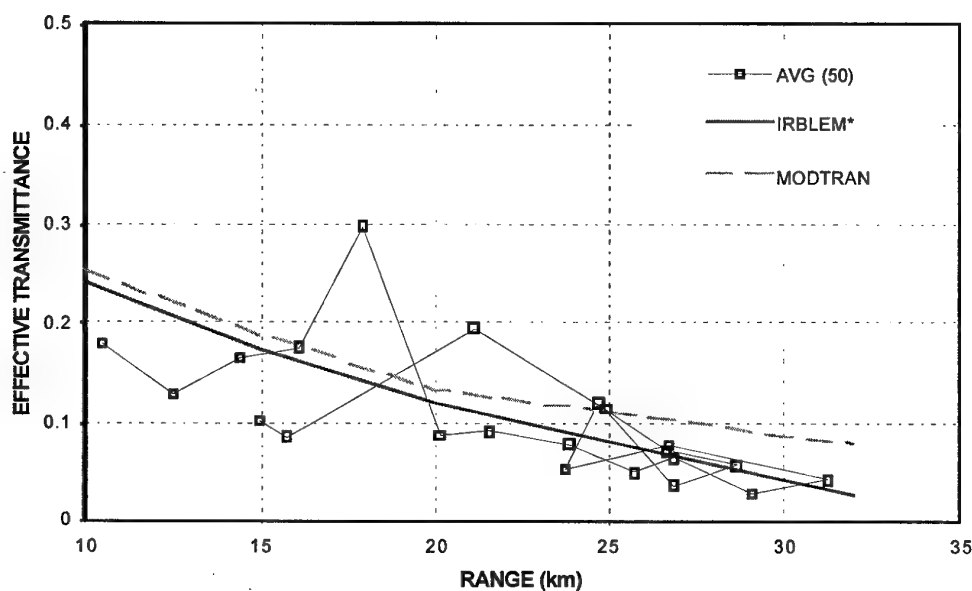


Fig. 2 TNO-FEL measurements in the 3-5 band for 16 July with IRBLEM\* and MODTRAN calculation

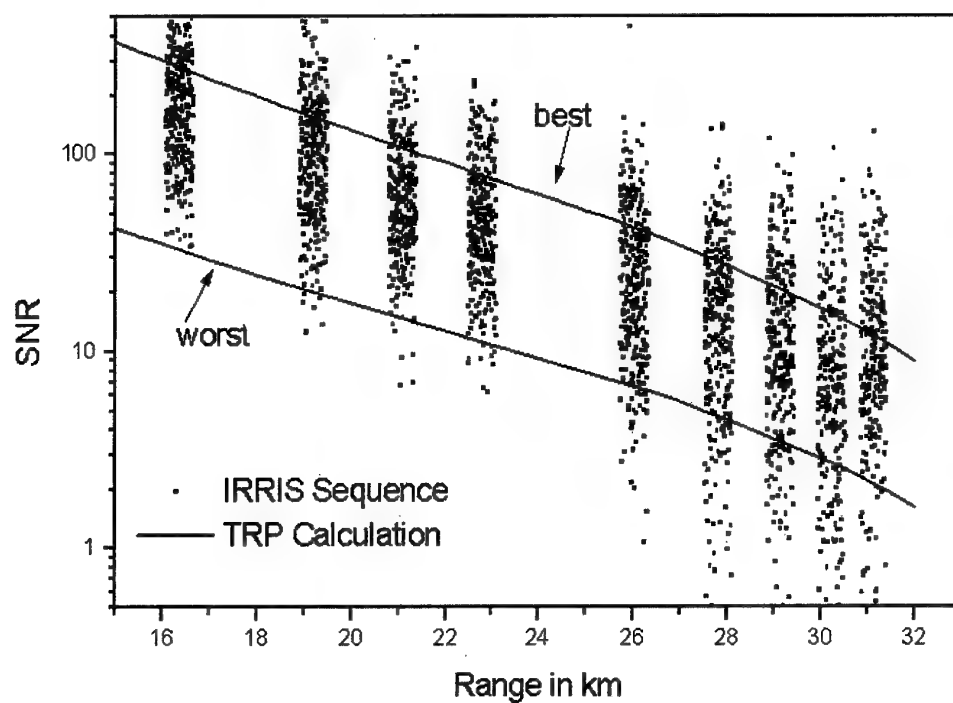


Fig. 3 FfO measurements in the 3-5 band for 16 July with TRP-IRBLEM\* calculation

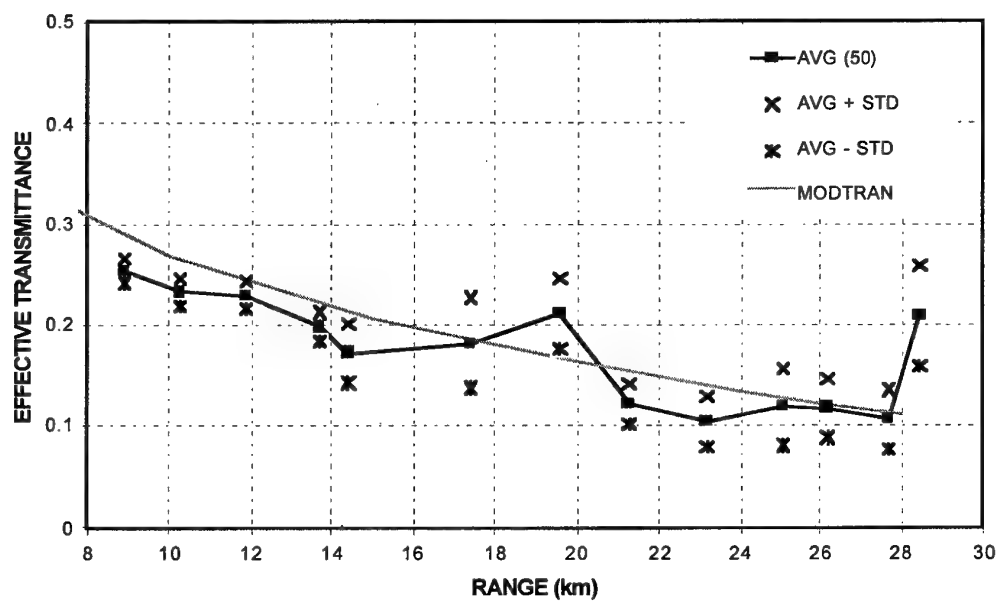


Fig. 4 TNO-FEL measurements in the 3-5 band for 22 July with MODTRAN calculation

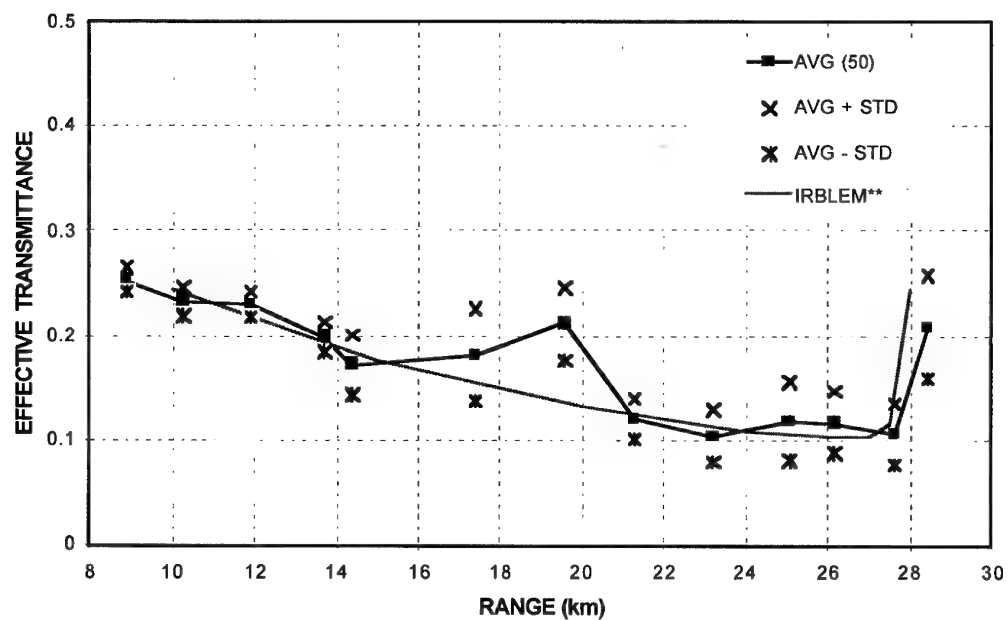


Fig. 5 TNO-FEL measurements in the 3-5 band for 22 July with IRBLEM\*\* calculation

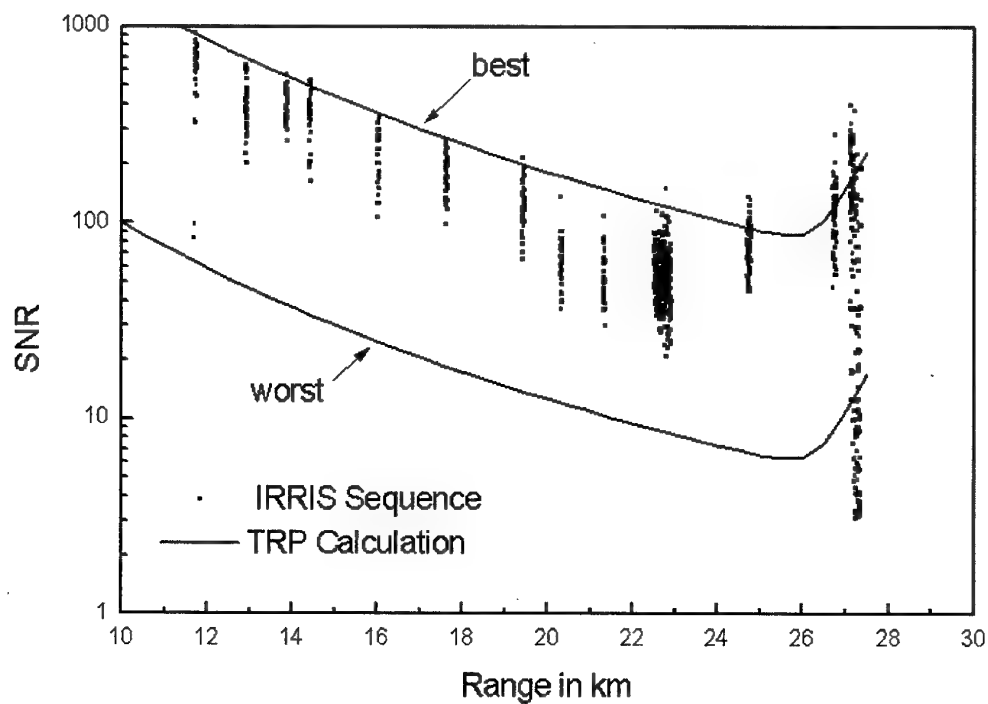


Fig. 6 FFO measurements in the 3-5 band for 22 July with TRP-IRBLEM\*\* calculation

## DEPENDENCE OF AEROSOL SIZE DISTRIBUTION ON DIFFERENT SEA BOTTOM TYPES

A. Zieliński

T. Zieliński

J. Piskozub

Institute of Oceanology, Polish Academy of Sciences  
ul. Powst. Warszawy 55, 81-712 Sopot, Poland

### SUMMARY

In the marine boundary layer over coastal areas aerosol size distribution and aerosol concentration strongly depend on wind speed, direction and duration as well as sea bottom type. Therefore, measurements were carried out in various seasons of the year taking into consideration all the above mentioned factors and different types of sea bottoms. The lidar based investigations of the marine boundary layer were conducted over coastal zones of the southern Baltic Sea.

### 1. INTRODUCTION

Coastal areas as sources of marine aerosols play important roles due to the fact that breaking waves occur in this area even at small wind speeds. Breaking waves create whitecaps and sea-spray droplets which consist of a large number of air bubbles essential for greater production of marine aerosols (Ref 1, 2). Concentration of air bubbles in breaking waves is four times higher in the breaker zone than in the ocean under the same weather conditions. Sea-spray droplets and droplets from bursting bubbles elevated into the marine boundary layer constitute marine aerosol (Ref 3, 4, 5, 6). Such mechanisms and sources of marine aerosols are well described theoretically and well investigated experimentally (Ref 7, 8). Based on results of many research findings, models have appeared dealing with problems of dependence of marine aerosol generation, transport and deposition from the marine boundary layer on various physical parameters of the atmosphere (Ref 9, 10, 11, 12, 13). Especially well described is the dependence of wind speed on concentration and size distribution of marine aerosol over the ocean. Such models, however, can not be directly applied to coastal areas for which only a little data is available. At present, an a full balance of aerosol fluxes in coastal areas can not be done. The available data for such areas are incomplete thus disallowing the determination of dependence of a particularly important parameter, roughness length, on fluxes of emission and deposition of marine aerosols (Ref 14, 15, 16). This parameter, as shown in (Ref 17) for developing and fully

developed roughness, in coastal areas, depends on the slope and shape of the sea bottom and it influences particle deposition velocity (Ref 18). Therefore, in coastal areas, sea bottom type influences deposition fluxes, and indirectly, concentration and size distribution of marine aerosols (Ref 19). The data collected from lidar based investigations were used to determine the influence of the sea bottom type on dynamics of marine aerosol in the marine boundary layer over coastal areas of the southern Baltic Sea under conditions of developing and fully developed roughness. In order to determine such dependencies empirical formulae which describe roughness length parameter were employed to calculate deposition velocities of aerosol particles of various sizes. These formulae include such factors as offshore distance, water depth and friction wind velocity (Ref 17).

### 2. THEORY

Since 1992 measurements have been taken from seven stations on the Polish coast of the Baltic Sea (17+19° E and 54.4+55° N) (Ref 14). The locations of the measuring stations are shown in figure 1.

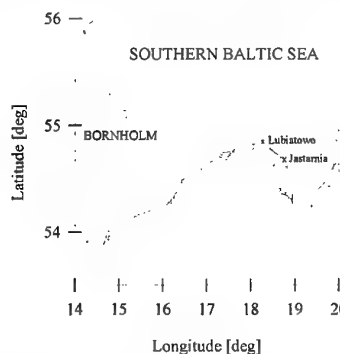


Fig. 1 Location of measuring stations.

The measurements were carried out in different seasons and at different stations in order to detect the influence of the type of wind and sea bottom type on aerosol size distribution and the level of aerosol concentration in the coastal zone. Therefore, wind speed and direction as well as wet and dry-bulb temperatures were recorded, in addition to other supporting information.

The air temperature varied from 278° K to 293° K, while the wind speed varied from 0.5 m/s to 19 m/s and the wind direction varied from NE to SW (Ref 14, 15). For calculations data obtained for southerly (i.e. offshore) winds have been neglected since in such cases the major contribution was from terrigenous and anthropogenic particles.

The lidar system FLS-12 has been installed in a van and stationed on the top of the dunes at a fixed distance of about 30 m from the sea. The inclination of the lidar has been easily changed, which allows for sounding the marine boundary layer at various altitudes. The FLS - 12 is a tunable laser system designed for remote sensing of the air in the VIS range of spectrum (400-670 nm). The source of UV pumping for the dye laser is a XeCl excimer laser (308 nm). The backscattered energy from various distances is collected by a Cassegranian configured telescope, which has a 280 mm diameter primary mirror and it is registered by separate channels of multichannel (8 channels) photoreceiver. A more detailed description of the lidar FLS-12 has been given previously (Ref 14). The backscattered signal was registered every 50 ns, that is every 7.5 m on the optical path. The lidar measurements were calibrated by simultaneous measurements with six stage cascade impactors and a laser particle counter (PMS-Particle Measurement System). The backscattered signal values for all wavelengths served as the basis for the determination of size distribution of aerosol particles and their concentrations at particular altitudes.

The comparative method, introduced by Potter (Ref 20), was used to derive these parameters. It was assumed that aerosols are comprised of optically homogeneous, non-absorbing, spheres, of size  $r \in [r_1, r_2]$ . Therefore, the extinction coefficient in the lidar equation can be defined as follows:

$$\alpha_{ij}(R_i, \lambda_j) = \int_{r_1}^{r_2} Q(r_i, \lambda_j) \cdot S(r) dr \quad (1)$$

where:  $S(r)$ -total, geometric cross-section of aerosol particles per unit volume,  $Q(r, \lambda_j)$ -dimensionless extinction coefficient,  $r$ -particle radius. Thus, the extinction coefficient may be replaced with the scattering coefficient and then functions  $S(r)$  and  $Q(r, \lambda_j)$  can be written as follows:

$$S(r) = a \cdot r^2 e^{(-br)} \quad (2)$$

$$Q(r_i, \lambda_j) = 2 - \frac{4}{\chi} \sin \chi + \frac{4}{\chi^2} (1 - \cos \chi) \quad (3)$$

where:  $\chi = 2\pi x_j (m-1)$ ,  $m$ -relative light refraction coefficient,  $\chi$ -Mie parameter:  $x_j = 2\pi r / \lambda_j$ ,  $a, b$ -distribution parameters. Function  $S(r)$  can be described by the Nakajima-Tanassara distribution

which is widely applied to determine the number of particles in unit volume in the size range from  $r_1$  to  $r_1 + dr$ , therefore,  $S(r) = n(r) = dN/dr$  (Ref 21). The shape of formulae (2) and (3) allow formula (1) to be solved in an analytical form. Formula (1) can also be used to determine the distribution parameters  $a$  and  $b$ . These distribution parameters are then used in the determination of aerosol size distribution and its concentration at particular altitudes for particles of sizes  $r \in [0.5; 5 \mu m]$  as follows:

-total concentration,

$$N_c(z_i, h_i) = \int_{0.5}^r n_r dr = \frac{a(z_i, h_i)}{b^2(z_i, h_i)} e^{[-0.5b(z_i, h_i)]} \quad (4)$$

-particle concentration from the range of sizes  $r_1$  to  $r_1 + dr$ ,

$$N_r(z_i, h_i) = N_c(z_i, h_i) f(r) \quad (5)$$

$f(r)$  is a normalized size distribution function,

$$f(r) = b e^{[-b(z_i, h_i)r]} \quad (6)$$

### 3. RESULTS AND DISCUSSION

For the coastal areas of the southern Baltic Sea in Jastarnia and Lubiato, which are characterized by sea bottom slopes of  $\tan \alpha = 0.014$  and  $\tan \alpha = 0.01$ , respectively, aerosol concentrations were determined in the marine boundary layer as a function of wind speed, direction and duration and under various weather conditions. The profiles of sea bottoms in the investigated area are shown in figure 2.

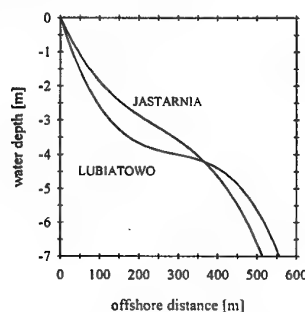


Fig. 2 Profiles of sea bottoms in Jastarnia and Lubiato.

The data collected from lidar based investigations were used to determine the influence of the sea bottom type on marine aerosol concentration, size distribution, and vertical gradients of concentration. Figure 3 shows the variations of total concentration of marine aerosol with wind speed for northerly



winds (i.e. onshore) and for two sea bottom slopes at an altitude of 4 m.

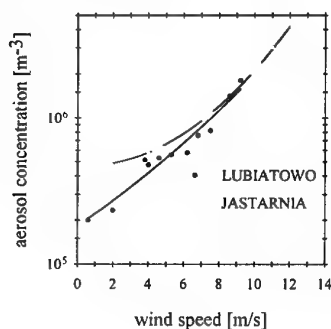


Fig. 3 Variations of aerosol concentration with wind speed.

Figure 3 reveals that in both cases total marine aerosol concentration increases with wind speed. In the range of wind speeds from 1 m/s to approximately 8 m/s the aerosol concentrations in the marine boundary layer were slightly higher for Jastarnia than for Lubiatoowo. The difference is highest at very slow wind speeds almost vanishing at speeds close to 8 m/s. For wind speeds faster than 8 m/s the difference is very small, however, values obtained for Jastarnia are still slightly higher.

A similar situation occurs for changes of total concentration gradient with altitude which is shown in figure 4. The data were collected at wind speeds of 9 m/s.

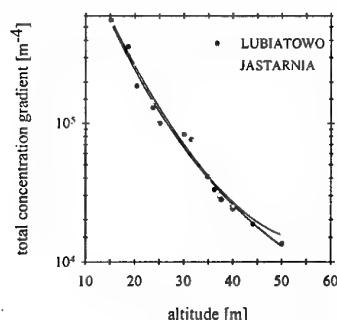


Fig. 4 Variations of aerosol total concentration gradients with altitude.

For both types of sea bottoms the total concentration gradient decreases with altitude and the difference between 10 m and 50 m is of about 1.5 order. There is a detectable difference between both sea bottom types at all altitudes, and values obtained for Jastarnia were slightly higher than for Lubiatoowo, and at altitude of 50 m the difference reached about 20%.

Differences occur when particles of various sizes are compared as in figure 5.

Similarly as in the case of the total concentration gradient, values decrease with altitude at both measuring stations and for particles of both sizes. However, the influence of sea bottom types on concentration gradients is more obvious. At lower altitudes, up to about 20 m, concentration gradients for particles of the same size were comparable at both stations. The difference appears at altitudes above 20 m reaching the magnitude of 2 orders at 50 m. It was revealed that at 50 m particles of size  $2.5 \mu\text{m}$  were practically non-existent in the marine boundary layer over Lubiatoowo, while in Jastarnia their number was still higher than the number of particles of  $1 \mu\text{m}$  in Lubiatoowo.

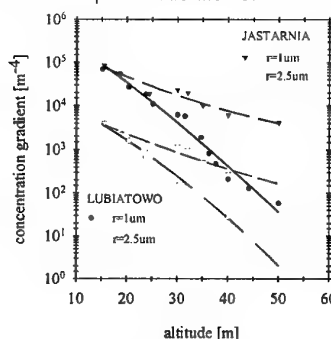


Fig. 5 Variations of aerosol concentration gradients with altitude.

Differences in aerosol concentrations and their gradients determined in marine boundary layers in Lubiatoowo and Jastarnia can be explained by influence of sea bottom type on emission and deposition fluxes of aerosols. These fluxes depend on roughness length parameter, which in coastal areas under various weather conditions is determined by sea bottom slope or water depth (Ref 17). For slow wind speeds, i.e. in the case of developing wavy motion, this parameter is proportional to ratio of the offshore distance and water depth, while for fast wind speeds i.e. fully developed wavy motion, the roughness length parameter is inversely proportional to water depth. For sea bottoms with smaller slopes, under conditions of developing wavy motion, the roughness length parameter is smaller than for sea bottoms with steeper slopes. In the latter case the average emission fluxes are higher than deposition fluxes (Ref 16). The decrease of deposition fluxes is caused by decrease of deposition velocity of particles (Ref 14). For fast wind speeds (fully developed wavy motion) the roughness length parameter is independent of sea bottom slope, and the sea bottom influence on average aerosol fluxes is negligible. By assuming that the average aerosol concentration in the marine boundary layer over the coastal area is a result of the balance of the two above mentioned fluxes, the differences of

concentrations at slow wind speeds and small differences at fast wind speeds shown in figure 3 can be easily explained. Changes of aerosol concentration gradients with altitude in Lubiatowo and Jastarnia (figures 4 and 5) were caused mainly by deposition fluxes, whose values linearly depended on particle deposition velocity. Such variations in size distribution are presented in figure 6. Data were collected at wind speeds of 9 m/s and at a distance of 100 m offshore.

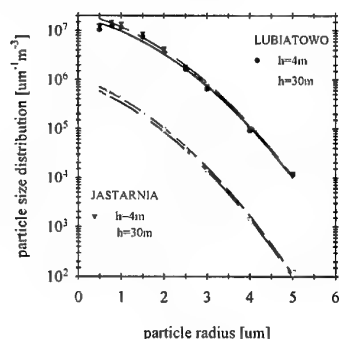


Fig. 6 Variations of aerosol size distribution with altitude.

In both cases at altitudes of 4 m and 30 m differences occur in size distribution for particles of radii ranging from 0.5  $\mu\text{m}$  to 2.5  $\mu\text{m}$ . These differences confirm the sea bottom influence on aerosol concentration. For particles of radii greater than 2.5  $\mu\text{m}$  these differences vanish, which means that the sea bottom influence on concentration of such particles in marine boundary layer in coastal areas is very small. Fluxes of such particles, due to relatively fast deposition velocity, (Ref 15) cause the fast decrease of particle concentration with altitude. This causes changes in size distribution of aerosols produced from over sea bottoms of various slopes with altitude and under various weather conditions.

Figure 7 presents variations of distribution parameter  $b$  with wind speed at three chosen altitudes at Lubiatowo and Jastarnia.

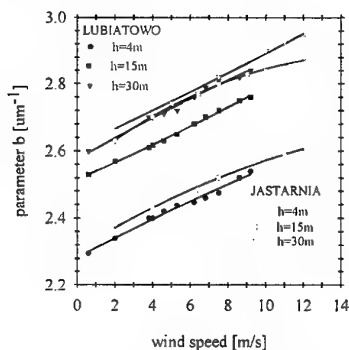


Fig. 7 Variations of distribution parameter  $b$  with wind speed and altitude.

In all cases values of distribution parameter  $b$  increase with wind speed, however there are significant differences with altitude and for both sea bottom slopes. The highest values were obtained for Jastarnia at 30 m and 15 m. They differ by about  $0.04 \mu\text{m}^{-1}$ . In the case of Lubiatowo values of parameter  $b$  at 30 m were comparable with Jastarnia at 15 m. Lubiatowo values at 15 m were lower by about  $0.08 \mu\text{m}^{-1}$  when compared with those at 30 m. At altitudes of 4 m parameter  $b$  was higher in Jastarnia than in Lubiatowo ( $0.04 \mu\text{m}^{-1}$ ) and the difference with altitude of 30 m reached  $0.24 \mu\text{m}^{-1}$ . Differences of distribution parameter  $b$  confirm that under the same weather conditions in marine boundary layers of Lubiatowo and Jastarnia generated marine aerosol is characterized by different size distribution. The maximum concentration occurs at  $r_m = 2/b$ . Figure 8 shows variations of aerosol concentrations as a function of particle size, at wind speed of 9 m/s, and altitudes of 4 m and 30 m in marine boundary layers of Lubiatowo and Jastarnia.

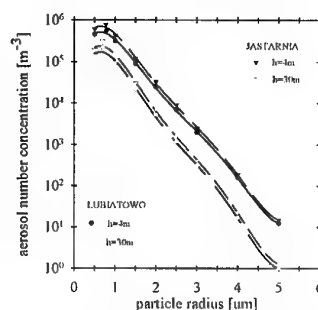


Fig. 8 Variations of aerosol number concentration with altitude.

This figure reveals the distinct maxima of aerosol size distribution in the investigated areas. With an increase of altitude these maxima shift towards particles of smaller sizes, which confirms the role of emission flux in the production of marine aerosols from over various sea bottom types. Also, a clear influence of sea bottom slope on aerosol concentration occurs. In Jastarnia, the average aerosol concentration is higher than in Lubiatowo under the same weather conditions. This means that with smaller sea bottom slope the marine aerosol concentration in coastal area increases. Similar results were obtained by Chomka and Petelski (Ref 16).

#### 4. CONCLUSIONS

Experimental results obtained for marine aerosol concentration in marine boundary layers of coastal areas show that sea bottom types influence both aerosol concentration and their size distribution.

Concentrations are higher for sea bottoms of smaller slopes than for bottoms of steeper slopes, under the same weather conditions. The maximum of aerosol size distribution is shifted towards smaller particles.

## 5. REFERENCES

1. Monahan E. C., Mac Niocall G., "Oceanic whitecaps and their role in air-sea exchange processes", D. Reidel Publ. Comp. Dordrecht, Holland, 1986, pp 129.
2. Resch, F. J., "Influence of wind generated spray on evaporation", J. Geophys. Res., 94, 1989, pp 909-918.
3. Resch F. J., Darozzes S. J., Afeti G., M., "Marine liquid aerosol production from bursting of air bubbles", J. Geophys. Res., 91, 1986, pp 1019-1029.
4. Blanchard D. C., Syzdek L. D., "Film drop production as a function of bubble size", J. Geophys. Res., 93, 1988, pp 3649-3654.
5. Wu J., "Bubbles in the near-surface ocean. A general description", J. Geophys. Res., 93, 1988, pp 587-590.
6. Wu J., "Comment on Film drop production as a function of bubble size" by D. C. Blanchard and Syzdek. J. Geophys. Res., 95, 1990, pp 7389-7391.
7. Monahan E. C., Spil D. E., Dawisan K. L., "Model of marine aerosol generation via whitecaps and wave distribution", 9th Conference on Aerospace and Aeronautical Meteorology, Omaha, Preprint volume, 1983, pp 147-158.
8. Wu J., "Bubble flux and marine aerosol spectra under various wind velocities", J. Geophys. Res., 97, 1992, pp 2327-2333.
9. Burk, S. D., "The generation, transport and deposition of marine aerosols, a turbulent modeling study" in Oceanic Whitecaps ed. E. C. Monahan and G. MacNiocall., D. Reidel Norwell Mass., 1986, pp 267-268.
10. Fairall C. W., Davidson K. L., "Dynamics and modelling of aerosols in the marine atmosphere boundary layer. in Oceanic whitecaps and their role in air-sea exchange processes", 1986, pp 195-208.
11. Fitzgerald J. M., "Numerical simulation of the evolution of the aerosol size distribution in a remote marine boundary layer" in Nucleation and Atmospheric Aerosols. ed. N. Fukuta and P. E. Wagner, A. Depak, Hampton, Va., 1992, pp 157-160.
12. Van Eijk A., G. de Leeuw, (1992), Modelling aerosol size distribution over the North Sea, J. Geophys. Res., 97, 14417-14429.
13. Gong, L. S., Barrie, A. L., Blanchet, P. J., "Modelling sea-salt aerosols in the atmosphere. 1 Model development". J. Geophys. Res., 102, 1997, pp 3805-3818.
14. Zieliński A., Zieliński T., "Aerosol fluxes and their gradients in the marine boundary layer over the coastal zone", Bulletin of the Polish Academy of Sciences, Earth Sciences, Vol. 44, No. 4, 1996, pp 203-211.
15. Zieliński T., "Aerosol masses and mass gradients in the marine boundary layer over the breaker zone", Oceanologia, 39 (3), 1997, pp 201-209.
16. Chomka M., Petelski T., "Modelling the sea aerosol emission in the coastal zone", Oceanologia, 39 (3), 1997, pp 211-225.
17. Panin G. N., Krivickij C. W., "Aerodinamicheskaja sherohovodnost povierhnosti vodojema", Izd. RAN, IWP, Moskwa, 1992, pp 134.
18. Carruthers D. J., Choularton T. C., "The microstructure of hill cap clouds", Quart. J. R. Met. Soc., 112, 1986, pp 113-129.
19. Zieliński A., Zieliński T., Piskozub J., "Aerosol size distribution function in the coastal area", Journal of Aerosol Science, Vol. 28, Suppl. 1, 1997, pp 41-42.
20. Potter J., "Two-frequency lidar inversion technique", Appl. Opt., 26 (7), 1987, pp 1250-1256.
21. Wells W. C., Gal G., Munn T. W., "Aerosol distribution in maritime air and predicted scattering coefficients in infrared", Appl. Opt., 16 (3), 1977, pp 634-659.

## ACKNOWLEDGEMENTS

This research is part of the State Committee for Scientific Research, Grant No. 6 P04E 03611.

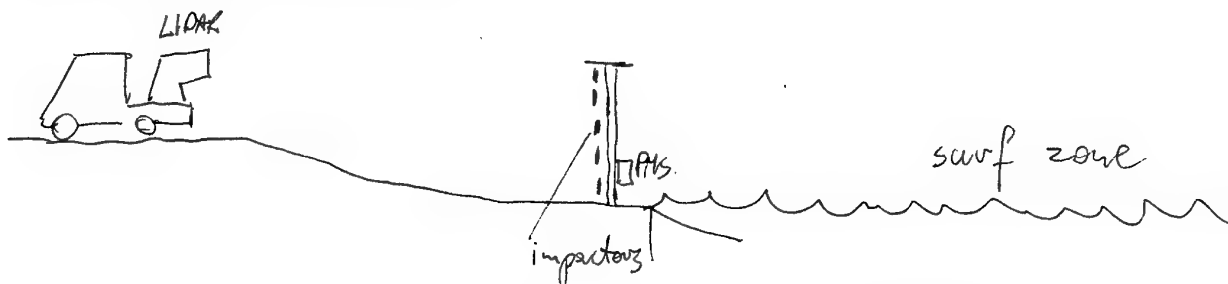
PAPER No. 38

DISCUSSOR'S NAME: C. R. Philbrick

COMMENT/QUESTION:

Please describe the geometrical arrangement of the experiment. How was the experiment arranged relative to the surf zone? Was it the same at both locations?

AUTHOR/PRESENTER'S REPLY:



In both cases the lidar and other supporting equipment was at fixed positions (distances) from the surf zone. the lidar was shot from the van across the surf zone reaching distances up to 600 - 700m, far beyond the surf zone range. The lidar was used at various altitudes (changeable system).

DISCUSSOR'S NAME: S. Gathman

COMMENT/QUESTION:

Is the land topography the same in both measurement sites?

AUTHOR/PRESENTER'S REPLY:

The land topography is the same in both measurement sites. There is a beach of about 40 to 60m wide and forest areas starting from the dunes going inland. The height of the trees is about + 5  $\frac{4}{5}$  6m.

PAPER No. 38

DISCUSSOR'S NAME: G. de Leeuw

COMMENT/QUESTION:

For a similar wave field, different sea bottom slopes will result in different widths of the breaker zone. Since the measurements were made at 100m from the beach, the wider surf zone will result in a more developed surf plume and hence higher concentrations at higher levels than for the narrower breaker zone. Hence the measured concentration differences at higher levels are rather a transport issue than a sea bottom issue.

AUTHOR/PRESENTER'S REPLY:

In all presented cases wind speed and direction were the same, therefore wave breaking was due to sea bottom conditions and the ranges of breaking zones were comparable. These results are being processed and they will be verified with the Chomka Model of Wave Energy Dissipation.

## HADES: Hot And Dusty Environment Survey.

A. R. TOOTH,  
Sowerby Research Centre, British Aerospace,  
Filton, Bristol, BS12 7QW, England.

J. ROGGE,  
Royal Military Academy,  
PO Box 90154,  
4800 RG Breda,  
The Netherlands.

### Abstract.

The possibility of future military conflicts in geographical regions that could be classified as 'desert' was, and remains, of growing concern to all NATO nations. The major concern related to military operations in desert environments was the effect of 'obscuration' caused by an increased dust loading of the atmosphere – the increased dust loading being primarily due to the movement of personnel and vehicles, the impact of artillery barrages, and the detonation of explosive devices such as mines.

The duration of the increased atmospheric dust loading depends on prevailing ambient conditions and the characteristics of the dust such as particle size. The effect of the suspended dust is to reduce the ability of electro-magnetic energy to propagate through the atmosphere and has the capability of denying 'lines of sight' between opposing forces thereby reducing the effectiveness of military sighting systems and communication links.

This paper is based on a joint survey called HADES, (Hot And Dusty Environment Survey), which was initiated by the delegates of the former Research Study Group RSG 15 of NATO (DRG) Panel 4. The aim was to review and, where possible, assess the effect of desert environments on military operations. Systems operating at wavelengths ranging from the visible through the infrared out to the milli-metric frequencies were of greatest concern.

### 1. Introduction.

This paper describes a survey that was conducted during 1994 and 1995 by the members of the former NATO Research Study Group AC/243 (Panel 4/RSG 15) on 'the characterisation of battle effects and related measurement techniques'. The group was concerned that the designers, evaluators, and users of military systems had insufficient information that related military electro-optical systems to their performance in hot and dusty environments. A survey, called HADES (Hot And Dusty Environment Survey), was initiated by the group and an overview of it is now reported.

During the course of the survey, possibly hundreds of documents were examined and their salient features used during the compilation of the final report. Classified reports were intentionally not reviewed, from the outset of the survey it was decided that the report should not contain any classified material. It was considered that this, acceptable omission, would enable the report and its findings to be distributed to the widest possible NATO audience without undue difficulty. Additionally, all of the references that have been quoted should be straightforwardly available.

The HADES report has been designed to present information primarily to the following groups of people: the Defence Research Group (DRG), Ministries and Departments of Defence, scientists, and military users.

### 2. Survey Rationale.

The possibility of future military conflicts in geographical regions that could be classified as 'desert' (hot and dusty rather than polar deserts) was, and remains, of concern to all NATO nations. The major concern related to military operations in desert environments was the effect of obscuration that is caused by an increased dust loading of the atmosphere. The increased amount of dust being primarily due to the movement of personnel and vehicles, the impact of artillery barrages, and the detonation of explosive devices such as mines. All of these rudimentary military activities have the capability of generating large quantities of dust which is subsequently lofted into the air. The dust can remain suspended in the atmosphere for varying amounts of time. The period of suspension depends on the prevailing ambient conditions, including meteorology, and the characteristics of the dust such as its particle size. The suspended dust reduces the propagation of electromagnetic energy through the atmosphere and has the capability of denying lines of sight between opposing forces thereby reducing the effectiveness of military sighting, aiming, tracking systems, and other 'communication' links.

The joint survey was designed to review existing material, and where possible assess the effects of desert

environments on military electro-optical systems. In particular, systems operating at wavelengths ranging from the visible through the infrared out to the millimetric wavelengths were of greatest concern.

### 3. Objectives of HADES.

The broad objectives of HADES were as follows:

- To characterise the desert (hot and dusty) environment in terms of its meteorology, and locate regions which exhibit such characteristics.
- To study the effects of desert environments on military electro-optical systems.
- To review the military implications of operations in desert environments.
- To identify where there is currently a lack of data available for desert environments and to indicate possible studies to help resolve the lack of appropriate data.

### 4. Scope of the Survey.

HADES was conducted over a two year period and involved Denmark, France, Germany, the Netherlands, United Kingdom and the United States.

Apart from the reviewing and assessment of many technical reports during the survey, detailed discussions were held with 'military advisors', primarily from the UK, who had direct experience of military operations in deserts. The results from these discussions, where relevant to the survey, have been included in the report. However some of the information that was provided can only be classified as 'anecdotal' and cannot be numerically substantiated.

It was immediately apparent, at the outset of the survey, that a considerable amount of relevant experimentation had already been conducted by various organisations. During the survey details of the majority of this experimentation was reviewed and reported on. In addition equations and models that had been developed were also reported and, where appropriate, examples of their use are given.

The report contains details of what constitutes a desert, and examples of the variability of different meteorological effects, such as temperature, humidity, visibility, atmospheric transmission etc, that can be expected in several specific locations are given.

Sections of the report are devoted to the characteristics of: desert environments, terrain and backgrounds, the natural (desert) atmosphere, and the battlespace atmosphere. Details of models for the prediction of desert related effects, and details of previous measurement programmes are also reported. However

the three most important sections are the Conclusions, Military Implications, and the Recommendations. Only details of these sections are given in this overview paper.

### 5. Conclusions.

The two most important conclusions that were drawn from the survey are:

1. Military operations in desert regions will be severely hampered by the environment. Although the above statement is perhaps obvious its importance is fundamental and should not be either taken for granted or underestimated.

Loose, dry surface dust will be lofted into the air by wind, vehicular movement (ground and low flying air activities), explosions or shockwaves from gunfire and missile launch. The atmospheric dust loading will be increased – all aspects of electro-optical system performance that rely on the propagation of electromagnetic energy through the atmosphere will be degraded.

In addition abrasion will occur to the optical surfaces of the sensors which are being deployed. Heat, dust and temperature changes will also have adverse effects on equipment reliability and will reduce the effectiveness of personnel.

2. Experimentation has shown that the effects of dust can be very different in areas that initially appear to be similar.

The dust which is produced, generally, has a broad particle size distribution however this distribution will greatly vary in different geographical areas. This variation will alter the obscuration characteristics of the atmosphere in terms of increased absorption and scattering which reduces atmospheric transmission.

Some locations although not explicitly considered to be desert (hot and dusty) can exhibit such characteristics under exceptional conditions, such as drought. Conditions such as these were experienced during the NATO BEST TWO trial which was conducted during August 1990 at Camp Mourmelon (150 km North East of Paris), France. During the trial dust conditions were unexpectedly experienced that were equal to any of the trials that were specifically designed for dust evaluations. These locations were not explicitly considered during this survey due to their unpredictability, although they should not be forgotten as their potential impact on any military operations in such areas could be severe.

### 6. Military Implications.

The most important military implications of the effect of dust are:

- a. The loss of target acquisition capability – targets will be masked inside and behind dust clouds in the visual and thermal wavebands.
- b. The loss of guided munition line of sight – increased dust loadings will reduce atmospheric transmission which will lead to a degradation of system performance.

However there is also a positive effect of vehicular dust; the long range detection of moving targets can be enhanced due to the cueing effects of the dust clouds that are created. For the shorter range detections it has been observed that the contrast of targets in front of the dust cloud is sometimes enhanced. The visualisation of the effect is different in the 3 to 5  $\mu\text{m}$  and the 8 to 12  $\mu\text{m}$  wavebands.

Although conditions that lead to increased dust loadings and the subsequent possible reduction in system performance are commonly found in desert type environments, such conditions can be found elsewhere. On many occasions, significant dust loadings can occur unexpectedly in non-desert locations (even in Europe), and it is essential that such eventualities are not underestimated.

Examination of experimental results indicates that due to the broad range of particle sizes contained within a dust cloud, all of the wavelengths from the visible to the far infrared will be similarly affected. However, under some conditions the longer wavelengths will be advantageous in desert environments.

Millimetre wavelength systems are only momentarily affected during the initial stages of an explosion when there are large particles present in the atmosphere. The larger particles quickly 'precipitate' from the dust cloud and at that time propagation through the cloud, at millimetre wavelengths, returns to normal.

Climatic conditions can be severe. Day time temperatures can be in the order of 40 to 50°C and the annual diurnal variation can vary by up to 80°C. Fierce winds can reach 35 m/s causing sand storms. The effects of such storms can be extensive and visibility impaired for significant periods of time. Dust storms can render all ground movements and low flying activities difficult and often impossible.

Dust can reduce the cross-country capability of combat vehicles and can damage weapons and equipment. The ingress of dust can significantly increase wear and tear on assemblies and sub-assemblies which leads to a need for more frequent technical servicing, and this, together with the logistic difficulties, imposes enormous demands on maintenance, and technical support. There is therefore an increased premium on equipment reliability and self sufficiency.

## 7. Recommendations.

The final objective of HADES was to identify where there is currently a lack of data available for desert environments, and to indicate where future experimentation is necessary in order to resolve the omissions. The following recommendations are considered to be appropriate:

- In order to provide the military user with the necessary information on the characteristics and the consequences of increased atmospheric dust loadings, it is recommended that studies should be conducted to characterise the different soil and dust types that are found in different geographical areas and to relate them to propagation effects in different wavebands. Ideally such a survey should cover world wide locations but could be realistically restricted to potential areas of conflict. It is considered that some of the required data are already available, albeit in many different reports.
- The potential exists for incorporating such characterisation data in Tactical Decision Aids (TDAs) which would aid the military users to assess their vulnerability to dust effects. With military assistance and guidance a Handbook on 'out-of-area' operations, in desert environments which would augment such TDAs could be developed.
- Collaboration is required for the evaluation of the operational performance of the next generation thermal imaging equipment and laser systems against increased atmospheric dust loading and other obscurants.
- Advances in weapon system technology may require more sophisticated models to assess their theoretical performance. In particular, an increased knowledge of multiple scattering, absorption, and emission within obscurant clouds will most likely be necessary.
- There is a need to establish the effects of obscurants on the electro-optical detection of moving targets. In particular there is a need to determine the search effectiveness of electro-optic sensors obscured environments. Data is required that allow search models to be further developed and validated. Data is also required for the analysis of the probability of detection, recognition and identification of targets moving in and out of defilade in clear and obscured environments.
- Many studies and experiments have been conducted that might partially resolve current and future requirements. It is considered essential that the data and subsequent results from those studies are not lost during the current reductions in defence spending. The effective use of data



repositories, such as the Atmospheric Aerosols and Optics Data Library (AAODL), should be encouraged.

#### **8. HADES Report Availability.**

The HADES report has been issued by NATO, the reference number is AC/243 (Panel 4) TR/19. Copies of the HADES report are available to NATO countries and requests for further information should be made directly through the appropriate national delegates.

#### **Acknowledgements.**

The authors of this review paper and the HADES report are firstly indebted to Dr. F.E. Niles, Senior US delegate of NATO Panel 4 Research Study Group 15 and Director (now retired) of the Atmosphere Simulation Division, Battlefield Environment Directorate, US Army Research Laboratory, White Sands Missile Range, New Mexico, USA, for guidance and access to his library of dust related material, and secondly to Dr. Roger Davis and his staff at the Science and Technology Corporation, Las Cruces, New Mexico, USA for their help in providing documentation and technical assistance. The members of NATO AC/243 (Panel 4 RSG. 15) are also thanked for their support.

Finally the authors would like to thank Dr. H.T.A. Pentecost (UK Senior delegate of RSG 15) of the Defence Research Agency, Fort Halstead, United Kingdom, for his support and assistance during the survey.

PAPER No.: 39

DISCUSSOR'S NAME: D. Clement

#### **COMMENT/QUESTION:**

Your message is clear. Implications appear to be significant. Could you report on any responses you received from the user community?

#### **AUTHOR/PRESENTER'S REPLY:**

The majority of responses have come from the weapon system community. Their interest was how much will the performance of systems be degraded in desert type climates.

PAPER No. 39

DISCUSSOR'S NAME: G. P. Anderson

COMMENT/QUESTION:

Are there any implications from the HADES study regarding the development and/or advantages for dust mitigation?

AUTHOR/PRESENTER'S REPLY:

The HADES report does not include information on dust mitigation. However, during the survey we found that some "traficability" trials had been conducted. The results from these trials are outlined and referenced in the final report.

There appears to be two related problems:

1. If you minimize the amount of dust generated/lofted into the air the visual/thermal signature becomes clearer and easier to acquire and recognise the target.
2. If you allow the dust to be naturally lofted into the air the detection of the vehicle improves.

## ATMOSPHERIC OPTICAL EXTINCTION MEASURED BY LIDAR

C. Russell Philbrick  
Daniel B. Lysak, Jr  
Applied Research Laboratory  
Penn State University  
PO Box 30  
State College PA 16804, USA

### SUMMARY

Two independent lidar techniques, one using Raman scatter in a monostatic configuration and one using the polarization ratio of the scattering phase function in a bistatic configuration have been developed to determine the optical properties in the lower atmosphere. The direct backscatter measured at the transmit wavelength of a monostatic lidar has been found to have limited utility in describing the important parameters because the measurement is a mixture of signals from molecular and particle scattering. A bistatic lidar technique has been used to demonstrate that useful information on number, size and distribution of particles is contained in measurements of the polarization ratio of the scattering phase function. An independent Raman lidar technique can be used to provide measurements of the molecular scattering profiles at several wavelengths through the lower atmosphere. The departures of the signal profile from the molecular density gradient then provide a direct measure of the optical extinction. The optical extinction profiles at visible and ultraviolet wavelengths are routinely measured today using Raman lidar.

### INTRODUCTION

We have been able to demonstrate that it is possible to measure the optical extinction and describe changes in the particle number, size, and distribution width of the optical scattering components using a bistatic lidar in the lower atmosphere [1, 2, 3]. The measurements were made using signals from a bistatic lidar technique which measures the polarization ratio of the scattering phase function. Additionally, the profiles of molecular species measured by Raman lidar techniques directly provide a measurement of the optical extinction from the gradients in the profile [4,5,6]. The Raman return signals scattered of the  $N_2$  and  $O_2$  components in the atmosphere

differ from the density scale height only by the extinction due to scattering losses along the transmitted and received paths. The factors which cause the extinction are particle scattering, molecular scattering and absorption. The scattering losses expected from molecular extinction are known directly from the density scale height and the molecular scattering cross sections of nitrogen and oxygen. The scattering losses from the particle component of the atmosphere can be separated by examining the gradient in the signal compared to the density gradient, thus providing extinction profiles of the particle scattering component of the lower atmosphere. The technique is able to provide the extinction profiles through clouds, as long as any signal remains to be detected. Many cases of cloud measurements have been obtained which have optical extinction coefficients up to the ranging up to  $10 \text{ km}^{-1}$ .

The profiles from the rotational Raman scattered signal at 530 nm (from the 532 nm transmitted beam of the 2<sup>nd</sup> harmonic of the Nd:YAG laser) provide a direct measure of the atmospheric aerosol extinction component at mid-visible wavelengths. The vibrational Raman 1<sup>st</sup> Stokes scatter signal from molecular nitrogen at 607 nm provides the simultaneous extinction at a second wavelength, which is sensitive to a slightly different size particle. The same measurement can be made from the rotational Raman scatter at other laser wavelengths from the 3<sup>rd</sup> or 4<sup>th</sup> harmonics of the laser transmitter (355 nm and 266 nm for the Nd:YAG laser). Example cases are used to describe the atmospheric optical properties using three wavelengths, 285, 530 and 607 nm.

### OPTICAL EXTINCTION FROM BISTATIC LIDAR SCATTERING PHASE FUNCTION

Single ended remote sensing instruments, whether using lasers, radars, or microwaves, have difficulties determining absolute extinction from

backscattered signals along a propagation path. This is due to the large variations in the ratio of the extinction (forward scattering) to the backward scattering components from different particle size distributions [7]. The bistatic linear array receiver was developed to provide useful information on the scattering phase function of the aerosols [1,2,3]. The bistatic remote receiver utilizes a linear photodiode array to image the radiation scattered from any high power CW or pulsed laser system. By observing the angular scattering variation along a horizontal path, where the distribution of scattering particles is relatively uniform, additional information that is obtained from the scattering angle phase function can. We have demonstrated a new technique to estimate particle density, size and distribution widths (of spherical scatters) by use of the unique information contained in the polarization ratio of the scattering phase function versus angle obtained from the ratio of signals parallel and perpendicular to the scattering plane.

Previous experiments with the bistatic lidar technique have used a scanning laser beam to attempt to reconstruct a scattering phase function from tropospheric aerosols [8,9,10]. The measurement technique presented in this paper does not attempt to reconstruct a scattering phase function of the particles. Instead, a ratio is obtained from the image of the scattering signal of two orthogonal polarization components as a function of angle, one in the scattering plane and one perpendicular to the scattering plane along a horizontal path, as shown in Figure 1. The use of a ratio cancels the effects of many measurement problems, including detector linearity and extinction differences due to different path lengths for each scattering angle. Figure 1 demonstrates the ability of the bistatic receiver to simultaneously image the backscattered radiation from an angle range of  $155^\circ$  to  $180^\circ$ , where the scattering function is most sensitive to the size of the particles. The assumption of a uniform horizontal path was verified with horizontal extinction profiles from the Raman lidar analysis during each data set [4,5]. The Penn State LAMP lidar [6] was alternately operated on a horizontal path and a vertical path. The LAMP lidar collected rotational Raman temperature profiles, vibrational Raman water vapor profiles, vibrational Raman nitrogen profiles, and aerosol/molecular scattering profiles at the fundamental laser wavelength of 532 nm, while the bistatic detector measured the angular scattering. The first tests of this measurement

technique were conducted in September 1995, during the CASE I (Coastal Aerosol Scattering Experiment) at Wallops Island, Virginia. This location was chosen for its humid coastal/marine environment and for an unobstructed 3.28 km horizontal path over a salt marsh. One of the goals of this research was to determine how well Mie theory [11], with a lognormal distribution of scatterers would describe actual aerosol data, in a humid coastal/marine environment [12]. Analysis of the data was made using a 9 parameter optimization fit of the polarization ratio versus angle from a model of polarization ratio from Mie scattering theory with trimodal lognormal size groups defined by size, width and number density in each group. The molecular scattering component had to also be added to the aerosol distribution model to obtain a satisfactory set of aerosol fit parameters. A polarizer was used on the receiver to measure the cross polarization to estimate the amount of multiple scattering and nonsphericity of the particles in the scattering volume. Results, which can be represented by trimodal lognormal size distributions, were obtained from both clear and hazy/misty nights. Extinction calculated from the size distributions has been compared with extinction from the Raman lidar at two different wavelengths. On calm evenings with high humidity and decreasing temperature, the inversions also show increasing particle sizes consistent with radiation fog formation. The results show remarkable agreement with a tri-modal aerosol distribution when using a spherical scattering model (Mie theory).

The measurements were made on a horizontal path under low wind and stable conditions so that the particle distribution should have been uniform as a function of angle. The analysis for the experiments performed required the assumption that the particle size and density were stable for more than 15 seconds, the minimum time to obtain a data set, and uniform over a scale of about 500 meters, the path corresponding to the range of scattering angles used,  $150$  to  $175^\circ$ . The magnitude of the scattered signal was nearly constant over the range of angles because the increase in surface brightness due to compression of the image on the detector off-sets the  $1/R^2$  decrease from the greater distance.

An example of the bistatic measurement technique is shown in Figure 2a, with the best fit of the model, and the corresponding trimodal distribution in Figure 2b. The time sequence of the changing

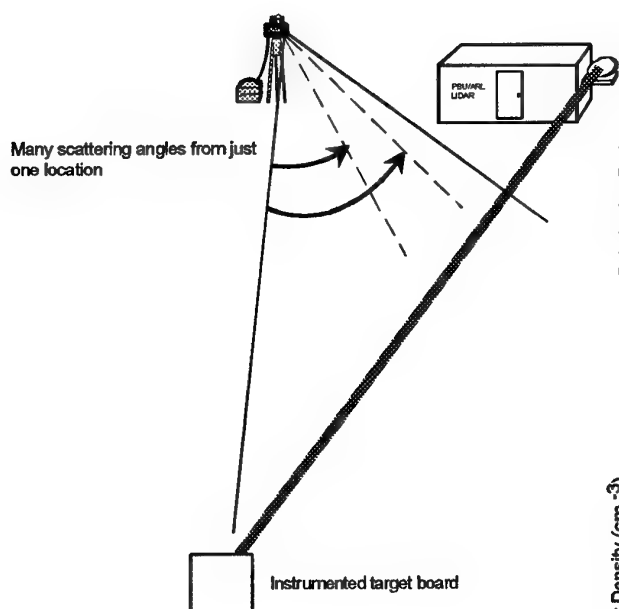


Figure 1. By operating in the horizontal mode, the bistatic lidar is able to collect radiation from many scattering angles, between  $155^\circ$  and  $180^\circ$ , from just one location.

particle size was followed over a period of several hours during this evening while the temperature decreased and the extinction increased as a radiative fog formed. The second mode of the distribution was found to narrow in distribution width as it increased from a radius of  $0.166 \mu\text{m}$  to  $0.237 \mu\text{m}$ . At the same time the third mode increased from a radius of  $6.46 \mu\text{m}$  to  $8.91 \mu\text{m}$ . This data set is most striking because the model follows almost every contour in the data between  $155^\circ$  and  $180^\circ$  as seen in Figure 2a. Not only does the model fit the data almost perfectly as the mode radii increased, but the calculated extinction coefficients are also the same as those measured by the Raman lidar. The extinction values from the calculated size distribution and the extinction values calculated from the Raman lidar profile at wavelengths of 532 and 607 nm are shown in Figure 2a. Figure 2b shows the particle properties derived for the data in the upper panel.

### OPTICAL EXTINCTION FROM RAMAN LIDAR

The molecular profiles from the Raman scatter signals provide direct measurements of the optical extinction. Figure 3 shows the visible and uv profiles measured when a thin cloud is present.

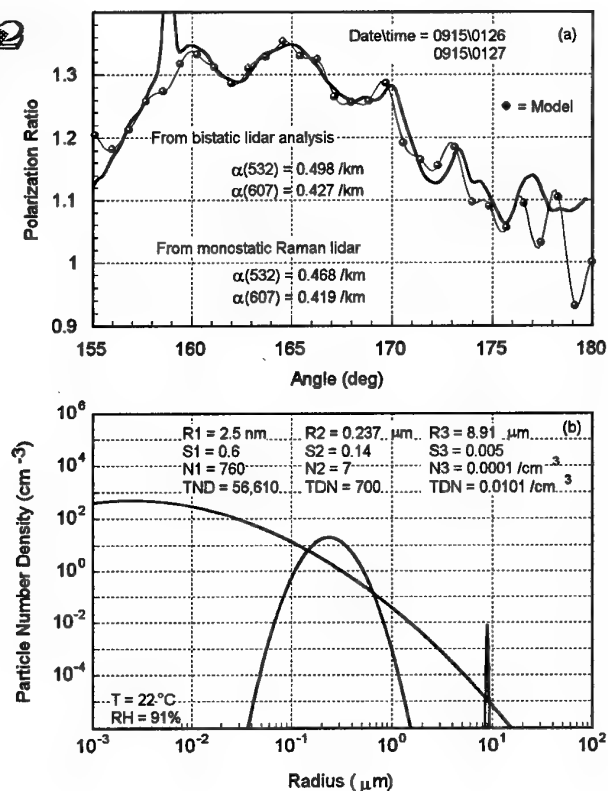


Figure 2. (a) An example of the bistatic lidar measurement technique, showing the best fit result from the ratio of the polarization scattering function versus angle from a Mie scattering theory model. The feature at  $159^\circ$  is due to a glint from an insect. The signal beyond  $175^\circ$  is ignored since these correspond to the last 2 km of the 3.2 km path. (b) The lognormal size distribution and density determined from the model fit to the data shown. The extinction values calculated from the particle distributions shown in (b) are listed in the panel (a) and compared with the simultaneously determined extinction from the Raman lidar analysis. The radiation fog mean radius grew from  $6.46 \mu\text{m}$  to  $8.91 \mu\text{m}$  in 2.5 hours (see Stevens dissertation [1] for several additional examples).

The signal from the fundamental transmitted wavelength at 532 nm exhibits a profile of combined molecular and particle scattering that is difficult to analyze for significant properties, except cloud height. However, analysis of the Raman signals can provide unique vertical profiles of the optical extinction.

The LAMP (Lidar Atmospheric Measurements Profiler) and LAPS (Lidar Atmospheric Profile Sensor) instruments use the molecular scattering properties of the species in the lower atmosphere to simultaneously measure profiles of ozone, water vapor, temperature, and optical extinction. The measurements can be made both daytime and nighttime because of the capability of the instrument to use the "solar blind" portion of the ultraviolet spectrum from the 4th harmonic of the Nd:YAG laser. The ozone profiles are obtained from a DIAL (Differential Absorption Lidar) analysis of the Raman shifted scatter of N<sub>2</sub> (285 nm) and O<sub>2</sub> (276 nm) which occur on the steep side portion of the Hartley absorption band of ozone. The water vapor profiles are obtained from the vibrational Raman scatter from the 2<sup>nd</sup> (532 nm) and 4<sup>th</sup> (266 nm) harmonics of the Nd:YAG laser. The temperature profiles are obtained from the rotational Raman profiles of the molecular nitrogen and oxygen components of the atmosphere.

The optical extinction profiles of the atmosphere are obtained from the gradients of the rotational Raman molecular profile and the N<sub>2</sub> vibrational Raman profiles measured at 530, 607 and 285 nm. The temporal resolution of the ozone and temperature profiles is about 30 minutes and the profiles of water vapor and optical extinction are obtained each minute. The wavelength dependent optical extinction can be used to describe changes in the particle size distribution as a function of altitude for the important small particles. These measurements can be interpreted to determine the air mass parameter and atmospheric optical depth.

Measurements of optical extinction are based upon gradients in the molecular profiles, using the N<sub>2</sub> vibrational Raman or a band of the rotational Raman lines. We have used the technique to measure the true optical extinction for clouds and aerosol layers. In order to calculate extinction due to aerosols from Raman lidar measurements, the following procedure is used:

- 1) Apply the range correction to the backscatter Raman shifted signal.
- 2) Correct for the attenuation due to molecular scattering on the way out at 532 nm and the Raman shifted wavelength on the way back to the lidar. The ground level molecular attenuation coefficients for 532 and 607 nm are known from the cross-sections for N<sub>2</sub> and O<sub>2</sub>.

$$\alpha_{m532} = 0.013 \text{ km}^{-1} \quad \alpha_{m607} = 0.007 \text{ km}^{-1}$$

- 3) The aerosol extinction coefficients at 530 nm and at 532 nm are assumed to be the same. Then using the 530 nm data, the altitude dependent extinction value for 532 nm can be calculated comparing the signal gradient with the atmospheric scale height using that part of the profile that is not affected by the telescope form factor (beyond about 1 km).

$$I(z) = I_0 e^{-2\alpha_{532} z}$$

$$I(z) = I_0 e^{-(\alpha_{532} + \alpha_{607}) z}$$

- 4) The extinction of the 607 nm is obtained by fitting the function to the 607 nm profile. This algorithm can only determine the sum of the two extinction paths but with the extinction determined at 532 nm, the extinction for 607 nm can be directly calculated. Figure 3 (upper panel) shows an example of the aerosol extinction profile. The Raman lidar equation can be written to emphasize the extinction at the transmit wavelength and the Raman scattered return wavelength. The optical extinction due to scattering and absorption is separated into the outgoing transmit wavelength path and the return path at the Raman shifted wavelength in the equation,

$$P_R(z) = \frac{\xi(z)}{z^2} N(z) \frac{\partial \sigma}{\partial \Omega} \exp\left(-\int^z (\alpha_{O,mol} + \alpha_{R,mol} + \alpha_{O,aer} + \alpha_{R,aer}) dz\right)$$

O - outgoing - 532 or 266 nm    R - return - 530 (rot), 607 (N<sub>2</sub>), 285 (N<sub>2</sub>) or 276 (O<sub>2</sub>) nm

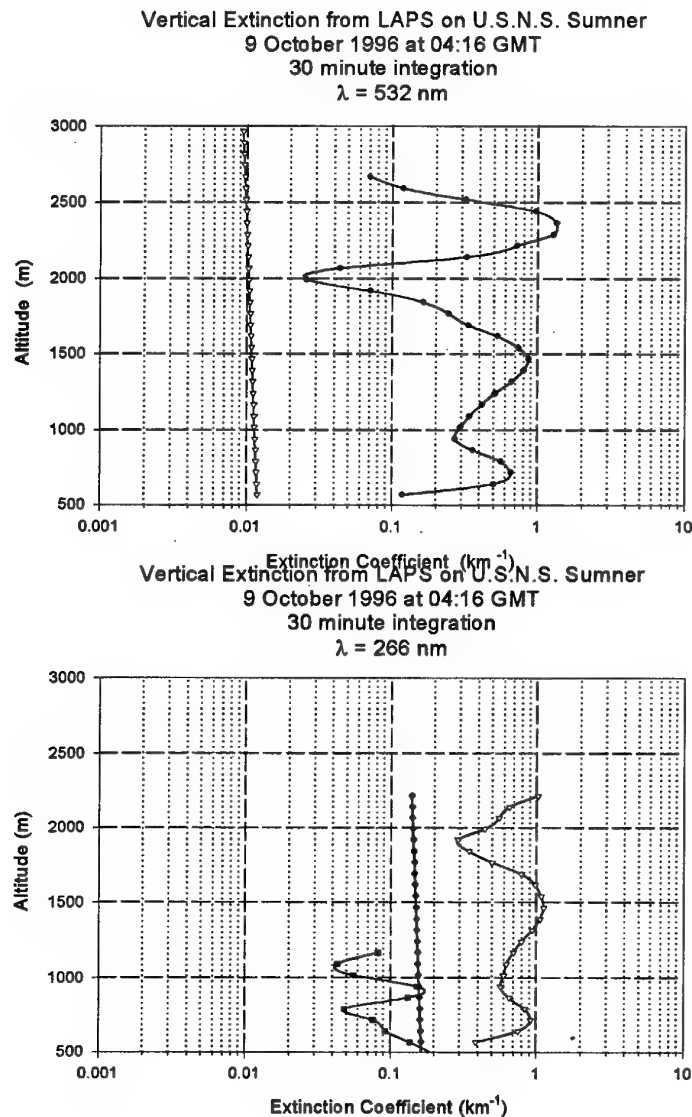


Figure 3. The optical extinction measured at visible and ultraviolet wavelengths from the LAPS Raman lidar on 9 October 1996. The extinction from molecular and aerosol scattering components are shown and the ozone absorption at 285 nm is based on the DIAL analysis of the Raman signals for  $\text{N}_2$  and  $\text{O}_2$ .

The relationship can be rewritten to solve for the optical extinction at the Raman shifted return wavelength. The first calculation is applied to the case when the extinction at the rotational Raman signal at 530 nm is measured. That wavelength is so close to the 532 nm transmit wavelength that no difference due to wavelength dependence of the scattering cross section exists. By first calculating the extinction at 532 nm from the 530 nm path and substituting this extinction as the aerosol extinction of the outgoing pulse, it

is possible to then calculate the optical extinction at 607 nm. This approach provides the 607 nm optical extinction from the  $\text{N}_2$  Raman without assuming any wavelength dependence.

The results in Figure 3 show the measured extinction profiles at visible (530 nm) and ultraviolet (285 nm) wavelengths which are ascribed to the scattering by the molecular and the aerosol components of the atmosphere are shown. In addition, the extinction at 285 nm due

to the measured tropospheric ozone profile is shown. It is interesting to note the general similarity between the visible and ultraviolet aerosol extinction values. The wavelength dependence of the aerosol extinction is seen to be relatively small in this case, but there are significant differences in the aerosol profiles. The molecular extinction profiles were calculated from the model profile of density. The molecular scattering cross-section between the visible and ultraviolet differ by the factor of  $\sim 12 (1/\lambda^4)$ . The total extinction at the ultraviolet wavelength is generally much greater than at the visible wavelength. However, as the aerosol extinction increases, it can make the total extinction at both wavelengths comparable, in clouds the visible extinction can be even larger.

The instrument provides a unique opportunity to simultaneously measure the variations in the ozone profile, while at the same time determining the atmospheric dynamics from variations in the water vapor profiles. These results, together with the temperature profiles and particle scattering optical extinction at several wavelengths will provide valuable input for investigations of the physical and chemical processes in the lower atmosphere, also for development of models of atmospheric pollution events.

Understanding of the atmospheric optical properties is critical for use and interpretation of many operational sensor systems. We have developed and used lidar instruments to provide measurements of the optical extinction at several wavelengths, to determine the spatial scales of particle scatters, and to determine particle properties from their scattering phase function. These investigations are conducted to provide a physical basis for describing optical propagation conditions for future tactical decision aids and for support of testing of advanced optical sensor systems.

## SUMMARY

Two independent approaches to measurement of the optical properties of the atmosphere have been successfully demonstrated and compared. One depends upon the determination of the aerosol description from the polarization ratio of the scattering phase function and provides the extinction at any wavelength calculated from the

number density, size and distribution width of the scattering particles, assuming the Mie scattering theory can be used to describe the particles. The second depends upon the fact that extinction produces a gradient in the Raman scatter profile of the principal molecular constituents. The Raman technique provides a reliable approach to obtain profiles of the molecular species which can be analyzed to directly determine the extinction at a wavelength. The "solar blind" spectral region has been found useful in measuring the daytime profiles of optical extinction and ozone absorption. Aerosol extinction measurements can be obtained at several wavelengths from the Raman molecular profiles. Simultaneous measurements of optical extinction at several wavelengths provides information on the variations in particle size, which can be particularly interesting around a cloud to determine whether it is in a growth phase or is dissipating.

## ACKNOWLEDGMENTS

The developments leading to the capability for measuring the optical extinction have been advanced through the efforts of several graduate students, particularly the work of T. D. Stevens and M. D. O'Brien. This work has been supported by the Navy through the program directed by J. Richter, SSD-SD. Our appreciation goes to Geary Schwemmer and NASA Goddard colleagues for the cooperative measurement program at Wallops Island VA.

## REFERENCES

- [1] Stevens, T. D., "Bistatic Lidar Measurements of Lower Tropospheric Aerosols," PhD Thesis for Penn State University, Department of Electrical Engineering, May 1996.
- [2] Stevens, T. D. and C. R. Philbrick, "Particle Size Distributions and Extinction Determined By a Unique Bistatic Lidar Technique," in Proceeding of IGARSS96 Conference on Remote Sensing for a Sustainable Future, Vol II pp 1253-1256, 1996.
- [3] Stevens, T. D. and C.R. Philbrick, "Atmospheric extinction from Raman lidar and a bistatic remote receiver," in Proc. Conf. IEEE topical Symp. CO-MEAS, 170, 1995.
- [4] O'Brien, M. D., T. D. Stevens and C. R. Philbrick, "Optical Extinction from Raman Lidar



- Measurements," in Optical Instruments for Weather Forecasting, SPIE Proceedings 2832, 45-52, 1996.
- [5] Philbrick, C. R. "Raman lidar measurements of atmospheric properties," in Proc. of Atm. Prop. and Remote Sensing III, SPIE 2222, p.922, 1994.
- [6] Philbrick, C. R., D. B. Lysak, T. D. Stevens, P. A. T. Haris and Y.-C. Rau. "Atmospheric measurements using the LAMP lidar during the LADIMAS campaign," in Proc. of the 11th ESA Symp. ESA-SP-355, p.223, 1994.
- [7] Hughes, H. G. and M. R. Paulson, "Double-ended lidar technique for aerosol studies," Appl. Opt. 27, 2273, 1988.
- [8] Reagan, J. A. and B. M. Herman, "Bistatic lidar investigations of atmospheric aerosols," in Proc. Conf. Radar Meteorol., 14th, p.275, 1970.
- [9] Devara, P. C. S. and P. Ernest Raj, "A bistatic lidar for aerosol studies," IETE Tech. Rev. Vol. 4, p.412, 1987.
- [10] Parameswaran, K., K. D. Rose, and B. V. Krishna Murthy, "Aerosol characteristics from bistatic lidar observations," J. Geophys. Res. Vol. 89, No. D22, p.2541, 1984.
- [11] Bohren, C. F. and D. R. Huffman, Absorption and Scattering of Light by Small Particles, Wiley-Interscience, New York, 1983.
- [12] Gathman, S. G., and Jensen, D. R., "Maptip (Marine aerosol properties and thermal imager performance): Aerosol Characteristics in a Coastal Region", Naval Command, Control and Ocean Surveillance Center, San Diego, CA. RDT and E Div., NTIS ID No.: AD-A300 25 Aug 1995.

# Lidar Remote Sensing of Adverse Weather for Performance Assessment of EO Sensors and Weapons

Luc R. Bissonnette, Gilles Roy, and Jean-Marc Thériault  
 Defence Research Establishment Valcartier  
 2459 Pie-XI Blvd. North  
 Val-Bélair, Québec, Canada, G3J 1X5  
 Tel.: 418-844-4437; FAX: 418-844-4511  
 E-mail: luc.bissonnette@drev.dnd.ca

## Abstract

It is a demonstrated fact that technology can provide a decisive edge in military operations. Sensors and weapons of ever increasing sophistication are constantly being fielded. To fully exploit the effectiveness of these systems, it is essential to know their performance limitations, especially in adverse weather where extinction conditions are highly variable. In this paper, we study the feasibility of using a lidar to measure on site and in real time the spatially resolved aerosol extinction. We have chosen the lidar because it is the only known instrument that can remotely detect and characterize fog and cloud droplets. The lidar has long been considered to fill this need but the shortcomings of the conventional solution methods have put serious limitations on its usefulness. At Defence Research Establishment Valcartier, we have defined and tested a novel multiple-field-of-view (MFOV) technique that solves many of the outstanding problems, particularly in adverse weather. The paper describes a proposed E-O systems performance calculation model based on MFOV lidar solutions and shows typical results derived from actual lidar measurements.

**Key words:** Lidar monitoring, Atmospheric transmittance, Detection ranges

## 1 INTRODUCTION

The operational performance of ultra-violet, visible and infrared wave weapon systems is very much dependent on weather conditions. Except for the effect of turbulence, their performance in clear atmosphere is mostly system limited, which is generally fixed, known and well modeled. Difficulties arise in adverse weather. Different systems perform differently and, above all, adverse weather is highly variable and unpredictable on the local operational scale. One possible solution is continuous monitoring with single-ended remote sensing devices. The forces equipped with such nowcasting devices would definitely have an edge in making weapons deployment decisions by adapting to or taking advantage of well characterized prevailing atmospheric conditions.

In this paper, we propose a visible and infrared systems performance calculation model based on on-line lidar monitoring. The chosen lidar is a multiple-field-of-view (MFOV) lidar which allows retrieval of both the extinction coefficient

and the effective droplet diameter of the precipitation, fog or cloud events that define adverse weather in the context of this paper. The main advantage of the MFOV technique is the access it provides to size information which permits scaling of the derived extinction coefficient to the lidar wavelength to any other wavelength of interest. Examples of thermal imagers performance calculations based on actual fog/cloud lidar measurements are presented. They show that the relative advantage of one infrared band over another can change in the course of changing adverse weather conditions.

## 2 PERFORMANCE MODEL

The objective of this study is the development of a prediction model of electro-optic systems performance in adverse weather based on lidar monitoring of the optical parameters of fog, clouds and precipitation droplets. We consider a generic imaging system and evaluate performance in terms of detection ranges of specified targets against the atmospheric background. Detection is defined by the strength of the target-to-background contrast seen by the imager relative to some suitable threshold.

The atmosphere affects infrared image contrast by transmission losses and background emission. Atmospheric emission is very complex to describe exactly. For the purpose of this study, we simplify the problem by neglecting direct sunlight scattering by the target and the atmosphere, and by assuming conservative scattering [1, 2] to estimate the atmospheric emissivity. Sunlight scattering can be significant in the mid infrared band where it can enhance or reduce target contrast depending on the target attitude with respect to direct and diffused sunlight. The conservative scattering approximation assumes that the radiation scattered away balances exactly the radiation scattered into the line of sight. In other words, scattering and absorption are considered indistinguishable from a radiance point of view [1]. For example, this is the default multiple scattering option used in MODTRAN [3]. Therefore, the mid infrared detection ranges calculated by the method of this paper are first-cut approximations that will have to be reviewed, particularly in the light of more advanced modeling of sunlight scattering and atmospheric emissivity.

According to the approximation of conservative scattering, the emissivity  $\epsilon_i$  of an atmospheric layer, delimited

by ranges  $R_i$  and  $R_{i+1}$  from the system receiver, is given by

$$\epsilon_i = [1 - \mathcal{T}(R_{i+1})/\mathcal{T}(R_i)], \quad (1)$$

where  $\mathcal{T}(R_i)$  is the atmospheric transmittance up to  $R_i$ . The spectral radiance of the layer is thus the product of  $\epsilon_i$  times the Planck function, and the received radiance is the emitted radiance attenuated by a factor equal to the transmittance  $\mathcal{T}(R_i)$ . Therefore, in the framework of this simplified model, the atmospheric effect on target contrast is completely determined by the range-resolved atmospheric transmittance  $\mathcal{T}(R)$ . Hence, the problem of calculating detection ranges reduces to specifying the transmittance  $\mathcal{T}(R)$  to far enough ranges to reach the limiting detection level.

Our interest is in adverse weather and, hence, in low altitudes. Under this condition, we believe it is sufficient to divide the atmosphere into three main layers: the boundary layer below cloud base, the cloud layer, and the clear sky above cloud top which, for the purpose of this study, is assumed aerosol and cloud free. To estimate detection ranges, we need the range-resolved transmittance along any slant path through this three-layer atmosphere. Models alone are not sufficient; the variability of the aerosol, fog, clouds and precipitation in the boundary layer requires continuous on-site monitoring. We propose to do this with the multiple-field-of-view lidar technique described in the following section. As will be seen, and this is particularly true for low-visibility conditions, the solutions retrieved from these lidar measurements are sufficiently detailed to estimate with good accuracy the particulate contributions  $\mathcal{T}_p(\lambda, R)$  to the transmittance at the wavelengths  $\lambda$  of interest. For the molecular contributions  $\mathcal{T}_m(\lambda, R)$ , we propose to use MODTRAN [3] as follows: the boundary layer below clouds is specified by a uniform average temperature and relative humidity derived from on-site measurements, and the clear sky above, by the default standard atmosphere model appropriate to the location. The band transmittance is then given by

$$\mathcal{T}(R) = \int_{\lambda_1}^{\lambda_2} d\lambda W(\lambda) \mathcal{T}_m(\lambda, R) \mathcal{T}_p(\lambda, R), \quad (2)$$

where  $W(\lambda)$  is the sensor spectral function, and  $\lambda_1$  and  $\lambda_2$  the limits of the bandpass. Instead of extending in each case the transmittance calculations to the top of the atmosphere, we plan to approximate the clear sky radiance for the semi-infinite layer above the clouds by tabulated brightness temperatures  $T_s(\theta)$ , where  $\theta$  is the elevation angle.

Under the simplified conditions outlined above, it is rather straightforward to derive the equations for the target-background contrast. Denoting by  $R$  the range to the target, by  $R_b$  the range to the cloud base or fog bank, by  $R_t$  the range to the cloud or fog layer top, by  $\bar{T}_a$  the average air temperature in the boundary layer below clouds, by  $\bar{T}_c$  the average cloud temperature over the lidar penetration depth, by  $T_s(\theta)$  the sky brightness temperature at the elevation angle of  $\theta$ , and by  $L_o$  the target radiance, we have for the contrast-to-noise ratio CNR

$$\text{CNR} = [L_o - B(T_s(\theta))] K \frac{\mathcal{T}(R)}{\text{NEP}}; \quad (3)$$

b) in the case where the target is within the clouds, i.e.  $R_b < R < R_t$ ,

$$\text{CNR} = [L_o - B(\bar{T}_c)] K \frac{\mathcal{T}(R)}{\text{NEP}} + [B(\bar{T}_c) - B(T_s(\theta))] K \frac{\mathcal{T}(R_t)}{\text{NEP}}; \quad (4)$$

and c) in the case where the target is below the clouds, i.e.  $R < R_b < R_t$ ,

$$\text{CNR} = [L_o - B(\bar{T}_a)] K \frac{\mathcal{T}(R)}{\text{NEP}} + [B(\bar{T}_a) - B(\bar{T}_c)] K \frac{\mathcal{T}(R_b)}{\text{NEP}} + [B(\bar{T}_c) - B(T_s(\theta))] K \frac{\mathcal{T}(R_t)}{\text{NEP}}, \quad (5)$$

where  $B$  is the Planck function and NEP is the noise equivalent power on a pixel. The geometric factor  $K$  is given by

$$K = \begin{cases} S_o A/R^2 & \text{if } p^2 R^2/f^2 S_o \geq 1, \\ p^2 A/f^2 & \text{if } p^2 R^2/f^2 S_o < 1, \end{cases} \quad (6)$$

depending on whether the pixel size is greater or smaller than the image size, where  $S_o$  is the target cross-section,  $A$  and  $f$  are, respectively, the aperture area and the focal length of the receiver optics, and  $p$  is the pixel size of the image plane sensor. The target radiance  $L_o$  reduces to the Planck function at the target temperature  $T_t$ , i.e.  $B(T_t)$ , if the target emissivity is close to unity.

### 3 MFOV LIDAR

Our objective is to continuously characterize adverse weather, defined by the presence of fog, clouds and precipitation, by lidar monitoring. Operating a lidar in such dense particulate media gives rise to multiple scattering contributions in the measured returns, e.g. Refs. 4-9. In the past, multiple scattering has been treated as an undesirable effect and correction factors have been proposed, for instance by Platt [10]. However, it has been recognized quite early [4, 5, 6] that retrievable information is included in the multiple scattering effects. In recent years, we have been developing at our laboratory measurement and inversion techniques [7, 9, 11, 12] to take advantage of this, in particular to try to derive particle size data from lidar returns.

Multiple scattering causes radiation to be rescattered into the receiver at angles greater than the divergence angle of the transmitted laser pulse. Therefore, one practical means of resolving the multiple scattering contributions consists in measuring the field-of-view dependence of the lidar returns. We have done this in two different ways. In an early experiment [7, 9], we used in the image plane of the receiver a large PIN photo-detector segmented in the form of concentric rings. Four discrete fields of view were thus obtained, namely 4, 13, 26 and 38 mrad. However, to take advantage

a) in the case where the target is above the clouds, i.e.

of the higher gain of APD detectors and to add flexibility to the number and values of the fields of view, we are currently experimenting with dynamically changing the receiver field of view by means of variable size masks rotated in front of a single detector [13]. Obviously, in this method, the returns at the different fields of view are not recorded simultaneously but sequentially. For most measurements reported here, the laser was pulsed at 100 Hz and the field-of-view masks were shifted at the same rate. Series of eight masks are used to define fields of view between 0.2 and 12 mrad. Hence, a complete sequence requires 0.07 s during which time the cloud must remain relatively stable for the measurements to be valid. The sequential approach would not be suitable for a scanning system but is very convenient for research needs.

Our lidar inversion method for exploiting multiple scattering is outlined in Ref. 11. It is applicable to scattering particles greater than the lidar wavelength, which is the case for fog, cloud and precipitation droplets at 1.06  $\mu\text{m}$ . Under this condition, half of the particulate extinction is due to diffraction scattering concentrated in a narrow peak centered on the laser axis. This means that a large fraction of the scattered radiation remains within the receiver field of view and can thus contribute substantially to the measured signal. Because nearly half of all scatterings are in the near forward direction, it follows that the multiply scattered radiation collected at small fields of view by a lidar receiver in a co-axial configuration has, for the most part, undergone a single backscattering at an angle close to 180° preceded and followed by near forward scatterings [14]. Hence, the field-of-view dependence of lidar returns is strongly related to the profile of the scattering diffraction peak. Diffraction theory tells us that the angular width of the peak is inversely proportional to the average diameter of the droplets. As a result, the MFOV measurements contain retrievable information on droplet size. Reference 11 describes the method used here to extract at each range of the MFOV returns the effective droplet diameter defined as the ratio of the third to the second order moment of the size distribution density function.

As discussed below, multiple scattering also contributes additional information to solve for the extinction coefficient. In general, the solution of the lidar equation requires the specification of a boundary value. In the case of single scattering lidars, the boundary value cannot be derived from the measured signal and must therefore be obtained by independent means. Moreover, it should preferably be specified at the far end of the lidar return to ensure stability [15]. Both conditions can seriously compromise the remote sensing capability of the lidar. In the MFOV inversion method [11] employed here, we use the multiple scattering contribution in lieu of a boundary value. By fitting the measured relative signal strength between the wide and narrow fields of view to an analytical expression valid in the limit of small multiple scattering contributions, we obtain the extinction coefficient at that range. This provides a reference to calibrate the lidar signal and thus eliminates the need for a boundary value.

In summary, the inversion of the MFOV lidar returns gives at each range bin a good estimate of the average or ef-

fective droplet diameter and a solution for the extinction coefficient. From these simultaneous solutions, it is possible, as shown in the following paragraphs, to estimate the extinction coefficient at any wavelength of interest.

Wavelength extrapolation is an important step toward calculating the spectral particulate transmittance  $T_p(\lambda, R)$  of Eq. 2. To do this, we first assume a parametrized function for the droplet size distribution, for example a modified gamma function of the form

$$\frac{dN}{dr} = N_0 r^a \exp(-br), \quad (7)$$

which is very suitable for fog and clouds, where  $r$  is the droplet radius, and  $N_0$ ,  $a$  and  $b$  are the parameters to be determined. According to cloud models developed by Deirmendjian [16] and fog models by Shettle and Fenn [17], the parameters  $a$  and  $b$  are, to a good approximation, linked together by the following empirical relation:

$$a = \begin{cases} 1.163 + 3.715 b^{0.65} & \text{for } b \leq 1.5, \\ 6.0 & \text{for } b > 1.5, \end{cases} \quad (8)$$

where  $a$  is dimensionless and  $b$  is in  $\mu\text{m}^{-1}$ . Thus, Eq. 7 is actually a two-parameter model that can be specified at each range bin  $R$  from the lidar solutions for the effective droplet diameter  $d(R)$  and extinction coefficient  $\alpha(\lambda_l, R)$ , where  $\lambda_l$  is the lidar wavelength, as explained below.

The effective diameter is defined by

$$d = 2 \frac{\langle r^3 \rangle}{\langle r^2 \rangle} = 2 \int_0^\infty r^3 \frac{dN}{dr} dr / \int_0^\infty r^2 \frac{dN}{dr} dr. \quad (9)$$

Using Eq. 7 for  $dN/dr$ , we have

$$d = 2(a + 3)/b. \quad (10)$$

Therefore, from the lidar-derived value of  $d$ , we can determine both  $a$  and  $b$  by solving numerically Eqs. 8 and 10.

By definition, the extinction coefficient at wavelength  $\lambda$  is

$$\begin{aligned} \alpha(\lambda, R) &= \int_0^\infty \pi r^2 Q_e(\lambda, r) \frac{dN}{dr} dr \\ &= \int_0^\infty N_0 \pi r^2 Q_e(\lambda, r) r^a e^{-br} dr, \end{aligned} \quad (11)$$

where  $Q_e(\lambda, r)$  is the extinction efficiency obtained by Mie calculations. Given the lidar-derived solutions for  $a$  and  $b$  obtained as described in the preceding paragraph, the extrapolation of the lidar extinction coefficient  $\alpha(\lambda_l, R)$  to other wavelengths is then straightforward, namely

$$\alpha(\lambda, R) = \alpha(\lambda_l, R) \frac{\int_0^\infty Q_e(\lambda, r) r^{a+2} e^{-br} dr}{\int_0^\infty Q_e(\lambda_l, r) r^{a+2} e^{-br} dr}. \quad (12)$$

Finally, the required particulate transmittance  $T_p(\lambda, R)$  of Eq. 2 is given by

$$T_p(\lambda, R) = \exp \left\{ - \int_0^R \alpha(\lambda, R') dR' \right\}. \quad (13)$$

The MFOV lidar method just described requires the presence of measurable multiple scattering effects. This is the case in fog and clouds but, in background aerosols, we have

not yet observed with our lidars any measurable contribution at fields of view greater than the pulse divergence. Because the size and concentration of background aerosol particles are small, the backscattered signal is mostly single scattering. Despite their relatively small extinction coefficients, background aerosols must nevertheless be taken into account in  $T_p(\lambda, R)$  because, in the absence of adverse weather, the detection ranges are long and significantly influenced even by small particulate extinction.

Under a single-pulse data recording procedure, which is the practical choice when scanning the environment is required as in the proposed application, we find that returns from background aerosols are detectable in the central field of view of our MFOV receiver up to a horizontal range of 2-3 km at the most. If fog or clouds are present within that range, we cannot discriminate the fraction contributed by the aerosol but this is irrelevant because the fog or clouds effects dominate. If the fog or clouds are farther away from the transceiver, or if they are completely absent, then the aerosol can and must be resolved. Multiple scattering is of no help in this case and conventional solution methods must be employed. As extensively discussed in the literature, there is no unique and accurate way of determining aerosol extinction from single scattering elastic lidar measurements. However, the same literature abounds with suggestions of measurement scenarios and approximate inversion methods for taking maximum advantage of the limited but nevertheless rich lidar information. In the following, we discuss how vertical profiles of aerosol data can be estimated when only single scattering returns are available.

The regions of single scattering contributions only are easily identified by the absence of signal in the fields of view greater than the pulse divergence. Compared with adverse weather, these are regions of good visibility that are not subject to rapid and large variations except in the vicinity of local sources such as fires, surf zones, white caps, etc. In most instances, there will exist a range of azimuthal directions and elevation angles where we can assume horizontal homogeneity. Under such conditions, the single scattering return signals  $P(h/\sin \theta_i)$  measured at different elevation angles  $\theta_i$  from ranges corresponding to the same height  $h$  can be related to the height-integrated extinction as follows [18]:

$$\int_0^h \alpha(\lambda_i, h') dh' = \frac{\sin \theta_i \sin \theta_{i+1}}{2[\sin \theta_{i+1} - \sin \theta_i]} \times \ln \left[ \frac{\sin^2 \theta_{i+1} P(h/\sin \theta_i)}{\sin^2 \theta_i P(h/\sin \theta_{i+1})} \right], \quad (14)$$

where  $\alpha(\lambda_i, h)$  is the aerosol extinction coefficient at the lidar wavelength  $\lambda_i$  and altitude  $h$ . The vertical profile of  $\alpha(\lambda_i, h)$  can thus be directly calculated from this equation or from Klett's solution [15] where the boundary value is replaced by the optical depth derived from Eq. 14. Another possibility proposed and tested by Kunz [19] is to solve the slant returns ( $\theta_i > 0$ ) by forward integration with the near end boundary value inferred by the slope method applied to the horizontal return ( $\theta_i = 0$ ). For the remaining directions of inhomogeneity caused by local sources, the single scattering lidar returns could be normalized by a return recorded

in one direction of homogeneity and the solution method developed by Evans [20] employed. Finally, the clear air solutions would need to be spatially extrapolated because, in good visibility, the useful lidar range is less than the detection ranges we want to calculate. Therefore, if scanning is performed, we can find in most situations ways of retrieving with reasonable accuracy the lidar extinction coefficient  $\alpha(\lambda_i, R)$  even in the absence of multiple scattering.

There remains to estimate from  $\alpha(\lambda_i, R)$  the extinction at mid and far infrared wavelengths. Since we have no data on particle size, shape and composition, we must use empirical scaling models. Unfortunately, the wavelength differences are large, which makes the ratio of the extinction coefficients dependent on the full particle size range and, therefore, sensitive to aerosol variability. For example, Trakhovsky and Shettle [21] concluded from numerical simulations using a number of different atmospheric aerosol models that the relation between the extinction coefficients at 1.06 and 10.6  $\mu\text{m}$  showed too much scatter to give an accurate scaling law. Having said that and in the absence of additional data, scaling still remains a practical option as long as we keep in mind the uncertainties involved.

Figure 1 illustrates the scatter that we can expect in trying to extrapolate the mid and far infrared extinction coefficients of background aerosols from the coefficient measured at the lidar wavelength of 1.06  $\mu\text{m}$ . The data are derived

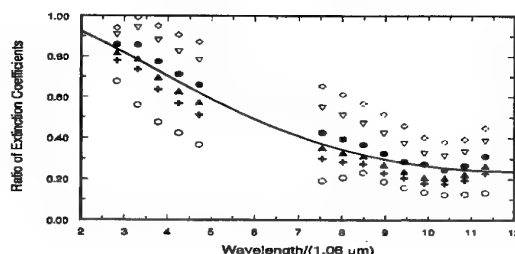


Figure 1: Wavelength scaling of extinction coefficients for MODTRAN maritime aerosol model; data sets are for various relative humidities; continuous curve is best fit to data.

from the MODTRAN maritime aerosol model for several relative humidities. The RMS scatter about the best fit curve is 27%. In the presence of fog or clouds, such uncertainties are inconsequential since the fog or cloud infrared extinctions, derived with good precision with the MFOV inversion method, are the dominant factor. In good visibility, the errors are potentially more serious. Fortunately, since we can expect that the errors fluctuate in sign over the long clear air paths, the integrated effect may still be acceptable.

Although the main emphasis is adverse weather, we believe that even in clear air lidar monitoring is still better than relying solely on models despite the shortcomings just discussed. At the very least, we have a continuously refreshed estimate of the infrared extinction profiles that may be crude but certainly more closely related to the prevailing conditions at the operation site than model

outputs. Moreover, should low visibility conditions set in or dissipate, MFOV lidar monitoring offers an immediate and accurate assessment of the resulting limitations or improvements. However, aerosol modeling remains essential for wavelength scaling where there is no multiple scattering signal.

## 4 RESULTS

Lidar probings of cloud decks were regularly performed with our experimental MFOV lidar. For these routine measurements, scanning was avoided to minimize eyesafety hazards; the lidar was instead pointed at a fixed near vertical elevation angle. For the illustrative CNR calculations of this paper, we have assumed horizontal homogeneity and trigonometrically transformed the vertical measurements to the elevation angles of interest.

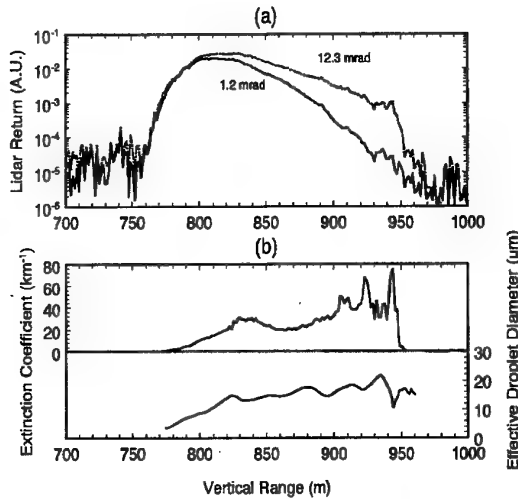


Figure 2: Example of MFOV cloud lidar returns for smallest and largest receiver fields of view (a) and corresponding solutions for extinction coefficient and droplet diameter (b)

One measurement example showing the raw lidar returns at the smallest and largest fields of view of our receiver, and the corresponding retrieved solutions for the extinction coefficient and droplet diameter is given in Fig. 2. This was the case of a stratiform cloud layer in an otherwise clear atmosphere. The two field-of-view returns are initially equal but, as cloud penetration increases, they deviate markedly to the point where the return at 12.3 mrad grows at cloud top to  $\sim 10$  times the strength of the return at 1.2 mrad. This is a clear illustration of multiple scattering contributions. Both returns finally drop to the noise level at approximately the same range indicating that the laser pulse has cleared the top of the cloud. Otherwise, if the signal fading were due to extinction, we would expect the signal at 12.3 mrad to outlive that at 1.2 mrad as we routinely observe from dense cloud layers. The lidar-derived solutions plotted in Fig. 2b give an extinction coefficient of  $30\text{--}40 \text{ km}^{-1}$  and an effective droplet diameter of  $15\text{--}20 \mu\text{m}$ . These numbers are consistent with expectations. For example, Chýlek *et al.* [22] propose for stratus clouds an effective

Table 1: Parameters of generic IRST

Parameter	Mid Infrared	Far Infrared
Band	$3.5 - 5 \mu\text{m}$	$8 - 11 \mu\text{m}$
Aperture Diameter	150 mm	150 mm
Focal Length	136 mm	136 mm
Pixel size	$30 \times 30 \mu\text{m}^2$	$30 \times 30 \mu\text{m}^2$
NETD ( $27^\circ\text{C}$ )	90 mK	20 mK

droplet diameter of  $16.6 \mu\text{m}$  and a liquid water content of  $0.29 \text{ g/m}^3$ , which corresponds, under the assumption of a constant efficiency factor of 2, to an extinction coefficient of  $50 \text{ km}^{-1}$ .

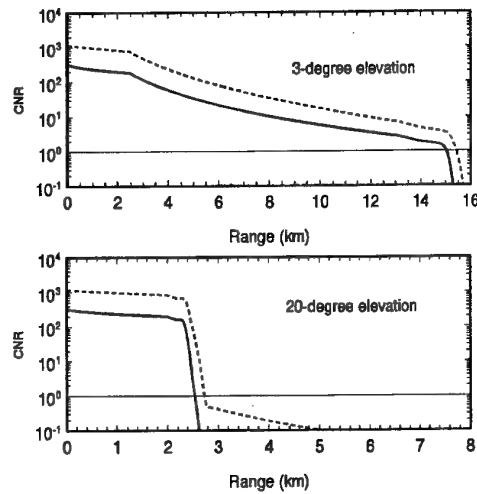


Figure 3: Contrast-to-noise (CNR) ratio, under stratus cloud layer of Fig. 2, of a 300 m/s,  $0.3 \text{ m}^2$  subsonic target as a function of range for a constant elevation viewing angle. Continuous curve: mid infrared; broken curve: far infrared. Top:  $3^\circ$  elevation; bottom:  $20^\circ$  elevation.

Using the lidar-derived cloud profiles of Fig. 2b, we have calculated with the method outlined in Sections 2 and 3 the contrast-to-noise ratios (CNR) of missile target images viewed at various elevation angles by a generic modern IRST. The relevant sensor data are summarized in Table 1. Two types of targets were considered: a) a 300-m/s subsonic missile with an effective area of  $0.3 \text{ m}^2$ , and b) a 1000-m/s supersonic missile with an effective area of  $0.45 \text{ m}^2$ . In both cases, we have assumed an emissivity of 0.8. Results at  $3^\circ$  and  $20^\circ$  elevations in the presence of the cloud of Fig. 2 are plotted in Figs. 3 and 4 for the subsonic and supersonic missiles, respectively. The small kink in the CNR curves of the top graphs of both Figs. 3 and 4 seen between 2 and 3 km corresponds to the transition from a resolved to an unresolved target, i.e. to the effect of the geometrical factor  $K$  of Eq. 6.

For the low-temperature subsonic target, Fig. 3 shows that the far infrared sensor has everywhere a higher CNR whether the target cruises below, within or above the clouds. At low elevations, the advantage of the far infrared is insignificant. Up to cloud base, both bands have a high CNR and hence excellent detection performance; once

in the clouds, because of the low slant angle, the extinction builds up sufficiently in both bands to make detection impossible with only a marginal range extension in the 8-11  $\mu\text{m}$  band. However, as the elevation angle increases, the cloud integrated attenuation decreases and we observe from Fig. 3 that the long wavelengths can become advantageous. For example at 20°, Fig. 3 shows that the target is almost detectable through the cloud in the far infrared band with a CNR close to unity, but completely masked in the mid infrared. At greater elevation angles, the target becomes clearly visible above the clouds in the 8-11  $\mu\text{m}$  band but remains completely hidden in the 3.5-5  $\mu\text{m}$  band.

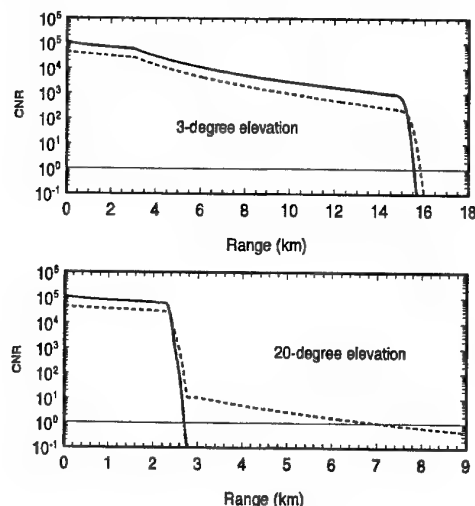


Figure 4: Contrast-to-noise (CNR) ratio, under stratus cloud layer of Fig. 2, of a 1000 m/s, 0.45 m<sup>2</sup> supersonic target as a function of range for a constant elevation viewing angle. Continuous curve: mid infrared; broken curve: far infrared. Top: 3° elevation; bottom: 20° elevation.

The high temperature results of Fig. 4 reveal an interesting feature. As a result of the high target temperature, the clear atmosphere target contrast is higher in the mid infrared but as soon as we reach the cloud, the situation quickly turns to the advantage of the far infrared. As in the previous case, the gain is not significant at low elevation. However, at higher angles, the cloud becomes transparent in the 8-11  $\mu\text{m}$  band; for example, the target remains detectable up to ~ 7 km at 20° elevation, i.e. a gain by a factor of more than 2.5 compared with the 3.5-5  $\mu\text{m}$  band.

The presence of clouds measured and characterized by the proposed lidar is valuable information even if the target is everywhere below cloud base. Cloud emission can make a difference. This is illustrated in Fig. 5 where the CNR calculated at 2° elevation for the overcast conditions of Fig. 2 is compared with the clear air case. At 2°, the 800-m cloud base gives a cloud-free range of 23 km. It follows that the transmittance is the same in both cases for all ranges less than 23 km. However, Fig. 5 shows that the radiance background created by the cloud layer is sufficient to reduce the target CNR by a factor of nearly 1.5. For a detection threshold chosen equal to CNR = 3, this translates into a detection range reduction of more than 1 km over 16 km.

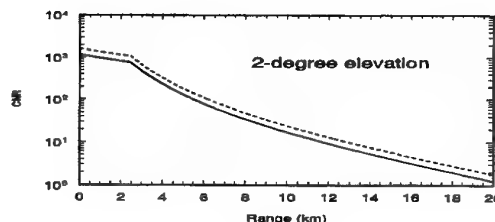


Figure 5: Contrast-to-noise (CNR) ratio of a 300 m/s, 0.3 m<sup>2</sup> subsonic target in the far infrared band as a function of range for an elevation angle of 2°. Broken curve: clear air; continuous curve: stratus cloud layer of Fig. 2.

No systematic validation of lidar-derived performance predictions such as depicted in Figs. 3-5 has yet been conducted. However, we participated with an early version of our MFOV lidar in a joint experiment that resulted in limited possibilities for comparison of predicted CNR with simultaneously recorded actual infrared images. One objective of the experiment, planned and carried out under the auspices of the former NATO Panel 4 RSG-8, was to verify the usefulness of lidars in providing real-time detection ranges for thermal imagers [23]. The experiment was called the Vertical Atmospheric Structure Trial 1992 (VAST92) and took place in the Fall of 1992 in the German Alps. Part of the measurements consisted in recording the images of a 0.22-m diameter calibrated blackbody target along a 30°-elevation, 2.3-km long slant path while making simultaneous MFOV lidar measurements close to the imagers axis. Highly variable fog or cloud layers regularly formed at middle altitudes between the valley station and the mountain top where the blackbody target was located. Unfortunately, most cloud/fog events remained opaque to both infrared bands. However, there occurred one event of a semi-transparent layer that was successfully probed by both the infrared imagers and the MFOV lidar. The results are shown in Figs. 6 and 7. The blackbody temperature for that event was set at 100° C.

In Fig. 6 are plotted the mid and far infrared detection probabilities predicted from the MFOV lidar returns with the method of this paper for the specific imagers and the specific blackbody target of the experiment. The lidar measurements were performed at a rate of 0.1 Hz but, to illustrate the trends more clearly, the 0/1 discrete probability values were averaged over a 1-min sliding window. The detection threshold was arbitrarily set at a CNR level of 3 for these calculations. The calculations of Fig. 6 predict that the blackbody target at 2.3 km should be undetectable by the mid infrared imager for most of the depicted 1-h measurement period except for a short interval around 10:00, and after 10:25 at which time the fog layer began to dissipate completely. By contrast, the target should remain fully detectable by the far infrared imager over the complete period. The imagers results shown in Fig. 7 confirm these general predictions. There is no target image in the mid infrared but a clearly defined spot in the far infrared. Strictly speaking, the prediction is not exact because at



10:00, i.e. at the time quoted for the recorded image of Fig. 7a, the predicted mid infrared detection probability is maximum. However, considering the synchronization errors between the lidar and the imagers, the uncertainties in the actual detection thresholds, the separation between the lidar and the imagers optical axes, and the rapid probability fluctuations shown in Fig. 6a, the prediction of marginal performance in the mid infrared compared with the far infrared is consistent with the recorded images.

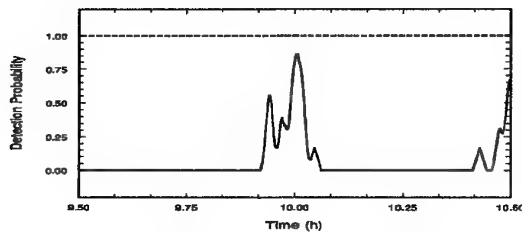


Figure 6: Lidar-derived, 1-min averaged detection probabilities of VAST92 target on 13 October 1992. Continuous curve: mid infrared imager; broken line: far infrared imager.

## 5 CONCLUSION

We have developed a simplified model to calculate the contrast-to-noise ratio (CNR) of a target seen through adverse weather. By neglecting target and atmospheric scattering of solar radiation into the line of sight and assuming conservative radiance scattering, we were able to formulate the CNR in terms of atmospheric transmittance alone. The adverse weather component to the transmittance is derived from on-site, real-time multiple-field-of-view (MFOV) lidar data and the molecular component, by MODTRAN calculations. The MFOV technique works well in adverse weather where the size and concentration of the scattering particles are sufficiently large for multiply scattered radiation to contribute to the measured lidar signals. For background aerosols, however, conventional solution methods must be employed along with model-based wavelength scaling and range extrapolation to compensate for the lack of particle size information, in the first case, and the limited useful range of clear air lidar soundings, in the second case.

CNRs of generic targets viewed by generic imagers were calculated from actual lidar data. Results showed that far infrared band imagers perform better in adverse weather for both low and high temperature targets at least for the conditions studied. Our general prediction of superior adverse weather performance in the far infrared is confirmed by the one case of simultaneous lidar and thermal imager data currently available to us. However, as expected, the advantage switches back to mid infrared for high temperature targets seen through clear air. The knowledge of such behaviors provided on-line by lidar monitoring, as proposed in this study, would give a definite advantage for selecting

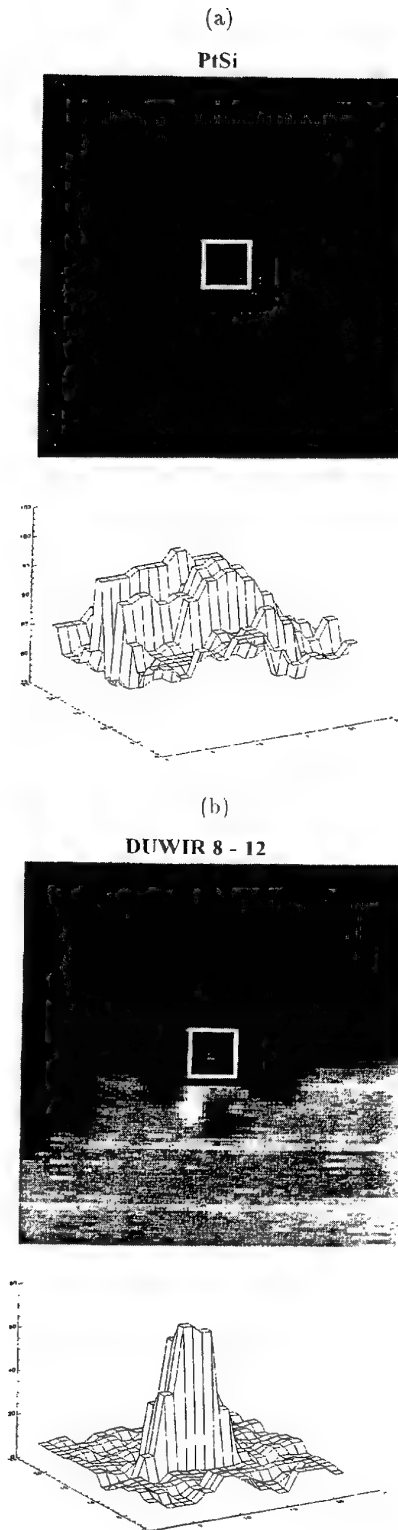


Figure 7: Infrared images and corresponding grey scale levels within windowed area of a  $100^{\circ}\text{C}$ , 0.22-m diameter blackbody source viewed along a  $30^{\circ}$  elevation, 2.3-km slant path through a cloud layer. (a) mid infrared; and (b) far infrared. Date was 13 October 1992 and time was 10:00.



the most favorable operating modes of surveillance imagers.

We have considered in this paper the surveillance scenario but it is evident that the lidar-based performance model of Sections 2 and 3 can be applied to tracking by enemy and defense weapons for optimal deployment decisions. Weather-coordinated weapons deployment may provide in some situations the sought after differential edge over opposing forces of equal hardware sophistication.

Future work will be devoted to refining the performance calculation model. The conservative scattering hypothesis needs to be revisited, and solar scattering by both the target and the atmosphere has to be taken into account. The accuracy of any solar scattering model will certainly be enhanced by the availability of lidar data from which real-time characterization of cloud cover can be derived. Finally, the complete approach needs extensive validation. To that effect, a decision has been taken and work has begun to build a demonstrator 10-Hz eyesafe, fieldable MFOV lidar capable of scanning in both azimuth and elevation at a slew rate of  $\sim 30^\circ/\text{s}$ .

## Acknowledgments

We are indebted to K. Stein and A. Kohnle of Forschungsinstitut für Optik for sharing the thermal images of Fig. 7.

## References

- [1] A. Ben-Shalom, B. Barzilai, A. Calib, A. Devir, S.G. Lipson, and U.P. Oppenheim, "Sky radiance at wavelengths between 7 and 14  $\mu\text{m}$ : measurement, calculation, and comparison with LOWTRAN-4 predictions," *Appl. Opt.*, Vol. 19, pp. 838-839 (1980).
- [2] R. Richter, "Some aspects of the atmospheric radiance model of LOWTRAN 6," *Int. J. Remote Sensing*, Vol. 6, pp. 1773-1777 (1985).
- [3] A. Berk, L.S. Bernstein, and D.C. Robertson, "MODTRAN: A moderate resolution model for LOWTRAN 7," GL-TR-89-0122 (U.S. Air Force Geophysics Laboratory, Hanscom Air Force Base, Mass., 1989).
- [4] R.J. Allen and C.M.R. Platt, "Lidar for multiple backscattering and depolarization observations," *Appl. Opt.*, Vol. 16, pp. 3193-3199 (1977).
- [5] S.R. Pal and A.I. Carswell, "Polarization properties of lidar scattering from clouds at 347 nm and 694 nm," *Appl. Opt.*, Vol. 17, pp. 2321-2328 (1978).
- [6] K. Sassen and R.L. Petrilla, "Lidar depolarization from multiple scattering in marine stratus clouds," *Appl. Opt.*, Vol. 25, pp. 1450-1459 (1986).
- [7] L.R. Bissonnette and D.L. Hutt, "Multiple scattering lidar," *Appl. Opt.*, Vol. 29, pp. 5045-5046 (1990).
- [8] C. Werner, J. Streicher, H. Herrmann, and H.-G. Dahn, "Multiple-scattering lidar experiments," *Opt. Eng.*, Vol. 31, pp. 1731-1745 (1992).
- [9] D.L. Hutt, L.R. Bissonnette, and L. Durand, "Multiple field of view lidar returns from atmospheric aerosols," *Appl. Opt.*, Vol. 33, pp. 2338-2348 (1994).
- [10] C.M.R. Platt, "Lidar and radiometer observations of Cirrus clouds," *J. Atmos. Sci.*, Vol. 30, pp. 1191-1204 (1973).
- [11] L.R. Bissonnette and D.L. Hutt, "Multiply scattered aerosol lidar returns: inversion method and comparison with *in situ* measurements," *Appl. Opt.*, Vol. 34, pp. 6959-6975 (1995).
- [12] G. Roy, L.R. Bissonnette, C. Bastille, and G. Vallée, "Estimation of cloud droplet size density distribution from multiple-field-of-view lidar returns," *Opt. Eng.*, Vol. 36, pp. 3404-3415 (1997).
- [13] G. Roy, L. Bissonnette, and C. Bastille, "Multiple-field-of-view lidar control systems," submitted to 19th International Laser Radar Conference, 6-10 July 1998, Annapolis, Maryland.
- [14] F. Nicolas, L.R. Bissonnette, and P.H. Flamant, "Lidar effective multiple-scattering coefficients in cirrus clouds," *Appl. Opt.*, Vol. 36, pp. 3458-3468 (1997).
- [15] J.D. Klett, "Stable analytical inversion solution for processing lidar returns," *Appl. Opt.*, Vol. 20, pp. 211-220 (1981).
- [16] D. Deirmendjian, "Far-infrared and submillimeter wave attenuation by clouds and rain," *J. Appl. Meteorol.*, Vol. 14, pp. 1584-1593 (1975).
- [17] E.P. Shettle and R.W. Fenn, "Models for the aerosols of the lower atmosphere and the effects of humidity variations on their optical properties," AFGL TR-79-0214 (U.S. Air Force Geophysics Laboratory, Hanscom Air Force Base, Mass., 1979).
- [18] G.J. Kunz, "Vertical Atmospheric Profile Measurements by Lidar," PHL 1982-49 (TNO Physics and Electronics Laboratory, The Hague, The Netherlands, September 1982).
- [19] G.J. Kunz, "Vertical atmospheric profiles measured with lidar," *Appl. Opt.*, Vol. 22, pp. 1955-1957 (1983).
- [20] B.T.N. Evans, "On the Inversion of the Lidar Equation," DREV Report 4343/84, November 1984.
- [21] E. Trakhovsky and E.P. Shettle, "Wavelength scaling of atmospheric aerosol scattering and extinction," *Appl. Opt.*, Vol. 26, pp. 5148-5153 (1987).
- [22] P. Chýlek, P. Damiano, and E.P. Shettle, "Infrared emittance of water clouds," *J. of the Atm. Sciences*, Vol. 49, pp. 1459-1472 (1992).
- [23] L.R. Bissonnette, D. Hutt, Y. Hurtaud, K. Stein, K. Weiss-Wrana, T. Trickl, W. Carnuth, G. Kunz, M. Moerman, E.A. Murphy, V. Turner, and F.D. Eaton, "Slant Path Lidar and Thermal Imaging Measurements," AC/243 (Panel 4) TR/18, published by Defence Research Establishment Valcartier, Québec, Canada, April 1995.

# **Measurement of the Distortion Generated in a Laser Beam's Characteristics Resulting from Passage through an Engine's Wake**

**D.H. Titterton  
WX3 Department, DERA Farnborough  
A2 Building, Room 1064  
Ively Road, Farnborough, Hants GU14 0LX  
United Kingdom**

## **1 Introduction**

This paper reports studies carried out to measure the change in characteristics and properties of a laser beam when propagating through a jet plume. The work comprised a ground trial conducted at a DERA range in the Autumn of 1995. The trial utilised an open air test bed employing a Phantom Spey 202 jet engine as the source of the plume. This trial involved using continuous wave laser beams propagating through the jet engine plume at a height of 2 m from the ground and over a horizontal atmospheric path. The scope of the trial was limited by the need to assess the magnitude of the problem, prior to embarking on a more definitive series of experiments.

The ability to direct a laser beam on to a distant target from an aircraft depends on a number of factors such as laser beam pointing stability, the pointing accuracy of the beam director, the motion isolation of the beam director and the variations in refractive index along the propagation path. The energy density incident on the distant target is determined by the energy emitted by the source, its divergence and the attenuation and modification produced by the atmospheric path. The location of the laser beam exit aperture on an airborne platform is clearly important, as it strongly influences those directions where the beam will need to pass through highly turbulent zones.

During normal propagation of a collimated laser beam through the atmosphere the energy is affected by turbulence generated by relatively small scale fluctuations in the refractive index of the air, this leads to scintillation effects. These changes in refractive index can result from variations in temperature and can be caused by absorption of solar energy, the consequence of which is that the beam can become defocused. In some circumstances, as the scale of the turbulence increases, the centroid of the beam can be seen to move about. Additionally, in the presence of moderate levels of turbulence there is the added phenomenon of constructive and destructive interference, which result in patches of low and high intensity. In general these effects can be predicted using existing theory. However, at very high turbulence levels, such as those occurring in plumes and wakes, there is no suitable validated theory to predict the effects on a laser beam and consequently practical measurements have to be made to assess beam spreading and motion of its centroid.

The effect of turbulence created in the plumes on the laser beam was studied at two wavelengths of 488 nm and 3.39  $\mu\text{m}$ . The results were recorded at two ranges 150 m and 800 m. The changes in the beam characteristics were observed and recorded using suitable cameras.

## **2 Experimental arrangement**

The experimental set-up consisted of three major parts:

- a) The transmitter cabin housing the laser sources.
- b) The engine facility and laser path.
- c) The far-field target board and imaging systems.

The general layout is shown schematically in Figure 1, below.

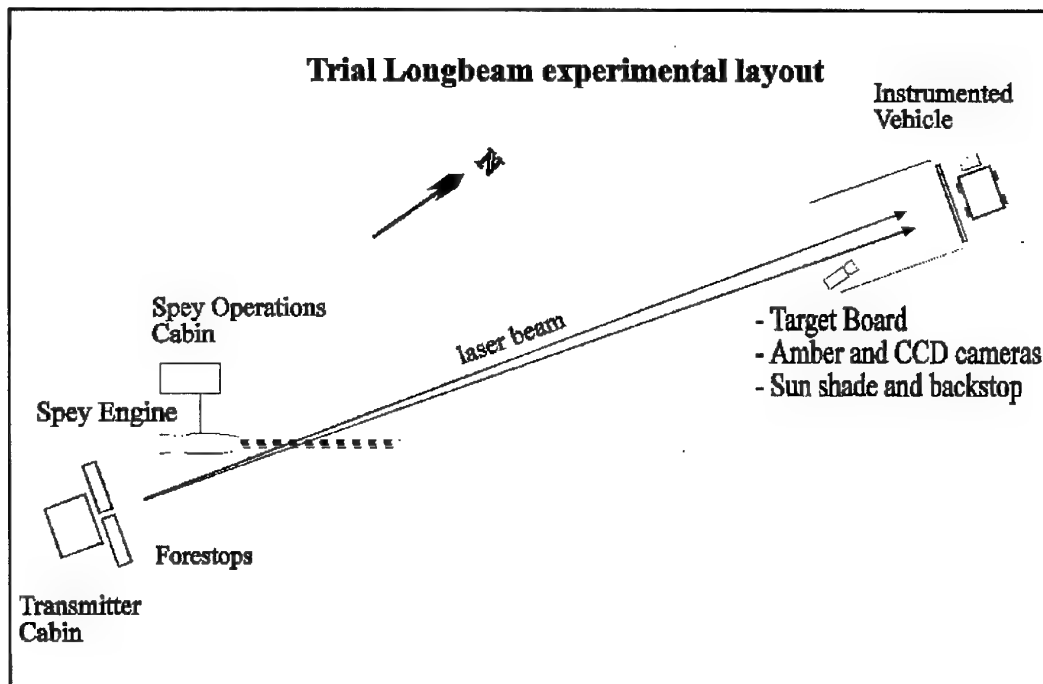


*Figure 1: Trial experimental layout*

## 2.1 The transmitter cabin and laser sources

The transmitter cabin housed the laser sources, beam expanding telescope, steering mirror, pointing telescope and CCD camera. A CCD camera was fitted on to the end of the aiming telescope to ensure that the laser operator could point the beam on to a retro-reflector placed on the target board, without having to look through the telescope for the retro-reflection with the unaided eye.

To reduce the inherent divergence of the laser beam, a beam expanding telescope with a "times 20" magnification was used. This gave a laser beam diameter at the output of the steering mirror of 16 mm and a divergence of 0.039 mrad for the argon ion laser. Similarly, the diameter and beam divergence of the helium neon laser was 31 mm and 0.14 mrad, respectively. The laser beam expanding telescope was adjusted to obtain a focused beam at the target. With the target board being at least 150 m away from the transmitter, the laser beam geometry at the target position was considered to be collimated.

Two different laser sources were used for this experiment, namely a continuous wave argon ion device emitting in the visible and a helium neon source emitting in the mid infrared. These lasers were selected as they were available and compatible with available camera recording equipment. Additionally, it was convenient to use a visible source for general alignment and viewing of the experimental effects, this source also had sufficient power to enable some comparatively long-range measurements to be made. The use of continuous wave laser sources avoided the need to synchronise the firing of the laser energy to the stare time of the camera and the operation of the recording equipment.

The performance of the laser sources used on the trial are summarised in table 1.

Laser source	Wavelength (nm)	Power (W)	Output beam dia. (mm)	Beam divergence (mrad)
Argon ion	488	0.27	0.8	0.78
HeNe	3390	0.0035	1.55	2.78

*Table 1: Summary of laser specifications.*

The laser beam propagated from the transmitter cabin at a height of 2 m above the ground, its path was notionally horizontal at a slight downward angle towards the target board positions, on a bearing of 023 with respect to "true" north. The angle between the engine longitudinal axis and the laser propagation path was 20°. The laser beam penetrated the plume at approximately 1 m downstream of the nozzle exit.

## 2.2 The engine facility and laser path

The Spey engine is a twin spool bypass engine with ten combustion chambers all radially located in an annular arrangement. At idle power the temperatures measured across the nozzle axis of the plume (comprising core + bypass air) are given in table 2.

Temperature (K)	Position from centre of jet pipe (mm)
633	0
598	100
543	167
512	216
472	260
467	277

*Table 2: Summary of engine exhaust temperatures.*

The temperatures generated through the centre of the plume at 1 and 10 m downstream from the end of the jet pipe were 631 K and 378 K.

The surface over which the laser beam propagated was solid concrete over the first 60 m of the path, followed by grass for the remaining path length.

Description	Bearing	Range (m)	Height Difference (m)
Engine	043.4	28.34	-0.157
Target 1	023.1	151.27	-1.058
Target 2	023.2	803.5	-0.753

*Table 3: Trial target range and laser path data.*

The positions of the Spey engine, target position 1 and target position 2 with respect to the transmitter output aperture are shown in table 3. The direction of the laser path had to be modified slightly to accommodate the longer range to the more distant target board.

The brightness of the helium neon laser and the methane absorption in the atmosphere limited the range of observations to 150 m.

### 2.3 The far-field target board and imaging equipment.

The far-field equipment comprised an imaging camera, video recording equipment and continuous wave power meter. The target board dimensions were 2.7 x 2.7 m and the surface of the board painted with a matt-white finish, to give maximum reflectivity.

The cameras used for imaging the image on the target board were the Amber Radiance 1 for the helium neon laser and a CCD colour camera for imaging the argon ion 488 nm laser. The specification for the two cameras is given in table 4.

Camera Type	Waveband ( $\mu\text{m}$ )	FOV ( $^{\circ}$ )	Integration time (ms)	Frame rates (fps)	Array size
Amber	3 - 5	10	1 and 2	60	256x256
Colour CCD	0.4 - 1.1	15	1 - 30	30 - 500	Not available

Table 4: Summary of camera specifications.

The output from the cameras was recorded on standard VHS video recorders.

### 2.4 Experimental method

The beam positioning mirror was adjusted so that the laser beam was centred on the target board and the appropriate camera positioned and focused to record the position of this beam on the target board. The camera then recorded data for a short period prior to the start-up of the jet engine. The camera continued to record the image of the laser beam received on the target board during this process, whilst the engine operated at "idle" power, moderate power and during shut down. The beam position was recorded for approximately 3-minute segments during this cycle of operations, for subsequent evaluation in the laboratory.

The background illumination on the target board was minimised by optical filtering and the erection of light shades. The limitations of the camera signal to noise ratio meant that only laser beams up to a certain size could be observed on the target board. This beam intensity limit was achieved at 150 m for the mid infrared laser source and about 800 m for the visible source.

A power meter placed near the centre of the target board was used to monitor the incident laser power before the engine was operated.

Weather data were accumulated during the runs recording visibility, temperature, wind speed and direction and humidity every hour.

The beam turbulence owing to normal atmospheric variations was evaluated by observing the recordings of the beam's behaviour during the period before engine start-up and after the engine was shut down. In general, the effect of natural atmospheric turbulence on the characteristics of the laser beams was found to be small or negligible during the period of this trial.

To calibrate the size of variations both in the beam spreading and beam deflections at the target board, a white plastic adhesive tape of dimensions 470 mm long and 25.4 mm wide was used as the aiming point and central reference.

### 3 Results

#### 3.1 Beam wander and spreading analysis.

A similar technique was used for both laser beam wavelengths, namely from frame-by-frame analysis of the image data from the video recordings with a digital storage oscilloscope. Measurements from the oscilloscope were taken as follows to determine the x- and y-components of the captured images:

- a) initially, the centre of the laser beam was adjusted to be in the middle of the oscilloscope's display screen before engine start-up. For subsequent frames, where the beam had moved in x-position owing to the presence of the jet plume, the pulse profile's peak-position shift was measured in microseconds with respect to the centre of the oscilloscope's display grid. The oscilloscope time-base was converted to a linear dimension by measuring the time difference between the ends of a 470 mm long calibration tape, illustrated in figure 2, hence the x-component of the new position was determined.
- b) The y-component was found by measuring the difference in lines from the reference video line (median vertical line 162). Each video line was scanned to identify the maximum peak profile of the spot which corresponded with the position of the centroid of the beam. The target board y-shift was found from the calibration that 25.4 mm on the board corresponded to 7 vertical lines on the video signal.
- c) The beam wander was calculated from (a) and (b) by taking the square root of the sum of the squares of the x- and y-components.
- d) The beam's radius was measured in the x-direction only and was recorded at the "zero power" levels by assessing the extent of the beam using the process described in step (a), above.

#### 3.2 Analysis of data recorded in the mid infrared.

Figure 2 shows the beam position and its size before engine start-up, in this case taken with the Amber camera. The beam's transverse profiles, taken from a single frame through its centre, are shown in Figure 3 and those of the horizontal strip of tape, used as a fixed reference, shown in Figure 4. After the initial runs this reference marker was changed to a "T" shape to give a better reference along both the abscissa and the ordinate.



Figure 2: Images on target board with engine off.

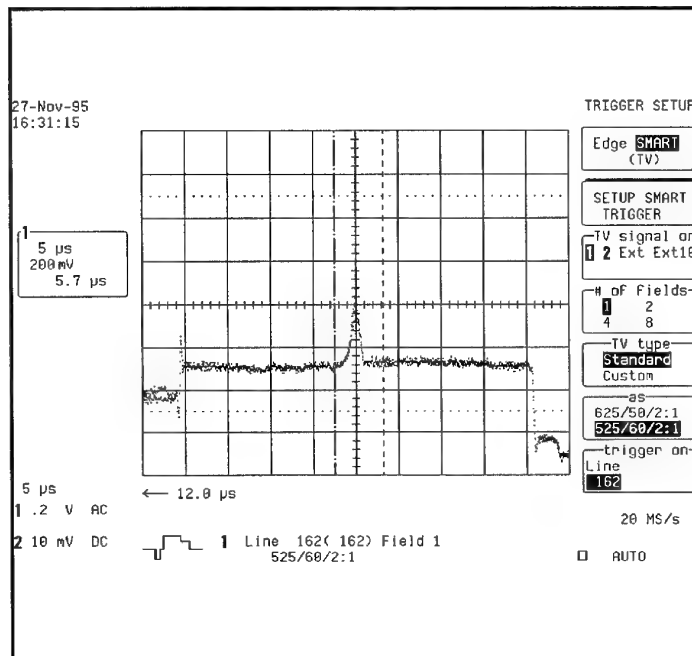


Figure 3: Scan through laser ( $3.39 \mu\text{m}$ ) profile at 150 m.

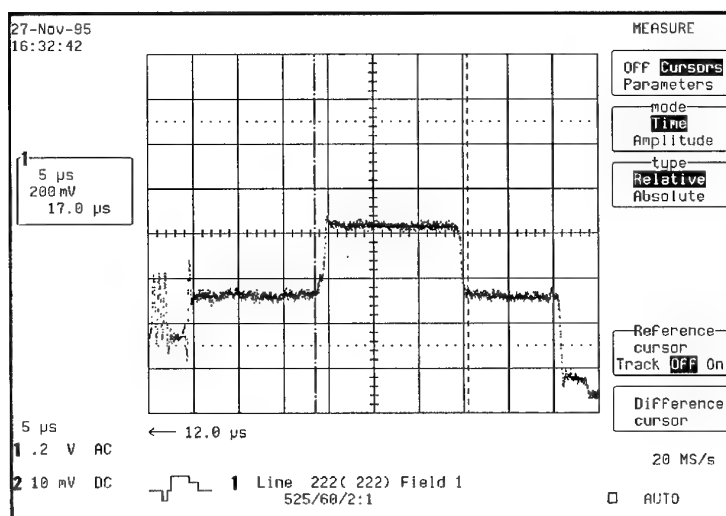


Figure 4: Scan through reference marker duration (470 mm long).

Images of the mid infrared waveband laser beam, observed on the target board, were also acquired by the instantaneous frame grabbing facility on the Amber camera. The sequence of pictures, shown below, were taken with the engine off (Figure 5), engine at idle (Figure 6), engine at a low throttle setting (Figure 7), and engine at a high throttle setting (Figure 8). The Amber camera used in these trials had an integration time of 2 ms and frame rate of 60 fps.

These images give some qualitative indication of the effect on the laser beam's characteristics after passing through the highly turbulent zone of the jet's plume, compared with normal propagation through the atmosphere. The pictures show that the laser beam undergoes spreading once the engine starts to run, and also, that the beam's characteristics have some slight sensitivity to engine speed.

Owing to low levels of laser power density falling on the target board and smaller spot size of the beam relative to the detector array, the intensity variations within the beam were not observable during this experiment.

A laser-power measurement at the target-board position was taken without the engine operating, using a detector with a  $1 \text{ cm}^2$  aperture; a power of  $300 \text{ } \mu\text{W}$  was recorded at a distance of 150 m from the transmitter position. The presence of atmospheric turbulence along the path resulted in some slight fluctuations in the beam's characteristics, and consequently the energy falling on the detector fluctuated slightly. Hence, direct measurements through the plume were not attempted, as they would not be very meaningful with this technique.

Direct measurements, taken over about 50 frames, showed that the beam size increased by a factor of three to four when the engine was operational, compared with the value recorded in the absence of a plume. Evaluation of the motion of the centroid of the beam, in the presence of a plume, indicated a mean beam wander radius of 14 mm with a standard deviation of 9 mm.

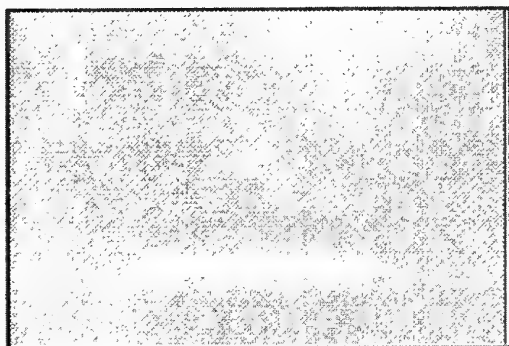


Figure 5: *Engine Off*

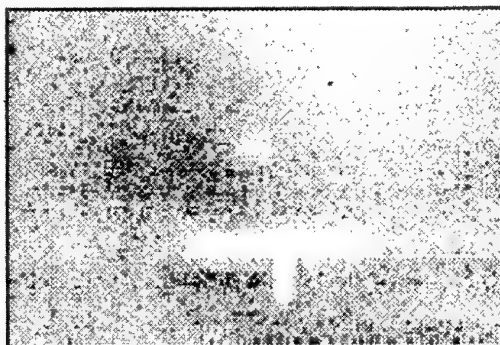


Figure 6: *Engine at idle*

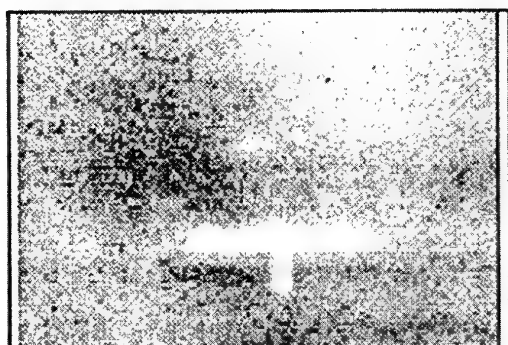


Figure 7: *Engine at low throttle*



Figure 8: *Engine at high throttle*



Examination of sequences of frames, during the shut-down of the engine, showed rapid variations in the beam profile through consecutive time frames. This indicated that the beam undergoes focusing and defocusing cycles during this period as the plume, and its effects, decay.

### **3.3 Analysis of data recorded in the visible.**

It was possible to record results with this argon ion laser at two ranges, 150 m and 800 m, owing to its greater output power.

In the case of the measurements made at the shorter range, investigation showed that the beam size increased by a factor of about nine in the presence of the engine's plume. However, the results from the longer-range measurements indicated a broadening of the beam by a factor of eleven during similar circumstances.

The motion of the centroid of the beam after passing through the plume, observed at the shorter range of 150 m, was found to move by about 65 mm on average with a standard deviation of 53 mm. The comparable statistics for the longer-range measurements, determined over a similar sample of 50 frames, showed a mean movement of 270 mm and a standard deviation of 220 mm. Clearly, the fluctuations about the mean value are much greater for the measurements made with a visible wavelength laser beam than those observed with the mid infrared beam.

These displacements, of the centroid, recorded at the two ranges convert to angular displacements (half angle) of 0.43 mrad at the shorter range and 0.34 mrad at the longer range. A similar comparison of the "half angle" measurements of beam spread showed a mean value close to one milliradian in both cases.

### **3.4 Comparison of recorded results**

Examination of the results recorded with the visible and the mid infrared laser beams show that the shorter wavelength energy experiences greater changes to its beam shape and position. The statistics also show that the centroid of the beam makes greater excursions about the centroid in the case of the shorter wavelength observations. The observations are shown in table 5, below.

For a given set of beam parameters, such as wavelength and divergence, it is anticipated that the angular expressions of beam wander and beam spreading to be the same at any range for a given path through the plume. Investigation of the data in table 5 recorded at the two different distances with the argon ion laser shows close correspondence between the observed values. However, it should be noted that the paths through the engine's plume were very similar, but not identical, as shown in table 3. The laser path to the more distant target board having a slightly longer path through the plume, which may explain the increased spread in its beam profile, but not its reduced beam wander statistics. Clearly, a more detailed study is required to investigate any such sensitivity to the angle of the laser path through a plume.

Range and laser wavelength	Average beam spread factor	Average beam wander	S.D. of beam wander
150 m and 3.39 $\mu\text{m}$	4	14 mm (0.1 mrad)	9 mm (0.06 mrad)
150 m and 488 nm	9	65 mm (0.43 mrad)	53 mm (0.35 mrad)
800 m and 488 nm	11	272 mm (0.34 mrad)	220 mm (0.27 mrad)

Table 5: Summary of results for trial (figures in brackets are angular conversions).

### 3.5 Comparison of results with theory

Theory [1,2] predicts that for a given turbulence condition, i.e. for a given value of the refractive index structure parameter  $C_n^2$ , the effects on the laser beam characteristics are approximately inversely proportional to wavelength. This suggests that the beam degradation should be about seven times worse when using visible light compared with mid infrared energy.

The results from this qualitative experiment confirm the trends predicted by the theory, particularly for the beam wander observations. However, there is less good agreement between the observation and theoretical prediction for the beam spread parameters. Clearly, further investigation is required in this area in future experiments.

## 4 Discussion

The effect of the increased spread of the beam means a reduction in the flux density on the target. In the case of the visible wavelength results, the increase in spread of a factor of 10 means a reduction in the power density of 100. For the mid infrared beam the reduction in power density is by a factor of 16.

The other aspect of importance is the effect of the increase in beam wander, which can reduce the time that the beam spends on a fixed target position. If the beam wander is interpreted as an error in the pointing stability, then the following equation can be used to estimate the time on target:

$$P_{(\text{time on target})} = \exp(-8\gamma^2/\beta^2)$$

where,  $\gamma$  is the pointing and tracking stability, and  $\beta$  is the beam divergence.

This equation implies that if the visible beam has a pointing and tracking stability of 0.4 mrad, from the increased beam wander, and a divergence of 1 mrad from the increased beam size, then the time on target reduced to 25% of that for the unperturbed beam. In the case of the mid infrared beam the time on target is reduced to 40% of that achieved with an unperturbed beam. In this calculation it was assumed that the pointing and tracking stability, resulting from the beam wander, was 0.1 mrad and the beam divergence was 0.3 mrad.

## 5 Conclusions

This trial indicated that the effects of turbulence experienced by a laser beam when passing through an engine plume resulted in increased levels of beam spreading and beam wander. Observations were recorded in the visible and in the mid infrared.

At a wavelength of 3.39  $\mu\text{m}$ , laser propagation through a jet engine plume was observed at a range of 150 m without any significant attenuation or absorption in the plume. At this range the beam spreading was found to increase by a factor of 4. The motion of the centroid of the laser beam, called beam wander, was found to have a mean value 0.1 mrad, with a standard deviation of 0.06 mrad.

The consequence of the increase in the beam size of this mid infrared beam is to reduce the power density on a target by a factor of 16, compared with the unperturbed beam. The effect of the increased beam wander is to reduce the time that the modified beam spends on a target to about 40% of the value for an unperturbed beam.

The effects of turbulence on the visible wavelength beam was to reduce the power density on a target by a factor of 100, owing to an increase in beam size by a factor of 10. The increased beam wander reduced the time on target to 25% of that for the unperturbed beam.

The observed effects of turbulence on the characteristics of the visible wavelength beam were much greater than the effects observed on the mid infrared beam. This trend was in line with the predictions of theory. However, the scaling between the observed effects at the two different wavelengths were slightly less than predicted by this theory.

## 6 References

1. A.N. Kolmogorov, "The local structure of turbulence in incompressible viscous fluid for very large Reynolds' numbers", Doklady Akad. Nank., USSR Academy of Sciences of USSR, New York, NY, Vol. 30, p 301, (1941).
2. The Infrared Handbook, Editors, W. L. Wolfe, et al, Chapter 6, ERIM, ONR Arlington. Va, (1978)

## 7 Acknowledgments

The author is grateful to the assistance of Messrs Turner and Din, of WX3/DERA, during these trials and also to the British MoD for financial support of this study.

© Copyright, British Crown Copyright 1998/DERA.

Published with the permission of the Controller of Her Britannic Majesty's Stationary Office.

PAPER No. 42

DISCUSSOR'S NAME: W. Cornette

COMMENT/QUESTION:

The turbulence of an aircraft plume is quite variable. Near the plume core, it is higher near the edge than in the center. Also, the gradients of Pressure, Temperature,  $H_2O$ , and  $CO_2$  cause the plume to act like a lens, both focusing/defocusing and bending the laser beam. Are there plans to scan the plume radially and axially to analyze this variability?

AUTHOR/PRESENTER'S REPLY:

Plans have been formulated to undertake a more extensive study which will involve the laser beam passing through various portions of the efflux. As you are aware, the report presented the findings of a qualitative study. The intention is that any follow-on work will be more definitive.

DISCUSSOR'S NAME: D. Clement

COMMENT/QUESTION:

A problem encountered frequently in this kind of experiment is microphony, meaning that vibrations jitter from the supersonic flow couples into the laser platform. Did you encounter this problem too, and what did you do to overcome it?

AUTHOR/PRESENTER'S REPLY:

The position of the low transmitter was chosen carefully, and evaluated by trial and error, to establish that there was no interference between the engine and the laser. Natural damping of the noise and vibration of the engine structure by choosing a suitable separation between the laser and the engine.

PAPER No.: 42

DISCUSSOR'S NAME: D. Clement

COMMENT/QUESTION:

If one wants to extrapolate your results and apply it to other cases, it would be highly desirable to understand the turbulence inside and outside the plume in a qualitative manner. Do you plan to work in this direction?

AUTHOR/PRESENTER'S REPLY:

A programme of research and investigation is currently underway. It is hoped to have results (which will be quantitative), available by December 1998.

# LEXTAB: LONG TERM EXPERIMENT ON TARGETS, ATMOSPHERE, AND BACKGROUNDS IN THE DESERT

Karin Weiss-Wrana, Alwin Dimmeler, Wolfgang Jessen  
Forschungsgesellschaft für Angewandte Naturwissenschaften e.V.  
Forschungsinstitut für Optik (FGAN-FfO)  
Schloss Kressbach  
D-72072 Tübingen, F. R. Germany  
Doc.: FGAN-FfO 1998/01

Leslie Balfour  
Electro-Optics Research & Development Unit (EORD)  
TECHNION R&D Foundation Ltd.  
Technion City, 32000 Haifa, Israel

## SUMMARY

As a joint effort of the FGAN-FfO and the EORD/TECHNION, the experimental program LEXTAB (Long term Experiment on Targets, Atmosphere, and Backgrounds) was commenced in 1997. With the test range located in the Negev desert, it aims on determining the temporal behaviour of atmospheric/ir parameters of target/background signatures in a desert environment. Data is going to be collected continuously for a period of at least one year at a time resolution of 5 minutes.

The measurements cover standard meteorological data, including visual range, downwelling short wave and long wave radiation, atmospheric infrared transmittance in two window regions (8 - 12  $\mu\text{m}$  and 3 - 5  $\mu\text{m}$ ) measured over a 488 m path, and radiometric temperatures of some typical nearby background elements (sand, rock).

After a general description of the LEXTAB concept and the LEXTAB station a first climatological survey from measurements at the LEXTAB range is presented.

The desert aerosol model from LOWTRAN 7 is unable to predict observed visual range statistics. New and more specific models are required.

The measured atmospheric broadband transmittance values were compared with theoretical systems-weighted values, calculated with the propagation model LOWTRAN 7 and MODTRAN 3.5 by using the corresponding measured meteorological parameters as input. For both ir windows MODTRAN 3.5 calculations yield higher transmittance values: the difference is negligibly small (about 1 %) in the case of the 8 - 12  $\mu\text{m}$  window (SW), for the 3 - 5  $\mu\text{m}$  (LW) about 3 % which is about equal to the estimated measurement accuracy. Examples of diurnal variations of measured and corresponding calculated transmittance values are given.

Examples for diurnal variations of uv radiation measured in two spectral bands and the corresponding ratio of the measured radiation in these two bands are given. The ratio shows a characteristic double peaked feature.

Results of computed thermal range statistics for a modern thermal imager are given. The variability in target/background temperature differences turns out to be the main factor for the variability in thermal range. Compared to this, atmospheric effects are of minor importance in this context.

The FGAN-FfO developed a thermal background model (THGM) for predicting thermal signatures of objects, with

emphasis on backgrounds. THGM is a semi-empirical model. By now sets of coefficients exist for two background types: "grassland" and "edge of forest", typical for moderate climatic zones. With the measurements at the LEXTAB range the model is extended to backgrounds typical for arid climates.

## 1. INTRODUCTION

Operations of electro-optical (E-O) systems in desert environments may be influenced by effects not found under moderate climatic conditions. Apart from the excessive temporal behaviour of signatures of targets and backgrounds, also atmospheric effects typical for desert regions like propagation through blowing dust and sand in the presence of high turbulence levels will affect systems performance. This can cause severe problems in system operation, or even prevent it.

The effectiveness of camouflage, concealment and deception (CCD) depends to a large extent on the actual environmental situation under which the targets are deployed. Since the environmental parameters usually change as a function of time-of-day and of season, CCD effectiveness can normally only be expressed in a statistical way. Existing data bases of target and background signatures as well as atmospheric data of arid climate zones are insufficient and adequate models practically do not exist.

A thorough study on the hot and dusty environment has recently been performed taking under consideration the performance of electro-optical systems on the meteorological situation and the contrast between targets and backgrounds [1].

To provide a statistically comprehensive data base and to develop an adequate predictive capability, the joint effort LEXTAB (Long term EXperiment on Targets Atmosphere and Backgrounds) was started in 1997 by the FGAN-FfO and the EORD/Technion (Haifa/ Israel) in the Negev.

## 2. TEST SITE, MEASURED QUANTITIES AND INSTRUMENTAL EQUIPMENT

The test site selected for carrying out LEXTAB is a test range near Mizpe Ramon in the Negev. This location is well suited for researching the influence of the desert environment on the performance of the E-O sensors and of CCD measures.

The following meteorological parameters are measured to quantify the environmental conditions:

- air temperature,
- relative humidity,
- atmospheric pressure,
- wind direction and velocity (2 m height),
- amount of precipitation,
- atmospheric visual extinction coefficient,
- global radiation (0.3 - 3  $\mu\text{m}$ ),
- indirect solar radiation (0.3 - 3  $\mu\text{m}$ ),
- soil temperature (10 cm depth).

Additionally, a modified net radiation meter (0.3 - 60  $\mu\text{m}$ ) is used to determine atmospheric longwave radiation. Furthermore the (effective) temperature is measured as the temperature of a black sphere, exposed to the ambient radiation field and subjected to convective heat exchange with ambient air.

The thermal background signature characteristics are registered by measuring the soil temperature and the radiometric temperature of two selected background elements (rocks and sand). All meteorological and target/background parameters are logged by an autonomous environmental station AME 67 (Hoffmann Messtechnik GmbH).

The total integrated transmittance in the visible and in two infrared bands, 8 - 12  $\mu\text{m}$  (LW) and 3 - 5  $\mu\text{m}$  (SW) band, is measured by a modified BARNES Atmospheric Infrared Transmissometer System (BAITS) of the FGAN-FFO. The transmittance range is 488 m long.

In addition to the meteorological station two uv radiation sensors (Scintec UV-S-290-T and UV-S-310-T) measure the level of atmospheric uv radiation in two spectral bands. The 280 - 315 nm band sensor with peak responsivity at 290 nm covers roughly the upper spectral end of the solar blind region whereas the 300 - 325 nm band sensor with peak responsivity at 310 nm measures radiation in the range above the solar blind region.

The local ozone concentration is monitored with a CDI 3100 system.

The measuring cycle for all parameters listed above is 5 minutes throughout.

### 3. FIRST LEXTAB ANALYSES

#### 3.1 General Climatological Evaluations

##### 3.1.1 Temperature and Humidity

First climatological surveys have been performed together with comparative studies based on earlier investigations on the climate of the Saudi-Arabian peninsula [2, 3].

The cumulative frequencies of occurrence of air temperature at the LEXTAB station in comparison to two further stations (Ovda and Beer Sheva) in the Negev (April 1986), as well as two stations located on the Saudi-Arabian peninsula, are presented in Fig. 1.

Obviously the temperatures at the LEXTAB site are considerably below the temperatures of the other stations. The higher values of the Saudi-Arabian stations can be explained mainly from their geographical location. Sharurah has the southernmost position and thus shows the highest temperatures. Hail, which is located more than 1000 m above sea level, is much more moderate in its temperature distribution. However, also in comparison to Beer Sheva and Ovda, both located in the Negev as well, the temperatures at the LEX-

TAB site are lower. This fact can only partly be explained by the height above sea level of approximately 500 m, but must probably also be attributed to local effects, e. g. plain terrain with relatively well pronounced ventilation. The comparatively low temperatures at the LEXTAB site are also observed during summer but, of course, on a higher level.

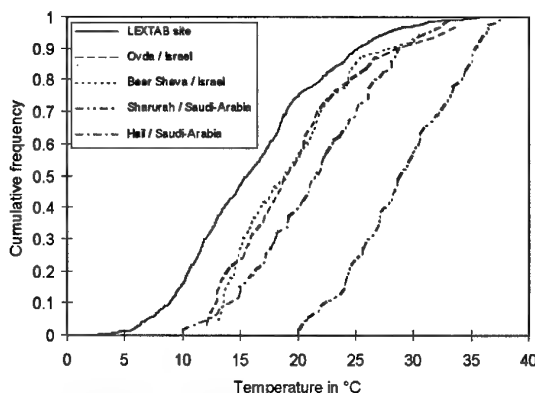


Fig. 1: Cumulative frequencies of occurrence of air temperature at five desert stations during April.

Atmospheric absolute humidity is one of the main factors determining atmospheric infrared transmittance. It turns out that in different desert regions this quantity can show a considerable variability. This is demonstrated in Figs. 2 and 3.

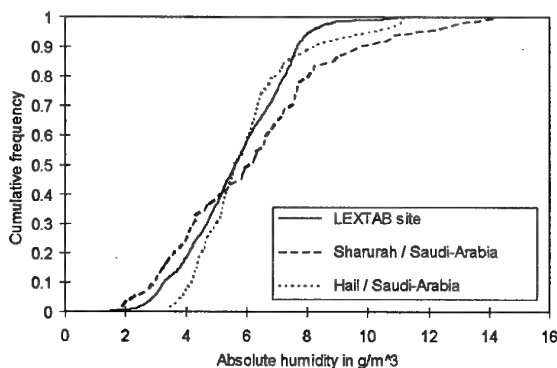


Fig. 2: Cumulative frequencies of occurrence of absolute humidity at three desert stations during April.

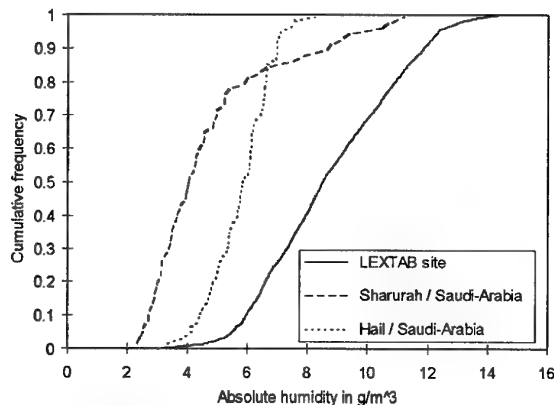


Fig. 3: Cumulative frequencies of occurrence of absolute humidity at three desert stations during July.

Whereas in April relatively small differences at the three stations with median values of absolute humidities around  $5 \text{ gm}^{-3}$  are observed, the situation changes drastically in July. During this month the absolute humidities at the LEXTAB site have doubled in comparison to those of Sharurah and have increased by a factor of 1.5 in comparison to Hail. These results demonstrate the extreme variability of environmental parameters in different desert regions and thus, of the resulting ir propagation conditions which have to be expected with respect to different geographical locations and seasons.

### 3.1.2 Visibility

Visibility is one of the controlling factors in atmospheric aerosol modelling by scaling the model aerosol size distributions according to visibility, as performed e. g. in the LOWTRAN 7 aerosol models [4, 5]. However, from earlier investigations [2, 3] it is known that the existing DESERT aerosol model from LOWTRAN 7 can not explain measured (or observed) visibilities to a sufficient degree of accuracy. For the first time project LEXTAB offers the opportunity for a more systematic investigation of this problem by providing visibility measurements collected over a longer period of time and with high temporal resolution.

The LOWTRAN 7 DESERT aerosol model was used for calculating atmospheric visual range (from extinction at  $0.55 \mu\text{m}$  via Koschmieders relation). Whereas for the original DESERT aerosol model [5] wind speed is the only driver for the desert aerosol extinction coefficient (resulting also in visual range predictions), the LOWTRAN 7 version [4] includes an additional visibility scaling allowing for observed visual ranges to be entered as input.

A comparison of visibilities from the DESERT model with measured visual ranges over a period of three months at a resolution of five minutes is presented in Fig. 4.

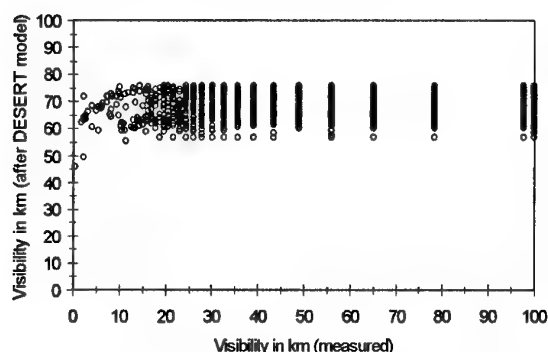


Fig. 4: Calculated visibility (from DESERT aerosol model) vs. visibility measured at the LEXTAB site, April - June 1997.

According to Fig. 4 measured visibilities at the LEXTAB site cover a wide range from below 1 km to more than 100 km. The bar pattern is due to the limited number of digits submitted and indicates the discrete steps in extinction coefficients as the originally measured quantity. It is obvious that the desert model is unable to predict the measured visual ranges correctly. Earlier investigations [3] based on synoptic weather data from desert regions had already revealed a similar behaviour. However, in this case only visual ranges up to ap-

proximately 20 km were documented due to visual ranges given by weather observers.

Due to these findings it seems extremely necessary to adjust existing or to develop new aerosol models for desert conditions.

### 3.2 Atmospheric Broad Band Transmittance

The development of a desert aerosol model requires measurements of the atmospheric transmittance. The measured total transmittance can be written as the product of aerosol and molecular transmittance. After calculating the molecular transmittance using simultaneous meteorological data the aerosol transmittance can be determined by dividing the measured total transmittance by the corresponding molecular part. The accuracy of these aerosol transmittance values depends on the accuracy of the measurements as well as on the accuracy of the atmospheric propagation model. Two propagation models can be used: LOWTRAN 7 with low spectral resolution ( $20 \text{ cm}^{-1}$ ) and MODTRAN 3.5 with moderate spectral resolution ( $2 \text{ cm}^{-1}$ ). MODTRAN 3.5 calculations are much more time consuming than LOWTRAN 7 calculations. The difference between systems-weighted transmittance values of LOWTRAN 7 and MODTRAN 3.5 calculations was investigated. The calculations were carried out for the propagation path of 488 m which corresponds to the transmissometer path length.

For both ir bands the MODTRAN 3.5 calculations yield slightly higher transmittance values. Figs. 5 and 6 demonstrate the diurnal variations of the molecular transmittance calculated with MODTRAN 3.5 and LOWTRAN 7. In the case of the 8 -  $12 \mu\text{m}$  band (LW) the difference is negligibly small (factor about 1.01), in the case of the 3 -  $5 \mu\text{m}$  band (SW) the difference is more significant but still small, the factor amounts to about 1.03. Calculations carried out for summer and winter conditions yield the same results.

It should be mentioned that this statement is valid only for the meteorological conditions met so far at the LEXTAB site, while for different climatic situations, for example hot and humid, the results may differ.

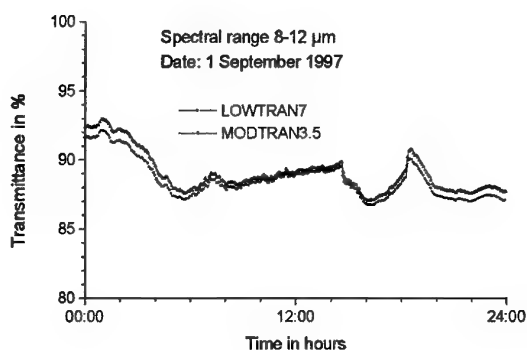


Fig. 5: Comparison between the diurnal variation of the systems-weighted molecular transmittance for the 8 -  $12 \mu\text{m}$  range calculated with MODTRAN 3.5 and LOWTRAN 7 (LEXTAB, 1 September 1997).



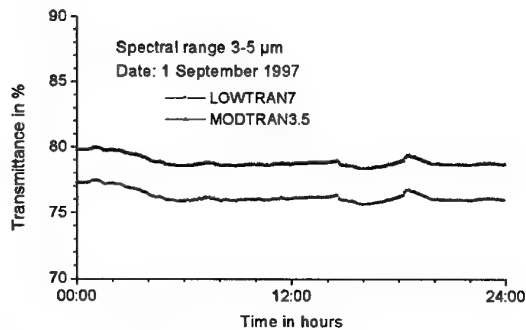


Fig. 6: Same as Fig. 5, for 3 - 5  $\mu$ m range.

The measured total transmittance values were compared with calculated systems-weighted transmittance values assuming two aerosol models: DESERT aerosol with the input parameter wind speed and RURAL aerosol with the input parameter visibility. Although the LOWTRAN 7 DESERT aerosol model is unable to predict the measured visual range, see 3.1.2, it was used as a first approximation.

Until now our transmittance measurements cover only atmospheric conditions with rather high visual ranges. For a general statement, transmittance values for low visual range would be necessary. It should be mentioned that the necessary parameters like wind speed and visibility are measured close to the receiver site. Limited variations of the visibility along the propagation path are possible (for example blown-up dust by dust devils or vehicles). These can not be measured.

The calculations were carried out with MODTRAN 3.5 and LOWTRAN7 for both ir ranges. As an example Figs. 7 and 8 demonstrate the results of the MODTRAN 3.5 calculations for 1 September 1997. In the LW, atmospheric extinction depends stronger on atmospheric water vapour content than in the SW. The two dips in the diurnal variation of the thermal ir range are mainly caused by higher values of absolute humidity. The wind speed varied from about 2 m/sec up to 8.8 m/s (5 min average) in the afternoon (at 16:00), this corresponds with the stronger difference between the corresponding molecular transmittance values and the calculated DESERT aerosol transmittance values. For the atmospheric conditions as measured on 1 September 1997 the measured diurnal variation of the total transmittance in the LW can be reproduced well by MODTRAN 3.5 calculations by applying both aerosol models.

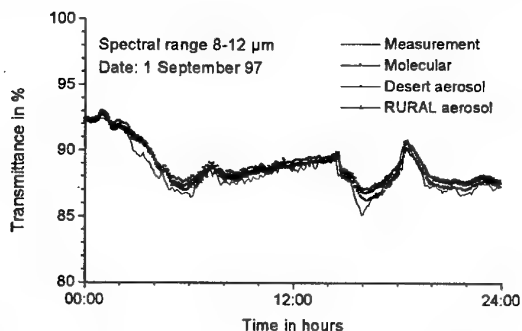


Fig. 7: Comparison between measured transmittance and transmittance values calculated with MODTRAN 3.5 for DESERT aerosol and RURAL aerosol model for the 8 - 12  $\mu$ m range (LEXTAB, 1 September 1997).

In the case of the SW the dips are much less significant. The agreement between the measured total transmittance and the corresponding MODTRAN 3.5 calculations is not as good as in the LW.

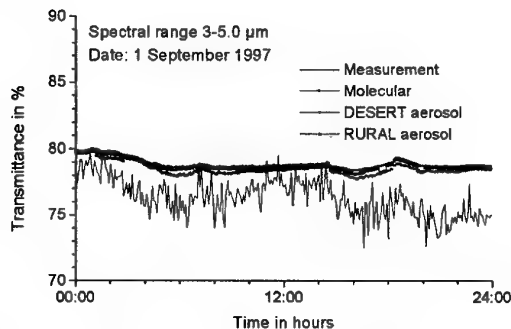


Fig. 8: Same as Fig. 7, for the 3 - 5  $\mu$ m range.

From Figs. 7 and 8 it can easily be seen that during this day the aerosol extinction was extremely low. Modelling the DESERT aerosol at the test site demands transmittance measurements for a dusty atmosphere (strong aerosol extinction).

### 3.3 Atmospheric Ultra-Violet Radiation

The calculation of range performance of uv systems requires information about the strength of the atmospheric uv radiation in different climatic regions. For this reason two uv sensors were additionally installed at the LEXTAB range.

Radiation in the uv is mainly absorbed by oxygen and ozone. In the uv region the absorption coefficient of these constituents increases strongly with decreasing wavelengths. For this reason the radiation measured in the 290 nm band is lower than the radiation measured in the 310 nm band.

Fig. 9 shows three examples for diurnal variations of the two uv bands as measured during summer (23 June 1997), fall (5 October 1997) and winter (14 December 1997). Due to the longer propagation path through the atmosphere during fall and winter compared to summer (larger solar zenith angles), the uv radiation is lower during winter.

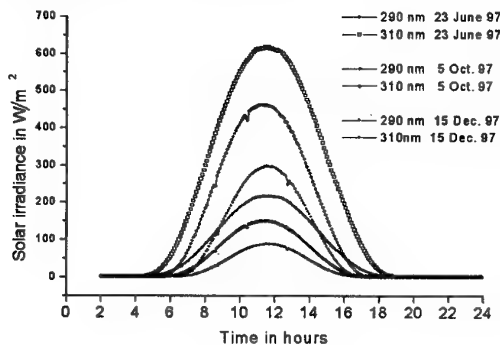


Fig. 9: Diurnal variation of the solar irradiance in the 290 nm band and 310 nm band as measured during 23 June, 5 October and 15 December 1997.

The ratio of the radiation in the 310 nm band to the 290 nm band was computed on a daily basis. For all days the diurnal variation of this ratio shows a characteristic double peaked feature. Shortly after sunrise and before sunset the ratio shows

its maximum. This is caused by the longer propagation path through the atmosphere. Under this condition the difference between the transmitted radiation in the two bands is more significant.

Fig. 10 shows the corresponding diurnal variations of the ratio for these three days. It is largest during winter. This is again an effect of a larger propagation path during winter.

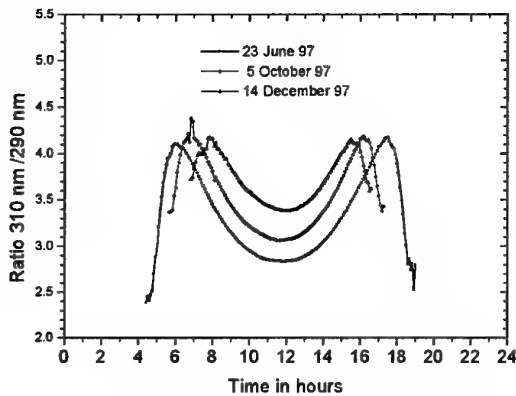


Fig. 10: Diurnal variations of the ratio of the irradiance in the 310 nm band to the 290 nm band as measured during 23 June, 5 October and 14 December 1997.

In the case of very small measured radiation values, before sunrise and after sunset, the calculated ratio is very sensitive against the accuracy of the sensors. For this reason a more detailed investigation of the steep decrease at both ends of the curve (before sunrise and after sunset) is planned for the near future.

### 3.4 Derivation of Thermal Ranges Statistics

The knowledge of range statistics for modern thermal imagers under arid climate conditions is of extreme importance. On the basis of a preliminary LEXTAB data set an estimate of such statistics was performed using the FGAN-FfO Thermal Ranges Model TRM [6].

Mathematically the range  $R$  of a thermal imager is determined as the intersection point of the Minimum Necessary Temperature Difference (MNTD) and the Effective Temperature Difference (ETD) of the system. Both functions are - besides others - a function of range  $R$ . The ETD is scaled by the absolute value of the initial target-to-background temperature difference  $\Delta T_0$ . Thus the following equation (1) has to be solved to calculate the thermal range  $R$  of a certain imager and for a certain observation task:

$$\text{ETD} = \Delta T_0 \cdot \tau_{\text{eff}}(R) = N \cdot \text{MNTD}(R), \quad (1)$$

where  $\tau_{\text{eff}}(R)$  is the effective, i. e. the spectrally averaged and systems-weighted atmospheric transmittance.  $N$  is a normalising factor, converting the MNTD valid for laboratory conditions to real meteorological conditions.

Using the LEXTAB data, range calculations were performed under the following assumptions:

- thermal imager: generic CMT system, 8 - 12  $\mu\text{m}$ , scanning,
- observation task: 50 % recognition probability,
- target size: 2.3 m x 2.3 m.

The MNTD was deduced from the MRTD (Minimum Resolvable Temperature Difference), calculated after the FGAN-FfO Thermal Range Model TRM [6]. The effective atmospheric transmittance was calculated via the SYTRAN code [7], because no reliable transmittance measurements were available at the point when the analysis was performed.

In contrast to earlier computations, the initial target/background temperature difference was no longer set only to a constant value (e. g. 2 K after STANAG 4347 [8]) but treated as a variable quantity with values depending on environmental conditions. In the present case, values were adopted from the LEXTAB data set, which provides radiative temperatures from two different elements (sand, rock). Due to the lack of temperatures from a real target, the temperature of "rock" was used instead. It is assumed that at least during daylight hours its thermal behaviour can represent a target to a sufficient degree. For comparisons calculations with a constant temperature difference of 2 K were carried out.

Equation (1) was solved by numerical means with respect to  $R$ , using LEXTAB meteorological data of one month (July). A statistical evaluation is plotted in Fig. 11, where the cumulative frequencies of occurrence of calculated thermal ranges for a generic imager are plotted.

The solid line refers to the case of variable target/background temperature difference. The dashed line indicates the results under the assumption of a fixed temperature difference of 2 K. Obviously the influence of the "weather" is fairly small, as can be seen from the nearly unique range of about 3 km, when assuming a fixed temperature difference. This changes drastically when considering the realistic (measured) signatures. The previous upper limit is exceeded by approximately 10 % in range, whereas on the lower end even ranges near zero are obtained. These can be attributed to situations where the temperature differences nearly vanish (cross-over points).

To summarise it can be said that for the situations considered thermal signatures play the dominating role, whereas the atmospheric extinction is of minor importance.

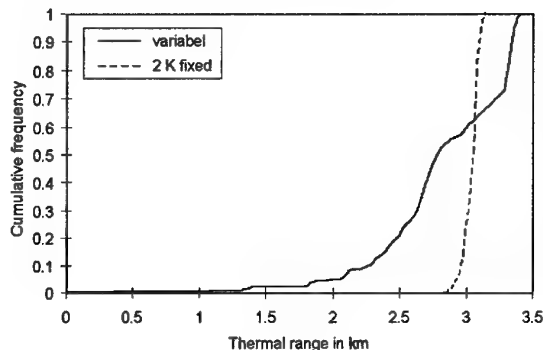


Fig. 11: Cumulative frequencies of occurrence of recognition ranges for a generic thermal imager in the 8 - 12  $\mu\text{m}$  region (50 %) for variable and fixed temperature differences at the LEXTAB site, July 1997.

An instructive example of temperature/signature variations as occurring under desert conditions is shown as Fig. 12.

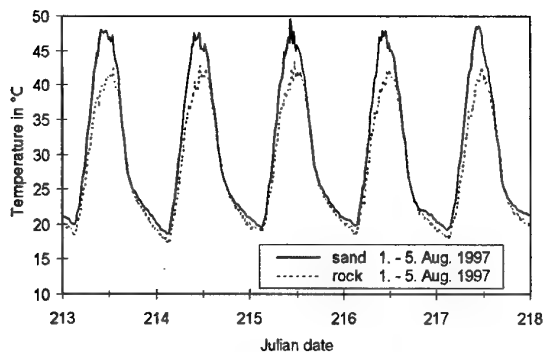


Fig. 12: Time series of radiometric temperatures of two typical background elements (sand and rock) at the LEXTAB site.

#### 4. MODELLING OF BACKGROUNDS IN ARID CLIMATES USING LEXTAB DATA

Dictated by the needs in performance assessment of both, ir imaging systems and ir camouflage technologies, the FGAN-FfO has developed a model for predicting thermal signatures of objects, with emphasis on backgrounds. The thermal background model (THGM) is a 1-dimensional, time dependent formulation of the heat transfer equation [9, 10]. The approach is semi-empirical, i. e. the coefficients quantifying the various heat transfer mechanisms of a given object are established by regressing the model results to time histories of measured object surface temperature.

Model coefficients exist by now for two typical middle European background types: "grassland" and "edge of forest". With the measurements at the LEXTAB range the FGAN-FfO is extending the set of coefficients of the THGM to backgrounds in arid climates.

Two surface temperatures are continuously measured by radiometers (8 - 12  $\mu\text{m}$ ) with the AME 67 at the LEXTAB station. These measurements are used for the determination of coefficients for the THGM. The surfaces are "sand" and "rock" (small heap of stones which were collected in the surroundings).

A first validation of the model has already taken place. During two field trials the two different background elements "sand" and "rock" [11, 12] were measured elsewhere. During these trials various backgrounds were measured for approximately 30 hours by imaging radiometers. The trials took place in the Negev desert in February and July 1996. Measurement results of a sandy surface in the Wadi Faran and a rocky surface at Mizpe Hagai are displayed in Figs. 13 and 14. Several different background elements were analysed in each image. Additionally the predicted temperatures of the THGM for "sand" and "rock" are plotted.

For the summer measurements (Fig. 13) it is possible to compute the surface temperatures within the bandwidth of the measured temperatures with one set of coefficients only. Surprisingly, this is the case for the coefficients determined with the surface element "rock" for Wadi Faran and for the coefficients determined with the element "sand" for Mizpe Hagai. In contrast to this result the coefficients "sand" yield better temperature predictions for the winter data (Fig. 14).

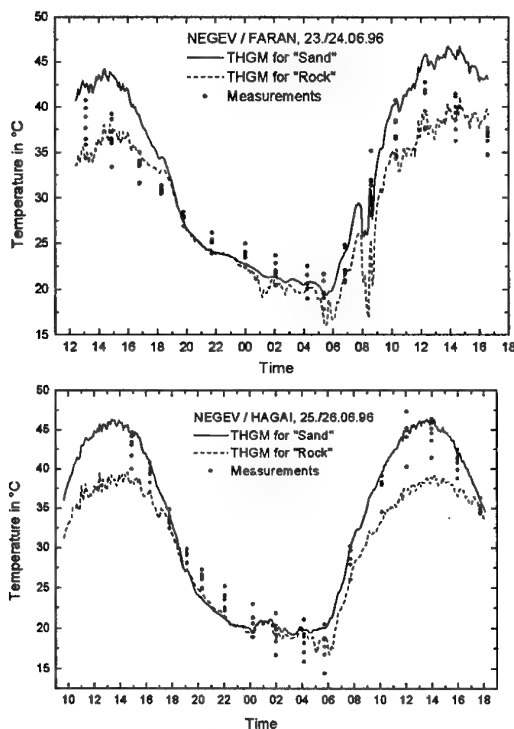


Fig. 13: Comparison between measured (points) and predicted (lines) surface temperatures (background types: "sand" and "rock") for the locations Wadi Faran (top) and Mizpe Hagai (bottom). Predicted time period: 23 - 26 June 1996.

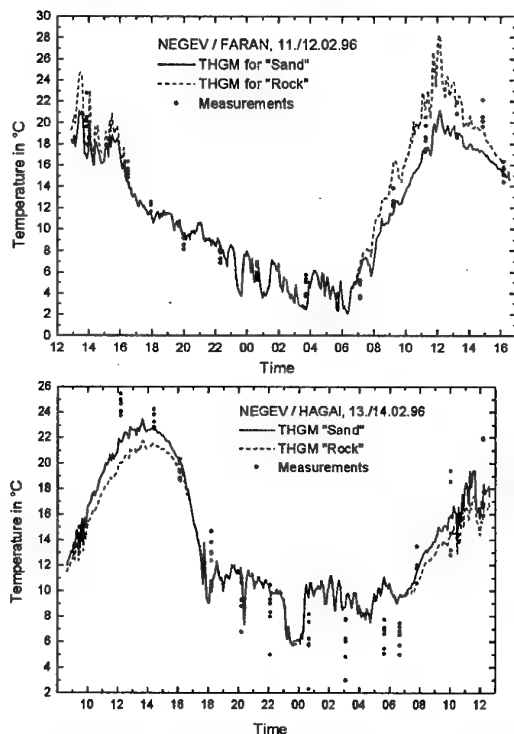


Fig. 14: Comparison between measured (points) and predicted (lines) surface temperatures (background types: "sand" and "rock") for the locations Wadi Faran (top) and Mizpe Hagai (bottom). Predicted time period: 11 - 14 February 1996.

However, the differences between the temperatures computed with the two sets of coefficients are significantly smaller for the winter data than for the summer data.

The prediction of the surface temperatures for the location Mizpe Hagai is partly outside the range of measured temperatures. This behaviour has to be investigated in future data analysis.

## 5. CONCLUSIONS

LEXTAB is a joint experiment of the FGAN-FfO, Germany, and the EORD, Israel. It offers the possibility for carrying out systematic measurements of environmental and target/background parameters for an extended time period and with high temporal resolution under desert conditions. The goal of the project is to establish a data base to study the statistical performance of electro-optical systems and CCD in a desert environment.

Air temperature and absolute humidity show an extreme variability in different desert regions and seasons. Thus it is expected that ir propagation differs significantly for different geographical locations and seasons.

Results of computed thermal range statistics for a modern thermal imager are given. The variability in target/background temperature differences turns out to be the main factor for the variability in thermal range. Atmospheric effects are of minor importance in this context.

It could be shown that the desert environment is far from being understood and being well described by existing models. This is especially true for an adequate modelling of the desert aerosol. The desert aerosol model from LOWTRAN 7 is unable to predict observed visual range statistics, which casts doubt on its ability to predict ir transmittance property. A main goal of LEXTAB is therefore to establish a data base on atmospheric extraction parameters which could be used for system performance evaluation and for the development of an improved desert aerosol model.

To derive realistic thermal imager performance ranges under desert conditions the FGAN-FfO target/background model was extended to include two backgrounds typical for arid climates, i. e. sand and rock.

For range performance calculations of uv systems, as used in multi-spectral sensors, the uv background, the strength of the solar uv irradiance was additionally measured in two adjacent spectral ranges. The diurnal variations of the ratio of uv irradiance in the 310 nm band and the 290 nm band show a characteristic feature with peaks shortly before sunrise and after sunset.

It is planned to continue the experiment so that a consistent data set is generated for a period of at least one year. Furthermore it is planned to include measurements of additional environmental parameters such as the atmospheric structure constant  $C_n^2$ , and of some experimental CCD measures.

## 6. REFERENCES

- [1] Tooth, A.R., H.T.A. Pentecost: "Hot and Dusty Environment Survey" (HADES), NATO AC/243 (Panel 4/RSG.13) TR/19, Nato unclassified.
- [2] Höhn, D.H., W. Jessen, D. Clement: "Atmospheric IR Transmittance Statistics in Arid Climates Based upon Synoptic Data from Selected Middle East Weather Stations", Battlespace Atmospheric Conference, San Diego, December 1996.
- [3] Jessen, W., D. Clement: "Infrared Propagation Statistics in Arid Climates after Synoptic Meteorological Data from nine Middle East Weather Stations", Report FGAN-FfO 1995/76.
- [4] Kneizys, F.X., E.P. Shettle, L.W. Abreu, J.H. Chetwynd, G.P. Anderson, W.O. Gallery, J.E.A. Selby, S.A. Clough: "Users Guide to LOWTRAN 7", AFGL-TR-88-0177, ERP No. 1010, August 1988.
- [5] Longtin, D.R., E.P. Shettle, J.R. Hummel, J.D. Price: "A Wind Dependent Desert Aerosol Model: Radiative Properties", AFGL-TR-88-0112, April 1988.
- [6] Wittenstein W., R. Gal, W. Schuberth: "Thermal Range Model TRM3", Report FGAN-FfO 1997/49.
- [7] Halavee, U., W. Jessen, A. Hirneth, A. Kohnle: "Systems-Weighted Infrared Broad-Band Atmospheric Horizontal Transmittance: The Computer Code SYTRAN", Report FGAN-FfO 1981/78.
- [8] Standardization Agreement STANAG 4347, NATO Military Agency for Standardization (MAS).
- [9] Höhn, D.H. (Ed.): "Jahresbericht FGAN-FfO 1990", (Annual) Report FGAN-FfO 1990/128.
- [10] Clement, D., W. Jessen: "A Background Model in the Thermal Infrared: Status, Validation, and Applications", Report FGAN-FfO 1993/41.
- [11] Dimmeler, A., D. Clement, R. Strobel, Y. Bushlin: "Background Properties in Arid Climates: Measurements and Analysis", Vortrag und Publ.: SPIE Symposium Aerospace/Defense Sensing and Controls, Orlando, FL, USA, 21.-25.04.97.
- [12] Dimmeler, A., D. Clement: "Results of Background Measurements Negev/Israel 1996", Treffen GE/IL MoA on CCD, EORD, Haifa, IL, 27.07.97, Report FGAN-FfO 1997/63.

## REPORT DOCUMENTATION PAGE

<b>1. Recipient's Reference</b>	<b>2. Originator's References</b> RTO-MP-1 AC/323(SET)TP/2	<b>3. Further Reference</b> ISBN 92-837-0001-5	<b>4. Security Classification of Document</b> UNCLASSIFIED/ UNLIMITED																						
<b>5. Originator</b> Research and Technology Organization North Atlantic Treaty Organization BP 25, 7 rue Ancelle, F-92201 Neuilly-sur-Seine Cedex, France																									
<b>6. Title</b> E-O Propagation, Signature and System Performance Under Adverse Meteorological Conditions Considering Out-of-Area Operations																									
<b>7. Presented at/sponsored by</b> The Sensors & Electronics Technology Panel Symposium held at the Italian Air Force Academy, Naples, Italy, 16-19 March 1998.																									
<b>8. Author(s)/Editor(s)</b> Multiple			<b>9. Date</b> September 1998																						
<b>10. Author's/Editor's Address</b> Multiple			<b>11. Pages</b> 352																						
<b>12. Distribution Statement</b> There are no restrictions on the distribution of this document. Information about the availability of this and other RTO unclassified publications is given on the back cover.																									
<b>13. Keywords/Descriptors</b> <table border="0"><tr><td>Electrooptics</td><td>Weather</td></tr><tr><td>Atmospheric studies</td><td>Reconnaissance</td></tr><tr><td>Mathematical models</td><td>Remote sensing</td></tr><tr><td>Optical detection</td><td>Battlefields</td></tr><tr><td>Meteorological data</td><td>Contamination</td></tr><tr><td>Target acquisition</td><td>Surveillance</td></tr><tr><td>Electromagnetic wave transmission</td><td>Signatures</td></tr><tr><td>Aerosols</td><td>Weapons systems</td></tr><tr><td>Coasts</td><td>Performance</td></tr><tr><td>Environments</td><td>Military operations</td></tr><tr><td>Models</td><td></td></tr></table>				Electrooptics	Weather	Atmospheric studies	Reconnaissance	Mathematical models	Remote sensing	Optical detection	Battlefields	Meteorological data	Contamination	Target acquisition	Surveillance	Electromagnetic wave transmission	Signatures	Aerosols	Weapons systems	Coasts	Performance	Environments	Military operations	Models	
Electrooptics	Weather																								
Atmospheric studies	Reconnaissance																								
Mathematical models	Remote sensing																								
Optical detection	Battlefields																								
Meteorological data	Contamination																								
Target acquisition	Surveillance																								
Electromagnetic wave transmission	Signatures																								
Aerosols	Weapons systems																								
Coasts	Performance																								
Environments	Military operations																								
Models																									
<b>14. Abstract</b> <p>This publication contains the papers presented at a specialists' meeting sponsored by the Sensors and Electronics Technology Panel of the RTO.</p> <p>The topics covered included:</p> <ul style="list-style-type: none"><li>• Theoretical and practical aspects of atmospheric propagation under adverse conditions</li><li>• Out-of-area operations, variations in weather conditions and propagation phenomena</li><li>• System optimisation techniques for out-of-area applications</li><li>• Modelling techniques</li><li>• Measurement programmes, including existing collaborations</li><li>• Applications of dual use technologies for adverse conditions (military/commercial).</li></ul>																									



## RESEARCH AND TECHNOLOGY ORGANIZATION

BP 25 • 7 RUE ANCELLE

F-92201 NEUILLY-SUR-SEINE CEDEX • FRANCE

Télécopie 0(1)55.61.22.99 • Téléc 610 176

## DIFFUSION DES PUBLICATIONS

RTO NON CLASSIFIEES

L'Organisation pour la recherche et la technologie de l'OTAN (RTO), détient un stock limité de certaines de ses publications récentes, ainsi que de celles de l'ancien AGARD (Groupe consultatif pour la recherche et les réalisations aérospatiales de l'OTAN). Celles-ci pourront éventuellement être obtenues sous forme de copie papier. Pour de plus amples renseignements concernant l'achat de ces ouvrages, adressez-vous par lettre ou par télécopie à l'adresse indiquée ci-dessus. Veuillez ne pas téléphoner.

Des exemplaires supplémentaires peuvent parfois être obtenus auprès des centres nationaux de distribution indiqués ci-dessous. Si vous souhaitez recevoir toutes les publications de la RTO, ou simplement celles qui concernent certains Panels, vous pouvez demander d'être inclus sur la liste d'envoi de l'un de ces centres.

Les publications de la RTO et de l'AGARD sont en vente auprès des agences de vente indiquées ci-dessous, sous forme de photocopie ou de microfiche. Certains originaux peuvent également être obtenus auprès de CASI.

## CENTRES DE DIFFUSION NATIONAUX

## ALLEMAGNE

Fachinformationszentrum Karlsruhe  
D-76344 Eggenstein-Leopoldshafen 2

## BELGIQUE

Coordinateur RTO - VSL/RTO  
Etat-Major de la Force Aérienne  
Quartier Reine Elisabeth  
Rue d'Evere, B-1140 Bruxelles

## CANADA

Directeur - Gestion de l'information  
(Recherche et développement) - DRDGI 3  
Ministère de la Défense nationale  
Ottawa, Ontario K1A 0K2

## DANEMARK

Danish Defence Research Establishment  
Ryvangs Allé 1  
P.O. Box 2715  
DK-2100 Copenhagen Ø

## ESPAGNE

INTA (RTO/AGARD Publications)  
Carretera de Torrejón a Ajalvir, Pk.4  
28850 Torrejón de Ardoz - Madrid

## ETATS-UNIS

NASA Center for AeroSpace Information (CASI)  
Parkway Center, 7121 Standard Drive  
Hanover, MD 21076

## FRANCE

O.N.E.R.A. (Direction)  
29, Avenue de la Division Leclerc  
92322 Châtillon Cedex

## GRECE

Hellenic Air Force  
Air War College  
Scientific and Technical Library  
Dekelia Air Force Base  
Dekelia, Athens TGA 1010

## ISLANDE

Director of Aviation  
c/o Flugrad  
Reykjavik

## ITALIE

Aeronautica Militare  
Ufficio Stralcio RTO/AGARD  
Aeroporto Pratica di Mare  
00040 Pomezia (Roma)

## LUXEMBOURG

Voir Belgique

## NORVEGE

Norwegian Defence Research Establishment  
Attn: Biblioteket  
P.O. Box 25  
N-2007 Kjeller

## PAYS-BAS

RTO Coordination Office  
National Aerospace Laboratory NLR  
P.O. Box 90502  
1006 BM Amsterdam

## PORTUGAL

Estado Maior da Força Aérea  
SDFA - Centro de Documentação  
Alfragide  
P-2720 Amadora

## ROYAUME-UNI

Defence Research Information Centre  
Kentigern House  
65 Brown Street  
Glasgow G2 8EX

## TURQUIE

Millî Savunma Başkanlığı (MSB)  
ARGE Dairesi Başkanlığı (MSB)  
06650 Bakanlıklar - Ankara

## AGENCES DE VENTE

## NASA Center for AeroSpace Information (CASI)

Parkway Center  
7121 Standard Drive  
Hanover, MD 21076  
Etats-Unis

## The British Library Document Supply Centre

Boston Spa, Wetherby  
West Yorkshire LS23 7BQ  
Royaume-Uni

## Canada Institute for Scientific and Technical Information (CISTI)

National Research Council  
Document Delivery,  
Montreal Road, Building M-55  
Ottawa K1A 0S2  
Canada

Les demandes de documents RTO ou AGARD doivent comporter la dénomination "RTO" ou "AGARD" selon le cas, suivie du numéro de série (par exemple AGARD-AG-315). Des informations analogues, telles que le titre et la date de publication sont souhaitables. Des références bibliographiques complètes ainsi que des résumés des publications RTO et AGARD figurent dans les journaux suivants:

## Scientific and Technical Aerospace Reports (STAR)

STAR peut être consulté en ligne au localisateur de ressources uniformes (URL) suivant:

<http://www.sti.nasa.gov/Pubs/star/Star.html>

STAR est édité par CASI dans le cadre du programme NASA d'information scientifique et technique (STI)

STI Program Office, MS 157A

NASA Langley Research Center

Hampton, Virginia 23681-0001

Etats-Unis

## Government Reports Announcements &amp; Index (GRA&amp;I)

publié par le National Technical Information Service

Springfield

Virginia 2216

Etats-Unis

(accessible également en mode interactif dans la base de données bibliographiques en ligne du NTIS, et sur CD-ROM)



Imprimé par le Groupe Communication Canada Inc.

(membre de la Corporation St-Joseph)

45, boul. Sacré-Cœur, Hull (Québec), Canada K1A 0S7



## RESEARCH AND TECHNOLOGY ORGANIZATION

BP 25 • 7 RUE ANCELLE

F-92201 NEUILLY-SUR-SEINE CEDEX • FRANCE

Telefax 0(1)55.61.22.99 • Telex 610 176

## DISTRIBUTION OF UNCLASSIFIED

## RTO PUBLICATIONS

NATO's Research and Technology Organization (RTO) holds limited quantities of some of its recent publications and those of the former AGARD (Advisory Group for Aerospace Research & Development of NATO), and these may be available for purchase in hard copy form. For more information, write or send a telefax to the address given above. **Please do not telephone.**

Further copies are sometimes available from the National Distribution Centres listed below. If you wish to receive all RTO publications, or just those relating to one or more specific RTO Panels, they may be willing to include you (or your organisation) in their distribution.

RTO and AGARD publications may be purchased from the Sales Agencies listed below, in photocopy or microfiche form. Original copies of some publications may be available from CASI.

## NATIONAL DISTRIBUTION CENTRES

## BELGIUM

Coordonateur RTO - VSL/RTO  
Etat-Major de la Force Aérienne  
Quartier Reine Elisabeth  
Rue d'Evere, B-1140 Bruxelles

## CANADA

Director Research & Development  
Information Management - DRDIM 3  
Dept of National Defence  
Ottawa, Ontario K1A 0K2

## DENMARK

Danish Defence Research Establishment  
Ryvangs Allé 1  
P.O. Box 2715  
DK-2100 Copenhagen Ø

## FRANCE

O.N.E.R.A. (Direction)  
29 Avenue de la Division Leclerc  
92322 Châtillon Cedex

## GERMANY

Fachinformationszentrum Karlsruhe  
D-76344 Eggenstein-Leopoldshafen 2

## GREECE

Hellenic Air Force  
Air War College  
Scientific and Technical Library  
Dekelia Air Force Base  
Dekelia, Athens TGA 1010

## ICELAND

Director of Aviation  
c/o Flugrad  
Reykjavik

## ITALY

Aeronautica Militare  
Ufficio Stralcio RTO/AGARD  
Aeroporto Pratica di Mare  
00040 Pomezia (Roma)

## LUXEMBOURG

See Belgium

## NETHERLANDS

RTO Coordination Office  
National Aerospace Laboratory, NLR  
P.O. Box 90502  
1006 BM Amsterdam

## NORWAY

Norwegian Defence Research Establishment  
Attn: Biblioteket  
P.O. Box 25  
N-2007 Kjeller

## PORTUGAL

Estado Maior da Força Aérea  
SDFA - Centro de Documentação  
Alfragide  
P-2720 Amadora

## SPAIN

INTA (RTO/AGARD Publications)  
Carretera de Torrejón a Ajalvir, Pk.4  
28850 Torrejón de Ardoz - Madrid

## TURKEY

Millî Savunma Başkanlığı (MSB)  
ARGE Dairesi Başkanlığı (MSB)  
06650 Bakanlıklar - Ankara

## UNITED KINGDOM

Defence Research Information Centre  
Kentigern House  
65 Brown Street  
Glasgow G2 8EX

## UNITED STATES

NASA Center for AeroSpace Information (CASI)  
Parkway Center, 7121 Standard Drive  
Hanover, MD 21076

## SALES AGENCIES

## NASA Center for AeroSpace Information (CASI)

Parkway Center  
7121 Standard Drive  
Hanover, MD 21076  
United States

## The British Library Document Supply Centre

Boston Spa, Wetherby  
West Yorkshire LS23 7BQ  
United Kingdom

## Canada Institute for Scientific and Technical Information (CISTI)

National Research Council  
Document Delivery,  
Montreal Road, Building M-55  
Ottawa K1A 0S2  
Canada

Requests for RTO or AGARD documents should include the word 'RTO' or 'AGARD', as appropriate, followed by the serial number (for example AGARD-AG-315). Collateral information such as title and publication date is desirable. Full bibliographical references and abstracts of RTO and AGARD publications are given in the following journals:

## Scientific and Technical Aerospace Reports (STAR)

STAR is available on-line at the following uniform resource locator:

<http://www.sti.nasa.gov/Pubs/star/Star.html>

STAR is published by CASI for the NASA Scientific and Technical Information (STI) Program  
STI Program Office, MS 157A  
NASA Langley Research Center  
Hampton, Virginia 23681-0001  
United States

## Government Reports Announcements &amp; Index (GRA&amp;I)

published by the National Technical Information Service  
Springfield  
Virginia 22161  
United States  
(also available online in the NTIS Bibliographic Database or on CD-ROM)



Printed by Canada Communication Group Inc.

(A St. Joseph Corporation Company)

45 Sacré-Cœur Blvd., Hull (Québec), Canada K1A 0S7